International Association for Hydrogen Energy

International Journal of Hydrogen Energy

IHTEC 2018

3rd International HYDROGEN TECHNOLOGIES Congress

www.ihtec2018.org

PROCEEDINGS

EDITORS
Ibrahim DINCER
Adnan MIDILLI
Hilmi YURDAKUL
Kadir AYDIN

ISBN: 978-605-66381-5-2



March 15-18, 2018
Asia Beach Resort Hotel
Alanya, Turkey









3rd International HYDROGEN TECHNOLOGIES Congress

March 15-18, 2018
Asia Beach Resort Hotel
Alanya, Turkey

PROCEEDINGS

EDITORS

Ibrahim DINCER
Adnan MIDILLI
Hilmi YURDAKUL
Kadir AYDIN

ISBN: 978-605-66381-5-2

INDEX

Preface	5
Committees	6
Scientific Program	7
Keynote Speakers	24
Proceedings	28

PREFACE

It is important to emphasize the importance of organizing the Third International Hydrogen Technologies Congress (initially started as the National Hydrogen Technologies Congress) which is considered another milestone in Turkey's hydrogen energy activities under the leadership of the National Hydrogen Energy Association.

It is also important to note that the National Hydrogen Energy Association was able to secure one of the next organizations of the 24th World Hydrogen Energy Congress first time in 2022, in Istanbul, Turkey. We are proud of being the organizers for this global event.

Anyway, we have now successfully completed our third congress in the area of hydrogen technologies, after organizing the first one in Istanbul, the second one in Cukurova University in Adana, the third one in Alanya Alaaddin Keykubat University which aimed to bring researchers, scientists, engineers and practitioners, who were working in the subject matter area, to provide a forum to exchange ideas, disseminate new research developments and discuss latest advances, new directions and priorities for a carbon-free future with hydrogen. The IHTEC-2018 conference has brought together four keynote speakers and over 140 participants from over 15 countries for a period of four days in order to discuss, disseminate and network on various aspects of hydrogen production processes ranging from its performance analysis and fuel cells, transportation, distribution, security, strategies and policies and those applications, through the topics, like renewable hydrogen production and technologies, biological hydrogen production and technologies, hydrogen strategies and policies, modeling, energy and exergy analysis, etc.

It is a great pleasure to mention that there have been numerous leading researchers attended and networked to share the newest ideas and latest technologies and developments. In addition, the conference delegates have benefited from the exchange of ideas, problems and solutions with a large number of technical experts, especially through the multiple workshops organized.

Furthermore, it is important to note that numerous individuals have contributed in significant ways to organize this conference and the workshops which made us take this pleasure to register our sincere appreciations to Prof. Dr. T. N. Veziroglu who has been the leader and father of all these activities which are essentially critical for sustainable hydrogen economy, and the chairs of the workshops Prof. Dr. Hikmet Karakoc and Assoc. Prof. C. Ozgur Colpan.

Moreover, we take this opportunity to warmly thank all congress keynote speakers, session chairs, oral and poster presenters (and co-authors), and all attendees, whose contributions and efforts will make this conference a great success.

Last, but not least we sincerely acknowledge the assistance, support and coordination provided by the Bros Congress Team.

Ibrahim DINCER
Adnan MIDILLI
Hilmi YURDAKUL
Kadir AYDIN

COMMITTEES

Honarary chairs

Veziroglu, T.N. / *USA*

Pinarbasi, A. / *Rector / Alanya / Turkey*

General Chair

Dincer, I. / *Canada / Turkey*

Congress Chair

Yurdakul, H. / *Turkey*

Congress Co-Chair

Aydin K. / *Turkey*

Technical Chair

Midilli, A. / *Turkey*

Executive Committee

Dincer, I. / *HTA/Turkey*
Eroglu, I. / *HTA/Turkey*
Gunes, H. / *Turkey*
Karaosmanoglu, F. / *HTA/Turkey*
Kadirgan, F. / *HTA/Turkey*
Kargi, F. / *HTA/Turkey*
Kaval, Y. /*HTA/Turkey*
Midilli, A. /*HTA/Turkey*
Solmaz, R. / *HTA/Turkey*
Tuncer, G. / *HTA/Turkey*
Yazici, S. /*HTA/Turkey*

Organizing Committee

Acikara, T. / *Turkey*
Kalinci, Y. / *Turkey*
Akbulut, U. / *Turkey*
Kucuk, H. / *Turkey*
Colpan, C.O. / *Turkey*
Mert, S.O. / *Turkey*
Dulgerbaki, C. / *Turkey*
Sener, E. / *Turkey*
Unal, F.A. / *Turkey*
Yurdakul, A. / *Turkey*

International Scientific Board

Veziroglu, T.N. / *USA*
Avaca, L.A. / *Brazil*
Azbar, N. / *Turkey*
Barbir, F. / *USA*
Baykara, S. / *Turkey*
Bolcich, J.C. / *Argentina*
Chen, W.H. / *China*
Dincer, I. / *Canada*
Eroglu, I. / *Turkey*
Fowler, M. / *Canada*
Gadalla, M. / *UAE*
Goltsov, V.A. / *Ukraine*
Goswami, Y. / *USA*
Hamdullahpur, F. / *Canada*
Hepbasli, A. / *Turkey*
Kakac, S. / *Turkey*
Karakoc, H. / *Turkey*
Karaosmanoglu, F. / *Turkey*
Kargı, F. / *Turkey*
Kendall, K. / *UK*
Koca, A. / *Turkey*
Kumbur, E.C. / *USA*
Li, X. / *Canada*
Mench, M.M. / *USA*
Midilli, A. / *Turkey*
Min, Z. / *China*
Miranda, P.E. / *Brazil*
Muradov, N. / *USA*
Naterer, G.F. / *Canada*
Ozkar, S. / *Turkey*
Ozturk, T. / *Turkey*
Rosen, M.A. / *Canada*
Sahin, O. / *Turkey*
Sahin, S. / *Turkey*
Sattler, C. / *Germany*
Sheffield, J.W. / *USA*
Veziroglu, E.A. / *USA*
Veziroglu, A. / *USA*
Yildiz, İ. / *Canada*
Yurum, Y. / *Turkey*

SCIENTIFIC PROGRAM

SCIENTIFIC PROGRAM

March 15, 2018

HALL - A	
08:00-09:00	Registration
09:00-09:30	**Opening Talks** **Hilmi Yurdakul** *(Congress Chair)* **İbrahim Dincer** *(President, National Hydrogen Energy Association)* **Ahmet Pinarbasi** *(Rector, Alanya Alaeddin Keykubat University)*
09:30-10:15	**Overview Talk-** Ibrahim Dincer **Alternative Dimensions of Hydrogen Energy and Future Directions**
10:15-11:00	**Keynote Speaker -** Richard Baker **Substituted Ceria-Based Materials for Applications in Solid Oxide Fuel Cell Electrolytes and Electrodes** **Chair:** Ibrahim Dincer
11:00-11:15	**Coffee Break**
11:15-12:00	**Keynote Speaker -** Wei-Hsin Chen **Recent Development in Hydrogen Separation and Purification through Pd-based Membrane Systems** **Chair:** Richard Baker
12:00-13:30	**LUNCH**

HALL - A	
13:30-15:00	**Session 1A: Biological Hydrogen Production** **Chair: Filiz Karaosmanoglu**
13:30-13:45	**(004) Hydrogen Production by Agar-Immobilized R. Capsulatus in Panel Photobioreactor** Kamal Elkahlout, Emrah Sagir, Siamak Alipour, Harun Koku, Ufuk Gunduz, Inci Eroglu, Meral Yucel
13:45:14:00	**(0050) Effect of Operational Variables on Biological Hydrogen Production by Dark Fermentation from Palm Oil Mill Effluent Using Response Surface Methodology** Azam Akhbari
14:00-14:15	**(0053) Multi-Objective Evolutionary Polynomial Regression Technique in Prediction of Bio-Hydrogen Production by Dark Fermentation Process** Azam Akhbari, Shaliza Ibrahim, Mohsen Vafaeifard, Isa Ebtehaj, Milad Khosravi, Hossein Bonakdari
14:15-14:30	**(0157) HHO Enrichment of Bio-Diesohol Fuel Blends in a Single Cylinder Diesel Engine** Mustafa Kaan Baltacıoğlu, Raif Kenanoğlu, Kadir Aydın
14:30-14:45	**(0154) Investigation of Optimum Hydraulic Retention Time (HRT) of Semi-batch Photofermentation Process in a Three-stage System** Melih Can Akman, Tuba Hande Erguder, Ufuk Gunduz, Inci Eroglu
14:45-15:00	**(0072) Direct Current Assisted Dark Fermentative Hydrogen Gas Production from Acid Hydrolysed Waste Paper Towel** Gulizar Onaran, Hidayet Argun
15:00-15:30	**Coffee Break**

SCIENTIFIC PROGRAM

HALL - B	
13:30-17:30	**Workshop – Hikmet Karakoc**
	Opening Remarks
13:30-15:00	**Session-I** **Session Chair: Adnan Midilli** • Battery Technology Overview – **Fatih Mutluel, TUBITAK MAM** • Battery Thermal Management System (TMS) – **Cihad Furkan Salman, TUBITAK MAM** • Battery Module/Package Development – **Ahmet Yayli, TUBITAK MAM** • Battery Management System (BMS) – **Turev Sarikurt, TUBITAK MAM**
15:00-15:30	**Coffee Break**
15:30-17:00	**Session-II** **Session Chair: C. Ozgur Colpan** • Analysis and Selection of Effective Battery Management System Architectures for Safety – **Melih Yildiz (Atilim University), T. Hikmet Karakoc (Anadolu University)** • Electric Mobility and Li Ion Based BMS Adaptation in Bozankaya Buses – **Emrah Dal (Bozankaya), Dursun Cicek (Bozankaya)** • Electrification Options in Aviation Systems –**Nader Javani (Yildiz Tech. University)** • Maintainability and Safety Parameters for Battery Design –**Melih Yildiz (Atilim University), T. Hikmet Karakoc (Anadolu University)**

HALL - C	
13:30-15:00	**Session 1C: Renewable Hydrogen Production** **Chair: Hadi Ganjehsarabi**
13:30-13:45	**(0192) Integrating of PEM Electrolyzer for Hydrogen Production in a Kalina Cycle Driven by Low-Grade Geothermal Energy** Hadi Ganjehsarabi
13:45-14:00	**(0097) Performance of Ni Incorporated Silica and Alumina Based Catalysts in Hydrogen Production from Biomass** Birce Pekmezci Karaman, Nurbanu Çakiryilmaz, Huseyin Arbag, Nuray Oktar, Gülşen Dogu, Timur Dogu
14:00-14:15	**(0030) Investigation of a Solar Driven Integrated TEG with PEM Electrolyzer System for Hydrogen Production** Murat Emre Demir, Ibrahim Dincer
14:15-14:30	**(0060) Hydrogen Production from Water as Photoelectrochemical by using Solar Light Irradiation** Rana Muhammad Zunain Ayaz, Duygu Akyüz, Özlem Uğuz, Irem Tanışık, Cevat Sarıoğlu, Fatma Karaca Albayrak, Ali Rıza Özkaya, Atıf Koca
14:30-14:45	**(0202) A Parametric Study on Exergetic Performance of Hydropower Integrated Hydrogen Production: A Case Study for East Black-Sea Region of Turkey** Adnan Midilli and Mert Ozsaban
15:00-15:30	**Coffee Break**

SCIENTIFIC PROGRAM

HALL - A	
15:30-17:15	**Session 2A: Pyrolysis, Gasification and Plasma Hydrogen production** **Chair: Inci Eroglu**
15:30-15:45	**(0027) In–situ and Downstream Desulfurization Ability of PbO and ZnO During Pyrolysis and Hydrogenation of a High–sulfur Lignite** Arzu Kanca, Deniz Uner
15:45-16:00	**(0089) Ni Catalyzed Methane Pyrolysis for H2 Generation under Concentrated Solar Irradiation** Celal Guvenç Ogulgonen, Atalay Çalışan, Deniz Uner, Serkan Kıncal
16:00-16:15	**(0068) Energy and Exergy Analyses of an Integrated Solar and Coal Gasification Combined Cycle for Hydrogen and Ammonia Production** Ahmed Hasan, Ibrahim Dincer
16:15-16:30	**(0098) Gasification of Sewage Sludge Enriched with Virginia Mallow for Higher Hydrogen Content in Syngas** Anna Poskart, Monika Zajemska, Stanisław Szwaja
16:30-16:45	**(0021) The Effects of Equivalence Ratio on a Downdraft Plasma Coal Gasifier** Zeki Yilmazoglu, Beycan Ibrahimoglu, Onurhan Gokalp
16:45-17:00	**(0155) Electrochemical Characterization of Carbon-Supported Bimetalic Pd-Zn Nanoparticles as Anode Catalyst for Direct Borohydride Fuel Cells** Ramiz Gultekin Akay, Merve Dogan Ozcan, Cenk Celik, Ayse Nilgün Akın
17:00-17:15	**(0222) Biohydrogen Production From Fruit And Vegetable Wastes Through Dark Dry Anaerobic Fermentation Under Thermophilic Condition** Haris Nalakath Abubackar, Okyanus Yazgın, Bensu Gunay, Kubra Arslan, Tugba Keskin Gundogdu, Nuri Azbar
17:15-17:30	**Coffee Break**

SCIENTIFIC PROGRAM

HALL - C	
15:30-17:15	**Session 2C: Hydrogen Fuel Cells** **Chair: Mehmet Suha Yazici**
15:30-15:45	**(0014) Microwave Assisted Synthesis of Pt/MWCNT Catalyst for High Temperature PEM Fuel Cell** Elif Damla Arica, Yılser Devrim
15:45-16:00	**(0085) Performance of CVD Graphene Supported PtxCoy Electrocatalysts for PEM Fuel Cell** Fatma Gül Boyacı San, Mehmet Suha Yazıcı
16:00-16:15	**(0005) A Field Application of a Fuel Cell Microcogeneration Unit** Cigdem Iyigün Karadag, Atilla Ersöz, Fatma Gül Boyacı San, Betül Erdör Türk, Emin Okumuş, Murat Kılıç, Egemen Akar, Nilüfer Topuz, Salih Obut, Özgür Can Korkmaz, Derya Aydemir
16:15-16:30	**(0153) A Labview-FPGA Based Process Control and Power Conditioning Prototype Application of a Fuel Cell Powered Range Extender for Unmanned Aerial Vehicles** Betul Erdor Turk, Mustafa Hadi Sarul
16:30-16:45	**(0174) System Design and Optimization of a Hydrogen Fuel Cell Vehicle in the Different Road Models** Yakup Hames, Kemal Kaya
16:45-17:00	**(0016) Development of Effective Cooling System for High Temperature PEM Fuel Cell** Yilser Devrim, Kubra Pehlivanoglu, Omer Erdemir, Celal Yılmaz, Huseyin Devrim
17:00-17:15	**(0181) The Impact of Boron Nitride Nanoparticles on Hydrogen Uptake Capacity over MWCNTs** Songul Kaskun, Muhammet Kayfeci
17:15-17:30	**Coffee Break**

SCIENTIFIC PROGRAM

17:45-18:30	POSTER Session 1 Chair: Ugur Akbulut
0055	Modeling of Syngas Production from Biogas via Tri-reforming Process Reiyu Chein, Wen Hwai Hsu
0058	Active Photocatalysts Designed by Sulphurization Method for Hydrogen Production Irem Tanışık, Duygu Akyüz, Rana Muhammad Zunain Ayaz, Özlem Uğuz, Cevat Sarıoğlu, Fatma Karaca Albayrak, Ali Rıza Özkaya, Atıf Koca
0093	Comparison of LFS of H2, CH4 at Elevated Temperatures Karol Grab Rogalinski, Stanislaw Szwaja, Michal Pyrc, Michal Gruca
0095	A Low Cost, Continuous H2-CH4 Sensor Assembly Celal Güvenç Oğulgönen, Atalay Çalışan, Deniz Üner, Serkan Kıncal
0099	Optimization of hydrogen release from anaerobic thermal processing of Virginia Mallow Anna Poskart, Monika Zajemska, Stanisław Szwaja, Aneta Magdziarz, Dorota Musiał
0103	Influence of Hydrogen Addition to Diesel Fuel on Smoke and Combustion Phases in a Compression Ignition Engine Stanislaw Szwaja, Romualdas Juknelevicius, Michal Gruca, Michal Pyrc
0105	A Comparative Thermodynamic Analysis of Alternatively Proposed Different Fuel System Models using Jet A Fuel Muhammet Yilanli, Önder Altuntaş, Emin Açıkalp
0107	The Effect of Support Material on the Hydrogen Adsorption-Desorption Characteristics of Ru/SiO2 and Ru/Vulcan Catalysts Mustafa Yasin Aslan, Deniz Üner
0110	Metal-Organic Frameworks as Hydrogen Evolution Catalysts Selçuk Demir, Emine Ülker
0112	Empirical Models for the Energy Consumption of Oil-in- Water Emulsion Treatment by Electro-coagulation Process Mohamed Tir
0115	Management of Hybrid System Operating in Grid–connected and Standalone Mode Houria Boumaaraf, Billel Boumaaraf, Abdelaziz Talha, Omar Bouhali
0117	Power Generation System Control of a Hybrid Renewable System PVT-diesel with Storage Billel Boumaaraf, Houria Boumaaraf, Abdelaziz Talha, Mohamed Salah Ait Cheikh
0119	The Relationship Between Fuel Flow Rate and Pressure Drop in a Direct Methanol Fuel Cell with Parallel Channels Anil Can Turkmen, Didem Demirtas, Hatice Esen, Cenk Celik
0122	Hydrogen Permeation Characteristics Through Palladium Membrane with/without Vacuume Shang Wei Lin, Wei Hsin Chen
0069	Heat Transfer and Pressure Drop Characteristics of Different Structured Micro-Pin-Fin Reactors Evren Yilmaz Yakin, Sinan Eren Yalcin, Tahir Hikmet Karakoc
0190	The Role of Temperature on Aluminium Oxide Embedded MWCNTs for Hydrogen Adsorption Songül Kaskun, Muhammet Kayfeci

SCIENTIFIC PROGRAM

March 16, 2018

HALL - A	
09:30-10:15	**Keynote Speaker: Bruno G. Pollet** **Current Status of Hydrogen and Fuel Cells in Norway** **Chair: Richard Baker**
10:15-10:30	**Coffee Break**
10:30-12:00	**Session 3A: Thermodynamic Analysis of Hydrogen Technologies** **Chair: Güngör Tuncer**
10:30-10:45	**(0044) Thermodynamic and Economic Analyses of a Renewable Energy Based Hydrogen Production System** Fatih Sorgulu, Ibrahim Dincer
10:45-11:00	**(0047) Thermodynamic Performance Assessment of Integrated Solar Energy System with Hydrogen Production** Fatih Yilmaz, Murat Ozturk, Resat Selbas
11:15-11:30	**(0064) Geothermal and Solar Driven Multigeneration System for Sustainable Buildings: A Thermodynamic Analysis** Tahir Abdul Hussain Ratlamwala, Hamed Alimoradiyan
11:30-11:45	**(0184) Thermodynamic Analysis of a New Solar Power Tower Based Integrated System for Hydrogen Production and Liquefaction** Yunus Emre Yuksel, Murat Ozturk, Ibrahim Dincer
11:45-12:00	**(0221) Thermodynamic Analysis of a Unique Integrated Photoelectrochemical System for Multigeneration Purposes** Canan Acar, Ibrahim Dincer
12:00-13:30	**LUNCH**

HALL - B	
10:30-12:00	**Session 1B: Exergy Analysis of Hydrogen Energy Systems** **Chair: Hikmet Karakoc**
10:30-10:45	**(0096) Diagnosis and Improvement of Hydrogen Demand/Supply Processes using Combined Pinch and Exergy Analysis** Fatma Alyer, Zehra Özçelik
10:45-11:00	**(0023) Optimum Energy and Life Cycle Cost Evalautaion of an Advanced Hydrogen Liquefaction Cycle Using Geothermal Power** Ceyhun Yılmaz
11:00-11:15	**(0065) Energy and Exergy Analyses of a Novel Ammonia Combined Power Plant Operating with a Gas Turbine and a Solid Oxide Fuel Cell** Muhammad Ezzat, Ibrahim Dincer
11:15-11:30	**(0079) A Parametric Study of the Performance of a Polymer Electrolyte Membrane Electrolyzer: Energy and Exergy Analyses** Ehsan Baniasadi, Ebrahim Afshari, Faeze Moradi Nafchi, Nader Javani
11:30-11:45	**(0041) Exergoeconomic Analysis and Optimization of a Concentrated Sunlight-based Integrated Photoelectrochemical Hydrogen and Ammonia Production System** Yusuf Bicer, Ibrahim Dincer
12:00-13:30	**LUNCH**

SCIENTIFIC PROGRAM

HALL - C	
10:30-12:00	**Session 3C: Hydrogen Fuel Combustion** **Chair: Stanislaw Szwaja**
10:30-10:45	**(0092) Analysis of the Turbocharged Internal Combustion Engine with Over-expanded Cycle Fueled with CNG and Hydrogen** Karol Grab Rogalinski, Stanislaw Szwaja
10:45-11:00	**(0102) Dilution of Fresh Charge for Reducing Combustion Knock in the Internal Combustion Engine Fuelled with Hydrogen Rich Gases** Stanislaw Szwaja
11:00-11:15	**(0147) Simulation of a Novel Alternative Fueled Hybrid Electric Vehicle (AF-HEV) with Hydrogen Enriched Internal Combustion Engine** Hüseyin Turan Arat
11:15-11:30	**(0196) A Numerical Study of Mild Flameless Combustion of Methane/hydrogen Mixtures in a Furnace** Mehmet Salih Cellek
11:30-11:45	**(0150) Colloidal Synthesis and Characterization of CuInS2 Nanoparticle for Solar Hydrogen Production** Cigdem Tuc Altaf, Nurdan Demirci Sankır
11:45-12:00	**(0131) Catalytic and Non-Catalytic Hydrogen Generation from Chemical Hydrides** Mehmet Sankir, Nazrin Abdullayeva
12:00-13:30	**LUNCH**

HALL - A	
13:30-15:00	**Session 4A: Borohydride Fuel Cells** **Chair: Ramazan Solmaz**
13:30-13:45	**(0215) Langmuir–Hinshelwood Kinetic Model to Capture the Manganese(0) Nanoparticles Supported on Ceria-catalyzed Hydrolysis of Sodium Borohydride** Sibel Duman, Saim Özkar
13:45-14:00	**(0148) Preparation And Characterization of Polyvinyl Alcohol/Chitosan Blended Anion Exchange Membranes for Direct Borohydride Fuel Cells** Tuncay Kadıoglu, Ramiz Gultekin Akay, Kursat Can Ata, Cenk Celik
14:00-14:15	**(0151) Novel Pd-Co/C Bimetallic Alloy Electrocatalyst for Direct Borohydride Fuel Cell Anode** Cem Gozlu, Cenk Celik, Ayse Nilgun Akın, Ramiz Gultekin Akay
14:15-14:30	**(0152) A Comparative Study on the Determination of Borohydride Permeability of Cation Exchange Membranes for DBFC** Kursat Can Ata, Tuncay Kadıoglu, Ramiz Gultekin Akay, Cenk Celik
14:30-14:45	**(0241) Effect of Inlet Air Temperature on Exergetic Performance of Hydrogen Production from Car Tires via Plasma Gasification** Handan Demirçay, Merve Mehan, Muhammed Emin Topal, Yildiz Kalinci, Senol Bayraktar, Ugur Akbulut, Haydar Kucuk, Hayati Olgun, Adnan Midilli, Ibrahim Dincer
15:00-15:30	**Coffee Break**

SCIENTIFIC PROGRAM

HALL - B	
13:30-18:20	**Workshop – C. Ozgur Colpan**
	Session Chair: İnci Eroğlu
13:30-13:35	Welcoming Remarks / **C. Özgür Çolpan**
13:35-13:55	Overview of Hydrogen and Fuel Cell Related Research at CERL in UOIT / **Ibrahim Dincer**
13:55-14:15	The Development and Production of Fuel Cell from TEKSIS's Point of View / **Hüseyin Devrim**
14:15-14:35	PEM Type Fuel Cell Research at TOBB ETU / **Mehmet Sankır**
14:35-14:55	Advances in the Fuel Cell Research in Dokuz Eylul University / **C. Özgür Çolpan**
14:55-15:15	Hydrogen & Fuel Cell Research in Atılım University / **Yılser Devrim**
15:15-15:35	Advances in the Fuel Cell Research in Sen Research Group (SRG), Dumlupinar University / **Fatih Şen**
15:35-16:00	**Coffee Break**
	Session Chair: T. Hikmet Karakoç
16:00-16:20	Fuel Cell Research in Atatürk University / **Ayşe Bayrakçeken Yurtcan**
16:20-16:40	Hydrogen & Fuel Cell Research and Demonstration Activities at MAM Energy Institute / **Suha Yazıcı**
16:40-17:00	Studies on the Development of Directly Fed Fuel Cell Catalysts at Van YYU / **Hilal Demir Kıvrak**
17:00-17:20	PEMFC Studies in Recep Tayyip Erdogan University / **Adnan Midilli**
17:20-17:40	Advances in the Fuel Cell Research in Çukurova University **Ebru Erünal**
17:40-18:00	Direct Borohydride Fuel Cell Studies in Kocaeli University **Cenk Çelik and R. Gültekin Akay**
18:00-18:20	Research and Development of Microbial Fuel Cell Technology at Yildiz Technical University / **Bestami Özkaya**

SCIENTIFIC PROGRAM

HALL - C	
13:30-15:00	**Session 4C: Material Applications for Hydrogen Energy Technologies** **Chair: Emmanuel Iheanyichukwu Iwuoha**
13:30-13:45	**(0091) Wireless High-Speed Continuous Sensing of Hydrogen Leak by a Quadrotor Drone** Kazuo Matsuura, Masahiro Inoue, Yuta Segawa, Takaya Kimura
13:45-14:00	**(0216) Green Dehydrogenation of Dimethylamine Borane Catalyzed by Nickel(0) and Copper (0) Nanoparticles** Hakan Demir, Ali Ozdemİr, Sibel Duman
14:00-14:15	**(0229) Graphene Oxide/Metal Organic Framework Nanocomposite with Improved Electrocatalytic Activity for Hydrogen Evolution Reaction** Emmanuel Iheanyichukwu Iwuoha, Mogwasha Daphney Makhafola, Kabelo Edmond Ramohlola, Thabang Ronny Somo, Gobeng Release Monama, Mpitloane Joseph Hato, Kerileng Midred Molapo, Kwena Desmond Modibane
14:15-14:30	**(0228) Copper(II) Phthalocyanine/Metal Organic Frameworks (Cupc/MOF) Composite with Improved Electrocatalytic Efficiency for Hydrogen Production** Emmanuel Iheanyichukwu Iwuoha, Gobeng Release Monama, Kwena Desmond Modibane, Kabelo Edmond Ramohlola, Kerileng Mildred Molapo, Mpitloane Joseph Hato, Mogwasha Daphney Makhafola, Gloria Mashao Mashao Mashao, Siyabonga Beizel Mdluli
14:30-14:45	**(0218) Highly Effective PVP-stabilized Rh-Ru Bimetallic Nanoparticles for the Dehydrogenation of Methylamine-borane in Water** Mehmet Gulcan, Yaşar Karatas
14:45-15:00	**(0128) Investigation of Hydrogen Fuel Usage Affects On Exergetic and Exergeeconomic Performances of a Turbojet Engine** Ozgur Balli, Yasin Şöhret, T. Hikmet Karakoc
15:00-15:30	**Coffee Break**

SCIENTIFIC PROGRAM

HALL - A	
15:30-17:00	**Session 5A: Modelling and Analysis of Hydrogen Energy Technologies** **Chair: Canan Acar**
15:30-15:45	**(0070) Kinetic and Electrochemical Analyses of a CuCl/HCl Electrolyzer** Reza Soltani, Ibrahim Dincer, Marc A. Rosen
15:45-16:00	**(0119) The Relationship Between Fuel Flow Rate and Pressure Drop in a Direct Methanol Fuel Cell with Parallel Channels** Anil Can Turkmen, Didem Demirtas, Hatice Esen, Cenk Celik
16:00-16:15	**(0088) Exergetic and Sustainability Analyses of Ammonia Usage in a Gas Turbine** Suleyman Kagan Ayaz, Onder Altuntas
16:15-16:30	**(0188) Thrust Modelling for a Solid Oxide Fuel Cell and Gas Turbine (SOFC/GT) Hybrid Propulsion System** Yasin Sohret, Arif Hepbasli, T. Hikmet Karakoc
16:30-16:45	**(0124) Exergetic Comparison of Various Flow Patterns in PEMFCs** Suha Orcun Mert, Muhammed Mucahit Toprak
17:00-17:15	**Coffee Break**

HALL - C	
15:30-17:00	**Session 5C: Hydrogen Production-1** **Chair: Figen Kadırgan**
15:30-15:45	**(0028) Maturity Impact on Hydrogen Production from Natural Gas and Coal: Examples from Dadaş Shale and Zonguldak Coals** Samil Sen, Huseyin Kozlu, Ilyas Erdal Kerey, Gungor Celik
15:45-16:00	**(0031) Investigation of Hydrogen Production through Thermochemical Cycles** Fatih Yilmaz, Resat Selbas, Murat Oztruk
16:00-16:15	**(0062) Photoelectrochemical Hydrogen Production Using cd(1-x)znxs and Its Modifications with Graphene Derivatives** Ozlem Uguz, Duygu Akyuz, Rana Muhammad Zunain Ayaz, Irem Tanısık, Cevat Sarıoglu, Fatma Karaca Albayrak, Ali Rıza Ozkaya, Atıf Koca
16:15-16:30	**(0073) Hydrogen Production from Melon and Watermelon Mixture by Dark Fermentation** Savas Turhal, Mansurali Turanbaev, Hidayet Argun
16:30-16:45	**(0166) Photocatalytic Hydrogen Production with Metal Oxide Bulk Structures** Gizem Yanalak, Abdalaziz Aljabour, Emre Aslan, Faruk Ozel, Imren Hatay Patir
16:45-17:00	**(0211) Hydrogen Gas Production from Wastewater by Electro-hydrolysis** Serkan Eker, Fikret Kargi
17:00-17:15	**Coffee Break**

SCIENTIFIC PROGRAM

17:00-18:00	POSTER Session 2 Chair: Suha Orcun Mert
0145	Ordered Mesoporous Carbons (OMC) Synthesized by Self-assembly Method and the Effects of Acidity and Carbon Source to Surfactant Ratio Silver Güneş, Fatma Çiğdem Güldür
0159	Bio-ethanol Reforming for Hydrogen and Methane Production Yuji Ando
0168	Electricity Generation and Wastewater Treatment with Microbial Fuel Cells Using Homemade Beer Wastewater Ömer Faruk Coşkun, Kürşat Can Ata, Ramiz Gültekin Akay
0182	Synthesis of Active and Reusable Nano Catalyst from Graphene Oxide (GO) Stabilized Pt-Ir Nanoclusters for DMAB Dehydrogenation Reaction at Room Temperature Fatih Sen, Esra Kuyuldar, Betül Sen
0183	Synthesis of Highly Active Pt-Rh Nanoclusters Stabilized on Graphene Oxide for Hydrogen Evolution Reaction Fatih Sen, Esra Kuyuldar, Betül Sen
0187	Energy and Exergy Analyses of an Integrated Hydrogen Production and Liquefaction System with Waste Material Gasification Yunus Emre Yüksel, Murat Öztürk, Ibrahim Dinçer
0191	A Comparative Study of Control Strategies for Vehicles with Hydrogen Fuel Cell/Battery/ Supercapacitor in the Electrical Grid-Independent Applications Yakup Hameş, Kemal Kaya
0200	Wood Char - Active Carbon Production for H2 Adsorption and Storage Yıldırım Tosun
0209	Biohydrogen Upgrading Towards a Cleaner Energy Production Emre Oguz Koroglu, Bestami Ozkaya, Ahmet Demir
0217	Hydrogen Generation from the Hydrolysis of Dimethylamine-borane at Room Conditions by Using Polyvidone Protected Ruthenium Nanocatalyst Mehmet Gülcan, Yaşar Karataş
0224	Optimization of Thermal Pre-treatment Conditions By Box-Wilson Method For Dark Fermentative Biohydrogen Production From Fruit and Vegetable Wastes Bensu Günay, Okyanus Yazgın, Kubra Arslan, Haris Nalakath, Tugba Keskin, Nuri Azbar
0225	Analysis of Biohydrogen Production via Dry Anaerobic Digestion of Fruit and Vegetable Waste Okyanus Yazgın, Bensu Günay, Haris Nalakath Abubackar, Tuğba Keskin Gündoğdu, Nuri Azbar
0230	Phase Transition and Photoelectrochemical Properties of Copper Oxide Photoelectrodes Fabricated by Electrodeposition İbrahim Y Erdoğan, Meral Balık, Veysel Bulut
0231	Enhanced Photoelectrocatalytic Performance of ZnO/Cu2O Photoelectrodes İbrahim Y Erdoğan, Ako Mahmood Qadir
0239	The Investigation of Three-dimensional Copper Nanodomes as Anode Materials for Direct Methanol Fuel Cells Fatih Baştürk, Handan Yüksel, Ramazan Solmaz
0240	Pt, Pd and Ag Modified NiCuZn Raney Electrodes for Alkaline Water Electrolysis Ramazan Solmaz, Ayşe Ongun Yüce, Ali Döner, Ibrahim Şahin, Gülfeza Kardaş
0104	Energy and Exergy Analysis of 1 kW Self-humidified PEM Fuel Cell Tayfun Özgür, Ali Cem Yakaryılmaz, Erdi Tosun, Mustafa Atakan Akar, Mustafa Özcanlı
0244	Mg60Ni40 Alloy Synthesis and Investigation of Hydrogen Storage Properties Gözde Bayazıt, Sefa Emre Sünbül, Sultan Öztürk, Kürşat Icin, Şadan Özcan

SCIENTIFIC PROGRAM

March 17, 2018

HALL - A	
09:00-10:30	**Session 6A: Hydrogen Energy Applications-1** **Chair: Can Ozgur Colpan**
09:00-09:15	**(0007) H_2 Adsorption on Cu(I)-ZSM-5: Exploration of Cu(I)-exchange in Solution** Ismihan Altıparmak, Busra Karakaya, Bahar Ipek
09:15-09:30	**(0082) Coke Minimization over Mesoporous Alumina Supported Ni Catalyst in Dry Reforming of Methane** Huseyin Arbag
09:30-09:45	**(0212) Electrohydrolysis Application on Metal Plating Wastewater to Produce Hydrogen Gas** Ebru Çokay, Yasin Gürler
09:45-10:00	**(0040) Bimetallic Particles for Ethanol Electro-oxidation** Hilal Demir Kivrak, Ebru Ozkan, Burak Yapıcı, Sumeyye Dogan, Shekiba Muhammady, Ozlem Sahin
10:00-10:15	**(0134) Synthesis and Characterization of Electrocatalyst with Graphene and Multi-Walled Carbon Nanotube Support Material** Guvenc Umur Alpaydin, Elif Damla Arica, Yilser Devrim, Can Ozgur Colpan
10:15-10:30	**(0108) SnS Photo-electrodes Produced by Sulfurization of Electrodeposited Sn Films for Photo-electrochemical Water Splitting** Sercan Soyoz, Bulut Sahin, Selim Demirci, Cevat Sarıoglu
10:30-10:45	**Coffee Break**

HALL - B	
09:00-10:30	**Session 2B: Hydrogen Evolution** **Chair: Kazuro Matsuura**
09:00-09:15	**(0057) The Effect of Co-catalyst and Novel Heterogeneous Active Photocatalysts for Hydrogen Evolution under Solar Energy** Duygu Akyuz, Ozlem Uguz, Irem Tanısık, Rana Muhammad Zunain Ayaz, Cevat Sarıoglu, Fatma Karaca Albayrak, Ali Rıza Ozkaya, Atıf Koca
09:15-09:30	**(0094) Water Splitting through the Pb/PbO Cycle** Atalay Calısan, Celal Guvenc Ogulgonen, Deniz Uner, Serkan Kıncal
09:30-09:45	**(0037) Comparison of Alcohol Electro-oxidation in Alkaline Medium** Ozlem Sahin, Ebru Ozkan, Hilal Demir Kivrak
09:45-10:00	**(0109) Zirconium Metal-Organic Framework Platform as a Heterogeneous Catalysts for Electrochemical Hydrogen Evolution** Emine Ulker, Selcuk Demir
10:00-10:15	**(0170) Hydrogen Evolution at the Water/DCE Interface Catalyzed by Cu2WS4** Faruk Ozel, Emre Aslan, Adem Sarilmaz, Imren Hatay Patir
10:15-10:30	**(0171) The Hydrogen Evolution Reaction Catalyzed by Metal Oxide and Metal Sulfide Catalysts at Soft Interfaces** Emre Aslan, Gizem Yanalak, Imren Hatay Patir
10:30-10:45	**Coffee Break**

SCIENTIFIC PROGRAM

HALL - C	
09:00-10:30	**Session 6C: Hydrogen Energy and Technologies-1** **Chair: Tanay Sıdkı Uyar**
09:00-09:15	**(0038) Electrocatalytic Performance of Pd Based Bimetallic Catalysts for Methanol Oxidation Reaction** Özlem Şahin, Ebru Özkan, Rabia Esra Takır,Abdullah Nadeesh, Hilal Demir Kıvrak
09:15-09:30	**(0039) Structure Sensitivity of Direct Alcohol Electro-oxidation Reaction Catalysts** Hilal Demir Kivrak, Ebru Ozkan, Ozlem Sahin
09:30-09:45	**(0013) Effect of Bipolar Plate Gas Flow Channel Pattern on Proton Exchange Membrane Fuel Cells Performance** Celal Yılmaz, Muhittin Bilgili, Yılser Devrim
09:45-10:00	**(0136) Performance Analysis of Compressor Assisted Single Effect Absorption Refrigeration Cycle Coupled with Heliostat Field** Chinedu Frank Okwose
10:00-10:15	**(0175) Integration of Renewable Energy Systems with Hydrogen Technologies** Alper Saydam, Tanay Sıdkı Uyar
10:15-10:30	**(0243) Design of Thin Film Membranes for Intermediate-Temperature Hydrogen Separation** Fatih Pişkin, Tayfur Öztürk
10:30-10:45	**Coffee Break**

HALL - A	
10:45-12:00	**Session 7A: Hydrogen Energy Policies and Strategies** **Chair: Sudi Apak**
10:45-11:00	**(0075) A Renewable Pathway Towards Increased Utilization of H_2 in Diesel Engines** Saket Verma, Abhishek Suman, Lalit M Das, Shubhash C Kaushik, Sudhir K Tyagi
11:00-11:15	**(0015) Turkey's Hydrogen Scenario and Hydrogen Production in the Thrace Basin versus Hydrogen Regulations and Standards** Erhan Atay, Sudi Apak
11:15-11:30	**(0090) Recent Trends of Hydrogen Utilization in Transportation** Kadir Aydın
11:30-11:45	**(0087) Maritime Industry and Future Hydrogen Production** Preeti Parikh, Yaqub Amani, Charles Munsch
12:00-13:30	**LUNCH**

SCIENTIFIC PROGRAM

HALL - B	
10:45-12:00	**Session 3B: Hydrogen Production-2** **Chair: Yılser Devrim**
10:45-11:00	**(0071) Steam Methane Reforming in Micro-reactors under Concentrated Solar Irradiation** Atalay Çalısan, Celal Guvenc Ogulgonen, Deniz Uner, Serkan Kincal
11:00-11:15	**(0081) Hydrogen Generation from Solid State NaBH4 by Using FeCl3 Catalyst for Portable PEMFC Applications** Inci Eroglu, Aslı Boran, Serdar Erkan
11:15-11:30	**(0100) Improvement of Operational Characteristics of Sesame Oil in a Compression Ignition Engine with Small Fraction of Hydrogen Enrichment** Tayfun Ozgur, Safak Yildizhan, Ceyla Ozgur, Kadir Aydın, Hasan Serin
11:30-11:45	**(0177) Effective TiO2 Supported Cu-Complex Catalyst in NaBH4 Hydrolysis Reaction to Hydrogen Generation** Dilek Kilinc
11:45-12:00	**(0195) Investigation of Hydrogen Generation from Sodium Borohydride Hydrolysis Reaction with Different Catalyst** Arife Saglam, Elif Damla Arıca, Yılser Devrim
12:00-13:30	**LUNCH**

HALL - C	
10:45-12:00	**Session 7C: Hydrogen Energy and Technologies-2** **Chair: Nader Javani**
10:45-11:00	**(0074) Electrochemical Impedance Modelling of a SOFC Button Cell and Parametric Analysis of the Cell Electrical / Electrochemical Performance** Yaser Mollaei Barzi, Rafat Mohammadi
11:00-11:15	**(0078) Experimental Characterization of Thin Electrolyte for Intermediate Temperature Solid Oxide Electrolysis Cell** Abdullah A. Alzahrani, Ibrahim Dincer
11:15-11:30	**(0084) Investigation of the Effect of Single Stage and Four-stage Clamping Pressure on Electrical Resistance of GDL** Mert Taş, Gülşah Elden
11:30-11:45	**(0083) Preparation of Nanostructured α-Fe2O3 Films from Electrodeposited Fe Films for Photoelectrochemical Water Splitting Performance** Selim Demirci, Cevat Sarıoğlu
12:00-13:30	**LUNCH**

13:30- 18:00	**SOCIAL PROGRAME (Damlataş Cave, Telpher Trip, Alanya Castle)**

SCIENTIFIC PROGRAM

March 18, 2018

HALL - A	
09:00-11:00	**Session 8A: Hydrogen Energy and Technologies-3** **Chair: Kadir Aydin**
09:00-09:15	**(0061) Hydrogen Storage Capacity Investigations of Pd Loading Ratio on MW-CNTs via Supercritical Fluid Deposition Method** Ebru Erunal, Fatma Ulusal, Sinan Büyükbayram, Selda Odabaşı, Bilgehan Güzel, Deniz Üner
09:15-09:30	**(0113) Enhancement of Hydrogen Charging in Metal Hydride-Based Storage Systems by Using Heat Pipe** Muhammet Kayfeci, Fawzi Elhamshri
09:30-09:45	**(0132) Artificial Neural Network Modelling of Hydrogen Storage Properties of LaNi4.75Al0.25 alloys based metal hydride vessels** Muhammet Kayfeci, Fevzi Bedir, Umran Elmas
09:45-10:00	**(0130) Gas (H2 and O2) Sensing Performance of ZnGa2O4 Thin Films Depending on Active Deep Energy Levels** Musa Mutlu Can, Shalima Shawuti, Namık Akçay, Gokhan Algun
10:00-10:15	**(0135) Axane Commitment for a Sustainable, Reliable, and Field Proven Power Source though Partnership with Laboratories and Design Efforts** Johan Andre, Marian Chatenet, Frédéric Maillard, Laetitia Dubau, Lionel Flandin, Corine Bas, Gilles De Moor, Olivier Lottin, Eric Claude, Elisabeth Rossinot, Nicolas Caqué
10:15-10:30	**(0160) A Design of Automated HHO System for Optimum Volumetric Efficiency** Mustafa Kaan Baltacioglu, Raif Kenanoglu, Kemal Kaya, Yakup Hames, Ertugrul Baltacioglu
10:30-10:45	**(0172) Effect of Channel Bend in Serpentine Flow Field Design Pattern for PEMFC** Mohammad Ziauddin Chowdhury, Yahya Erkan Akansu, Omer Genc, Serkan Toros, Yusuf Sahin
10:45-11:00	**(0234) Effects of Rice Husk Particle Size on Biohydrogen Production under Solid State Fermentation** Serpil Özmıhçı, Zülfiye Velioğlu Tosuner
11:00-12:00	**World Hydrogen Day and Closing Ceremony**

SCIENTIFIC PROGRAM

HALL - B	
09:00-11:00	**Session 4B: Applications on Hydrogen Energy and Technologies** **Chair: Johan Andre**
09:00-09:15	**(0197) An Investigation of the Mild Flameless Combustion Behaviour of Methane and Hydrogen Fuels under the Various Preheating Levels in a Furnace** Mehmet Salih Cellek
09:15-09:30	**(0173) Numerical Investigation of Conventional Flow Field Patterns in Proton Exchange Membrane Fuel Cell** Mohammad Ziauddin Chowdhury
09:30-09:45	**(0205) Metal-Schiff Base Complex Catalyst in KBH4 Hydrolysis Reaction for Hydrogen Generation** Dilek Kılınc, Ömer Şahin
09:45-10:00	**(0233) Bio-Hydrogen Production from Waste Rice Husk Using Co-Culture** Serpil Özmıhçı, Gülsün Gizem Taylan
10:00-10:15	**(0199) Mathematical Modeling of a Flowing Electrolyte-Direct Methanol Fuel Cell Using Comsol Multiphysics** Omer Faruk Atacan, David Ouellette, Deniz Yımaz, Pasa Yaman, Can Ozgur Colpan
10:15-10:30	**(0042) Development of a Mathematical Model for a HT-PEMFC Stack Based Cogeneration System** Yagmur Nalbant, Can Ozgur Colpan, Yilser Devrim
10:30-10:45	**(0125) Quasistatic Model Based Analysis of Direct Methanol Fuel Cell System for Hybrid Vehicular Applications** Mustafa Umut Karaoğlan, Alper Can Ince, Can Özgür Çolpan, Nusret Sefa Kuralay
10:45-11:00	**(0232) Turkey's Hydrogen Scenario and Hydrogen Production in the Thrace Basin versus Hydrogen Regulations and Standards** Sudi Apak
11:00-12:00	**World Hydrogen Day and Closing Ceremony in Hall A**

KEYNOTE SPEAKERS

Substituted Ceria-based Materials for Applications in Solid Oxide Fuel Cell Electrolytes and Electrodes

Richard Baker

School of Chemistry, University of St Andrews

Partially substituted (or 'doped') cerium oxide materials are of great interest for applications in SOFC components. By the careful choice of dopant identity and quantity, doped cerias can be endowed with very high oxygen ion conductivity, electronic conductivity, catalytic activity for reduction-oxidation and reforming reactions, or a combination of all three. We have developed methods for the preparation of high purity doped cerias with nanoscale particles. Impurities – even a few ppm of Si – have a strongly deleterious effect on ionic conductivity at grain boundaries while high surface area nanoparticles are desirable for applications in SOFC anodes where the material must catalyse the fuel oxidation, or re-forming, reaction. This presentation will review our very recent work in which two sets of ceria-based materials were prepared for application either as electrolytes or as anode materials in SOFCs. First, the effect of multiple doping of ceria with combinations of Gd, Nd and Sm on oxygen ion conductivity, materials microstructure and, therefore, suitability for use in SOFC electrolytes will be described. A composition was found which shows better performance at intermediate temperatures than singly Gd- or Sm-doped cerias. Second, the use of nanostructured doped cerias, with and without addition of an active metal function, as anode catalysts will be covered and the important effect of preparation method on ultimate performance will be highlighted.

Recent Development in Hydrogen Separation and Purification through Pd-based Membrane Systems

Wei Hsin Chen

National Cheng Kung University, Distinguished Professor, Department of Aeronautics and Astronautics

Global climate change and fossil fuel depletion have driven the need to shift energy use from the conventional carbon cycle to hydrogen cycle. One of the prime advantages of consuming hydrogen as a fuel is zero emissions of carbon dioxide and other pollutants. Hydrogen can be produced from fossil fuels, biomass, and hydrocarbons. However, in most conversion processes, hydrogen-rich gases rather than pure hydrogen are produced. When hydrogen is separated from hydrogen-rich gases using membranes, palladium (Pd) has demonstrated its excellent features of high hydrogen permeability and selectivity. In addition to hydrogen separation and purification, Pd-based membranes can also be thought of as a potential tool to fulfill CO2 capture. In this talk, recent development in hydrogen separation and purification in Pd-based membrane systems such as hydrogen permeation, concentration polarization, and membrane permeance measurement will be introduced. The interfacial and bulk mass transfer phenomena of hydrogen in Pd-based membrane system will be underlined. The presentation will also show hydrogen permeation in Pd membrane tube systems approached by computational fluid dynamics (CFD), demonstrating the potential of simulations as a tool to aid in membrane system designs.

Current status of hydrogen and fuel cells in Norway

Bruno G. Pollet

Norwegian University of Science and Technology (NTNU)

Norway's strategy is structured around five closely interrelated themes addressing: (i) energy supply security, (ii) a fully-integrated energy market, (iii) energy efficiency, (iv) decarbonising the economy and (v) research, innovation and competitiveness. Climate change is one of the policy priorities of Norway. The country is a heavy producer of renewable energy and electricity generation that originate almost entirely from hydroelectric power plants (over 99%). There is also a large potential in wind power, off-shore wind power and wave power, as well as the production of bio-energy from biomass. Although, Norway has limited resources in solar energy, it is one of the world's largest producers of solar grade silicon and silicon solar cells. Hydrogen Energy has been identified by Norway as an alternative fuel with the potential for a substantial contribution to reduce petroleum dependence and greenhouse gases emissions in the long term. The Norwegian government supports the potential role of hydrogen for Norway in the transition to a zero-emission society [1,2]. In line with the EU, Hydrogen and Fuel Cell Technologies (HFCTs) have been identified as a key area of research priority for Norway [1-3]. For example, the White Paper on Norway's energy policy [2] explicitly describes the national hydrogen priorities, which focus on research and development within production, storage and use of hydrogen. Indeed, among the renewable energy sources, HFCTs are considered as a key technology of the 21st century, not only because of its high efficiency in heat and electricity generation, but also because of its potential role in attaining sustainable energy system. It is also envisaged that HFCT will be integrated into "intelligent" energy networks, with conventional and distributed renewable electricity systems. Also, they enable flexible and adaptable fueling strategies, according to local resources, with fossil, bio-fuels or synthetic fuels to reduce impact on air pollution and climate change. For a few years, Norway has put significant effort in HFCT R&D through national and international projects as well as in implementing a hydrogen infrastructure. This presentation will highlight the main HFCT projects in Norway.

PROCEEDINGS

Hydrogen production by agar-immobilized *R. capsulatus* in panel photobioreactor

[1]Kamal Elkahlout, [2]Emrah Sagir, [3]Siamak Alipour, [4]Harun Koku, [2]Ufuk Gunduz, [4]Inci Eroglu, [2*]Meral Yucel

[1] Islamic University of Gaza, Department of Biology and Biotechnology, Gaza, Palestine
[2] Middle East Technical University, Department of Biological Sciences, Ankara, 06800, Turkey
[3] University of Maragheh, Department of Chemical Engineering, Maragheh, P. O. Box 55181-83111, Iran
[4] Middle East Technical University, Department of Chemical Engineering, Ankara, 06800, Turkey

* E-mail: meraly@metu.edu.tr

Abstract
Biological hydrogen production is attractive since biological methods can use cheap and renewable resources for hydrogen production. In this study, a novel panel photobioreactor (1.4 L) was constructed from Plexiglas with a network of nylon fabric support for agar immobilized bacteria complex. Two strains of *Rhodobacter capsulatus* DSM 1710 wild-type strain and *R. capsulatus* YO3 (uptake hydrogenase deleted mutant) with cell concentrations of 2.5 and 5.0 mg dcw/mL agar, respectively were entrapped by 4% (w/v) of agar. The system was operated for 72 to 82 days in a sequential batch mode utilizing acetate as substrate at 30 ^{0}C under continuous illumination in indoor conditions. The pH was between 6.7 and 7.9 during the sequential hydrogen production. The highest hydrogen productivities of 0.68 mmol H_2/L/h and 0.96 mmol H_2/L/h were obtained by *R. capsulatus* DSM 1710 and *R. capsulatus* YO3 respectively.

Keywords: *Rhodobacter capsulatus*, biological hydrogen production, immobilized bacteria, photobioreactor, sequential batch process

I. Introduction

Hydrogen presents itself as an ideal alternative energy carrier that can meet all the conditions for a clean, renewable and, locally produced energy resource. Hydrogen is a clean and promising energy carrier. Biological hydrogen production presents an environmentally friendly option by utilizing renewables and consuming less energy compared to thermochemical and electrochemical production pathways (Meher Kotay and Das, 2008). Although a variety of processes are available for hydrogen production, a sustainable, long-term, cost-effective and commercial production system is still required to be developed for the energy demand in the world (IEA, 2015).

Purple non-sulfur bacteria (PNSB) are a versatile group capable of producing hydrogen under various growth conditions (Basak et al. (2014)). They have the ability to grow under anaerobic and light conditions to produce molecular hydrogen (Koku et al. 2002). PNSB has been widely used in hydrogen production studies on various substrates including organic acids and sugars so far (Kars and Gunduz, 2010).

Immobilization of cells offers many advantages over suspended culture systems such as providing higher cell concentrations and stability, eliminating cell washout problems, protecting against shear damage, and allow working with smaller reactor volumes compared to suspension cultures (Elkahlout, 2011). Amongst the various immobilization methods, cell entrapment is a promising method to immobilize the cells. Agar is considered as suitable for this purpose as it is durable, cheap, biodegradable material for entrapment (Xie et al. 2012, Sagir et al. 2017).

This study demonstrates indoor photofermentative hydrogen production by agar-immobilized *Rhodobacter capsulatus* DSM 1710 wild type strain and *R. capsulatus* YO3 in a panel photobioreactor. Acetate was used as the sole carbon source for the immobilized culture with a two-sided continuous tungsten illumination system. Biohydrogen production was carried out in the sequential batch mode including consecutive 5-7 rounds throughout 72-82 days.

II. Experimental Set-up and Procedure

Two strains of *Rhodobacter capsulatus* the DSM 1710 wild-type strain and the YO3 uptake hydrogenase deleted mutant, (Ozturk etal. 2006), were used in this study. Activated suspended cultures (50 mL, OD_{660}: 2.0) were transferred to a 500 mL transparent screwed bottle containing 450 mL of 20/10 mM (acetate/glutamate) growth medium. Growth temperature and illumination intensity were 30^{0}C and 200 W/m^2, respectively. The pellets were collected after 2-3 days by centrifugation at 10000 g for 20 min and they were re-suspended in 10 mL of basal medium (Biebl and Pfennig, 1981). Agar (4% w/v) was used to entrap and immobilize the bacteria. The effect of acetate concentration (60 mM, 80 mM, and 100 mM) on hydrogen productivity has been investigated in agar entrapted small scale photobioreactors previously by Elkahlout et al. (2016), and optimal acetate concentration was found as 60 mM. Glutamate (4 mM) was used as nitrogen source for the culture.

The frame parts sandwiched a network cloth made of nylon. The aim of using the cloth network was to provide a supporting medium for agar gel. The frame was put horizontally on a glass panel and then 200 mL of the bacteria-agar complex was poured into the inner part of the frame to fill completely. Another glass panel was used to cover the molten agar inside the frame to prevent flooding out while passing the frame for cooling in the refrigerator (4 ^{0}C). The reactors were then closed and filled with hydrogen production medium and then the reactor was flushed with argon for 15 minutes. The outer dimensions of the panel reactor were 29 cm x 29 cm x 4 cm. The

employed panel reactor (1.4 L empty volume) was made of two Plexiglass panels which sandwiched a frame made from PVC (Fig. 1). The frame and the two panels are fitted together as one piece by metal screws which were positioned in from each other by regular distances. Each round (R) was a sequential batch and the spent effluent was discarded at the end of the batch. Then, the reactor was washed with basal medium and the new fresh medium was supplied. For each round, 1 L hydrogen production medium (Acetate/Glutamate, 60 mM/4 mM) was added to the reactor.

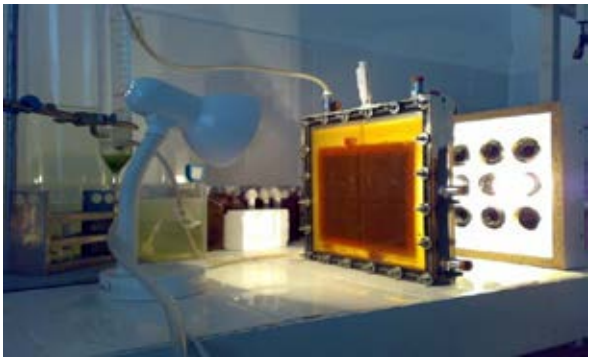


Fig. 1: A photograph of the experimental setup

III. Analysis

Daily 2 mL hydrogen production medium was taken and used for analysis of organic acids. The HPLC instrument was Varian Prostar type provided with the computerized system using prostar workstation software. For analysis of acetate,100 µl of the sample was injected automatically to the injection port. Analysis process was operated at 0.3 mL/min flow rate by using sulfuric acid (0.008 N) as the mobile phase. The run time was adjusted at 25 minutes while the temperature was 35°C. The system used MetaCarb 87H column, 300x7.8 mm. For detection, PDA detector was employed at 210 nm wavelength. The evolved gas was collected by water displacement method using glass graduated cylinders. Gas composition analysis was done by using Agilent type GC system, 6890N version N.05.06100 provided with computerizing system and network analysis software. For analysis of gas composition, 100 µl was aspirated from the gas collection bottles and then injected into the injection port specified for gas analysis. The instrument was operated at 140°C oven temperature for 9 minutes run time and flow rate at 22.3 mL/min. The GC system was equipped with a packed column of the type Supelco 12390U, Carboxen 1000. The inert gas argon was used as the carrier gas. The evolved gas was composed of 99% H_2 and 1% CO_2. Four separate reactors (D1, D2, Y1, Y2) were operated (two for each strain).

IV. Results and discussions

Reactor D1 (*Rhodobacter capsulatus* DSM 1710) was operated for four sequential batches designated as R1-R4 for 67 days. Throughout all rounds, illumination was applied on both sides of the reactor. Table 1 lists total hydrogen production of photobioreactors in each round. During the first round R-1, 3.9 L hydrogen was produced, it decreased to 2.15 L in the second round (R-2). Hydrogen production increased in the third round (R-3) to 3.64 L and then decreased to 1.47 L in the 4th round. The values of pH during operation of this reactor exhibited an increase over 7.6 and even more than 7.8, especially during R-2 and R-4 operations. During R-1 and R-3, pH was tending to be stable between 6.7 and 7.9 (Fig. 2).

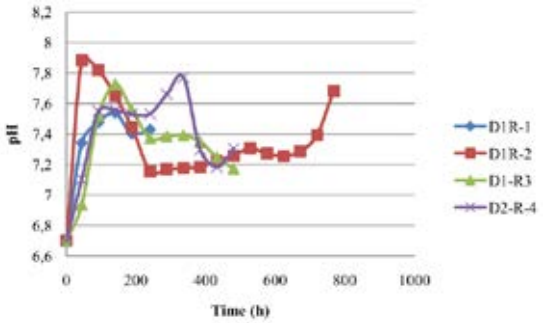


Fig. 2: pH change of *Rhodobacter capsulatus* DSM 1710 (Reactor D1) during the sequential hydrogen production. R-1, R-2, R-3 and R-4 indicate the consecutive rounds.

Reactor D2 (*Rhodobacter capsulatus* DSM 1710) was operated for 82 days. Hydrogen production increased from the first round (2.6 L) to round 4 (3.25 L). The maximum hydrogen productivity of 0.96 mmol H_2/L/h was achieved by *Rhodobacter capsulatus* DSM 1710. These results correlate well with previously reported values (0.54-2.0 mmol H_2/L/h) in small-scale studies by Elkahlout et al. (2016).

Tab. 1: Total hydrogen production of photobioreactors in each round.

Reactors-strains	**Round 1** H_2 (L)	**Round 2** H_2 (L)	**Round 3** H_2 (L)	**Round 4** H_2 (L)	**Round 5** H_2 (L)	**Round 6** H_2 (L)	**Round 7** H_2 (L)	**Cumulative** H_2 (L)
D1-DSM1710	*3.9*	*2.15*	*3.64*	*1.47*	-	-	-	*11.2*
D2-DSM1710	*2.6*	*1.65*	*1.7*	*3.25*	*3.0*	-	-	*12.2*
Y1- YO3	*4.4*	*3.85*	*4.6*	*4.2*	*4.0*	*1.2*	-	*22.3*
Y2- YO3	*5.0*	*4.0*	*5.2*	*5.0*	*4.9*	*4.5*	*4.4*	*33.0*

Reactor Y2 (*R. capsulatus* YO3) was operated for seven sequential batches designated as R1-R7 for 72 days. The reactor produced 33.0 L of hydrogen with an average of total hydrogen produced per round per reactor as 4.72 L of hydrogen. The maximum hydrogen productivity of 0.68 mmol H_2/L/h was obtained by *R. capsulatus* YO3.

Reactor Y1 (*R. capsulatus* YO3) was operated for seven sequential batches designated as R1-R7 for 69 days. By the end of sixth round (R-6) black precipitation started to form in the reactor with an uncharacteristic odor, suggesting contamination a rotten-egg smell. Total hydrogen gas produced was 22.3 L, considering the operation period of R-1 to R-6 that corresponded to average hydrogen produced per round per reactor as 4.15 L of hydrogen. During the last round the immobilized bacteria showed very low activity and produced only 1.22 L of hydrogen. The values of pH during operation of this reactor ranged between 6.7 and 8.0 (Fig. 3).

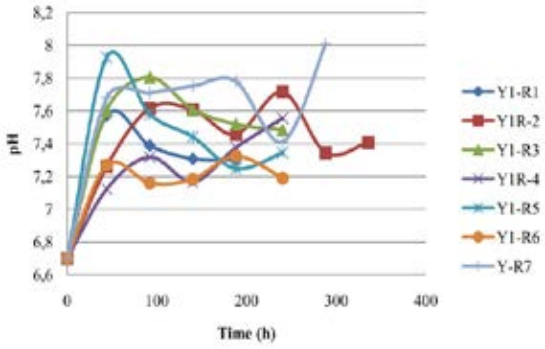


Fig. 3: pH change of *Rhodobacter capsulatus* YO3 (Reactor Y1) during the sequential hydrogen production. R-1, R-2, R-3, R-4, R-5, R-6 and R-7 indicate the consecutive rounds.

V. Conclusions

Biohydrogen production was realized through photofermentation by agar-immobilized *Rhodobacter capsulatus* on acetate. The scaling up of the agar immobilized system improved the stability and long-term hydrogen production. The range of pH change was between 6.7 and 7.9 throughout the overall processes, thereby indicating pH stability of the system. This work demonstrated that this system was reproducible and stable for long-term large-scale operations. The maximum hydrogen productivity of 0.96 mmol H_2/L/h was achieved by *Rhodobacter capsulatus* YO3. The highest hydrogen yields of 2.68 and 3.3 mol H_2/mol acetate were obtained by *Rhodobacter capsulatus* DSM 1710 and YO3, respectively.

Acknowledgements

This study has been supported by Middle East Technical University BAP program and by the EU 6th FP project "HYVOLUTION-019825".

References

Basak N., Jana A.K., Das D., Saikia D., Photofermentative molecular biohydrogen production by purple-non-sulfur (PNS) bacteria in various modes: the present progress and future perspective, International Journal of Hydrogen Energy, 39:6853-6871, (2014).

Biebl H., Pfennig N., Isolation of members of the family Rhodospirillaceae. In: Starr M.P., Stolp H., Truper H.G., Balows A., Schlegel H.G., editors. The prokaryotes. Springer-Verlag, 267-273, (1981).

Elkahlout K., Phototrophic hydrogen production by agar-immobilized *Rhodobacter capsulatus*, Ph.D Thesis, Middle East Technical University, Turkey, (2011).

Elkahlout K., Alipour S., Eroglu I., Gunduz U., Yucel M., Long-term biological hydrogen production by agar immobilized *Rhodobacter capsulatus* in a sequential batch photobioreactor, Bioprocess and Biosystem Engineering, 40, 589-599, (2016).

International Energy Agency, Technology Roadmap, Hydrogen and Fuel Cells, (2015).
https://www.iea.org/publications/freepublications/publication/TechnologyRoadmapHydrogenandFuelCells.pdf

Kars G., Gunduz U., Towards a super H2 producer: improvements in photofermentative biohydrogen production by genetic manipulations, International Journal of Hydrogen Energy, 35, 6646-6656, (2010).

Koku H., Eroglu I., Gunduz U., Yucel M., Turker L., Aspects of the metabolism of hydrogen production by *Rhodobacter sphaeroides*, International Journal of Hydrogen Energy, 2:1325-1329, (2002).

Meher Kotay S., Das D., Biohydrogen as a renewable energy resource prospects and potentials, International Journal of Hydrogen Energy, 33, 258-263, (2008).

Ozturk Y., Yucel M., Daldal F., Mandaci S., Gunduz U., Turker L., Hydrogen production by using *Rhodobacter capsulatus* mutants with genetically modified electron transfer chains, International Journal of Hydrogen Energy, 31, 1545-1552, (2006).

Sagir E., Alipour S., Elkahlout K., Koku H., Gunduz U., Eroglu I., Yucel M., Scale-up studies for stable, long-term indoor and outdoor production of hydrogen by immobilized *Rhodobacter capsulatus,* International Journal of Hydrogen Energy, 42, 22743-22755, (2017).

A Field Application of a Fuel Cell Microcogeneration Unit

[1]*Çiğdem İyigün Karadag, [1]Atilla Ersöz, [1]Fatma Gül Boyacı San, [1]Betül Erdör Türk, [1]Murat Kılıç, [1]Emin Okumuş, [1]Egemen Akar, [1]Nilüfer Topuz, [1]Salih Obut, [1]Özgür Can Korkmaz, [2]Derya Aydemir
[1] TÜBİTAK Marmara Research Center, Energy Institute, P.O.21, 41470, Gebze/Kocaeli, Turkey
[2] Republic of Turkey Ministry of Energy and Natural Resources General Directorate of Renewable Energy, Eskişehir yolu 7. km No:166, 06520 Çankaya/Ankara, Turkey

* E-mail: cigdem.karadag@tubitak.gov.tr

Abstract
In this study, the production process of hydrogen rich gas using natural gas as a feedstock has been investigated for a fuel processing system including autothermal reformer, water gas shift (WGS) (high and low temperature) and preferential oxidation reactors. The resulting gas stream has been introduced to a low temperature fuel cell unit. These two main process parts have been integrated as a 2 kWe micro cogeneration unit as a whole. In the process, the raw natural gas is cleaned, its hydrocarbon content is reformed, CO content is shifted (via WGS reactor) and finally H_2 rich stream is fed to a low temperature PEM fuel cell unit. The conceptual design of the fuel cell stack components (bipolar plate and membrane electrode assembly) has been performed. The bipolar plates with a novel flow field design have been produced. The preliminary single cell performance tests have been performed for 225 cm^2 active area. 2 kWe fuel cell system has been integrated and performance tests have been performed.
Keywords: "Reforming, hydrogen, fuel cell, PEM, microcogeneration"

I. Introduction

Cogeneration (or Combined Heat and Power (CHP)) is seen to have the potential to primary energy savings and greenhouse gas emissions reduction when compared with large power stations. Cogeneration is the combined production of electrical and thermal energy from a single primary energy source. In residential applications, cogeneration provides electricity and heat (for hot water and space heating) for the household (Ellamla, 2015; Staffel, 2013). Fuel cells are energy conversion devices capable to convert the chemical energy of hydrogen into electricity, while a fraction of the unused energy becomes available as heat. In a fuel cell, electricity is produced from the electrochemical reaction of fuel on the anode side and an oxidant on the cathode side, with the concomitant flow of ions through the electrolyte and electronic current in an external circuit. A fuel processing unit converts hydrocarbon to hydrogen for use in a fuel cell. Fuel cells, specifically the polymer electrolyte membrane (PEM) fuel cell and the solid oxide fuel cell (SOFC), are considered as an alternative to combustion based technologies utilized to meet heating requirements. This is because they exhibit high efficiencies, low emissions and noise levels, modularity, and a low heat-to-power ratio (Murugan, 2016, Milcarek, 2017).

In this study, the production process of hydrogen rich gas using natural gas as a feedstock has been investigated for a fuel processing system and the resulting gas stream has been introduced to a low temperature fuel cell unit. These two main process parts have been integrated as a 2 kWe micro cogeneration unit as a whole. A fuel cell based cogeneration system requires power conditioning and control units which are responsible for power DC to AC power conversion and chemical process management. This study also focuses on a real time embedded control system unit which is designed for both hydrogen reformer/fuel cell and data acquisition of the power converter. An embedded data acquisition and control system has been designed to provide a self-regulated process of the hydrogen reformer unit. This work is a part of a national project entitled "A Field Application of a Fuel Cell Microcogeneration Unit" supported by Republic of Turkey Ministry of Energy and Natural Resources General Directorate of Renewable Energy.

II. Experimental Set-up and Procedure

The simplified block diagram of the microcogeneration system is given in Figure 1. Natural gas is used as a feedstock and reformed into hydrogen rich gas. Autothermal reforming is used as an efficient and cheaper technique. The fuel processing system includes several reactors like autothermal reformer (ATR), water-gas shift (WGS) and preferential oxidation (PROX). In ATR, natural gas is converted into hydrogen rich gas composition. However, the hydrogen rich gas consists of carbon monoxide (CO) that is very harmful for anode catalysts in the fuel cell. Therefore, CO is decreased below %1 with WGS reactors, than to ppm levels with PROX reactors.
Fuel cell consists of bipolar plates, membrane electrode assembly including membrane and catalyst, and fuel cell hardware. Polymer composite bipolar plates are produced and flow channels are processed. Nafion XL membranes are pretreated before use. Catalyst slurry is applied on gas diffusion layers through ultrasonic spray technique. The PEM fuel cell system includes the fuel cell module, blower and humidifier. There are power conditioning and control units which are responsible for power DC to AC power conversion and chemical process management.

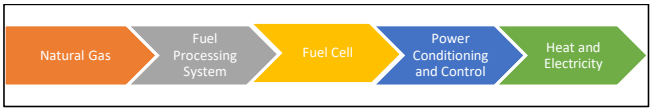


Fig.1: Simplified block diagram of the microcogeneration system

III. Analysis

The ASPEN-HYSIS Version 9 software has been utilized for the simulations and calculations of the fuel processing reactions.

The catalytic properties limit applicable operational parameter ranges such as S/C, O_2/C and operation temperatures and pressures. The durability of the ATR membrane reformer is governed by the thermal durability of the catalysts by coke formation.The main process variables are investigated using equilibrium reactor conditions. The thermodynamic equilibrium system calculations are based on minimizing the Gibbs free energy. The overall process is modeled using ASPEN-HYSYS. The equilibrium temperature and outlet compositions of the reformer are calculated with simulation studies. For all cases, reactor simulation calculations are performed under adiabatic conditions.

IV. Results and discussions

The design of fuel processing system consists of several studies:

- The construction of the process flow diagram including all instruments,
- Determination of the design parameters for fuel processing system,
- Process simulation studies,
- Construction of process flow diagram (PFD),
- Recognition of technical needs and process restricts.

The process flow diagram of the whole system is given in Figure 2. Requirements of main and sub-units are determined by process simulations. The most critical parameters for catalytic reactors are studied. Design and construction of reactors are realized according to the optimum operating conditions. Finally, reactors and sub-units will be integrated to obtain a prototype unit.

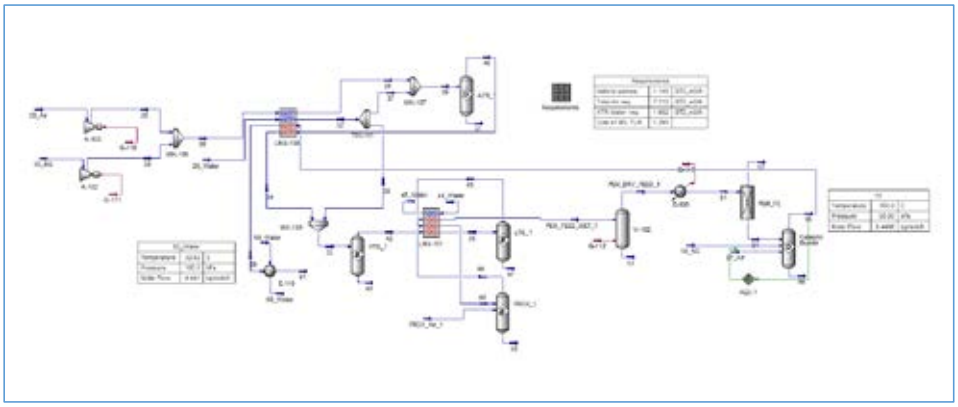


Fig. 2: Process flow diagram of the microcogeneration system

The fuel cell stack consists of bipolar plates, membrane electrode assembly, gaskets, current collectors and fuel cell hardware. Bipolar plates are prepared in house, and different designs are proposed for anode, cathode and cooling plates. The flow channel designs and channel depths are different for anode and cathode plates due to different reaction dynamics, stoichiometric ratio and water accumulation reasons. Anode part consists of 15 channels where cathode side has 25 channels. Channel depth of anode plates is 0.55 mm, where 0.65 mm channel depth is designed for the cathode side. Symmetric cooling plates are designed for both anode and cathode.

Membrane electrode assembly (MEA), which is the heart of the fuel cell consists of catalysts, membrane and gas diffusion layers. All of the electrochemical reactions are performed on MEA. The characteristics of membrane electrode assembly is summarized in Table 1.

Tab. 1: Characteristics of fuel cell MEA

Membrane	Nafion XL
Gas diffusion layer	Sigracet 29 BC
Anode catalyst	%60 PtRu/C
Cathode catalyst	%20 Pt/C
Anode catalyst loading	2 mg/cm^2
Cathode catalyst loading	0.5 mg/cm^2

Before system integration, single cell tests are performed at 25 cm^2 active area. At 0.6 V, 350 mW/cm^2 power

density is achieved with pure hydrogen and oxygen; 220 mW/cm^2 with hydrogen and air. 225 cm^2 active area is proposed for the fuel cell system, therefore the bipolar plates and MEA area produced in this dimension. Produced fuel cell module is seen in Figure 3. The module consists of 30 cells with 350 mm height, 400 mm length and 190 mm width.

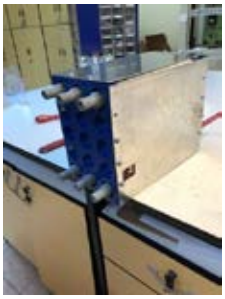


Fig.3: Fuel cell module

The preliminary results of the fuel cell performance tests are summarized in Table 1. The tests are carried under 1.2:2 stoichiometry of simulated reformate gas composition (45%H_2 and 55% N_2) and air.

Tab. 2: Preliminary fuel cell performance data

Voltage (V)	Current (A)	Power (W)
16.99	100.0	1699
15.94	120.0	1912
15.26	130.0	1984
15.05	135.0	2032
15.04	135.0	2031

V. Conclusions

Fuel cell microcogeneration systems are energy efficient systems that are used worldwide. It is possible to increase total energy efficiency up to 90%. By the increase in the system efficiency, the electrical and heating costs for the households can decrease up to 30%. All countries have programmes to increase the awareness of fuel cells. Fuel cell microcogeneration systems are manufactured by several companies, however, technology is still developing towards full commercialisation. Financial incentives are also important to bring it within the reach of an average household.

In conclusion, fuel cell based microcogeneration system with a natural gas fuel processor is designed for this study. Process simulation and designs are performed. 2 kWe fuel cell stack is integrated and tested. This study also focuses on a real time embedded control system unit which is designed for both hydrogen reformer/fuel cell and data acquisition of the power converter. An embedded data acquisition and control system is designed to provide a self-regulated process of the hydrogen reformer unit. The integration of all the systems and field tests are the future work.

Acknowledgements

This research was supported by Republic of Turkey Ministry of Energy and Natural Resources General Directorate of Renewable Energy (ETKB YEGM).

References

Ellamla, H.R., Staffell, I., Bujlo, P., Pollet, B.G. “Current status of fuel cell based combined heat and power systems for residential sector” J. Power Sources 293, 312-328, (2015).

Milcarek, R. J., Ahn, J. , Zhang, J. **“**Review and analysis of fuel cell-based, microcogeneration for residential applications: Current state and future opportunities” Science and Technology for the Built Environment, DOI: 10.1080/23744731.2017.1296301, (2017).

Murugan, S., Horak, B. “A review of micro combined heat and power systems for residential applications” Renewable and Sustaninable Energy Reviews, 64, 144-162, (2016).

Staffell, I., Green, R. “The cost of domestic fuel cell micro-CHP systems” International Journal of Hydrogen Energy, 38 (2), 1088-1102, (2013).

H_2 Adsorption on Cu(I)-ZSM-5: Exploration of Cu(I)-exchange in Solution

[1]Ismihan Altiparmak, [1]Busra Karakaya, [1*]Bahar Ipek,
[1] Middle East Technical University, Chemical Engineering Department, Ankara, 06800, Turkey

* E-mail:bipek@metu.edu.tr

Abstract
Lightweight and economical onboard H_2 storage systems are long sought for efficient utilization of H_2 in fuel-cell vehicles. Cu(I)-exchanged zeolites have high potential as adsorbents since they show much higher H_2 binding energies and higher storage capacities than other adsorbents at ambient temperature. Here we show a new Cu(I)-exchange method in liquid media that proves to be successful especially for mesoporous zeolites with easier Cu(I) diffusion. With this new exchange method, H_2 storage capacities as high as 0.03 wt% at 50 °C and 300 mmHg were achieved on [Al] and [B]-ZSM-5 with initial heats of H_2 adsorption as high as 95 kJ/mol and average heat of adsorption values of 20 kJ/mol.

Keywords: Zeolite, H_2 storage, acetonitrile, Cu(I)-exchange

I. Introduction

H_2 production from renewable sources enables zero-carbon emissions via H_2 fueled fuel-cell vehicles. Among hydrogen storage systems including liquid H_2 storage (~30 K) and compressed gas storage (at pressures up to 70 MPa), use of nanoporous adsorbents are known to be advantageous with operating temperatures near ambient temperature and pressures below 10 MPa (Broom et al., 2016). To reach the 2020 Department of Energy H_2 storage capacity target of 5.5 wt.% using nanoporous adsorbents, these materials should have relatively high H_2 adsorption enthalpies and high pore volumes. For instance, metal organic frameworks (MOFs) with surface areas reaching 6240m^2/g (with a pore volume of 3.6 cm^3/g) are reported to achieve H_2 storage capacity values as high as 8.6 wt.% at -196 °C (at a pressure of 120 bar) (Furukawa et al., 2010). Despite the high H_2 storage capacity at -196 °C, MOFs show 1.5 wt.% H_2 storage at ambient temperature (at 100 bar) (Kaye et al., 2007). These low H_2 capacity values at ambient temperature is related to the low H_2 binding energies (the highest for MOFs reported to be 12.3 kJ/mol for Co_2-*m*dobdc (Kapelewski *et al.*, 2014)) observed on MOFs, and an optimum H_2 binding energy of 20 kJ/mol is suggested for maximum H_2 delivery (Bae and Snurr, 2010).

Cu(I)-exchanged zeolites were reported to result in respectively higher H_2 binding energies reaching 73– 39 kJ/mol values resulting in a H_2 adsorption capacity of 0.045 wt.% at 1 bar and 298 K (Cu-ZSM-5, Georgiev et al. 2007). This unusual strong interaction between the Cu(I) adsorption sites and H_2 has been explained by increased cation (3dπ)→H_2 (σ*) back donation specific to zeolites, rendering Cu(I)-exchanged zeolites potential adsorbents for H_2 (Kozyra and Piskorz, 2016).

Cu(I)-exchange of the zeolites are conventionally performed using either solid-state (Drake et al., 2006) or vapor-phase (Turnes Palomino et al., 2000; Sen et al., 2014) exchange of CuCl with NH_4^+ or H^+-form of zeolites. These methods are known to result in Cl residuals on zeolites with Cl/Al ratios as high as 0.48 (Zhang et al. 2006), which is undesirable since pure monoatomic Cu(I) cations are expected for a successful Cu(I) exchange. An alternative solid-state ion-exchange has also been reported by Shwan et al., which includes physical mixing of the zeolite with CuO or Cu_2O salts followed by heat treatment with NH_3 (Shwan et al., 2015). Even though this method proves to be a Cl free method, presence of unreacted Cu_2O and CuO islands on the zeolite crystals indicate formation of heterogeneous Cu species in/or zeolite particles.

Here, we report a new method to exchange Cu(I) in liquid CuCl/acetonitrile solution, which enables homogeneous contact of soluble Cu(I) cations with zeolite crystals. H_2 storage capacities at 50 °C and differential heat of H_2 adsorption values of Cu(I)-exchanged [Al]-ZSM-5, [B]-ZSM-5 and mesoporous [B]-ZSM-5 were also investigated.

II. Experimental Set-up and Procedure

Aluminum ([Al]-ZSM-5) and Boron ([B]-ZSM-5) containing ZSM-5 were used for H_2 storage in this work.

[Al]-ZSM-5 was synthesized hydrothermally using a procedure similar to that reported by Zhang et al. 2017. Firstly, 0.05 g $NaAlO_2$ (Riedel-de Haen, 44% Na_2O, 55% Al_2O_3, 1%H_2O) and 0.6 g NaOH (Merck, 99%) were dissolved in 101.25 mL H_2O and stirred at room temperature for 12 h. Afterwards, 6.425 g tetraethyl orthosilicate (TEOS, Merck, 98%) was added drop wise under agitation. Then 2.1 g tetrapropylammonium bromide (TPABr, Merck, >99%) was added and stirred for additional 12 h. All the prepared gels were transferred into Teflon-lined 35 mL autoclaves and heated under static conditions at 175 °C for 3 days. Synthesized zeolite was separated by vacuum filtration, washed with de-ionized water, dried at 100 °C and calcined at 550 °C (heating rate 1 °C/min) for 5 h.

[B]-ZSM-5 was synthesized hydrothermally following the procedure reported by Sanhoob et al., (2017) with a gel formula of 1.0SiO_2:0.1TPAOH:35.5 H_2O: 0.1$B(OH)_3$. After the hydrothermal zeolite was calcined at 550 °C (heating rate 2 °C/min) for 5 h.

Mesoporous [B]-ZSM-5 was synthesized following a modified version of a procedure reported by Xue et al., 2017. A gel having molar composition of 1SiO_2:0.128H_3BO_3:0.13Na_2O:0.14HDA:0.1CTABr:60H_2O. Firstly, 1.04 g

NaOH (Merck) and 0.792 g H_3BO_3 were dissolved in 108 g de-ionized water. Then, 3.72 g cetyltrimethylammonium bromide (CTABr, Sigma Aldrich, 98%) and 1.66 g 1,6-diaminohexane (HDA, Sigma Aldrich, 98%) were added and dissolved. After that 6.01 g fumed silica (Sigma Aldrich, 99.8%) was added. After obtained mixture was stirred for 6 h at room temperature, it was transferred into Teflon-lined autoclaves and heated under static conditions at 150 °C for 14 days. The product was recovered by vacuum filtration and washed with de-ionized water, dried in air, and calcined at 580 °C (heating rate 1 °C/min) for 10 h to remove CTABr and HDA.

NH_4^+-form of the zeolites were obtained by exchanging >1 g of calcined zeolites in 500 mL of 0.2 M (M = mol/L) NH_4NO_3 (Merck, 95%) aqueous solution (500 mL DI water and 8 g NH_4NO_3). The solution was stirred for 3 hours at 80 °C for ion-exchange, and then the zeolite was filtered, washed with 250 mL de-ionized water and dried at 80 °C. This exchange procedure was repeated three times. Finally, exchanged zeolite was treated at 550 °C (heating rate 1 °C/min) for 5 h to obtain H^+-form of the zeolites.

500 mg of H^+-[Al]-ZSM-5, H^+-[B]-ZSM-5 and mesoporous H^+-[B]-ZSM-5 were exchanged with Cu(I) in 250 mL of 0.01 M CuCl/acetonitrile solution at room temperature for 6 hours to obtain Cu(I)-ZSM-5. Acetonitrile/CuCl solution is purged with N_2 (Oksan, 99.99%) for 10 minutes before introducing H^+-zeolites that were dehydrated at 150 °C for 6 hours to minimize the water content of the zeolites. After 6 hours of exchange, the zeolites were filtered, washed with 250 mL acetonitrile and dried at a temperature of 80 °C in air. Cu(I)-exchanged zeolites were treated in air at 400 °C (heating rate of 2 °C/min) for 3 h to remove remaining acetonitrile from the crystals.

The characterization of the prepared samples were performed using X-ray diffraction (Rigaku Ultima-IV diffractometer, λ=1.5418 Å), surface area and pore volume analyzer (Micromeritics Tristar II 3020) and a scanning electron microscope (QUANTA 400F Field Emission SEM).

H_2 Adsorption isotherms and differential heat of adsorption measurements were conducted on a Seteram C-80 Tian-Calvet calorimeter coupled to a multiport high-vacuum Pyrex glass manifold backed by a turbo molecular pump (Varian, Minitask, Uner and Uner, 2005). Approximately 220 mg of air exposed Cu(I)-exchanged samples was loaded into the sample port and treated at 250 °C, 200 °C, 150 °C, 100 °C each for 2 h under vacuum (for auto-reduction of Cu(II) to Cu(I)) before cooling to 50 °C. At 50 °C, the free space of the sample cell was calculated by dosing 100 mmHg of He (Oksan, >99.9%) inside a known volume, then expanding it into the sample cell. After the sample was degassed at 50 °C for 1 h, the H_2 adsorption isotherms and differential heats of adsorption values were obtained by introducing 5-400 mmHg of H_2 into the sorption chamber at 50 °C.

III. Results and discussions

X-ray diffraction of synthesized zeolites showed pure MFI patterns with high crystallinity (Figure 1).

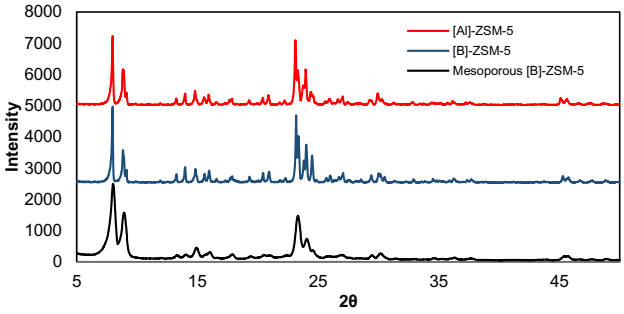


Fig. 1: XRD patterns of prepared zeolites (λ=1.5418 Å)

Morphologies of the Cu(I)-exchanged zeolites can be seen in Figure 2. [Al]-ZSM-5 and [B]-ZSM-5 particle sizes were observed to be around 2–5 µm; whereas, mesoporous [B]-ZSM-5 crystals are composed of adjoined small crystals forming a bigger crystal of 10 µm. Pore volumes of the calcined samples and elemental analysis of Cu(I)-exchanged samples are given in Table 1. [B]-ZSM-5 prepared using CTABr resulted in mesopores ranging from 2 nm to 50 nm and a mesopore volume of 0.14 cm^3/g.

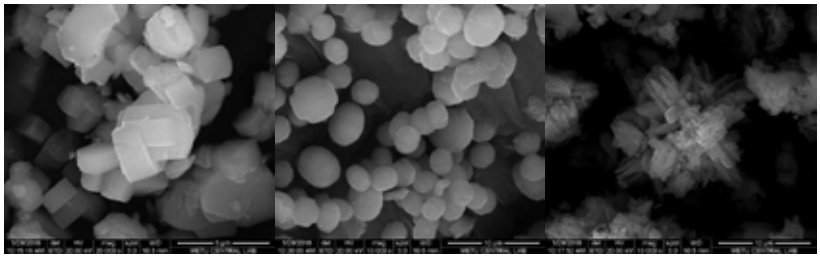


Fig. 2: SEM micrographs of Cu(I)-exchanged zeolites. From left to right: Cu(I)-[Al]-ZSM-5, Cu(I)-[B]-ZSM-5 and mesoporous Cu(I)-[B]-ZSM-5

Cu(I)-exchange of [Al]-ZSM-5, [B]-ZSM-5 and mesoporous [B]-ZSM-5 using a 0.01 M CuCl/acetonitrile solution was achieved successfully with Cu/Al or Cu/B ratios between 0.52 and 0.78. For Cu(I)-[B]-ZSM-5 and mesoporous Cu(I)-[B]-ZSM-5, similar Cu/B ratios obtained by EDX and ICP-OES method (0.66 versus 0.51 for Cu(I)-[B]-ZSM-5 and 0.78 versus 0.79 for mesoporous Cu(I)-[B]-ZSM-5) indicate homogeneous Cu(I) exchange of the zeolite crystals. Cl content of the zeolites observed with the EDX method was lower than 0.1 mol %, resulting in Cl/Al or Cl/B ratios reported in Table 1. Higher Cu content of the mesoporous [B]-ZSM-5 when compared to [B]-ZSM-5 sample at the same conditions indicates easier diffusion of Cu(I) cations inside the zeolite pores.

Tab. 1: Micropore and mesopore volumes of the calcined samples and elemental analysis of Cu(I)-exchanged [Al]-ZSM-5, [B]-ZSM-5, mesoporous [B]-ZSM-5.

Samples	V_{mic} (cm^3/g)[a]	V_{mes} (cm^3/g)[b]	Si/Al or Si/B[c]	Cu/Al or Cu/B	Cl/Al or Cl/B	Cu content (μmol Cu/g)
[Al]-ZSM-5	*0.134*	*0.020*				
[B]-ZSM-5	*0.126*	*0.052*				
Mes-[B]-ZSM-5	*0.093*	*0.143*				
Cu-[Al]-ZSM-5			*40±5*	*0.55±0.12*	*0.05±0.05*	*221*
Cu-[B]-ZSM-5			*54.7*	*0.66±0.04*	*0.12±0.04*	*196*
Mes-Cu-[B]-ZSM-5			*101*	*0.78±0.08*	*0.08±0.08*	*127*

a: Micropore volume was calculated using t-plot method from N_2 adsorption data at -196 °C.
b: Meseopore volume was calculated by subtracting the micropore volume from single point pore volume obtained at P/P_0=0.98
c: Elemental analysis was obtained by EDX at 20 keV

H_2 adsorption isotherms obtained at 50 °C showed similar H_2 storage capacities on a per gram of zeolite basis (150 (0.030), 103 (0.020) and 130 (0.026) μmol H_2/g (wt. %) at 300 mmHg H_2 pressure for Cu(I)-[Al]-ZSM-5, Cu(I)-[B]-ZSM-5 and mesoporous Cu(I)-[B]-ZSM-5 respectively, see Figure 3.a). When the H_2 storage capacities were reported on a mol H_2/ mol Cu basis at the same conditions, it was observed that capacity of Cu(I)-[B]-ZSM-5 was similar to Cu(I)-[Al]-ZSM-5 (0.53 versus 0.68), which were lower than that of mesoporous Cu(I)-[B]-ZSM-5 (1.03) at 300 mmHg H_2 pressure.

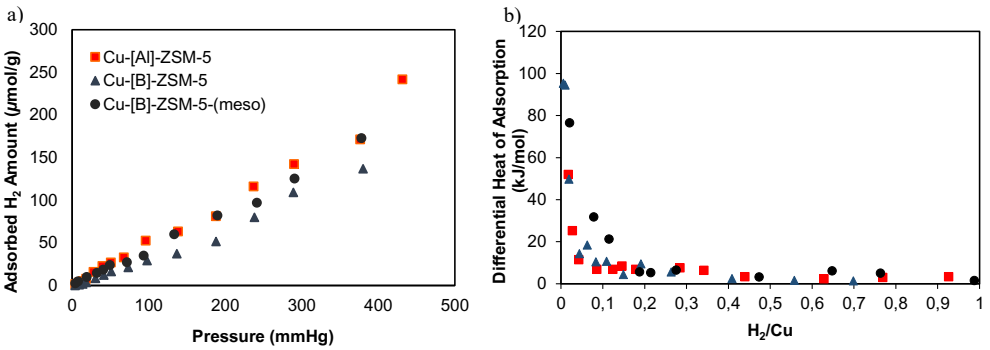


Fig. 3: a.H_2 adsorption isotherms, b. Differential heat of H_2 adsorption values obtained at 50 °C for Cu(I)-[Al]-ZSM-5, Cu(I)-[B]-ZSM-5 and mesoporous Cu(I)-[B]-ZSM-5

Differential heat of H_2 adsorption values on Cu(I)-exchanged samples for 10–400 mmHg H_2 pressure range can be seen in Figure 3.b. The initial heat of adsorption values observed on Cu(I)-[Al]-ZSM-5, Cu(I)-[B]-ZSM-5 and mesoporous Cu(I)-[B]-ZSM-5 were: 52, 95 and 76 kJ/mol H_2 respectively, which are consistent with reported isosteric heat of adsorption values of 73– 39 kJ/mol for Cu(I)-[Al]-ZSM-5 (Georgiev, Albinati and Eckert, 2007). Differential heat of adsorption values ranged between 20 and 30 kJ/mol up to H_2 pressures of 30 mmHg, and stayed constant near 10 kJ/mol for a significant portion of the pressure range (30–240 mmHg). Similar trends for H_2-Cu(I) interaction strength on [Al]-ZSM-5 and [B]-ZSM-5 samples indicate similar Cu(I) locations on MFI framework showing a range of H_2 adsorption heats between ~-50 and -10 kJ/mol and explain similar H_2 storage capacities (on a per Cu basis) on these samples. On mesoporous Cu(I)-[B]-ZSM-5, higher differential heat of adsorption values (higher than 10 kJ/mol) observed for H_2/Cu values between 0 and 0.2, consistent with the observed higher H_2 adsorption capacity of mesoporous Cu(I)-[B]-ZSM-5 on a per Cu basis.

IV. Conclusions

Cu(I)-exchanged [Al]- and [B]-ZSM-5 showed promising H_2 storage capacity values reaching 0.03 wt.% at 50 °C and 300 mmHg pressure and initial heats of adsorption as high as 95 kJ/mol. Cu(I)-[B]-ZSM-5 showed similar H_2 binding energies to those of Cu(I)-[Al]-ZSM-5, resulting in similar H_2 storage capacities on a per Cu basis. Mesoporous-microporous [B]-ZSM-5 was successfully synthesized and Cu(I) exchanged in CuCl/Acetonitrile liquid solution with remaining trace amounts of Cl in the crystals. Mesoporous Cu(I)-[B]-ZSM-5 showed higher differential

heats of H_2 adsorption (80–20 kJ/mol) resulting in higher H_2/Cu ratios at similar conditions when compared to microporous [Al]- and [B]-ZSM-5, which is related to better diffusion of Cu(I) cations through the mesopores during the exchange.

Acknowledgements
This research was supported by the TUBITAK BIDEB 2232 project 117C024. Supports of Prof. Dr. Deniz Uner for the microcalorimetry are gratefully acknowledged.

References

Bae, Y. S. and Snurr, R. Q., Optimal isosteric heat of adsorption for hydrogen storage and delivery using metal-organic frameworks, Microporous and Mesoporous Materials, 132, 300–303, (2010).

Broom, D. P., Webb, C. J., Hurst, K. E., Parilla, P. A., Gennett, T., Brown, C. M., Zacharia, R., Tylianakis, E., Klontzas, E., Froudakis, G. E., Steriotis, T. A., Trikalitis, P. N., Anton, D. L., Hardy, B., Tamburello, D., Corgnale, C., van Hassel, B. A., Cossement, D., Chahine, R. and Hirscher, M., Outlook and Challenges for Hydrogen Storage in Nanoporous Materials, Applied Physics A, 122, 151, (2016).

Drake, I. J., Zhang, Y., Briggs, D., Lim, B., Chau, T. and Bell, A. T., The local environment of Cu + in Cu-Y zeolite and its relationship to the synthesis of dimethyl carbonate, Journal of Physical Chemistry B, 110, 11654–11664, (2006).

Furukawa, H., Ko, N., Go, Y. B., Aratani, N., Choi, S. B., Choi, E., Yazaydin, A. O., Snurr, R. Q., O'Keeffe, M., Kim, J. and Yaghi, O. M., Ultrahigh Porosity in Metal-Organic Frameworks, Science, 329, 424–428, (2010).

Georgiev, P. A., Albinati, A. and Eckert, J,. Room temperature isosteric heat of dihydrogen adsorption on Cu(I) cations in zeolite ZSM-5, Chemical Physics Letters, 449, 182–185, (2007).

Kapelewski, M. T., Geier, S. J., Hudson, M. R., Stück, D., Mason, J. A., Nelson, J. N., Xiao, D. J., Hulvey, Z., Gilmour, E., FitzGerald, S. A., Head-Gordon, M., Brown, C. M. and Long, J. R., M2 (m -dobdc) (M=Mg, Mn, Fe, Co, Ni) Metal–Organic Frameworks Exhibiting Increased Charge Density and Enhanced H2 Binding at the Open Metal Sites, Journal of the American Chemical Society, 136, 12119–12129, (2014).

Kaye, S. S., Dailly, A., Yaghi, O. M. and Long, J. R., Impact of preparation and handling on the hydrogen storage properties of Zn4O(1,4-benzenedicarboxylate)3 (MOF-5), Journal of the American Chemical Society, 129, 14176–14177, (2007).

Kozyra, P. and Piskorz, W., A comparative computational study on hydrogen adsorption on the Ag^{+}, Cu^{+}, Mg^{2+}, Cd^{2+}, and Zn^{2+} cationic sites in zeolites, Physical Chemistry Chemical Physics, 18, 12592–12603, (2016).

Sanhoob, M. A., Muraza, O., Shafei, E. N., Yokoi, T. and Choi, K. H., Steam catalytic cracking of heavy naphtha (C12) to high octane naphtha over B-MFI zeolite, Applied Catalysis B: Environmental, 210, 432–443 (2017).

Sen, D., Kim, C. W., Heo, N. H. and Seff, K. Using CuCl vapor to ion exchange copper into zeolite Na-Y. Single crystal structure of |Cu30Na30Cl9|[Si 121Al71O384]-FAU containing Cu16Cl7 21+, Cu4Cl7+, Cu3Cl2+, and Cu2+, Microporous and Mesoporous Materials, 185, 16–25, (2014).

Shwan, S., Skoglundh, M., Lundegaard, L. F., Tiruvalam, R. R., Janssens, T. V. W., Carlsson, A. and Vennestrøm, P. N. R., Solid-State Ion-Exchange of Copper into Zeolites Facilitated by Ammonia at Low Temperature, ACS Catalysis, 5, 16–19, (2015).

Turnes Palomino, G., Bordiga, S., Zecchina, A., Marra, G. L. and Lamberti, C., XRD, XAS, and IR characterization of copper-exchanged Y zeolite, Journal of Physical Chemistry B, 104, 8641–8651, (2000).

Uner, D. and Uner, M., Adsorption calorimetry in supported catalyst characterization: Adsorption structure sensitivity on Pt/-Al2O3, Thermochimica Acta, 434, 107–112, (2005).
Xue, T., Liu, H., Zhang, Y., Wu, H., Wu, P. and He, M., Synthesis of ZSM-5 with hierarchical porosity: In-situ conversion of the mesoporous silica-alumina species to hierarchical zeolite, Microporous and Mesoporous Materials, 242, 190–199, (2017).

Zhang, C., Chen, H., Zhang, X. and Wang, Q., TPABr-grafted MWCNT as bifunctional template to synthesize hierarchical ZSM-5 zeolite, Materials Letters, 197, 111–114, (2017).

Zhang, Y., Drake, I. J. and Bell, A. T., Characterization of Cu-ZSM-5 prepared by solid-state ion exchange of H-ZSM-5 with CuCl, Chemistry of Materials, 18, 2347–2356, (2006).

Effect of Bipolar Plate Gas Flow Channel Pattern on Proton Exchange Membrane Fuel Cells Performance

[1,2*]Celal Yılmaz, [1]Muhittin Bilgili, [3]Yılser Devrim
[1] Gazi University, Faculty of Engineering, Mechanical Engineer, Eti Mh. Yükseliş Sk. No: 5, Ankara, 06500, Turkey
[2] Teksis İleri Teknolojiler, METUTECH, Silikon blok No:29 ODTÜ, Çankaya, Ankara, 06800, Turkey
[3] Atılım University, Faculty of Engineering, Energy Systems Engineering, Kızılcaşar Köyü İncek, Ankara, 06836, Turkey

* E-mail: impcelal@gmail.com

Abstract
Fuel cell technology is used in many industries because it is long lasting, quiet, wide application area, zero emission and high efficiency. In this study, the bipolar plate gas flow channel pattern that influence the fuel cell performance curve was investigated. The effect of fuel cell performance was investigated by using three-dimensional computational fluid dynamics (CFD). Three different gas flow channel patterns (parallel type, parallel in serpentine type (PIS) and custom type (CU)) have been designed. Bipolar plate anode and cathode flow channel models on 5cm^2 active area were modeled and single cell solutions were made with Ansys Fluent fuel cell module. In the numerical simulations, reactant feed pressure, humidification level, operating temperature, channel width, height dimensions were kept constant, and the effect of different gas flow channel designs on performance was investigated. In these analyses, temperature distribution, pressure drop, distributions of reactant concentrations and polarization curves were determined numerically. Experimental study was conducted to verify numerical results. In the experiment, hydrogen and air were used as the reactant gas. Fuel cell experiments on 5cm^2 active area were made with test station. Polarization curves were plotted using values of current and voltage data. The physical validity of the computational fluid dynamics model was compared with the experimental results conducted. Based on the simulation results, a custom gas flow pattern design showed the best performance curve.

Keywords: Flow Channel Design, Fluent Fuel Cell, Bipolar Plate, Channel Geometry, CFD

I. Introduction

The bipolar plate flow channel patterns have a significant effect on fuel cell performance. There are many different flow channel patterns in the literature. The features of these patterns are different from each other. The flow channel patterns with 5cm^2 active area of three different geometries were investigated. As a result of the literature research, it has been determined that as the number of flow channels decreases, the performance of the cell increases and the number of flow channels affects the performance more than the flow channel geometry by Limjeerajarus (2015). The flow field is a tree-shaped geometry that connects the central nozzle to the periphery of the bipolar plate. The results show that the tree-shaped flow models provide a relatively low-pressure drop and at the same time provide equal flow distribution by Gutierrez (2013). At an experimental study of the flow field of fuel cells, the pin-type flow field showed the worst performance and the serpentine type flow channel pattern gave the best performance by Liu (2014). Um and Wang (2004) studied the gas transport and electrochemical phenomena in the channel geometry. They has shown that the model with segmented type channel exhibits better results. Alvarado (2011) et al. investigated three structural flow channel patterns of fuel cell. Each pattern created is a fractal extension of the original pattern. As a result, the structural flow channel pattern has shown a low-pressure drop. Kloess (2009) et al. offered new flow channel designs for bipolar plates on fuel cell. These designs combined the advantages of serpentine and interdigitated models of bipolar plate flow channel. The results, the leaf and lung design had a lower pressure drop than the serpentine and interdigitated flow models.

The purpose of this work is to contribute to the new patterns and improve the performance of the bipolar plate gas flow channel. In addition, the study highlights the flooding phenomenon and performance losses on the fuel cell.

II. Experimental Set-up and Procedure

Membrane electrode assemblies (MEAs) based of Nafion 212 membrane (Ion Power, Inc., USA) were fabricated by Ultrasonic Coating Technique by Devrim (2015). 35 BC gas diffusion layers (SGL Technologies GmbH, Germany) were used for gas diffusion electrode (GDE) preparation. Catalyst inks were coated onto GDL by using Sono-Tek ultrasonic coating instrument (Exacta Coat, Sono-Tek Corporation, USA) operating at 120 kHz. Coating inks were comprised of 70 wt.% Pt/C catalyst in a mixture of water/isopropyl alcohol. The Pt loading of anode and cathode electrodes was kept 0.4 mg Pt/cm^2.

Performances of fabricated MEA's were measured via the fuel cell test station (TECHYS HYGO FCTS-H2ME 500). The MEAs were tested in a single cell (Model: FC05-01 SP REF, ElectroChem Inc., USA) with a 5 cm^2 active area which have same pattern and dimensions of PIS model type. Fuel cell was operated at atmospheric pressure and cell temperature was set to 65^{o}C. Atmospheric air and pure hydrogen (99.99%) were used as reactant gases.

III. Numerical Analysis

The cross sections of the channel patterns were designed as a square profile with constant dimension for each channel patterns. The geometric shapes of the patterns are given in Figure 1 and Figure 2. And the geometric dimensions of the flow channel patterns are given in Table 1.

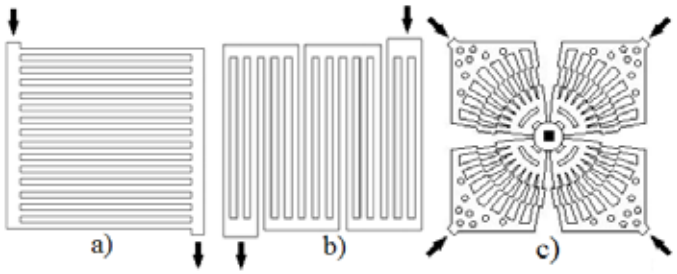


Fig. 1: The flow channel patterns of 2D view a) Parallel type, b) PIS type, c) CU type

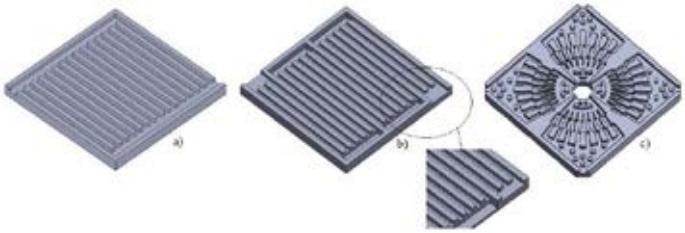


Fig. 2: The flow channel patterns of the bipolar plate a) Parallel type, b) PIS type, c) CU type

Tab. 1: Fuel cell bipolar plate geometric dimensions

Physical Dimensions	Parallel	PIS	CU	Units
Channel Height	0,75	0,75	0,75	mm
Channel Width	0,75	0,75	0,75	mm
Flow Channel Cross Section	0,5625	0,5625	0,5625	mm^2
The fuel cell Active Area	5	5	5	cm^2
Current Collector Thickness	2	2	2	mm
Diffusion Layer Thickness	0,325	0,325	0,325	mm
Catalyst Layer Thickness	0,015	0,015	0,015	mm
Membrane Thickness	0,05	0,05	0,05	mm

In order to solve problem, the following assumptions accepted.

- The geometric model is modelled in 3D, steady state and multi-phase.
- The gas continuous flow in the channel and fully developed flow is acceptable.
- Membrane is assumed to be a homogeneous structure and no gas pass.
- The reactants species assumed as ideal gas.
- Gas diffusion layers and catalyst layers are isotropic.
- The flow is incompressible by Bilgili (2011).

Tab. 2: Physical parameters of fuel cell models.

Parameters	Values	Units
Anode/Cathode of Porosity GDL	0.75	-
Anode/Cathode of Porosity CL	0.50	-
Anode/Cathode Contact Angle	165	°
Anode/Cathode Surface-volume ratio	350000	(1 / m)
Membrane Equivalent weight	1100	(kg $kmol^{-1}$)
Inlet temperature	338	K
Operation pressure	1	bar
Anode/Cathode Relative Humidity	100	%
Stoichiometry of Anode	1.2	-
Stoichiometry of Cathode	2.5	-

IV. Results and discussions

The purpose of this study is to investigate the infulence of flow channel patterns on the performance of fuel cell. The fuel cell experimental study was performed by using PIS flow channel pattern. Numerical analysis of model was verified by the experimental results, which is the case of PIS channel pattern. The numerical analysis of the PIS type model and experimental method that has the same physical parameters and geometric dimensions are given in Table 1 and Table 2. Polarization curves were obtained for both the experimental results and the numerical solutions as seen on Figure 3. A small deviation at the values of current densities had occurred with expiremantal result of PIS type. According to numerical study, the best performance curve was obtained for the CU type and differences of that with the other models had occured at some potential value about 11%.

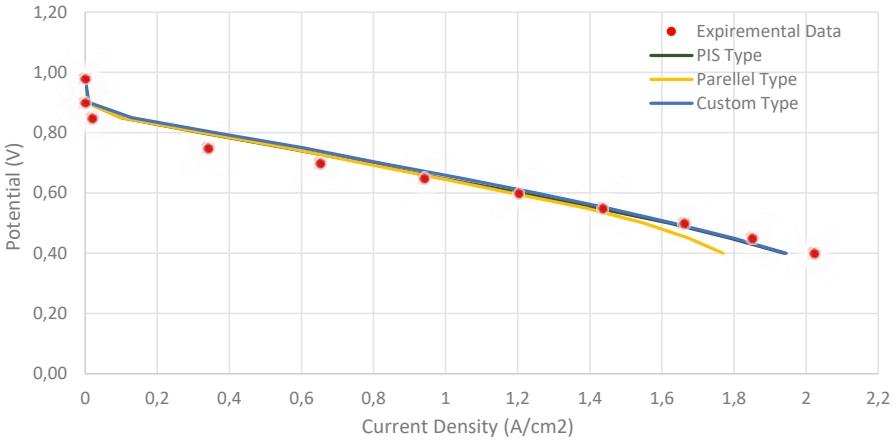


Fig. 3: Polarization curves of different types of flow channel models

The results show that the differences on the polarization curves are dominant in low potential region. The CU type channel pattern have given the best result among three different channel patterns. The parallel type flow channel pattern have given the worst polarization curve as seen in Figure 3. This difference is generally due to flood phenomena at the low potential region. PIS type and CU type flow patterns show quite close performance curves according to numerical analysis results.

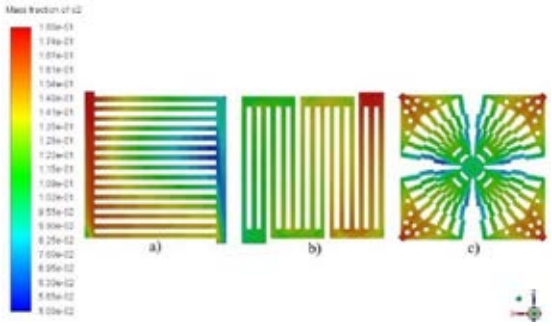


Fig. 4: O_2 mass fraction cathode channel at 0.6V cell voltage a) Parallel type, b) PIS type, c) CU type

The flow rate of the reactants must be equal or greater than the rate of consumption of the electrochemical reactions in the cell. Reactants can not supply adequately and distributed in the channel pattern, resulting in devastating effect on the fuel cell. Because of this, the negative cell voltage appears at the regions that the reactants cannot reach. This causes membrane disruption on fuel cell. In order to cope with such problems, adequate gas flow quantity and appropriate gas flow channel patterns are required by Zhang (2008). As we expected, while the distribution of PIS and CU type was more uniform, it was determined that the concentrations of the reactants in the parallel pattern were uneven in some regions as seen in Figure 4.

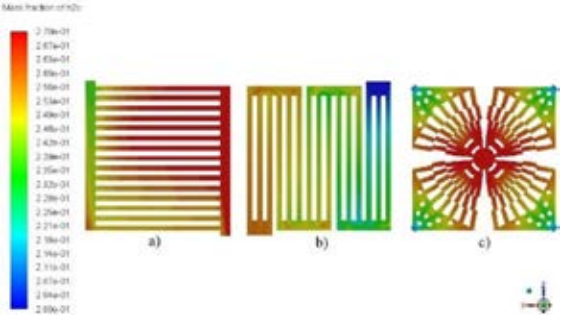


Fig. 5: H_2O mass fraction cathode channel at 0.6V cell voltage a) Parallel type, b) PIS type, c) CU type

The PIS and CU type models have better performance than parallel models because these have more uniform water production. The parellel type, in some zone electrochemical reaction is slow as seen Figure 5. Also, water cannot be removed from the flow channels because of the reactant distribution. These zones are saying in stagnant areas. As seen from Figure 5, the parallel type pattern has more than stagnant regions than the other.

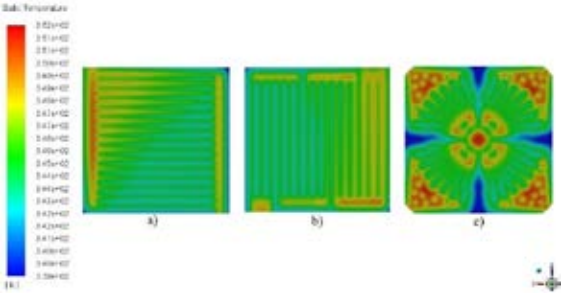


Fig. 6: Temperature cathode cl/memb.interface at 0.6V cell voltage a) Parallel type, b) PIS type, c) CU type

The fuel cell non-homogeneous temperature distribution can cause a decrease of fuel cell performance (Barbir, 2005). The PIS type model has the most uniform temperature distribution at the catalyst a membrane interface. The parallel and CU patterns have some zone dominant temperature distribution. In the fuel cell excessive temperature gradient, above 80 degree, on the membrane can cause increase mechanical stresses, the local overheating. Eventually, the life of fuel cell reduces. In order to guarantee long cycle membrane life, the temperature differences are acceptable on the membrane to be 5°C (Pasaogulları, 2009). The parellel and PIS type of pattern, the temperature gradient on the membrane surface appears to be around 7°C.

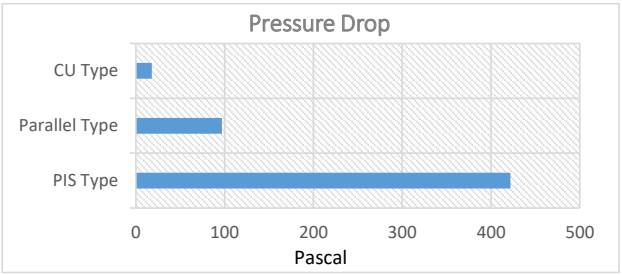


Fig. 7: Pressure drop of different channel patterns

The high-pressure drop can remove accumulated water in the channel of cell, but increases the auxiliary power loading of fuel cell. The ideal flow channel shape is expected to overcome the flooding phenomenon with low-pressure drop (Chao, 2017). Pressure drop in the parallel flow field is low, but water accumulate in the channels due to channel pattern design. As seen in Figure 5, causing high-pressure losses, the flooding and stagnant region in the channel leads to many problems like the reactants cannot transmitted to the catalyst surface. Especially in the fuel cell with large active area, pressure drop can reach great values. The difference of the pressure drop between the CU type and the PIS type patterns are about 95% (Figure 7).

V. Conclusions

Polarization curves were obtained for three different flow patterns by using numerical analyses. The numerical analysis was verified with the experimental results of PIS channel pattern. As a result, flow channel patterns can influence the cell performance as negatively or positively. Therefore, the researchers need to be careful in choosing flow channel patterns of the fuel cell. The PIS and CU channel patterns showed the best performance curve and the parallel type of flow channel showed the worst performance curve. However, the PIS flow channel pattern had the highest-pressure drop value. By taking into account the pressure drop and polarization curves, the CU model is recommended for application.

References

Barbir, F., Pem Fuel Cells Theory and Practice. Elsevier Academic Press, London, 207-43 (2005).
Bilgili M. 3-dimensional analysis of the effect of semi cylindirical blocks in flow channels on pem fuel cell performance. Doctoral Thesis. Gazi University Institute of Science and Technology (2011).

Chao W., Qinglei Z., Shuiyun S., Xiaohui Y., Fengjuan Z., Xiaojing C., Junliang Z., The respective effect of under-rib convection and pressure drop of flow fields on the performance of PEM fuel cells. Scientific Report; 7:43447 (2017).

Kloess J.P, Wang, X, Liu J, Shi Z, Guessous L. Investigation of bio-inspired flow channel designs for bipolar plates in proton exchange membrane fuel cells. Journal of Power Sources, 188:132–40 (2009).

Limjeerajarus N, Charoen-amornkitt P. Effect of different flow field designs and number of channels on performance of a small PEFC. International Journal of Hydrogen Energy, 40: 7144-58 (2015).

Liu H, Li P, Juarez-Robles D, Wang K and Hernandez-Guerrero A. Experimental study and comparison of various designs of gas flow fields to PEM fuel cells and cell stack performance. Frontiers in Energy Research, 2:1-8 (2014).

Lorenzini-Gutierrez D, Hernandez-Guerrero A, Ramos-Alvarado B, Perez-Raya I, Alatorre-Ordaz A. Performance analysis of a proton exchange membrane fuel cell using tree-shaped designs for flow distribution. International Journal of Hydrogen Energy, 38: 14750–63 (2013).

Pasaogulları U. Heat and water transport models for polymer electrolyte fuel cells. Handbook of fuel cells. Chichester, UK, (2009)

Ramos-Alvarado B, Hernandez-Guerrero A, Elizalde-Blancas F, Ellis M.W. Constructal flow distributor as a bipolar plate for proton exchange membrane fuel cells. International Journal of Hydrogen Energy, 36: 12965–76 (2011).

Um S, Wang C. Three-dimensional analysis of transport and electrochemical reactions in polymer electrolyte fuel cells. Journal of Power Sources, 125: 40–51 (2004).

Yılser Devrim, Huseyin Devrim, Inci Eroglu, Development of 500 W PEM fuel cell stack for portable power generators, International Journal of Hydrogen Energy, Volume 40, Issue 24, 7707-7719 (2015).

Zhang, J., Pem Fuel Cell Electrocatalyst and Catalyst Layers Fundementals and Applications, Springer, Canada,1-50 (2008).

Microwave Assisted Synthesis of Pt/MWCNT Catalyst for High Temperature PEM Fuel Cell Application

Elif Damla Arıca, Yılser Devrim
Atılım University, Department of Energy Systems Engineering, Ankara, 06836, Turkey

E-mails: aelifdamla@gmail.com, yilser.devrim@atilim.edu.tr

Abstract
In this study, the preparation of Platinum (Pt) catalyst on Multi Walled Carbon Nanotube (MWCNT) support material was prepared by Microwave Synthesis Method for high temperature proton exchange membrane fue cell (HT-PEMFC) applications. Prepared catalyst was analyzed with X-Ray Diffraction (XRD), Transmission Electron Microscopy (TEM), BET surface area analysis and corrosion tests. 20-40% Pt loading was observed on the MWCNT support material at different microwave conditions. Gas diffusion electrodes (GDE) were fabricated by an ultrasonic coating technique with Pt/MWCNT catalyst. Polybenzimidazole (PBI) membrane based Membrane Electrode Assembly (MEA) was prepared for observe the HT-PEMFC performance of the Pt/MWCNT catalyst. The MEA was tested in a single HT-PEMFC with a 5 cm^2 active area at 160^oC without humidification. A comparison of their performance with the commercial Pt/C catalyst is also presented. The experimental results suggested that the Pt/MWCNT catalyst is promising catalyst options for HT-PEMFC applications.

Keywords: PEM, Fuel Cell, High Temperature PEMFC, Multi Walled Carbon Nanotube (MWCNT), Catalyst, Microwave

I. Introduction

Fuel cell is an electrochemical device that produces electricity by using fuel in one step and by nature of one step process provides high efficiency when compared with multi-step processes. In other words fuel cells are electrochemical devices that have capacity to produce electricity when it is fed.

PEM fuel cells can be examined in two subtitles with regard to its working temperatures: Low Temperature PEMFC (LT-PEMFC) and High Temperature PEMFC (HT-PEMFC). LT-PEMFCs have widespread use however, for PEM fuel cells working at high temperature increased the performance of fuel cells because of increasing the kinetic and water transport capacity also decreasing the liquid water saturation (Xing et al, 2014).

In many studies, new membranes, catalysts, electrochemical reaction mechanisms and kinetic and electrode materials and preparation for PEMFC technologies are discussed. On the other hand, it is a significant disadvantage for PEMFCs that catalysts and membranes are easily poisoned and costly (Ehsai et al, 2010). The use of noble metals (usually platinum) as catalysts and the financial consequences of the quantities of these noble metals create a significant problem for using. Consequently, the catalyst should be providing to use small amount platinum and high surface area as long term targets (Zhang et al, 2015). Support materials are an important ingredient in corrosion and Pt dissolution/consolidation. Some carbon support materials can increase the electrochemical use of Pt metal, thereby reducing the amount of Pt required. According to studies done on MWCNTs are widely used as support materials because of their structural properties, homogeneously dispersed catalyst precipitates and high conductivity, high corrosion resistance, etc. (Mikhaylova et al, 2011).

In this paper, Pt supported MWCNT catalysts were synthesized by microwave-assisted synthesis. Pt loading of the prepared Pt/MWCNT catalysts was successfully achieved between 20 and 40%. The microwave condition of was used with different powers and different durations, and the effect was also observed at the same time.

II. Experimental Set-up and Procedure

Pt/MWCNT catalysts were prepared by microwave assisted method. The main materials used for synthesis Pt/MWCNT were Chloroplatinic acid hydrate (99.9%, Sigma-Aldrich, USA) and MWCNT (outer diameter: 48-78 nm, Nanografi, Turkey), $CH_3CH(OH)CH_3$ (IPA, Merck, Germany), EG (99%, Sigma-Aldrich,USA) and nitrogen gas (>99.98%, Linde). The pH adjustment was done with NaOH (98-100.5%, Sigma-Aldrich, USA) and HNO_3 (65%, Sigma-Aldrich, USA). Finally, acetone was used in washing process.

Briefly, required amount of MWCNT was dispersed into 24 mL EG and 6 mL IPA (v/v 4:1) under ultrasonic mixing for 1 hour. At the end of 1 hour Chloroplatinic acid hydrate was added to the mixture and ultrasonic treatment continues for 10 minutes. After mixing Pt and MWCNT in the solution of EG and IPA, the pH of the mixture was adjusted to 12 with 1 M NaOH in EG (Bharti et al, 2017), the alkaline mixture was stirred under N_2 atmosphere for 30 minutes in ultrasonic mixing. Then the mixture placed into microwave oven and five different catalysts were prepared by operating the microwave at different power values at different times. Five different syntheses were named Pt/MWCNT-1 (600W, 60sec), Pt/MWCNT-2 (600W, 80sec), Pt/MWCNT-3 (800W, 40sec), Pt/MWCNT-4 (800W, 60sec) and Pt/MWCNT-5 (800W, 80sec). After the mixture reaches room temperature the required amount of acidic solution of 0.2 M HNO_3 was added to the solution to lower the pH value between 2 to 4. Finally, the catalyst stirring for 12 hours and washed with acetone then the catalyst solution dried at 80 °C.

Cyclic voltammeter test is used for electrochemical surface area calculations. The CV tests were done with potentiostat (Wonatech ZIVE-SP2 Potentiostat/Galvanostat/FRA). Detailed information for the calculations is

explained in next chapter. The cyclic voltammetry tests were done with $HClO_4$ solution (70-72%, Sigma-Aldrich, USA) and the preparation process of catalyst was done with IPA and deionized water (Sigma-Aldrich, USA) as solvents and Nafion 15% dispersion (Ion Power, Inc, USA). The cyclic voltammetry tests were compared with commercial Pt/C catalyst.

III.Analysis

First of all the Pt loading characterization of Pt/MWCNT catalyst was determined by TGA analysis. The test was done between room temperature to 900°C in air atmosphere. The weight lost together with the change in temperature is recorded and consequently the percentage of Pt in the catalyst is determined. Results of the test for Pt/MWCNT-1, Pt/MWCNT-2, Pt/MWCNT-3, Pt/MWCNT-4 ve Pt/MWCNT-5 microwave conditions and percentages are given in Tab.1.

Tab. 1: Microwave condition and % Loading of Pt for catalysts

Catalyst	Power (W)	Time (s)	% of Pt Loading
Pt/MWCNT-1	600	60	29.16
Pt/MWCNT-2	600	80	40.12
Pt/MWCNT-3	800	40	4.18
Pt/MWCNT-4	800	60	24.05
Pt/MWCNT-5	800	80	29.23

IV.Results and discussions

XRD analysis is used to determine the size of the Pt nanoparticle. Fig. 1. gives the Pt characteristic diffraction corresponding to Pt (111), Pt (200), Pt (220) and Pt (311) peaks for Pt / MWCNT-4 catalyst.

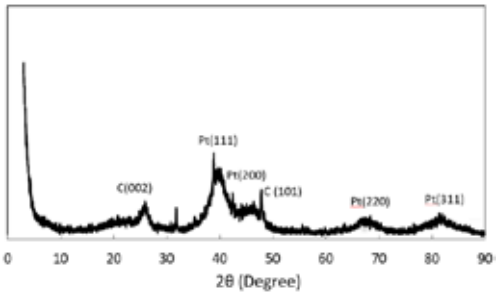


Fig. 1: XRD graph of Pt/MWCNT-4 catalyst.

The Sherer equation (equation 1) is used to calculate the mean Pt particle size using the XRD graph (Heydari and Gharini, 2016). The equation was given in below;

$$d = \frac{0.89 \times \lambda}{B_{2\theta} \times \cos(\theta)} \quad (1)$$

In the equation d is the average particle size in nm, λ is the wavelength of the X-Ray used in diffraction and which equal to 1.5406 A, B is the maximum peak in the diffraction pattern peak width in half max (radian) and finally θ is the angle of maximum peak. The average particle size of Pt in Pt/MWCNT-4 catalyst was estimated to be 2.8 nm. Finally, homogenous distribution of Pt particle in support material is another important factor to increase the efficiency of electrochemical activity of catalyst (Wang et al, 2005). TEM image of the synthesis Pt/MWCNT catalyst was given in Fig. 2. Homogenous distribution of the Pt particles were observed on MWCNT:

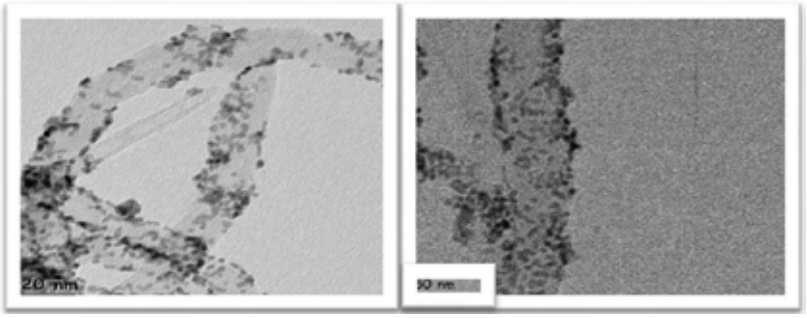


Fig. 2: TEM image of Pt/MWCNT-4 catalyst.

CV tests were done to evaluate electrochemical surface area (ECSA) of catalysts. The tests were done in 0.1 M $HClO_4$ aqueous solution with 0.1 V/s scan rate at room temperature and it is aimed to calculate corrosion amounts for after 1000 cycles. ECSA formula is given in equation 2.

$$ECSA\left(\frac{cm^2}{g}\ of\ Pt\right) = \frac{Q_H(\frac{\mu C}{cm^2})}{K(\frac{\mu C}{cm^2})\times L\ (g\ of\ Pt\ per\ cm^2)} \quad (2)$$

The maximum peak value for all samples was obtained at cycle 20 for this reason the peak values of all catalysts samples were compared for cycle 20 in the Fig. 3.

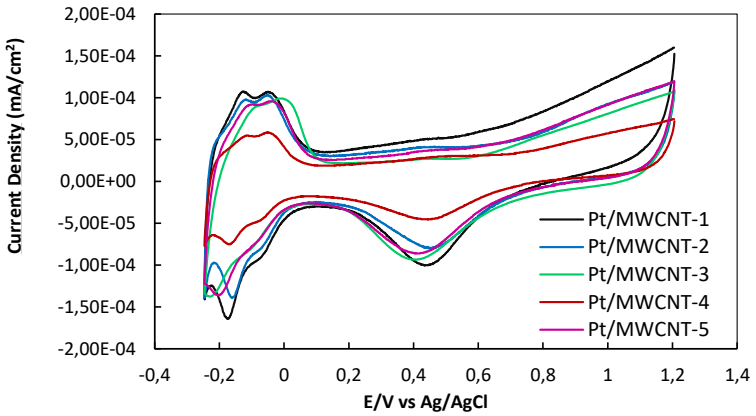


Fig. 3: CV graph for all samples at cycle 20.

Comparison of all sample's ECSA value for cycle 20 given in Tab.2. As we mentioned earlier, the comparisons for all samples are made in cycle 20 because the catalysts show the highest peak values at the 20th cycle. Pt/MWCNT-1 gives the highest ECSA value (50.06 cm^2/g). In addition, when we compare all samples, the Pt/MWCNT-1 has the lowest loss at the end of 1000 cycles. Commercial Pt/C catalyst has higher ECSA value (197.57 cm^2/g) than other samples at the end of 20th cycle but we can say that the Pt/MWCNT-1 sample performs better result in terms of % Pt loss at the end of 1000 cycle. Pt/MWCNT-1 sample is selected for comparison because in the CV test we can get most stable result from this sample. According to Bharti and Cheruvally, Pt use of MWCNT supported catalyst is more efficient than carbon and grapheme support catalyst (Bharti et al, 2017). Our test result does not support their idea which may be due to the fact that the Pt nanoparticle of the Pt/C commercial catalyst is quite large. On the other hand, the smaller size of the Pt nanoparticle in the catalyst leads to a better catalytic activity (Li et al, 2010). For this reason, it may be possible for the Pt/C commercial catalyst to provide a better catalytic result. Mirzaei and his friends have encountered a similar result when comparing carbon and carbon nanotube sample in their work, and they have concluded that this result may be due to the particles size of the Pt nanoparticle in the carbon support (Mirzai et al, 2017).

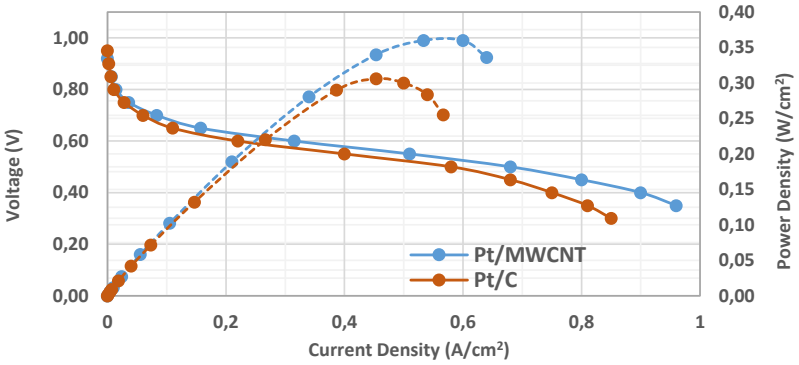


Fig. 4: Voltage vs current density graph for HT-PEMFC.

Performance tests were done dry H_2/Dry air (1.5/2.5), Tcell =160°C condition on 5 cm^2 active area HT-PEMFC the curve of voltage vs current density was given in Fig. 4. The power densities obtained for Pt/MWCNT catalysts (0.35 W/cm^2) in this study are higher than the values of Pt/C catalysts (0.31 W/cm^2).

V. Conclusions

In this study synthesis of Pt/MWCNT catalyst were prepared by microwave assisted synthesis at different microwave conditions for HT-PEMFC application. The best ECSA value was obtained from the Pt/MWCNT-1 sample. The loading of Pt on support material was changed between % valueof 20-40 and the most effective result was obtained in Pt/MWCNT-4 catalyst therefore, the Pt/MWCNT-4 catalyst was sent to XRD analysis and the particle size was measured as 2.8 nm. It was found that smaller and well dispersed Pt particles were deposited onto the MWCNT surface through MW method. Finally, catalyst was tested with HT-PEMFC an active area of 5 cm^2 and maximum power density measured 0.35 W/cm^2 and current density at 0.6 V was found to be 0.315 A/cm^2.

Acknowledgement

This study is supported by The Scientific and Technological Research Council of Turkey (TUBITAK) 1001 (Grant number: 214M301) Project.

References

Altergy units replace batteries in Caribbean telecom deployment. (2015). Fuel Cells Bulletin, 2015(4), p.6.

Bharti, A., Cheruvally, G., & Muliankeezhu, S. (2017). Microwave assisted, facile synthesis of Pt/CNT catalyst for proton exchange membrane fuel cell application. International Journal of Hydrogen Energy, 42(16), 11622-11631.

Ehsani, M., Gao, Y. and Emadi, A. (2010). Modern electric, hybrid electric, and fuel cell vehicles. Boca Raton (Fla.): CRC Press.

Heydari A,Gharibi H. Fabrication of electrocatalyst based on nitrogen doped graphene as highly efficient and durable support for using in polymer electrolyte fuel cell J. Power Sources 2016 ;325 :808-815.

Li, Y., Gao, W., Ci, L., Wang, C. and Ajayan, P. (2010). Catalytic performance of Pt nanoparticles on reduced graphene oxide for methanol electro-oxidation. Carbon, 48(4), pp.1124-1130.

Mikhaylova, A., Tusseeva, E., Mayorova, N., Rychagov, A., Volfkovich, Y., Krestinin, A. and Khazova, O. (2011). Single-walled carbon nanotubes and their composites with polyaniline. Structure, catalytic and capacitive properties as applied to fuel cells and supercapacitors. Electrochimica Acta, 56(10), pp.3656-3665.

Mirzaei, F., Parnian, M. and Rowshanzamir, S. (2017). Durability investigation and performance study of hydrothermal synthesized platinum-multi walled carbon nanotube nanocomposite catalyst for proton exchange membrane fuel cell. Energy, 138, pp.696-705.

Wang ZB, Yin GP, Shi PF. Stable PteRu/C catalysts prepared from new precursors by thermal reduction for direct methanol fuel cell. J Electrochem Soc 2005;152. A2406-A12.

Xing, L., Liu, X., Alaje, T., Kumar, R., Mamlouk, M. and Scott, K. (2014). A two-phase flow and non-isothermal agglomerate model for a proton exchange membrane (PEM) fuel cell. Energy, 73, pp.618-634.

Turkey's hydrogen scenario and Hydrogen production in the Thrace Basin versus hydrogen regulations and standards

Erhan Atay[1], Sudi Apak[2]

[1]Department of Ind. Ing, Esenyurt University, Istanbul, Turkey
[2]Department of Economics, Trakya University, Edirne, Turkey

Access to cheap energy is vital to economic growth. It is well known that energy will be a blade runner issue for the 2050s world. The idea of renewable energy has been a hot topic in recent years, as it has been heavily debated in both the business and investing world. But, today technological race is between volatile fossil fuels such as natural gas and renewable energy sources. Nowadays, an attractive environmental framework has been established in Turkey for the development of renewable energy. This has resulted in a strong increase of investors' interest, especially in the Thrace Basin mainly due to their renewable energy potential related to recently natural gas discovery at the Black sea region.♀

The paper aims to estimate the market share of hydrogen energy products in the economy considering the financial introducing of hydrogen energy investments at Thrace Basin-Istranca area in Turkey. Therefore, hydrogen energy and hydrogen products markets are growing rapidly. Turkey should support investments in the areas of hydrogen energy and technologies that have been developing all over the world. Thus, this research aims to analysis a comprehensive evaluation of the renewable energy in reducing CO2 emissions to environmental protection for the Thrace Basin local area in Turkey.

Renewable energy in the Thrace basin which is a risk-mitigation measure against oil price volatility by replacing conventional generation with arguments in favor of hydrogen energy applications to the local environment commonly framed in terms of economic development and energy security.

Keywords: Thrace basin, The EU, Black sea, hydrogen energy, Agriculture in Thrace.

Development of Effective Cooling System for High Temperature PEM Fuel Cell

[1*] Yılser Devrim, [2]Kübra Pehlivanoğlu, [2]Ömer Erdemir, [2]Celal Yılmaz, [2]Hüseyin Devrim
[1] Atılım University, Energy Systems Engineering Department, Ankara, Turkey
[2] Teksis İleri Teknolojiler Ltd. Şti., METU Technopolis, Silikon Blok No:29, 06800 Ankara, Turkey Affiliation University, Faculty,

* E-mail: yilser.devrim@atilim.edu.tr

Abstract
High-temperature Proton Exchange Membrane Fuel cell (HT-PEMFC) has gained a lot of attention in recent years. It is due to a number of its unique features, such as higher CO tolerance, faster kinetics and simpler balance-of-plant design as compared to their traditional and low-temperature PEMFC (LT-PEMFC). One of the most common problems in HT-PEMFC systems is to be able to produce a system that has the gas and cooling liquid leak-tightness. Effective cooling system is critical for safe and efficient operation of HT-PEMFC stacks with high power. The present work is aimed at promoting the development of more effective encapsulated liquid cooling strategies for HT-PEMFC stack. Special liquid cooling system was designed to safely circulate this liquid in the system without any leakage. The stack temperature was effectively regulated by the liquid cooling system based on on-off control system. The use of a 10 cell HT-PEMFC is demonstrated, with a nominal power of ≈400 W at 0.5 A/cm^2. A maximum power of 500 W was obtained from the stack.

Keywords: PEM, fuel cell, high temperature, PBI, stack cooling, PEMFC.

I. Introduction

Fuel cell systems have gained attention in recent years and seem to be one of the most suitable alternatives for especially fossil fuel based power generation systems (Budak, 2018). Among different types of fuel cells, proton exchange membrane fuel cell (PEMFC) is considered to be the most promising candidate for the next generation power source for transportation, stationary, auxiliary and portable applications (Wang, 2011). High temperature proton exchange membrane fuel cells (HT-PEMFC) can be operated in the temperature range between 120°C and 200°C and have a number of potential advantages compared to low temperature PEMFC (LT- PEMFC), e.g., no need for humidification, high CO tolerance, and simplified heat management of the PEMFC system (Zhang, 2006; Song, 2011). Polybenzimidazole (PBI) membranes with doping some strong acids are used in HT-PEMFC because of their high thermal chemical stability. Base PBI membrane has low proton conductivity and when doped with strong acid it provided high proton conductivity.

Effective cooling is critical for safe and efficient operation of HT-PEMFC stacks for high power. The generated heat must be effectively removed to avoid overheating of the stack components. The cooling methods and cooling system designs also influence the power consumption, volume and mass of the HT-PEMFC stack. The cooling system design has a direct impact in meeting the durability, cost, and performance targets for commercialization (Zhang, 2012). Liquid coolant is the most common method of removing waste heat from higher power HT-PEMFC stacks (Larminie, 2006). Waste heat is transferred from the cells with the bipolar plates and into the liquid coolant which flows through separate cooling channels between selected cells. Heated coolant is then pumped to a separate heat exchanger where it is either rejected to ambient or used for alternative purposes such as heating (Fly, 2016).

This study concentrates on the investigation of different cooling strategies regarding the HT-PEMFC stack. Two cooling methods to maintain operating temperature in stacks with large active areas were analyzed. In the first cooling system the thermo oil flows through capsuled cooling cells, which are arranged between every fifth electrochemical cell. In the second method heat transfer oil flows through the HT-PEMFC stack in internal cooling channels used insulated copper pipes that are located on the backside of the cathode-side bipolar plate. In this study effect of cooling system on HT-PEMFC application was studied at 160°C. Polarization curves were measured in order to quantify the cell performance for all conditions. The results from this work can provide better understanding on liquid based cooling strategies of HT-PEMFC systems.

II. Experimental Set-up and Procedure

The HT-PEMFC stack consists of ten cells, each with an active area of 163.5 cm^2. Graphite bipolar plates with custom designed prepared by CNC machining. Current collectors were made up gold coated copper plates to improve electrical conductivity and corrosion resistant. Tab.1 summarizes the HT-PEMFC stack components and design parameters.

The HT-PEMFC stack temperature was controlled by the two different thermo oil based cooling&heating system based on on-off control system. In the first method, HT-PEMFC stack with thermo oil based liquid cooling have been designed and demonstrated with additional inserted cooling plates (Fig. 1a). The oil flows through capsuled cooling cells, which are arranged between every fifth cell. A five port cooling channel was used in cooling plates. In the second method heat transfer oil flows through the HT-PEMFC stack in internal channels that are located on the backside of the cathode-side bipolar plate (Fig. 1b). Insulated Copper pipes were used in these channels to separate thermo oil and prevent liquid leakage. Heat is removed from the liquid cooled stack via circular cooling channels in the bi-polar plates between cells.

Tab. 1:HT-PEMFC stack components and design parameters

Design Parameters	
Active Area	163.5 cm^2
Membrane	H_3PO_4 doped PBI
Catalyst loading	1 mg/cm^2
Flow pattern	Serpentine
Bipolar plate	Graphite
Current collectors	Gold coated copper
End Plates	Aluminium
$P_{anode}=P_{cathode}$	1.2 atm
$\lambda_{anode}= \lambda_{cathode}$	1.2/2.5
Cell Number	10
Cooling liquid	Thermo-oil
Humidification	Dry anode & cathode

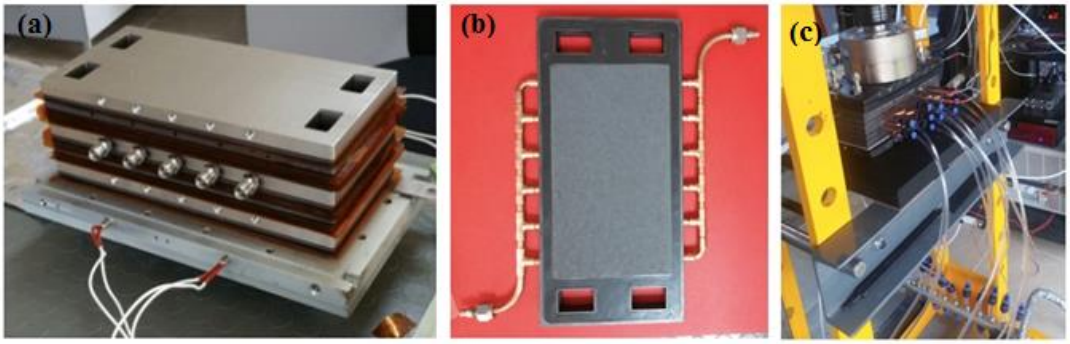


Fig. 1: a) Capsulated cooling plate b) New-cooling design c) HT-PEMFC stack with new cooling design

III. HT-PEMFC Performance Tests

High temperature performance tests were performed by the HT-PEMFC test station. The test station equipped with a reactant gas supply unit, electronic load, data logger computer, was used to performance test of the stack. The current and voltage of the cellswere monitored and logged throughout the operation by the test software. When the outlet temperature of the coolant has reached 120°C, air and H_2 were fed to the stack. Dry N_2 was used to verify that there were no leaks of reactant gases. Anode side gas stream from high-pressure tank was fed to the test cell via electronic mass flow controllers. After compressor, air was fed to dryer to supply dry air. The dry air was fed to the cell by using compressor and controlled via another mass flow controller. All tests were run with a stoichiometric ratio of 1.2 at the anode using H_2 and 2.5 using dry air at the cathode.

IV. Results and discussions

In the first cooling method the thermo oil flows through capsuled cooling cells, which are arranged between every fifth electrochemical cell. The capsuled stainless steel cooling cells showed no sealing problems during operation. The temperature difference was distributed sufficiently homogeneous over the stack. However, due to the different expansion properties of the graphite and metal bipolar plates, the graphite plates were broken during the cooling of the stack.

Generally, for internal cooling, thermo oil flows through the HT-PEMFC stack in internal channels that are located on the backside of the cathode-side bipolar plate. A penetration of termo oil into the MEA can be observed, which will lead to non-reversible MEA degradation up to the total failure of the stack for internal cooling. Due to the sealing problem of the internal oil cooling method, new desing was used with copper wire cooling pipes inserted the internal cooling channels and thermo oil was used in these pipes. The copper pipes placed to the cooling channels are insulated with a special material to electrically isolate. By means of new design the very small temperature differences within the active area and each cells of the stack were obtained.

The HT-PEMFC performance results of 10 cells stack at 160°C are shown in Fig.2. The termo oil was was fed to the system using the circulator. A temperature difference of ± 5°C was also determined on the bipolar plates of the HT-PEMFC stack. The low temperature difference between the bipolar plates indicates that efficient cooling was achieved new cooling system.

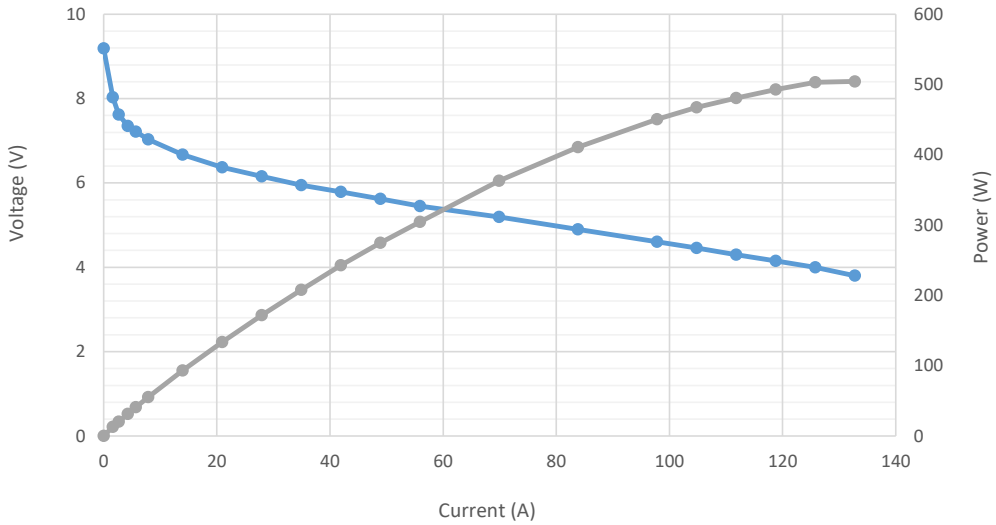


Fig. 2: HT-PEMFC stack performance at 160oC using dry H_2 and air for new design cooling system.

V. Conclusions

In this work, the effect of cooling system on HT-PEMFC stack was studied at 160°C using dry H_2 and air. Thermo-oil based cooling has proven very suitable because of the high heat transport capacity of the oil. Two different cooling system were investigated to balance the temperature and the homogenous temperature gradients within the stack. The internal oil cooling of every f cell with capsuled stainless steel cooling cells showed no sealing problems but it has caused to crack of bipolar plates during cooling period due to the differenr thermal expansion of the graphite and steel. HT-PEMFC stack temperature was efficiently regulated by the new designed on-off liquid cooling system without any leakage and bpola plate crack during cooling. A maximum power of 500 W was obtained from the HT–PEMFC stack.

Acknowledgements

This study was supported by The Scientific and Technological Research Council of Turkey (TUBITAK) ut nder project EUREKA TUBITAK 1509-9130085.

References

Budak, Y., Devrim, Y., Investigation of micro-combined heat and power application of PEM fuel cell systems, Energy Conversion and Management, 160, 486–494, (2018).

Fly, A., Thring, R.H., A comparison of evaporative and liquid cooling methods for fuel cell vehicles,International Journal of Hydrogen Energy, 41, 14217-14229, (2016).

Larminie, J., Dicks, A., Fuel Cell Systems Explained, (2nd ed.), Wiley, (2006).

Song, T.W., Choi, K.H., Kim, J.R., Yi, J.S., Pumpless thermal management of water-cooled hightemperature proton exchange membrane fuel cells," Journal of Power Sources, 196(10), 4671-4679, (2011).

Wang, Y., Chen, K.S., Mishler, J., Cho, S.C., Adroher, X.C., A review of polymer electrolyte membrane fuel cells: technology, applications, and needs on fundamental research, Applied Energy, 88, 981-1007, (2011).

Zhang, J., Xie, Z., Tang, Y., Song, C., Navessin, T., Shi, Z., Song, D., Wang, H., Wilkinson, D., High temperature PEM fuel cells, Journal of Power Sources, 160 (2), 872-891, (2006).

Zhang, G., Kandlikar, S.G., A critical review of cooling techniques in proton exchange membrane fuel cell stacks, International Journal of Hydrogen Energy, 37, 2412-2429, (2012).

In–situ and downstream desulfurization ability of PbO and ZnO during pyrolysis and hydrogenation of a high–sulfur lignite

[1]Arzu Kanca, [2*]Deniz Uner
[1] Ataturk University, Department of Chemical Engineering, Erzurum, 25240, Turkey.
[2] Middle East Technical University, Department of Chemical Engineering, Ankara, 06800, Turkey.

* E-mail: uner@metu.edu.tr

Abstract
This study addresses in–situ and downstream sulfur capture ability of lead oxide (PbO) in comparison to zinc oxide (ZnO) during the pyrolysis and hydrogenation of high–sulfur Tuncbilek lignite. Sulfidation reaction thermodynamics of these two compounds was compared to most commonly used metal oxides i.e., FeO, MnO, and CaO. The equilibrium conversions indicated superior performance of PbO and ZnO towards sulfidation reactions at high temperatures. The final compounds formed after each process were observed by X-ray diffractometer (XRD) and Diffuse Reflectance Infrared Fourier Transformation Spectroscopy (DRIFTS). XRD analyses results revealed that PbO can be used as hot gas sulfur trap during pyrolysis and hydrogenation processes, while ZnO can hold up sulfur only in the presence of hydrogen. Furthermore, both PbO and ZnO show the superior sulfur capture performance in the presence of hydrogen when they were used as adsorbents located after the reactor (downstream) at ambient conditions.

Keywords: Pyrolysis, hydrogenation, sulfidation of PbO and ZnO

I. Introduction

Hydrogen sulfide (H_2S) removal is one of the major problems resulting from high sulfur containing coal. In addition to the positive effects on environmental waste minimization and hydrogen and sulfur recovery, high temperature desulfurization process prevents the decrease in overall efficiency of the power generation systems. As a result, hot gas desulfurization process is a special research interest. For most of these metal oxides, the sulfidation reactions are favorable thermodynamically at relatively low temperatures, requiring cooling of the hot gas (Westmoreland and Harrison 1976, Vamvuka, Arvanitidis et al. 2004, Yi 2004).

Meng et al. (Meng, de Jong et al. 2010) summarized the desulfurization studies in a comprehensive review paper. According to the review study, sulfur adsorbents should have high sulfur capture capacity, fast kinetics, easy regenaration ability, and mechanical and thermal stability as main features. They classified the desulfurization as in–situ desulfurization produced by Ca based sorbents and downstream desulfurization performed by metal oxides, supported metal oxides, and mixed metal oxides. The sulfur capturing performance of CaO, ZnO, FeO, CuO, and MnO were also critically evaluated in their article (Meng, de Jong et al. 2010).

The oxides of Ca, Zn, Mn, and Fe are some of the sulfur sorbents and the several combinations of these metals may increase the sulfur removal efficiency. Despite the disadvantages of a toxic compound such as Pb, very high free energies of formation of PbS from PbO and the utilization of PbO as an efficient sulfur adsorbent/absorbent merits investigation. Lamoreaux et al. (Lamoreaux, Hildenbrand et al. 1987) compiled the thermodynamic and experimental studies in literature on the high temperature vaporization behavior of several metal oxides including PbOx. According to thermodynamic calculations, condensed phase PbO is stable at above 527ºC under reducing (10-15 bar), oxidizing (0.2 bar) and neutral conditions. PbO polymers (Pb_2O_2, Pb_3O_3, Pb_4O_4, Pb_5O_5, Pb_6O_6) were found as the primary species in the vapor phase under neutral and oxidizing media, while atomic Pb was the main species under reducing condition (Lamoreaux, Hildenbrand et al. 1987).

II. Experimental Set-up and Procedure

The pyrolysis and hydrogenation reactions were conducted in a home built reactor system equipped with a home built furnace with temperature control ranging from 40ºC to 800ºC under a temperature ramp of 5ºC/min. Approximately 500 mg of sample was placed in a quartz reactor fastened by quartz wool at both ends. Pyrolysis was conducted under 200 cc/min N_2 flow. Hydrogenation reactions were conducted under a hydrogen flow rate of 50 cc/min.

In order to follow the sulfur capture ability of PbO and ZnO at reaction conditions mentioned above, lignite samples were mixed with MeO (commercial PbO and ZnO) in the MeO to coal weight ratio of 2 to 1. The downstream sulfidation performance of these materials were also tested by using a fixed bed of glass fragments coated with either ZnO or PbO.

III. Analysis

The extent of the sulfidation reactions were followed by XRD and DRIFTS. The XRD experiment was performed using a Rigaku-Miniflex diffractometer using Cu Ka-ray radiation (l=1.5405 Aº) operating at 30 kV and 15 mA. DRIFTS measurements were conducted using a Perkin Elmer Spectrum 100 FTIR spectrometry in diffuse reflectance mode. After the sample was diluted with a non-absorbing material (KBr), the mixture was placed in a sample holder. 16 scans were collected with 4 cm^{-1} resolution in the range of 4000 cm^{-1}–450 cm^{-1}.

IV. Results and discussions

Sulfidation thermodynamics

The equilibrium conversions of sulfidation reactions of CaO, FeO, MnO, ZnO and PbO based on the data collected from (Barin 1989) were presented in Figure 1. It is clear from the results presented in Figure 1 that sulfidation reactions of all of these oxides are favorable especially at temperatures less than 227ºC. However, equilibrium conversion values decrease with increasing temperature for CaO, FeO, MnO, and ZnO. Due to high free energies of formation of the sulfide, PbO sulfidation reaction is the most favorable at high temperatures.

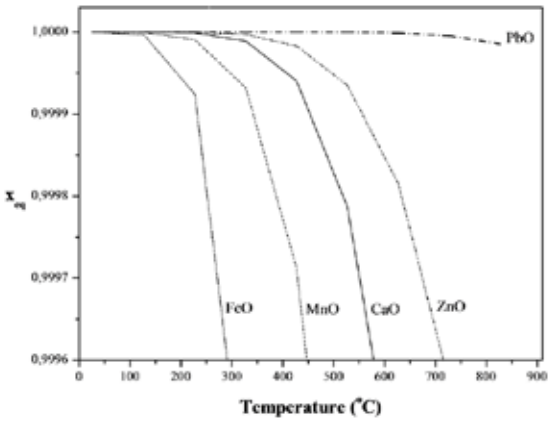


Fig. 1: Equilibrium conversions of CaO, MnO, PbO, ZnO, and FeO reduction with H_2S.

MeS formation

After the pyrolysis and hydrogenation processes was presented in the absence of MeO, the structural changes during the pyrolysis and hydrogenation processes tested in the presence of PbO and ZnO were investigated. The XRD patterns of unprocessed lignite (Figure 2a), the pyrolysis and hydrogenation residues of lignite–PbO mixtures (Figure 2b and 2c), and commercial PbO (Figure 2d) as a reference compound are presented in Figure 2. As seen in the figure, XRD pattern of unprocessed lignite (Figure 2a) is different from XRD patterns of pyrolysis (Figure 2b) and hydrogenation residues (Figure 2c), while XRD patterns of residues are similar to each other. This finding justifies that coal crystalline structure has changed during pyrolysis and hydrogenation.

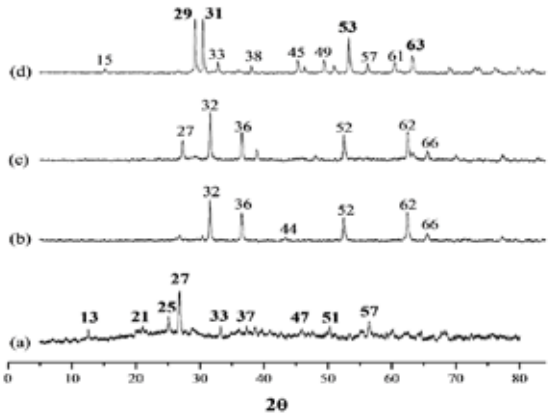


Fig. 2: XRD patterns of (a) unprocessed lignite, (b) PbO/coal=2 after pyrolysis, (c) PbO/coal=2 after hydrogenation, and (d) commercial PbO.

The XRD patterns of unprocessed lignite (Figure 3a), pyrolysis and hydrogenation residues of ZnO/coal=2 samples (Figure 3b and 3c), and commercial ZnO (Figure 3d) are shown in Figure 3. The first observation is the change in coal crystalline structure after pyrolysis process in the presence of ZnO (Figure 3a and 3b). Furthermore, XRD patterns of pyrolysis (Figure 3b) and hydrogenation (Figure 3c) residues are different from each other. As seen in Figure 3b, there is no change observed in XRD pattern of ZnO/ coal=2 pyrolysis residue and commercial ZnO.

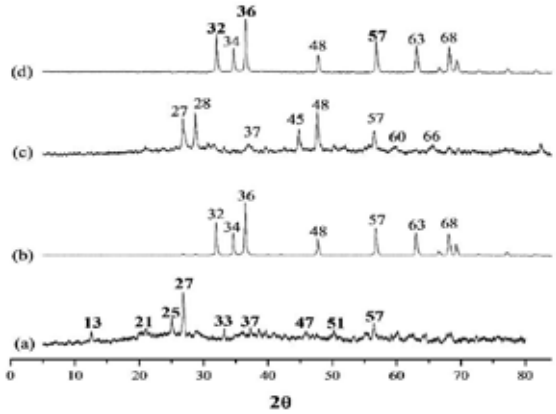


Fig. 3: XRD pattern of (a) pure coal, (b) ZnO/coal=2 after pyrolysis, and (c) ZnO/coal=2 after hydrogenation, and (d) commercial ZnO.

Although XRD pattern of ZnO/coal=2 sample after hydrogenation (Figure 3c) shows that characteristic ZnO peaks are still present in the ZnO hydrogenation residue, the new peaks at 27º, 29º, 45º, 60º, and 66º were also formed during hydrogenation. The specific Bragg angle values of ZnS were reported as 29º, 48º, and 56º (Balaz, Balintova et al. 1997, Nanda, Sapra et al. 2000, Li and Tang 2007, Ashwini, Pandurangappa et al. 2012). As a result, these new peaks can indicate the formation of ZnS and sulfur capture ability of ZnO in the temperature range of 40ºC to 800ºC under 50 cc/min H_2 flow.

As mentioned in experimental part, in addition to in–situ sulfur capture behaviors of PbO and ZnO tested at reaction conditions, the downstream sulfidation reaction of these oxides were examined under ambient conditions only during hydrogenation. XRD patterns of PbO and ZnO coated glass fragments after hydrogenation are illustrated in Figure 4. The Bragg angle values of PbO doped glass fractures are observed at 31º, 30º, 53º, 63º, 45º, 50º, 61º, and 69º, while in the presence of ZnO coated glass fractures, these values are 36º, 56º, 63º, 68º, 31º, 47º, 34º, and 69º.

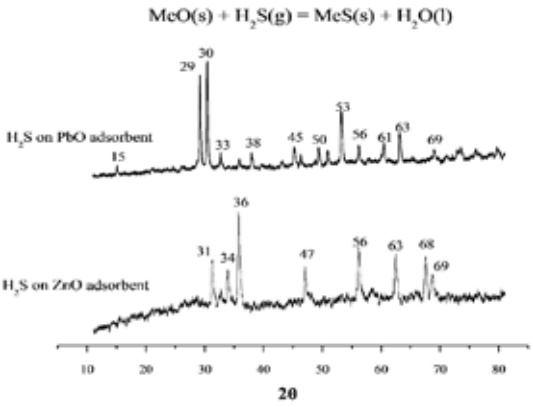


Figure 6. XRD results of downstream part of PbO and ZnO after hydrogenation process.

The possible sulfur containing Zn and Pb compounds and their Bragg angle values were collected in Table 1. The peaks at 30º, 63º, and 69º were found to be related to sulfur containing Pb. Similarly, the peaks at 36º, 47º, and 56º can be considered as the possible sulfidation products of Zn.

Tab. 1: XRD databank for Pb and Zn based compounds.

Substances	2Θ		
PbS	30.1	26.0	43.1
PbS	54.0	69.0	71.0
$PbOPbSO_4$	26.7	30.3	30.3
$PbSO_4$	24.6	35.1	41.4
$PbSO_4$	21.5	29.0	44.0
ZnS	28.6	47.5	56.3
$ZnSO_4$	21.4	35.3	41.7

V. Conclusions

In conclusion, thermodynamic calculations indicated the superior hot gas desulfurization performance of PbO during the pyrolysis and hydrogenation processes. The comparison of PbO with respect to ZnO indicated that PbO can capture sulfur during both pyrolysis and hydrogenation while ZnO sulfidation was found to be possible only for hydrogenation process at reaction conditions. The favorable downstream sulfur hold up performance of these two compounds were also reported during hydrogenation process. Further studies are in progress to justify the PbS and ZnS formation during pyrolysis and hydrogenation processes of high sulphur lignites.

Acknowledgements

The authors are grateful for Turkish Coal Enterprises for coal samples and partial financial support for this project. One of the authors (A.K.) is supported by the State Planning Organization under the auspices of OYP program.

References

Barin I., Ed., Thermochemical data of pure substances, New York : VCH, (1989).

Lamoreaux R. H., Hildenbrand D. L., and Brewer L., High-temperature vaporization behavior of oxides. 2: Oxides of Be, Mg, Ca, Sr, Ba, B, Al, Ga, In, Tl, Si, Ge, Sn, Pb, Zn, Cd, And Hg, Journal of Physical and Chemical Reference Data, 16(3), 419-443, (1987).

Meng X. M., de Jong W., Pal R., and Verkooijen A. H. M., In bed and downstream hot gas desulphurization during solid fuel gasification: A review, Fuel Processing Technology, 91(8), 964-981, (2010).

Vamvuka D., Arvanitidis C., and Zachariadis D., Flue gas desulfurization at high temperatures: A review, Environmental Engineering Science, 21(4), 525-547, (2004).

Westmoreland, P. R. and Harrison D. P., Evaluation of candidate solids for high-temperature desulfurization of low-btu gases, Environmental Science & Technology, 10(7), 659-661, (1976).

Maturity Impact on Hydrogen Production from Natural Gas and Coal: Examples from Dadaş Shale and Zonguldak Coals

***Şamil Şen*[1], Hüseyin Kozlu[2], Ilyas Erdal Kerey[3], Güngör Çelik[4]**

[1]Geology Department, Istanbul University, Istanbul, Turkey
[2]Turkish Petroleum, Exploration Group, Ankara, Turkey
[3]Civil Engineering Department, Istanbul Rumeli University, Silivri, Turkey
[4]Mining Department, Istanbul University, Istanbul, Turkey

98% of the hydrogen production is made by natural gas reforming and coal gasification. Simplifed formules are CH4 + ½O2 → CO + 2H2 (+ heat), CH0.8 + O2 + H2O → CO + CO2 + H2 and CO + H2O → CO2 + H2 (+heat). Thus, carbon and hydrogen contents of the natural gas and coals are very important to hydrogen production and low carbon dioxide gas emission. According to organic geochemical studies, increase in the maturity of shale (gas source rock) and coal with Time-Temperuture Index cause to decrase of Total Organic Carbon (TOC) and Hydrogene Index (HI). For example, maturity increase in the Dadaş shale and Zonguldak coals were caused to decrease in the TOC and HI. In addition, HI has recently been used to maturity indicator of oil and gas (biogenic gas, wet gas-condensate and dry gas) generation from shale and coals.

Keywords: Maturity, Hydrogen Production, Natural Gas, Coal

Investigation of a solar driven integrated TEG with PEM electrolyzer system for hydrogen production

*[1]Murat Emre Demir, [1,2]Ibrahim Dincer
[1]University of Ontario Institute of Technology, Faculty of Engineering and Applied Science, 2000 Simcoe Street North, Oshawa, Ontario L1H 7K4, Canada
[2]Yildiz Technical University, Faculty of Mechanical Engineering, Istanbul, 34349 Turkey

* E-mail: murat.demir@uoit.ca

Abstract
In this study, an integrated solar thermal driven system is conceptually developed for hydrogen, electricity and hot water production and thermodynamically analyzed. The proposed system consists of a solar dish collector, latent heat storage subsystem, proton exchange membrane (PEM) electrolyzer, thermoelectric generator (TEG) and hydrogen storage medium. The TEG unit is sandwiched between the latent heat storage and the heat exchanger. The water is pumped from a reservoir to a heat exchanger where it is heated before electrolysis to improve the overall system performance with a novel configuration, consisting a solar dish collector and a thermoelectric generator embedded with a heat exchanger. After the water leaves the heat exchanger, it enters the PEM electrolyzer for water splitting. The electricity needed for the PEM electrolyzer is supplied by the TEG. While the produced hydrogen is sent to a storage medium, unreacted excessive hot water is sent to the residential heating subsystem. NaOH is selected as the phase change substance and Bi_2Te_3 is chosen for the TEG. The COMSOL Multiphysics software package is used for the numerical modelling of the thermoelectric generator. The remaining elements of the integrated system are analyzed in Engineering Equation Solver (EES). The overall energy and exergy efficiencies are determined to be 6.5% and 6.4%, and H_2, hot water and electric power generation capacity of the system are then calculated.

Keywords: Hydrogen production; power production; solar energy; thermoelectric generator; thermal energy storage; energy; exergy; efficiency

I. Introduction

Energy is one of the significant factor for industrial developments, human welfare, global politics and the environment. To maintain our daily works, we are dependent on ample and continuous energy supply is. The World Bank data of energy consumption indicates that, 78% of global demand is met by fossil fuels. Furthermore, utilization of carbon-based fuels pollutes the environment in crucial levels. Fossil fuels are responsible for 87% of the carbon emissions caused by humans (World Bank, 2016). Thus, seeking for an alternative is not only reasonable, but it is now obligatory. It is of importance to focus renewables as a clean energy source. However, renewables are not reliable source without hybrid systems or energy storage options. Hydrogen (H_2) is a promising candidate to address these issues and can be utilized as an energy carrier due to its features such as having better conversion efficiency, being able to be yielded from water without carbon emissions, abundant presence in nature (Acar, Dincer, and Naterer 2016). Solar energy can be used in various H_2 generating applications including, artificial photosynthesis, photo-fermentation, PV-electrolysis, photo-electrolysis and thermochemical water splitting processes. The H_2 production via water electrolysis is one of the practical approaches without consumption of fossil.

The suggested system is presented in Fig. 1. The system consists of a solar dish collector, latent heat storage subsystem, proton exchange membrane (PEM) electrolyzer and thermoelectric generator (TEG), water and hydrogen storage mediums. First, the water is pumped from the reservoir to the heat exchanger where it is heated before electrolysis. The group of devices consisted of solar dish collector, thermoelectric generator embedded with a heat exchanger enhances the overall system performance in 5 ways. First, as the water passes through a heat exchanger and is heated the electrolysis efficiency increases and results in high yield hydrogen. Secondly, the TES system stores and provides the energy for the system when the solar irradiance is unavailable which allows the system being operated without interruption. Thirdly, as the thermoelectric generator rejects its heat to the water from TEG`s top side, a high-temperature gradient is formed between the bottom and the top side of the TEG which results in an increase of the induced thermoelectricity and heat to electricity efficiency. The fourth benefit of the solar subsystem is the availability of adjusting the system`s working range. Since the solar illumination is not directly focused on the TEG but the latent heat storage system, the thermoelectric device is prevented from overheated which may lead burning and malfunctioning of the device. By arranging the type and amount of phase change material in the thermal storage system, it is possible to adjust the operation range of the thermoelectric generator. Finally, the last main advantage of the solar subsystem is it eliminates the requirement of a voltage regulator. To maintain a constant thermoelectric output, it is of importance to keep the temperature difference between hot and cold sides of the TEG. Since the phase change of material occurs under constant temperature, the temperature fluctuations due to the variation of solar irradiance can be avoided by the presence of PCM. Hence voltage variations generated by the TEG is also avoided. After the water leaves the heat exchanger, it enters the proton exchange membrane electrolyser for water splitting. The TEG supplies the

electricity for the PEM electrolyser. While the produced hydrogen is sent to a storage medium, unreacted hot water is sent to the residential heating subsystem.

The COMSOL Multiphysics software package is utilized for the numerical modeling of the thermoelectric generator (COMSOL Inc n.d.). The remaining elements of the integrated system are analyzed in the Engineering Equation Solver (EES). The overall energy and exergy efficiencies of each system component are determined, and H_2, hot water, electric power generation capacity of the system is then calculated.

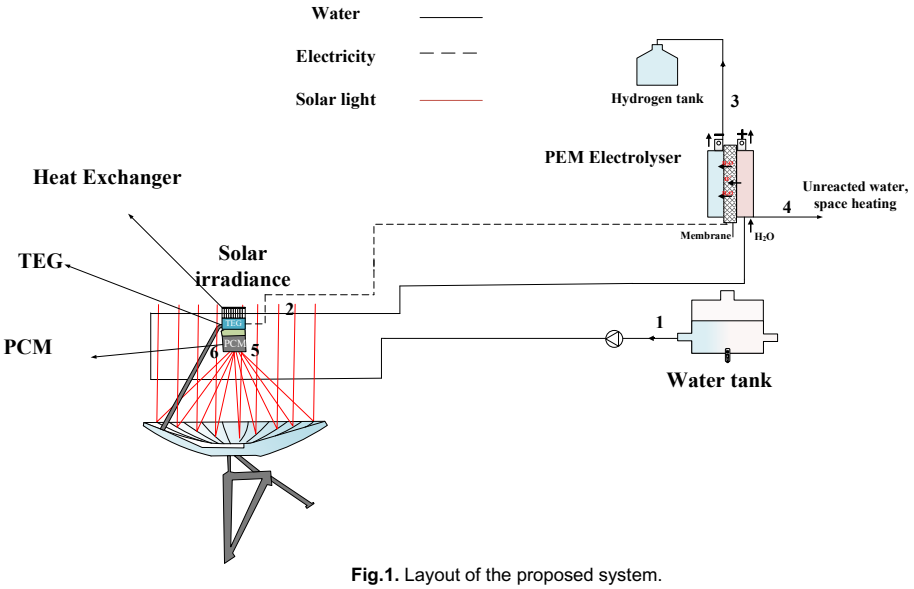


Fig.1. Layout of the proposed system.

II. Thermodynamic analyses

The thermodynamic analysis of the suggested system is carried out for four subsystems including solar dish collector, latent heat storage subsystem, thermoelectric generator unit and PEM electrolyser. All the system elements are explained in detail in this section. Firstly, the theoretical maximum reflected solar irradiance by the solar dish is obtained. By taking into account losses due to solar dish`s formation and material (reflectivity, the cosine effect, the shades and blocking effect) and heat losses through the surface of the receiver by convection and radiation actual captured solar heat is obtained. Then the transferred heat from PCM-TEG unit to water is obtained numerically by COMSOL. The numerical model also gives the temperature distribution on the legs of TEG and generated electricity by the TEG unit. PCM storage tank`s storage capacity and heat losses then calculated. A mathematical model (Demir and Dincer 2017) is built for the PEM electrolyser to estimate the produced hydrogen and system efficiency. The overall exergy losses for all components and their exergy efficiencies are tabulated in Table1. To assess the performance and behavior of the integrated system the following assumptions are made.

- The only chemical reaction takes place in the PEM electrolyser.
- The changes in the kinetic and potential energies are negligible.

In this study, PCM and water stream is utilized as the heat source and heat sink for the thermoelectric generator. To examine the performance and behavior of the TEG, modeling the heat transfer on the TEG has a vital significance. COMSOL Multiphysics software package is utilized to model and simulate the non-isothermal and turbulent fluid flow in the heat exchanger. k-ϵ model is selected in order to model the turbulent flow through the thermoelectric generator module. The continuity and momentum relations of the fluid flow is performed under steady-state conditions.

The outputs of the numerical solution are used in EES to obtain overall energy and exergy efficiencies of the system. The mesh structure and dimensions of the TEG module are presented in Fig. 2. A rectangular cross-sectional channel is placed at the top of the TEG unit and the bottom part of the TEG unit is connected to the PCM tanks surface to create and maintain the temperature difference between the sides of the TEG. In the numerical model, it is assumed that the hot side temperature of the thermoelectric leg is equal to the melting temperature of the selected PCM. Thermoelectric properties of the thermoelectric materials used in this study are tabulated in Table 2. Hydrogen, electricity and hot water production capacities are also determined.

Tab. 1: Exergy efficiency and exergy destruction rate definitions for the system components.

Component	Exergy Destruction Plus Loss Rate Definition	Exergy Efficiency Definition
PCM	$\dot{E}x_{d,PCM} = \dot{E}x_6 - \dot{E}x_5 - \dot{Q}_{out}\left(1-\frac{T_0}{T_{melt}}\right) + \dot{Q}_{in}\left(1-\frac{T_0}{T_{melt}}\right)$	$\psi_{PCM} = 1 - \frac{\dot{E}x_{d,PCM}}{\dot{Q}_{in}\left(1-\frac{T_0}{T_{melt}}\right)}$
HEX	$\dot{E}x_{d,HEX} = \dot{m}_2 ex_2 - \dot{m}_1 ex_1 - \dot{Q}_{HEX}\left(1-\frac{T_0}{T_{TEG,cold}}\right)$	$\psi_{HEX} = \frac{\dot{m}_2 ex_2 - \dot{m}_1 ex_1}{\dot{Q}_{HEX}\left(1-\frac{T_0}{T_{TEG,cold}}\right)}$
Thermoelectric Generator	$\dot{E}x_{d,TEG} = \dot{m}_1 ex_1 - \dot{m}_2 ex_2 - \dot{W}_{out,TEG}$	$\psi_{TEG} = \frac{\dot{W}_{out,TEG}}{(\dot{m}_1 ex_1 - \dot{m}_2 ex_2)}$
Solar Receiver	$\dot{E}x_{d,SR} = \dot{m}_6 ex_6 - \dot{m}_5 ex_5 + \dot{Q}_{SR}\left(1-\frac{T_0}{T_{sun}}\right)$	$\psi_{SR} = \frac{(\dot{m}_6 ex_6 - \dot{m}_5 ex_5)}{\dot{Q}_{SR}\left(1-\frac{T_0}{T_{sun}}\right)}$
PEM Electrolyzer	$\dot{E}x_{d,El} = \dot{W}_e + \dot{m}_{H_2O} ex_{H_2O} - \dot{m}_{H_2} ex_{H_2}$	$\psi_{El} = \frac{\dot{m}_{H_2} ex_{H_2}}{\dot{W}_e + \dot{m}_{H_2O} ex_{H_2O}}$

Tab. 2: Properties of the thermoelectric materials(COMSOL Inc n.d.).

Thermoelectric Material	k (W/m K)	σ (S/m)	μS (V/K)
n & p type Bi_2Te_3	1.9	111,110	± 192 (negative value for n, positive value for p type)

The PEM electrolyser considered in this study is driven by the induced thermoelectricity. The heated water stream enters the electrolyser for decomposition. While the produced hydrogen is sent to the storage for later usage, unreacted water is utilized for domestic heating. The energy efficiency of the reactor is defined as the ratio between the energy input to the electrolyser and theoretical maximum amount of heat released by combustion of the yielded hydrogen. By taking into account all the system inputs and outputs, the overall energy and exergy efficiencies of the system are defined as follows:

$$\eta_{ov} = \frac{\dot{m}_{H_2} HHV_{H_2} + \dot{W}_{net,e} + \dot{m}_{H_2O}(\Delta h)}{\dot{Q}_{solar}}, \quad \psi_{ov} = \frac{\dot{m}_{H_2} HHV_{H_2} + \dot{W}_{net,e} + \dot{E}x_4}{\dot{E}x^{Q_{solar}}} \tag{1}$$

As the water input to the PEM electrolyser is relatively high compare to the produced hydrogen, its effect dominates the efficiency definition. In order to better understand the system performance another efficiency definition is used in which exludes the water flow energy for space heating is

$$\eta_{ov,2} = \frac{\dot{m}_{H_2} HHV_{H_2} + \dot{W}_{net,e} + \dot{m}_{H_2O}(\Delta h)}{\dot{Q}_{solar}}, \quad \psi_{ov,2} = \frac{\dot{m}_{H_2} HHV_{H_2} + \dot{W}_{net,e} + \dot{E}x_4}{\dot{E}x^{Q_{solar}}} \tag{2}$$

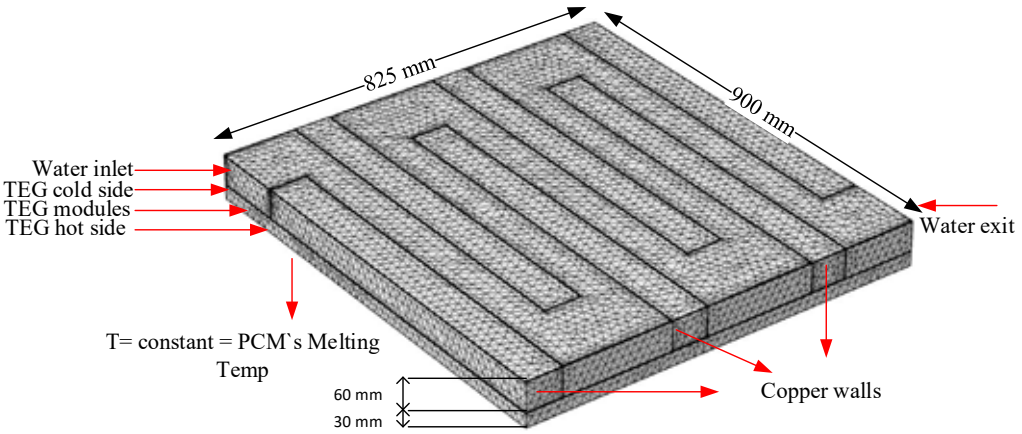


Fig. 2: TEG unit used in the study.

III. Results and discussions

The thermodynamic calculations of the system components are performed by both EES and COMSOL Multiphysics software. The overall energy and exergy efficiencies of the system overall system for the cases where unreacted water is sent for space heating applications are calculated as 93.7% and 9.3% respectively. As the most of the heat is utilized for district heating and solar heat used as heat in the final product, the energy efficiency is obtained considerably high. On the other hand, the quality of the energy is drastically drop in the heat exchanger part. PCM at 323°C is used for heating water from about 25°C to 44°C which results in a massive entropy generation and exergy destruction for that part. Hence energy efficiency is found high where the exergy efficiency is obtained relatively low. In order to better understand the system performance another efficiency definition is used which excludes the space heating load on the overall system ($\eta_{ov,2}$ and $\psi_{ov,2}$). These energy and exergy efficiencies are found to be 6.5% and 6.4%. The overall exergy losses calculated as 779 kW for the combined system.

The Bi2Te3 based TEG produces 67.4 kW electricity with a heat to electricity efficiency of 8.5%. 33.7 kW of the thermoelectric power is utilized for electrolysis process. Based on the developed mathematical model, the electrolyser is producing 12.32 kg H2/day with a 77.4% energy efficiency. It is obtained that by increasing the water`s temperature from 25°C to 44.2°C it is possible to enhance electrolyser efficiency by 4.7%. Which also means by rejecting heat from the TEG to the water stream, 1.1 kg more hydrogen can be manufactured, besides the induced thermoelectric power.

IV. Conclusions

In this study, a solar-driven system including TEG, PEM electrolyzer and latent heat storage system, for electricity, hydrogen (H_2) production and space heating is proposed and analyzed thermodynamically. The concluding remarks are stated as follows:

- The overall energy efficiency of the system is calculated as be 6.5% (93.7% if the water stream is utilized in district heating).
- The overall exergy efficiency of the system is calculated as 6.4%(9.3% if the water stream is utilized in district heating).
- The electrical energy output of the system is 33.71 kW.
- The heating capacity of hot water is calculated as 724.6 kW.
- The total hydrogen production capacity per day is 12.32 kg.
- The hydrogen production is improved by 1.1 kg/day by increasing the operating temperature of PEM with from 25°C to 44.4°C.
- The PCMs lead less temperature fluctuation for the TEG, which provides a constant rate of power.

References

Acar, Canan, Ibrahim Dincer, and Greg F. Naterer. 2016. “Review of Photocatalytic Water-Splitting Methods for Sustainable Hydrogen Production.” *International Journal of Energy Research* 40(11): 1449–73.

COMSOL Inc. “COMSOL Multiphysics® Modeling Software.” www.comsol.com.

Demir, Murat Emre, and Ibrahim Dincer. 2017. “Development of A Hybrid Solar Thermal System With TEG and PEM For Hydrogen And Power Production.” *International Journal of Hydrogen Energy*.

World Bank. 2016. “Fossil Fuel Energy Consumption.” *Data, Energy: Fossil fuels consumption*. http://data.worldbank.org/indicator/EG.USE.COMM.FO.ZS.

Investigation of Thermochemical Cycles for Hydrogen Production

[1*]Fatih YILMAZ, [2]Reşat SELBAŞ, [3]Murat OZTURK
[1]Department of Electrical and Energy, Vocational School of Technical Sciences, Aksaray University, 68100, Aksaray, Turkey
[2]Department of Energy System Engineering, Faculty of Technology, Suleyman Demirel University 32100, Isparta, Turkey
[3]Department of Mechatronic Engineering, Faculty of Technology, Suleyman Demirel University 32100, Isparta, Turkey

*E-mail: fatiyilmaz7@gmail.com

Abstract:
Hydrogen is one of the most promising fuel options for the future, and it is considered as a green energy carrier. Clean and sustainable hydrogen production pathways have become very important nowadays. Thus, thermochemical or hybrid cycles, one of the sustainable hydrogen production methods, has begun to gain importance in recent years. In this study, we investigated the hydrogen production ways with sustainable chemical methods. In this regard, the most commonly worked cycles in literature, which are the magnesium chlorine (Mg-Cl), copper chlorine (Cu-Cl) and sulfur iodine (S-I) thermochemical cycles, have been reviewed for hydrogen production. The general energy and exergy efficiencies of these cycles are presented as in the form of tables. Also, hydrogen production performance with these cycles are discussed and presented in terms of the pros and cons.

I. Introduction

A sustainable production and use of energy sources are one of the challenges faced by in today's society. Therefore, practical studies in improving of new methods, and also the reasonable use of energy sources are the critical important issues. For these mitigations, hydrogen energy has been become attractive in the recent years. The hydrogen economy presents a compelling vision of an energy future for the nation and world, which is, in the large quantities, clean, flexible and secure (Argonne National Laboratory, 2003). However, nowadays about 95% of hydrogen production is from fossil fuel sources, such as coal, oil and natural gas (Ewan and Allen, 2005). So, the negativity effect of hydrogen energy production and consumption continues. Therefore, for a sustainable and more environmentally friendly world, it is necessary to address the environmentally friendly hydrogen production methods such as thermochemical cycles. In this regard, many researchers, in recent years they have been working on the subject of hydrogen production, economy etc. (Balta et al. 2016).

Orhan et al. (2008), have presented a cost analysis of thermochemical cupper chlorine (Cu-Cl) cycle for nuclear based hydrogen generation. They have studied that various types of cost such as operation, maintenance, capital invest and fixed charges etc. Lewis and Masin (2009), have proposed alternative thermochemical cycles. They have defined nine cycles. Balta et al. (2016), have investigated a comparative assessment of chlorine family thermochemical cycles for hydrogen generation. They have examined that copper chlorine (Cu-Cl), magnesium chlorine (Mg-Cl), iron chlorine (Fe-Cl) and vanadium chlorine (V-Cl) cycles, which are driven by heat and/or electricity. Balta et al. (2012), carried out energy and exergy analyses of Mg-Cl thermochemical cycle for hydrogen generation. According to results of their study, the energy and exergy efficiency of this cycle have been calculated as 63.63% and 34.86%, respectively. Ozcan and Dicer (2014), have performed that performance evaluations of Mg-Cl hybrid thermochemical cycle for hydrogen generation. As can be understand from their study, the Mg-Cl cycle can compete with other lower temperatures of thermochemical water splitting cycles. Some of researcher (Carty et al., 1981; Beghi, 1986; Balte et al., 2010; Ozcan and Dincer, 201; Yilmaz and Selbas, 2017) published several studies on the various thermochemical cycles for hydrogen production over the last 40 years.

In this study, hydrogen production with Mg-Cl, Cu-Cl and S-I by thermochemical cycle was examined. In this regard, the energy and exergy efficiencies of these cycles were compared according to these studies in the literature. In this paper, these cycles are discussed and compared in terms of their pros and cons.

II. Thermochemical cycles

Thermochemical cycles are a good candidate, in which water splits into hydrogen and oxygen using a series of chemical reactions. All chemical intermediates are recycled internally within the process so that water is the only raw material and hydrogen and oxygen are the only products (Yildiz et al. 2006). Thermochemical processes include a thermal disassociation of water into hydrogen and oxygen through a series of thermally driven chemical reactions. The general schematic diagram of hybrid and thermochemical cycle is presented in Fig. 1.

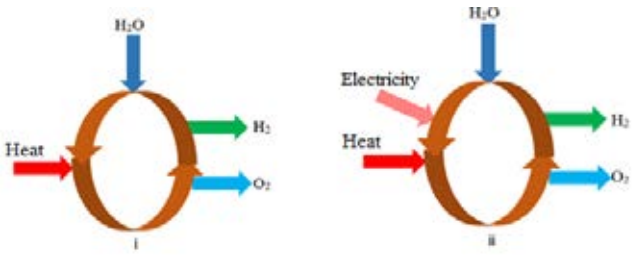


Fig. 1: The schematic diagram of thermochemical (i) and hybrid (ii) cycle

Mg-Cl Thermochemical cycle

In this study, three-step Mg-Cl thermochemical cycle is considered, and thermochemical cycles are given in Table 1. This cycle consists of three step that are step I, occurs at about 450 °C, step II is occurs 500 °C and the last step of Mg-Cl cycle is hydrogen production step occurs. The electrochemical reaction takes place in the last step at 80°.

Tab.1: The steps of the Mg-Cl cycle and temperatures

$MgCl_2 + H_2O = 2\,HCl + MgO$	450 °C
$MgO + Cl_2 = MgCl_2 + ½\,O_2$	500 °C
$2\,HCl = Cl_2 + H_2$	80 °C

Cu-Cl Thermochemical cycle;

In the literature, there are different configurations of Cu-Cl cycle. But, the most common investigated is four-step of Cu-Cl cycle. The Cu-Cl thermochemical cycle steps are given in Table 2. The maximum temperature requirement in this cycle is calculated approximately 500 °C. In additional, the electrochemical reaction takes place in the third step at 1000 °C.

Tab. 2: The steps of the Mg-Cl cycle and temperatures

$2CuCl_2+H_2O=2CuCl+2HCl+½O_2$	400-500 °C
$4CuCl+H_2O=2CuCl_2+2Cu$	25-80 °C
$CuCl_2(aq)=CuCl_2(s)$	>100 °C
$2Cu+2HCl=2CuCl+H_2$	430-475 °C

S-I Thermochemical cycle;

The S-I cycle is usage of the both heat and electricity to produce hydrogen from water at a maximum process temperature of 850 °C. As given in Table 3, the S-I cycle consists of the following three chemical reactions (Ozturk et al., 1994, 1995):

Table 3: The steps of the Mg-Cl cycle and temperatures

$H_2SO_4 \rightarrow H_2O+SO_2+ ½\,O_2$	850 °C
$I_2+SO_2+2H_2O \rightarrow 2HI+H_2SO_4$	120 °C
$2HI \rightarrow H_2+I_2$	450 °C

III. Analysis

The mass balance equations for steady state flow can be written as below;

$$\sum \dot{m}_{in} = \sum \dot{m}_{out} \quad (1a)$$

or

$$\sum \dot{m}_{R} = \sum \dot{m}_{P} \quad (1b)$$

where $\dot{m}$ is the mass flow rate, and the subscript in stands for inlet and out for outlet and also subscript R stands for reactants and P for products. The general energy balance can be expressed in the rate form as;

$$\dot{E}_{in} - \dot{E}_{out} = \Delta \dot{E}_{s} \quad (2)$$

which becomes ;

$$\dot{Q} - \dot{W} = \sum \dot{m}_{out} h_{out} - \sum \dot{m}_{in} h_{in} \quad (3)$$

where $\dot{Q}$ and $\dot{W}$ denote heat and work, respectively. The heat transfer for a chemical process involving no work is determined from the energy balance. For a steady-state reaction process, the energy balance reduces to;

$$\dot{Q} - \dot{W} = \sum n_P \left(\bar{h}_f^\circ + \bar{h} - \bar{h}^\circ\right)_P - \sum n_R \left(\bar{h}_f^\circ + \bar{h} - \bar{h}^\circ\right)_R \quad (4)$$

where $\bar{h}_f^\circ$ is specific enthalpy of formation, $\bar{h}^\circ$ is specific enthalpy at reference state and $\bar{h}$ is specific enthalpy in kJ/kmol, n stands for number of moles and subscripts R and P represents reactants and products, respectively. The last step of S-I cycle reaction III, involves electrolysis, the amount of electrical energy demand is calculated

using the Nernst equation in a given state, depending on the change in Gibbs free energy, ΔG, as shown by [14].

$$\Delta G = -nFE \quad (5)$$

where F denotes Faraday's constant, which is taken as 96485 C/mol, E is the cell potential of the cells and n is the number of moles of electrons exchanged in an electrochemical reaction. Electrical energy demand is determined by;

$$W_{el} = -\Delta G \quad (6)$$

After writing mass, energy and exergy balances for the system, the enthalpy and entropy values of each compound and elements of thermochemical cycles are evaluated with Shomate equations.

$$\bar{h} - \bar{h}_0 = AT + B\frac{T^2}{2} + C\frac{T^3}{3} + D\frac{T^4}{4} - E\frac{1}{T} + F - H \quad (7)$$

$$\bar{s} = A\ln(T) + BT + C\frac{T^2}{2} + D\frac{T^3}{3} - E\frac{1}{2T^2} + G \quad (8)$$

$$\eta_{overall} = \frac{LHV_{H2}}{\sum \dot{Q} + W_{el}} \quad (9)$$

$$\psi_{overall} = \frac{Ex_{H2}}{\sum E\dot{x}_Q + W_{el}} \quad (10)$$

where $\dot{Q}$ is the heat supplied to the cycle, as the lower heating value of hydrogen which is taken as 239.92 kJ/mol. W_{el} is the electrical energy demand for the electrolysis step in the thermochemical reaction.

4. Results and discussions

In this study, a performance assessment of three steps Mg-Cl cycle, four steps Cu-Cl cycle and three steps S-I cycle, which are commonly used in literature for hydrogen production, are investigated. Shomate equations are used for thermodynamic calculations of these cycles. Energy and exergy efficiencies of these cycles are presented in Table 4.

Tab. 4: Energy and exergy efficiencies of some thermochemical cycles in literature

Cycle	Type	Required max. temperature	Energy efficiency	Exergy efficiency	References
Mg-Cl	Hybrid	550 °C	43.7	52	Ozcan and Dincer (2016)
			18.8	19.9	Ozcan and Dincer (2014a)
			18.18	19.5	Balta et al. (2014)
			37.4	71	Ozcan and Dincer (2014b)
			16.31	17	Ozcan and Dincer (2017)
			63.63	34.86	Balta et al. (2012)
Cu-Cl	Hybrid	500-550 °C	66.92	72.06	Ratlamwala and Dincer (2012)
			21.67	19.35	Balta et al. (2010)
			40.2	48.2	Ratlamwala and Dincer (2013)
			55.4	66	Ozbilen et al. (2014)
			45	10	Orhan et al. (2009)
			43	70	Orhan et al. (2012)
S-I	Hybrid	850 °C	43.85	62.39	Yilmaz and Selbas (2017)
			40.86	-	Zhang et al. (2013)
			66.3	-	Zhou et al. (2007)

Many researchers have evaluated the performance of hydrogen production through thermochemical or hybrid cycles in the literature with energy efficiency. Mg-Cl and Cu-Cl thermochemical cycles are more prominent in these studies. The energy efficiency for hydrogen production range between 18-65% for Mg-Cl cycle and 15-66% for Cu-Cl cycle according to previous studies. However, these values vary according to the heat source of the system. As a source of heat, it is usually studied with solar, geothermal and nuclear energies sources.

5. Conclusions

In this paper, we performed a reviewed of Mg-Cl, Cu-Cl and S-I cycles for hydrogen production. Moreover, the energy and exergy efficiencies of these cycles are compared and presented. As a result, Mg-Cl and cu-Cl cycles are generally studied in the literature because of the good potential in low temperature cycles. Nevertheless, the work on the S-I cycle is scarce. The S-I cycle must be further developed to compete with the Mg-Cl and Cu-Cl cycles.

References:

Argonne National Laboratory. Basic research needs for the hydrogen economy. Report of the basic energy sciences.

Balta MT, Dincer I, Hepbasli A. Geothermal-based hydrogen production using thermochemical and hybrid cycles: a review and analysis. Int J Energy Res 2010;34(9):757-75.

Balta, M. T., Dincer, I., & Hepbasli, A. (2010). Energy and exergy analyses of a new four-step copper–chlorine cycle for geothermal-based hydrogen production. Energy, 35(8), 3263-3272.

Balta, M. T., Dincer, I., & Hepbasli, A. (2012). Energy and exergy analyses of magnesium-chlorine (Mg-Cl) thermochemical cycle. International Journal of Hydrogen Energy, 37(6), 4855-4862.

Balta, M. T., Dincer, I., & Hepbasli, A. (2016). Comparative assessment of various chlorine family thermochemical cycles for hydrogen production. International Journal of Hydrogen Energy, 41(19), 7802-7813.

Beghi GE. A decade of research on thermochemical hydrogen at the joint research centre. ISPRA Int J Hydrogen Energy 1986;11(12):761-71.

Carty RH, Mazumder MM, Schreider JD, Pangborn JB. Thermochemical hydrogen production1e4. Chicago, IL: Gas Research Institute for the Institute of Gas Technology; 1981. GRI-80/0023. workshop on hydrogen production, storage and use. May 13-15, 2003. p. 3

Ewan BCR, Allen RWK. A figure of merit assessment of the routes to hydrogen. Int J Hydrogen Energy 2005;30:809-19.
Lewis, M. A., & Masin, J. G. (2009). The evaluation of alternative thermochemical cycles–part II: the down-selection process. International Journal of Hydrogen Energy, 34(9), 4125-4135.

Orhan, M. F., Dincer, I., & Naterer, G. F. (2008). Cost analysis of a thermochemical Cu–Cl pilot plant for nuclear-based hydrogen production. International Journal of Hydrogen Energy, 33(21), 6006-6020.

Orhan, M. F., Dincer, I., & Rosen, M. A. (2009). Efficiency analysis of a hybrid copper–chlorine (Cu–Cl) cycle for nuclear-based hydrogen production. Chemical Engineering Journal, 155(1-2), 132-137.

Orhan, M. F., Dinçer, İ., & Rosen, M. A. (2012). Efficiency comparison of various design schemes for copper–chlorine (Cu–Cl) hydrogen production processes using Aspen Plus software. Energy conversion and management, 63, 70-86.

Ozbilen, A., Dincer, I., & Rosen, M. A. (2014). Development of new heat exchanger network designs for a four-step Cu–Cl cycle for hydrogen production. Energy, 77, 338-351.

Ozcan, H., & Dincer, I. (2014a). Energy and exergy analyses of a solar driven Mg–Cl hybrid thermochemical cycle for co-production of power and hydrogen. International Journal of Hydrogen Energy, 39(28), 15330-15341.

Ozcan, H., & Dincer, I. (2014b). Performance investigation of magnesium–chloride hybrid thermochemical cycle for hydrogen production. International Journal of Hydrogen Energy, 39(1), 76-85.

Ozcan, H., & Dincer, I. (2016). Modeling of a new four-step magnesium–chlorine cycle with dry HCl capture for more efficient hydrogen production. International Journal of Hydrogen Energy, 41(19), 7792-7801.

Ozcan, H., & Dincer, I. (2017). Energy and exergy analyses of a solar based hydrogen production and compression system. *International Journal of Hydrogen Energy*, *42*(33), 21414-21428.

Ozturk, I.T., Hammache, A., Bilgen, E., 1995. An improved process for H2SO4 decomposition step of the sulfur–iodine cycle. Energy Conversion and Management 36 (1), 11–21.

Oztüurk, I.T., Hammache, A., Bilgen, E., 1994. A new process for oxygen generation step for the hydrogen producing sulphur–iodine thermochemical cycle. Transactions of IChem., Part A 72, 243–250.

Ratlamwala, T. A. H., & Dincer, I. (2012). Energy and exergy analyses of a Cu–Cl cycle based integrated system for hydrogen production. Chemical engineering science, 84, 564-573.

Ratlamwala, T. A. H., & Dincer, I. (2013). Performance assessment of solar-based integrated Cu–Cl systems for hydrogen production. Solar Energy, 95, 345-356.

Yildiz B., Hohnholt K. J. and Kazimi M. S., —Hydrogen production using high-temperature steam electrolysis supported by advanced gas reactors with supercritical CO2 cycles, Nuclear Technology, Vol. 155, pp. 1-21, 2006.

Yilmaz, F., & Selbaş, R. (2017). Thermodynamic performance assessment of solar based Sulfur-Iodine thermochemical cycle for hydrogen generation. Energy, 140, 520-529.

Zhang, Y., Zhou, Z., Wang, J., Wang, Z., Zhou, J., & Cen, K. (2013). Thermal efficiency evaluation of the thermochemical H2S splitting cycle for the hydrogen and sulfur production. International Journal Of Hydrogen Energy, 38(2), 769-776.

Zhou, J., Zhang, Y., Wang, Z., Yang, W., Zhou, Z., Liu, J., & Cen, K. (2007). Thermal efficiency evaluation of open-loop SI thermochemical cycle for the production of hydrogen, sulfuric acid and electric power. International journal of hydrogen energy, 32(5), 567-575.

Comparison of Alcohol Electro-oxidation in Alkaline Medium

***Ozlem Sahin*[1], Ebru Özkan[1], Hilal Demir Kivrak[2]**

[1]*Department of Chemical Engineering, Selcuk University, Konya, Turkey*
[2]*Department of Chemical Engineering, Yüzüncü Yıl University, Van, Turkey*

Direct alcohol fuel cells (DAFCs) are most promising renewable and clean energy devices for portable applications due to numerous advantages over similar devices fed with hydrogen. Alcohols, such as methanol, ethanol, and ethylene glycol exhibit high volumetric energy density, and their storage and transport are much easier than hydrogen. However, the oxidation kinetics of the alcohols is much slower than hydrogen fueled polymer electrolyte fuel cells. Therefore, remarkable efforts have been made to discover more effective electrocatalysts for DAFCs. In this case, numerous work has been done to study the electrooxidation of alcohol on Pt-based catalysts in alkaline medium. Palladium could be a good candidate as catalyst due to many advantages such as, less expensive, higher activity and more resistant to poisoning species than Pt. Pd-based catalysts with different structures have been investigated by many research groups to improve the activity and stability towards alcohol oxidation. These researches have shown that bimetallic catalysts could be preferred with improved electrocatalytic activies than monometallic catalysts. Moreover, core-shell structures with noble metal shells are of great importance in chemical catalysis due to their enhancing properties to substrate oxidation. In the present study, the oxidation reaction was investigated in order to compare the activity of catalysts for different alcohols. The electrocatalytic activity of the both core –shell and bulk alloy palladium-based catalysts toward oxidation reaction has been examined by electrochemical techniques such as cyclic voltammetry, chronoamperometry, electrochemical impedance spectroscopy.

Keywords: Alcohol electro-oxidation, methanol, ethanol, ethylene glycol

Electrocatalytic Performance of Pd Based Bimetallic Catalysts for Methanol Oxidation Reaction

***Ozlem Sahin*[1] , Ebru Özkan[1], Rabia Esra Takır[1], Abdullah Nadeesh[1], Hilal Demir Kivrak[2]**

[1]*Department of Chemical Engineering, Selcuk University, Konya, Turkey*
[2]*Department of Chemical Engineering, Yüzüncü Yıl University, Van, Turkey*

Nanotechnology can offer clean solutions about generation, storage and utilization of energy. Nanomaterials are utilized as catalysts in fuel cells being favorable sources of direct electricity generation for electronic devices and transportation. Direct methanol fuel cells (DMFCs) have the advantageous to convert chemical fuels to electricity with high efficiency. Methanol oxidation reaction is the main reaction occurring in the anode of a DMFC. It is well known that Pt is considered as the most efficient catalysts for the electro-oxidation of methanol. However, the main problem encountered in DMFCs is the loss of active sites due to CO poisoning of the catalysts and high cost of Pt would restrict their applications. Thus, development of more efficient and durable nanocatalysts is required. Therefore, a great deal of research has been focused on improving the catalyst performance for methanol electro-oxidation. Different methods have been adopted to increase the catalysts activity and reduce the Pt loadings in DMFC. Also, several non-platinum catalysts have recently been synthesized to overcome the above problems. For this aim, palladium could be utilized as electrocatalyst with significant electrocatalytic activity. Bimetallic catalysts could be preferred with enhanced electrocatalytic activies than monometallic ones. The activity of catalysts could be also improved by the core-shell structures. Moreover, core-shell nanoparticles with thin noble metal shells are of great importance in chemical catalysis due to their enhancing properties to substrate oxidation. In this study, the electrocatalytic activity of the both core-shell and alloy palladium-based catalysts toward the methanol oxidation reaction has been examined by electrochemical techniques.

Keywords: Bimetallic catalysts, methanol electro-oxidation, fuel cells

Structure Sensitivity of Direct Alcohol Electrooxidation Reaction Catalysts

***Hilal Demir Kivrak*[1], Ebru Özkan[2], Özlem Sahin[2]**

[1]*Van Yuzuncu Yıl University Chemical Engineering Department, Van Turkey*
[2]*Selcuk University Chemical Engineering Department, Konya Turkey*

Over the last few decades, advanced catalysts have been extensively studied to increase the catalyst activity in fuel cell applications. Especially, bimetallic nanoparticles with core-shell structures composed of two distinct metal elements display enhanced catalytic properties due to the lattice strain formed between the core and shell regions. By changing their components and morphologies, their relevant physical, electrical, or chemical performances can be modified. Nanoparticles with different shapes and structures usually display differ¬ent activity and selectivity. Generally, these structures can improve the activity of the catalysts. Core-shell structures exhibit properties distinct from their alloy structures. Different analytical techniques can be employed to characterize the nanostructure of the core–shell particles. Comparison of different techniques is necessary in order to determine the overall structure. In this study, the structural characterization of Pd and Pt based bimetallic and trimetallic catalysts evaluated by BET, SAXS, XRD, SEM-EDS, TEM, and chemisorption analysis. Surface morphologies and particle size of these catalysts were determined and related the electrocatalytic activities. In conclusion, one could note that there is strong structure sensitivity for alcohol electrooxidation reaction for these catalysts.

Keywords: alcohol oxidation, structure sensitivity, fuel cells

Bimetallic Particles for Ethanol Electro-oxidation

***Hilal Demir Kivrak*[1], Ebru Özkan[2], Burak Yapıcı[2], Sümeyye Doğan[2], Shekiba Muhammady[2], Ozlem Sahin[2]**

[1]Department of Chemical Engineering, Yüzüncü Yıl University, Van /Turkey
[2]Department of Chemical Engineering, Selcuk University, Konya/Turkey

Electrocatalytic energy conversion plays an important role in the development of sustainable energy technologies for decreasing consumption of fossil fuels. The development of alternative power sources is an important issue at present. In this case, direct alcohol fuel cells (DAFCs) have attracted considerable interest for mobile applications such as electric vehicles and other portable devices. Among several fuels which can be used in DAFCs, ethanol is the most promising fuel due to its safety and high energy density. Moreover, it can be produced from agricultural products and fermentation of biomass.

Platinum (Pt) based catalysts can be utilized for electro-oxidation of ethanol due to its high activity and stability. However, it is required to develop better catalysts for ethanol oxidation due to the slow reaction kinetics and electrode poisoning. In this case, palladium (Pd) has better electrocatalytic activity than Pt. Although Pd has been known to be a suitable catalyst for electrooxidation of ethanol in alkaline media, it is required to improve the catalytic activities of the catalyst to form alloy structures. In this study, the electrocatalytic activity of the different bimetallic nanoparticles toward the ethanol oxidation reaction has been investigated by cyclic voltammetry, chronoamperometry, electrochemical impedance spectroscopy techniques in alkaline media.

Keywords: Bimetallic nanoparticles, ethanol electro-oxidation, fuel cells.

Exergoeconomic Analysis and Optimization of a Concentrated Sunlight-based Integrated Photoelectrochemical Hydrogen and Ammonia Production System

[1,2] Yusuf Bicer and [2,3] Ibrahim Dincer
[1] Division of Sustainable Development, College of Science and Engineering, Hamad Bin Khalifa University, Qatar Foundation, Doha, Qatar.
[2] Clean Energy Research Laboratory, Faculty of Engineering and Applied Science, University of Ontario Institute of Technology, 2000 Simcoe Street North, Oshawa, Ontario L1H 7K4, Canada
[3] Faculty of Mechanical Engineering, Yildiz Technical University, Istanbul, Turkey

Emails: ybicer@hbku.edu.qa; ibrahim.dincer@uoit.ca

Abstract
This work presents a comprehensive study undertaken to cover exergoeconomic analysis and optimization of an integrated system for photoelectrochemical (PEC) hydrogen and electrochemical ammonia production. The integrated system consists of a solar concentrator, spectrum splitting mirrors, a photoelectrochemical (PEC) hydrogen reactor, a photovoltaic (PV) module, an electrochemical ammonia reactor and support mechanisms. Thermodynamic and exergoeconomic analyses are initially conducted to determine the performance of the integrated system namely; efficiency and total cost rate. The obtained performance parameters are then optimized to yield the minimum cost rate and maximum efficiency under given constraints of the experimental system. The highest capital costs are observed in photoelectrochemical hydrogen and electrochemical ammonia reactors because of high procurement costs and electricity inputs. The optimized values for exergy efficiency of the integrated system range from 5% to 9.6%. The overall efficiencies are mainly affected by the photovoltaic (PV) and photoelectrochemical (PEC) cell areas and solar light illumination. The optimum efficiencies are found to be 8.7% and 5% for the multi-objective optimization of hydrogen production and integrated ammonia production systems, respectively. When the exergy efficiency of the integrated system is maximized and total cost rate is minimized, the total cost rate of the system is calculated to be about 0.2 $/h.

Keywords: Hydrogen; ammonia; photoelectrochemical; solar energy, exergoeconomics; optimization.

I. Introduction

As the energy consumption of mankind increases, seeking for various power generation and storage alternatives emerges. Rather than conventional sources, renewable energy resources are main solution for a cleaner and sustainable world. Extensive utilization of solar energy-based hydrogen and ammonia production systems will be extremely important for achieving global sustainability in both developing and industrialized countries. Two of the major uses of hydrogen are for methanol and ammonia production. These chemicals are crucial for the world economy because they are the feedstock for many other major products. Since their production is heavily dependent on natural gas at the moment, alternative (clean, sustainable, cost-effective) hydrogen and ammonia production techniques are currently being investigated.

A solar energy-driven process, photoelectrochemical water splitting for hydrogen generation, has numerous benefits over other methods mainly; avoiding safety concerns, reducing energy necessities, and improving system control by selecting a low temperature process instead of the high temperature techniques. On the other hand, Haber-Bosch ammonia synthesis is an energy intensive technique having high temperature and pressure levels. Alternatively, electrochemical routes can be employed to reduce the temperature and pressure level of the ammonia formation reaction.

Previously, we have reported experimental studies of photoelectrochemical hydrogen production (Bicer and Dincer, 2017a, 2017b, 2017c), electrochemical ammonia synthesis (Bicer and Dincer, 2017d) and integrated hydrogen and ammonia production system (Bicer and Dincer, 2017e, 2017f). Those studies contained mostly experimental results where economic considerations were not included. This study, however, presents exergoeconomic analysis of producing hydrogen and ammonia in an integrated fashion via cleaner techniques namely; photoelectrochemical hydrogen production and electrochemical ammonia production. The experimental system for which the exergoeconomic analysis is conducted, can be found in our previous research (Bicer and Dincer, 2017e, 2017f).

II. Analysis

The exergoeconomic analysis in this study is mostly based on the actual experimental system and components. The equipment costs of the experimental system are first introduced to be used in the capital cost factors. The experimental systems are divided into three main sub-systems; (i) Photoelectrochemical hydrogen production reactor, (ii) Electrochemical ammonia production reactor and (iii) Integrated system comprising of solar light concentrator and spectrum splitter, PV cell and support mechanism.

The PEC hydrogen production reactor is used under concentrated and split spectrum. Therefore, the solar concentrator, dielectric mirrors and PVs are included in the integrated system costs. These two sub-systems for hydrogen and ammonia production are integrated in the experimental setup which yield the total system capital cost. The support mechanism used in the integrated system consists of wood and metal parts. The highest cost is for the PEC hydrogen production reactor which corresponds to about 68% of total capital cost.

The exergoeconomic analyses are performed for the experimental integrated system. Exergy cost for the streams in any cost rate balance is given as follows (Bejan et al., 1996; Lazzaretto and Tsatsaronis, 2006):

$$\dot{C} = c\,\dot{Ex} \quad (1)$$

Here, c is in given in \$/kWh and $\dot{Ex}$ is given in W. The capital costs of the components is given as $\dot{Z}$ in \$/h. Typical cost rate balance for a component is given below (Bejan et al., 1996; Lazzaretto and Tsatsaronis, 2006):

$$\sum \dot{C}_{in} + \dot{W}\,c_{in} + \dot{Z} = \sum \dot{C}_{out} + \dot{W}\,c_{out} \quad (2)$$

CRF refers to capital recovery factor and depends on the interest rate and equipment life time, and is determined here as follows:

$$CRF = \frac{i\,(1+i)^n}{(1+i)^n - 1} \quad (3)$$

Here, i denotes the interest rate and n the total operating period of the system in years. Total costs for each of the components in the system are needed in \$/h in order to use them in cost rate balance equations. The capital cost and the operating and maintenance costs are added. The total costs are then divided by the number of hours in a year to get a cost in \$/h. Operating and maintenance costs are assumed to be a ratio of the capital costs as follows:

$$OM = CC\ OM_{ratio} \quad (4)$$

where OM_{ratio} depends on the type of application and material.

The capital costs of the equipment are calculated based on the experimental setup costs. The total cost balance is written as follows:

$$TCC = CRF\,(CC + OM) \quad (5)$$

The annual investment cost rate of any component, $\dot{Z}$ is calculated for the components of the experimental integrated system. It is the summation of the annual capital investment cost rate and the annual O&M cost rate and defined as follows:

$$\dot{Z} = \frac{TCC}{t_{operation}} \quad (6)$$

where $t_{operation}$ is the total operational hours in a year.

The cost rate of exergy destruction for each component is expressed as follows (Bejan et al., 1996; Lazzaretto and Tsatsaronis, 2006):

$$\dot{C}_D = c\,\dot{Ex}_d \quad (7)$$

Summation of additional cost caused by exergy destruction, $\dot{C}_D$ and final capital and operating cost rate $\dot{Z}$ gives a critical parameter named as total cost rate $\dot{C}_D + \dot{Z}$:

$$\dot{C}_{total} = \dot{C}_D + \dot{Z} \quad (8)$$

Total cost rates of the system consists of the total investment cost and cost of exergy destruction. In general, the smaller the sum of this parameter, it means that the component is more cost effective. Therefore, this parameters is taken as optimization function in the optimization analyses.

The exergoeconomic factor, which is a measure of system effectiveness in terms of cost, obtained through exergoeconomic analysis is given as follows (Bejan et al., 1996; Lazzaretto and Tsatsaronis, 2006):

$$f = \frac{\dot{Z}}{\dot{Z} + \dot{C}_D} \quad (9)$$

The exergoeconomic variables $\dot{Z}$ and $\dot{C}_D$ provide the significance of component in the system optimization, whereas the variable f exergoeconomic factor is a relative measure of the component cost effectiveness.

The following financial parameters shown in Table 1 are used in the exergoeconomic analysis.

Tab.1: The financial and operational cost parameters used in the exergoeconomic analyses.

Parameter	Value
Interest rate	7%
Lifetime of all components	10 years
Calculated capital recovery factor	0.1424
Calculated hydrogen cost	3.24 $/kg
Calculated ammonia cost	0.84 $/kg
Cost of electricity	0.06 $/kWh
Cost of thermal energy	0.02 $/kWh
O&M percentage of capital cost	2.2%
System annual operation hours	2500 hours

The exergy cost rates balance of the components in the integrated system are written below:

Fresnel lens:

$$\dot{E}x_1\, c_1 + \dot{Z}_{FRESNEL} = \dot{E}x_2\, c_2 + \dot{E}x_{d_{FRESNEL}}\, c_{Ex_{d_{FRESNEL}}} \quad (10)$$

The inlet and outlet streams (#1 and #2) of the Fresnel lens are sunlight. Therefore, the cost of light is taken as zero for c_1 and c_2. The final capital and operating cost rate of the components are calculated using the purchased equipment costs and O&M ratios.

Dielectric mirror:

$$\dot{E}x_2\, c_2 + \dot{Z}_{MIRROR} = \dot{E}x_3\, c_3 + \dot{E}x_4\, c_4 + \dot{E}x_{d_{MIRROR}}\, c_{Ex_{d_{MIRROR}}} \quad (11)$$

The inlet and outlet streams (#2 and #4) of the dielectric mirror are sunlight. Therefore, the cost of light is taken zero for c_2, c_3 and c_4.

PV:

$$\dot{E}x_3\, c_3 + \dot{Z}_{PV} = \dot{E}x_{Electricity}\, c_{Electricity} + \dot{E}x_{Heat}\, c_{Heat} + \dot{E}x_{d_{PV}}\, c_{Ex_{d_{PV}}} \quad (12)$$

The inlet stream (#3) of the PV is sunlight. Therefore, the cost of light is taken zero for c_3. $\dot{E}x_{Heat}$ is the exergy rate of calculated heat dissipation from the PV.

PEC:

$$\dot{E}x_{H_2O}\, c_{H_2O} + \dot{E}x_{Electricity}\, c_{Electricity} + \dot{E}x_4\, c_4 + \dot{Z}_{PEC} = \dot{E}x_{O_2}\, c_{O_2} + \dot{E}x_{H_2}\, c_{H_2} + \dot{E}x_{d_{PEC}}\, c_{Ex_{d_{PEC}}} \quad (13)$$

One of the inlet stream (#4) of the PEC reactor is sunlight. Therefore, the cost of light is taken zero for c_4.

Ammonia Reactor (AR):

$$\dot{E}x_{H_2} c_{H_2} + \dot{E}x_{N_2} c_{N_2} + \dot{E}x_{Electricity} c_{Electricity} + \dot{Z}_{AR} = \dot{E}x_{NH_3} c_{NH_3} + \dot{E}x_{d_{AR}} c_{Ex_{d_{AR}}} \quad (14)$$

The cost rate of water and nitrogen are taken as zero in the calculations.

III. Optimization Study

Engineering Equation Solver (EES) is used for optimization purposes. EES requires lower and upper bounds to be set for each independent variable. Careful selection of the bounds and the guess value(s) of the independent variables improves the likelihood of finding an optimum. The main performance parameters in the integrated system including the constraints are given in Table 2. The constraints of the decision variables in this study are selected as listed in Table 2.

Tab. 2: The selected decision variables and constraints in the integrated system.

Variable	Lower	Upper	Unit
A_{PV}	0.03	0.05	m^2
$A_{cell,PEC}$	0.025	0.093	m^2
i (interest rate)	1	10	%
I_3	1500	3000	W/m^2
I_4	1500	3000	W/m^2

Lifetime	5	40	years
T_o	290	310	K

Most of the constraints are defined based on the experimental measurements and component specifications. Interest rate and lifetime of the system are defined within actual limits observed in the practice.

Three objective functions are considered here for optimization: (i) exergy efficiency maximization of hydrogen production, (ii) exergy efficiency maximization of ammonia production and (iii) total cost rate minimization for the complete system based on the following formulas:

Exergy efficiency (Hydrogen production):

$$\eta_{\text{ex,integrated system},H_2} = \frac{(\dot{m}_{H2}\, ex_{H_2} + \dot{W}_{PV} - \dot{W}_{in,PEC})}{Ex_{I_{r_3}}\, A_{PV} + Ex_{I_{r_4}}\, A_{PEC,cell}} \quad (15)$$

Exergy efficiency (Ammonia production):

$$\eta_{\text{ex,integrated system},NH_3} = \frac{\dot{m}_{NH3}\, ex_{NH_3} + \dot{W}_{PV} - \dot{W}_{in,PEC} - \dot{W}_{in,NH_3}}{Ex_{I_{r_3}}\, A_{PV} + Ex_{I_{r_4}}\, A_{PEC,cell} + \dot{m}_{N_2}\, ex_{N_2}} \quad (16)$$

The total cost rate of the system is minimized using the following cost function obtained from the exergoeconomic analysis.

Total cost flow rate:

$$\dot{C}_{total} = \dot{C}_{D,total} + \dot{Z}_{total} = \dot{C}_{D.FRESNEL} + \dot{C}_{D,MIRROR} + \dot{C}_{D,PEC} + \dot{C}_{D,PV} + \dot{C}_{D,AR} + \dot{Z}_{FRESNEL} + \dot{Z}_{MIRROR} + \dot{Z}_{PEC} + \dot{Z}_{PV} + \dot{Z}_{AR} \quad (17)$$

Optimum values are obtained for minimized cost and maximized exergy efficiency. The objective functions are initially optimized with single-objective and then combined for multi-objective optimization purposes by giving equal weighting factors.

IV. Results and discussions

The main findings of the exergoeconomic assessment is based on stream exergy rates and corresponding exergy destruction ratios. The cost rates and costs of exergy destructions for each component are tabulated in Table 3. The highest capital cost is observed in PEC reactor because of high purchased cost and electricity input. Secondly, ammonia reactor has highest cost rate. These two reactors are the only electricity consuming devices resulting in a larger cost rates. Furthermore, since PV generates electricity, the total cost rate is quite lower than other components.

Tab. 3:The exergoeconomic results of the components in the integrated system

Component	Cost Rate of Exergy Destruction - $\dot{C}_D$ ($/h)	Exergoeconomic Factor - f (%)	Total Cost Rate - $\dot{C}_{total}$ ($/h)	Annual Investment Cost Rate - $\dot{Z}$ ($/h)
Ammonia reactor	0.07295	42.46	0.1268	0.05384
Fresnel Lens	0.004365	50	0.008731	0.004365
Dielectric Mirror	0.03911	50	0.07823	0.03911
PEC	0.1596	59.27	0.3918	0.2322
PV	0.003902	54.4	0.008559	0.004656
TOTAL	0.2799	54.42	0.6141	0.3342

Since the PEC reactor capital cost is the highest contributor to the system cost, a parametric study is conducted to investigate the effect on the total cost rates as shown in Fig 1a. In case the PEC reactor can be built in a more cost effective way corresponding to about 2000 US$, the total exergy destruction cost rate decreases to 0.1641 US$/h whereas total exergoeconomic factor increases to 57.1%. Also, the exergoeconomic factor of PEC reactor component increases to 72.7% from 54.41%.

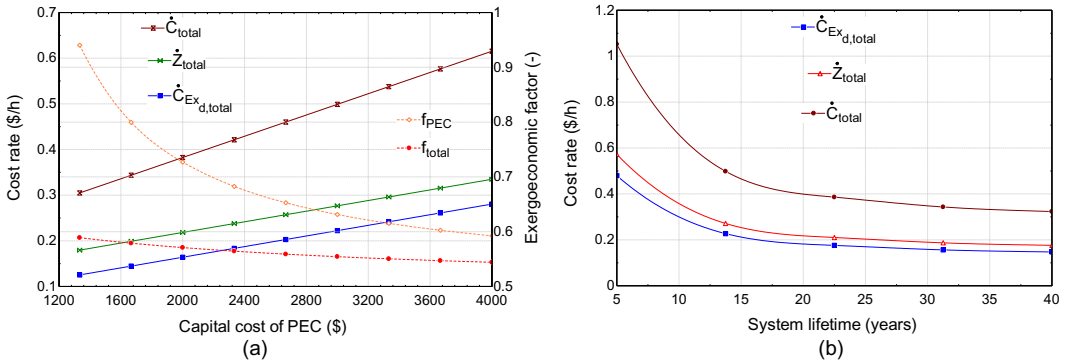


Fig. 1: (a) The effects of PEC reactor capital cost on the system cost rates and exergoeconomic factors and (b) the effects of system total lifetime on the system cost rates.

The lifetime of the system and components has also important role in the total cost rate as shown in Fig. 1b. Each component can have different lifetime periods. For example, the PEC electrodes may need to be replaced in two years whereas the solar concentrator may have up to ten years operation. In the base case, the system lifetime is taken to be 10 years for the experimental system that corresponds to about 0.6141 $/h total cost rate. However, in case the lifetime can be increased up to 40 years, the total cost rate can be decreased down to 0.3233 $/h.

The exergy efficiencies of the integrated hydrogen and ammonia production systems are maximized whereas the total cost rates are minimized using the optimization toolbox of Engineering Equation Solver. The genetic algorithm optimization is performed for 64 generations where the maximum mutation rate is 0.2625 and number of individuals (populations) is 16. Larger values for the maximum mutation rate cause the algorithm to search more aggressively for an optimum at locations distant from the current optimum. Smaller values focus the search more around the current optimum.

At first, the exergy efficiencies for hydrogen and ammonia production systems are individually optimized to be maximized. The total cost rate obtained from the exergoeconomic analyses is then optimized to be minimized. Finally, the exergy efficiency of integrated ammonia production system (since it is the complete process) and total cost rate are combined in an optimization function having same weighting factors of 0.5.

In the single objective optimization, the optimum efficiency for the integrated ammonia production system is found to be 6.96%. The optimum PEC cell area is very close to lower bound. However, the optimum PV cell area is very close to upper bound due to higher power generation. The system performance is mostly affected by the ambient temperature and irradiation on the PV cell. Similarly, in the single objective optimization results for the hydrogen production, the optimum efficiency is calculated as 9.69%. The optimum PEC cell area is equal to lower bound. However, the optimum PV cell area is very close to upper bound due to higher power production. On the other hand, in the single objective optimization results for the total cost rate of the overall system, the optimum total cost flow rate is found to be 0.131 $/h. The irradiances on the PEC cell and PV cell are desired to be higher in this case to lower the unit cost for energy production. Furthermore, the area of the PEC cell is close to upper bound and PV cell area is close to lower bound implying the higher efficiency for power production. The total cost rate of the system is mostly affected by the interest rate and lifetime of the system.

Table 4 shows the summary of the optimization results for each objective function. The obtained values are optimum for the specific objective whereas the in the last two columns, the optimum parameters for the multi-objective function are presented combining the exergy efficiency of the ammonia and hydrogen production system and total cost rate of the overall system.

Tab. 4: Comparison of optimized values and base case values for design parameters of the integrated system.

Decision Parameter	Base Case	Best Exergy Efficiency (Ammonia)	Best Exergy Efficiency (Hydrogen)	Best Total Cost Rate	Multi-Objective Best Exergy Efficiency (Ammonia) and Best Total Cost Rate	Multi-Objective Best Exergy Efficiency (Hydrogen) and Best Total Cost Rate
APEC (m^2)	0.025	0.02542	0.025	0.08435	0.02609	0.02554
APV (m^2)	0.040	0.04991	0.04991	0.03585	0.04971	0.04572
Interest rate (-)	0.07	0.04231	0.09077	0.01	0.01046	0.01652
Irradiation on PV (W/m^2)	2238	2828	2847	2640	2018	2103
Irradiation on PEC (W/m^2)	2102	1523	1500	2750	1516	1542
Lifetime (year)	10	31.6	27.99	40	24.56	27.95
Ambient temperature (K)	298	290.8	290.9	290.3	299.7	300.7

The irradiance levels on the PEC cell and PV cell are in the range of 1500 W/m^2 to 3000 W/m^2. The overall efficiencies are mainly affected by the PV and PEC cell areas and solar light illumination. The lower area of the PEC cell results in higher efficiencies because the increasing the cell area alone does not increase the hydrogen production significantly (there is a limitation on the concentrated sunlight area). On the other hand, less Fresnel lens area is favored because the illuminated area on the dielectric mirrors remain similar to the base case. This is due to the distance of the mirror from the focal area of the Fresnel lens. In this way, there is less power input to the system, however, the amount of generated useful products remain constant or slightly decrease.

V. Conclusions

Based on the conducted exergoeconomic analyses, the following conclusions and future study recommendations are noted:

- The system capital cost is mainly dominated by the photoelectrochemical reactor and electrodes.
- In case the system lifetime is taken to be 10 years for the experimental system, the total calculated cost rate is about 0.6141 $/h. However, in case the lifetime can be increased up to 40 years, the total cost rate can be decreased down to 0.3233 $/h.
- The developed system for ammonia production can be applied in various sectors ranging from solar fields to remote communities for producing multiple commodities such as heating, cooling, power generation, energy storage, etc.
- Other renewable energy options can be easily integrated to this system to produce clean ammonia. Any type of renewable electricity would make the process environmentally friendly. Therefore, there is a high potential for utilization of renewable energy in electrochemical ammonia synthesis applications for energy conversion and storage.

Acknowledgement

The authors acknowledge the support provided by the Natural Sciences and Engineering Research Council of Canada.

References

Bejan, A., Tsatsaronis, G., Moran, M.J., 1996. Thermal design and optimization. Wiley.

Bicer, Y., Dincer, I., 2017a. Performance evaluation of a photoelectrochemical hydrogen production reactor under concentrated and non-concentrated sunlight conditions. Int. J. Hydrogen Energy. https://doi.org/10.1016/j.ijhydene.2017.08.122.

Bicer, Y., Dincer, I., 2017b. Electrochemical impedance spectroscopic assessment and analysis of a newly developed photoelectrochemical cell. Chem. Eng. Process. Process Intensif. 117, 141–153.

Bicer, Y., Dincer, I., 2017c. Experimental investigation of a PV-Coupled photoelectrochemical hydrogen production system. Int. J. Hydrogen Energy 42, 2512–2521.

Bicer, Y., Dincer, I., 2017d. Electrochemical Synthesis of Ammonia in Molten Salt Electrolyte Using Hydrogen and Nitrogen at Ambient Pressure. J. Electrochem. Soc. 164, H5036–H5042.

Bicer, Y., Dincer, I., 2017e. Performance assessment of electrochemical ammonia synthesis using photoelectrochemically produced hydrogen. Int. J. Energy Res. 41(14), pp.1987-2000.

Bicer, Y., Dincer, I., 2017f. Assessment of a Sustainable Electrochemical Ammonia Production System Using Photoelectrochemically Produced Hydrogen under Concentrated Sunlight. ACS Sustain. Chem. Eng. 5, 8035–8043.

Lazzaretto, A., Tsatsaronis, G., 2006. SPECO: A systematic and general methodology for calculating efficiencies and costs in thermal systems. Energy 31, 1257–1289.

Development of a mathematical model for a HT-PEMFC stack based cogeneration system

[1*]Yagmur Nalbant, [1,2]Can Ozgur Colpan, [3]Yilser Devrim
[1]Dokuz Eylul University, School of Natural and Applied Sciences, Mechanical Engineering Department, Buca, Izmir, 35397, Turkey
[2]Dokuz Eylul University, Faculty of Engineering, Mechanical Engineering Department, Buca, Izmir, 35397, Turkey
[3]Atilim University, Faculty of Engineering, Energy Systems Engineering, Incek, Ankara, 06836, Turkey

* E-mail: yagmurnalbant.yn@gmail.com

Abstract
High temperature-proton exchange membrane fuel cells (HT-PEMFC) operating between 160°C and 200°C are suitable for cogeneration applications in which electricity and hot water are produced. In this study, a mathematical model of a cogeneration system, which includes an ethylene glycol cooled HT-PEMFC stack, a heat exchanger, and a pump, is developed. The stack is fed with pure hydrogen at the anode side and air at the cathode side. This model is based on a one-dimensional and semi-empirical fuel cell model and simple thermodynamic model for the heat exchanger. This model is validated using in-house experimental data. The effect of anode stoichiometry ratio on the electrical and fuel utilization efficiencies are examined. In addition, the average temperature of hot water is calculated for each month for a case study.

Keywords: High temperature-proton exchange membrane fuel cell, semi-empirical, cogeneration, mathematical model.

I. Introduction

Proton exchange membrane fuel cells have already commercialized in portable, stationary, and vehicle applications. These fuel cells can be classified into two according to their operating cell temperature: low temperature-proton exchange membrane fuel cell (LT-PEMFC) and high temperature-proton exchange membrane fuel cell (HT-PEMFC). LT-PEMFCs and HT-PEMFCs generally operate at cell temperatures of 60-80°C and 120-200°C, respectively (Rosli et al., 2016). LT-PEMFC and HT-PEMFC use Nafion® membrane and phosphoric acid (PA) doped polybenzimidazole (PBI) membrane, respectively. PBI membrane is generally preferred for higher temperature operation as they have high proton conductivity and high thermal and chemical stabilities at these conditions (Nalbant et al., 2017). HT-PEMFCs are more advantageous than LT-PEMFCs in terms of their water and thermal management and carbon monoxide (CO) poisoning tolerance. Main advantages of HT-PEMFCs can be given as (i) faster electrochemical reaction rate, (ii) simpler water and thermal management, and (iii) higher CO poisoning tolerance. In addition, waste heat produced from HT-PEMFCs can be used to generate other beneficial forms of energy (e.g. hot water and space heating). Aside from their advantages, HT-PEMFCs have some disadvantages such as slow start up, higher material degradation rate, and difficulty in thermal insulation (Rosli et al., 2016).

In the literature, several studies on HT-PEMFC based CHP (combined heat and power) systems have been conducted. For example, Supra et al. (2013) designed a HT-PEMFC stack including encapsulated cooling cells that use heat transfer oil and experimentally investigated the temperature distribution in the HT-PEMFC. They applied energy balance for HT-PEMFC stack, and found the temperature and voltage differences between each cell as 8.3 K and 0.047 V, respectively. Arsalis et al. (2011) developed the model of a micro-CHP residential system based on HT-PEMFC using the Engineering Equation Solver (EES) software. Four parameters (fuel cell operating temperature, steam-to-carbon ratio, combustor temperature, and hydrogen stoichiometry) were studied to determine the effect of these parameters on the overall performance. The highest efficiency of the cogeneration system was found as 83.08%. In another study, Arsalis et al. (2015) developed the model of a HT-PEMFC based micro-CHP system, which includes heat pump instead of thermal storage tank for residential demands. This system was optimized through genetic algorithm using thermophysical parameters for different loads. The efficiency of the total system was found as 81.5%. Jannelli et al. (2013) compared the performance of integrated cogeneration systems based on three different PEMFCs through numerical models, which were validated using experimental data. The maximum electric and cogeneration efficiencies for HT-PEMFC based system were found as 40% and 79%, respectively; while the highest cogeneration efficiency was found as 80% for LT-PEMFC based system. This study showed that HT-PEMFC has higher electric efficiency and lower cogeneration efficiency than those of LT-PEMFC.

According to the findings of the literature survey, there are no studies on modeling of HT-PEMFC based cogeneration systems that use semi-empirical fuel cell model. The aim of this study is to develop a mathematical model for a HT-PEMFC stack based cogeneration system to investigate the effect of anode stoichiometry ratio on the electrical and cogeneration efficiencies and to obtain the average temperature of hot water calculated for each month.

II. Experimental

Experiments which were carried out with different operating temperatures and Pt loadings, were used to calibrate thin film thicknesses of anode and cathode for semi empirical model of HT-PEMFC. The details of the experiments

including the materials, the preparation of the MEA, and the performance tests were explained in Nalbant et al (2017). High temperature performance tests were obtained using the HT-PEMFC (TECHYS HYGO FCTS-H2ME 500) test station. The test station equipped with a gas handling unit, an electronic load (BK Precision, USA), a control and data logger computer, was used to test the HT-PEMFC. A computer-based control and data acquisition system of test station collected and multiplexed the respective signals and fed them into the PC for the overall system control. The current and voltage of the cell were monitored and logged throughout the operation by the test software. Non-humidified H_2/Air was fed in co-flow to the HT-PEMFC without any applied back pressure. After compressor, air was fed to dryer to supply dry air. Constant stoichiometry values were chosen for all performance tests. The reactant gases were supplied by mass-flow controllers at constant stoichiometry of 1.2 for anode side and 2.5 for cathode side. After steady state was achieved, starting with the OCV value, the current-voltage data was logged by changing the load. The polarization curves were obtained by measuring the current density with the stepwise decrement of voltage from OCV to 0.3 V, with an interval of 0.05 V.

III. Model Description

A mathematical model for a HT-PEMFC stack based cogeneration system is developed. HT-PEMFC stack is fed with pure hydrogen at the anode side and with air at the cathode side. In this section, the modeling of the main components (HT-PEMFC stack and heat exchanger (HEX)) in the cogeneration system is presented. The schematic diagram of the cogeneration system and the control volume used in the energy balance for the HT-PEMFC stack are shown in Fig. 1, and the working parameters are tabulated in Tab. 1.

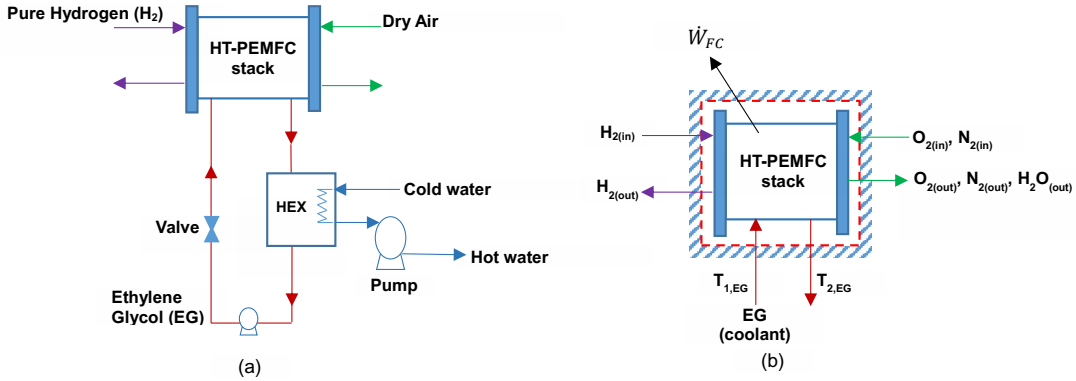


Fig. 1. (a) Schematic diagram of the cogeneration system and (b) the control volume used in the energy balance of the HT-PEMFC stack.

Tab. 1: Operating parameters of the cogeneration system.

Parameters	Value
Current density (i) at 0.6 V	0.42 A/cm^2
Active Area (A_{cell})	150 cm^2
Number of cells (N_{cell})	13
Mass flow rate of coolant ($\dot{m}_{coolant}$)	0.019 kg/s
Specific heat capacity of coolant ($c_{p,coolant}$)	2.84 kJ/kg-K
Anode and cathode temperatures (T_a, T_c)	160 °C
Inlet temperature of coolant ($T_{1,EG}$)	95 °C

III.1. Fuel cell stack

The details of the one dimensional and semi-empirical model for a HT-PEMFC is given in Nalbant et al. (2017). Only hydrogen and oxygen are the reactant gases, and N_2 is the inert gas. The single cell voltage (V_{cell}) can be calculated as follows;

$$V_{cell} = V_{rev} - \eta_{act,a} - |\eta_{act,c}| - \eta_{ohm} \quad (1)$$

where, V_{rev} is the reversible cell voltage, $\eta_{act,a}$ and $\eta_{act,c}$ are the activation losses at the anode and cathode, respectively, and η_{ohm} is the ohmic loss.

The activation losses for the anode and cathode are shown in Eqs. (2) and (3), respectively. The total ohmic losses for both proton and electron transfer are calculated as shown in Eq. (4).

$$\eta_{act,a} = \frac{\bar{R}\cdot T_{cell}}{\alpha_a \cdot F} \sinh^{-1}\left(\frac{i}{2\cdot i_{0,a}}\right) \quad (2)$$

$$\eta_{act,c} = \frac{\bar{R}\cdot T_{cell}}{\alpha_c \cdot F} \cdot \sinh^{-1}\left(\frac{i}{2\cdot i_{0,c}}\right) \quad (3)$$

$$\eta_{ohm} = i \cdot ASR_{ohmic} \quad (4)$$

where, $\bar{R}$, F, α, i, i_0, T_{cell}, and ASR_{ohmic} are universal gas constant, Faraday's constant, charge transfer coefficient, current density, exchange current density, cell temperature, and area specific resistance, respectively.

It is assumed that each cell in the stack has the same performance. Thus, the stack voltage (V_{stack}) can be obtained multiplying the cell voltage with the number of cells (N_{cell}); and the power density ($\dot{W}''_{FC}$) of the stack can be found multiplying the current density with stack voltage.

$$V_{stack} = N_{cell} \cdot V_{cell} \quad \text{and} \quad \dot{W}''_{FC} = i \cdot V_{stack} \quad (5)$$

An energy balance around the control volume of the fuel cell stack (Eq. (6)) is applied to find the outlet temperature of coolant. Here, HT-PEMFC stack is assumed as adiabatic. The control volume for energy balance is given in Fig. 1 (b). Molar flow rates of species, which are required to solve Eq. (5), are given in Tab. 2.

$$0 = \sum\left(\dot{n}''_i \bar{h}_i\right)_{in} - \sum\left(\dot{n}''_i \bar{h}_i\right)_{out} - \dot{W}''_{FC} \quad (6)$$

Tab. 2: Molar flow rate of chemical species.

Inlet molar flow rates of species	Outlet molar flow rates of species
$\dot{n}''_{H_2,in} = \lambda_{H_2} \cdot \frac{i}{2 \cdot F} \cdot N_{cell}$	$\dot{n}''_{H_2,out} = (\lambda_{H_2} - 1) \cdot \frac{i}{2 \cdot F} \cdot N_{cell}$
$\dot{n}''_{O_2,in} = \lambda_{O_2} \cdot \frac{i}{4 \cdot F} \cdot N_{cell}$	$\dot{n}''_{O_2,in} = (\lambda_{O_2} - 1) \cdot \frac{i}{4 \cdot F} \cdot N_{cell}$
$\dot{n}''_{N_2,in} = \frac{x_{N_2}}{x_{O_2}} \dot{n}''_{O_2,in}$	$\dot{n}''_{N_2,out} = \dot{n}''_{N_2,in}$
$\dot{n}''_{H_2O,in} = 0$	$\dot{n}''_{H_2O,out} = \dot{n}''_{H_2O,gen} = \frac{i}{2 \cdot F} \cdot N_{cell}$

To calculate the outlet temperature of coolant ($T_{2,EG}$), Eq. (6) can be rewritten as shown in Eq. (7).

$$0 = \left(\dot{n}''_{H_2,in}\bar{h}_{H_2} + \dot{n}''_{O_2,in}\bar{h}_{O_2} + \dot{n}''_{N_2,in}\bar{h}_{N_2}\right) - \left(\dot{n}''_{H_2,out}\bar{h}_{H_2} + \dot{n}''_{O_2,out}\bar{h}_{O_2} + \dot{n}''_{N_2,out}\bar{h}_{N_2} + \dot{n}''_{H_2O,out}\bar{h}_{H_2O}\right) + \dot{n}''_{coolant}\bar{c_p}_{coolant}\Delta T_{EG} - \dot{W}''_{FC} \quad (7)$$

III.2. Heat exchanger

The heat exchanger in the system is used to cool the fuel cell stack and to heat the tap water. According to the calculations, the temperature of the coolant increases 10°C while it cools HT-PEMFC stack. The outlet temperature of hot water can be calculated using the energy balance shown in Eq. (8).

$$T_{W,out} = T_{W,in} + \frac{\dot{n}''_{coolant}\bar{c_p}_{coolant}(T_{2,EG} - T_{1,EG})}{\dot{n}''_{water}\bar{c_p}_{water}} \quad (8)$$

III.3. System modeling

To asssess the performance of the HT-PEMFC stack based cogeneration system, the electrical efficiency and the fuel utilization efficiency are selected. The electrical efficiency ($\eta_{electrical}$) is calculated by dividing the fuel cell power output to the chemical energy of hydrogen supplied to the cogeneration system. The fuel utilization efficiency (FUE) is defined as the ratio between the total amount of useful energy to the chemical energy of hydrogen.

$$\eta_{electrical} = \frac{\dot{W}_{FC}}{\dot{n}''_{H_2,in} \cdot LHV_{H_2}} \quad (9)$$

$$FUE = \frac{\dot{W}_{FC} + \dot{n}''_{water}\bar{c_p}_{water}(T_{W,out} - T_{W,in})}{\dot{n}''_{H_2,in} \cdot LHV_{H_2}} \quad (10)$$

IV. Results and discussions

IV.1. The effect of anode stoichiometry ratio

Fig. 2 shows the effect of anode stoichiometry ratio on the electrical efficiency. Anode stoichiometry ratio mainly affects the molar flow rate of hydrogen as shown in Tab. 2. According to Fig. 2, it is found that when the anode stoichiometry ratio increases, the molar flow rate of hydrogen increases, and the electrical efficiency for the system decreases. The electrical efficiencies at 0.42 A/cm^2 for 1.2, 2.0, and 2.5 stoichiometries were calculated as 40%, 25%, and 18%, respectively. Fuel utilization efficiencies for 1.2, 2.0, and 2.5 stoichiometries were calculated 85%, 52%, and 39%, respectively. The decrease of fuel utilization efficiency at this current density is found to be 54% when the anode stoichiometry ratio increases from 1.2 to 2.5.

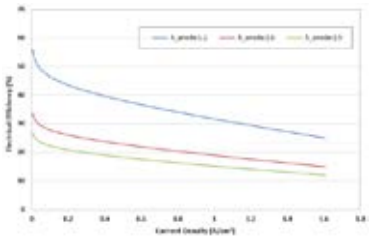
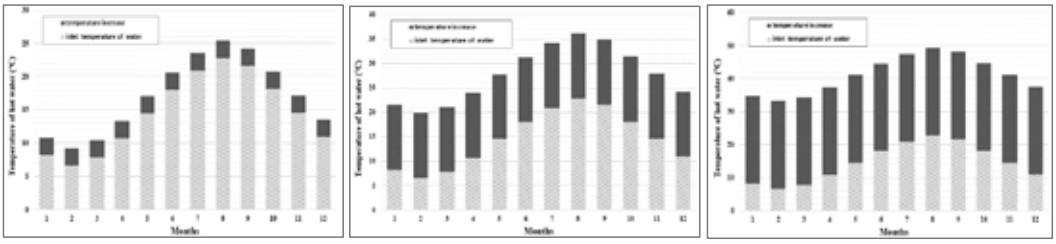


Fig. 2. The effect of anode stoichiometry ratio on the electrical efficiency.

IV.2. The average temperature of hot water for each month

In houses, the ideal temperature for taking shower is between 33°C and 38°C. The temperatures of pre-wash, wash, and rinsing in a dishwasher are 30-35°C, 50-60°C, and 80-90°C, respectively. The average temperature of water in a washing machine is 20-90°C for different program levels. Fig. 3 shows that the temperature increases at 0.42 A/cm^2 and 1.61 A/cm^2 were found as 2.62 °C and 13.30 °C, respectively. In addition, the temperature increases at 1.61 A/cm^2 for 13 and 26 cells were found as 13.30°C and 26.60°C, respectively. The results show that this cogeneration system is suitable for the house needs discussed above.



(a) (b) (c)

Fig. 3. The average temperature of hot water for each month at (a) 0.42 A/cm^2 for 13 cells, (b) 1.61 A/cm^2 for 13 cells, and (c) 1.61 A/cm^2 for 26 cells.

V. Conclusions

A mathematical model of a cogeneration system, which includes a semi-empirical modeled HT-PEMFC stack, a heat exchanger, and a pump, is developed. This model is validated using the experimental results such as the temperature difference between the inlet and outlet coolant streams and the fuel utilization efficiency. The effect of anode stoichiometry ratio on the electrical and fuel utilization efficiencies were investigated. Morever, the temperature of hot water used for the household needs was calculated for different current densities and number of cells in the stack. The main findings derived from this study are as follows.

- When the anode stoichiometry ratio increases, the electrical and fuel utilization efficiencies decrease. The decrease of fuel utilization efficiency at 0.42 A/cm^2 is found to be 54% when the anode stoichiometry ratio increases from 1.2 to 2.5.
- When both the current density and number of cells increase, the hot water temperature increases.
- HT-PEMFC stack based cogeneration system is suitable for the fundamental needs in the house.

Acknowledgements

This study is supported by The Scientific and Technological Research Council of Turkey (TUBITAK) 1001 (Grant number: 214M301) Project.

References

Arsalis, A., Nielsen, M. P., & Kær, S. K., Modeling and parametric study of a 1kW e HT-PEMFC-based residential micro-CHP system. International Journal of Hydrogen Energy, 36(8), 5010-5020, (2011).

Arsalis, A., Kær, S. K., & Nielsen, M. P., Modeling and optimization of a heat-pump-assisted high temperature proton exchange membrane fuel cell micro-combined-heat-and-power system for residential applications. Applied Energy, 147, 569-581, (2015).

Jannelli, E., Minutillo, M., & Perna, A., Analyzing microcogeneration systems based on LT-PEMFC and HT-PEMFC by energy balances. Applied Energy, 108, 82-91, (2013).

Nalbant, Y., Colpan, C. O., & Devrim, Y., Development of a one-dimensional and semi-empirical model for a high temperature proton exchange membrane fuel cell. International Journal of Hydrogen Energy, in-press (2017).

Rosli, R. E., Sulong, A. B., Daud, W. R. W., Zulkifley, M. A., Husaini, T., Rosli, M. I., ... & Haque, M. A., A review of high-

temperature proton exchange membrane fuel cell (HT-PEMFC) system. International Journal of Hydrogen Energy, 42(14), 9293-9314, (2017).

Supra, J., Janßen, H., Lehnert, W., & Stolten, D., Temperature distribution in a liquid-cooled HT-PEFC stack. International journal of hydrogen energy, 38(4), 1943-1951, (2013).

Thermodynamic and Economic Analyses of a Renewable Energy Based Hydrogen Production System

[1,2*]Fatih Sorgulu and [1,3]Ibrahim Dincer
[1] Faculty of Mechanical Engineering, Yildiz Technical University, Besiktas, Istanbul, Turkey
[2] Faculty of Technology, Kahramanmaras Sutcu Imam University, Elbistan, Kahramanmaras, Turkey
[3] Faculty of Engineering and Applied Science, University of Ontario Institute of Technology, Oshawa, Ontario, Canada

* E-mail: fatihs@yildiz.edu.tr

Abstract
We have been facing drastic issues as a result of conventional energy sources and their ultimate environmental impacts. Renewable energy sources with hydrogen as an energy carrier are considered promising alternatives to overcome such issues. Integrating hydrogen energy systems with renewable energy sources is a rational way to supply energy demand and therefore to vanquish environmental issues, such as global warming and increased CO_2 emissions. In the current study, both solar and wind energies are employed to provide the required electric power for a university campus, as included, and an electrolyzer system in order to produce hydrogen. The hydrogen produced by the electrolyzer is utilized as fuel in stationary cogeneration units and fuel cell vehicles. In this way, a renewable energy based university campus is established. Furthermore, hydrogen energy carriers such as methylcyclohexane, ammonia, and formic acid, which are proposed among promising solutions to store hydrogen are evaluated and compared technically and economically. The current integrated system is analyzed thermodynamically and economically to assess its performance. It is aimed to compare the results with the conventional systems to show its advantages through calculation of electricity cost per kWh and hydrogen cost per liter. The results show how to establish a smart university campus where the energy is provided by renewable sources in a more efficient and sustainable way.

Keywords: Electrolyzer, Fuel cell, Hydrogen Production, Solar energy, Wind energy

I. Introduction

Global energy demand is supplied mainly by fossil fuel resources. However, energy demand has been increasing drastically, particularly in developing and developed countries. According to the Ministry of Energy and Resources (2017), electricity consumption increased up to 4.8% and exceeded to 278.4 billion kWh in Turkey in 2016. Also, in 2017 (January to July), 35% of electricity consumption is provided by renewable energies and hydropower. Based on 2023 plan, this rate should be improved to meet the requirements.

Renewable energy source based electricity production has numerous advantages particularly in terms of environmental impact. Renewable energy based power plants such as wind turbines, solar PV panels, biomass and geothermal have zero or low CO_2, NO_x and SO_2 emissions. Furthermore, electricity cost through renewable energy source is decreasing rapidly. However, fluctuation of particularly wind and sunshine is one of the limitations of these power plants. Thus, a storage system is require to overcome this problem. Considering hydrogen as a promising energy carrier to provide sustainability, they are more focused for the storage purpose. Excess electricity can be utilized for the water electrolysis and produced hydrogen can be stored for the intermittent situations.

Ozlu etal. (2012) evaluated the electricity, heating and cooling demands by determining various systems such as ground and air source heat pump, photovoltaic panel, wind turbine and fuel cell systems. Authors also assessed the renewable energy based integrated systems with the fuel cell systems and carried out thermodynamic, economic and environmentally studies by considering weather conditions, electricity cost and loads in Ontario, Canada.

Biniwale etal. (2008) reviewed the dehydrogenation of cycloalkanes such as methylcyclohexane, cyclohexane and decalin as useful reaction for storage of hydrogen in chemical hydrides. They evaluated liquid organic hydrides using catalytic reaction pair of dehydrogenation of cycloalkanes.

In the current study, a renewable energy based integrated system is thermodynamically analyzed in order to evaluate its performance. Furthermore, proposed system is compared with conventional systems economically and thermodynamically to prove its superiority.

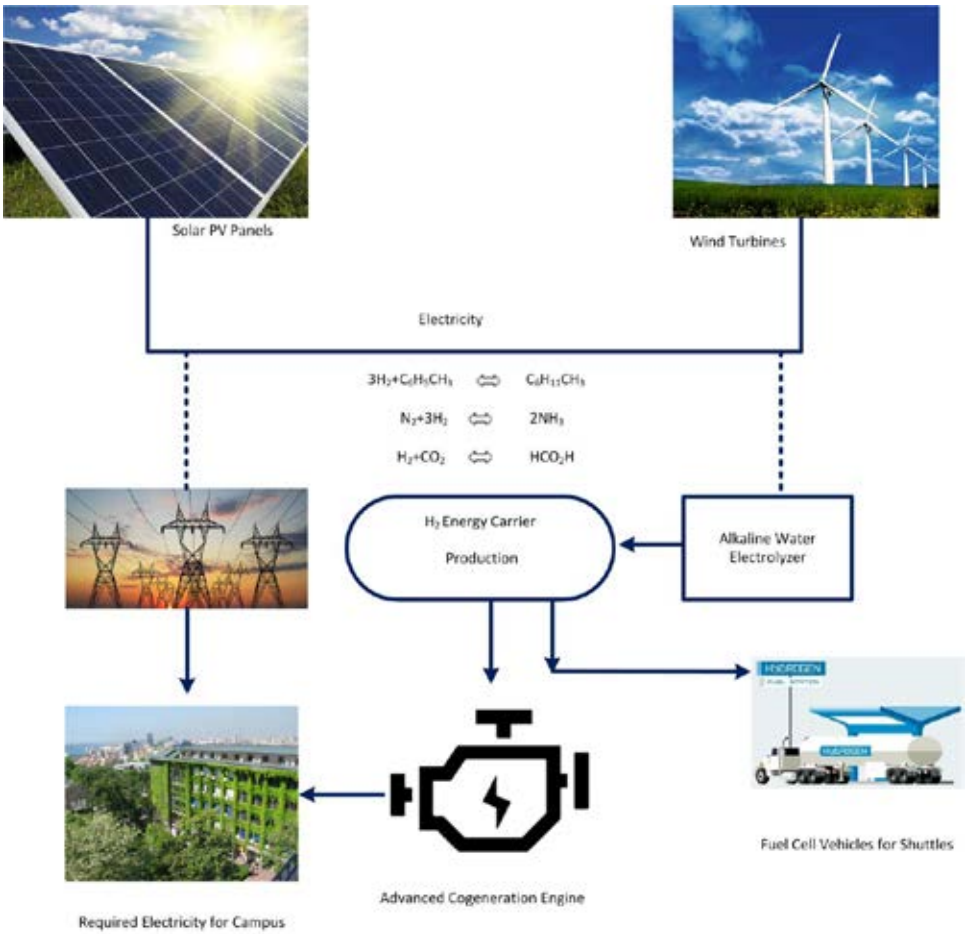


Fig. 1: A schematic diagram of the proposed system

II. System Description

As shown in Fig. 1, proposed system represents how to supply energy demand for Yıldız Technical University Campus located in Istanbul. Solar PV panels and wind turbines are determined as the main sources to provide the required energy. Previous study by Advanced Industrial Science and Technology (2017) have been considered. As shown below, Hydrogen is stored by converting into methylcyclohexane ($C_6H_{11}CH_3$), ammonia (NH_3) and formic acid (HCO_2H). Eventually, stored hydrogen carrier products are utilized to produce electricity when wind speed and solar radiation intensity is not enough to meet energy demand.

$3H_2+C_6H_5CH_3 \leftrightarrow C_6H_{11}CH_3$; $N_2+3H_2 \leftrightarrow 2NH_3$; $H_2+CO_2 \leftrightarrow HCO_2H$

III. Analysis

Note that Electricity and fuel demand are supplied by solar energy and wind energy. Hydrogen is produced by using excess electricity. Produced hydrogen is utilized to meet both electricity and fuel demands. Tab. 1 shows the solar parameters for the Istanbul, Turkey. According to Turkish State Meteorological Service, hours of sunshine change between 2.96 to 11.17 hours in a day. Tab. 2 tabulates the wind parameters for Istanbul.

Tab. 1: Solar Parameters for Istanbul by Turkish State Meteorological Service (2017)

Month	Sunshine hours (h)	Average solar intensity ($kWh/m^2 \times day$)	Average solar flux (W/m^2)	Monthly production (MWh)
January	3.46	2.00	578.03	210.00
February	4.43	2.57	580.14	269.85
March	5.32	4.20	789.47	441.00
April	6.85	5.28	770.80	554.40
May	8.61	6.30	731.71	661.50
June	10.51	6.79	646.05	712.95
July	11.17	6.79	607.88	712.95
August	10.14	6.07	598.62	637.35
September	7.83	5.09	650.06	534.45
October	5.22	3.74	716.48	392.70
November	3.85	2.37	615.58	248.85
December	2.96	1.80	608.11	189.00
Mean	6.70	4.42	657.74	462.44
Total	80.35	53.00	7892.93	5565.00

Tab. 2: Wind Parameters for Istanbul by Kayaci and Demir (2018) and Turkish State Meteorological Service (2011)

Month	Average wind speed (m/s)	Average wind speed at 100 m (m/s)	Power (kW)	Power density (kW/m^2)	Monthly electricity production (MWh)
January	2.60	5.02	608.00	0.076	153.22
February	2.70	5.21	680.89	0.086	171.58
March	2.70	5.21	680.89	0.086	171.58
April	2.40	4.63	478.21	0.060	120.51
May	2.40	4.63	478.21	0.060	120.51
June	2.40	4.63	478.21	0.060	120.51
July	3.10	5.99	1030.55	0.129	259.70
August	3.00	5.79	934.00	0.117	235.37
September	2.40	4.63	478.21	0.060	120.51
October	2.40	4.63	478.21	0.060	120.51
November	2.40	4.63	478.21	0.060	120.51
December	2.90	5.60	843.68	0.106	212.61
Mean	2.616667	5.05	637.27	0.08	160.59
Total	-	-	7647.26	0.96	1927.11

IV. Results and discussions

In this study, an integrated system is modified to meet required electricity for a university campus by renewable energy. Hydrogen is utilized to provide sustainability. Alkaline water electrolyzer is utilized to produce hydrogen. Furthermore, hydrogen is stored through converting into hydrogen carrier products. 5565 MWh electricity production is gained by solar PV panels. Solar PV area is calculated to be 10000 m^2 (100m×100m). Six wind turbines are selected to utilize to produce 1927.11 MWh electricity power in each of the turbines.

The necessary electricity and renewable electricity production can be seen in Fig. 2. Both wind and solar energies are intermittent sources of energy. This leads to fluctuations in the daily generated electricity, even hourly. Excess electricity is utilized to produce hydrogen by water electrolyzer. Thereafter, when the wind and solar energies are not enough, electricity would be generated by employing the hydrogen by advanced cogeneration engine.

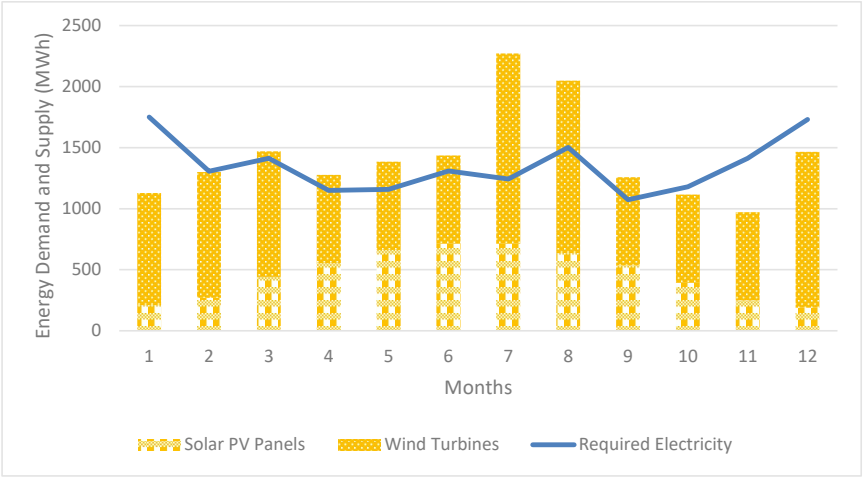


Fig. 2: Energy Demand and Supply

Fig. 3 shows the change in wind speed and power production by attitude. The wind speed increases with an increase in attitude as follows:

$$\frac{V_1}{V_2} = \left(\frac{H_1}{H_2}\right)^n \quad (1)$$

Here, H, V and n represent the attitude (m), velocity (m/s) and environmental factor, respectively.

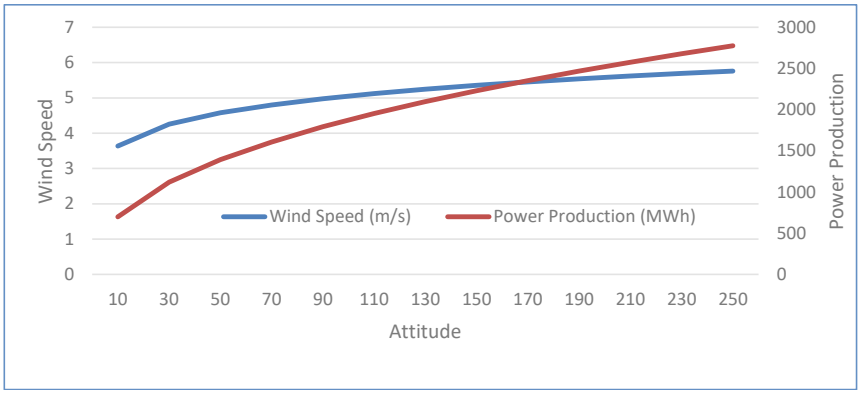


Fig. 3: Change in wind speed and power production by attitude

Fig. 4 also shows the change in amount of hydrogen generation by various wind speed and solar radiation intensity. By increasing wind speed, solar radiation and also hours of sunshine, excess electricity increase. So, available electricity for electrolyzer increase.

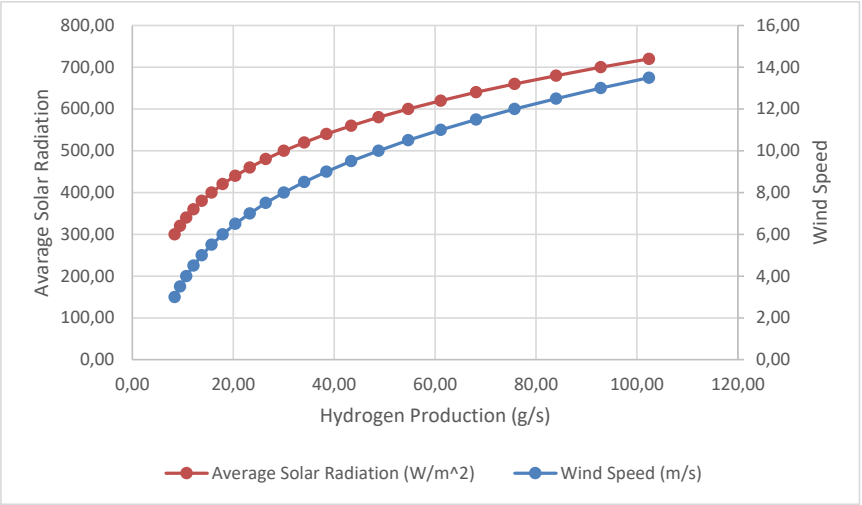


Fig. 4: Change in hydrogen production by various wind speed and solar radiation intensity.

V. Conclusions

In this study, an integrated system is modified in order to provide electricity and fuel consumptions in a university campus by renewable energy. Hydrogen is selected to achieve sustainability. The main findings of this study are given as follows:

- Electricity consumption of the university is determined as 15,523 MWh in 2016.
- 5565 MWh electricity production is gained by solar PV panels.
- Six wind turbines is selected to utilize to gain 1927.11 MWh electricity power each of turbine.

References

Advanced Industrial Science and Technology. Hydrogen Energy Carrier Team. Website: http://www.aist.go.jp/fukushima/en/unit/HyCaT_e.html [accessed: 15/12/2017].

Biniwale RB, Rayalu S, Devotta S, Ichikawa M., Chemical hydrides: A solution to high capacity hydrogen storage and supply, International Journal of Hydrogen Energy, 33, 360-365 (2008).

Kayaci N., Demir H., Long time performance analysis of ground source heat pump for space heating and cooling applications based on thermo-economic optimization criteria, Energy and Buildings, 163, 121-139 (2018).

Ozlu S., Dincer I., Naterer GF., Comparative assessment of residential energy options in Ontario, Canada, Energy and Buildings, 55, 674-684 (2012).

Republic of Turkey, Ministry of Energy and Resources. Website: http://www.enerji.gov.tr/en-US/Pages/Electricity [accessed: 25/12/2017].

Turkish State Meteorological Service, Section of statistics. Goztepe Station, Istanbul, Turkey (2011).

Turkish State Meteorological Service. Website: https://www.mgm.gov.tr/veridegerlendirme/il-ve-ilceler-istatistik.aspx?m=ISTANBUL [accessed: 20/12/2017].

Thermodynamic performance assessment of integrated solar energy system with hydrogen production

Fatih YILMAZ*, Murat ÖZTÜRK** Reşat SELBAŞ***,
*Department of Electrical and Energy, Vocational School of Technical Sciences, Aksaray University, 68100, Aksaray, Turkey
** Department of Mechatronic Engineering, Faculty of Technology, Suleyman Demirel University 32100, Isparta, Turkey
*** Department of Energy System Engineering, Faculty of Technology, Suleyman Demirel University 32100, Isparta, Turkey
*E-mails: fatiyilmaz7@gmail.com ; muratozturk@sdu.edu.tr ; resatselbas@sdu.edu.tr

Abstract
In this paper, the thermodynamic performance analysis of solar energy based integrated system with hydrogen production is investigated. This multigeneration system is consisted of seven main sub-systems, such as i-) parabolic collector system, ii-) Rankine cycle with two turbines, iii-) ORC with two turbines, iv-) hydrogen production and storage system, v-) drying process, vi-) heat pump process, and vii-) double effect absorption cooling system, for power, hydrogen, heating, cooling, drying and hot water production. In addition to that, the effects of some design parameters and reference temperature on the exergetic performance and exergy destruction rate for solar energy based integrated system with hydrogen production are investigated. The energy and exergy efficiencies of multigeneration system are calculated as 54.87% and 48.24%, respectively.

Keywords: Solar energy, hydrogen, integrated system, thermodynamic analysis, design parameters.

I. Introduction

Since the industrial revolution, the use of fossil-based fuels continues to increase in order to meet the world's need for energy consumption**.** In parallel to the energy demand is increasing (Ozturk and Dincer, 2013). Because of the use of fossil fuels, the environmental problems have arisen such as global warming acid rain, climate change etc.. So it has become important to logically use of energy sources. In this regard, the renewable energy based multigeneration power production system offers many advantages. These system consists of many processes using single energy input to the system (El-Emam and Dincer 2018).

When the literature is examined, there is a lot of work related to the solar energy assisted multigeneration power production system. Bicer and Dincer (2016), have proposed a performance assessment and analyses of renewable energy based multigeneration system. They conducted an energy and exergy efficiencies analyses of solar PV/T and geothermal based multigeneration system. Also, the energy and exergy efficiencies of they suggested study calculated as 11% and 28%, respectively. Khalid et al. (2015) suggested a solar and geothermal based multigeneration system. In their study, the total exergy efficiency of the system calculated as 39.7%. Yüksel et al. (2016), have examined a thermodynamic performance assessment of a new solar based multigeneration system. According to their study, the exergy efficiency of parabolic through solar collector is 43.14%. Some studies in the literature are presented as follows (Al-Sulaiman et al. 2011; Ezzat and Dincer, 2016; Balta et al. 2016; Leiva-Illanes et al. 2017).

In this study, the thermodynamic performance analysis of solar energy based integrated system with hydrogen production is investigated. In addition to that, the effects of some design parameters and reference temperature on the exergetic performance and exergy destruction rate for solar energy based integrated system with hydrogen production are investigated.

II. System Description and Analyses

The schematic diagram of solar energy based integrated system with hydrogen production is illustrated in Fig. 1. As seen from this figure, the parabolic dish collector (PDC) working fluid (molten salt that consists of 60% $NaNO_3$, 40% KNO_3 by weight) is pumped from cold storage tank (CST) to the PDC, where it is heated up to 580°C. Then, the hot working fluid is pumped from the collector to the hot storage tank (HST), where it is stored and pumped as a continuous flow. The leaving hot working fluid supplies heat to drive a steam Rankine cycle with two turbines, such as high-pressure turbine (HPT) and low-pressure turbine. To give heat power at the maximum allowable temperature, the heat transfer fluid of Rankine process can be selected with a high critical temperature range. To produce hydrogen, the PEM electrolyzer sub-system is utilized. Furthermore, to recover heat power more efficiently, turbine-I and turbine-II in the organic Rankine cycle (ORC) are combined because the temperature range of these turbines is convenient for extra power production. R245fa is chosen as a working fluid for ORC-sub-system. The rejected heat energy from ORC can be transferred to the double effect absorption cooling system (DEACS) to produce cooling. After heating the DEACS working fluid in the generator-I, the waste heat of dish collector working fluid is extracted through HEX-II by blowing air across it. The produced hot air in HEX-II is passed through the wet products for the drying aims. The hot working fluid coming from the HEX-II at point 6 is passed through the heat pump evaporator between points states 6 and 7 where the heat pump working fluid absorbs its heat. Then, heat pump working fluid rejects its heat between points states 19 and 16 to keep the high temperature of heated area. Then, the cold working fluid of PDC goes to the CST at point 7.

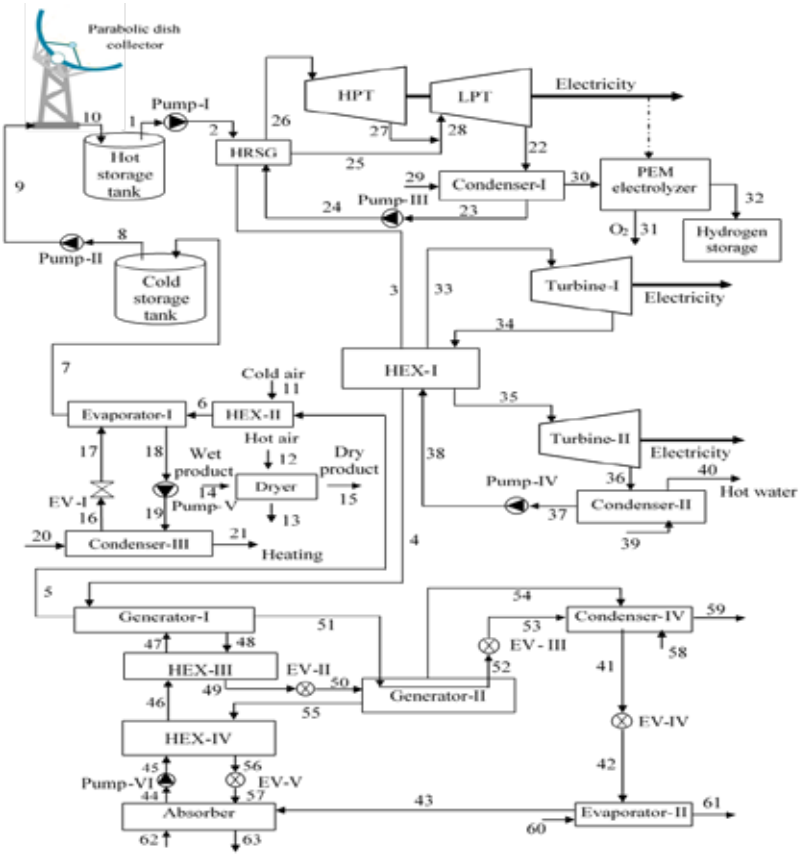


Fig. 1: Schematic diagram of solar energy based integrated system with hydrogen production

III. Thermodynamic analysis

In this section, the general mass, energy, entropy and exergy balance equalities for steady-state and steady-flow conditions are given based on the thermodynamic laws and operating conditions of integrated system for multi-generation to develop a clear understanding of systematic approach. The general mass, energy, entropy and exergy balance equations can be defined as follows, respectively (Dincer and Rosen, 2012)

$$\sum \dot{m}_i = \sum \dot{m}_e \quad (1)$$

$$\sum \dot{m}_i h_i + \sum \dot{Q}_i + \sum \dot{W}_i = \sum \dot{m}_e h_e + \sum \dot{Q}_e + \sum \dot{W}_e \quad (2)$$

$$\sum \dot{m}_i s_i + \sum \frac{\dot{Q}_{cv}}{T_o} + \dot{S}_{gen} = \sum \dot{m}_e s_e \quad (3)$$

$$\sum \dot{m}_i ex_i + \sum \dot{E}x_i^Q + \sum \dot{E}x_i^W = \sum \dot{m}_e ex_e + \sum \dot{E}x_e^Q + \sum \dot{E}x_e^W + \dot{E}x_D \quad (4)$$

where $\dot{m}$ is the mass flow rate, the subscripts i and e are the inlet and outlet conditions, $\dot{Q}$ and $\dot{W}$ are the heat flow and power rates, s is the specific entropy, $\dot{S}_{gen}$ is the entropy generation rate, $\dot{E}x_Q$ and $\dot{E}x_W$ indicate the exergy transfer rates associated with heat and boundary or shaft work, respectively.

$$\dot{E}x_Q = \left(1 - \frac{T_o}{T}\right)\dot{Q} \quad (5)$$

$$\dot{E}x_W = \dot{W} \quad (6)$$

The flow associated specific exergy of a system part (i) can be defined as follows;

$$ex_i = ex_{ph,i} + ex_{ch,i} + ex_{ke,i} + ex_{pe,i} = \quad (7)$$

The kinetic, potential and chemical parts of exergy appear in the above equation are assumed to be negligible during the course of this paper as the changes in velocities, within the process parts are unimportant compared to the contributions of other indicators, and also there is no chemical reaction. The specific physical exergy parts can be written as follows;

$$ex_{ph} = h - h_o - T_o(s - s_o) \quad (8)$$

where h and h_o are specific enthalpies, and s and s_o are the specific entropies at the real case and the reference environment states, respectively. The energy and exergy efficiency equations can be defined as follows;

$$\eta = \frac{\sum \text{useful output energy}}{\sum \text{input energy}} = 1 - \frac{\sum \text{energy loss}}{\sum \text{input energy}} \quad (9)$$

$$\psi = \frac{\sum \text{useful output exergy}}{\sum \text{input exergy}} = 1 - \frac{\sum \text{exergy loss}}{\sum \text{input exergy}} \quad (10)$$

IV. Results and discussions

The exergy destruction rate, exergy destruction ratio and exergy efficiency of solar energy based integrated system and its sub-systems are illustrated in Table 1. As seen from this table, the PDC and Rankine cycle have the maximum exergy destruction rate among the other sub-systems. Also, the dryer sub-system has the maximum exergy efficiency, and DEAC sub-system has the lowest exergy efficiency.

Tab. 1: Thermodynamic analysis outputs of integrated system and its sub-components

Sub-systems	Exergy destruction rate (kW)	Exergy destruction ratio (%)	Exergy efficiency (%)
Parabolic Dish collector	24,750	33.70	42.14
Rankine cycle	18,400	25.06	41.86
PEM-electrolyzer	7,840	10.68	33.67
Double effect absorption cooling	8,780	11.96	15.07
Dryer	5,745	7.82	67.85
Heat pump	7,920	10.78	26.97
Whole system	73,435	100	43.57

The effect of ambient temperature on the exergy destruction rate and exergy efficiency of solar based integrated system is shown in Fig. 2. As ambient temperature changes from 0°C to 40°C, the exergy destruction rate of integrated system decreases from 78,435 kW to 70,398 kW, while exergy efficiency of integrated system increases from 38.55% to 46.57%.

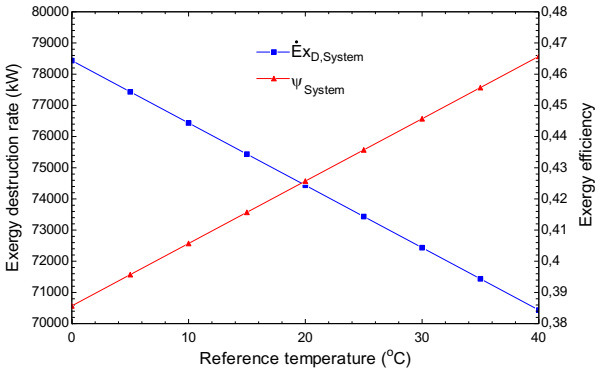


Fig. 2: Effect of ambient temperature on the integrated system exergy destruction rate and exergy efficiency

Fig. 3 shows that the changes of exergy destruction rate and exergy efficiency with respect to solar radiation flux. As solar radiation flux increases from 500 W/m^2 to 1000 W/m^2, the exergy destruction rate increases from 70,650 kW to about 75,510 kW, and also the exergy efficiency of whole system increases from nearly 40% to 45.24%.

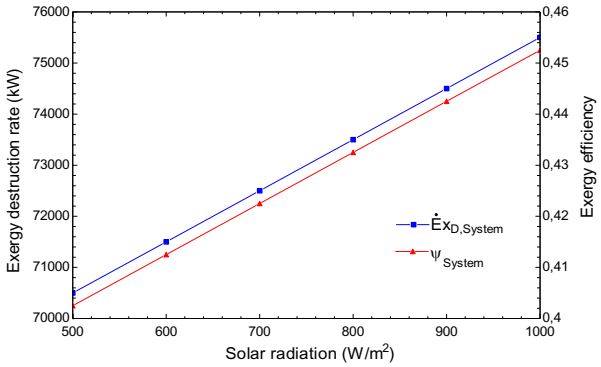


Fig. 3: Effect of solar radiation on the integrated system exergy destruction rate and exergy efficiency

Fig. 4 shows how solar radiation flux effects the total power and hydrogen production rate from whole system. As solar radiation flux increases from 500 W/m^2 to 1000 W/m^2, both of the power and hydrogen production rate increase because rising solar radiation flux has positive effect on the integrated system performance.

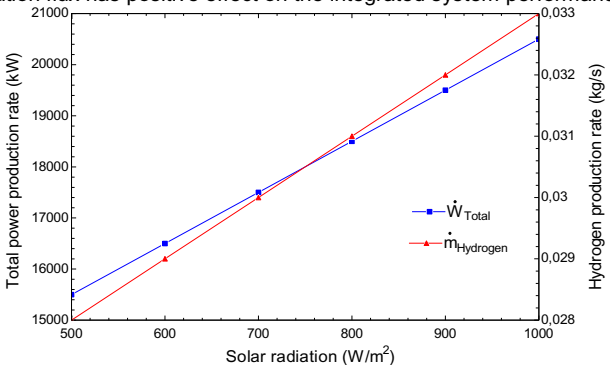


Fig. 4: Effect of solar radiation on the total power and hydrogen production rate

The impact of absorption chiller evaporator temperature both the on energetic coefficient of performance (COP_{en}) and exergetic coefficient of performance (COP_{ex}) is shown in Fig. 5. Based on the analysis outputs, as the absorption chiller evaporator temperature increases from 5°C to 20°C, the COP_{en} increases from about 0.76 to 0.85. On the other hand, with the same temperature change, the COP_{ex} decreases from about 0.26 to 0.14.

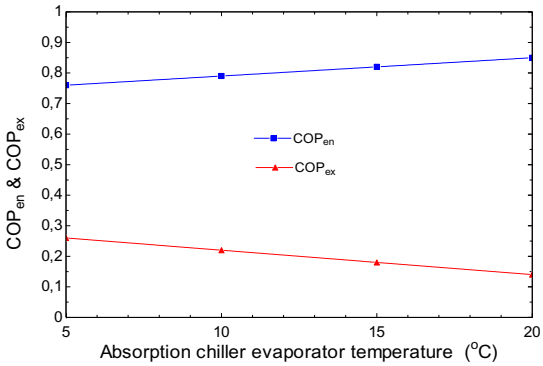


Fig. 5: Effect of absorption chiller evaporator temperature on COP_{en} and COP_{ex}

V. Conclusions

In this study, the thermodynamic analysis of PDC based integrated system for hydrogen production is analyzed. The exergy destruction rate, exergy destruction ratio and exergy efficiency of integrated system and its sub-systems are presented. The parametric analysis is performed in order to see how some variables effect the integrated system performance. The parametric variables of this study are the reference temperature and solar radiation flux. Some concluding outputs are given as

- The parameters, namely reference temperature and solar radiation flux, have great influence on the multigeneration system efficiency.
- Also, the multigeneration energy production system has much higher exergy rate than the other production systems such as trigeneration, cogeneration or single generation.

References

Al-Sulaiman FA, Dincer I, Hamdullahpur F. Exergy modeling of a new solar driven trigeneration system. Solar Energy 2011;85(9):2228e43.

Balta, M. T., Kizilkan, O., & Yılmaz, F. (2016). Energy and exergy analyses of integrated hydrogen production system using high temperature steam electrolysis. International Journal of Hydrogen Energy, 41(19), 8032-8041.

Bicer, Y., & Dincer, I. (2016). Analysis and performance evaluation of a renewable energy based multigeneration system. Energy, 94, 623-632.

Dincer, I., Rosen, M.A. "Energy, Environment, and Sustainable Development". Elsevier: Oxford, 2012.
El-Emam, R. S., & Dincer, I. (2018). Investigation and assessment of a novel solar-driven integrated energy system. Energy Conversion and Management, 158, 246-255.

Ezzat MF, Dincer I. Energy and exergy analyses of a new geothermal–solar energy based system. Sol Energy 2016;134:95–106.

Khalid, F., Dincer, I., & Rose.n, M. A. (2015). Energy and exergy analyses of a solar-biomass integrated cycle for multigeneration. Solar Energy, 112, 290-299.

Leiva-Illanes R, Escobar R, Cardemil JM, Alarcón-Padilla D-C. Thermoeconomic assessment of a solar polygeneration plant for electricity, water, cooling and heating in high direct normal irradiation conditions. Energy Convers Manage 2017;151:538–52.

Ozturk, M., & Dincer, I. (2013). Thermodynamic analysis of a solar-based multi-generation system with hydrogen production. Applied Thermal Engineering, 51(1-2), 1235-1244.

Yuksel, Y. E., Ozturk, M., & Dincer, I. (2016). Thermodynamic performance assessment of a novel environmentally-benign solar energy based integrated system. Energy Conversion and Management, 119, 109-120.

Modeling of Syngas Production from Biogas via Tri-reforming Process

Reiyu Chein*, *Wen Hwai Hsu

Dept. of mechanical engineering, National Chung Hsing University, Taiwan

The tri-reforming (TR) process was employed for syngas production from biogas at elevated pressures in this study. In the TR process air and H2O were added simultaneously as the reactants in addition to the main biogas components. The effects of various operating parameters such as pressure, temperature, and reactant composition on the reaction performance were studied numerically. From the simulated results it was found that CH4 and CO2 conversions can be enhanced and higher H2/CO ratio can be obtained by increasing the amount of air. However, decreased H2 yield could result due to the reverse water-gas shift (WGS) reaction. Higher CH4 conversion and H2/CO ratio can be obtained with the increased H2O addition. However, negative CO2 conversion could result due to WGS and reverse CO2 methanation reactions. The dry reforming reaction resulting in positive CO2 conversion can only be found at high reaction temperature. For all cases studied, low or negative CO2 conversion was found because of CO2 production from methane oxidation, water-gas shift, and reverse CO2 methanation reactions. It was found that the CO2 conversion can be enhanced in the TR process by a small amount of added H2O. It was also found that the first-law efficiency increases with the increased reaction temperature because of higher H2 and CO yields. The second-law efficiency was found to decrease with increased temperature because of higher exergy destruction due to more complete chemical reaction at high temperatures.

Keywords: Biogas, tri-reforming process, CH4/CO2 conversion, H2/CO ratio, first-law/second-law efficiency.

The Effect of Co-catalyst and Novel Heterogeneous Active Photocatalysts for Hydrogen Evolution Under Solar Energy

***Duygu Akyüz*[1], Özlem Uğuz[2], Irem Tanışık[2], Rana Muhammad Zunain Ayaz[2], Cevat Sarıoğlu[3], Fatma Karaca Albayrak[2], Ali Rıza Özkaya[1], Atıf Koca[2]**

[1]*Department of Chemistry, Marmara University, Istanbul, Turkey*
[2]*Department of Chemical Engineering, Marmara University, Istanbul, Turkey*
[3]*Department of Metallurgy and Materials Engineering, Marmara University, Istanbul, Turkey*

In recent years, heterogeneous photocatalysts has received much research interest because of its powerful potential applications in clean energy production and environmental remediation. The heterogeneous photocatalysts for hydrogen evolution from water by using solar energy need to decrease active and stable co-catalysts using of expensive and rare elements.Transition metals including chalcogenides (CdS, ZnS etc.) have long time been one of the most promising inorganic photocatalysts for hydrogen production[1, 2]. However, the photo-corrosion, recombination rates and efficient charge transfers of these photocatalysts are the most serious problems which constrains its development. Here, we report the design and fabrication of reduced graphene oxide (RGO) doped-cadmiumzincsulfide (RGO-Cd0.6Zn0.4S) nanocomposite by using solvothermal method. Synthesized nanocomposite loaded with different noble metals (Ru, Rh, Pt) as co-catalyst via photodeposition. The heterogeneous photocatalysts were characterized with SEM, TEM, XRD and UV-Vis diffuse reflectance spectroscopy. The obtained photocatalyst were tested in photocatalytic reactor for photocatalytic hydrogen production and investigated effect of co-catalyst on photoactivity.

Acknowledgement: We thank to The Scientific and Technological Research Council of Turkey (TUBITAK, Project Number: 116M567) for its financial support.

Keywords: Heterogeneous photocatalyst, Hydrogen production, Solar energy, Reduced graphene oxide.

Active Photocatalysts Designed by Sulphurization Method for Hydrogen Production

***Irem Tanışık*[1], Duygu Akyüz[2], Rana Muhammad Zunain Ayaz[1], Özlem Uğuz[1], Cevat Sarıoğlu[3], Fatma Karaca Albayrak[1], Ali Rıza Özkaya[2], Atıf Koca[1]**

[1]Department of Chemical Engineering, Marmara University, Istanbul, Turkey
[2]Department of Chemistry, Marmara University, Istanbul, Turkey
[3]Department of Metallurgy and Materials Engineering, Marmara University, Istanbul, Turkey

Hydrogen is the most abundant element in the nature. Since hydrogen can be transported into a renewable and non-polluting energy resource, it is considered as the future energy. Hydrogen is produced mostly from the fossil fuels. Since the sun is primary and renewable energy source, photocatalytic hydrogen production becomes a current issue[1, 2]. For photocatalytic hydrogen production from water, several photocatalysts have been tested. In order to increase hydrogen energy efficiency, it is known that CdxZn(1-x)S is an efficient photocatalyst for hydrogen production. Therefore, in here, we synthesised CdxZn(1-x)S nanoparticles on graphene derivatives by using thermal sulphurization method by using elemental sulphur as the sulphur source. Then, characterization of compounds for determining crystal systems, lattice parameters, band gap and surface morphologies, was done by various techniques including X- Ray diffractometer, scanning electron microscopy and UV-VIS-NIR spectrophotometer. Finally the GO/ CdxZn(1-x)S and RGO/ CdxZn(1-x)S composites were tested as active photocatalysts for hydrogen evolution reactions and basic photocatalytic parameters were analysed.

Acknowledgement: We thank to The Scientific and Technological Research Council of Turkey (TUBITAK, Project Number: 116M567) for its financial support.

Keywords: Photocatalyst, Hydrogen production, Solar energy, Graphene and graphene derivate, Sulphurization.

Hydrogen Production from Water as Photoelectrochemical by Using Solar Light Irradiation

Rana Muhammad Zunain Ayaz[1], Duygu Akyüz[2], Özlem Uğuz[1], Irem Tanışık[1], Cevat Sarıoğlu[3], Fatma Karaca Albayrak[1], Ali Rıza Özkaya[2], Atıf Koca[1]

[1]Department of Chemical Engineering, Marmara University, Istanbul, Turkey
[2]Department of Chemistry, Marmara University, Istanbul, Turkey
[3]Department of Metallurgy and Materials Engineering, Marmara University, Istanbul, Turkey

The ever increasing population and growing demand of energy, we cannot rely on exhaustible energy resources anymore. Introducing Hydrogen as a sustainable, and trustworthy energy carrier and its production through Photoelectrochemical (PEC) reactions, was an important development. The reported in literature, doping of ZnS with transition metal cations improves the absorbance of ZnS in visible region of light. Cd1−xZnxS, which is the solid solution of CdS and ZnS, has controllable band structure and excellent performance under visible light irradiation [1, 2]. But desired efficiency of Cd1−xZnxS is still a milestone to reach. On contrary, a strictly two-dimensional material, graphene oxide, possesses exceptionally high crystal and electronic quality, improved effective electron transfers and exhibits enhancement of specific surface area. We synthesized, which Cd1−xZnxS photocatalysts supported GO and/or rGO by sulphurization method for obtain photo-electrodes possess higher photoelectrochemical responses such as a higher anodic photo-current density, and a higher solar to hydrogen conversion efficiency under visible light irradiation. Obtained photo-electrodes were tested for hydrogen production from water as photoelectrochemical under solar light irradiation and photoelectrochemical hydrogen production system was optimized with respect to all system components.

Acknowledgement: We thank to The Scientific and Technological Research Council of Turkey (TUBITAK, Project Number: 116M567) for its financial support.

Keywords: Photocatalyst, Hydrogen production, Solar energy, photo-electrodes, photoelectrochemistry.

Hydrogen Storage Capacity Investigations of Pd Loading Ratio on MW-CNTs via Supercritical Fluid Deposition Method

[1*]Ebru Erünal, [2]Fatma Ulusal, [3]Selda Odabaşı, [2]Bilgehan Güzel, [3]Deniz Üner
[1] Çukurova University, Ceyhan Engineering Faculty, Chemical Engineering Department, Ceyhan, Adana, 01950, Turkey
[2] Çukurova University, The Faculty of Arts And Sciences, Chemistry Department, Sarıçam, Adana, 01100, Turkey
[3] Middle East Technical University, Faculty, Department of Chemical Engineering, Çankaya, Ankara, 06800, Turkey

* E-mail:eerunal@cu.edu.tr

Abstract

A new bipyridyl precursor that provides reduction at moderate conditions was employed for $scCO_2$ deposition to prepare 1% and 4% Pd doped multi walled carbon nanotube (CNT) materials for hydrogen storage. Temperature programmed desorption (TPD) and reduction (TPR) performance as a function of Pd loading on these materials were compared together with pristine carbon nanotubes. The BET surface areas were determined for pristine CNT as 176 m^2/g with a pore size of 17.6 nm, for %1 Pd/CNT 199.62 m^2/g with a pore size of 21.82 nm and for %4 Pd/CNT 205.22 m^2/g with a pore size of 19.36 nm. TPR measurements revealed a Pd hydride formation on the doped materials since hydrogen decomposition peaks for both doped materials were observed while no decomposition was observed for pristine CNT. Pd loading ratio was found to have a strong effect on PdH_x formation due to the estimated hydrogen decomposition from these sites as 118 µmole/g sample for 4% Pd doped CNT and 8.38 µmole/g sample for 1% Pd doped.

Keywords: Hydrogen storage, multi-walled carbon nanotubes, temperature programmed reduction, temperature programmed desorption, supercritical fluid deposition

I. Introduction

The decrease in fossil energy sources and other long-term environmental problems caused by fossil fuel usage lead to the development of alternative technologies that utilize hydrogen which is considered as one of the promising renewable and clean energy sources. Safe storage of hydrogen at ambient temperatures and moderate pressures is one of the important issues that should be overcome in order to be able to use hydrogen energy in daily life applications (Schapplach and Züttel ,2001; Jena, 2011). Carbon nanotubes (CNTs) which are doped with transition metals are attractive hydrogen storage materials due to their low mass density, high surface area, narrow and nanometer pore size distribution (Sakintuna et al. 2007). Palladium (Pd) shows a strong hydrogen adsorption performance when dispersed on CNTs because of the spillover process resulting in migration of hydrogen atoms through the metal particles and diffusion into the CNT supports (Zacharia et al., 2005). The dispersion of Pd atoms on CNTs, which directly depends on the synthesis method, is very effective on the spillover mechanism. Among different synthesizing routes by which it is harder to control the nanoscale particle shape and size with desirable dispersion, supercritical carbon dioxide ($scCO_2$) deposition is a powerful method to prepare well-dispersed nanoparticles among these techniques dependent on the deposition method. Generally precursors of acetylacetonate derivatives like $Pd(acac)_2$ or hexafluoroacetylacetonate ($Pd(hfa)_2$) which require high temperature or pressure conditions during reduction phase of $scCO_2$ deposition are used. In this study, new bipyridyl derivative precursors that enable reduction at moderate conditions are synthesized and exploited to prepare Pd doped CNTs via $scCO_2$ deposition method in order to have a good dispersed material. The hydrogen storage performance at moderate pressure and ambient temperature as a function of Pd loading ratio was tracked via temperature programmed desorption (TPD) and reduction (TPR) analysis.

II. Experimental Set-up and Procedure

All materials were used without further purification. Multiwall Carbon Nanotube (CNT) was purchased from Sigma-Aldrich with a purity of ≥95%. The nanotubes have an outer mean diameter of 6–9 nm with a diameter distribution of 5.5–6.6 nm and the average length was reported as 5 µm in product specifications sheet. Palladium chloride and 2,2'bipyridyl materials were purchased from ABCR GmbH (both with a purity of 99%). For adsorption experiments, ultrahigh pure grade (99.999%) of Hydrogen (H_2), Argon (Ar) and Helium (He) gases (purchased from Linde) were used. Details of precursor synthesizing and $scCO_2$ deposition are given in Erünal et al. (2017). The deposition conditions were 2500 psi CO_2 and 80°C while reduction was carried out with 10.3 bar H_2. The experimental setup is shown in Fig.1.

Temperature Programmed Reduction (TPR) and Temperature Programmed Desorption (TPD) analysis of CNT and Pd/CNT were carried out on Micromeritics 2720 Instrument. H_2-TPR experiments (ca. 20 mg) were performed in the presence of 25 ml/min, 10% H_2 balance Ar flow up to 800°C with a temperature ramp of 5°C/min. After H_2-TPR profiles were obtained, the samples were cooled down to room temperature with a flow of 10% H_2 balance Ar. TPD experiments were performed immediately after cooling of the samples up to room temperature. TPD profiles of the samples were recorded in the presence of He flow up to 800°C with a temperature ramp of 5°C/min.

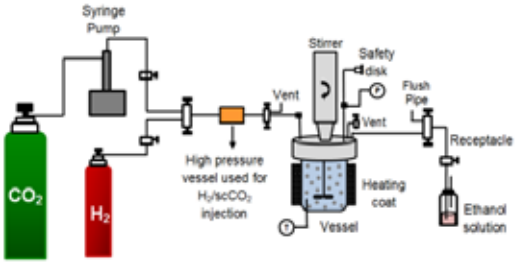


Fig. 1: Supercritical CO_2 deposition reactor system

III. Analysis

The quantitative analysis of palladium was done by ICP-OES (Perkin Elmer 2100 DV). The surface morphology was analyzed with XRD (Rigaku Miniflex CuK_α, λ=0.154nm). BET analyses were recorded at 77.4 K. XRD spectra can be seen in Fig. 2. Similar peaks were observed for both samples while Pd peaks are sharper and more distinct on 4%Pd doped material as expected. Besides, the broader peak between 67-70° designates PdH_x which can be better observed on other support materials like γ-Al_2O_3 as shown in Ulusal et al. (2017) but with CNT supports, they can't be distinguished well from XRD spectrum. Addition to XRD analyses, the surfaces were characterized with BET measurements as 176 m^2/g with a pore size of 17.6 nm for pristine CNT, 199.62 m^2/g with a pore size of 21.82 nm for % 1 Pd/CNT and 205.22 m^2/g with a pore size of 19.36 nm for % 4 Pd/CNT. The doping enhances surface area of pristine CNT. Hence, as Pd loading ratio increases, the increase in surface area has not changed drastically. This can be attributed to the slight decrease in pore volume of higher Pd loaded material.

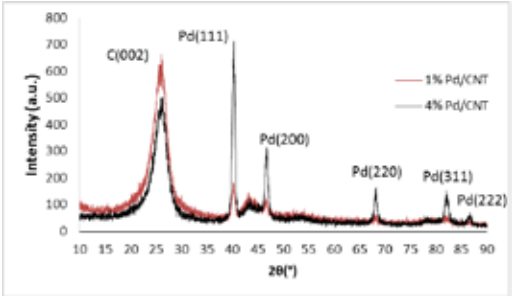
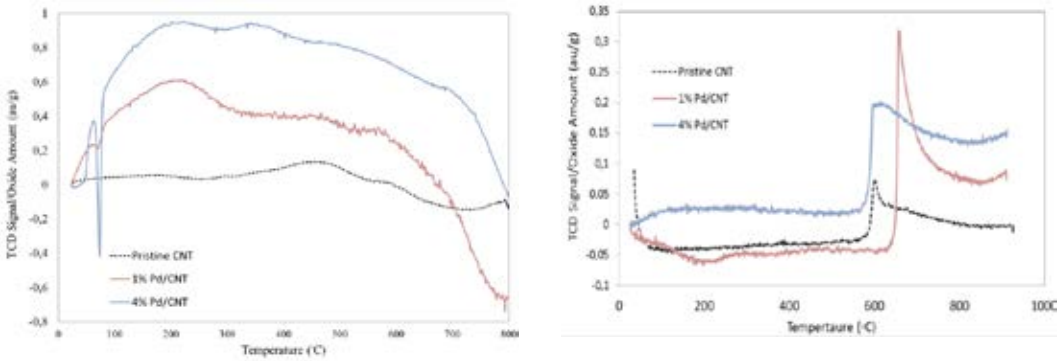


Fig. 2: XRD Spectra of a) 1%Pd doped CNT b) 4%Pd doped CNT

IV. Results and discussions

Hyrdogen uptake capacity was tracked according to temperature programmed reduction (TPR) and desorption (TPD) performances as a function of Pd loading and compared together with pristine CNTs in Fig. 3.a&b. Both doped samples show a hydrogen decomposition peak during TPR experiments around 60°C. This sharp decomposition peak show PdH_x sites that can not be easily detected with XRD due to the strong Pd(220) site peak as seen in Fig. 2. Hence, a recent study by Ulusal et al. (2017) showed that PdH_x sites can be easily detected for different supports with XRD. The initial hydrogen decomposition of 4% Pd/CNT was calculated approximately 118 µmole/g sample while for 1% Pd/CNT, it was found around 8.38 µmole/g sample. It is understood that hydrogen occupies these cites not linearly as a function of Pd ratio. This phenomenon can be attributed to the relation between Pd loading ratio and applied pressure during reduction under $scCO_2$ conditions together. Therefore, this decomposed hydrogen is a result of reduction during sample preparation and shouldn't be considered as the stored hydrogen within the materials. Still TPR esperimetns showed that at moderate temperatures below 70°C, this hydrogen emanating from PdH_x sites within the material can still be utilized. On the other hand, as temperature increased, the increase in hydrogen uptake capacities for both Pd doped materials can be tracked in Fig. 3.a. This is due to the spillover mechanism which was discussed extensively in literature by Yoo et al. (2004), Zacharia et al. (2005) and Prins (2012). Temperature programmed desorption (TPD) results under He flow can be seen in Fig. 3.(b). For pristine CNT, an intense peak around 40°C tailing until 100°C corresponds to hydrogen desorption at moderate temperatures. This phenomenon can not be seen on doped materials. Apart from that peak both Pd/CNTs and pristine CNT exhibit similar desorption behaviour at higher temperatures around 600°C with 1% Pd doped material has the highest intensity. The hydrogen desorption at these high temperatures is associated with the aromatization of C-C bonds saturated during hydrogen storage period as explained by Erünal et al. (2017). Similar to these findings, Yamanaka et al. (2004) also reported the decrease of hydrogen desorption temperature of CNTs when coated with metals which act as a catalyst. This was related to the nature of strong C–H bonds during adsorption on pristine CNTs. The whole hydrogen uptake as a function of temperature between 100-600°C was calculated as 8.7 µmole/ g sample, 5.9 µmole/ g sample for 4% Pd/CNT and 1% PdCNT while for pristine CNT

hydrogen uptake between room temperature and 760°C was calculated as 1.3 µmole per g sample.



(a) (b)

Fig. 3. a) Temperature Programmed Reduction (TPR) b) Temperature Programmed Desorption (TPD) of Pristine CNT (dashed black lines), 1% Pd/CNT(solid red lines) and 4% Pd/CNT materials (Blue solid lines)

V. Conclusions

Pd was successfully loaded in different amount on CNTs through $scCO_2$ deposition with new bipyridyl precursors that provide reduction at moderate conditions. The enhancement of hydrogen uptake as a function of increased Pd loading was oberserved together with the enhancement of surface areas. According to TPR experiments PdH_x formation on both of the doped materials was verified. Hyrdogen amounts on these sites were estimated approximately as 118 µmole/g sample for 4% Pd doped CNT while for 1% Pd doped it was around 8.38 µmole/g sample. Moreover, TPR experiments around showed spillover effect in means of hydrogen dissociation by Pd atoms. It is predicted that these atoms can be used to saturate the C-C double bonds in CNT structure. Consequently, the peaks obtained during TPD experiments around 600°C for both doped and undoped materials was attributed to the decomposition of these cyclic saturated compounds to aromatics.

Acknowledgements

Prof. Dr. Ramazan Esen for XRD measurements and and Atalay Çalışan for BET measurements is greatly acknowledged.

References

Erünal E., Ulusal, F., Aslan, M.Y., Güzel B., Üner D. Enhancement of hydrogen storage capacity of multi-walled carbon nanotubes with palladium doping prepared through supercritical CO_2 deposition method, International Journal of Hydrogen Energy, https://doi.org/10.1016/j.ijhydene.2017.12.058 (2017).

Jena P. Materials for hydrogen storage: past, present, and future. Journal of Physical Chemistry Letters, 2, 206-211 (2011).

Prins R. Hydrogen Spillover. Facts and Fiction. Chemical Reviews, 112, 2714-2738 (2012).

Sakintuna B., Lamari-Darkrim F., Hirscher M. Metal hydride materials for solid hydrogen storage: a review. International Journal of Hydrogen Energy, 32, 1121-1140 (2007).

Schlapbach L., Züttel A. Hydrogen-storage materials for mobile applications. Nature, 414,353-358, (2001).

Yamanaka S., Fujikane M., Uno M., Murakami H., Miura O. Hydrogen content and desorption of carbon nano-structures. Journal of Alloys and Compdounds, 366, 264-268 (2004).

Yoo E., Gao L., Komatsu T., Yagai N., Arai K., Yamazaki T., Matsuishi K., Matsumoto T., Nakamura J. Atomic hydrogen storage in carbon nanotubes promoted by metal catalysts. Journal of Physical Chemistry B,108, 18903-18907 (2004).

Zacharia R., Kim K.Y., Fazle Kibria A.K.M., Nahm K.S. Enhancement of hydrogen storage capacity of carbon nanotubes via spill-over from vanadium and palladium nanoparticles. Chemical Physics Letters, 412, 369-375 (2005).

Photoelectrochemical Hydrogen Production Using Cd(1-x)ZnxS And Its Modifications with Graphene Derivatives

***Özlem Uğuz*[1], Duygu Akyüz[2], Rana Muhammad Zunain Ayaz[1], Irem Tanışık[1], Cevat Sarıoğlu[3], Fatma Karaca Albayrak[1], Ali Rıza Özkaya[2], Atıf Koca[1]**

[1]*Department of Chemical Engineering, Marmara University, Istanbul, Turkey*
[2]*Department of Chemistry, Marmara University, Istanbul, Turkey*
[3]*Department of Metallurgy and Materials Engineering, Marmara University, Istanbul, Turkey*

Photoelectrochemical hydrogen production is one of the most trending approaches to generate renewable energy source having no hazard on the environment. In this concept, the use of semiconductors is of great importance to determine the efficiency of the overall process. To capture a large share of the solar spectrum and obtain a better output from the hydrogen production process, narrow bandgap energy, proper conduction band position, slow recombination rate and high stability are the most important characteristics to consider. Composites such as TiO2, CdS, WO3, ZnO, ZnS, and GaAs, etc. are the most commonly used materials for photoelectrochemical hydrogen production studies. Nevertheless, the efficiencies which can be obtained by utilizing these materials as semiconductors are low because of their limitations, such as stability, efficiency, electron-hole recombination and etc. Thus, different strategies are developed to achieve better efficiencies, slow recombination rate and high stability. In this regard, utilization of Cd1-xZnxS type photocatalysts can be thought to be a good solution to provide a semiconductor material with a controllable band structure by causing a higher electron mobility, and electrochemical stability [1,2].

In this study, Cd(1-x)ZnxS composites having different ratios of graphene derivatives (graphene oxide, and/or reduced graphene oxide GO/rGO) were synthesized by solvethermal methods. Prepared samples were coated on the indium tin oxide (ITO) electrodes with different coating techniques. After the samples were characterized by both structurally and morphogically by SEM, FTIR, XRD, UV-vis diffuse reflectance spectroscopy analyses, photoelectrochemical hydrogen production by water splitting were conducted under simulated solar light irradiation. The results obtained from the required analyses and hydrogen production experiments were discussed with respect to types, compositions and morphology of the semiconductor composites, electrolyte system, and electrode modification techniques. And finally the results were compared with the literate to predict technological feasibility of the active structures.

Acknowledgement: We thank to The Scientific and Technological Research Council of Turkey (TUBITAK, Project Number: 116M567) for its financial support.

Keywords: Photoelectrochemical hydrogen production,cadmium zinc sulfide, graphene oxide, reduced graphene oxide.

Energy and Exergy Analyses of a Novel Ammonia Combined Power Plant Operating with a Gas Turbine and a Solid Oxide Fuel Cell

M.F Ezzat[1,2], I. Dincer[1]
[1]Faculty of Engineering and Applied Science, University of Ontario Institute of Technology,
2000 Simcoe Street North, Oshawa, Ontario, L1H 7K4, Canada.
[2]Automotive and Tractor Engineering Department, Faculty of Engineering, Minia University, Egypt.

* E-mail: muhammad.ezzat@uoit.ca, ibrahim.dincer@uoit.ca

Abstract
This study deals with a new combined power plant that is using only ammonia as a fuel for trigeneration purpose. The system comprises two main powering sources, a gas turbine running on ammonia and using hydrogen as a promoter, and an ammonia fed solid oxide fuel cell. The waste heat from the gas turbine exhaust gases will be reovered using rankine cycle to generate an additional electric power, the residual thermal energy from the exhaust gases will be used to operate an absorption chiller to provide refrigeration for the industry. The electricity generated from the rankine cycle will be supplied to an ammonia electrolyzer to produce hydrogen, which can be stored for other application use and supplied to the gas turbine to function as a combustion promoter. The system is analysed thermodynamically using the first and second law of thermodynamics. Moreover, Exergy destruction of the different combined power plant units is determined. Furthermore, a comprehensive parametric study has been carried out to investigate the effect of varying ambient conditions, operating and design parameters on the overall performance of the combined system and subsystems.

Keywords: Ammonia; Hydrogen; Solid oxide fuel cell; Gas turbine; Energy; Exergy; Efficiency

I. Introduction

The concept of integrating gas turbine (GT) with solid oxide fuel cell (SOFC) in power plants is introduced and analysed many years ago. Ide et al. (1989) compare the overall efficiencies of three different fuel cell power generation systems. One of the systems comprises SOFC unit, natural gas reformer and a power recovery gas turbine. Massardo and Lubelli (2000) examined the performance via the theoretical simulation of a combined cycle consists of internal reforming solid oxide fuel cell (IRSOFC) and GT. Granovskii et al. (2007) carried out second law analyses for two SOFC–gas turbine systems to identify their efficiencies and abilities to produce power at various rates of oxygen transport via the SOFC electrolyte. Haseli et al. (2008) studied the exergetic performance of a high-temperature solid oxide fuel cell (SOFC) combined with a conventional recuperative gas turbine (GT) plant. They determined the exergy efficiency of the overall plant and the exergy destruction rate of each component in the system. It is also found that augmenting the turbine inlet temperature (TIT) leads to a mitigation in the energetic and exergetic efficiencies of the cycle and enhanced the total specific power output of the system. Moreover, increasing compressor pressure ratio results in an upsurge in the exergy destruction rate of the system. Ishak et al. (2012) integrated direct ammonia solid oxide fuel cell with a gas turbine (DA-SOFC/GT) in a novel combined cooling, heating and power (CHCP) cycle. The integration strategy is compared for oxygen ion-conducting solid oxide fuel cells (SOFC-O) and hydrogen proton-conducting solid oxide fuel cells (SOFC-H). The results show that SOFC-H integrated system provides better performance compared to SOFC-O option. For instance, SOFC-H based integrated system achieved an energetic and exergetic efficiencies of 81.1% and 74.3% respectively, while the SOFC-O based integrated system reaches an energetic and exergetic efficiencies of 76.7% and 69.9% respectively. The systems are more evaluated via a comprehensive parametric study to study the influence of changing the operating conditions and parameters on the overall energetic and exergetic performance of the systems.

Fossil fuels account for 78% of the world final energy consumption in 2014 (REN21 2016), which results in the release of huge amounts of greenhouse gases emissions. Therefore, replacing fossil fuels with clean and carbon free fuels would result in a significant reduction in these harmful emissions. One good option is to use ammonia as a fuel. Ammonia has the potential to replace fossil fuels in power production applications. Particularly, that ammonia can be combusted in an environmentally benign way producing nitrogen and water, Moreover, ammonia-specific energetic cost is around 13.3$ for every GJ which way less than other fossil fuels such as gasoline and compressed natural gas, which have the specific energetic cost of 29.1$/GJ and 38.3$/GJ respectively as asserted by Zamfirescu and Dincer (2008). Ammonia is also categorized as a sustainable fuel, and it can be easily manufactured utilizing the process of Haber-Bosh as stated by Dincer and Zamfirescu (2011). Integrating the energy systems for producing multiple useful outputs has proven to enhance the energy system performance and increase its efficiency (Dincer and Rosen 2013). Furthermore, the multigeneration approach can provide better cost effectiveness, and make the energy systems more sustainable with less environmental impact (I. Dincer and Zamfirescu 2012). For instance, Ezzat and Dincer (2016) proposed an integrated system for multigeneration purpose. They exploited geothermal energy (single flash stage power plant) and solar energy to produce various valuable outputs such as space heating, electricity, hot water, and refrigeration for the industry for residential applications. The energetic and exergetic efficiencies are found to be 69.6% and 42.8%, respectively.

Siddiqui and Dincer (2017) developed a novel solar-based multigeneration system integrated with an ammonia fuel cell and solid oxide fuel cell-gas turbine combined cycle to generate electric power, hydrogen, cooling and hot

water. The results showed that the overall multigeneration system energetic and exergetic efficiencies are found to be 39.1% and 38.7%, respectively. In this paper ammonia gas turbine and ammonia fed SOFC are combined to produce electric power. The non-utilized hydrogen and ammonia leaving the solid oxide fuel system are supplied to the combustor along with ammonia from the liquid ammonia tank to produce more power from GT system, at which hydrogen can enhance and increase the temperature of the combustion inside the combustor. Moreover, the exhaust released from the gas turbine is used to run Rankine cycle to produce additional electricity that can be used to operate ammonia electrolyte cell to produce hydrogen. The remaining heat in the exhaust gases is used to run an ammonia absorption chiller to produce cooling for industrial application.

II. System description

Fig.1 shows the proposed combined SOFC-GT system. The system comprises liquid ammonia tank, SOFC, compressor, combustor, gas turbine, Rankine cycle, Absorption chiller system (ACS), Ammonia electrolyte cell (AEC), two electric generators and an inverter to change the DC current obtained from the SOFC to AC current. As shown from the figure, the pressurized ammonia at 11 bar enters the SOFC at state point 1 at which it will be decomposed thermally into hydrogen and nitrogen using the heat generated from the SOFC due to thermodynamic irreversibilities. Air enters the compressor at state 4 and divided into two streams. The first stream leaves the compressor from state 5 and will be supplied to the SOFC, while the compressed air, which leaves the compressor from state 6 will be supplied to the combustor. Electrochemical reaction occurs in the SOFC between the supplied air and the decomposed hydrogen leading to the production of an electric power from state 8 which will be supplied for residential application after its current is changed from DC to AC. The remaining hydrogen and ammonia released from the anode of the SOFC at state 7 and will be supplied to the combustor along with an additional amount of liquid ammonia from ammonia tank. The combustion occurs in the combustor resulting in the release of high temperature exhaust gases, which will be used to run the gas turbine that is coupled with an electric motor to generate additional electric power from the system. The generated power supplies the compressor with the required electricity and any additional electricity will be directed to the residential use. The remaining thermal energy in the exhaust gases will be used to operate the RC to produce electricity that can be supplied to the AEC for hydrogen production and to run an ammonia ABS to produce cooling for industrial application. The electricity generated from the RC generator supplies the AEC at state 19, while liquid ammonia supplies the AEC at state 2. The provided electricity will decompose ammonia electrochemically into hydrogen, which leaves the AEC at state 20, and nitrogen, which leaves the AEC at state 21 as shown in the figure.

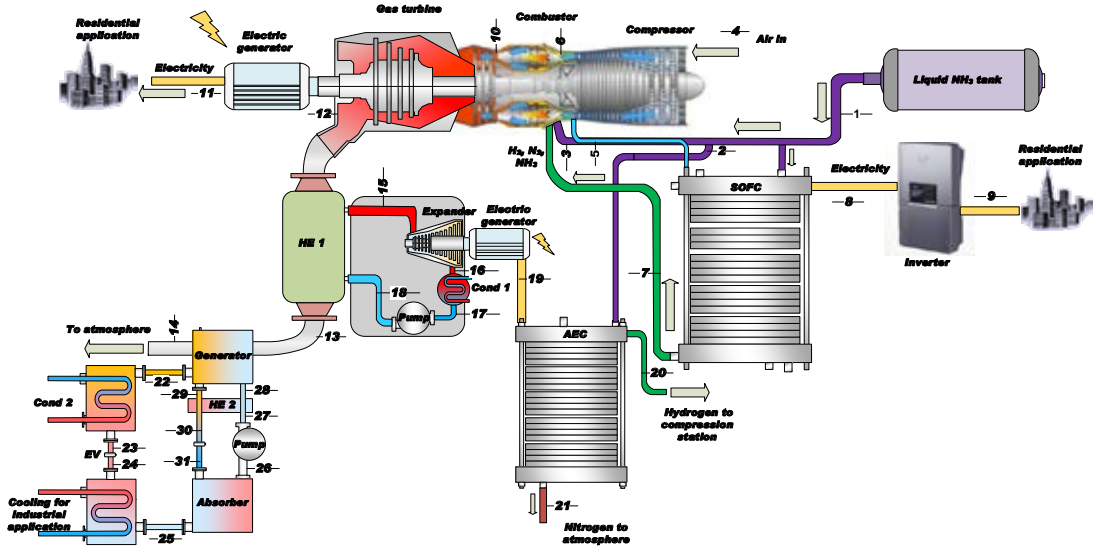


Fig. 1: Schematic of the combined SOFC-H-GT power plant

III. System analysis

The introduced integrated system is analyzed thermodynamically, and all the enthalpies, mass flow rates, pressures, exergies, and temperatures of the flows entering and leaving the system are identified and determined. Exergy destruction rates of the main components are also calculated to allocate the irreversible system losses. The mathematical modeling is executed utilizing the Engineering Equation Solver (EES) software. The following assumptions are taken into consideration in the system modelling:

- The reference temperature T0 = 298 K and reference pressure P0 = 101.325 kPa.
- The variations in the kinetic and the potential energies and exergies are ignored.
- The pressure losses are negligible. The pressure loss in pressure regulators are only considered.
- The combustion occurs completely in the combustor.

III. 1. Thermodynamic analysis

This section will include thermodynamic analysis for the main component of the system along with the energy and exergy efficiencies definition for the primary units in the system and the overall system.

The specific total exergy of flow can be written as follows:

$$ex_{flow} = ex^{ph} + ex^{ch} + ex^{ke} + ex^{pe} \quad (1)$$

The physical exergy can be expressed by the following equation:

$$ex^{ph} = (h - h_0) - T_0(s - s_0) \quad (2)$$

The chemical exergy for any gaseous mixture can be expressed as:

$$ex^{ch}_{mix} = \sum y_i ex^{ch}_i + RT_0 \sum y_i \ln y_i \quad (3)$$

III.1.1 Ammonia electrolyte cell

The molar flow rate of the hydrogen that can be obtained from the AEC unit can be calculated by:

$$\dot{N}_{H_2,out} = \frac{J_{AEC}}{3F} \quad (4)$$

The theoretical electrolysis voltage of liquid NH3 at any temperature can be calculated using Nernst's equation (Dong et al. 2016):

$$Er_{AEC} = -\frac{\Delta G^o}{3F} + \frac{RT_{AEC}}{3F} \ln(P_{N_2}^{0.5} P_{H_2}^{1.5}) \quad (5)$$

where P_{H_2} is the partial pressure of H_2, and P_{N_2} is the partial pressure of N_2

The required electrolysis voltage can be calculated by adding all the AEC resistances (activation, concentration and ohmic) to reversible cell voltage as expressed in the following equation:

$$E_{AEC} = Er_{AEC} + E_{act_{AEC}} + E_{ohm_{AEC}} + E_{conc_{AEC}} \quad (6)$$

The power required by the AEC for the electrolysis process unit can be determined as follows:

$$P_{AEC} = J_{AEC}\ E_{AEC}\ A_{cell}\ n_{cells} \quad (7)$$

III.1.2 Solid oxide fuel cell

The cell actual potential can be calculated as follows

$$E_{SOFC} = E_{r,SOFC} - E_{act} - E_{con} - E_{ohm} \quad (8)$$

where E_{SOFC} is the cell practical voltage, $E_{r,SOFC}$ is the cell reversible voltage, E_{act} represents the activation polarization, E_{con} refers to the concentration polarization and E_{ohm} denotes the ohmic polarization.

The reversible cell voltage can be calculated using Nernst equation as follows:

$$E_{r,SOFC}(T, P_i) = E_{r,SOFC}(T, P) + \frac{RT}{2F} \ln\left(\frac{P_{H_2} P_{O_2}^{\frac{1}{2}}}{P_{H_2O}}\right) \quad (9)$$

The amount of power that can be produced by every single cell can be obtained from the following equation:

$$\dot{W}_{cell} = E_{SOFC} \times J_{SOFC} \times A_{cell} \quad (10)$$

Here, J_{SOFC} is the fuel cell current density and A_{cell} is the geometric cell area.The overall stack power can be calculated by the equation below:

$$\dot{W}_{stack} = n_{fc} \times \dot{W}_{cell} \quad (11)$$

where n_{fc} is the number of cells in the fuel cell stack.

III.1.3 Combustor

The combustor is feed by two streams, the non-utilized fuel from the SOFC and fuel supplied from liquid ammonia tank, energy and exergy balance equations on a rate basis for the combustor can be written as follows:

$$\dot{N}_7 h_7 + \dot{N}_3 h_3 + \dot{N}_6 h_6 = \dot{N}_{10} h_{10} + \dot{Q}_{loss} \quad (12)$$

$$\dot{N}_7 ex_7 + \dot{N}_3 ex_3 + \dot{N}_6 ex_6 = \dot{N}_{10} ex_{10} + \dot{E}x^{Q_{loss}} + \dot{E}xd_c \quad (13)$$

III.1.4 Absorption chiller system

The heat supplied to the generator in the absorption chiller is defined as:

$$\dot{Q}_{Gen} = \dot{m}_{13}(h_{13} - h_{14}) \quad (14)$$

The outlet condition of the generator can be obtained by applying the following energy and exergy balance equations:

$$\dot{Q}_{Gen} + \dot{m}_{28} h_{28} = \dot{m}_{29} h_{29} + \dot{m}_{22} h_{22} \quad (15)$$

$$\dot{Q}_{Gen}\left(1 - \frac{T_o}{T_{s_{Gen}}}\right) + \dot{m}_{28} ex_{28} = \dot{m}_{29} ex_{29} + \dot{m}_{22} ex_{22} + \dot{Ex}_{d_{Gen}} \quad (16)$$

The cooling effect which takes place in the evaporator of absorption chiller cycle can be obtained using the following

equations:

$$\dot{Q}_{ABS,eva} = \dot{m}_{25}(h_{25} - h_{24}) \quad (17)$$

$$\dot{Q}_{ABS,eva}\left(1 - \frac{T_0}{T_{s_{eva2}}}\right) + \dot{m}_{24}\, ex_{24} = \dot{m}_{25} ex_{25} + \dot{E}x_{d_{eva2}} \quad (18)$$

III.1.5 Energy efficiencies

The energy efficiency of the SOFC system can be determined as follows:

$$\eta_{sys,Fc} = \frac{\dot{W}_{Fc}}{(\dot{N}_1 h_1 - \dot{N}_7 h_7)} \quad (19)$$

The energy efficiency of the AEC unit can be defined as follows:

$$\eta_{AEC} = \frac{\dot{N}_{20} h_{20}}{\dot{N}_2 h_2 + \dot{W}_{RC}} \quad (20)$$

The energetic COP of the absorption cooling system can be expressed as follows:

$$COP_{en,ABS} = \frac{\dot{Q}_{ABS,eva}}{\dot{N}_{13} h_{13} + \dot{N}_{14} h_{14}} \quad (21)$$

The energy efficiency of the overall system can be calculated as follows:

$$\eta_{sys} = \frac{\dot{W}_{SOFC} + \dot{W}_{turb} - \dot{W}_{comp} + \dot{N}_{20} h_{20} + \dot{Q}_{ABS,eva}}{\dot{N}_1 h_1} \quad (22)$$

III.1.6 Exergy efficiencies

The exergy efficiency of the SOFC system can be determined as follows:

$$\psi_{sys,Fc} = \frac{\dot{W}_{Fc}}{(\dot{N}_1 ex_1 - \dot{N}_7 ex_7)} \quad (23)$$

The exergy efficiency of the AEC unit can be defined as follows:

$$\psi_{AEC} = \frac{\dot{N}_{20} ex_{20}}{\dot{N}_2 ex_2 + \dot{W}_{RC}} \quad (24)$$

The exergetic COP of the absorption cooling system can be expressed as follows:

$$COP_{ex,ABS} = \frac{\dot{Q}_{ABS,eva}\left(1 - \frac{T_0}{T_{s_{eva2}}}\right)}{\dot{N}_{13} ex_{13} + \dot{N}_{14} ex_{14}} \quad (25)$$

The exergy efficiency of the overall system can be calculated as follows:

$$\psi_{sys} = \frac{\dot{W}_{SOFC} + \dot{W}_{turb} - \dot{W}_{comp} + \dot{N}_{20} h_{20} + \dot{Q}_{ABS,eva}\left(1 - \frac{T_0}{T_{s_{eva2}}}\right)}{\dot{N}_1 ex_1} \quad (26)$$

IV. Results and discussions

A parametric study is carried out on the proposed combined system for comprehensive performance evaluation. The analysis and assessment considered both, first and second law of thermodynamics. Fig.2 shows the variation of the fuel cell and overall system energy and exergy efficiencies with the fuel cell current density. Increasing the fuel cell current density from 100 to 1500 mA/cm^2 results in a decrease in the overall system energy and exergy efficiencies from 51.8 to 46.25% and from 43.84 to 42.8% respectively. Moreover, the same increase in the current density leads to a decrease in the fuel cell energy and exergy efficiencies from 71.6 to 42% and from 73 to 42.9% respectively. Furthermore, increasing the fuel cell current density from 100 to 1500 mA/cm^2 leads to an increase in the fuel cell and overall system exergy destruction rate from 356.4 to 11360 kW and from 2685 to 16184 kW respectively. The declination behaviour in the fuel cell and overall system energetic and exergetic efficiencies and the upsurge in the exergy destruction rate of the fuel cell and overall system can be interpreted by the fact that increasing the fuel cell current density leads to an upsurge in the overpotential losses of the fuel cell represented in ohmic, concentration and activation polarization. The increase in these loses reduces the fuel cell practical voltage and consequently reduce the power output and the overall efficiency of the fuel cell system. However, for the same power output, increasing the fuel cell current density will reduce the number of the required cells and consequently will reduce the cost of the fuel system. Fig.3 displays the variation of the fuel cell, RC and gas turbine output power, the fuel cell and overall system exergy destruction rate, and the energetic and exergetic efficiencies of the overall system with the molar flow rate of the ammonia entering the SOFC. Increasing the ammonia molar flow rate from 7 to 140 $kmol/h$ results in an increase in the fuel cell, RC and gas turbine output power from 339 to 6781 kW and from 95.33 to 297.5 kW and from 790 to 1364 kW respectively. Moreover, the augmentation of the ammonia molar flow rate from 7 to 140 $kmol/h$ leads to an increase in the exergy destruction rate of the fuel cell and overall system from 231.5 to 4271 kW and from 2441 to 7883 kW. Furthermore, the overall energetic and exergetic efficiencies of the overall system increased from 44.73 to 58.61% and from 35.75 to 54% respectively with the increase of the ammonia molar flow rate from 7 to 140$kmol/h$. The increase in the overall energy and exergy efficiencies can be interpret by the tremendous increase in the output power from the fuel cell compared to the increase in the gas turbine output power, which improves the system performance.

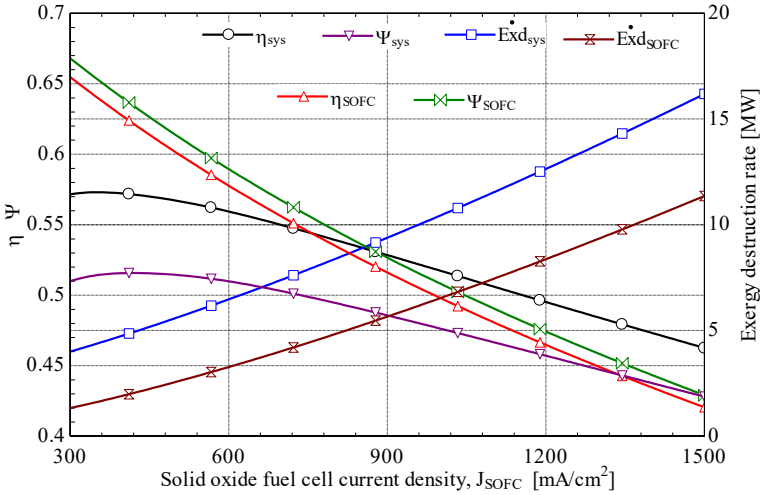


Fig. 2: Variation of the SOFC and overall energy and exergy efficiencies and exergy destruction rate of the fuel cell and the overall system with the solid oxide fuel cell current density.

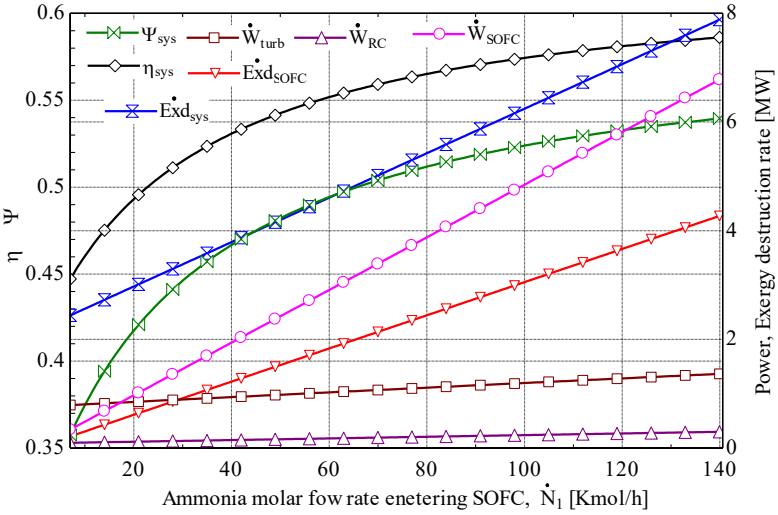


Fig. 3: Variation of the SOFC, RC and gas turbine output power, overall energy and exergy efficiencies and exergy destruction rate of the fuel cell and the overall system with the ammonia molar flow rate entering SOFC.

V. Conclusions

A novel combined cycle comprises ammonia fed SOFC and ammonia gas turbine is developed and analysed using energy and exergy approaches. The present system is able to produce hydrogen, provide electric power for residential application and cooling for industrial application. The purpose of the introduced integrated energy system is to provide an alternative environmental clean options via the utilization of sustainable and carbon free fuels in power plants. Energy and exergy efficiencies and exergy destruction rate of all system main units are evaluated and determined. In this regard, the following findings are summarized from the current study:

- The overall energy and exergy efficiencies of the system are found to be 56.7% and 51.5% respectively.
- The overall energy and exergy efficiencies of the SOFC system are found to be 60% and 61.4% respectively.
- The overall energy and exergy efficiencies of the AEC unit are found to be 81.3% and 79.7% respectively.
- The energetic and exergetic COPs of the absorption chiller cycle are obtained as 0.73 and 0.43 respectively.
- The SOFC and gas turbine output power are found to be 4069 and 1127 kW respectively.
- The maximum exergy destruction rate is found in the SOFC with 2563 kW followed by the combustor with 2122 kW, and the exergy destruction in the AEC is found to be 120.8 kW.
- The system can provide cooling output of 252.9 kW and is able to produce 36.75 kg of hydrogen per hour with electrolysis power of 212 kW.

Nomenclature

A	Area, m^2
E	Cell voltage, V
Er	Reversible cell voltage, V
$\dot{E}x$	Exergy rate, kW
ex	Specific exergy, $kJ/kmol$
F	Faraday constant, C/mol
G	Gibbs free energy, $kJ/kmol$
h	Specific enthalpy, kJ/kmol
J	Current density, A/cm^2
$\dot{N}$	Molar flow rate, $mole/min$
n	Number of moles
P	Pressure, bar
PEI	Electrolysis power, kW
$\dot{Q}$	Heat rate, kW
R	Gas constant, $kJ/kmol.K$
T	Temperature, $°C\ or\ K$
$\dot{W}$	Power, kW
Y	Molar fraction

Greek Letters

η	Energy efficiency
ψ	Exergy efficiency

Subscripts

0	Ambient conditions
$1,2,\ldots.i$	State Points and numbers
Act	Activation
Ch	Chemical
Conc	Concentration
$cool$	Cooling
Ke	Kinetic
ohm	Ohmic
Pe	Potential
Ph	Physical
sys	System
$turb$	Turbine

Acronyms

ABS	Absorption chiller system
AEC	Ammonia electrolyte cell
$cond$	Condenser
Eva	Evaporator
GT	Gas turbine
HE	Heat exchanger
Pr	Pressure regulator
RC	Rankine cycle
$SOFC$	Solid oxide fuel cell

References

Dincer I., Zamfirescu C., Renewable-Energy-Based Multigeneration Systems, *International Journal of Energy Research,* 36 (15), 1403-1415, (2012).

Dincer I., Rosen M., A., Chapter 14 - Exergy Analysis of Integrated Trigeneration and Multigeneration Systems, In *Exergy (Second Edition)*, 303–317, (2013).

Dincer I., Zamfirescu C., Ammonia as a Potential Substance, In *Sustainable Energy Systems and Applications*, 203–232, (2011).

Dong B., X., Tian H., Wu Y., C., Bu F., Y., Liu W., L., Teng Y., L., Guo-Wang Diao, G., W., Improved Electrolysis of Liquid Ammonia for Hydrogen Generation via Ammonium Salt Electrolyte and Pt/Rh/Ir Electrocatalysts, International

Journal of Hydrogen, 41 (33), 14507-1518, (2016)

Ezzat M. F., Dincer I., Energy and Exergy Analyses of a New Geothermal-Solar Energy Based System, *Solar Energy,* 134, 95–106, (2016).

Granovskii M., Dincer I., Rosen M., A., Performance Comparison of Two Combined SOFC-Gas Turbine Systems, *Journal of Power Sources,* 165 (1), 307–314, (2007).

Haseli Y., Dincer I., Naterer G., F., Thermodynamic Analysis of a Combined Gas Turbine Power System with a Solid Oxide Fuel Cell through Exergy, *Thermochimica Acta,* 480 (1–2), 1–9, (2008).

Ide H., Yoshida T., Ueda H., Horiuchi N., Natural Gas Reformed Fuel Cell Power Generation Systems-a Comparison of Three System Efficiencies, In *Proceedings of the 24th Intersociety Energy Conversion Engineering Conference*, 1517–1522, (1989).

Ishak F., Dincer I.,. Zamfirescu C., Energy and Exergy Analyses of Direct Ammonia Solid Oxide Fuel Cell Integrated with Gas Turbine Power Cycle, *Journal of Power Sources,* 212, 73–85, (2012).

Massardo A., F., Lubelli F., Internal Reforming Solid Oxide Fuel Cell-Gas Turbine Combined Cycles (IRSOFC-GT): Part A—Cell Model and Cycle Thermodynamic Analysis, *Journal of Engineering for Gas Turbines and Power,* 122 (1), 27-35, (2000).

REN21. 2016. *Renewables 2016 Global Status Report*.

Siddiqui O., Dincer I., Analysis and Performance Assessment of a New Solar-Based Multigeneration System Integrated with Ammonia Fuel Cell and Solid Oxide Fuel Cell-Gas Turbine Combined Cycle, *Journal of Power Sources,* 370, 138–154, (2017).

Zamfirescu C., Dincer I., Using Ammonia as a Sustainable Fuel, *Journal of Power Sources* 185 (1), 459–465, (2008).

Modelling and assessment of an integrated gasification combined cycle using waste tires for hydrogen production

Ahmed Hasan, and Ibrahim Dincer
Clean Energy Research Laboratory, Faculty of Engineering and Applied Science, University of Ontario Institute of Technology
2000 Simcoe Street North, Oshawa, Ontario L1H 7K4, Canada

E-mails: ahmed.hasan@uoit.ca, ibrahim.dincer@uoit.ca

Abstract
In this paper, waste tires as a feedstock for an Integrated Gasification Combined Cycle (IGCC) are modeled and assessed thermodynamically. Tire gasification is found to be a viable solution for leftover tire waste in the world. The hydrogen production to feed rate ratio is found to be 0.154, which is competitive to high-quality coals, such as Illinois No.6, that had a ratio of 0.157(Al-Zareer et al. 2016), making tires an excellent feedstock to produce hydrogen. The net power output from the Brayton and Rankine cycle are found to be as follows: 7,602 kW and 6,899 kW. The systems energy and exergy efficiencies obtained are 34.1% and 32.9%.

Keywords: Hydrogen production, Energy, Exergy, Efficiency, Tires, Gasification

I. Introduction

As the use of vehicles increases around the world, due to more developing countries becoming developed, tire disposal is becoming a large problem around the world. Many tires are disposed of in landfills, leaving them to slowly decompose or even burned, which implicates serious environmental problems/hazards. There have been initiatives to recycle and re-purpose tires, about thirty-five percent of tires on average get recycled, and fifty percent is used to produce Tire Derived Fuel (TDF) in the U.S according to the EPA. However, this leaves about fifteen percent of the tires to decompose in landfills in the U.S... In 2003, approximately 290 million tires were disposed of in the U.S (EPA). Using tires as a fuel is very feasible, as studies have shown by the EPA that tires have up to twenty-five percent more energy than coal.

According to a comparative study (Atal and Levendis, 1995) between coal and waste tires, combustion behavior were analyzed. The study was conducted on tires and pulverized bituminous coal particle sizes that included 75-90 μm and 180-212 μm particles. The combustion was conducted at a gas temperature of 1450K in air; it was found that during pyrolysis coal experienced swelling, melting and large blowholes, which the tires did not experience. During the char combustion phase, the peak flame temperatures for tires were in the range of 2000-2100K in comparison, the coals chars temperature was burning with a flame temperature of 1850 -2000K. However, the char burnout time was significantly shorter than that of tires.

A study (Leung and Wang 2003) was conducted with a laboratory scale fluidized bed gasifier to study the gasification characteristics of tire powder. The granulated tires were gasified in air at a temperature ranging from 350-900ºC. The results have shown that both equivalence ratio (ER), tire feed rate and particle size have a large impact on the outcomes of their gasification, specifically bed temperature, gas yield, gas heating value, the gas product composition, the volatile release ratio, and secondary reaction temperature. The char and oil yields were found to be within the following ranges 24-37% and 0-37%. Furthermore, over 90% of volatile release and 18% fixed carbon conversion. The energy recovery was also found to be within the range of 15%-38%.

II. System Description and Simulation

Gasifier

The simulation is based on the Gibbs free energy model, as it can be used with various carbonaceous materials such as tires in Aspen. According to Al-Zareer et al., the Gibbs free energy minimization approach model had slightly larger error values than that of the kinetics-based model on Aspen Plus, where the error range was found to be 4.1%-6.55%. In this study, the pyrolysis reaction is conducted by using a yield reactor, which decomposes the tires based on the proximate and ultimate analysis (Ismail et al. 2017) to their primary elements. After pyrolysis in the Ryeild reactor in the Aspen flow sheet, the RGibbs reactor is used for the following reactions associated with gasification, where the syngas is produced. The gasifiers operating temperature and temperature are as follows 1460ºC and 2400 kPa. The tires are fed to the gasifier at ambient conditions ($T_0 = 298K, P_0 = 101.325\ kPa$).

Water Gas Shift Membrane Reactor (WGSMR)

Following the gasification of the tires, the syngas leaves the gasifier, and the flow expands in a turbine where the syngas pressure and temperature decrease to meet the Water Gas Shift Membrane Reactors (WGSMR) operating conditions. The operating conditions for the WGSR are obtained from Augustine et al., and are stated as follows: $T = 723K, P = 1400kPa$ and a conversion rate to hydrogen of 98%.The excess heat from the syngas is then used to power an integrated combined cycle. The thermal energy from the syngas to the combined cycle is done using a counter flow heat exchanger. Apart from the syngas, the WGSR is supplied with steam to complete the shift reaction (1). The WGSR includes a membrane that separates hydrogen from the flow.

$$CO + H_2O \leftrightarrow CO_2 + H_2 \quad (1)$$

Combined Cycle

The combined cycle in this system consists of a simple Rankine and Brayton cycle as a proof of concept. The operating conditions of the Brayton cycle are as follows $r = 8.08, T_{Turbine} = 1297K, T_0 = 298K$. The turbine and compressor isentropic efficiency are taken as follows: 92.2% and 59.4%. The operating conditions for the Rankine cycle were as follow: $T_{Turbine} = 723K, T_{Condensor} = 291K, P_{Turbine} = 5MPa, and\ P_{Condensor} = 10kPa$. The turbine and pump isentropic efficiencies are taken as follows: 72% and 90%. Figure 1 displays the Aspen flowchart of the system.

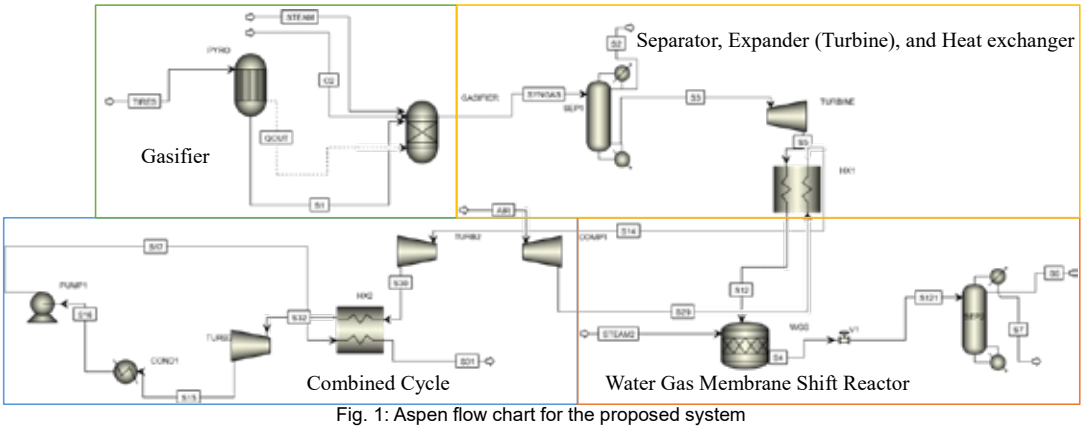


Fig. 1: Aspen flow chart for the proposed system

III. Analysis

The physical exergy of the tires is considered to be zero as it enters the system, at ambient temperature and pressure conditions. As estimates for the chemical exergy are lacking in the literature, an estimate using a correlation factor for solid biomass where O/C<2 is used eq.1 [Cohce 2010]. The tires composition based on the oxygen to carbon ratio is within this relation.

$$\beta = \frac{1.044 + 0.0160\frac{\mathrm{H}}{\mathrm{C}} - 0.3493\frac{\mathrm{O}}{\mathrm{C}}\left(1 + 0.0531\frac{\mathrm{H}}{\mathrm{C}}\right) + 0.0493\frac{\mathrm{N}}{\mathrm{C}}}{1 - 0.4124\frac{\mathrm{O}}{\mathrm{C}}} \quad (1)$$

The chemical exergy of the tires can then be estimated by using the tires lower heating value.

$$\mathrm{ex_{ch}} = \beta \mathrm{LHV_{tires}} \quad (2)$$

Table 1 summarises the compositions values of the tires as well as other types of coals used around the world. The ultimate and proximate analysis of the tires were based on a study conducted by Ismail et al.. As for the lower heating value of tires, it is estimated through a tool provided by deltawayenergy.

Tab. 1: Proximate and ultimate analysis of waste tires and various coal types

		Illinois (Wen, 1968)	Elibistan (El-Emam et al. ,2012)	Waste Tires (Ismail et al. 2016)
Proximate analysis	Moisture	0.20	16.30	1.5
	Fixed Crabon	58.01	35.73	30
	Volatile matter	26.46	35.03	55
	Ash	15.53	12.93	13.5
Ultimate analysis	C	73.90	48.76	75
	H	6.24	3.25	7
	N	0.71	1.27	0.3
	Cl	0.37	0.00	0
	S	1.77	3.67	1.5
	O	1.32	13.79	2.7
	Ash	15.53	12.93	13.5
Heating Values	HHV(MJ/kg)	28.1	18.6	36.5 (dai et al.,2001)
	LHV (MJ/kg)	24.1	17.8	19.9

The energy and exergy analyses of the overall system take into account the power produced from the combined cycle, the hydrogen produced and the feedstock for the gasifier, which in this case are tires. The overall energy and exergy efficiencies of the systems are written as follows:

$$\eta_{\mathrm{Overall,sys}} = \frac{\dot{\mathrm{m}} * \mathrm{LHV_{H_2}} + \sum \dot{\mathrm{W}}_{\mathrm{turbine}}}{\dot{\mathrm{m}} * \mathrm{LHV_{tires}}} \quad (3)$$

$$\psi_{Overall,sys} = \frac{\dot{m} * LHV_{H_2} + \sum \dot{W}_{turbine}}{\dot{m} * Ex_{tires}} \quad (4)$$

4. Results and discussion

After the simulations were performed on the IGCC plant, it was found that the optimal conversion rate in the gasifier would produce syngas with a composition of 65% carbon monoxide and 3.6% hydrogen. To achieve that conversion rate it was found that ideally, the oxygen and steam supply rate should be 40% and 18% of the feed composition. Figure 2 represents the CO production rate from the gasifier relative to the varying oxygen and steam mass flow rates with a constant tire feed rate held at 12kg/s.

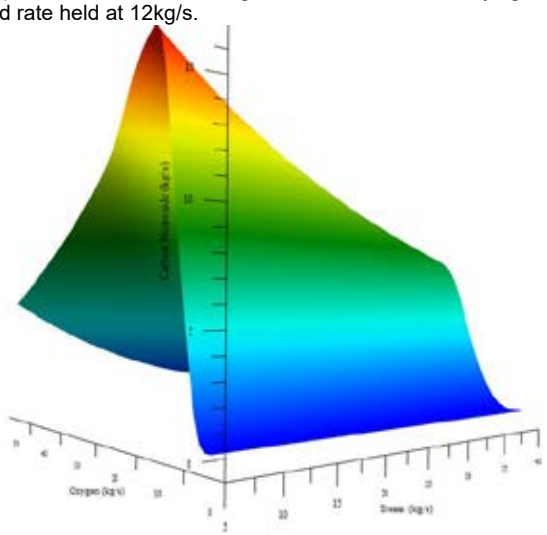


Fig. 2: Carbon monoxide production rate with oxygen and steam feed rates

As seen in figure 3 the WGSR achieves peak conversion when the steam mass flow rate reached 8.28kg/s. The peak hydrogen production was 1.85 kg/s, and the lowest carbon monoxide mass flow rate was 0.36kg/s. It should be noted that the steam mass flow rate increase after it reached 8.23 kg/s did not affect the CO and H_2 conversion rate.

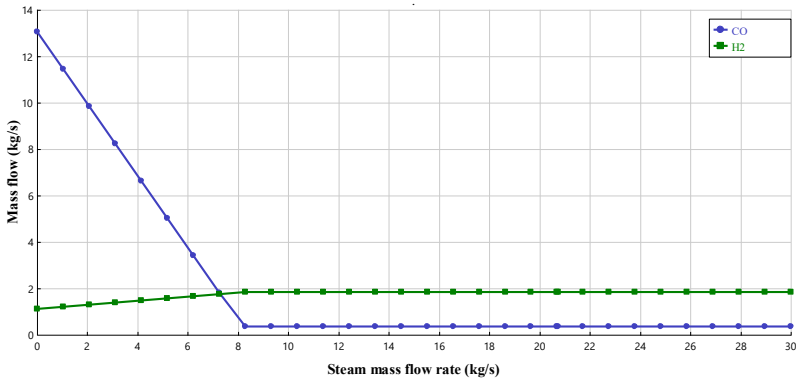


Fig. 3: Hydrogen production rate and carbon monoxide conversion rate in the WGSR with various steam feed rates

The syngas's excess thermal energy exiting the gasifier was used to provide thermal energy to the combined cycle via a heat exchanger. The net power output from the Brayton and Rankine cycle were as follows: 7,602 kW and 6,899 kW. The expanding turbine used to reduce the pressure of the syngas as its entering the WGSR was producing 1209 kW. The energy and exergy efficiency of the overall system was found to be 34.1% and 32.9%.The hydrogen production rate to feed rate ratio was compared to other studies that used coal to justify waste tires as a feedstock. The current hydrogen to fuel ratio of this system was found to be 0.154, compared to Al-Zareer et al. study it was found that the ratio for Elbistan and Illinois No.6 coal were as follows 0.132 and 0.157 making tires a viable feedstock for gasifiers.

V. Conclusions

The integrated tire gasification combined cycle system proposed in this paper is a viable solution for left over tire

waste in the world. The systems energy and exergy efficiencies obtained were 34.1% and 32.9% respectively, which is competitive with coal gasification. The hydrogen production to feedstock rate ratio was 0.154, which is also competitive to one of the higher quality coals available, such as Illinois No.6, which had a ratio of 0.157, making tires a good source to produce hydrogen. To conclude this study, tire waste is a rising problem and using it as a feedstock for gasifiers is more environmentally benign than simply piling tires in a landfill.

References

Al-Zareer, M., Dincer, I., and Rosen, M. (2017). Modeling and performance assessment of a new integrated gasification combined cycle with a water gas shift membrane reactor for hydrogen production. *Computers & Chemical Engineering*, 103, pp.275-292.

Al-Zareer, M., Dincer, I., and Rosen, M. (2017). Development of an integrated system for electricity and hydrogen production from coal and water utilizing a novel chemical hydrogen storage technology. *Fuel Processing Technology*, 167, pp.608-621.

Archive.epa.gov. (2018). *Tire-Derived Fuel | Scrap Tires | US EPA*. [online] Available at: https://archive.epa.gov/epawaste/conserve/materials/tires/web/html/tdf.html [Accessed 18 Feb. 2018].

Atal, A. and Levendis, Y. (1995). Comparison of the combustion behavior of pulverized waste tyres and coal. *Fuel*, 74(11), pp.1570-1581.

Augustine, A.S., Ma, Y.H., and Kazantzis, N.K., 2011. High-pressure palladium membrane reactor for the high-temperature water–gas shift reaction. Int. J.Hydrogen Energy 36 (9), 5350–5360.

Cohce, M., Dincer, I. and Rosen, M. (2010). Thermodynamic analysis of hydrogen production from biomass gasification. *International Journal of Hydrogen Energy*, 35(10), pp.4970-4980.

Deltawayenergy.com. (2018). *LHV Tool - Deltaway Energy*. [online] Available at: http://www.deltawayenergy.com/wte-tools/lhv-tool/ [Accessed 25 Feb. 2018].

Dai, X., Yin, X., Wu, C., Zhang, W. and Chen, Y. (2001). Pyrolysis of waste tires in a circulating fluidized-bed reactor. *Energy*, 26(4), pp.385-399.

El-Emam, R.S., Dincer, I., and Naterer, G.F., 2012. Energy and exergy analyses of an integrated SOFC and coal gasification system. J. Hydrogen Energy 37 (2),1689–16979.

Ismail, H., Abbas, A., Azizi, F. and Zeaiter, J. (2017). Pyrolysis of waste tires: A modeling and parameter estimation study using Aspen Plus ®. *Waste Management*, 60, pp.482-493.

Leung, D. and Wang, C. (2003). Fluidized-bed gasification of waste tire powders. *Fuel Processing Technology*, 84(1-3), pp.175-196.

Wen, C.Y., 1968. Noncatalytic heterogeneous solid-fluid reaction models. Ind. Eng.Chem. 60 (9), 34–54.

Heat Transfer and Pressure Drop Characteristics of Different Structured Micro-Pin-Fin Reactors

***Evren Yilmaz Yakin*[1], Sinan Eren Yalcin[2], Tahir Hikmet Karakoc[3]**

[1]*Evren Yilmaz Yakin, Eskisehir Osmangazi University, Graduate School of Natural and Applied Sciences, Eskisehir, Turkey*

[2]*Sinan Eren Yalcin, Nisantasi University School of Civil Aviation, Program of Airframe and Powerplant Maintenance, Istanbul, Turkey*

[3]*T. Hikmet Karakoc, Anadolu University, Faculty of Aeronautics and Astronautics, Department of Airframe and Powerplant Maintenance, Eskisehir, Turkey*

Proton Exchange Membrane Fuel Cells (PEMFC) are potential power sources when compared with internal combustion engines and conventional batteries due to several reasons such as low emissions, low costs, low operating temperatures, high efficiency, high energy density, quick start up, and compactness. Without any combustion, electricity can be generated, and water and heat can be the only products. However the need for hydrogen supply is a critical factor for reliable operation of the PEMFC. One of the most attractive approach is to overcome the hydrogen production limitation is to use microstructured reactors. Thus the optimal design of the micro reactor is a key factor for PEMFC development.

Although significant improvements have been made in the microreactor flow systems, its thermal management still remains the challenge. Its cooling rate can be improved by increasing coolant flow rate and surface heat transfer area, but this also increases the pumping power. Recently, micro structured reactors have gained an increasing interest due to its large surface area, energy density, high heat and mass transfer, and short reaction time.

Here in this study, we aim to perform several numerical experiments to study the heat transfer and pressure drop rates of different micro pin fin structured reactor configurations. Based on the results, the pin-fin structures' thermofluidic characteristics will be obtained and a better one will be proposed.

Keywords: micro-pin-fin reactor, pressure drop, heat transfer, optimal design

Kinetic and electrochemical analyses of a CuCl/HCl electrolyzer

Reza Soltani, Ibrahim Dincer and Marc A. Rosen
Faculty of Engineering and Applied Science, University of Ontario Institute of Technology (UOIT), 2000 Simcoe St. North, Oshawa, ON L1H 7K4, Canada

E-mails: reza.soltani1@uoit.net, ibrahim.dincer@uoit.ca, marc.rosen@uoit.ca

Abstract

The CuCl/HCl electrolyzer is the electrochemical step of the CuCl thermochemical water splitting process for hydrogen production. In this study an electrochemical analysis is carried out on the electrolysis cell from a kinetic electrochemistry perspective. At 25℃ the activation overpotential of the anode half-reaction is found to be around 53 mV for a current density of 0.5 $\mathrm{A.cm^{-2}}$ while the activation overpotential of the cathode half-reaction for the same condition is about 87 mV. An increase in working temperature decreases the overpotential of the anode half-reaction and increases the magnitude of the cathode half-reaction activation overpotential. The value of the Ohmic overpotential of the cell membrane is almost 1000 times smaller than the activation overpotentials of the electrode half-reactions for the same temperature and current density. A higher working temperature results in a lower membrane ohmic overpotential. The required voltage to trigger electrolysis for a current density of 0.5 $\mathrm{A.cm^{-2}}$ is found to be 0.53 V at 25℃, and it increases to 0.59 V at 80℃. However, a higher temperature results in a better electrochemical efficiency for the electrolysis process examined.

Keywords: Hydrogen production, electrolysis, electrochemical analysis, kinetic analysis, efficiency.

I. Introduction

A Canadian team of researchers, led by University of Ontario Institute of Technology (UOIT), has been extensively involved in Cu-Cl cycle research, including effort to develop an integrated lab-scale demonstration (Naterer et al., 2013). Regarding the electrochemical step (electrolysis) of the CuCl cycle, as well as other steps, much research has been carried out. Atomic Energy of Canada Limited (AECL) demonstrated hydrogen production by a CuCl electrolyser continuously for several days (Sadhankar et al., 2006). They reported that electrolysis is feasible at considerably low potentials (0.6-0.7 V) at a current density of 0.1 $\mathrm{A.cm^{-2}}$ using inexpensive materials (Naterer et al., 2011). The Pennsylvania State University (PSU) has published extensive results on the cycle through comprehensive experiments and theoretical development (Naterer et al., 2010). Data regarding kinetics of the anode half-reaction such as transfer coefficient, exchange current density and symmetry factor of reaction have been determined by Hall et al. (2014). These data are used in this study to develop the overpotential model of the cell. Furthermore, a kinetic study on the hydrogen evolution reaction (HER) at the cathode was conducted by Hall et al. (2015) in concentrated $\mathrm{HCl(aq)}$ that released some useful kinetic parameters for this study. In this study a CuCl/HCl cell is studied in a non-equilibrium state through a kinetic analysis. The activation overpotentials of the anode and cathode half-reactions as well as the Ohmic overpotential of the cell membrane are modelled.

II. CuCl/HCl Electrolysis

In the CuCl/HCl electrolyzer cell the intake streams are HCl(aq) and CuCl(aq), which are generated from hydrolysis and thermolysis steps of a four-step copper-chlorine cycle, respectively and the outlet streams are hydrogen gas and $CuCl_2$(aq). The anode and cathode half-reactions, respectively, follow:

$$\mathrm{Anode\ half-reaction:\ CuCl(aq) + HCl(aq) \longrightarrow CuCl_2(aq) + H^+(aq) + e^-} \quad (1)$$

$$\mathrm{Cathode\ half-reaction:\ H^+(aq) + e^- \longrightarrow 0.5H_2(g)} \quad (2)$$

In this study results regarding the equilibrium electrochemistry are used from our previous work (Soltani et al., 2016), which show that the following reaction is the dominant electrolysis reaction occurring for the selected anolyte concentration of 2 $\mathrm{mol.l^{-1}\ CuCl(aq)}$ and 10 $\mathrm{mol.l^{-1}\ HCl(aq)}$:

$$\mathrm{CuCl_3^{2-}(aq) + H^+(aq) \longrightarrow CuCl_3^-(aq) + 0.5H_2(g)} \quad (3)$$

Therefore this reaction is used for the kinetic analysis in this study. In addition in this study the catholyte concentration is taken to be 11 $\mathrm{mol.l^{-1}\ HCl(aq)}$. The favourable effect of the presence of $\mathrm{HCl(aq)}$ stops the copper species from migrating into the catholyte from the anolyte. The presence of HCl(aq), especially at high concentrations, strongly affects the equilibrium potential of the HER.

III. Kinetic Analysis

The kinetic analysis is carried out in this study to develop polarization curves for half-cell and full-cell reactions of the CuCl/HCl electrolyser. In other words, the activation and Ohmic overpotentials within the cell are calculated. Then, the required potential for operating the electrolysis unit can be determined:

$$E_{cell} = -\left(|E_{D,cell}| + |\eta_{anode}| + |\eta_{cathode}| + |\eta_{ohmic}|\right) \quad (4)$$

Subsequently the voltage and current efficiency of the cell as well as its overall electrochemical efficiency can be determined. The total activation overpotential of a single electrode is due to the contribution of charge transfer (electron transfer) overpotential and mass transfer overpotential:

$$\eta_{electrode} = \eta_{et} + \eta_{mt} = \eta_{emt} \quad (5)$$

where η_{et} denotes the imperfection corresponding to the electron transfer process and η_{mt} the overpotential corresponding to the mass transfer process, and η_{emt} is the total overpotential of each half-reaction. The anodic and cathodic currents of each electrode half-reaction can be determined as follows:

$$i_{electrode} = i_{anodic} + i_{cathodic}$$

$$i_{anodic} = i_{\circ,electrode}\left[1 - \frac{i_{electrode}}{i_{lim,anodic}}\right]\exp\left\{\frac{(1-\alpha)z_r F\eta_{electrode}}{RT}\right\} \quad (6)$$

$$i_{cathodic} = -i_{\circ,electrode}\left[1 - \frac{i_{electrode}}{i_{lim,cathodic}}\right]\exp\left\{\frac{-\alpha z_r F\eta_{electrode}}{RT}\right\} \quad (7)$$

where $i_{\circ,electrode}$ is the exchange current density of the electrode, which is called the dynamic equilibrium current of the electrode. The assumption of zero current leakage in the examined cell is invoked, so the cathode receives the same amount of current as the anode provides:

$$i_{cathode} = -i_{anode}$$

In order to determine the resistance of the proton exchange membrane (PEM) to hydrogen ion transport, which is referred to as the Ohmic overpotential of the cell, the same procedure is employed as used for a water electrolyzer membrane. Overall, the Ohmic overpotential is a function of the humidification, thickness and temperature of the membrane, which is assumed to be the same as the temperature of the anolyte and catholyte. The cell Ohmic overpotential as follows:

$$\eta_{ohmic} = R_{PEM} \times i_{cell} \quad (8)$$

where R_{PEM} denotes Ohmic resistance of PEM, and i_{cell} represents the overall cell current.

IV. Results and discussions

Figure 1(a) shows that considering only electron transfer (dashed line) for activation overpotential leads to an incorrect result, as the solid line can be validated by experimental released reports. Therefore, both electron and mass transfer effects should be taken into account to obtain adequately accurate and realistic results. At a 0.5 $A.cm^{-2}$ current density, the anode activation overpotential is observed to be -0.053 V. In addition, as Figure 1(b) shows, at a conversion degree other than 5%, the overpotential results are not observed to be on a proper trend, which is simply due to the fact that the kinetic parameters used are from references corresponding a 5% conversion degree. Since in the literature, a logarithmic presentation of current and activation overpotential is reported for the HER, the logarithmic graph is initially obtained to assess if the developed model is valid compared to the relevant studies. Figure 2(a) shows a proper trend and shape of the overpotential for the HER of the studied cell. The activation overpotential of the HER is calculated to be 0.083 V to obtain the desired current density of 0.5 $A.cm^{-2}$ (Figure 2(b)). Note that Figure 2(a) is developed only to compare the trend of results with those of other reports in the literature. Otherwise, Figure 2(b) is used in this study to determine the corresponding overpotential.

As other results, The exchange current density of the anode half-reaction increases with temperature that is a better (higher) current density is reported for a higher temperature at constant applied potential. The activation overpotential of the anode half-reaction decreases as exchange current density rises. The activation overpotential of the anode decreases dramatically as temperature rises from room temperature and then plateaus at around 0.030 V. In addition, the magnitude of the activation overpotential of the HER increases as temperature increases; here, the exchange current density of the HER is assumed constant.

The Ohmic overpotential of the PEM is found to have values on the order of microvolts, which is almost 1000 times smaller than activation overpotentials. For a specific membrane thickness, the temperature rise decreases the Ohmic overpotential steadily, while for a certain temperature membrane thickness the temperature rise linearly increases the value of Ohmic overpotential.

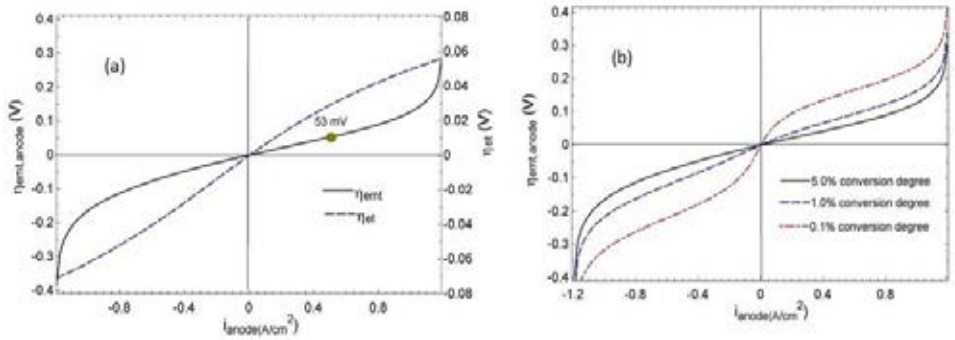


Fig. 1: Activation overpotential of dominant anode half-reaction: (a) 5% Cu(I)→Cu(II) conversion degree. Red dot presents corresponding overpotential at cell current density of 0.5 A.cm^{-2}; (b) various Cu(I)→Cu(II) conversion degrees.

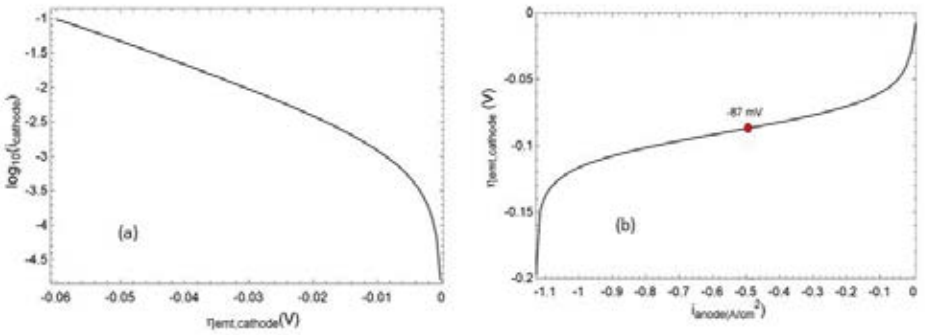


Fig. 2: Current-activation overpotential of HER: (a) Logarithmic; (b) non-logarithmic and red dot presents corresponding overpotential at cell current density of 0.5 A.cm^{-2}. Kinetic data are used considering Pt cathode electrode; data from (Hall et al., 2015).

V. Conclusions

The main findings the present kinetic analysis are as follows:

- At a 5% anolyte conversion degree and 25 ℃, the anode half-reaction activation overpotential is 53 mV. This value decreases to around 30 mV with an increase of temperature to 80 ℃.
- In term of voltage efficiency, 60℃ is the most suitable working temperature for the electrolyzer.
- The electrochemical efficiency of CuCl/HCl electrolysis ranges from 10% to 70% for a temperature range of 25℃ to 80℃.
- The magnitude of the overall required potential for electrolysis at a 5% anolyte conversion is between 0.53 V and 0.59 V as temperature rises from 25℃ to 80℃.

It is believed that in future studies on CuCl/HCl electrolysis it would be worthwhile to determine experimentally the precise kinetic parameters of the anode and cathode half-reactions for various concentrations and temperatures.

References

Hall D.M., Akinfiev N.N., LaRow E.G., Schatz R.S., Lvov S., Thermodynamics and efficiency of a CuCl(aq)/HCl(aq) electrolyzer, Electrochimica Acta, 143, 70-82, (2014).

Hall D.M., LaRow E.G., Schatz R.S., Beck J.R., Lvov S., Electrochemical kinetics of CuCl(aq)/HCl(aq) electrolyzer for hydrogen production via a Cu-Cl thermochemical cycle, Journal of the Electrochemical Society, 162(1), F108-F114, (2015).

Naterer G., Suppiah S., Stolberg L., Lewis M., Wang Z.L., Daggupati V., Gabriel K., Dincer I., Rosen M.A., Spekkens P., Canada's program on nuclear hydrogen production and the thermochemical Cu–Cl cycle, International Journal of Hydrogen Energy, 35(20), 10905-10926, (2010).

Naterer G., Suppiah S., Stolberg L., Lewis M., Ferrandon M., Wang Z.L., Dincer I., Gabriel K., Rosen M.A., Secnik E., Clean hydrogen production with the Cu–Cl cycle–progress of international consortium, I: experimental unit operations, International Journal of Hydrogen Energy, 36(24), 15472-15485, (2011).

Naterer G., Suppiah S., Stolberg L., Lewis M., Wang Z.L., Dincer I., Rosen M.A., Gabriel K., Secnik E., Easton E.B., Progress of international hydrogen production network for the thermochemical Cu–Cl cycle, International Journal of Hydrogen Energy, 38(2), 740-759, (2013).

Sadhankar R.R., Li J., Li H., Ryland D.K., Suppiah S., Future hydrogen production using nuclear reactors, In EIC Climate Change Technology, IEEE, 1-9, (2006).

Soltani R., Dincer I., Rosen M.A., Electrochemical analysis of a HCl(aq)/CuCl(aq) electrolyzer: equilibrium thermodynamics. International Journal of Hydrogen Energy, 41(19), 7835-7847, (2016).

Steam Methane Reforming in Microreactors under Concentrated Solar Irradiation

Atalay Çalışan, C. Güvenç Oğulgönen, Deniz Üner, *Serkan Kıncal
Middle East Technical University, Chemical Engineering Department, Ankara, 06800, Turkey

* E-mail: skincal@metu.edu.tr

Abstract

In this work, steam methane reforming is carried out on 200CPSI mullite monoliths, loaded with Ni or Pd catalysts encapsulated in a 200mm long 316 grade stainless-steel reactor placed in front of a 70 cm diameter parabolic mirror with a 30x30mm focal area. The reactor-dish assembly was mounted on a dual axis solar tracker. Measured reaction temperatures varied significantly due to weather conditions, enabling the characterization of the relationship between conversion, temperature and extent of reaction. Peak H_2 yields of ~99% were demonstrated on both materials, with the average in the range of 50-70%. The discontinuities in the water supply in the feed prevented sustainable >90% yields. Hourly production rates were between 0.05-0.10 moles of H_2. Differences between the two catalysts and the advantages of running multiple micro reactors will be discussed along with the possibilities of improving the average yield levels by a more efficiently designed water feeding strategy.

Keywords: SMR, Concentrated Solar Irradiation

I. Introduction

Methane steam reforming is the most common industrial process used for almost the 50% of the world's hydrogen production (Lulianelli, Liguori, Wilcox, & Basile, 2016) On paper, the reaction simply produces H_2, CO, CO_2, and CH_4 in various proportions depending on the reaction conditions dictated by the end use of the gas mixture desired (Van Hook,1980).

$$\mathrm{CH_4 + H_2O \rightarrow CO + 3H_2} \qquad \Delta H^0_{298K} = 206\ \mathrm{kj/mol}$$
$$\mathrm{CO + H_2O \rightarrow CO_2 + H_2} \qquad \Delta H^0_{298K} = 165\ \mathrm{kj/mol}$$
$$\mathrm{CH_4 + 2H_2O \rightarrow CO_2 + 4H_2} \qquad \Delta H^0_{298K} = -41\ \mathrm{kj/mol}$$

The computed equilibrium compositions of the system at 1 atm as a function of temperature show that the equilibrium conversions of methane for reforming reactions exceed 90% at 1000 K, making the reaction system a good candidate for solar heating to high temperatures (Kodama, 2003). Solar reforming of methane with steam has been studied over 20 years using both indirect and direct heating of the catalyst for the efficient absorption of concentrated solar energy (Levitan, Rosin, & Levy, 1980) (Böhmer, Langnickel, & Sanchez, 1991) (Muir, Hogan, Skocypec, & Buck, 1994) (Kodama et al., 2000) (Tamme, Buck, Epstein, Fisher, & Sugarmen, 2001). In direct heating systems, the reactant gas mixture and/or the catalyst are heated directly by the solar radiation using a reactor with a quartz windows as aperture to run the endothermic reforming reaction (Kodama, 2003). The advantages of this reactor / receiver system are listed as low heat losses due to high solar flux capability, fast response to thermal transients due to compact, low mass receiver – reactors and improved overall efficiency (Buck, Muir, & Hogan, 1991).

Ni is the commercially preferred SMR catalyst due to its optimal stability and cost. On the other hand, Pd offers high rates and selectivities due to the facile oxygen transfer between Pd and the supporting oxide. The facile oxygen transfer at the Pd/CeO_2 interface results in rapid removal of coke deposited during methane decomposition, and inhibits coke build up during the reaction (Farrauto et al., 1992).

II. Experimental Set-up and Procedure

The reaction was studied on 30x30x10mm, 200CPSI mullite monoliths coated respectively with:

1. 13.6 wt% Ni
2. 1.0 wt% Pd in CeO_2

The monoliths were loaded into the solar reactor with the 30x30 facing the focused solar irradiation, as seen in Figure 1(c). In this same image the blue tubing providing the feed gases to the front face of the monolith can be seen on the left side. The white tubing towards the back collects the effluent gases and delivers them to the gas analysis unit, while monitoring the temperature of the effluent by a J-type thermocouple. The window facing the focused solar rays is a 3mm thick, 96mm diameter quartz piece. A side-view of the reactor chamber is shown in Figure 1(b), the K-type thermocoulple leads can be seen extending out from the back of the reactor (top of the picture). This thermocouple is embedded into the monolith and holds the monolith in place while monitoring its internal temperature. The parabolic dishes used for concentration are 70cm in diameter and are shown in Fig. 1(a). The effluent gases are analyzed with an array of 3 solid state (SnO based) sensors that have varying levels of sensitivity towards CH_4 and H_2 and allow for real time monitoring of the gas composition (more specifically MQ4, MQ6 and MQ8 by Hanwei Electronics, China). They also pass through a more sensitive total combustible gas analyzer (namely a Honeywell XCD) for validation. Two O_2 sensors (sensitive ppm and percentage levels by the Southland Sensing Ltd) connected to two EMD-485 sensor board are used to track O_2 levels. The O_2 levels are monitored prior to experimentation to confirm purging of all O_2 from the system. The entire set-up is automated

through a Lab-VIEW interface complemented with a NI USB-6343 A/D converter with digital I/O capabilities.



(a) 2x2 array of 70cm parabolic dishes mounted on a dual axis solar tracker with 4 reactors installed.



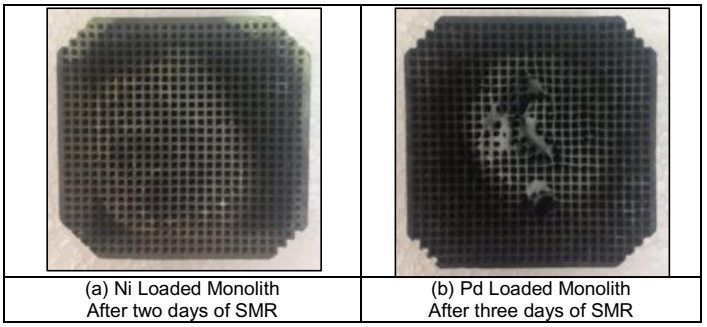
(b) Close-up of the reactor – face down



(c) Reactor mounted at focus – monolith inside, facing mirror

Fig. 1 – Pictures of the solar-thermal reactor set-up - the solar tracker is installed at METU, Ankara campus

Continuous SMR reactions took place on 19th and 20th of August using the Ni loaded monolith. CH_4 is fed to the reactor, diluted to 4% in Ar, at a total gas flowrate of 200sccm. Due to the limited in-house capabilities and the long distance between the utilities and the reactor-dish assembly, water had to be fed through a peristaltic pump with a long feeding line (>10m). Water is fed "in excess" however takes time to reach saturation due to transport limitations and the way water is fed to the reactor. Once saturation happens, spikes of high conversion are observed when liquid droplets reach the reactor and evaporate instantaneously. Figure 2(a) shows the Ni monolith after 2 days of SMR reaction. Significant coking can be seen around the 30x30mm focal area.



(a) Ni Loaded Monolith After two days of SMR

(b) Pd Loaded Monolith After three days of SMR

Fig. 2 – Monolith pictures after the continuous SMR experiments

Continuous SMR reactions on the Pd loaded monolith took place during August 22th to 24th, 2017. The feeding strategy is exactly the same as Ni coated monolith experiments; hence the same initially rising and the subsequent spiky periods are observed. Significant coking is apparent at the end of the 3 days but this is a gradual build-up. What is also unique about this particular monolith is the regions of molten mullite (MP ~1700°C), Fig. 2(b). This is attributed to the catalytic combustion of CH_4 prior to cracking/SMR reactions, with trace amounts of residual O_2 in the system, taking localized temperatures to very high levels (Farrauto et al., 1992). Also note that this melting has happened in different locations. These likely correspond to the different focal points at the beginning of the experiment each day.

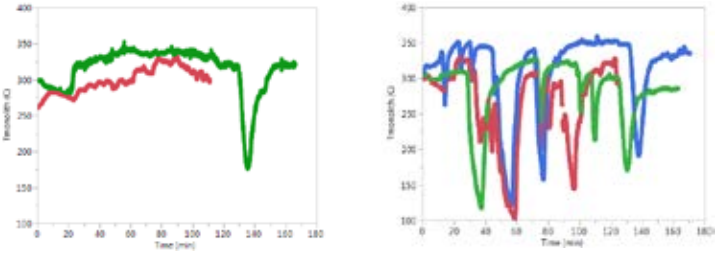
III. Results and discussions

Fig. 3 and Fig. 4 show the monolith temperature and total irradiation (same inclination as the mirrors) measurements of the Ni and Pd monoliths during the day. In this, and all the following plots, RED, BLUE and GREEN colors refer to day 1, 2 and 3 testing respectively. For the Ni coated monolith, these were August 19th and 20th, 2017. The three days of testing for the Pd coated monolith were the 22nd through the 24th of August, 2017. The main conclusion here is that the solar irradiation directly drives the reaction temperature and eventually the extent of reaction, an expected result.

For the Ni monolith, Day 1 was a sunny day with cloudy patches, particularly later in the day, resulting in a shorter run. Day 2 was a more consistent day averaging monolith temperatures of 330°C. The dip in the temperature at ~140min is due to the cell phone tower shadow located 10 m away from the reactor-dish assembly.

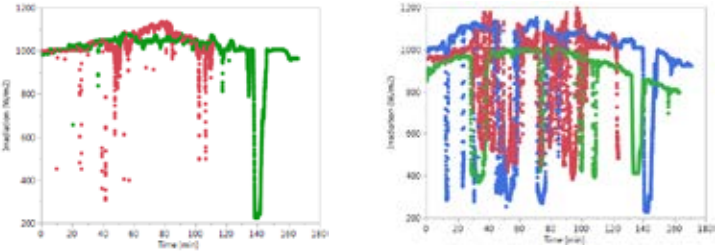
For Pd coated monolith, Day 3 has the highest achieved monolith temperatures followed by Days 2 and 1. All three days contain intermittent cloud coverages where as only day 2 and 3 attained the completion of the experimental

procedure. Day 1 had to be stopped early due to complete and consistent cloud presence, eliminating any possibility of the reactions going forward.



(a) Ni loaded monolith (b) Pd loaded monolith

Fig. 3: Temperature trends for the monoliths during the SMR reactions



(a) Ni loaded monolith (b) Pd loaded monolith

Fig. 4: Solar Irradiation trends for the monoliths during the SMR reactions

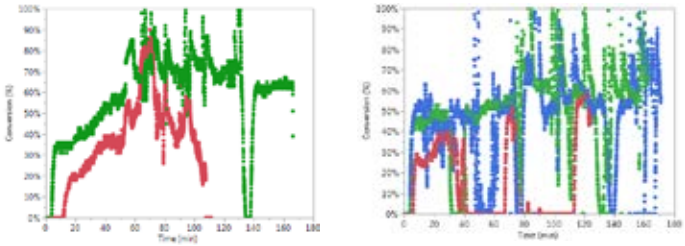
In Fig. 5 and Fig. 6, the reaction characteristics are captured, first in terms of instantenous CH_4 conversion and then for overall H_2 production. For the Ni coated monolith, the 40-50°C temperature difference between the two days manifests itself in the conversion levels as well. There is an initial period of around 60min of consistently rising conversion levels, likely the amount of time it takes for water to saturate the entire system. The water is fed by injection in liquid from at a distance approximately 12m away from the reactor itself.

Once saturation conditions are reached, liquid water also reaches the reactor and then there are spikes in conversion, corresponding to the instances in time where droplets reach the reactor enclosure and instantaneously evaporate, saturating the entire enclosure with excess water. These events are accompanied by small temperature drops as well since the latent heat is required to evaporate the liquid water.

Pd catalyst does not show the slow increase in conversion climbing to its eventual level much more rapidly. It too shows spikes later in operation once liquid water makes its way onto the monolith. Note that CH_4 conversion does not necessarilty imply full SMR reaction completion. In fact there is strong evidence in Fig. 2 that both monoliths also facilitate the thermal cracking of CH4, depositing C on the surfaces as indicated by the black color. One might qualitatively argue that there is more coke deposition on the Pd coated monolith. So in the first stages of operation, before H_2O is available on the monolith surface to facilitate the SMR reaction sequence, the Pd coated monolith may be more effective in CH_4 cracking. Unfortunately the effluent gases were not analyzed for the intermediate products of the SMR reaction sequence, so this argument cannot be supported qualitatively.

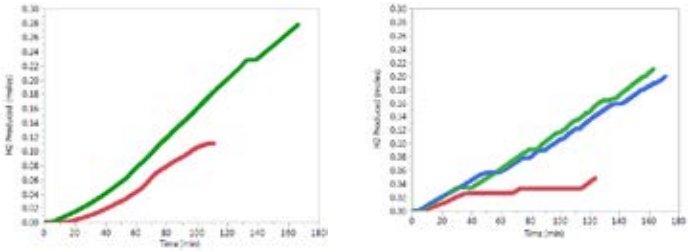
Another possible explanation could be provided by the observation of the molten regions on the Pd coated monolith. These regions suggest that at some point in the reaction sequence, the temperatures exceeded the melting point of mullite – which is around 1700°C. There is no evidence of this on the monitoring thermocouple but this thermocouple is actually 15mm away from the surface of the monolith that receives the concentrated irradiation. So the very high local temperatures at the surface could have enhanced the activation of the catalyst or elevated the reaction rates simply due to reaction kinetics. However this does not sound very plausible since it is clear that this temperature spike was instantenous and short-lived, as is not detected by the monitoring thermocouple.

For the Ni coated monolith, Day 1 produces 0.11 moles of H_2 in about 110mins with another 0.28 moles in 165mins in Day 2. Difference is driven by temperature and the associated lower conversion levels. For the Pd loaded monolith, the first day production is very low – only around 0.05 moles in 125mins due to the failing sun-light. The latter two days are somewhat similar, around 0.20 moles with the final day producing slightly less than the first day. This is interesting because the final day irradiation and temperature levels were better. This might be the result of a predominant coking mechanism.



(a) Ni loaded monolith (b) Pd loaded monolith

Fig. 5: CH_4 conversion for Ni (left) and Pd (right) coated monoliths



(a) Ni loaded monolith (b) Pd loaded monolith

Fig. 6: H_2 produced on Ni (left) and Pd (right) coated monoliths

V. Conclusions

This work demonstrates the feasibility of carrying out SMR reactions on a micro-reactor scale on Ni and Pd coated catalysts. It is seen that production on Pd catalyst is slightly less than the Ni catalyst, however, the weight based loading of Pd is 1% while that of Ni is 13.6%. In other words, very comparable activities were monitored despite almost 15 fold lower Pd loading in comparison to Ni. This indicates superior activity of Pd/CeO_2 catalysts. Coking seems to be a pre-dominant mechanism of catalyst poisoning, which can be mitigated by more consistent water vapor delivery.

Acknowledgements

Funding for this project is provided by TUBITAK 1003 program under the grant no 213M006.

References

Böhmer, M., Langnickel, U., & Sanchez, M. (1991). Solar steam reforming of methane. *Solar Energy Materials*, *24*(1-4), 441–448.

Buck, R., Muir, J. F., & Hogan, R. E. (1991). Carbon dioxide reforming of methane in a solar volumetric receiver/reactor: the CAESAR project. *Solar Energy Materials*, *24*(1-4), 449–463.

Iulianelli, A., Liguori, S., Wilcox, J., & Basile, A. (2016). Advances on methane steam reforming to produce hydrogen through membrane reactors technology: A review. *Catalysis Reviews*, *58*(1), 1–35. https://doi.org/10.1080/01614940.2015.1099882

Farrauto, R. J., Hobson, M.C., Kennelly, T., & Waterman E.M., Catalytic chemistry of supported palladium for combustion of methane, Appl. Catal. Gen. 81 (1992) 227–237. doi:10.1016/0926-860X(92)80095

Kodama, T. (2003). High-temperature solar chemistry for converting solar heat to chemical fuels. *Progress in Energy and Combustion Science*, *29*(6), 567–597. https://doi.org/10.1016/S0360-1285(03)00059-5

Kodama, T., Ohtake, H., Matsumoto, S., Aoki, A., Shimizu, T., & Kitayama, Y. (2000). Thermochemical methane reforming using a reactive WO 3/W redox system. *Energy*, *25*(5), 411–425.

Levitan, R., Rosin, H., & Levy, M. (1989). Chemical reactions in a solar furnace—direct heating of the reactor in a tubular receiver. *Solar Energy*, *42*(3), 267–272.

Tamme, R., Buck, R., Epstein, M., Fisher, U., & Sugarmen, C. (2001). Solar Upgrading of Fuels for Generation of Electricity. *Journal of Solar Energy Engineering*, *123*(2), 160. https://doi.org/10.1115/1.1353177

Direct Current Assisted Dark Fermentative Hydrogen Gas Production from Acid Hydrolysed Waste Paper Towel

[1]Gülizar Onaran,[1*]Hidayet Argun
[1] Pamukkale University, Engineering Faculty, Department of Environmental Engineering, Kınıklı Campus Pamukkale, Denizli, 20070, Turkey

* E-mail: hargun@pau.edu.tr

Abstract
One of the main constraints in batch operated dark fermentative hydrogen production is the sharp decrease of the pH due to the fast formation of volatile fatty acids. Therefore pH is generally adjusted to neutral levels using alkaline solutions. However, alkaline addition results in salt accumulation in the media limiting microbial activity. In this study, DC was applied to the dark fermentation media to control the pH as an alternative to alkaline addition. Acid hydrolysed waste paper towel was used as substrate and electrical current was only applied to raise acidic pH to the neutral level. In this context, the effects of applied voltage (0.25-3 V), substrate concentration (5-40 g/L at 1 V) and electrode distance (0.3-1.3 cm at 1 V) on pH regulation and hydrogen production performance were assessed. Most convenient conditions resulting most efficient hydrogen production and pH control were obtained at 1 V, 20 g glucose/L and 0.5 cm electrode distance.

Keywords: Dark fermentation, bio-hydrogen, waste paper towel, direct current

I. Introduction

Bio-hydrogen is expected to be an ideal fuel in the future due to its promising properties such as high energy content, renewable production way and environmental friendly usage (Paramesh et al., 2017). Among different bio-hydrogen production methods dark fermentation (DF) is an emerging process that enables the use of carbohydrate containing wastes as substrate (Argun et al., 2017). Spore forming *Clostridia* species are the most known bacteria able to convert carbohydrates into H_2, CO_2 and volatile fatty acids (VFA) at anaerobic conditions (Argun and Kargi, 2011). However, DF requires the strict control of operation conditions to maintain effective H_2 production (Argun and Kargi, 2011). One of the most important operating parameter to be controlled in DF is the pH. The pH in DF usually decreases due to VFA formation and drops sometimes to 3-4 which steers microorganisms to shift towards solvent production such as acetone, butanol and ethanol (Valdez-Vazquez and Poggi-Varaldo, 2009). Therefore sharp pH drops are not desired and the pH is kept at 5.5-6. pH control is accomplished manually or automatically and the most common alkalines used for neutratlization are NaOH, KOH and different buffers. However, the use of those alkalines triggers the increase of the conductivity and salt formation to levels haltering microbial activity. In this context the use of milder pH regulation methods are essential for more effective DF. In this study H_2 was produced from acid hydrolysed waste paper (WPT) towel by DF and the pH was controlled by applying DC current to the media only when required and the conditions resulting most effective H_2 production with DC current assistance were determined accordingly.

II. Experimental Set-up and Procedure

DF experiments were carried out in 300 mL gas tight serum bottles at 36 ^oC in an incubator. The substrate was waste paper towel (WPT) hydrolysate which was obtained by autoclaving 50 (w/v) dried WPT at 130 ^oC, pH: 1 for 15 min. The WPT was collected from the toilet paper bins at the Engineering Faculty of Pamukkale University. The inoculum was obtained from the anaerobic wastewater treatment plant of MONDİ paper factory that is located in the city of İzmir-Turkey. The seed sludge was boiled for one hour at pH: 5.9 to eliminate any methanogenic activity and was grown on a synthetic growth media whose C/N/P/Fe ratio was adjusted to 100/2/0.2/0.125 with NH_4Cl, KH_2PO_4 ve $FeSO_4.7H_2O$. The carbon source was 10 g/L glucose that was obtained by autoclaving 20 (w/v) WPT at 135 ^oC, pH: 1 for 15 min. The growth media was also supplemented with 0.2 g/L $MgSO_4.7H_20$ and 0.1 g/L L.cysteine.HCl. Inoculum addition was carried out by transferring the tenth the working volume and the C/N/P/Fe ratio was adjusted to 100/5/9/0.28 (Argun and Onaran, 2017). Additionally bottles were supplemented with 0.2 g/L $MgSO_4.7H_20$ and 0.1 g/L L.cysteine.HCl. Bromothymol blue (BB) was used as pH indicator during fermentation and DC current was instantly applied to only adjust the color. The color of BB turns from blue to yellow when the pH decreases below 6 (Argun and Dao, 2017).

Three sets of experiments were carried out to investigate the effects pH adjustment with DC-current application. In the first set of experiments the effects of applied voltage were studied by varying the DC voltage between 0.25-3.0 V. All other conditions ($Glucose_o$: 5.1 g/L, COD_o: 5.73 g/L, V_o: 140 mL, conductivity: 5 ms/cm, distance between electrodes: 0.5 cm) were kept constatnt except the applied voltage (0.25-3.0 V). In the second step of experiments only the initial glucose concentration was varied between 5.0-40.0 g/L and all other parameters were kept constant (Voltage: 1.0 V, pH: 6.8, V_o: 100 mL, distance between electrodes: 0.5 cm). Aluminium electrodes were used in the experiments and DC current was obtained from a power supply (TT-T-ECHNI-C MCH-303T). During the third step of experiments the distance between the electrodes was varied between 0.3-1.3 cm and other parameters were the same (Voltage: 1.0 V, pH: 6.5, $Glucose_o$: 21.44 g/L).

Liquid and gas samples were subjected to analytical measurements to follow the performance of the fermentations. The hydrogen percentage of the gas samples were determined using a gas chromatogram (GC-Agilent 7820) equipped with Supelco, Carboxen™ 1010 PLOT Fused Silica Capillary Column, 30m x 0.53 mm (U.S. Patents 5-549-445 ve 5-607-580). Nitrogen was used as carrier gas (8 mL/min). The oven, inlet, detector temperatures of the GC were 110°C, 230°C and 250°C, respectively. Total gas measuement was carried out using the water displacement method and the cumulative hydrogen volume was calculated using the following equation (Logan et al., 2002):

$$V_{H2,\,i} = V_{H2,i\,-1} + V_W \quad C_{H2,i} + V_{G,i}\,C_{H2,i} - V_{G,i-1}\,C_{H2,\,i-1} \qquad (1)$$

The meanings of the letters in Eq.(1) are as following:

$V_{H2,i\,-1}$ and $V_{H2,\,i}$:Cumulative H_2 volumes (mL) calculated for (i-1) th and (i^{th}) condition,
V_W :Total amount of gas (mL) that was measured with water displacement
$C_{H2,i}$ and $C_{H2,\,i-1}$: Measured H_2 percentage at (i^{th}) and (i-1) th condition,
$V_{G,i}$ and $V_{G,i-1}$: Headspace volume at (i^{th}) and (i-1) th condition

The cumulative H_2 volumes and time data were correlated with the Gompertz equation (Eq. 2) as shown below (Lee et al. 2008) and the constants were determined by regression analysis with the software Statistica (trial version).

$$H(t) = P\,\exp\left\{-\exp\left[\frac{R_m\,e}{P}(\lambda - t)\right] + 1\right\} \qquad (2)$$

where P is the maximum H_2 production potential (mL), Rm is the maximum rate of H_2 production (mL/h), λ is the Lag time (h) and e is 2.718.

Liquid analyses were carried out after centrifuging the sample at 5000 rpm for five minutes. Liquid samles were subjected to
Glucose (DuBois et al., 1956), total volatile fatty acid (TVFA) (TVFA kit of Merck Spectroquant, 1.01763. 0001), suspended solid and chemical oxygen demand (COD) concentrations (APHA, 2012).
The hydrogen yield (HY) was calculated by dividing the total cumulative H_2 volume to the consumed amount of substrate.

III. Results and discussions

The results for DC current assisted DF experiment is presented in Table 1. HY and Rm values increased by increasing the voltage from 0.25 to 1.5 V and then decreased at 3.0 V. Lowest and highest yield values were obtained at 0.25 V (49.05 mLH_2/gCOD and 0.237 molH_2/mol glucose) and 1.50 V (192.77 mLH_2/gCOD and 0.516 molH_2/mol glucose), respectively. As can be seen the highest yield is lower than the theoretical maximum yield which is 4 molH_2/mol glucose or 550 mLH_2/gCOD when glucose is the sole carbon source in DF for hydrogen production. The reason for lower yield were probably due to high sulphate concentration and high conductivity level as a result of acid hydrolysis inhibiting microbial activity. Or the possibility of the presence of hydrogen consuming microorganisms originating from the inoculum might have caused hydrogen consumption which eventually decreased the yield. The hydrogen formation rate showed a similar trend as the HY with the variation of the voltage. The Rm values increased from 0.354 to 1.270 mLH_2/h by increasing the voltage from 0.25 to 1.50 and then decreased to 0.844 mLH_2/h at 3.0 V. Low HY and Rm values at voltages higher than 1.50 migth be a result of aluminium inhibition on microbial activity. Since the aluminium release is proportional with the increase of the applied voltage. The maximum hydrogen percentage increased from 8.4 to 31.1% by increasing the voltage from 0.25 to 1.0 V and then decreased at higher voltages.

Tab. 1: Comparison of the hydrogen production performance at different voltages.

Voltage	Cumulative H_2 (mL)	Yield (mLH_2/gCOD)	Yield (molH_2/mol glucose)	Rm (mLH_2/h)	Max. H_2 (%)
0.25	10.714	49.05	0.237	0.354	8.4
0.50	18.179	75.49	0.309	0.592	18.21
1.00	32.431	142.11	0.511	0.899	31.12
1.50	42.102	192.77	0.516	1.270	23.94
3.00	21.967	72.64	0.280	0.844	12.58

IV. Conclusions

pH control was investigated by DC in dark fermentative hydrogen production from WPT hydrolysate. In this context effects of voltage, substrate concentration and electrode distance on hydrogen yield and rate were evaluated and most convenient conditions were determined at 1 V, 20 g glucose/L and 0.5 cm electrode distance. pH was effectively controlled using DC current, however more efficient results could be obtained with an automatically controlled DC supply. Moreover, dark fermentative hydrogen production performance can be enhanced by treating the hydrolysate for sulphate, 5-HMF and salt removal which are forming during acid hydrolysis.

Acknowledgements
This study was supported by TUBİTAK with a grant number 113Y184. Also the full conference attendance was financially supported by Pamukkale University Scientific Research Projects Coordination Unit (PAÜ-BAP) with a grant number 2018KRM002-030. The authors are thankful for TUBİTAK and PAÜ-BAP for their support.

References

APHA, 2012. Standard Methods for the Examination of Water and Wastewater, American Water Works Association/American Public Works Association/Water Environment Federation.

Argun, H., Dao, S., 2017. Hydrogen Gas Production from Waste Peach Pulp by Natural Microflora. Waste and Biomass Valorization 0, 0. doi:10.1007/s12649-017-9990-1

Argun, H., Kargi, F., 2011. Bio-hydrogen production by different operational modes of dark and photo-fermentation: An overview. Int. J. Hydrogen Energy 36, 7443–7459. doi:10.1016/j.ijhydene.2011.03.116

Argun, H., Onaran, G., 2017. Effects of N/C, P/C and Fe/C ratios on dark fermentative hydrogen gas production from waste paper towel hydrolysate. Int. J. Hydrogen Energy 42, 14990–15001. doi:10.1016/j.ijhydene.2017.04.289

Argun, H., Pelin, G., Kapdan, I.K., 2017. Biohydrogen Production Potential of Different Biomass Sources, in: Singh, A., Rathore, D. (Eds.), Biohydrogen Production: Sustainability of Current Technology and Future Perspective. Springer India, New Delhi, pp. 11–48. doi:10.1007/978-3-319-02904-7

DuBois, M., Gilles, K.A., Hamilton, J.K., Rebers, P. a., Smith, F., 1956. Colorimetric Method for Determination of Sugars and Related Substances. Anal. Chem. 28, 350–356. doi:10.1021/ac60111a017

Lee, K., Hsu, Y., Lo, Y., Lin, P., Lin, C., Chang, J., 2008. Exploring optimal environmental factors for fermentative hydrogen production from starch using mixed anaerobic microflora. Int. J. Hydrogen Energy 33, 1565–1572. doi:10.1016/j.ijhydene.2007.10.019

Logan, B.E., Oh, S.E., Kim, I.S., Van Ginkel, S., 2002. Biological hydrogen production measured in batch anaerobic respirometers. Environ. Sci. Technol. 36, 2530–2535. doi:10.1021/es015783i

Paramesh, K., Lakshmana Reddy, N., Shankar, M. V., Chandrasekhar, T., 2017. Enhancement of biological hydrogen production using green alga Chlorococcum minutum. Int. J. Hydrogen Energy 43, 3957–3966. doi:10.1016/j.ijhydene.2017.09.005

Valdez-Vazquez, I., Poggi-Varaldo, H.M., 2009. Hydrogen production by fermentative consortia. Renew. Sustain. Energy Rev. 13, 1000–1013. doi:10.1016/j.rser.2008.03.003

Hydrogen Production from Melon and Watermelon Mixture by Dark Fermentation

[1]Savaş Turhal, [1]Mansurali Turanbaev,[1*]Hidayet Argun
[1] Pamukkale University, Engineering Faculty, Department of Environmental Engineering, Kınıklı Campus Pamukkale, Denizli, 20070, Turkey

* E-mail: hargun@pau.edu.tr

Abstract
Fruit wastes offer a potential substrate and inoculum source for dark fermentative hydrogen gas production. Moreover, the utilization of fruit waste in dark fermentation enables waste reduction beside fuel production. In this context melon and watermelon mixture was selected as a source for hydrogen production and the effects of initial fruit mixture concentration (0.74-37 g TS/L) on hydrogen production yield and rate was studied using natural microflora and heat treated anaerobic sludge in batch experiments. Hydrogen was effectively produced by the natural microflora at 37 gTS/L (3.95 $mLH_2/mL_{reactor}$, 6.45 mLH_2/h). However, hydrogen yield and rate increased significantly by inoculating the fruit mixture with heat treated anaerobic sludge at the same substrate concentration (4.84 $mLH_2/mL_{reactor}$, 28.09 mLH_2/h). Inoculated melon and watermelon mixture was found to be a potential source for hydrogen production however the initial substrate concentration needs to be adjusted properly for efficient productivity.

Keywords: Bio-hydrogen, dark fermentation, natural microflora, melon, watermelon

I. Introduction

The extensive consumption of fossil fuels led to the investigation for alternative clean and sustainable energy sources (Sinha and Pandey, 2011). In this context hydrogen gas (H_2) is considerd as one of the potential fuels due to its superior properties such as high energy content and environmental friendly usage (Hallenbeck et al., 2012). However, H_2 is not readily available and is usually produced by conventional high energy demanding complex processes such as steam reforming, electrolysis and pyrolysis (Dincer and Acar, 2014). Alternatively H_2 can be produced by a biological process called dark fermentation (DF) where bacteria convert carbohydrates into volatile fatty acids, H_2 and CO_2 at mild conditions (Levin et al., 2004). Carbohydrates can be found in different types of wastes such as agricultural, industrial and municipal wastes whose disposal account for huge amount of efforts and energy. Moreover, regulations restrict the direct disposal of those wastes in landfills and require a certain reduction in the total carbon content. Therefore H_2 production from carbohydrate containing wastes offer distinct advantages such as waste disposal beside H_2 production. The maximum H_2 formation yield in DF can be calculated as 525 mL H_2/ g COD when glucose is used as the carbon source in the substrate (35 ^oC, 1 atm) (Singh, 2013). However, obtained yields in real applications are lower because of microbial constrictions (Argun et al., n.d.). In this study, H_2 was produced from melon and watermelon mixture by DF under different inoculation conditions. Both melon and watermelon are rich in carbohydrates and may account for a significant portion in municpal and agricultural wastes escpecially during the summer times. The aim was to compare the H_2 production performance of inoculated and not inoculated waste mixtures.

II. Experimental Set-up and Procedure

Substrate

The melon and watermelon waste used in this study was obtained from a local market in the city of Denizli-Turkey. The wastes were mixed with same amount after knife chopping and passing through a blender. This mixture was stored in a deep refrigerator at -18 ^oC and used when needed. The composition of the waste mixture used in this study is presented in Table 1.

Tab. 1: The composition of waste mixture used in this study.

Parameter	Content
COD	*96.59 g/L*
Total sugar	*83.84 g/L*
Total phosphorous	*5.55 gDW/kg*
Total nitrogen	*0.098 %*
Total solids	*7.4%*
Volatile solids	*94%*
Ash	*0.39%*
Water content	*92.6%*
Lignin	*10.29%*
Total organic carbon	*55.33%*

Inoculum

The inocula used in this study was anaerobic sludge (ANS) obtained from Pakmaya Baker's Yeast Company

located in İzmir-Turkey. The sludge was boiled for one hour (pH: 5.5) in order to eliminate methane forming microorganisms then it was grown on molasses for 20 h prior inoculation. The total sugar concentration of the growth media was 20 g/L and the C/N/P/Fe ratio was adjusted to 100/2/0.5/0.125 by using NH_4Cl, KH_2PO_4 and $FeSO_4.7H_2O$. Additionaly the media was supplemented with 0.2 g/L $MgSO_4.7H_2O$ and 0.1 g/L L.cysteine-HCl.

Experimental procedure

Experiments were done in serum bottles (310 mL) at 36 °C, pH: 5.5-6.0 and the working volume was 80 mL. Two sets of experiments were done to understand the effects of inoculation. The TS concentration (0.74-37 g TS/L) was varied within the same range during the experiments with and without inoculation. The pH of the media was kept between 5.5-6.0 manually using 5 M NaOH solution.

Analytical methods and calculations

A gas chromatograph (GC-Agilent 7820A) was used to determine the hydrogen percentage in the biogas. The oven, back inlet and back detector (TCD) temperatures of the GC were 110°C, 230°C, 250°C, respectively. Liquid samples were subjected to TS, VS, ash, water content, TOC, TKN, TP, glucose and volatile fatty acid (VFA) analyses. TS, VS, ash, water content and glucose concentrations were determined according to the standard methods (Eugene W. Rice, Rodger B. Baird, Andrew D. Eaton, 2012) and phenol-acid method (DuBois et al., 1956), respectively. All other analyses were done as described in our previous study (Argun and Dao, 2016). The hydrogen yield (HY) was calculated by dividing the cumulative hydrogen volume to the working volume of the reactor. Cumulative H_2 and time data were correlated with the Gompertz (Lee et al., 2008) (Eq. 2) equation and the coefficients were determined using the regression analysis tool of the software Statistica (trial version):

$$H(t) = P \exp\left\{-\exp\left[\frac{R_m e}{P}(\lambda - t)\right] + 1\right\} \quad (1)$$

where; P is the maximum hydrogen production potential in (mL), R is the hydrogen production rate in (mL H_2/h) and λ is the lag phase (h).

III. Results and discussions

Fig.1 presents the variation of HY and the final TVFA concentration with TS concentration when no inoculation was applied to the waste mixture. Both HY and TVFA concentrations increased by increasing the TS of the waste which was probably a reason for the increase in the sugar concentration. The sugar concentration increased from 1 to 10 g/L by increasing the TS from 0.74 to 37 g/L. TVFA formation showed a similar trend with the HY and the TVFA concentration increased from 0.44 to 5.49 g/L by increasing the TS from 0.74 to 37 g/L. Maximum HY and TVFA concentration were obtained at 37 gTS/L as 3.95 $mLH_2/mL_{reactor}$ and 5.49 gTVFA/L, respectively.

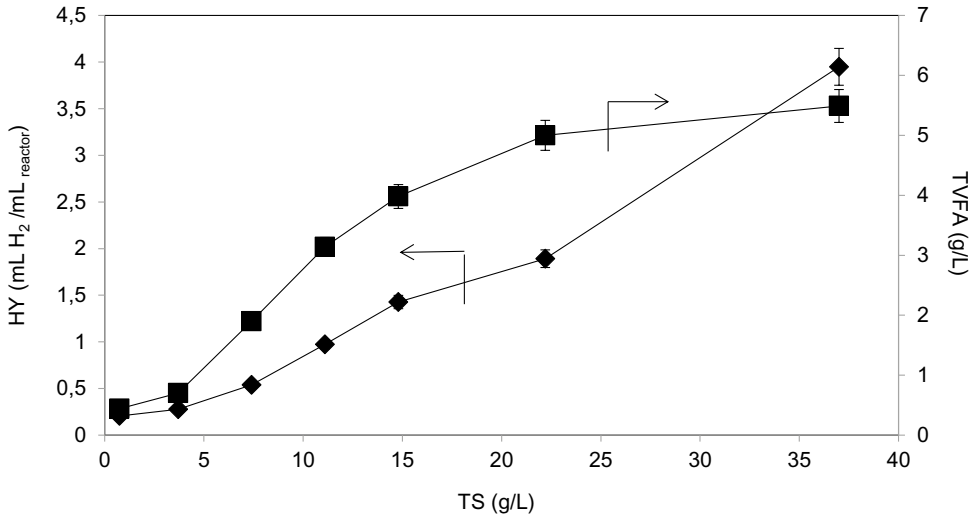


Fig. 1: Variation of HY (♦) and final TVFA concentration (■) with the TS concentration of the waste without inoculation.

A similar trend was observed for HY and TVFA concentration as in Fig. 1 when inoculation was applied. However, obtained HY and final TVFA concentrations were higher compared with the results presented in Fig. 1 indicating that inoculation contributed to some extend for hydrogen and TVFA formation. The maximum HY and TVFA concentration were obtained at 37 gTS/L as 4.84 $mLH_2/mL_{reactor}$ and 11.15 gTVFA/L, respectively when inoculation was used. The maximum hydrogen formation rates for non-inoculated and inoculated cultures were obtained at 37

gTS/L and 11.1 g/L as 6.47 and 42.90 mLH_2/h, respectively.

IV. Conclusions

Hydrogen gas production from melon and watermelon mixture by dark fermentation was studied at different TS concentrations with and without inoculation. The natural microflora in the waste was capable of producing effective H_2. However, inoculation increased the H_2 formation rate significantly. When the waste mixture was directly subjected to fermentation then HY decreased both for inoculated and non-inoculated conditions probably due to high sugar input and formation of high TVFA resulting in product inhibition. Finally it can be concluded that inoculation of melon and watermelon mixture at proper sugar concentration can significantly enhance the H_2 production performance compared with non-inoculated DF.

Acknowledgements

This study was supported by TUBİTAK with a grant number 113M994. Also the full conference attendance was financially supported by Pamukkale University Scientific Research Projects Coordination Unit (PAÜ-BAP) with a grant number 2018KRM002-030. The authors are thankful for TUBİTAK and PAÜ-BAP for their support.

References

Argun, H., Dao, S., 2016. Hydrogen gas production from waste peach pulp by dark fermentation and electrohydrolysis. Int. J. Hydrogen Energy 41, 11568–76. doi:10.1016/j.ijhydene.2015.11.170

Argun, H., Pelin, G., Kapdan, I.K., n.d. Biohydrogen Production Potential of Different Biomass Sources, in: Singh, A., Rathore, D. (Eds.), Biohydrogen Production: Sustainability of Current Technology and Future Perspective. Springer India, New Delhi, pp. 11–48. doi:10.1007/978-3-319-02904-7

Dincer, I., Acar, C., 2014. Review and evaluation of hydrogen production methods for better sustainability. Int. J. Hydrogen Energy 40, 11094–11111. doi:10.1016/j.ijhydene.2014.12.035

DuBois, M., Gilles, K.A., Hamilton, J.K., Rebers, P. a., Smith, F., 1956. Colorimetric Method for Determination of Sugars and Related Substances. Anal. Chem. 28, 350–356. doi:10.1021/ac60111a017

Eugene W. Rice, Rodger B. Baird, Andrew D. Eaton, L.S.C., 2012. Standard Methods for the Examination of Water and Wastewater. Am. Water Work. Assoc. Public Work. Assoc. Environ. Fed. 1469.

Hallenbeck, P.C., Abo-Hashesh, M., Ghosh, D., 2012. Strategies for improving biological hydrogen production. Bioresour. Technol. 110, 1–9. doi:10.1016/j.biortech.2012.01.103

Lee, K.S., Hsu, Y.F., Lo, Y.C., Lin, P.J., Lin, C.Y., Chang, J.S., 2008. Exploring optimal environmental factors for fermentative hydrogen production from starch using mixed anaerobic microflora. Int. J. Hydrogen Energy 33, 1565–1572. doi:10.1016/j.ijhydene.2007.10.019

Levin, D.B., Pitt, L., Love, M., 2004. Biohydrogen production: Prospects and limitations to practical application. Int. J. Hydrogen Energy 29, 173–185. doi:10.1016/S0360-3199(03)00094-6

Singh, R., 2013. Fermentative Biohydrogen Production Using Microbial Consortia, in: Gupta, V.K., Tuohy, M.G. (Eds.), Biofuel Technologies Recent Developments. Springer, Heidelberg, pp. 273–299. doi:10.1007/978-3-642-34519-7

Sinha, P., Pandey, A., 2011. An evaluative report and challenges for fermentative biohydrogen production. Int. J. Hydrogen Energy 36, 7460–7478. doi:10.1016/j.ijhydene.2011.03.077

Experimental Characterization of Thin Electrolyte for Intermediate Temperature Solid Oxide Electrolysis Cell

[1,2,*]Abdullah A. AlZahrani, [1]Ibrahim Dincer
[1] University of Ontario Institute of Technology, Faculty of Engineering and Applied Science, Oshawa, L1H 7K4, Canada
[2]Umm Al-Qura University, College of Engineering and Islamic Architecture, Department of Mechanical Engineering, Makkah, Saudi Arabia

*E-mail: abdullah.alzahrani@uoit.ca

Abstract
High temperature solid oxide electrolysis is an important pathway to efficient and sustainable hydrogen production from water. However, a major limitation of this technology is the high operating temperature that increases degradation, particularly at high steam intake concentrations. This paper reports an experimental performance and characterization results of a thin electrolyte-supported solid oxide cell operating in fuel/electrolysis cell modes at temperatures of 750℃, and 850℃. The experiment examines the impact of high steam to hydrogen ratios up to 95/5, in addition, the cell performance at compositions of 50/50 and 90/10 are reported. Therefore, the performance parameters such as the open circuit potential and *J–V* curves are measured and compared with theoretical values and relevant literature. Furthermore, the electrochemical impedance spectroscopy (EIS) is performed at both operating modes electrolysis and fuel cell.

Keywords: Solid oxide fuel cell, electrolysis, hydrogen production.

I. Introduction

High temperature solid oxide electrolysis is a promising technology with various hydrogen production applications. The deployment of this technology can revolutionize hydrogen storage and subsequently the use of hydrogen as a renewable energy carrier which perceived as one of the key success of renewables. Furthermore, hydrogen demand in many industries has been relying on conventional hydrogen production methods that have significant disadvantage of emitting carbon dioxide.

Hydrogen production through high temperature solid oxide electrolysis has one of the highest conversion efficiencies (Annabelle Brisse, Schefold, and Zahid 2008), compared with other sustainable methods hydrogen production technologies such as low temperature electrolysis and thermochemical cycles (Dincer 2012). Experimental investigations showed a maximum efficiency of 52.7% achieved by a 30-cell solid oxide electrolysis stack (Q. Li et al. 2014). The fact that Solid Oxide Electrolysis Cells (SOECs) are made of all solid components and requires no catalysts are other advantages that reflect on the design flexibility and the cost of the cell components (X. Li 2005). Though SOCs are produced in several designs such as tubular, monolithic, and planar, the planar cell design is currently being extensively pursued, due to the simple manufacturing and installation procedures, and the high volumetric power density.

Solid oxide electrolysis takes place at high temperatures in the range of 500–1000℃. A high temperature is required for the oxygen ion electrolyte to reach a practical conductivity. The solid oxide cell electrolyte is made of a dense ceramic layer fabricated of materials such as the commonly used yttria-stabilized zirconia (YSZ). The electrolyte is positioned between two electrodes: an oxygen electrode, which is the anode electrode with respect to the electrolysis process, and a hydrogen electrode, which is the cathode electrode. The typical material used for SOCs electrolyte is YSZ, usually composed of zirconium oxide (ZrO_2) doped with 8–0 mol% yttrium oxide (Y_2O_3). The conventional oxygen electrode is fabricated from strontium-doped lanthanum (LSM) while the cathode is made of nickel/yttria-stabilized zirconia (Ni/YSZ) cermet.

The electrolyte conductivity depends on operating temperature and significantly reduces at low operating temperatures, i.e., below 600℃ (AlZahrani and Dincer 2015). Nevertheless, YSZ, a widely accepted electrolyte material, has a higher ohmic resistance (~30 Ω.cm) than both an alkaline solution and proton exchange membrane even at as high a temperature as 900–1000℃ (Dincer and AlZahrani 2018). The high operating temperature of the SOECs reduces the electric power required for the electrolysis process while increasing the heat demand. It also enhances electrochemical reaction kinetics. However, several disadvantages arise with increasing the operating temperatures such as limiting material options for cells manufacturing and increasing degradation rate. Therefore, and in an effort to reduce the electrolysis cell operating temperature, a thin electrolyte layer (as low as 10–50 μm) has been fabricated to optimize the tradeoff between cell performance and operating temperature.

Ebbesen et al. tested a hydrogen electrode (Ni/YSZ) supported planar cell in an electrolysis mode for synthetic fuel production from steam and carbon dioxide (Ebbesen, Graves, and Mogensen 2009). Different ratio combinations of a mixture of H_2O, H_2, and CO_2 were supplied to a Ni/YSZ electrode active area of 16 cm^2 at temperatures between 750–850℃. The current density-voltage (J-V) curves were then measured, in addition to the durability and characterization tests that were performed. The reported results showed a feasible operation of a Ni/YSZ electrode with these mixtures and also indicated a long-term degradation of 0.003–0.006 mV/h, detected while operating at -0.25 A/cm^2. Moreover, Brisse et al. experimentally measured the performance of a SOEC consisting of Ni/YSZ as a hydrogen electrode, YSZ as an electrolyte, and LSM as an oxygen electrolyte (A Brisse,

Schefold, and Zahid 2008). This study revealed a considerable influence in the change in absolute humidity, which may be attributed to the steam diffusion at the hydrogen electrode. The degradation rate over 160 hours of continuous operation was observed to be minimal. Laguna-Bercero et al. (Laguna-Bercero, Skinner, and Kilner 2009) measured the performance of a SOEC with electrodes of LSM/YSZ and LSCF. They also used the EIS method to characterize electrodes. The ASR is evaluated for LSM/YSZ and LSFC/YSZ while operating at 800℃ and 70% steam concentration; the ARS values are 0.93 and 0.79 Ω cm^2, respectively.
The literature covers various aspects of SOECs testing and characterization, however, few studies considered the SOECs testing under high steam to hydrogen feed. The impact of operating under high steam to hydrogen ratio is significant as the designers may not choose such operating conditions, but due flow arrangement or reactant distribution such high steam concentration may develop. Therefore, it of great importance to examine operating in such conditions. The current paper presents a thin-electrolyte supported cell performance under steam to hydrogen composition ratios of 50/50, 90/10, and 95/5. In these cases, the open cell potential (OCV), current density-potential (J-V) curves, and electrochemical impedance spectroscopy EIS are measured and reported.

II. Experimental Set-up and Procedure

The cell used for testing is a planar SOC, usually called a button cell. The *NextCell 2.5* provided by *NexTech Materials* is used in the current experimental work. This cell is an electrolyte-supported cell, the design of which is advantageous for sealed operations. The cell specifications are listed in Table 1.

Tab: 1. Material and dimensions of the *NextCell 2.5* (data from (fuelcellmaterial 2008)).

Component	Diameter	Thickness	Material
Electrolyte	*25 mm*	*0.13-0.17 mm*	*YSZ*
Hydrogen electrode	*12.5 mm*	*~50 µm*	*NiO-GDC/NiO-YSZ*
Oxygen electrode	*12.5 mm*	*~50 µm*	*LSM/LSM-GDC*

The installation of the cell within the casing is shown in Fig. 1. The cell is sandwiched between two meshes to allow for uniform gas distribution over the electrodes active area. At the oxygen electrode, precious metals (commonly Pt) are used for current collection; the selection usually depends on the operating temperature as well as the desired conductivity. Ni mesh can be used for current collection at the hydrogen electrode. Platinum wires are preferred for current transmission and voltage measurements, but also nickel wire can be used. In addition to the exploded schematic view shown in Fig. 1 presents the main components arrangement in the cell fixture, high temperate gaskets are used to reduce or eliminate gas leakage from the cell fixture. The testing gas compositions and testing procedure is given in Table 1.

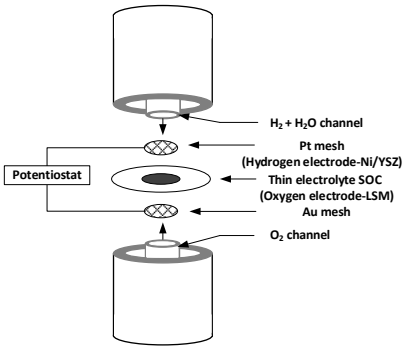


Fig. 1: The layout of the button cell installation in the testing fixture.

Tab. 2: The combination of tests performed on SOC cells.

Cell No.	Temperature	Fuel gas compositions (vol.%) out of 200 ±1.6 sccm	Oxygen gas compositions (vol.%) out of 200 ±1.6 sccm	Operating mode
1	750 ± 5 ℃	100 H_2	100 Air	FC
		50 H_2/50 H_2O	100 Air	FC/EC
		10 H_2/90 H_2O	100 Air	FC/EC
		05 H_2/95 H_2O	100 Air	FC/EC
	850 ± 5 ℃	50 H_2/50 H_2O	100 Air	FC/EC
		10 H_2/90 H_2O	100 Air	FC/EC
		05 H_2/95 H_2O	100 Air	FC/EC

III. Analysis

By supplying a DC power to the solid oxide electrode terminals, the water vapor, fed to the cathode side, is reduced to hydrogen and oxygen ion by electron consumption, as shown in the following half-cell reaction:

$$H_2O + 2e^- \rightarrow H_2 + O^{2-} \quad (1)$$

The oxygen ions O^{2-}, produced at the cathode side, migrate through the electrolyte to the anode side, creating an internal balancing ion current whereas, at the anode, oxygen ions are oxidized, releasing electrons and forming oxygen, as shown in the following half-cell reaction:

$$2O^{2-} - 2e^- \rightarrow O_2 \quad (2)$$

These reactions, at the microscopic level, occur at the triple phase boundary (TPB), which is where electrons, ions, and reactant gas intersect.
The reversible cell potential is then determined at standard T and P conditions as

$$E_r = -\frac{\Delta g}{nF} \quad (3)$$

At any operating pressure or temperature, the SOEC reversible cell potential at equilibrium is given by Nernest equation as

$$E_r(T, P_i) = E_r - \frac{RT}{nF} \ln\left(\frac{P_{H_2} {P_{O_2}}^{1/2}}{P_{H_2O}}\right) \quad (4)$$

The power density required by each cell is calculated as

$$P = J\,E \quad (5)$$

The area specific resistance (ASR) of the cell is determined as

$$ASR = \frac{\Delta V}{\Delta J} \quad (6)$$

IV. Results and discussions

In Fig. 2, summarizes the measurements of the OCV at five different reactant gas compositions and at operating different temperatures. This figure also illustrates the stability of the cell performance before other measurements can be taken. At a temperature of 750℃ and 100% volumetric hydrogen feed to the fuel electrode compartment, the cell shows an OCV of 1.293 V. Now, calculating the Nernst potential based on the equation (4) reveals a theoretical OCV value of 1.294 V which is in close agreement with the measured value. The discrepancy between the measured and calculated OCV is 1 mV that represents an error of 0.07%. While this minor drop in voltage may be attributed to wiring and other leakage losses, the close match between the two values can be related to the pure reactants used and the good conductivity of the wiring and current collection system. When the hydrogen gas concentration reduced to 50% and the steam increased to 50%, the corresponding cell measured OCV is 0.9628 V. The calculated Nernst potential is 0.9895 V. The difference in potential, in this case, increases to 26.65 mV. Further reduction in the hydrogen concentration to 10% while increasing the steam concentration to 90% led to an OCV of 0.8632 V. Compared with the theoretical value at the same condition of 0.8926 V; the discrepancy increases more than the double to 29.39 mV. Lastly, the OCV measurement made at fuel electrode gas compositions of 5% hydrogen and 95% steam is 0.823 V. The corresponding Nernst potential calculated to be 0.8597 V. While the difference is 36.65 mV.

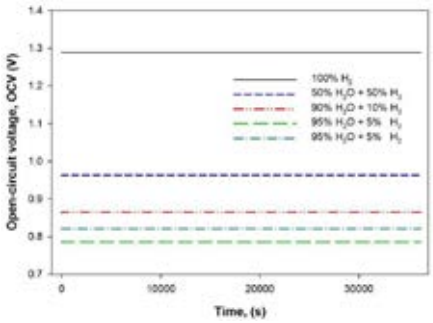


Fig. 2: The OCV measurements at stable conditions of different reactant gas compositions.

The performance of the cell operating in fuel cell mode under three different reactant gas compositions is presented in Fig. 3 through the *J–V* curve measurements. The operation at a hydrogen to steam volumetric composition of 1:1 shows an OCV of about 0.9601 V, and with increasing the current density the cell potential reduces to reach a voltage of 0.5 V at a current density of 0.356 A/cm^2. This corresponds to a power density of 0.178 W/cm^2. A more practical voltage in the range of 0.7–0.6 V is achieved while drawing a current density in the range of 0.179–0.2536 A/cm^2, at this range the calculated ASR is about 1.34 Ω cm^2.

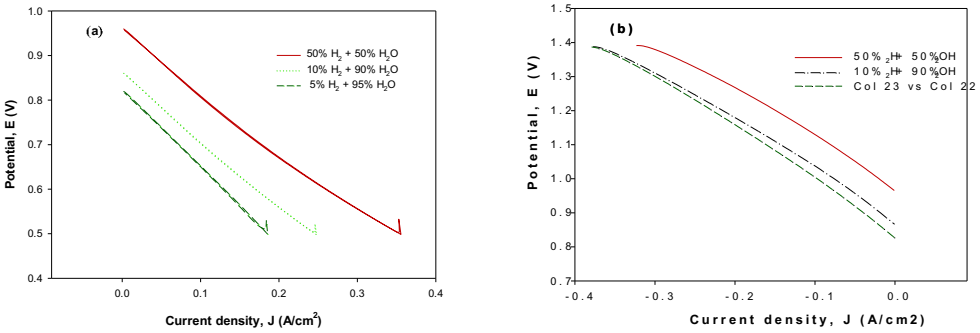


Fig. 3: The *J–V* curve measurements at a temperature of 750℃ reactants compositions of 50% H_2 + 50% H_2O, 10% H_2 + 90% H_2O, and 5% H_2 + 95% H_2O for (a) a SOFC mode, and (b) SOEC mode.

As a response to the reduction in the hydrogen concentration from 50% to 10%, the cell potential reduces and the recorded OCV at 10% hydrogen and 90% steam is 0.8608 V. The minimum measured of 0.5 V is at a current density of 0.2461 A/cm^2. At such low hydrogen concentration, the cell shows a higher ASR calculated to be about 1.5 Ω cm^2. For the research curiosity, the hydrogen concentration is further reduced to 5% while the remaining 95% is water. While it is unlikely such condition would be the desired valued set by an operator for a fuel cell, but it might be the case in some localized area within the cell/stack due to geometrical limitation or high current density operating. Therefore, it worth examination. In this case, the cell OCV is about 0.82 V and the cell potential reduces to 0.5 V while operating at a current density of 0.1862 A/cm^2. The calculated ASR is about 1.751 V.

The impedance spectra of the SOC are presented in Fig. 4(a), and 4(b) for the temperature of 750℃ and 850℃, and gas compositions of 50%, 90%, and 95% steam concentrations. The Figures show further increase in the cell resistance at higher steam concentrations. In the case of 750℃, the concentrations of 50% and 90% showing reasonable performance but at 95% the cell may encounter considerable performance degradation. Similarly, In Fig. 4(b), the high steam concentration led to significant reduction in the cell performance and thus damage in the cell structure. This is due to the increased concentration and temperature of 850℃. Further analysis using Figs. 4(a), and 4(b), will include equivalent circuit analysis and the complex impedance analysis.

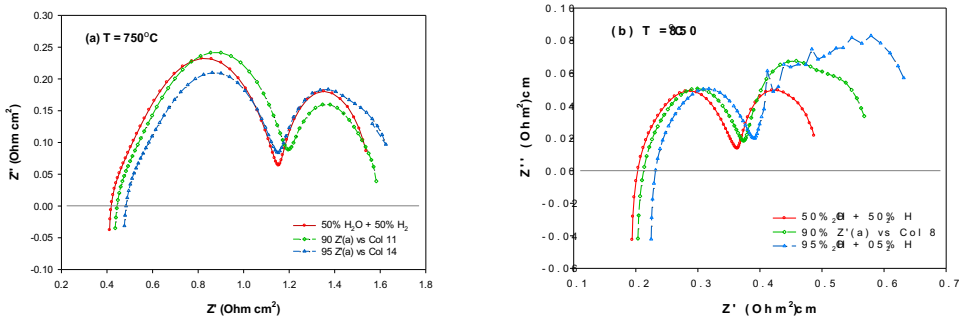


Fig. 4: The electrochemical impedance spectra at different reactant concentrations while operating at temperature of (a) 750℃. and (b) 850℃.

V. Conclusions

An electrolyte supported solid oxide button cell was tested in fuel cell and electrolysis cell mode at various steam/hydrogen compositions. The cell has an electrolyte of about 130–170 µm thickness, while the electrodes were 50 µm each. Two operating temperatures considered 750℃ and 850℃, while the fuel electrode was tested at steam to hydrogen volume compositions of 50/50, 90/10, and 95/5. The test examines the impact of high steam/hydrogen ratio of 95/5 on the cell performance, namely the cell potential and resistances compared with low

ratios, i.e., 50/50 and 90/10. By fixing the gas composition at the oxygen electrode, the influence of increasing the steam concentration in the fuel electrode on the electrode polarization can be identified. The results show significant effect of high steam concentration on the electrode resistance. In particular, at high operating temperature of 850°C the fuel electrode performance degraded at a higher rate and the polarization resistance increased from R_p=0.2847 Ω cm^2 at 95/5 at 50/50 to R_p=0.4014 Ω cm^2 at 95/5. Therefore, such high steam concentration should be avoided to maintain low degradation rate and extend the cell lifetime.

Acknowledgments
This research was supported by Umm Al-Qura University (UQU), Makkah, Saudi Arabia which is gratefully acknowledged.

References
AlZahrani, Abdullah A., and Ibrahim Dincer. Design and Analysis of a Solar Tower Based Integrated System Using High Temperature Electrolyzer for Hydrogen Production. International Journal of Hydrogen Energy 41, 8042–56 (2015).

Brisse, A, J Schefold, and M Zahid. High Temperature Water Electrolysis in Solid Oxide Cells. International Journal of Hydrogen Energy 33, 5375–82 (2008).

Brisse, Annabelle, Josef Schefold, and Mohsine Zahid. High Temperature Water Electrolysis in Solid Oxide Cells. International Journal of Hydrogen Energy 33, 5375–82 (2008).

Dincer, Ibrahim. Green Methods for Hydrogen Production. International Journal of Hydrogen Energy 37, 1954–71 (2012).

Dincer, Ibrahim, and Abdullah A. AlZahrani. 4.25 Electrolyzers. In Comprehensive Energy Systems, 1st ed., Oxford: Elsevier. 4:985–1025, (2018)

Ebbesen, Sune Dalgaard, Christopher Graves, and Mogens Mogensen. Production of Synthetic Fuels by Co-Electrolysis of Steam and Carbon Dioxide. International Journal of Green Energy 6, 646–60 (2009).

Fuelcellmaterial. “NEXTCELL-2.5.” 2008. http://www.fuelcellmaterials.com/site/sofc-components/ (accessed Jan 15, 2018).

Laguna-Bercero, M.A., S.J. Skinner, and J.A. Kilner. Performance of Solid Oxide Electrolysis Cells Based on Scandia Stabilised Zirconia. Journal of Power Sources 192, 126–31 (2009).

Li, Qingshan, Yifeng Zheng, Wanbing Guan, Le Jin, Cheng Xu, and Wei Guo Wang. Achieving High-Efficiency Hydrogen Production Using Planar Solid-Oxide Electrolysis Stacks. International Journal of Hydrogen Energy 39, 10833–42 (2014).

Li, X. Principles of Fuel Cells. Taylor & Francis (2005).

A Parametric Study of the Performance of a Polymer Electrolyte Membrane Electrolyzer: Energy and Exergy Analyses

Ehsan Baniasadi[1], Ebrahim Afshari[1], Faeze Moradi Nafchi[1], Nader Javani[2]

[1]University of Isfahan, Department of Mechanical Engineering, Faculty of Engineering, Hezar Jerib Ave., Isfahan, Iran
[2]Yıldız Technical University, Yildiz Campus, Faculty of Mechanical Engineering, Department of Mechanical Engineering, Istanbul, Turkey

In this paper, an analytical model is developed to study the performance of a PEM electrolyzer. The concentration over-potential as well as resistance losses of other electrolyzer components are modeled and the effect of different parameters including temperature, pressure, membrane thickness, the width and height of channel, electro-osmotic drag coefficient and current density on the performance of the electrolyzer are investigated. In addition, the effect of these parameters on the energy and exergy efficiency of PEM electrolyzer are studied. The results indicate that by increasing current density, the voltage of the electrolyzer increases and energy and exergy efficiencies decrease. Increase of temperature, decrease of pressure, decrease of membrane thickness and increase of current density of the anode and cathode electrodes lead to decrease of voltage of the electrolyzer and increase of energy and exergy efficiencies. The results indicate that the electrolyzer voltage increases by increasing the dimensions of the channel due to increase of the ohmic over potential. Moreover, it is concluded that electro-osmotic drag coefficient has not a considerable effect on the performance of the electrolyzer.

Keywords: PEM electrolyzer, Exergy, Membrane thickness, Channel geometry, Electro-osmotic drag coefficient

Hydrogen Generation from Solid State $NaBH_4$ by Using $FeCl_3$ Catalyst for Portable PEMFC Applications

[1*]Aslı Boran, [2]Serdar Erkan, [3]Inci Eroglu,
[1,3] Middle East Technical University, Chemical Engineering Department, Ankara, 06800, Turkey
[2] Erdes Teknoloji Kimya Endüstriyel Tasarım Kontrol ve Dış Ticaret Ltd. Şti., Büyükesat Mahallesi Seyyah Sok. 9/6 G.O.P., Ankara, 06680, Turkey

E-mails: yurdakulasli@gmail.com, erkanserdar@gmail.com, ieroglu@metu.edu.tr

Abstract
Being boron based compound, sodium borohydride, $NaBH_4$, is a convenient hydrogen storage material for applications like unmanned air vehicles. There are several issues behind commercialization of hydrogen gas generator by $NaBH_4$ hydrolysis systems. This study aims to find solution to the problems of $NaBH_4$ hydrolysis system by highlighting three main contributions. First, the usage of solid state $NaBH_4$ enables to increase the durability and the gravimetric H_2 storage capacity of the system in order to meet US DOE targets. Second, solid $NaBH_4$ usage decreases the system's weight since it does not require a separate fuel storage tank, which is very important for portable, on demand applications. Finally, the system's cost is decreased by using accessible and effective non precious catalyst such as ferric chloride, $FeCl_3$, The maximum hydrogen generation rate obtained was 2.6 L/min and the yield was 2 L H2/g NaBH4 with an efficiency of 76% at the most promising condition. Moreover, the novel solid $NaBH_4$ hydrogen gas generator developed in the present work was integrated to a PEM fuel cell and tested at the optimum operating conditions.

Keywords: Sodium Borohydride, Hydrogen Generation, PEM Fuel Cell, Portable Application

I. Introduction

There is no doubt that the world needs a renewable, sustainable energy source to maintain the existence of human kind. Today's economy based on fossil fuels may replace itself by named "hydrogen based economy" due to the depletion of fossil fuel reserves and negative impact on nature.

There are several technical barriers in front of the hydrogen infrastructure that must be addressed before commercialization. One of the most crucial obstacles behind hydrogen economy is the hydrogen storage. This present work will focus on hydrolysis of solid $NaBH_4$ for hydrogen generation in order to be a solution of "hydrogen storage".

The stoichiometric hydrolysis reaction can be written as follows:

$$NaBH_4 + 2H_2O \longrightarrow NaBO_2 + 4H_2 + heat \quad (1)$$

The reaction is highly exothermic with a heat of reaction of -217kJ/mol. The reaction rate is strongly dependent on initial $NaBH_4$ concentration (Wang et al., 2017).

If water is in excess, the reaction is expressed as in Equation 2.

$$NaBH_4 + (2+x)H_2O \xrightarrow{catalyst} NaBO_2.xH_2O + 4H_2 + heat \quad (2)$$

where, x is called "*hydration factor*".

In literature, throughout all studies, the main idea is to design a sodium borohydride hydrolysis reactor system together with fuel cell for commercial applications. Most of the continuous hydrolysis reactor systems in literature uses stabilized $NaBH_4$ solution as a fuel and solid catalyst which was placed in a reactor. Kim et al. (2007) worked with 20% $NaBH_4$, 1% NaOH and Co-B/Ni foam as catalyst obtained 76% yield. They also noted that as NaBH4 concentration increases, the yield decreases. Oronzio et al. (2009) used 20% NaBH4, 10% NaOH and Ru catalyst. They obtained 90% efficiency but, they found that $NaBO_2$ separation was needed.

Within the scope of this work, solid $NaBH_4$ was mixed with different amounts of water and H_2 generation kinetics has been determined by using $FeCl_3$ as catalyst. The optimum condition of the hydrogen generator was integrated with a single PEMFC and the performance of the system was tested.

II. Experimental Set-up and Procedure

As a hydrogen generation reactor, a reactor made from tempered glass which had an internal volume of 290 mL and cover diameter of 7.5cm was used.

Iron (III) chloride hexahydrate ($FeCl_3$) supplied from MERCK® and solid state sodium borohydride ($NaBH_4$) (was supplied from National Reasearch Institute of Boron (BOREN) with a purity of ≥96) was used in experiments. Water having a pH of 7.39 and conductivity of 37.1 µs/cm was used as reactant in the experiments. Figure 1 shows the experimental setup for kinetic experiments.

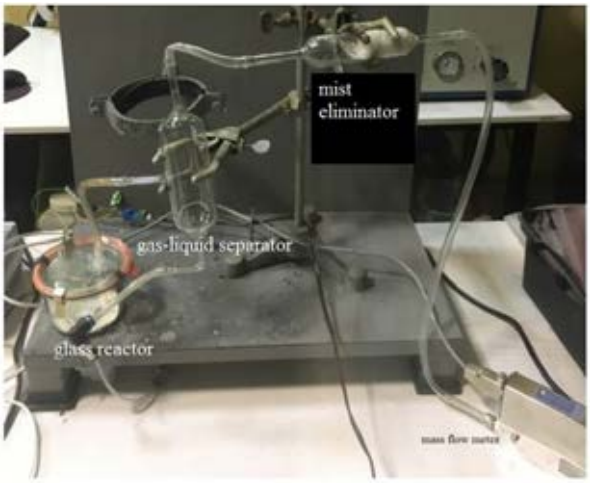


Fig. 1: Photograph of experimental setup of kinetic experiments for hydrolysis of $NaBH_4$ (b)

As can be seen from Figure 1, experimental setup is composed of 4 main parts which are; a glass hydrolysis reactor, a gas-liquid separator , a mist eliminator in order to prevent the liquid drops coming from reactor and a mass flow meter (Bürkert®, Model No: 8705). The mass flow meter is connected to the computer with RS485. So, H_2 generation flow rate was directly measured and monitored online by using Reliance 5.0 program. H_2 generation rate was recorded in every 1 second.

Two different procedures were applied for start-up of hydrogen generation from hydrolysis of $NaBH_4$ experiments. In the first case, Case 1, desired amount of solid $NaBH_4$ and solid catalyst were placed in the reactor. Required quantity of water at room temperature was injected directly into the reactor with a syringe (100mL) in order to start the hydrolysis reaction. In the second case, Case 2, only the solid $NaBH_4$ was placed in the reactor. The solid catalyst was dissolved in the desired amount of water and catalyst solution was obtained. This catalyst solution at room temperature was injected with a syringe (100mL) into the reactor which contains only solid $NaBH_4$. H_2 generation rate was monitored starting with the injection of catalyst solution.

The developed solid $NaBH_4$ hydrolysis system is integrated to a single Polymer Electrolyte Membrane Fuel Cell, PEMFC having an active area of 100 cm^2. Fuel Cell performance was measured and recorded by test station. Figure 2 shows the picture of integrated system.

The Membrane Elactrode Assembly (MEA) of the PEMFC was prepared by the ultrasonic coating manufacturing procedure given previously by Erkan (2011) and Erkan and Eroglu (2015). For the preparation of MEA's first catalyst ink solution was prepared and then coated on gas diffusion layer (GDL) by using SONOTEK Exacta Coat equipment.

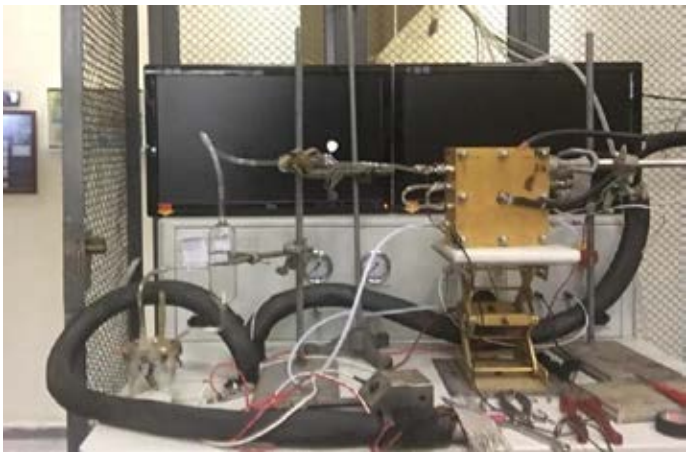


Fig 2: Integrated NaBH4 hydrolysis reactor with a single PEMFC.

III. Analysis

"*H_2 Generation Yield*" was defined as liter of H_2 produced per grams of $NaBH_4$ according to the Equation 3.

$$Yield = \frac{Total\ H_2\ produced(L)}{Amount\ \text{of}\ \mathrm{NaBH_4}(g)} \tag{3}$$

"Efficiency %" was defined according to Equation 4.

$$Efficiency(\%) = \frac{Total\ H_2\ \text{Generated}(L)}{Theoretical\ H_2\ \text{Generated}(L)} \times 100 \tag{4}$$

Mean H_2 generation rate was calculated from Equation 5 as follows where t_1 is duration:

$$Mean\ H_2\ generationrate = \frac{Total\ H_2\ produced(@t = t_1)}{\text{Duration}(t_1)} \tag{5}$$

IV. Results and discussions

Case 1 and Case 2 procedure that was explained in Section II was followed in kinetic experiments and compared with each other. Table 1 shows the results of kinetic experiments.

Tab. 1: Results of the kinetic experiments conducted at different hydration factors by using $FeCl_3$ catalyst

$NaBH_4$ amount (g)	H_2O amount, Hydration Factor x	$FeCl_3$ amount (g)	Total H_2 Generated (L)	Duration (min)	Mean H_2 generation rate (L/min)	Yield (L H_2/g $NaBH_4$)	Efficiency %
5.0	4.8g, x=0	0.5 (Case 1)	0.72	9	0.08	0.14	6
5.0	14.3g, x=4	0.5 (Case 1)	7.49	8	0.95	1.5	58
5.0	33.3g, x=12	0.5 (Case 1)	8.22	11	0.71	1.6	64
5.0	52.3g, x=20	0.5 (Case 1)	7.30	17	0.42	1.5	56
5.0	4.8g, x=0	0.5 (Case 2)	0.88	3	0.26	0.18	7
5.0	14.3g, x=4	0.5 (Case 2)	7.33	12	0.59	1.5	57
5.0	33.3g, x=12	0.5 (Case 2)	8.03	16	0.49	1.6	62
5.0	52.3g, x=20	0.5 (Case 2)	7.84	20	0.38	1.6	61
10.0	9.50g, x=0	1.0 (Case 2)	6.25	5	1.11	0.63	24
10.0	47.6g, x=8	1.0 (Case 2)	19.34	17	1.07	1.9	74
10.0	**66.6g, x=12**	**1.0 (Case 2)**	**19.72**	**17**	**1.17**	**2.0**	**76**

As can be seen from Table 1, the maximum H_2 generation efficiency (76%) is obtained with 10g $NaBH_4$, hydration factor of x=12 when 1.0g of $FeCl_3$ catalyst was dissolved in water and injected to the reactor (Case 2). This condition is found to be promising to be tested in prototype reactor for fuel cell applications.

The performance of the integrated system is recorded by the test station. Figure 3 shows the picture of integrated PEMFC system. For performance tests, the fuel cell voltage was kept constant at 0.55V and air flow rate of 0.56 L/min for all experiments. Before solid $NaBH_4$ system integrated to the PEM fuel cell, fuel cell was tested with pure hydrogen and compared with the hydrogen supply coming from developed solid $NaBH_4$ hydrolysis system. Figure 3 shows the fuel cell operation data with pure H_2. Figure 4 shows the fuel cell operation with integrated $NaBH_4$ hydrolysis system that is composed of fresh catalyst and $NaBH_4$. Fuel cell temperature was 40℃ for both experiments. One can compare the fuel cell performance with pure hydrogen and solid $NaBH_4$ system from Figures 3 and 4. The maximum power achieved by pure hydrogen was 20W with a current of 35A. The slightly higher performance was obtained by developed solid $NaBH_4$ hydrolysis system. This is because of generated hydrogen coming from hydrolysis reaction contains some humidity that enhances the fuel cell performance.

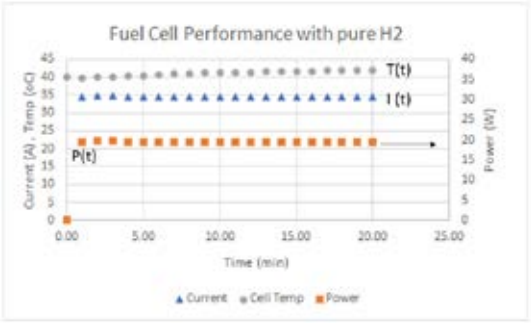


Fig. 3: Fuel cell performance for pure H_2 at constant cell voltage of 0.55V

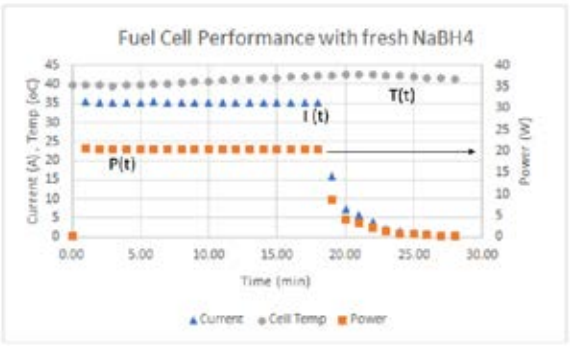


Fig. 4: Fuel cell performance of integrated $NaBH_4$ hydrolysis system at 0.55V

V. Conclusions

In the present work an original, portable solid $NaBH_4$ hydrolysis system has been developed for hydrogen generation. This system has been successfully integrated to a PEM fuel cell. This system can be stored for a long time and it can be used in demand.

Hydration factor is found to be one of the most critical parameter for solid state $NaBH_4$ hydrolysis reaction. When stoichiometric amount of water was used, H_2 generation occurs at a very slow rate and efficiency. So, excess water is needed for solid state H_2 generation from $NaBH_4$. As a result of kinetic experiments, the optimum H2 generation conditions was obtained with 10g $NaBH_4$, hydration factor of x=12 and 1.0g of $FeCl_3$ catalyst as in Case 2.The developed system that runs with $NaBH_4$ under optimum conditions can supply 20W and 35A for 18 minutes that is enough to charge the battery of a notebook.

Acknowledgements

Dr. Aslı Boran acknowledges the scholarship given by Turkish Scientific and Research Council, TUBITAK.

References

Erkan S., Development of 100W portable fuel cell system working with sodium borohydride, PhD Thesis, Middle East Technical University, Turkey (2011).

Erkan S., Eroglu I., Ultrasonic spray coating technique for high-performance PEM fuel cell electrode manufacturing. In: Dincer I., Colpan C., Kizilkan O., Ezan M. (eds) Progress in Clean Energy, Volume 2. Ch.34 Springer, Cham (2015).

Kim S.J., Lee J., Kong K.Y.,Jung C.R., Min I.G., Lee S.Y., Kim H.J., Nam S.W., Lim T.H., Hydrogen generation system using sodium borohydride for operation of a 400 W scale polymer electrolyte fuel cell stack. Journal of Power Sources 170,412-418 (2007).

Oronzio R., Monteleone G., Pozio A., De Francesco M., Galli S., New reactor design for catalytic sodium borohydride hydrolysis" International Journal of Hydrogen Energy 34,4555-4560 (2009).

Wang M.C., Ouyang L.Z., Liu J.W., Wang H., Zhu M., Hydrogen generation from sodium borohydride hydrolysis accelerated by zinc chloride without catalyst: A kinetic study. Journal of Alloys and Compounds, 717, 48-54 (2017).

Coke Minimization over Mesoporous Alumina Supported Ni Catalyst in Dry Reforming of Methane

Hüseyin Arbağ

Chemical Engineering Department, Gazi University, Ankara, Turkey

Biogas can be converted to hydrogen rich syngas by dry reforming of methane. In fact, CO2 reforming of methane can be considered as one of the important steps of production of valuable chemicals from biogas. Syngas with a H2/CO molar ratio of one is suitable to produce liquid hydrocarbons via Fischer-Tropsch synthesis and/or direct synthesis of dimethyl ether. In the present study, activity of mesoporous alumina supported nickel catalysts was tested in dry reforming of methane. Mesoporous alumina was synthesized following a hydrothermal route. Ni was incorporated into the structure of alumina materials by impregnation method. Mg was co-impregnated or sequentially impregnated into the Ni based catalyst. The synthesized catalysts were characterized by XRD, N2 adsorption/desorption, TPR, SEM-EDX, CO2-TPD and TG techniques. Nitrogen adsorption/desorption analysis showed that these catalysts had uniform mesoporous size distribution. The TPR analysis of the catalysts showed that Mg incorporation changed the reduction temperature of the Ni catalysts. All catalysts showed stable activity during 4 h activity test. Mg impregnation decreased the activity of the Ni based catalyst in terms of methane and carbon dioxide conversion. The result of TG analysis showed that impregnation Mg onto the Ni based catalyst did not help to decrease the coke deposition over Ni catalyst. However, co-impregnation of Mg and Ni decreased the coke deposition significantly due to the formation of a Ni and Mg mixed oxide.

Acknowledgements: Gazi University Research Fund (06/2016-12 and 06/2017-03) grants are acknowledged

Keywords: Hydrogen, Mesoporous Alumina, Ni, dry reforming

Preparation of Nanostructured α-Fe2O3 Films from Electrodeposited Fe Films for Photoelectrochemical Water Splitting Performance

Selim Demirci*, *Cevat Sarıoğlu

Department of Metallurgical and Materials Engineering, Marmara University, Istanbul, Turkey

Hematite (α-Fe_2O_3) has been extensively studied for photoelectrochemical (PEC) water splitting. The aim of this study is the fabrication of α-Fe_2O_3 photoanodes in order to apply in the hydrogen production area. In this study, nanostructured α-Fe_2O_3 photoanodes structures were prepared on indium-doped tin oxide (ITO) coated glass by thermal oxidation of electrodeposited Fe films at different temperature in the air atmosphere. The effect of electrodeposition parameters of Fe such as duration, current etc. on photoelectrochemical water splitting was investigated. The crystal phase structure, surface morphology, and optical properties of the α-Fe_2O_3 photoanodes were characterized using an X-ray diffractometer (XRD), scanning electron microscopy (SEM) and UV–VIS spectrophotometer, respectively. PEC performances of the α-Fe_2O_3 photoanodes were determined in the 0.1 M NaOH electrolyte solution. The results showed that electrodeposition parameters influenced the PEC performances of α-Fe_2O_3 photoanodes. Electrodeposition method could be good candidate for production of efficient α-Fe_2O_3 photoanodes for enhancement of PEC performance.

Keywords: Electrodeposition, Fe film, Hematite, Hydrogen generation, thermal oxidation, Photoelectrochemical Properties (PEC)

Investigation of the Effect of Single Stage and Four-Stage Clamping Pressure on Electrical Resistance Of GDL

[1]Mert Taş, [1*]Gülşah Elden
[1] Erciyes University, Engineering Faculty, Energy Systems Engineering, Kayseri, 38039, Türkiye

* E-mail: gulsah@erciyes.edu.tr

Abstract
Polymer electrolyte membrane fuel cells which generate power have a very wide application area such as portable, transport and stationary systems. The generating power with electrochemical reactions by fuel cell is directly related to the cell performance that changing with the properties of cell components. Gas diffusion layer (GDL) which is one of the cell components provides electron, water, fuel and oxidant transport with anisotropic porous structure. The anisotropic electrical resistances occurring due to structure of GDL can cause low cell performance. The purpose of this study is to investigate experimentally the effects of single stage (8 bar) and four-stage (2,4,6 and 8 bars) clamping pressure on the electrical conductivity of GDL. To achieve this purpose, the anisotropic electrical resistances were separately measured for gas diffusion layer and its with microporous layer using four probe conductivity measurement system. The electrical conductivities were calculated from the obtained values and these conductivities were integrated into three dimensional numerical models to analyse fuel cell performance and the distribution of electrical current density over GDL. It was observed that the electrical resistance values under gradual clamping pressure were mode stable than directly one.

Keywords: PEM fuel cell, Micro-porous and porous gas diffusion layer, Electrical resistance measurement, 3D anisotropic modelling

I. Introduction

Polymer electrolyte membrane (PEM) fuel cells which are scalability and eco-friendly are energy conversion systems. Although ohmic, kinetic and mass transport loses are observed in PEM fuel cell, these systems have high efficiency. These loses adversely affect fuel cell performance and decrease PEM fuel cell efficiency. Operating conditions and material structures cause of ohmic loses which one of the types of loses occured in PEM fuel components.

A study that measure of anisotropic gas diffusion layer resistance has been conducted by Todd et al (2015). To analyze anisotropic electrical resistance using four point probe method, samples are prepared as a square form. According to results, in-plane electrical resistance increases with increasing strain. However through-plane resistance decreases with increasing strain. Wilde et al. has been conducted an experimental study which is about structural and physical properties on GDL. They used commercial GDL and tried to find out the effect of clamping pressure on GDL properties. As a result, clamping pressure affect the resistance up to spesific point sharply but the higher pressure has less effect on through-plane resistance (Wilde, 2004). Mason et al has studied that effect of clamping pressure on through-plane resistance and fibres structure for commercial GDL (Mason, 2012). They investigate that GDL thickness and through-plane resistance decreases while clamping pressure increasing. The anisotropic conductivity effect on 3D PEM fuel cell computational modelling has been conducted by Zhou et al (2006). They set up a model by parametric in-plane and through-plane conductivity and tried to find out current density distribution and performance of PEM fuel cell. The effect of anisotropic conductivity on PEM fuel cell has been analysed using parametric conductivity values by Ismail et al. (2012).

This paper is targeted to find out single-stage and four-stage clamping pressure effect on anisotropic porous and micro-porous GDL resistance and PEM fuel cell performance. In-plane and through plane resistances are measured single stage and four-stage clamping pressure using four point probe conductivity measurement system. To analyse the effect of anisotropic electrical conductivity on performance, PEM fuel cell model which is single phase, 3D were established.

II. Experimental Set-up and Procedure

Commercially available porous and micro-porous gas diffusion layers (Sigracet SGL 34 BA and 34 BC respectively) are examined. Gas diffusion layer samples are prepared as square formation (3cm x 3cm) and assembled to conductivity cell according to directions that X and Y represent in-plane and z direction represents through-plane.

Experiments are performed using designed system that combined pneumatic compression unit, compressor, conductivity measurement cell and four point probe resistance measurement system. Fig 1.a. illustrates the front view of the conductivity measurement cell plate. This cell has two plates which have gold-plated pins placed square formation. Also, these plates were producted by material which has electrical insulation. Compression is controlled by compressor regulation for single stage (8bar) and four stage compression (2, 4, 6 and 8 bar). Single stage resistance measurement is conducted after single-stage compression to 8 bars for 60 minutes. For four-stage compression, the sample is compressed for 60 minutes every stage.

To measure of anisotropic electrical resistance, four point probe technique is used (Versastat 3). While DC current is supplied by two probe, voltage is measured by other two probe. The resistance of current axis is

calculated by Ohm's Law. Fig 1.b and Fig 1.c. illustrate to through-plane resistance measuring configurement and in-plane measuring configurements, respectively.

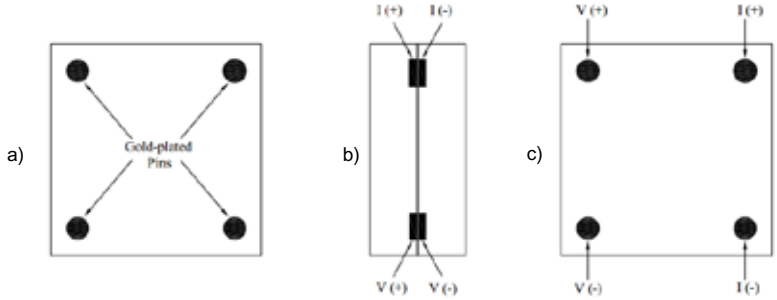


Fig.1: Conductivity measurement cell a) Front view of measurement cell, b) Through-plane resistance measurement configuration, c) In-plane resistance measurement configuration

III. Computational Model

The aim of this paper is to investigate the effect of anisotropic conductivity on performance and current density distribution of PEM fuel cell. Single phase, 3D PEM fuel cell model established by using COMSOL Multiphysics 4.2a software. The model consists of components which are anode and cathode channel, anode and cathode gas diffusion layer, anode and cathode catalyst layer and membrane. Figure 2 demonstrates fuel cell components, mesh construction and interface measuring potentials of PEM fuel cell (Elden and Tas, 2018).

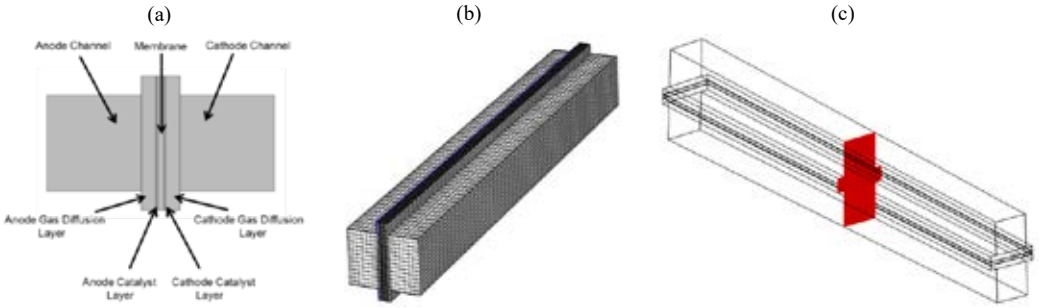


Fig.2: PEM fuel cell model a) PEM fuel cell components, b) mesh construction, c) Interface that measuring current density distribution and potentials (Elden and Tas, 2018).

Used assumptions in this model listed below and conservation equations listed in Table 1. Also, source terms and boundry conditions are listed in Table 2.

- Flow is in steady state.
- Cell temperature is constant.
- Hydrogen, oxygen and water are in gas phase and all gases are assumed in ideal gas.
- Contact resistances are ignored.

Tab. 1: Conservation equations.

Continuity equation	$\nabla(\varepsilon\rho\vec{u}) = 0$
Navier Stokes Equation	$\nabla(\varepsilon\rho\vec{u}\vec{u})=-\varepsilon\nabla P+\nabla^{*}\left(\varepsilon\mu^{eff}\nabla u\right)+S_u$
Darcy Law	$u=-\frac{k_p}{\mu}$
Stephan-Maxwell equation	$\rho\vec{u}\nabla m_i=\nabla\left[\rho\varepsilon m_i\sum_{j=i}^{N}D_{ij}\left\{\frac{M}{M_i}\left(\nabla m_i+m_i\frac{\nabla M}{M}\right)\right\}\right]$
Charge conservation equation	$\nabla.(k_e^{eff}\nabla\Phi_e)+S_\Phi=0$

Tab. 2: Source terms using equations and boundary conditions

Equations	Flow Channels	GDL	Catalyst Layer	Membrane
Momentum	$S_u=0$	$S_u=-\nabla P\frac{k_p}{\mu}$	$\vec{u}=0$	$\vec{u}=0$
Species	$S_k=0$	$S_k=0$	$S_k=-\nabla n_d F I_e-s_k jnF$	$S_k=-\nabla n_d F I_e$
Charge	$S_\Phi=0$	$S_\Phi=0$	$S_\Phi=j$	$S_\Phi=0$
Boundary Conditions				
$U_{in,anode}= U_{a,in}$, $U_{in,cathode}= U_{c,in}$				
$c_{H2,anode}=c_{H2,a}$; $c_{O2,cathode}=c_{O2,c}$; $c_{H2O,anode}=c_{H2O,a}$; $c_{H2O,cathode}=c_{H2O,c}$				

IV. Results and discussions

IV.I. Results of experiments

Fig. 3. shows validation of the through-plane resistance of porous and micro-porous GDL with SGL Sigracet GDL datasheet. As is shown in Fig. 3, measurement results are less than maximum resistance of GDL's in datasheet. Furthermore, the resistance values of single stage compression have higher resistance than four stage compression.

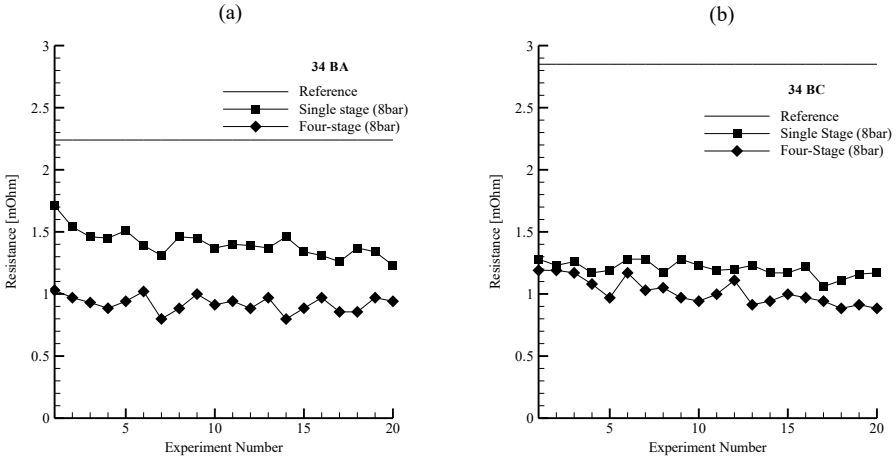


Fig 3. Validation of experiments with datasheets a) Porous GDL (34 BA) b) Micro-porous GDL (34 BC)

Electrical conductivity were calculated from the measured electrical resistance via equation (1) where transport resistance to conductivity; ρ is conductivity, R is resistance, A is sample area, l is the length of sample.

$$\rho = \frac{RA}{l} \quad (1)$$

Fig 4. illustrates conductivity values of four-stage compression for porous and micro-porous GDL. As clamping pressure is increased from 2 bar to 8 bar, in-plane conductivities (XX,XY and YY directions) are linearly decreased for both porous and micro-porous GDL. Deformations can be occured on these fibre directions with the increase of clamping pressure and this can be reason of the decreasing in-plane conductivity. Fig 4.d illustrates through-plane conductivity of porous and micro-porous GDL. Conductivity is almost linearly increased by increasing clamping pressure. Clamping pressure reduces the distance between fibres ,therefore, through plane conductivity is increased.

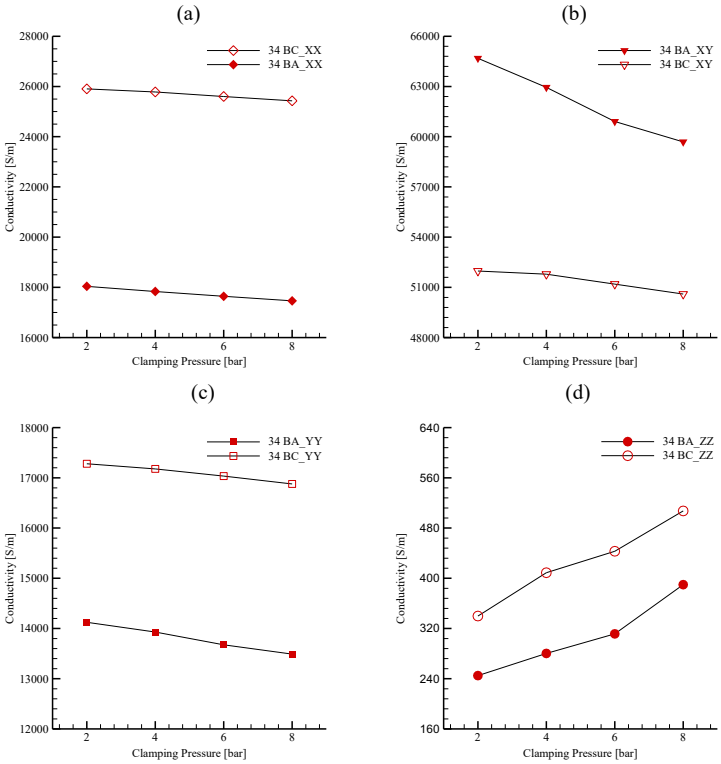


Fig.4: The variation of GDL conductivity depending on four-stage clamping pressure a) X direction, b) XY direction, c) YY direction, d) ZZ direction.

IV.II. Results of computational model

The computational model is established using Comsol software and the model was validated with experimental and numerical study of Ismail et al (2012). When the model results and reference study values are compered in Fig. 5, these results be in similarity each other.

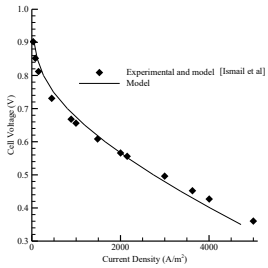


Fig. 5: Validation of numerical model

V. Conclusions

In this paper, the effects of single-stage and four-stage compression on porous and micro-porous gas diffusion layer conductivity are investigated. As the clamping pressure increases, in-plane conductivities are decreased. But, as increasing clamping pressure, through-plane conductivity increased. Consequently, when four-stage compression conductivity results were compered with single-stage compression, four-stage compression ensures higher through-plane conductivity. Thus PEM fuel cell performance and current density distribution are positively affected by the four-stage compression.

Acknowledgements

The authors would like to thank the Scientific Research Projects Unit of Erciyes University for funding and supporting the project under the contract no: FYL-2017-7235.

References

Todd D., Schwager M., Merida W., Three-dimensional anisotropic electrical resistivity of PEM fuel cell transport layers as functions of compressive strain, Journal of the Electrochemical Society, 162(3), 265–272, (2014).

Wilde P. M., Mandle M., Murata M., Berg N., Structural and physical properties of GDL and GDL/BPP combinations and their influence on PEMFC performance', Fuel Cells, 4(3), 180–184, (2004).

Mason T. J., Millichamp J., Neville T.P., El-kharouf A., Pollet B.G., Brett D.J.L., Effect of clamping pressure on ohmic resistance and compression of gas diffusion layers for polymer electrolyte fuel cells, Journal of Power Sources, 219, 52–59, (2012).

Zhou T., Liu H., Effects of the electrical resistances of the GDL in a PEM fuel cell, Journal of Power Sources, 161, 444–453, (2006).

Ismail M. S., Hughes K.J., Ingham D.B., Ma L., Pourkashanian M., Effects of anisotropic permeability and electrical conductivity of gas diffusion layers on the performance of proton exchange membrane fuel cells, Applied Energy, 95, 50–63, (2012).

Elden G., Taş M., Numerical investigation of anisotropic electrical conductivity effects in proton exchange membrane fuel cell, Special issue, 2–6, (2018).

Technische, I., GDL 34 & 35 Series Gas Diffusion Layer datasheet, 1–2,(2009).

Performance of CVD graphene supported Pt_xCo_y electrocatalysts for PEM Fuel Cell

Fatma Gül Boyacı San, Sümeyye Dursun, Mehmet Suha Yazıcı
TUBITAK Marmara Research Center, Energy Institute, 41470, Gebze, Kocaeli, TURKEY

E-Mails: fatmagul.boyaci@tubitak.gov.tr; suha.yazici@tubitak.gov.tr

Abstract
Graphene is an attractive support material for fuel cell catalysts and electrodes due to good electronic conductivity, high durability, mechanical and chemical stabilities. Platinum/cobalt (Pt/Co) nanoparticles have emerged as one of the most promising electrocatalyst in polymer electrolyte membrane (PEM) fuel cell. In this study, graphene grown by chemical vapor deposition (CVD) is utilized as catalyst support after nickel foam is removed and transferred onto the membrane. Graphene supported Pt_xCo_y electrocatalysts (Pt_3Co, Pt_2Co, PtCo, $PtCo_2$, $PtCo_3$) are prepared by sodium borohydride reduction method at room temperature. Unit cell of anode (CVD graphene supported Pt_xCo_y)//membrane (nafion)//cathode (Vulcan XC-72 supported Pt) is compressed to prepare membrane electrode assembly (MEA). Fuel cell performance tests indicate activity increase in the following trend: $Pt_3Co < Pt_2Co < PtCo < PtCo_2 \leq PtCo_3$. The $PtCo_3$ electrocatalyst has shown 2 times higher performance than that of Pt_3Co electrocatalyst at 0.55V.

Keywords: catalyst, fuel cell, Pt/Co, graphene

I. Introduction

Carbon supported platinum (Pt) is still the most used electrocatalyst in polymer electrolyte membrane fuel cells (PEMFCs). On the other hand, it has problems due to the overpotential for the oxygen reduction reaction (ORR) in the excess of 300 mV. In PEMFCs, Pt-alloys with various transition metals such as Co, Cr, Ni, etc. have been studied and shown superior electrocatalytic activity for the ORR, when compared to pure Pt (Jung et al 2015). Amongst the Pt based electrocatalysts (alloy or bimetallic), the PtCo catalyst has attracted much attention due to its high activity and stability in acidic environment. The enhancement in measured activity over Pt by modification Pt with transition metals is due to various factors including reduction of the Pt oxidation state, changing of surface composition, suppression of Pt oxide formation, formation of a new electronic structure with higher Pt 5d orbital vacancies and decrease in the Pt–Pt bond distance (Özaslan 2012, Jung et al 2015, Jung and Popov 2017, Baronia et al 2017). On the other hand, under the fuel cell operating conditions the transition metals can dissolve and not only cause decreasing of electrocatalyitc activity but also degradation of membrane due to migration of the metal into the ionomer (Cai et al 2015).

The durability of carbon supported PtCo catalysts is studied by several authors. Yu et al found that the cell performance enhancement by PtCo/C over Pt/C catalyst was sustained over 2400 cycles and the overall performance loss of the PtCo/C MEAs was less than that of the Pt/C MEA. Arico et al. reported that the potential cycling test at 130°C in a pressurized PEMFC showed a better stability for the PtCo alloy than pure Pt/C (Jung et al 2015). Rao et al (2011) studied synthesis and electrocatalytic oxygen reduction activity of graphene supported Pt_3Co nanoparticles which are prepared by ethylene glycol reduction method. Maximum power densities of 790 and 875 mW/cm^2 were obtained with graphene supported Pt and Pt_3Co, respectively.

Catalyst support material plays an important role to enhance the fuel cell performance. Carbon based materials such as carbon black, carbon fiber, carbon nanotube, fullerene and graphene are potential materials as a support for PEMFC. On the other hand, the oxidation of carbon black support hinders its use for electrode applications. Graphene is attractive candidate due to superior properties such as good electronic conductivity, large surface area, mechanical and chemical stabilities. The 2-D planar structure of the carbon sheet allows both the edge planes and basal planes to interact with the catalyst nanoparticles. This results with enhanced electrocatalytic activity and durability of graphene supported metal electrodes compared to amorphous carbon supported electrodes [Rao et al 2011, Sharma and Pollet 2012].

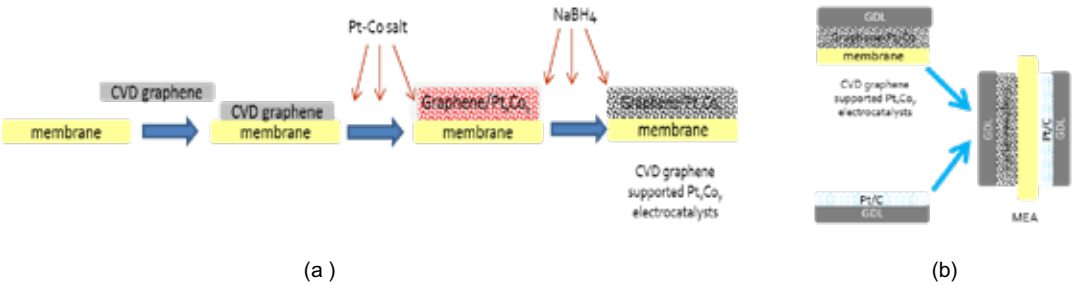
Aim of this study is to better understand the effect of CVD graphene supported Pt_xCo_y catalyst on fuel cell performance. Pt_xCo_y electrocatalysts having Pt:Co atomic ratio of 3:1, 2:1, 1:1, 1:2, 1:3 are prepared on CVD graphene, using sodium borohydride reduction method at room temperature. The effect of the composition on the fuel cell performance is investigated.

II. Experimental

Chloroplatinic acid ($H_2PtCl_6 \cdot 6H_2O$, Alfa Aesar) and cobalt chloride ($CoCl_2$, Alfa Aesar) sulfuric acid (H_2SO_4, Merck), hydrogen peroxide (H_2O_2, Alfa Aesar, 30% in water) and sodium borohydride ($NaBH_4$, Merck) are used to prepare the electrocatalysts. Nafion XL membrane and Sigracet 29BC are used as electrolyte and gas diffusion layer (GDL). CVD process is utilized to grow graphene on metal structures that are processed at 850-1035 ^oC. Metal support is etched away to obtain self-supporting continuous-phase graphene structure. Electrode prpeparation is schematically shown in Figure 1. First, graphene structures (5cm^2) are transferred onto pretreated Nafion XL membrane. Second, desired amounts of chloroplatinic acid and cobalt chloride are dropwise added onto CVD graphene to prepare PtCo electrocatalysts having Pt:Co atomic ratio of 3:1, 2:1, 1:1, 1:2, 1:3 (named as Pt_3Co/G,

Pt_3Co/G,Pt_2Co/G, PtCo/G,$PtCo_2$/G and $PtCo_3$/G) at room temperature. Then freshly prepared $NaBH_4$ is added dropwise to the metal precursor loaded graphene. Finally, resulted structure is washed with ultrapure water to remove undesired contaminants and treated using 0.5 M H_2SO_4. For the cathode electrode, conventional electrocatalyst ink is prepared and painted on carbon paper (Sigracet 29BC) with Pt loading of 0.1 mg cm^{-2}.

Unit cell of anode (graphene supported Pt_xCo_y)/membrane (nafion)/cathode (Vulcan XC-72 supported Pt) is hot pressed at 100 °C using a pressure of 30 kg/cm^2 for 5 min to prepare MEA. Schematic diagram for preparation steps of MEA is given in Fig.1b. Performance tests are carried out in a 5 cm^2 active area cell hardware. MEA is placed between two graphite plates with a single serpentine flow field with rectangular channels of 1 mm width and 1 mm depth. Silicon gaskets are used for sealing between the electrode and the bipolar plate. The humidified hydrogen and oxygen are supplied to anode and cathode side at the constant stoichiometry of 1.5 and 2, respectively.



(a) (b)

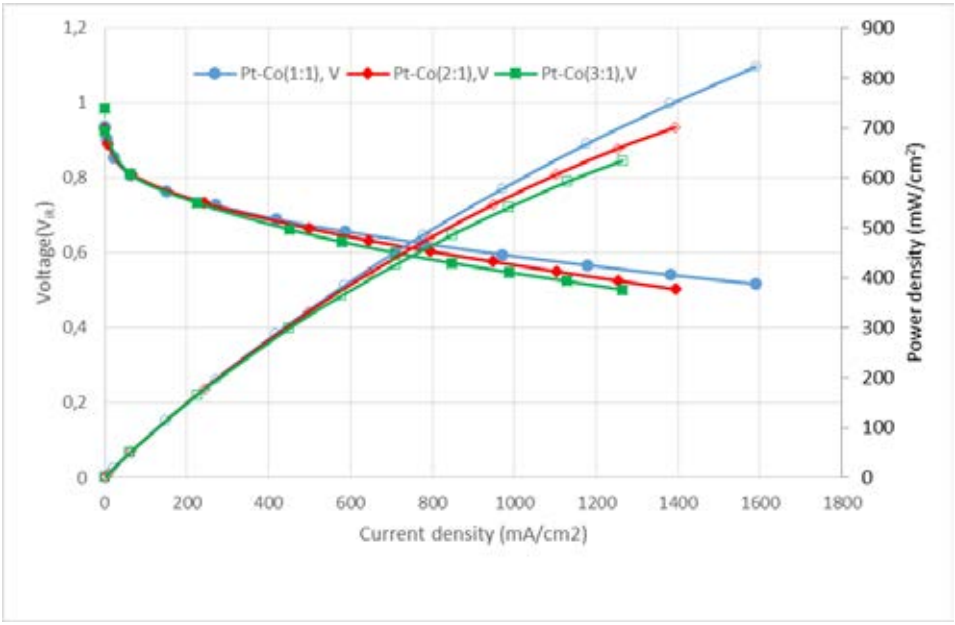
Fig.1: Schematic of graphene/Pt_xCo_y electrode preparation steps (a) and MEA formation (b)

Single fuel cell performance is investigated by polarization measurements at the cell temperature of 60°C and atmospheric pressure. Voltage versus current density data are collected for each graphene supported Pt_xCo_y electrocatalysts.

III. Results and Discussion

It is difficult to load catalyst onto continuous phase CVD grown graphene by conventional approaches. Graphene is highly hydrophobic and very sensitive to water and hydrophobic surfaces. This newly developed approach to put graphene first onto membrane prevents agglomeration and reduced surface area during catalyst loading.

The single cell performance curves of MEAs (Pt_3Co/G, Pt_2Co/G and PtCo/G) are presented in Fig. 2a. PtCo catalyst gives relatively better performance. The performance of the fuel cell decreases with increasing Pt amount. The maximum power densities of 634, 700, and 822 mW/cm^2 are obtained for the CVD graphene supported Pt_3Co, Pt_2Co and PtCo anode, respectively at the same operating conditions. At the next step, the electrocatalytic properties of PtCo/G, $PtCo_2$/G and $PtCo_3$/G for anode are investigated by increasing cobalt amount (Fig. 2b). Electrocatalytic performance increases with increasing the Co content of the electrocatalysts. The highest power density of 1200 mW/cm^2 is obtained for the CVD graphene supported $PtCo_3$ catalyst. In addition, it can be seen from Fig. 2b that activation and ohmic losses at low current region are significantly reduced with increasing Co content. The enhancement of the fuel cell performance can attributed to the increased d-electron vacancy and increased oxygen adsorption as well as weakened O-O bonds (Rao et al (2011), Jung et al (2016), Lohrasbi et al (2016)). Cell resistivities are also monitored during the fuel cell tests. The highest membrane resistivity is obtained for CVD graphene supported Pt_3Co. However, resistivity increases at high current densities. This may have to do with water management and drying of the membrane at high current densities. For Pt_3Co/G and Pt_2Co/G, higher resistivity is observed at low current density. This response may be due to $Co(OH)_2$ precipitation in membrane.



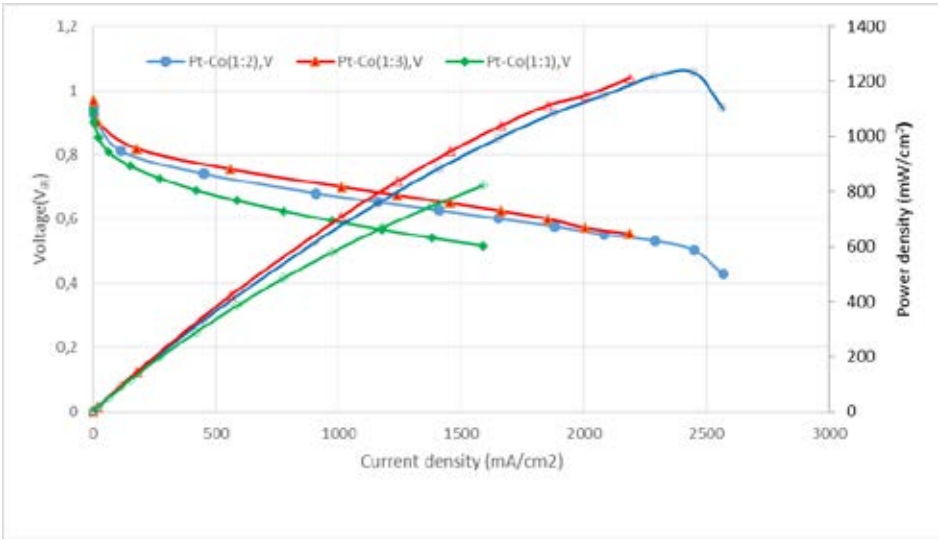


Fig.2: Single cell performance of MEA with CVD graphene supported Pt_3Co, Pt_2Co,PtCo (a), PtCo, $PtCo_2$,$PtCo_3$ (b).

In another approach, PtCo electrocatalyst is precipitated on the graphene and transferred onto gas diffusion layer (GDL). As seen in Fig. 3, maximum power density obtained at 0,5 V is 525 mW/cm^2. Performance of the fuel cell is lower with this approach compare to the one step process on the membrane as seen in Fig. 2. The decrease in the MEA performance is attributed to the catalyst losses in the separation step. After measurements, MEA is treated with H_2SO_4 and tested again at the same conditions. After the pretreatment of MEA, the performance is increased by 48 %.

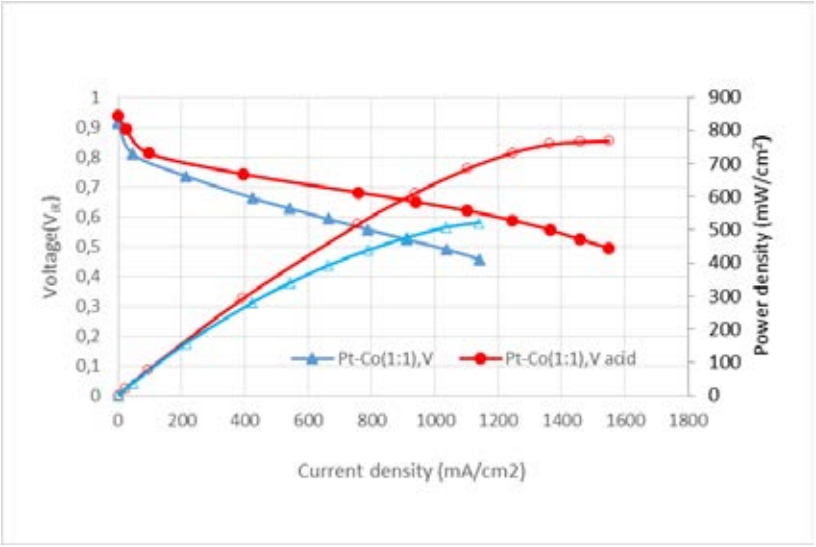


Fig. 3: The effect of the acid treatment of MEA on PEMFC performance.

IV. Conclusions

CVD supported PtxCoy nanoparticles are prepared on membrane by sodium borohydride reduction method. Thus, the agglomeration and decreasing the surface area of graphene sheets are prevented. The results shows that $PtCo_3$/G electrocatalyst exhibits 2 times higher performance than that of Pt_3Co/G under same fuel cell conditions. The electrocatalytic enhancement for $PtCo_3$/G has been attributed to the Pt electronic structure change due to the presence of metal, Pt-Pt distance and d-electron density in Pt. Post-test acid tratement seems to be a valuable option to enhance performance.

Acknowledgements

Financial support provided by the TUBITAK-ARDEB through 1003 program under contract #215M302 (Developing Cobalt-Boron-Nitrogen doped Oxygen Electrode (Cathode)) is greatly acknowledged.

References

Baronia R, Goel J, Tiwari S, Singh P, Singh D, Singh SP, Singhal SK. 2017. Efficient electro-oxidation of methanol using PtCo nanocatalysts supported reduced graphene oxide matrix as anode for DMFC. International Journal of Hydrogen Energy. 42 (15) 10238-10247.

Cai Y, Kongkanand A, Gu W, Moylan TM. 2015. Effects of Cobalt Cation on Low Pt-loaded PEM Fuel Cell Performance. ECS Transactions, 69 (17) 1047-1061.

Jung W, Xie T, Kim T, Ganesan P, Popov BN, 2015. Highly Active and Durable Co-Doped Pt/CCC Cathode Catalyst for Polymer Electrolyte Membrane Fuel Cells. Electrochimica Acta 167, 1-12.

Jung WS, Popov BN 2017. New Method to Synthesize Highly Active and Durable Chemically Ordered fct-PtCo Cathode Catalyst for PEMFCs. ACS Applied Materials Interfaces. 19;9(28):23679-23686.

Lohrasbi E, Javanbakht M, Mozaffari SA. Synthesis of Graphene-Supported PtCoFe Alloy with Different Thermal Treatment Procedures as Highly Active Oxygen Reduction Reaction Electrocatalysts for Proton Exchange Membrane Fuel Cells. Ind. Eng. Chem. Res. 55, 34, 9154-9163.

Özaslan M, Hasch F, Strasser P. 2012 Oxygen Electroreduction on PtCo3, PtCo and Pt3Co Alloy Nanoparticles for Alkaline and Acidic PEM Fuel Cells. Journal of The Electrochemical Society, 159 (4) B394-B405.

Rao CV, Reddy ALM, Ishikawa Y, Ajayan PM. 2011 Synthesis and electrocatalytic oxygen reduction activity of graphene-supported Pt3Co and Pt3Cr alloy nanoparticles, Carbon, 249:932-936.

Sharma S, Pollet BG. 2012. Support materials for PEMFC and DMFC electrocatalysts—A review, Journal of Power Sources 208: 96–119.

Maritime Industry Role in Future of Hydrogen Economy

Yaqub M. Amani, Preeti Parikh and Charles Munsch
State University of New York Maritime College, 6 Pennyfield Avenue, Bronx, New York, 10465, USA

E-mail: yamani@sunymaritime.edu;pparikh@sunymaritime.edu; cmunsch@sunymaritime.edu

Abstract
The impact of global warming is clear from the unfolding events witnessed worldwide. The world needs a new accelerated approach to meet the energy demand and reverse the processes that causes further instability in earth atmosphere. The objective of this paper is to introduce a novice idea for production of hydrogen. Maritime administration commissioned NS Savanah in 1962. The nuclear-powered cargo ship was by with a total power generating capacity of seventy-five megawatts. The international ports did not allow the ship to dock due to fears that radiation from nuclear powered ship may cause problems related to human health. Recognizing this fact, we offer to utilize this class of vessels for production of hydrogen, provided all safety measures regarding this class of ships are strictly applied and the ship operates faraway from population centers. The proposed scenario for such a scheme, based on the newest technological advances made in the fields of hydrogen production and autonomous cargo ships for hydrogen transfer to designated platforms. The economic viability of this process, comparative emission of greenhouse gases and production capacity of a platform similar to NS Savanah are topics addressed in this paper.
Keywords: hydrogen, power generation, shipping, maritime, climate change, energy

I. Introduction

The new discoveries in hydrogen storage technologies and methods make it possible to accelerate the transition from fossil fuel to hydrogen fuel. The latest developments in Liquid Organic Hydrogen Carrier (LOHC) enables efficient and safe storage of hydrogen through binding hydrogen to Dibenzyltoluene $C_{21}H_{20}$. This biodegradable chemical is nontoxic, non-mutagenic, non-carcinogenic, recyclable and noncombustible. It has high volumetric energy density. Storage density of LOHC is 21 times that of compressed hydrogen gas at 70 bar and 8.5 times that of a Lithium-ion battery (G. D0 etal. 2016). This process is simple catalytic hydrogenation and dehydrogenation of $C_{21}H_{20}$. Hydrogenation process is an exothermic reaction and the reaction parameters are 50-bar at 150C. The hydrogenation process is an endothermic and the reaction parameters are 1-bar and 300C. Furthermore, the logistic performance of LOHC (Bérubé, etal, 2007) compared to compressed hydrogen gas at 250 bar is impressive. A typical 40-ft truck will carry five times amount of hydrogen in kilograms than in compressed form. These facts establish safe and efficient means for hydrogen transportation by ships and trucks for power production. The introduction of this high energy density liquid and its safe transportation to local power generating stations will shorten the time to implement a decentralized power distribution system. Since hydrogen fuel cell produces DC power, it eliminates power conversion to AC and eases the path to implementation of DC micro-grids (H. Technologies 2017]). The only way to accelerate the implementation of micro-grids and guarantee a sustainable future is to make hydrogen available at lower price than fossil fuels. This can be achieved by conversion of all offshore wind, distant solar, wave and tidal electric power outputs to hydrogen. Utilizing these resources for hydrogen production will not be sufficient if not augmented by nuclear power. The choices are:

a. To continue using fossil fuel for 81% of electric power generation and let the majority of world population live without the privileges of modern technologies.
b. Using vast world oceans to augment hydrogen production by deploying nuclear powered ships.
c. Designing oceangoing vessels with extendable solar and wind turbines, to harvest the solar and wind energies for onboard hydrogen generation.
d. Delivery produced hydrogen, to shore side power generating platforms.
e. Utilizing nuclear power by removing the power plants to safe distances from population centers and using modern reactors to produce hydrogen.

II. Methodology

To demonstrate the logistics of using nuclear power for hydrogen production, data from NS Savanah is used. The future design of ocean going vessels to produce hydrogen utilizing atomic power will be simpler and more efficient than results presented.

The following data, related to NS Savanah, obtained from The American Society of Mechanical Engineers (Scott 1963):

Engine power: 16.42 MW

Reactor Capacity: 75 MW

Length: 182 m
Width: 23.8m
Gross Tonnage: 15,868 tons.

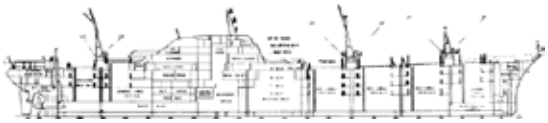


Fig.1: Side view of NS Savanah.

Only 60% of total onboard electric power generated used to calculate amount of hydrogen production. Commercially available hydrogen generating stations designed for indoor applications and rated at 3000 cubic meter per hour of hydrogen is used (Scott 1963) Each unit consumes 15 MW, thus three units will be installed on board of this ship. Each unit has 600 m^2 of footprint and all three will occupy 43.5% of total area of one of the upper decks. Deploying hydrogenation units, with capacity to absorb 100m^3 of hydrogen per hour in form of hydrogenated LOHC requires 160 l/hr. of $C_{21}H_{20}$ per unit. Ninety hydrogenation units or equivalent capacity needed for infusion of hundred percent hydrogen generated on board. The footprint for hydrogenation units is about 112m^2. Fig. (2), depicts scheme of hydrogen production for any platform. The two arrows at right and left of drawing points loading and unloading of recyclable LOHC to possible transfer modes. LOHC storage size for hydrogenated and dehydrogenated depends on how frequent it is recycled. The assumption for analysis presented in figure (3), is that every twenty-four hours autonomous tanker ships recycle LOHC transfer the sored content for use on marine hydrogen power generating platforms.

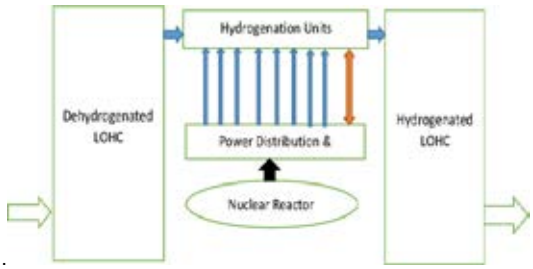


Fig. 2: The scheme of hydrogen production for any platform

III. Analysis

The use of nuclear energy to produce hydrogen away from population centers reduces cost for transmission of power to distant location. Although this paper will not discuss design of ships to augment hydrogen production, it is possible to use existing nuclear power generating facilities and convert them for hydrogen production to meet the needs of decentralized grid. Under these conditions, the reactor will operate under optimum conditions without load changes and make the operation of nuclear power generating plants more efficient than operating as a part of centralized distribution systems.

Figure (3) presents percentage storage size for LOHC relative to total cargo space available for cargo in NS Savanah for twenty-four hour continuous operation of hydrogen generators as function of total reactor power output. The medium for hydrogen storage is only for conveying the concept of pure hydrogen economy. As it previously mentioned, there are other possibilities that may arise as result of wide spectrum of materials with higher hydrogen to carrier storage capacity. The weight percentage of hydrogen for LOHC is 6.32% and some researchers show 7.2% in solids.

Using the promenade deck for electrolysis and lower deck for hydrogenation units. Hydrogenation units are twenty feet trailers each requiring 160 l/hr. of dehydrogenated LOHC. Cargo holds space can serve to store equal amount of $C_{21}H_{20}$ for hydrogenation for transport and recycled dehydrogenated $C_{21}H_{20}$.

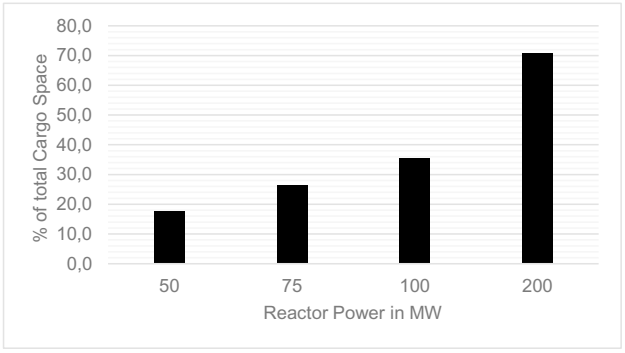


Fig.3: The percentage storage size for LOHC

A plot of monthly hydrogen production versus reactor power depicted in Figure (4). This demonstrates the significant economic benefits of hydrogen production by this method using 60% of reactor power. Notice that the monthly income for ships like NS Savanah is close to five million US dollars, assuming average price is $4 per kilogram of hydrogen. We recognize that a more detailed economic analysis of hydrogen production by the methodology proposed in this paper is required. These analysis, include nuclear fuel prices, maintenance and other related costs, which can be modeled on existing nuclear power plants. A more practical way for future of this technique for hydrogen generation is to put more research funds on small molten-salt Thorium reactors, which has les radioactivity and decay time. This will serve two purposes:

1. Provides world with low cost hydrogen and helps transition to distributed power generation a reality.
2. The small reactors can serve as powerhouse for cargo ships and eliminates vast amounts of Carbon dioxide, Nitro oxides and Sulphur oxides from current combustion engine ships.

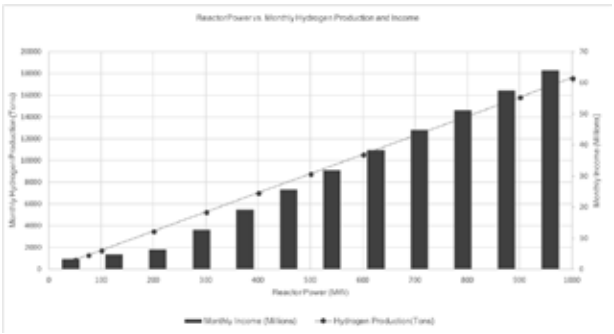


Fig. 4: Monthly economic benefits of hydrogen production

IV. Conclusions

There is an urgent need to reduce fossil fuel consumption for electric power generation. The investment per kilowatt on fuel cell are very close to combustible fuels and every year falling at rates that makes future of hydrogen as main fuel for electricity production hopeful. Hydrogen prices and means of production are the only obstacle to an accelerated transition to zero emission stationary power generation. The transportation industry, both marine and on land, can benefit, if the scheme for hydrogen production is feasible. A feasibility study addressing the following items is necessary to come to a consensus regarding production by this method.

- A comparative economic study of nuclear powered ships, reactor construction, installation and fuel costs with equivalent power generated by other means.
- Hydrogen storage current and future technologies and ease of transferring hydrogen from hydrogen production sites to electric power generation platforms.
- Environmental effects of using nuclear power to produce hydrogen away from population centers verses producing electric power by other means.
- The effects of low price hydrogen on implementation of micro-grids.
- The new wideband semiconductors switches at power transfer junctions and distribution center are promising and will reduce the cost and losses incurred in such processes.
- Cost analysis of transporting hydrogen from remote nuclear-powered hydrogen production facilities to local area electric power providers, versus construction of transmission lines and including the losses in transmission lines.
- Using remote nuclear power to switch to zero emission electric power generation technique reduces health care costs incurred due to emissions form fossil fuels.

These studies will give us a more detailed analysis, advantages and disadvantages of hydrogen production using nuclear technology. Given the advancements in hydrogenation units and liquid hydrogen carriers, hydrogen production can lead to large economic benefits in the supply of energy to general population. However, the more important advantage of using nuclear power to produce hydrogen energy lies in the possibility to initiate reversal of climate change from the adverse effects of fossil fuel emission. As the safety of nuclear reactors are advancing, it is time for humanity to decide to use nuclear power or not to use it at all. We propose that all industry and world leaders should compromise to use nuclear power for peaceful purposes, as opposed to using it for other means and to develop safeguards to protect humanity from its harmful effects. There is no doubt that the climate change is already causing economic stress in developed countries and more hardship in underdeveloped countries. There are two pathways for future of humanity. Continue accepting the slow pace of renewable energy entry to market and let the planet experience violent climate change, or to find similar and better methods for a fast transition to zero emission.

References

G. Do, P. preuster, R. Aslam, A Bosmann, K. Muller, W. Arlt, and P Wasserscheid, , "Hydrogenation of the liquid organic hydrogen," *Reaction Chemistry and Engineering,* p. 313–320, 2016.

Vincent Bérubé, Gregg Radtke, Mildred Dresshelhaus, Gang Chen, "Size Effects On The Hydrogen Storage Properties Of Nanostructured Metal Hydrides: A Review," International Journal of Energy Research, 14 March 2007.

H. Technologies, "Liquid Organic Hydorgen Carrier Energy Storage," 2017.

F. M. Scott, "N.S. Savannah," Patiots Point Naval And Maritime Museum, Mt. Pleasant, South Carolina, 1963.

Other References

Y. Amani C. Strez “Simulation of Engine Room for hydrogen powered ship” IAMU, Oct. 2012

Y. Amani, AGA-11, 2010, South Korea, “Hydrogen Based Shipping Industry”

Y. Amani, ITU Nov. 2010, Istanbul Turkey, “A Pioneering Hydrogen Fueled Cargo ship”

Y. Amani and Catherine Strez, Charlie Munsch, IAMU, June 2011, Gdynia Poland “Comparative Analysis of Combustion verses Hydrogen Fueled Cargo Ship”

Parag Upadhyay, Yaqub Amani, Navigation conference June 2011, Gdynia, Poland, “Integrating Modular Hydrogen Fuel Cell Drive for Ship Propulsion”

Y. Amani, Hydrogen Based Shipping Industry” Oct. 2010, IAMU, AGA11, Proceedings

Exergetic and Sustainability Analyses of Ammonia Usage in a Gas Turbine

Süleyman Kağan Ayaz*, *Önder Altuntaş

Department of Airframe and Powerplant Maintenance, Anadolu University, Eskişehir, Turkey

The world surface temperature increased by 0.6 °C in the 20th century and in the literature, there is a wide consensus that the temperature increase of 2 °C is an irreversible point. Low carbon economy is of great importance in decreasing global warming effects of energy systems. Ammonia, if produced in a sustainable way, can be used in energy systems in an environmentally benign way, producing only water vapour and nitrogen. This carbon free fuel can be stored and transported more easily than hydrogen or methanol and can be found easily since it is extensively used in agricultural industry. This study focuses on effects of using ammonia in a general gas turbine engine used for ground operations. The gas turbine model have been developed using the sotware EBSILON® Professional. Effects of ammonia fraction in compared to other fuels such as methane, hydrogen and kerosene is the main concern of this paper. Energetic, exergetic and sustainability analyses have been carried out for optimising power generation utilising ammonia fuel blends.

Keywords: Ammonia, gas turbine, exergy analysis, sustainability

Ni Catalyzed Methane Pyrolysis under Concentrated Solar Irradiation

C. Güvenç Oğulgönen, Atalay Çalışan, Deniz Üner, *Serkan Kıncal
Middle East Technical University, Chemical Engineering Department, Ankara, 06800, Turkey

* E-mail: skincal@metu.edu.tr

Abstract
Solar thermal methane pyrolysis over nickel in a pilot scale solar reactor is reported. The 316 SS reactor with a quartz window on one end allowed effective energy collection from a 70cm diameter parabolic mirror, such that solar irradiation was focused on the 30x30mm face of the 30x30x10mm, 200CPSI mullite monolith. Blank and 1.645g Ni monoliths were tested. Inlet flow stream during pyrolysis with 4% CH_4 or during regeneration with 4.2% O_2 mixture was fed to the irradiated side of the monolith. The pyrolysis and de-coking reactions were implemented in sequence. The effect of the ambient weather conditions on the relationship between conversion, temperature and the extent of coking was monitored. Repeatable, peak H_2 yields of ~95% were demonstrated at 100 mmol/h peak production rates. Pyrolysis and and regeneration cycles were complete within one hours each. Blank monoliths yield two orders of magnitude lower conversions under the same conditions.

Keywords: Methane Pyrolysis, Concentrated Solar Irradiation, Ni /mullite

I. Introduction

Hydrogen production by methane cracking is emerging as an efficient method of producing CO free hydrogen (Weger, Abanades, and Butler 2017). The reaction proceeds by depositing coke over a surface that can activate C-H bonds with subsequent hydrogen evolution. The challenge of the present day technologies is to manage the carbon deposited on the catalytically active surface.

The existing bottlenecks of the process can be shortlisted as managing the deactivation by coke deposition, and a potential CO_2 footprint problem at the end of the full cycle. If the thermal energy needed to drive this mildly endothermic reaction can be provided by concentrated solar energy a step forward will be taken for a CO free hydrogen generation for fuel cell applications(Rodat, Abanades, and Flamant 2011; Abanades, Kimura, and Otsuka 2014; Pregger et al. 2009).

The process is inherently unsteadystate due to the carbon buildup step. The major drawback of the carbon build up is the catalyst deactivation. The buildup carbon can inhibit the reaction by blocking the active sites over metal and carbon based catalyts (Serrano, Botas, and Guil-Lopez 2009; Snoeck, Froment, and Fowles 1997; Hazra et al. 2009). Eventually, the built up carbon fills the micro and macropores, and can congest the flow. The steady operation of such systems require periodic regeneration without a major damage to the catalytic activity. If the coke build-up involves carbon filament (CF) or carbon nanotube (CNT) formation, the metallic catalysts are usually lifted off from the support to the tip of the nanotubes. The reneneration by oxidation can lead to the loss of the active metal by volatilaziation, or sintering. Alternative solutions to catalytic systems have also been proposed, such as using a molten metal reactor where the carbon can be retrieved as a commercial product (Geissler et al. 2016).

Conducting chemical conversions using solar radiation is a challenging problem, due to the intermittent nature of solar radiation. In addition, temporal fluctuations in the incident radiation are reflected in the productivity, and yields. The commercial success of any process utilizing solar radiation depends strongly on the engineering ability to assess and circumvent the problems associated with the temporal fluctuations of the solar energy and inherently couple endotherms and exotherms of cyclic processes to the solar influx cycles. In this paper, we report the results obtained on solar thermal methane cracking conducted on Ni coated on a mullite monolith. The temporal and day to day variations of the process are reported.

II. Experimental Set-up and Procedure

The 30x30x10mm, 200 cpsi mullite monoliths used in this work were coated with Ni by a modified incipient wetness procedure, without any wascoat layer. In order to ensure the surface cleanliness and also introduce additional surface roughness, the monoliths were first etched in 2 M HCl solution in an ultrasonic bath, followed by hot water elutriation of the residual chlorine. Hot water elutriation was repeated with fresh water until there was no sign of residual chlorine elutriated in the water as tested by $AgNO_3$ (Merck CAS # 7761-88-8) additon.The monoliths were subsequently dried at 80 °C overnight and calcined at 500 °C for 3 hours. An appropriate amount of $Ni(NO_3)_2{\cdot}6H_2O$ (Merck CAS# 13478-00-7) salt was dissolved in deionized water, stirred for 30 min at room temperature. A known amount of this solution was carefully drop coated with the help of a pastor pipet on both sides of the monolith. The monolith was dried at 80 °C and the coating procedure was repeated until the desired metal loading was achieved. After the final layer was coated, the monolith was calcined in air at 600°C for 5 hours. The calcined sample had a loading of 12.8 wt% Ni/mullite.

The monoliths were loaded onto the solar reactor with the 30x30 facing the focused solar irradiation, as seen in Figure 1(c). In this same image the blue tubing providing the feed gases to the front face of the monolith can be

seen on the left side. The white tubing towards the back collects the effluent gases and delivers them to the gas analysis unit, while monitoring the temperature of the effluent by a J-type thermocouple. The window facing the focused solar rays is a 3mm thick, 96mm diameter quartz piece. A side-view of the reactor chamber is shown in Figure 1(b), the K-type thermocoulple leads can be seen extending out from the back of the reactor (top of the picture). This thermocouple is embedded into the monolith and holds the monolith in place while monitoring its internal temperature. The parabolic dishes used for concentration are 70cm in diameter and are shown in Figure 1(a). This 2x2 array of mirrors used in the study is mounted on a dual axis solar tracker that tracks the position of the sun based on the latitude of the installation and the solar time. On the picture, the mirrors are covered with their protective covers.

The effluent gases are analyzed with an array of 3 solid state (SnO based) sensors that have varying levels of sensitivity towards CH_4 and H_2 and allow for real time monitoring of the gas composition (more specifically MQ4, MQ6 and MQ8 by Hanwei Electronics, China). They also pass through a more sensitive total combustible gas analyzer (namely a Honeywell XCD) for validation. During the coke burning stages, two O_2 sensors (sensitive ppm and percentage levels by the Southland Sensing Ltd) connected to two EMD-485 sensor board are used to track O_2 levels. The O_2 levels are also monitored prior to experimentation to confirm purging of all O_2 from the system. The entire set-up is automated through a Lab-VIEW interface complemented with a NI USB-6343 A/D converter with digital I/O capabilities.



(a) 2x2 array of 70cm parabolic dishes mounted on a dual axis solar tracker with 4 reactors installed.



(b) Close-up of the reactor – face down



(c) Reactor mounted at focus – monolith inside, facing mirror

Fig. 1: Pictures of the solar-thermal reactor set-up - the solar tracker is installed at METU, Ankara campus

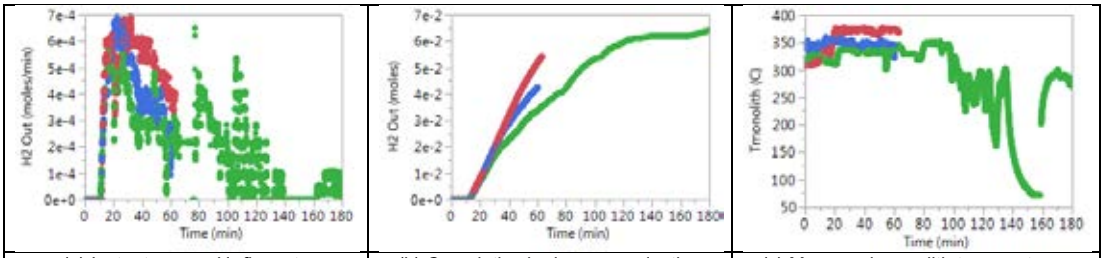
The experiments whose results are reported in this paper were conducted between August 11th and 17th, 2017. The total gas flow was 200sccm for all cases, with Ar as balance.

Day 1. Methane cracking on Ni with 4% Methane, followed by coke burning with 4.2% O_2. – Full Sun
Day 2. Methane cracking on Ni with 4% Methane all day – cloudy conditions, variable temperature
Day 3. Coke burning on Ni with 4.2% O2 – clouds were present towards the end
Day 4. Control run methane cracking on blank monolith with 4% Methane.

Once the monoliths were loaded in the reactor, the reactor volume was purged with 200sccm Ar overnight, during which time the O_2 concentration was monitored to ensure the completion of purging. The Ar flow was continued until the monolith was at focus and attained the reaction temperature before either CH_4 or O_2 was introduced.

III. Results and Discussion

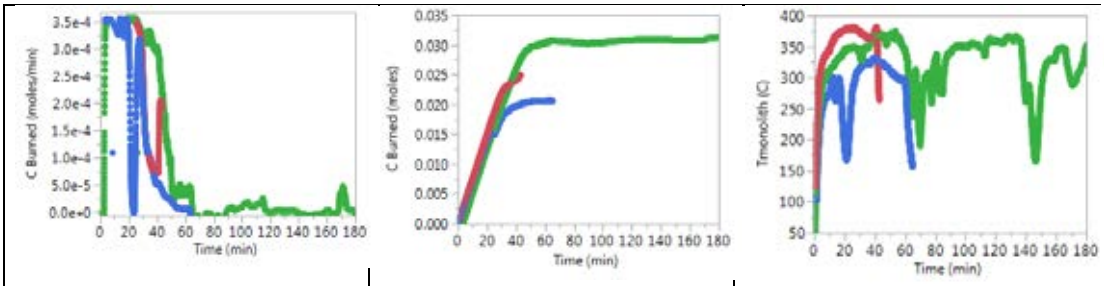
The results of experiments detailed above will be reported and evaluated here. The first reaction conducted on the monolith was methane cracking using 4% CH4 in Ar with 200sccm total flow rate under bright solar radiation. The monoliths were placed in the reactor shown in Figure 1 b and c without any further treatment and installaed in the focal point of the solar collector. The time dependent effluent hydrogen yields are shown in Figure 2(a) and (b), where the instantaneous and cumulative amounts are indicated, respectively. The time variation of the temperatures, driven by solar irradiation conditions, are also shown in Figure 2(c). Note that these temperatures are monitored by a thermocouple that is embedded about 15mm into the 30mm thick monolith, it is only a proxy for the reaction temperature. Higher temperatures exist particularly on the front face, as a function of the exact location of the point of focus. The reaction sequences were such that the experiment continued for either 60 or 180 minutes. On the same figure the results of two subsequent measurements on the same monolith are also reported. Data in Figure 1 a clearly show the fluctuations in the hydrogen effluent amounts, especially in coherence with the fluctuations in temperature during the extended perios of operation. The limited size of the solar collector would maintain a high temperature and sustain these temperatures at the relatively warm external conditions. However, the sensitivity of the system performance to the external temperatures is explicitly demonstrated by the data presented in this figure.



(a) Instantaneous H_2 flowrate | (b) Cumulative hydrogen production | (c) Measured monolith temperatures

Fig.2: Hydrogen yields on three different sequences of methane cracking. RED line is the first CH4 cracking cycle (60min), GREEN is the second cycle (180min), BLUE is the third cycle (60min)

The oxidation of the deposited coke was also carried out under solar irraditation. The flow was switched to 4.2% O_2 in Ar, and the effluent O_2 was monitored to account for the burning of coke. These runs were continued until the effulent O_2 was stabilized near the inlet values, indicating that there was no longer any C left to burn. The resulting instantaneous and cumulative de-coking results for all three sequences of coke regeneration are reported in Figure 3. The results also include the temperature trends, in very similar fashion to the CH_4 cracking results for Figure 2. The same color coding is used to refer to the sequences. Finally, Table 1 summarizes the total H_2 production and de-coking amounts along with an efficiency calculation, capturing the effectiveness of the de-coking step. The blue trace in Figure 2 also demonstrated the thermal sensitivity of the process. Ar around 20 min. the a quench in the system temperature (Figure 2c) resulted in a sharp decrease in ethe effluent carbon amounts (Figure 2a).



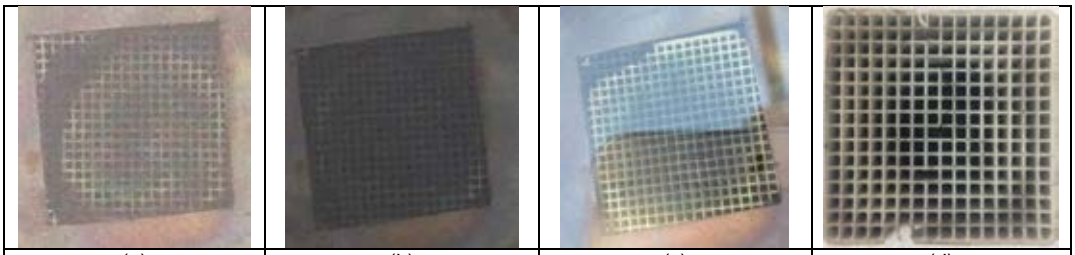
(a) Instantenous de-coking rate | (b) Cumulative carbon burnt | (c) Measured monolith temperatures

Fig. 3: The de-coking rates and totals during regeneration, along with the temperature profiles. RED line is the first cycle (60min), GREEN is the second cycle (180min) and BLUE is the third cycle (60min)

Table 1. Quantitative summary of hydrogen production during methane cracking and carbon burning during regeneration.

Cycle No	H_2 produced (moles)	C produced (moles)	C from before (moles)	C burned (moles)	Efficiency	
					Daily	Cumulative
1	54.5	27.25	0	24.9	91.4%	N/A
2	64.4	32.2	2.35	31.2	96.9%	90.3%
3	42.7	21.35	3.35	20.7	97.0%	83.8%

At the end of each day, the visual inspection and recording of the monoliths were also performed. The pictures of the monoliths at the end of Day 1, 2 and 3 are shown in Figure 4. Included here is the picture of the reference, blank monolith that went through the same methane cracking cycle as the GREEN line in Figure 2. The pictures in Figure 4 a and c clearly show that the color is non uniform. This is probably due to the loss of Ni metal during coke regeneration. Coking over nickel catalysts is a well known process/artefact of the reforming reactions. The generally agreed mechanism of carbon growth is the dissolution of carbon in Ni followed by carbon growth with the catalyst on the tip of the carbon fibers or nanotubes. Under these conditions, during regeneration by combustion, Ni metal is removed from the surface by the gas flow also. The lighter color of Figure 4 c in comparison to figure 4 a indicates the loss of metas in peripheral regions. This color change is also indicative of the temperature nonuniformity in the monoliths, as can be inferred by the different rates of carbob build up, and Ni metal elimination.



(a) (b) (c) (d)

Fig. 4: Monoliths after the reactions (a) end of day 1 – 1hr cracking followed by 1hr de-coking; (b) end of day 2 – 3hrs of cracking only; (c) end of day 3 – 3hrs of de-coking only; (d) blank monolith after 3hrs of cracking.

IV. Conclusions

In this paper, we summarized the results of hydrogen production by methane cracking over Ni coalted monoliths using a solar collector of 80 cm diameter and a home built solar thermal reactor. Systematic measuements revealed reproducible results in terms of hydrogen production rates followed by consistent carbon removal rates. The temperature sensitivity of the process to the external conditions and the ability to follow the reaction effluents in tandem with temperature fluctuations revealed that the process time constants are inherent to the reactor and the peripheral transfer lines do not contribute too much dead volume especially fro the concentration measurements. In the absence of Ni, monoliths were inactive for methane cracking. Coke regeneration have deactivated the catalyst, most probably due to the loss of Ni during regeneration excursions. The catalyst loss was attributed to the color change of the monoliths. Despite the bottlenecks indicated, the feasibility of the presented process lies in the small scale solar concentrator design.

Acknowledgements

Funding for this project is provided by TUBITAK 1003 program under the grant no 213M006.

References

Abanades, Stephane, Hiroyuki Kimura, and Hiroyuki Otsuka. 2014. “Hydrogen Production from CO2-Free Thermal Decomposition of Methane: Design and on-Sun Testing of a Tube-Type Solar Thermochemical Reactor.” *Fuel Processing Technology* 122 (June): 153–62. https://doi.org/10.1016/j.fuproc.2014.02.002.

Geissler, T., A. Abanades, A. Heinzel, K. Mehravaran, G. Mueller, R. K. Rathnam, C. Rubbia, et al. 2016. “Hydrogen Production via Methane Pyrolysis in a Liquid Metal Bubble Column Reactor with a Packed Bed.” *Chemical Engineering Journal* 299 (September): 192–200. https://doi.org/10.1016/j.cej.2016.04.066.

Hazra, M., E. Croiset, R. R. Hudgins, P. L. Silveston, and A. Elkamel. 2009. “EXPERIMENTAL INVESTIGATION OF THE CATALYTIC CRACKING OF METHANE OVER A SUPPORTED Ni CATALYST.” *Canadian Journal of Chemical Engineering* 87 (1): 99–105. https://doi.org/10.1002/cjce.20087.

Pregger, Thomas, Daniela Graf, Wolfram Krewitt, Christian Sattler, Martin Roeb, and Stephan Moeller. 2009. “Prospects of Solar Thermal Hydrogen Production Processes.” *International Journal of Hydrogen Energy* 34 (10): 4256–67. https://doi.org/10.1016/j.ijhydene.2009.03.025.

Rodat, Sylvain, Stephane Abanades, and Gilles Flamant. 2011. “Co-Production of Hydrogen and Carbon Black from Solar Thermal Methane Splitting in a Tubular Reactor Prototype.” *Solar Energy* 85 (4): 645–52. https://doi.org/10.1016/j.solener.2010.02.016.

Serrano, D. P., J. A. Botas, and R. Guil-Lopez. 2009. “H-2 Production from Methane Pyrolysis over Commercial Carbon Catalysts: Kinetic and Deactivation Study.” *International Journal of Hydrogen Energy* 34 (10): 4488–94. https://doi.org/10.1016/j.ijhydene.2008.07.079.

Snoeck, J. W., G. F. Froment, and M. Fowles. 1997. “Filamentous Carbon Formation and Gasification: Thermodynamics, Driving Force, Nucleation, and Steady-State Growth.” *Journal of Catalysis* 169 (1): 240–49. https://doi.org/10.1006/jcat.1997.1634.

Weger, Lindsey, Alberto Abanades, and Tim Butler. 2017. “Methane Cracking as a Bridge Technology to the Hydrogen Economy.” *International Journal of Hydrogen Energy* 42 (1): 720–31. https://doi.org/10.1016/j.ijhydene.2016.11.029.

Recent Trends of Hydrogen Utilization in Transportation

Kadir Aydın
Çukurova University, Department of Automotive Engineering, Adana, 01330 TURKEY

E-mail: kdraydin@gmail.com

Abstract
Today's transportation sector depends almost entirely on fossil fuels, emits more than 20% of all CO_2 emissions – and is almost certain to grow significantly in the years ahead. Latest predictions show that CO_2 emissions will increase by about 35% by 2050. Hydrogen usage is one of the solutions for the reducing of the emissions created by transportation. In the transport sector hydrogen is now used almost exclusively in fuel cells. Hydrogen fuel cell systems are suitable for virtually all means of transport. Passenger cars, buses and material handling vehicles have technically reached series-production readiness, are not far off that point, or are already in the early stages of commercialisation. Fuel cell passenger cars now offer the same features as those powered by internal combustion engines. Buses have undergone more intensive testing with hydrogen and fuel cells than any other form of transport. Light rail and road vehicles for the transport of goods may benefit from bus technology. Of all modes of transport, industrial trucks have the largest numbers of fuel cell electric vehicles. Commercial aircraft and merchant ships can use fuel cells as an efficient and clean energy provider for auxiliary power units.

Keywords: Hydrogen, fuel cell, transportation, renewable energy, ammonia.

I. Introduction

Environmental stress to planet earth has stimulated a quest for innovation in the energy system on a global scale. There is profound interest in fostering a cleaner future for present and future generations, evidenced by the 148 nations who ratified the 2015 Paris Climate Accord. These nations agree that the remedy for environmental stress requires capping greenhouse gas (carbon) emissions as soon as possible, and holding global temperature rise this century to 2°C at a minimum and 1.5°C ideally. Achieving this target requires reducing emissions minimum by 40% until 2050. Average emissions per kilometer need to decrease by more than 70%, despite an increase in more carbon-intensive freight and air traffic. Hydrogen offers an elegant solution to this environmental crucible. As a highly flexible energy carrier, hydrogen can deliver a holistic – clean, integrated and multi sector– systems approach to energy that will contribute decisively to solving the environmental problem and securing earth's energy future De Valladares (2017).

Hydrogen's relationship to renewables cannot be overemphasized. Hydrogen with a low-carbon footprint has the potential to facilitate significant reductions in energy-related CO_2 emissions. Thus, use of renewable feedstocks for hydrogen production is very attractive from the environmental perspective. Today, the world is witnessing significant growth in the installed capacity of renewables (primarily wind and solar). Onshore wind is the leader, accounting for over one-third of the renewable capacity and generation increase. Solar PV follows, accounting for another third of deployment. Hydropower is also growing and accounts for one-fifth of new renewable additions, and over a quarter of the growth in renewable energy electricity generation Japanese Member update (2017). As a result of this growth, the electricity grid must sometimes restrict uptake of renewable electricity when the grid is full (saturated) in order to balance electricity supply and demand. Consequently, renewable electricity production is curtailed. However, use of hydrogen for storage of renewable electricity (converted via water electrolysis) is a game changer. Hydrogen and electricity are in fact complementary energy carriers: hydrogen can be converted to electricity, and electricity can be converted to hydrogen.

Hydrogen is the most abundant and lightest of the elements. It is odorless and nontoxic. It has the highest energy content of common fuels by weight -- nearly three times that of gasoline. Hydrogen is not found free in nature and must be "extracted" from diverse sources: fossil energy, renewable energy, nuclear energy and the electrolysis of water. A separate energy source (electricity, heat or light) is required to "produce" (extract or reform) the hydrogen. Today, most hydrogen is made from fossil energy using steam methane reforming (SMR) of natural gas, followed by partial oxidation (POX) and autothermal reforming (ATR), which combines SMR and POX processes De Valladares (2017). Hydrogen generated by electrolysis from renewable energies produces the lowest greenhouse gas emissions. The primary energy input for electrolysis based on conventional electricity is high, whereas that for natural gas and biogas reforming and for renewable electrolysis is low. However, electrolysis from renewable electricity uses a high proportion of renewable primary energy and only small amounts of fossil primary energy. As an "industrial gas," hydrogen is already a big global business with strong fundamentals. The hydrogen generation market is expected to be valued at $115.25 billion USD in 2017 and grow to $154.74 billion USD in 2022. This market comprises two segments: "merchant" hydrogen - i.e., hydrogen generated on site or in a central production facility and sold to a consumer by pipeline, bulk tank or cylinder truck delivery; and "captive" hydrogen - hydrogen produced by the consumer for internal use and consumed at the point of usage.

Like electricity, hydrogen is an "energy carrier". It can be used in a full range of applications in all sectors of the economy: transportation, power, industry, and buildings. Since fuel cell electric vehicles (FCEVs) are emission-free at the tailpipe, use of hydrogen in the transport sector positively impacts urban air quality, whether or

not the hydrogen feedstock is produced from a renewable source. Hydrogen can be used for difficult to electrify applications or applications that currently use diesel. Electrification via the grid or with batteries is not an inherently superior or even viable solution for some applications. Heavy duty-transport, non-electrified trains, and maritime transport are examples of applications that are battery-challenged. Hydrogen can be used as a substitute for diesel, e.g., to power non-electrified trains. Germany alone has some 4,000 diesel powered train cars De Valladares (2017).

The efficient storage of hydrogen is regarded as an important precondition for the spread of fuel cell technology in the transport sector. Since hydrogen has a low volumetric energy density, in motor vehicles it is usually carried in compressed form in pressurised cylinders. 700 bar is now the established storage pressure for passenger cars. By contrast, the storage space in buses (on the roof) is less constrained than in passenger cars. Therefore, buses can use high-pressure storage tanks at 350 bar. Fuel cell passenger cars currently have a range of around 500 km. With the current vehicle technology, this requires around 4 to 6 kg of hydrogen, depending on the vehicle, driving style and driving conditions. A passenger car needs a tank capacity of around 100 to 150 litres to store 4 to 6 kg of hydrogen at 700 bar. The petrol tanks on modern compact and mid-size cars have a capacity of 50 to 60 litres, while executive cars and light commercial vehicles carry 70 to 80 litres of fuel. In addition to the volume and weight of the fuel, the weight of the tank system is relevant, since heavy tank systems increase rolling, grade and acceleration resistance and hence the fuel and energy consumption of a vehicle. Vehicle tanks for liquid fuels have a very favourable ratio of transported energy content to overall mass of tank system plus content. Similar to batteries in a hybrid gasoline vehicle, fuel cell vehicles also need a (smaller) traction battery. Depending on the drivetrain configuration, the battery adds additional weight. Nevertheless, fuel cell vehicles achieve ranges comparable to those of internal combustion engine cars because of their higher drive efficiency. Finally, the gravimetric storage density of hydrogen tank systems is significantly higher than that of battery electric vehicles. Current battery technology achieves storage densities of 0.3 MJ/kg, and 1.116 MJ/kg is considered achievable in the medium to long term. As a consequence, battery electric vehicles have much shorter ranges and the vehicle weight is greater.

The most important advantages of hydrogen and fuel cells in road transport are the higher efficiency of the energy converter, zero-pollutant operation (in fuel cells) and functionality comparable to established IC engined vehicles. For automotive applications, low-temperature polymer electrolyte membrane fuel cells are now used almost exclusively. In the PEM fuel cell, hydrogen is converted with oxygen to water. The technology has a high degree of maturity and is characterised by a simple setup, fast response to load changes, good cold start properties and a high power density.

Fuel cells achieve their highest efficiency under low loads. At part load they can achieve efficiencies roughly twice those of heat engines. In addition, if the passenger compartment needs to be heated, vehicles with fuel cells can draw heat from the fuel cell stack's coolant circuit, thereby avoiding power losses for auxiliary air heaters of up to around 5 kW as compared with battery electric vehicles. However, as the PEM fuel cell operating temperature of 80 to 85°C cannot be exceeded significantly, additional electrical power for cooling the stack is needed. Moreover, operation in extremely hot regions represents a technical challenge. In addition to the fuel cell stack, a fuel cell vehicle also has a traction battery (usually lithium-ion or nickel-metal hydride rechargeable batteries). Electrical energy from the fuel cell or from regenerative operation of the powertrain (recuperation) can be temporarily stored in this battery. The traction battery also serves to cover short-term power peaks. The traction battery is operated at a much higher voltage than the current vehicle electrical system (12 V).

The electric powertrain of fuel cell electric vehicles, i.e. electric motors and power electronics, is no different from the drive for battery electric vehicles. If the fuel cell stacks feed electrical energy directly into the electric motor as and when required, this is described as a fuel cell-dominant system. If the fuel cell stack only supplies the traction battery, which in turn is the sole energy supply for the electric motor, this type of vehicle is referred to as a battery electric vehicle with range extender.

II. Results and discussions

At today's cost structures fuel cell passenger cars are not yet competitive. But in an ambitious climate scenario involving rapid technological advances and market development, automotive fuel cell technology would quickly become much more cost-effective. In addition, production costs for hydrogen (from renewables) could fall in the medium to long-term, and – with lower hydrogen infrastructure costs – it could be distributed more cheaply as a fuel. At the same time, internal combustion drive systems are becoming more expensive, and in urban and metropolitan areas they are often subject to local usage restrictions as a result of stricter air quality regulations. As a consequence, (locally) emission-free fuel cell electric vehicles powered by hydrogen are becoming increasingly attractive in comparison to cars with an internal combustion engine, and not on cost grounds alone. If the gap between the purchase costs of fuel cell cars and battery electric cars can be closed as production numbers increase, fuel cell cars can also offer an alternative to (locally) emission-free battery electric vehicles. That is because, with comparable ownership costs, fuel cell electric vehicles offer further advantages over battery electric vehicles, such as greater comfort, longer range and shorter charging times. By contrast, if battery electric vehicles are improved in terms of comfort, range or charging time, they will become more expensive and will lose any economic advantages they may have over fuel cell electric vehicles.

As of the beginning of 2017, there are 281 hydrogen refuelling stations and more than 4,000 hydrogen-powered vehicles worldwide. Hydrogen refuelling stations and fuel cell vehicle fleets are concentrated in

the USA, Western Europe and Asia/Japan. The infrastructure of hydrogen refuelling stations and the number of hydrogen-powered vehicle in the world has to grove very fast to achieve the climate action goal of limiting the global temperature rise to 2°C. Achieving the Paris Climate Accord target, the number of fuel cell vehicles in three key markets (USA, selected European passenger car markets and Japan) will increase to some 113 mln units by 2050. This is based on new FCEV registrations rising to 1 mln each in the EU and USA in 2030 and to around 10 mln in all the regions in question in 2050. Based on these FCEV fleet scenarios, a hydrogen consumption of around 10 mln t of hydrogen (per year) has been estimated for the 113 mln FCEVs in 2050. If efficient petrol cars are superseded by FCEVs, this will lead to savings – depending on the petrol vehicle type (hybrid or petrol only) – of 38 to 68 mln t of petrol and over 190 mln t of traffic-related CO_2 emissions in 2050 Shell (2017).

III. Conclusions

Liquid ammonia contains more hydrogen by volume than compressed hydrogen or liquid hydrogen. Ammonia could be stored on-board a motor vehicle where the elemental hydrogen and nitrogen are separated just before the hydrogen is fed into the fuel cell or internal combustion engines. Ammonia cracking reaction requires less energy cost compared to alternative hydrogen carriers. Renewable energy based hydrogen and ammonia production arises as one of the most sustainable solutions of today's critical energy, environmental and sustainability issues. Since solar and wind energy cannot be directly stored or continuously supplied, it is required to convert solar and wind energy to a storable type of energy. Ammonia is a significant candidate as a sustainable energy carrier. Hydrogen can be produced from electrolysis of water and nitrogen can be produced from air to form green ammonia using renewable energy like solar and wind energy. Oxygen which is released during the water electrolysis and air separation processes can be converted to ozone, which has high commercial value, using plasma energy. Green ammonia is the ideal energy currency because it can be efficiently manufactured from green electricity, easily transported to where it is needed, and then converted back into electricity Aydin and Un (2017).

References

Aydin, K., Un, C., Renewable Hydrogen Production from Ammonia for Automotive Industry, 8th International Conference on Hydrogen Production (ICH2P-2017), Brisbane, Australia, 29-31 July 2017.

De Valladares, M.R., Global Trends and Outlook for Hydrogen, (December 2017).

Japanese Member update, IEA HIA ExCo Meeting 77 in Oslo, Norway, 14-16 February 2017.

Shell, Hydrogen Study, Energy of the Future Sustainable Mobility through Fuel Cell and H_2, (2017).

Wireless High-Speed Continuous Sensing of Hydrogen Leak by a Quadrotor Drone

[1*]Kazuo Matsuura, [2]Masahiro Inoue, [2]Yuta Segawa, [3]Takaya Kimura
[1] Ehime University, Graduate School of Science and Engineering, 3 Bunkyo-cho, Matsuyama, Ehime, 790-8577, Japan
[2] Kyushu University, Faculty of Engineering, Department of Earth Resources Engineering, 744 Motooka, Nishi-ku, Fukuoka, Fukuoka, 819-0395, Japan
[3] Ehime University, Faculty of Engineering, Department of Mechanical Engineering, 3 Bunkyo-cho, Matsuyama, Ehime, 790-8577, Japan

* E-mail: matsuura.kazuo.mm@ehime-u.ac.jp

Abstract
Continuous hydrogen sensing by a quadrotor drone is presented. The present system consists of a drone, semiconductor-type hydrogen sensor, wireless microcontroller module, boot converter and batteries. After investigating the relationship between leak amount and the spatial distribution of hydrogen concentration in the absence of the drone, sensing experiments are conducted with the drone hung above the leak source. The rotational speeds of the blades are also varied. The results show that the present system can successfully detect leaked hydrogen in spite of the downwash of the quadrotor drone.

Keywords: hydrogen safety, hydrogen sensor, drone, wireless, continuous sensing

I. Introduction

The usage of hydrogen has been growing in our daily lives. Hydrogen leakage is anticipated in various occasions ranging from production to consumption. Because system degradation and human error are inevitable and also hydrogen can be easily ignited even by weak magnitude of static electricity, quick, flexible and reliable sensing techniques of leaked hydrogen are required. Broadly speaking, current methods of hydrogen sensing can be categorized into stationary measurement, portable probing and laser measurement. In the stationary measurement, because the location of a hydrogen sensor is fixed, some time is required until hydrogen reaches the location from the leak source. In the portable probing, measurement becomes difficult when human access is difficult. In the laser measurement such as Raman scattering method based on ultraviolet rays[a)], an optical system is not necessarily cheap. On the other hand, if we can develop a system such that an inexpensive hydrogen sensor is attached on a rapidly-flying vehicle and hydrogen is measured within an acceptable accuracy, we can realize a new quick, flexible and reliable method.

In this study, we present a new wireless high-speed continuous sensing system with a semiconductor-type hydrogen sensor installed on a quadrotor drone. Its system operation and ability to measure leaked hydrogen with and without rotor blade rotation are investigated.

II. Experimental Set-up and Procedure

II.A Drone with hydrogen sensor

A MQ-8 gas sensor of Zhengzhou Winsen Electronics Technology Co., Ltd.[b)] is used. This sensor is of semiconductor-type, and its detection range is around 0-1000 ppm. The input voltage is 5 V, and the output voltage is around 1-4 V for the range. The 5 V input is supplied from batteries through a boost converter. In order to send the signals of the output voltage to PC wirelessly in real-time, a wireless microcontroller module named TWELITE DIP[c)] of MONO WIRELESS Inc. is used. The input voltage of TWELITE DIP is 2.3-3.6 V. The range of voltage represented on PC is around 0-2 V.

As shown in Fig. 1, the wireless hydrogen sensor system is installed on a quadrotor drone RC Logger, RC EYE One Xtreme of CEI Conrad Electronic International (HK) Ltd[d)]. The total length of the drone is 225 mm, and the rotor diameter is 138 mm. The maximum loading weight excluding the main LiPo battery is 100 g. The total weight of the present sensor system is 38 g, so the drone can easily lift the system without losing maneuverability.

II.B Hydrogen leakge

100% hydrogen is relased from the leak source, which is a rectangular slot with the size of 1cm×1cm. Leak flow rates of 5 and 10 L/min are considered. The spatial distribution of hydrogen concentration above the leak source is confirmed also by Raman scattering measurement conducted separately.

II.C Experimental condition

Experimental conditions are summerized in Table 1. The appearance of the measurement with and without the drone is shown in Fig. 2. To gain an insight into the spatial distribution of leaked hydrogen, Case 1 is conducted. In Cases 2-6, the leak flow rate is set 5 L/min and the leak is continued for 10 sec. The location of the hydrogen sensor is about 50 cm above the leak source. The speed of blade rotation is varied in these cases by inclining the throttle lever of the transmitter. In particular, Case 2 is the case without rotation, and Case 3 is the state of stand-by with blade rotation.

III. Results and Discussion

Experimental results are summarized in Table. 1. In Case 1, hydrogen concentration is about 0.5% at the height of

20 cm above the leak source. Therefore, an atmosphere of hydrogen is successfully created by the present

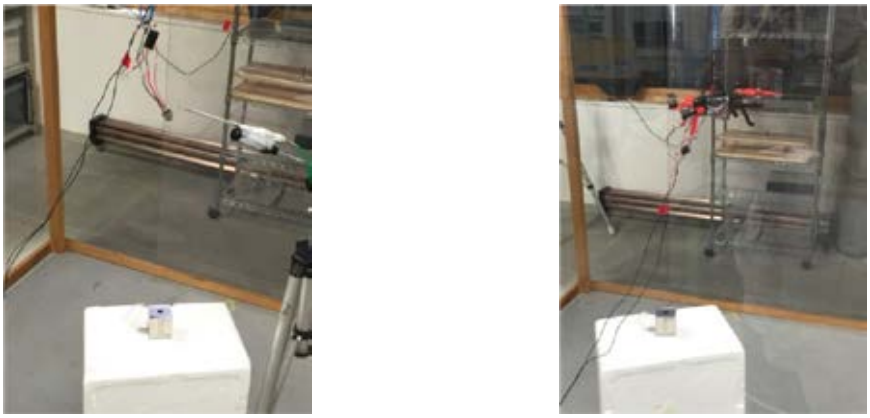
Tab.1: Experimental conditions for the hydrogen sensing

Case	H2 leak flow rates, duration	Blade rotation	H2 signal (Experimental results)
1	10L/min, 10 sec	No drone	H2 conc. is approx. 0.5% at the height of 20 cm above the leak source
2	5 L/min, 10 sec	No	Over Range of TWELITE DIP within zero point a few seconds since the leak start
3	ditto	Yes, Stand-by condition	The voltage rised up to 1600 mV
4	ditto	Yes, 25% Full Throttle(FT)	The voltage rised up to 1400 mV
5	ditto	Yes, 50% FT	The voltage rised up to 2000 mV
6	ditto	Yes, 100% FT	The voltage rised up to 2000 mV



(a) View from the top side (b) View from the bottom side

Fig. 1: Wireless hydrogen sensing system by a quadrotor drone



(a) Without the drone (b) With the drone

Fig. 2: Measurement of the spatial distribution of H2 with and without the drone

experimental system. In Cases 2-6, evident hydrogen signals are captured in spite of the downwash of the quadrotor. It is therefore confirmed that the present system can detect hydrogen leak successfully.

IV. Conclusions

By installing wireless hydrogen sensor system on a drone, high-speed-flying continuous hydrogen sensing system is developed. Sensing tests were conducted with and without blade rotation. It is confirmed that the present system works successfully, and also that the present system can detect leaked hydrogen in spite of the downwash from the quadrotor drone.

Acknowledgements

This study was supported by the Ministry of Education, Culture, Sports, Science and Technology (MEXT) through a Grant-in-Aid for Scientific Research (C), 15K04759, 2015. The hydrogen leak experiments were conducted at the laboratory of Prof. M. Inoue in Kyushu University.

References

Ninomiya H., Yaeshima, S., Ichikawa K., Fukuchi, T., Raman lidar system for hydrogen gas detection, Optical Engineering, 46(9), 094301, 1-5 (2007).
http://www.hwsensor.com
https://mono-wireless.com/jp/products/TWE-Lite-DIP/index.html.
https://www.droneart.com/

Analysis of the Turbocharged Internal Combustion Engine with Over-expanded Cycle Fueled with CNG and Hydrogen

Karol Grab Rogalinski, Stanislaw Szwaja

Department of Mechanical Engineering and Computer Science, Czestochowa, Poland

Nowadays one of the major challenges regarding internal combustion (IC) engine operation is to reduce exhaust toxic emission at higher engine loads. There are several technologies and methods as eg. exhaust gases after-treatment systems, applying alternative fuels and modifications to engine combustion systems by applying an over-expanded cycle system, that was under investigation and results are presented in this paper. It is especially important in high power stationary gas fueled engines working for heat and power generation (CHP). Hydrogen is crucial component in syngas and hythane (H2-CH4) is considered as a component which significantly reduces CO2, THC and CO in exhaust gases from the IC engine. However, on the other hand, hydrogen as secondary fuel blended primary gas is willing to generate engine knock, that might lead to damage the engine in short-term future. Knock combustion affects not only for engine reliability but also emissions, efficiency and performance, what can be observed in analysis of the combustion parameters. In this work results from investigation on knock intensity in the IC engine with the over-expanded cycle system and fueled with hydrogen rich gases is presented. The test engine used for investigation worked as a classical Otto cycle based engine and after modifications, it worked with over-expanded cycle system. In these both cases two fuels were used: CNG (Compressed Natural Gas) and hydrogen. Moreover, the engine was equipped with charging system to increase its performance as well as to compensate losses caused by use of the over-expanded cycle. The over-expanded cycle in this case was done through applying early intake valve closure before BDC (Bottom Dead Centre). The boost positive pressure was varied from 0 to 0.6 bar. On the basis of the performed tests parameters as follows: IMEP, COVIMEP, knock intensity and engine efficiency were obtained. The results confirmed that running the engine with over-expanded cycle makes it possible to reduce intensity of the knock from both these fuels by approximately 50% with increase in engine efficiency of nearly 1.5%.

Keywords: gas engine, hydrogen, over-expanded cycle, knock combustion

Comparison of LFS of H2, CH4 at Elevated Temperatures

***Karol Grab Rogalinski*, Stanislaw Szwaja, Michal Pyrc, Michal Gruca**

Department of Mechanical Engineering and Computer Science, Czestochowa University of Technology, Czestochowa, Poland

The paper presents results of case studies on laminar flame speed (LFS) of different gaseous fuels such as hydrogen, methane and mixture of hydrogen and methane in percentage share by volume 20%/80% (hydrogen/methane). LFS is one of the parameters which describes properties of flame propagation during combustion process. On the basis of the LFS analysis at various temperatures the conclusions of the behavior for the tested fuel can be stated, what in consequence can be used to explain phenomenon called combustion knock which might occur during combustion in the spark ignited reciprocating piston engine. The experiment was performed at temperature range from 25 to 100°C, as it is typical for fresh air-gas mixture in the intake manifold of both a naturally aspirated and a boosted engines. The test stand used for the experiment consists of the following: a one side open tube equipped with a spark plug which initiates combustion, a mixing system for feeding the tube with homogeneous air-fuel mixture and measuring system which allows to measure LFS of the flame along the tube. Modeling LFS was done with aid of Chemkin program. Results from both experiment and computer calculations were used to present LFS vs. temperature and tube length. As observed, hydrogen addition to methane dramatically shorten ignition delay, what contributes to faster flame development and increases LFS. These properties are used in methods for knock prediction in the piston engine fueled with hydrogen rich gases.

Keywords: laminar flame speed, hydrogen, knock prediction

Water Splitting Through the Pb/PbO cycle

[1]Atalay Calisan, [2]Celal Guvenc Ogulgonen, [3]Deniz Uner, [4*]Serkan Kincal
[1] Middle East Technical University, Department of Chemical Engineering, Universiteler Mahallesi Dumlupinar Bulvari No:1, Çankaya, Ankara, 06800, Turkey

* E-mail: skincal@metu.edu.tr

Abstract

This work reports the studies conducted on the feasibility of the Pb/PbO cycle for the splitting of H_2O for H_2 production. The reaction cycle ($Pb + H_2O \rightarrow PbO + H_2$ and $PbO \rightarrow Pb + O_2$) was first studied by flowing moist Ar gas over a small molten Pb surface, demonstrating the feasibility of reaction kinetics. Bench-scale experiments showed that conversions up to ~35% can be reached at 950 °C. The water splitting performance of Pb was also tested in pilot scale test system by doping Pb on mullite. High solar flux leads to vaporization of Pb resulting activity loss. Despite its relatively high vapor pressure and toxic nature, Pb was found as a good candidate for this cycle, owing to the thermodynamic feasibility of the Pb/PbO cycle and cost – compared to other possible metals.

Keywords: Water splitting, thermochemical, Pb/PbO_x couple

I. Introduction

The worldwide energy demand together with the environmental concerns has boosted the research on the utilization of renewable energy sources. Hydrogen as a critical energy carrier can be a solution for future energy demand and economy. Among the candidate process, two-step thermochemical process by using solar power is an emerging technology. In this process, a redox pair is cycled through two distinct steps such as thermal decomposition/reduction and oxidation. Metal oxides are heated to high temperatures to thermally desorb its oxygen so that vacancies are formed in the first step. The reduced metal oxides are oxidized under H_2O atmosphere so that one oxygen atom fills the formed vacancy. The overall process can be described by the following steps:

Thermal Decomposition/Reduction Step: $MeO_x \xrightarrow{h\nu} MeO_{x-1} + 1/2\ O_2$

Oxidation Step: $MeO_{x-1} + H_2O \rightarrow MeO_x + H_2$

The redox pairs for solar thermochemical processes are expected to have moderate or low operational temperatures, high thermal stability, and good cyclic performance and high overall efficiencies. Some examples for such materials such as 1700°C for ZnO (Schunk et al. 2008), 1500°C for SnO_2 (Abanades et al. 2008), 2000°C for CeO_2 (Chueh et al. 2010) and 1200°C for Fe_3O_4 (Roeb et al. 2009) were investigated during two-step solar thermochemical water splitting cycles. Operation of such materials requires high-temperature operation during thermal decomposition step. Therefore, mixed metal oxides such as spinel oxides (Kostoglou, Lorentzou, and Konstandopoulos 2014) and perovskites (Jiang et al. 2014) were investigated to increase oxygen evolution rate at lower temperatures and to improve structural stability. Nevertheless, the temperature needed for the O_2-releasing step is still higher than 1200 °C.

Lead, as a potential redox material, offers a wide range of oxidation state depending on the temperature and oxygen concentration. Buttler and Copp (1956) studied the intermediate crystal structures of lead oxides during the thermal decomposition of PbO_2 in the air. The change in oxidation state of lead follows the following decomposition pathway $PbO_2 \xrightarrow{150\,^\circ C} PbO_{1.98} \xrightarrow{200\,^\circ C} PbO_{1.965} \xrightarrow{270\,^\circ C} PbO_{1.952} \xrightarrow{293\,^\circ C} PbO_{1.74} \xrightarrow{343\,^\circ C} PbO_{1.568} \xrightarrow{384\,^\circ C} PbO_{1.34}$. Otto (1966) showed the similar decomposition steps as $PbO_2 \xrightarrow{270\,^\circ C} PbO_{1.56} \xrightarrow{345\,^\circ C} PbO_{1.44} \xrightarrow{367\,^\circ C} PbO_{1.33} \xrightarrow{570\,^\circ C} PbO$ The involvement of PbO_2 and PbO determines the x value in PbO_x such as $5PbO_2 \cdot 4PbO$, $4PbO_2 \cdot 5PbO$, and $3PbO_2 \cdot 6PbO$.

II. Experimental Set-up and Procedure

Water splitting experiments were conducted in two different lab-scale experimental setups. In the first part, the lead rod was put into 316-stainless steel boat. This boat was inserted into 25mm OD quartz reactor and supported by quartz wool from both sides. Prior to water splitting, the lead was heated to 950°C with a heating rate of 10°C/min under 100cm^3/min Ar flow for removal of any residual oxygen. Then, the reactor was cooled down to room temperature under same flow. Water was supplied to the reactor by passing the 100 cm^3/min Ar through the bubbler. The excess water at the reactor exists trapped in the condenser held at liquid nitrogen bath. The reactor was heated up to 800°C at a rate of 10°C/min. The product gas was analyzed by Teledyne XTC-2000 Hydrogen Transducer.

In the second part, 5.6cm ID, ~30cm tall reactor equipped with a thermocouple and a bubbler (~3mm ID SS tube) dipped into molten lead inside a homemade furnace. The reactor was loaded with ~2kg of lead (7.6 to 8.1cm height in the operating temperature range). Ar was used as carrier gas (200cm^3/min), a peristaltic pump was used to supply liquid H_2O which vaporized inside the reactor and reacted with Pb. Honeywell XCD sensor was used to track combustibles (H_2 in the case) after the reactor effluent was diluted by 500 cm^3/min air and passed through silica gel to remove excess water vapor. After Pb oxidation at various temperature levels between 600-950°C, the

bath was heated to 1000°C, and pure Ar was flown through – very little O_2 was measured – higher temperatures could not be explored due to material limitations and Pb evaporation.
Water splitting performance of lead was also tested in pilot scale solar reactor system. Prior o the experiment lead doped monolith was prepared by impregnating the lead acetate to the mullite monolith. Lead doped monolith was calcined at 500°C for 3 hours. After the calcination, it was calculated that approximately1.65gr Pb was doped on mullite. The pilot scale experiments were performed in the solar thermal reaction set up shown in Figure 1.



(a) 2x2 array of 70cm parabolic dishes mounted on a dual axis solar tracker with 4 reactors installed.
(b) Close-up of the reactor – face down
(c) Reactor mounted at focus – monolith inside, facing mirror

Fig. 1: Pictures of the solar-thermal reactor set-up - the solar tracker is installed at METU, Ankara campus

III. Thermodynamic Analysis

Thermodynamic evaluation of a two-step thermochemical water splitting process was carried out to find out the limits of the favorability of Pb oxidation by H_2O, temperature, pressure and the gas compositions. Based on the thermodynamic calculations, lead oxidation by utilization the oxygen of H_2O is possible at high H_2O and low H_2 partial pressures. The favorability increases as temperature increases since the potential area of PbO shifts to higher H_2 content. The temperature has a particular drawback due to a loss of oxidation steps such as Pb_3O_4 and Pb_2O_3.

Thermodynamic driving force towards thermal decomposition was shown in Fig. 2. Starting from the highest oxidation state, the decomposition of PbO_2 follows the reaction pathway of $12\mathrm{PbO_2} \rightleftharpoons \mathrm{Pb_{12}O_{19}} + 5/2\,\mathrm{O_2} \rightleftharpoons 6\mathrm{Pb_2O_3} + 1/2\,\mathrm{O_2} \rightleftharpoons \mathrm{Pb_{12}O_{17}} \rightleftharpoons \mathrm{Pb_{12}O_{17}} + 1/2\,\mathrm{O_2} \rightleftharpoons 4\mathrm{Pb_3O_4} + 1/2\,\mathrm{O_2} \rightleftharpoons 12\mathrm{PbO} + 2\mathrm{O_2} \rightleftharpoons 12\mathrm{Pb} + 6\mathrm{O_2}$. The oxide forms other than PbO can decompose at a relatively high oxygen environment. The decomposition reaction of $2\mathrm{PbO} \rightleftharpoons 2\mathrm{Pb} + \mathrm{O_2}$ needs high temperature and low O_2 content in the atmosphere.

Equilibrium calculations were conducted by Gibbs free energy minimization method. The equilibrium concentration of water splitting by lead and thermal decomposition of lead monoxide was calculated under the assumption of 1 mol Pb and 1 mol PbO was heated under 1 mol of water and 1 mol of Ar environment respectively. The equilibrium compositions during water splitting and thermal decomposition were given in Fig. 3. Lead oxidation by water starts at 200 °C. The rate of hydrogen production increases as a function temperature. Overall hydrogen production reaches to 0.0004 mol (conversion 0.0004%) which is relatively low. Higher oxidation states of Pb are not observed since these oxides (Pb_3O_4, PbO_2, etc.) are stable at high temperature and low oxygen environment. During the regeneration step of lead, PbO starts to decompose by following $PbO \rightleftharpoons Pb + O_2$ reaction after the melting point of PbO which is around 900 °C.

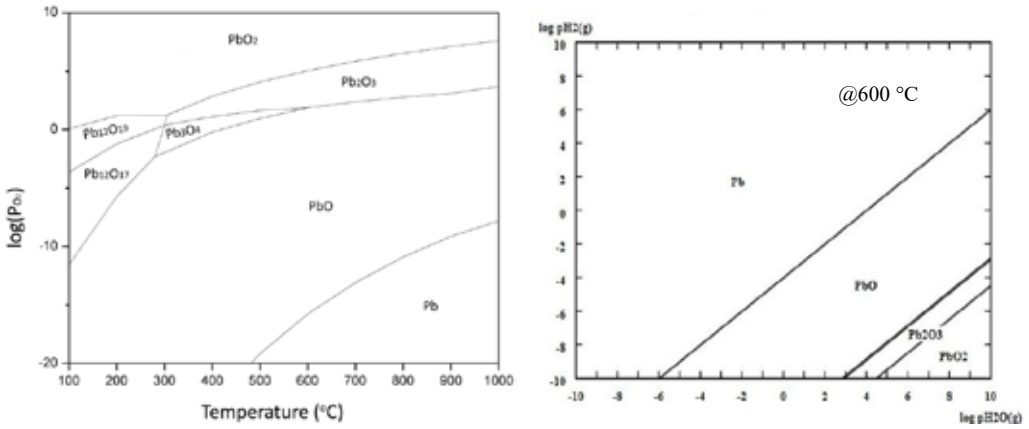


Fig.2: Predominance diagram of Pb-O system (left) and Pb-H-O system (right)

IV. Experimental Results and Discussions

Water splitting performance of molten lead media was tested in several different experimental setups as explained in the methods section. Lead can react with quartz and replace silicon atoms in glass at high temperatures. Therefore, a stainless steel reactor has to be used.

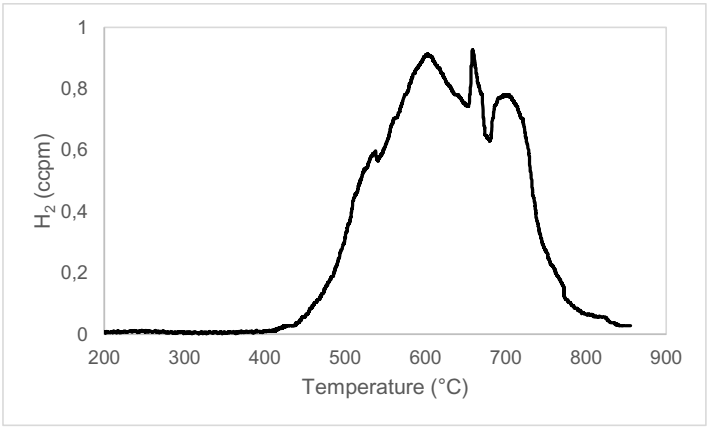


Fig. 3: Hydrogen production profile during TPWS

Lead was placed into a small stainless steel boat and placed in the quartz reactor. Prior to the experiment, any oxide scale existed on the lead surface was removed by heating under inert Ar atmosphere. The oxygen-free surface was then heated under argon+H_2O mixture flow for water splitting experiment as shown in **Hata! Başvuru kaynağı bulunamadı.**. Water splitting by molten lead started after 400°C. The rate of hydrogen production increased with temperature. The hydrogen production rate reached to its maxima around 600°C. Thereafter, the water splitting reaction started to slow down. The fluctuations around 660°C was due to flow problems observed in the condenser. The overall hydrogen production was calculated as 0.12mmol H_2/g Pb.

In the second experimental part, the approximately 2kg lead was loaded into cylindrical stainless steel reactor. Argon+H_2O mixture was bubbled through the bottom of the reactor. The conversion was summarized in Table 1 with respect to the lower and upper 10% percentiles and the median as a function of temperature. Due to the excess amount of lead, the decline in hydrogen production rate seen in **Hata! Başvuru kaynağı bulunamadı.** was not observed in the large scale measurement reported in Table 1. The deviation in the conversion was probably due to the problems related to feeding efficiency of the water pump.

Water splitting performance of lead-doped monolith was also tested in the pilot-scale solar reactor setup. Lead doped monolith was heated under direct solar irradiation in the pilot-scale solar reactor. The Pb-monolith was thermally decomposed for removing oxygen in the first heat-up cycle. After the thermal decomposition, water splitting experiment was performed, but hydrogen could not be detected. Post experiment monolith photo (**Hata! Başvuru kaynağı bulunamadı.**) shows that due to control issues on solar irradiation, the temperature could not be regulated so that all Pb vaporized during the first thermal decomposition experiment.

Table 1 Conversion of hydrogen depending on the reaction temperature

Temperature (°C)	Conversion (mean)	Conversion (max)	Conversion (min)
600	2.29%	6.41%	0.95%
650	2.38%	6.40%	0.95%
700	4.61%	8.67%	0.99%
750	9.40%	13.48%	5.68%
800	13.97%	19.00%	8.82%
850	18.87%	24.81%	12.63%
900	29.29%	35.33%	23.97%
950	34.96%	35.71%	34.40%



Fig. 4: The picture of monolith after the experiment

V. Conclusions

The technical feasibility of Pb/PbO cycle on water splitting was demonstrated in a molten metal bath reactor. The attraction of oxygen to Pb was thermodynamically favorable at the studied temperature range. Water splitting on Pb needs high P_{H2O}/P_{H2} ratio. The oxidized lead can decompose at 900 °C under an inert environment. Experiments were conducted at several experimental setups under constant heating conditions. The maximum hydrogen yield was obtained as 34.96% at 950 °C. Despite the toxicity of lead, Pb/PbO cycle was found as a suitable candidate for thermochemical water splitting reaction.

Acknowledgements
Financial support from TUBITAK through 1003 program under the 213M006, from METU Research Coordination Center (BAP-08-11-DPT.2013K120500-2) are gratefully acknowledged. A.C. is grateful to TUBITAK for graduate scholarship through 2211 program.

References

Abanades S., Charvin P., Lemont F., Flamant G., Novel Two-Step SnO_2 /SnO Water-Splitting Cycle for Solar Thermochemical Production of Hydrogen, International Journal of Hydrogen Energy, 33, 6021-6030, (2008).

Butler G., Copp JL., The Thermal Decomposition of Lead Dioxide in Air, Journal of the Chemical Society, 725–735, (1956).

Chueh WC., Falter C., Abbott M., Scipio D., Furler P., Haile SM., Steinfeld A., High-Flux Solar Driven Thermochemical Dissociation of CO_2 and H_2O using Nonstoichiometric Ceria, Science, 330, 1797-1801, (2010).

Jiang Q., Tong J., Zhou G., Jiang Z., Li Z., Li C., Thermochemical CO2 Splitting Reaction with Supported $La_xA_{1-x}Fe_yB_{1-y}O_3$ (A = Sr, Ce, B = Co, Mn; $0 \leqslant X, Y \leqslant 1$) Perovskite Oxides, Solar Energy, 103, 425–437, (2014).

Kostoglou M., Lorentzou S., Konstandopoulos, AG., Improved Kinetic Model for Water Splitting Thermochemical Cycles Using Nickel Ferrite, International Journal of Hydrogen Energy, 39, 6317–6327, (2014)

Otto EM., Equilibrium Pressures of Oxygen over Oxides of Lead at Various Temperatures, Journal of The Electrochemical Society, 113, 525–527, (1966).

Roeb M., Neises M., Säck JP., Rietbrock P., Monnerie N., Dersch J., Schmitz M., Sattler C., Operational Strategy of a Two-Step Thermochemical Process for Solar Hydrogen Production, International Journal of Hydrogen Energy, 34, 4537–4545, (2009).

Schunk LO., Haeberling P., Wepf S., Wuillemin D., Meier A., Steinfeld A., A Receiver-Reactor for the Solar Thermal Dissociation of Zinc Oxide, Journal of Solar Energy Engineering, 130, 21006–21009, (2008)

A Low Cost, Continuous H2-CH4 Sensor Assembly

C. Güvenç Oğulgönen, Atalay Çalışan, Deniz Üner, *Serkan Kıncal
Middle East Technical University, Chemical Engineering Department, Ankara, 06800, Turkey

* E-mail: skincal@metu.edu.tr

Abstract
This work reports on a low cost sensor assembly that is capable of monitoring H2 and CH4 mixtures diluted in inert gases on a real time basis. The sensors are SnO based solid state technology, demonstrating different levels of sensitivity to H_2 and CH_4 as well as higher hydrocarbon gases. These sensors are built into a custom made sampling chamber, with a reduced volume so as to improve response times. This sequence of solid state sensors is complemented by an industrial grade flammable gas sensor that generates a separate reading for total combustible gases to be used as an additional confirmation. The technique is based on the theoretical response curves of the sensors with calibration sequences implemented to ensure accuracy of response curve parameters. The lowest detection limit for H_2 and CH_4 is on the order of a few 100ppm, and maximum levels in the 10000ppm range are possible. The confirmation sensor kicks in at around 4000ppm of total combustibles. The sample gas also needs some injection of dry air to ensure proper sensor functionality – the ratio of the sample gas to air can be tuned to ensure confirmation to the sensitivity range, in case the sample gas is too concentrated. Calibration and confirmation sequences are reported in detail.

Keywords: gas sensor, H_2 and CH_4

I. Introduction

A very significant cost item for studying reaction pathways for H_2 production from hydrocarbons, mainly but not limited to CH_4, is the capability to monitor the composition of the effluent gases to keep track of conversion and yield as a function of reaction conditions.

A widespread approach is gas-chromatography (GC) equipment installed with multiple sensors, does not provide the capability for real time analysis as the separation of the gas mixture takes in the order of tens of minutes – in addition to the cost on the order of a few $10K. Particularly when one desires the capability to take the equipment to the field in order to study pilot scale reactors, the costs climb even higher.

Another approach is to use field tested standalone sensors, widely implemented in the petroleum refining industry. Unfortunately, relatively low cost such sensors operate based on the combustion of the sample gas and cannot differentiate between the different species of the flammable components in the mixture. Modifying this approach a little further, one may implement a flammable gas sensor along with an IR sensor and perhaps a standalone thermal conductivity detector – providing for different sensitivity levels for the various gas components. However, the combined cost of such a system easily runs into the same level as a GC.

The approach detailed and demonstrated in this study takes this idea of using multiple sensors of varying sensitivity levels and implements it using solid-state (SnO) based detectors. 3 different such sensors, namely the MQ-4 (methane), MQ-6 (propane) and MQ-8 (hydrogen) models manufactured by Hanwei Electronics, China – the gas in parenthesis referring to the highest but not exclusive sensitivity.

The sensors were imbedded into a gas flow chamber constructed from a block of polyimide, the gas flow volume was minimized to ensure fast response. Sensors were supplied by a 5V signal from an independent power supply and the response was monitored by Arduino boards, digitizing the analog sensor response into a USB port on a control PC. The sensor assembly was placed on a portable frame that allowed for easy transportation for field measurements.

The whole sensor assembly along with the data acquisition hardware is below $100. The limitations and capabilities of the set-up are reported with extensive calibration experiments. Sensor signals are a strong function of total gas flowrate – as there is no internal temperature control capabilities integrated into the sensors. There is good repeatability for individual sensors but a large sensor to sensor variation. The sensing circuit can be modified by different load resistors to adjust the sensitivity range. The approach can potentially sense as many different gases as there are sensors.

II. Sensor Set-up Description

The specific sensors used in the sensor array is listed in Table 1. The total cost of the sensors are around $1300. The supporting infrastructure, that includes the hardware components to house the sensors and provide power as well as digitizing the signals to be tracked by a PC are pictured in Figure 1. The costs of this infrastructure is around $200, keeping the total cost slightly below $1500.

Tab. 1:List of sensors used and vendor information

Sensor	Vendor	Cost	Specifications
Sensepoint XCD(1)	Honeywell Analytics, ABD	$980	4000-40000ppm total combustibles
MQ-4(2)	Zhengzhou Winsen Electronics Technology Co. Ltd., China	$6	300-10000ppm CH_4
MQ-6(3)		$6	300-10000ppm C_2H_6
MQ-8(4)		$6	100-1000ppm H_2

(1) http://www.honeywellanalytics.com/en/products/Sensepoint-XCD
(2) http://www.winsen-sensor.com/products/semiconductor-gas-sensor/mq-4.html
(3) http://www.winsen-sensor.com/products/semiconductor-gas-sensor/mq-6.html
(4) http://www.winsen-sensor.com/products/semiconductor-gas-sensor/mq-8.html

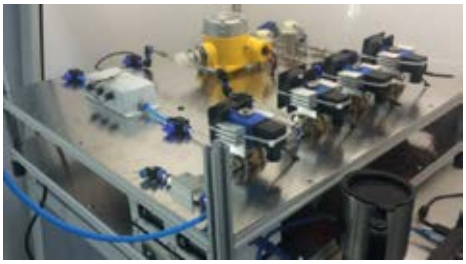


Fig. 1: The integrated sensor assembly

III. Theory and Basis of Operation

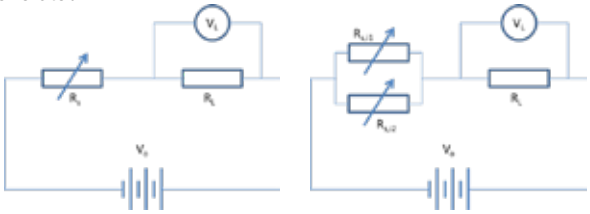
According to the specification sheets of the MQ-X series of sensors, their response to different gases is given by an exponential relationship best represented by

$$R_s = A \cdot ppm^B$$

Where Rs is the sensor resistance, ppm is the concentration in ppm and the coefficients of A and B take on a set of different values for each gas-sensor pair. The circuit schematic that is used to carry out measurements on a single gas is shown in Fig. 2(a). In this view, the sensors is simply a variable resistor so one can easily derive the VL vs concentration relationship based on the Ohm's law and re-arrange into a format that is convenient for performing calibrations to extract the sensor coefficients *A* and *B*:

$$ln\left(\frac{V_o + V_L}{V_L} R_L\right) = B \cdot ln(ppm) + ln(A)$$

a sequence of voltage measurements, V_L, are taken at known concentration levels followed by appropriate scaling to generate a linear relationship whose slope gives *B* and intercepts yields *A*. In this way the constants for each sensor-gas pair can be generated.



(a) Single gas (b) Mixture of gases

Fig. 2: Sensor electrical schematics

If these sensors are then subjected to multiple gases, they behave as parallel variable resistors as depicted in Fig. 2 (b). The individual sensor response to each gas can then be written in the form

$$R_{s,ij} = A_{ij} \cdot ppm_j^{B_{ij}}$$

Where the subscripts i denote the sensor and j denotes the gas, with ij referring to the gas-sensor pair for which the coefficients were derived from individual calibrations. The combined resistance of each sensor to a mixture of tow gases can be written as

$$\frac{1}{R_{s,i}} = \frac{V_o + V_{L,1}}{V_{L,1}} R_L = \frac{1}{A_{i1} \cdot ppm_1^{B_{i1}}} + \frac{1}{A_{i2} \cdot ppm_2^{B_{i2}}}$$

in which the left side is measured and all Aij, Bij values have been generated through calibrations. There are two unknowns here, ppm_1 and ppm_2, so an additional equation is needed. This equation is generated by the second sensor that has different levels of sensitivity to the gas pair being analyzed – resulting the in the following pair of coupled non-linear equations

$$\frac{1}{R_{s,1}} = \frac{V_o + V_{L,1}}{V_{L,1}} R_L = \frac{1}{A_{11} \cdot ppm_1^{B_{11}}} + \frac{1}{A_{12} \cdot ppm_2^{B_{12}}} \qquad \frac{1}{R_{s,2}} = \frac{V_o + V_{L,2}}{V_{L,2}} R_L = \frac{1}{A_{21} \cdot ppm_1^{B_{21}}} + \frac{1}{A_{22} \cdot ppm_2^{B_{22}}}$$

In principle, this approach can be extended into a mixture of n gases, provided that there are at least n sensors with varying sensitivity levels to the different gas species, in order to generate the required relationships.

III. Calibration Results and Discussions

The calibration results for H_2 and CH_4, separately diluted in Ar, are shown in Fig. 3 below. The resulting fits to the expected exponential sensor behavior are confirmed with all correlation coefficients on the order of 0.99. The load resistance for these tests were 9600 ohm for both sensors and a supply voltage of 5V is used.

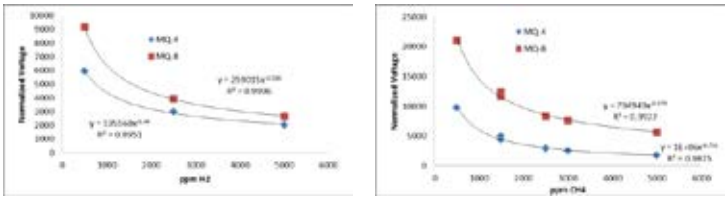


Fig. 3: Calibration Curves for H_2 (left) and CH_4 (right) diluted in Ar

The calibrated sensors are then subjected to the known binary mixtures listed in Table 2 for confirmation of the assumed independent reaction of individual gases in a gas mixture.

Table 2: Tests with known binary mixtures of H_2 and CH_4

CH_4 (ppm)	H_2 (ppm)	MQ-8 (V)	MQ-4 (V)
2500	2500	4.23	3.87
2000	3000	4.25	3.87
500	4500	4.06	3.77
4500	500	4.31	3.71

These measured responses are compared to the predicted voltage based on the theory outlined in the previous section in Fig. 4 – where the correlation between the measured and predicted values is quite reasonable. The actual concentrations are predicted within a 10% error margin.

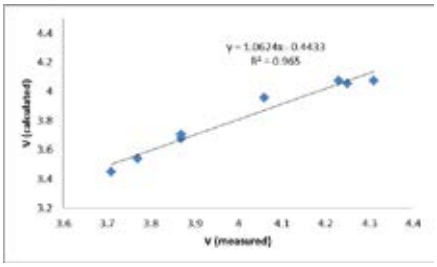


Fig. 4: Correlation of measured and predicted values for the binary gas mixtures

IV. Conclusions

The simple and cost effective sensor array assembly has been proven to be able to predict binary gas mixture compositions to within 10%. This is a very powerful finding, particularly for applications where real time monitoring of gas compositions is required. Real time monitoring requirements are particularly important for monitoring reactions under solar irradiation where reaction conditions are subject to fluctuations on the order of seconds for which more established methods that depend on separation of the species, such as GC, is simply not capable of delivering a signal. Furthermore, the small footprint allows one to be able to set-up measurements in the field, where it is difficult to transport and set-up bulky equipment. The set-up however is sensitive to total gas flow as well as gas temperature since no active temperature control is provided for the sensor housing. This shortcoming is addressed through performing multiple calibrations for different total gas temperature and flow conditions. Furthermore, the sensors are also sensitive to moisture content and hence the gas mixture to be analyzed needs to be free of water – easily achievable by passing the gas through a desiccant at the inlet.

Acknowledgements

Financial support was provided by TUBITAK through the 1003 program under project 213M006.

Performance of Ni Incorporated Silica and Alumina Based Catalysts in Hydrogen Production from Biomass

***Birce Pekmezci Karaman*[1], Nurbanu Çakıryılmaz[1], Hüseyin Arbağ[1], Nuray Oktar[1], Gülşen Doğu[1], Timur Doğu[2]**

[1]Department of Chemical Engineering, Gazi University, Ankara, Turkey
[2]Department of Chemical Engineering, Middle East Technical University, Ankara, Turkey

One of the most promising alternative fuel is hydrogen because of its high energy content and reduced greenhouse gas emissions as compared to fossil fuels. Biomass-based hydrogen production is recognized as promising resources for hydrogen production. In this study, steam reforming of acetic acid, as a model compound of biomass source, was performed over silica and alumina based mesoporous materials. Silicate structured mesoporous SBA-15 was synthesized following a hydrothermal procedure and mesoporous alumina (MA) catalyst was prepared by using EISA method. Nickel was incorporated into the structure of catalysts by impregnation method. The physical and structural properties of these catalysts were investigated by characterization methods such as X-ray diffraction (XRD), N2 adsorption-desorption, Transmission electron microscopy (TEM) and thermal analysis (TGA-DTA) techniques. Multipoint BET surface area values of SBA-15 and mesoporous alumina were 652 and 229 m^2/g, respectively. TEM images of the 5Ni@SBA-15 catalyst are consistent with the nitrogen adsorption/desorption analysis and proved the presence of ordered cylindrical mesopores. XRD pattern of silica and alumina based catalysts showed that Ni particles were rather well dispersed on catalysts structure. The performances of the SBA-15 and MA supported Ni based catalysts were highly stable and highly active in steam reforming of acetic acid. Both 5Ni@MA and 5Ni@SBA-15 catalysts showed complete acetic acid conversion with a similar hydrogen selectivity (% 58) values. However, TGA result of the spent catalysts showed that coke deposition over the 5Ni@MA catalyst (% 46) was higher than the 5Ni@SBA-15 catalyst (% 8).

Acknowledgements: Financial support of Gazi University Researcher Fund (BAP 06/2015-05 BAP-06/2016-08) TUBITAK 214M578 are gratefully acknowledged.

Keywords: Hydrogen, Acetic acid, Steam reforming, SBA-15, Alumina, Nickel

Gasification of Sewage Sludge Enriched with Virginia Mallow for Higher Hydrogen Content in Syngas

***Anna Poskart*[1], *Monika Zajemska*[2], *Stanisław Szwaja*[1]**

[1]*Faculty Of Mechanical Engineering And Computer Science, Czestochowa University of Technology, Czestochowa, Poland*
[2]*Faculty of Production Engineering and Materials Technology, Czestochowa University of Technology, Czestochowa, Poland*

The article presents results from investigation of gasification of sewage sludge enriched with biomass from Virginia Mallow in order to obtain a hydrogen-rich syngas. In the analysis, the content of hydrogen in the syngas produced during gasification of dried sewage sludge and Virginia Mallow in a mass ratio of 50/50% was determined. Sewage sludge contains about 50% organic compounds, however, it is a substance difficult to further energy utilization. The dried sludge can be subjected to thermal processing of gasification at temperature above 800°C. However, there are some difficulties in obtaining this temperature due to high content of mineral substances transforming into large amounts of ash during gasification. Thus, it has been proposed a solution based on mixing a high energy component with the sewage sludge in order to improve the gasification parameters. Due to the restrictions on the use of fossil fuels, it was decided to apply for this purpose a dried Virginia Mallow, which is considered as an energy plant with fast and high annual weight gain. The analysis was carried out as an experiment and also as modeling using the Chemkin program. The analysis was based on a 0-dimensional simulation model. A detailed chemical mechanism developed by the CRECK Modeling Group, "Biomass mechanism", has been implemented for the calculations. The mechanism is dedicated to the chemical analysis of processes occurring during thermal biomass conversion. The calculations were carried out for a gasification temperature of 850°C. Obtained results showed that hydrogen content in syngas can increase up to approximately 12%. Furthermore, calculations performed for the case of gasification of the sewage sludge without biomass enrichment showed a three times smaller content of hydrogen than in syngas produced from gasification of sewage sludge with Virginia Mallow.

Keywords: syngas, hydrogen, gasification, Virginia Mallow, sewage sludge, modeling

Optimization of Hydrogen Release from Anaerobic Thermal Processing of Virginia Mallow

***Anna Poskart*[1], Monika Zajemska[2], Stanisław Szwaja[1], Aneta Magdziarz[3], Dorota Musiał[2]**

[1]*Faculty Of Mechanical Engineering And Computer Science, Czestochowa University of Technology, Czestochowa, Poland*

[2]*Faculty of Production Engineering and Materials Technology, Czestochowa University of Technology, Czestochowa, Poland*

[3]*Faculty of Metals Engineering and Industrial Computer Science, AGH University of Science and Technology in Krakow, Krakow, Poland*

This article presents investigation of the temperature and residence time influence on hydrogen content in processing gas (torgas, pyrolysis gas and syngas) obtained from the thermal processing of Virginia Mallow heated from ambient temperature to 800°C with temperature rise rate of approximately 40°C/min along the tube length of 1 m. The thermogravimetric tests were carried out in order to determine parameters of torrefaction and pyrolysis processes. As part of the TGA analysis, the weight loss over time was determined. Based on the designated data, computer simulations were carried out using the CHEMKIN-PRO computer software. A detailed chemical mechanism including 137 compounds and 4533 chemical reactions was implemented for the calculations. The hydrogen content in the torgas was analyzed for a variable temperature range between 200÷325°C and residence time from 1 to 60 minutes. Hydrogen content in the pyrolysis gas was analyzed for a temperature profile up to 800°C and a residence time of up to 60 minutes. Results from simulations have shown that the content of hydrogen increased with increasing either residence time in the reactor or the torrefaction temperature. The highest value equaled 0.6% was recorded for a residence time of approx. 19 minutes and a temperature of 250°C. The further increase in temperature and extension of residence time of the sample in the reactor leads to a decrease in the hydrogen content in torgas below 0.1%. This is because significant hydrogen amounts were released during torrefaction in which hydrogen appeared in PAH compounds.

Keywords: hydrogen, thermal processing, Virginia Mallow, torrefaction, pyrolysis, TGA analysis

Improvement of Operational Characteristics of Sesame Oil in a Compression Ignition Engine with Small Fraction Of Hydrogen Enrichment

Tayfun Özgür, Şafak Yildizhan, Ceyla Özgür, Kadir Aydın, Hasan Serin

Department of Automotive Engineering, Çukurova University, Adana, Turkey

Methods of the improvement of performance and emission characteristics of the internal combustion engines such as biodiesel and hydrogen (H2) usage particularly for compression ignition engines are widely investigated by many researchers all over the world with the awareness of depletion of fossil sources and environmental issues. Also, to eliminate the drawbacks of biodiesel usage such as lower performance and higher carbon dioxide (CO2) and oxides of nitrogen (NOx) is one of the most important popular studies recently. Hydrogen enrichment to biodiesel is a promising alternative method since H2 molecules do not contain carbon atoms. Also the high energy content of H2 (120 Mj/kg) makes it a signifant candidate for the enriching the bio-based renewable fuels. This study explores the effect of small fraction of H2 (5 litre per minute) enrichment to sesame oil biodiesel (SOB) on the performance and emission characteristics of an unmodified compression ignition engine. In the study, fatty acid composition of sesame oil was determined by using gas chromatography (GC) prior to convert it to biodiesel by two stage transesterification. GC measurement results showed that sesame oil has Palmitic acid (C16:0), Stearic acid (C18:0), Oleic acid (C18:1), Linoleic acid (C18:2), Linolenic acid (C18:3), Eicosenoic acid (C20:1), 12.54, 6.09, 44.10, 35.11, 1.02, 1.14 by wt%, in its composition, respectively. The most significant property of SOB was its pour point and measured as -15 oC. Also, calorific value of SOB was 9.71% lower than conventional diesel fuel. The engine experiments showed that operating engine with SOB (100%) increased brake specific fuel consumption (BSFC), CO2 and NOx emissions. But enriching the SOB with H2 gas improved BSFC up to 8.34% while decreasing CO2 emissions up to 16.29%.

Keywords: Hydrogen, Biodiesel, Sesame, Compression ignition engine

Dilution of fresh charge for reducing combustion knock in the internal combustion engine fuelled with hydrogen rich gases

[1*]Stanislaw Szwaja
[1] Czestochowa University of Technology, Faculty of Mechanical Engineering and Computer Science, Dabrowskiego 69, Czestochowa, 42-201, Poland

* E-mail: szwaja@imc.pcz.czest.pl

Abstract
Although, trend for pure hydrogen use as the only fuel for internal combustion (IC) engines in vehicles is decreasing, but hydrogen is commonly burnt in high power stationary engines for heat and power generation. Hydrogen can appear either as a single gas or as a component in processing gases eg. syngas, hythane and coke gas. Hence, problems concerning effective hydrogen combustion in the IC engines is still current. The most crucial is problem with so-called hydrogen combustion knock, which is harmful to the engine. Paper presents results from experimental investigation focused on dilution of air-fuel mixture for reducing the combustion knock. Dilution can be realized by both exhaust gas recirculation (EGR) and making the combustible mixture lean. It is known that both lean mixtures and EGR can be successfully applied not only for reducing NOx content in exhaust gases but also for reduction of combustion knock in SI engines. From this point of view, both these techniques can be also effective for knock elimination in the internal combustion engine fueled with hydrogen rich gases. Results from this investigation show that applying EGR is more effective than making combustible air-gas mixture lean. Comparison between EGR and lean mixture impact on knock intensity was possible after recalculating these parameters from mass percentage to molar percentage of diluent. Then, it was found that EGR is approximately twice more effective in knock reduction than lean mixtures.

Keywords: hydrogen, combustion, engine, EGR, lean mixture

I. Introduction

Combustion knock occurring in the internal combustion (IC) spark ignited (SI) engine is a phenomenon, which is sensitive to several quantities. They can influence on knock intensity at various impacts. They can be distinguished as follows:

- Temperature of preignition gases – it has significant impact on an induction time (preignition reactions) and strongly impacts on combustion knock as stated by d'Adamo etal. (2017), and Jamrozik and Tutak (2010). Compression ratio is the most crucial parameter influencing on the preignition temperature as observed by Szwaja and Naber (2013).
- O-H ratio, which, among others, depends on either exhaust gas recirculation (EGR) or lambda – relative equivalence ratio – from investigation by Merola etal. (2007).
- Oxygen dilution in the intake charge – provided by EGR.
- Presence of hot spots and exhaust residuals – they can work as extra sources for uncontrolled air-fuel self-ignition.
- Engine load – higher engine load requires higher amounts of fuel, hence, energy releasing during combustion also influences knock intensity - by Merola etal. (2009).

In practice, knock can be reduced by either applying exhaust gases recirculation (EGR) or fueling the engine with lean air-fuel mixture. In these both measures additional agent is present in the combustible mixture: exhaust gases from EGR or extra air in lean mixtures. Hence, these agents can be considered as diluents, which contribute to knock reduction as stated among others, by Nande etal. (2008) for EGR gases and by Szwaja and Naber (2008) for air-gas lean mixtures.

As mentioned, impact of EGR and lean mixture on knock is known, but there is no knowledge in the available literature on their effectiveness in comparison to each other. Hence, there is no information presenting which measure is more effective for knock reduction. This paper presents results from engine tests focused on knock reduction by applying both EGR and lean mixtures. The fuel used for tests is coke gas and hydrogen. Numerous works on applying hydrogen rich gases as fuel to the SI engine was conducted by Szwaja (2017). Investigation presented in this paper concerns impact of these both measures on reducing combustion knock intensity in the spark ignited (SI) reciprocating engine fueled with hydrogen rich gases. Investigation involves hydrogen and coke gas as fuels to the internal combustion (IC) engine. Coke gas is a by-product from gasification of pit coal associated with water-gas reforming process. In general, it consists of 50-70% hydrogen, hence, it is high-value fuel for effective power generation.

II. Experimental Set-up and Procedure

Fundamental tests were conducted on the research engine and then the results were used for verification and calibration of a model of high power output gas fuelled engine. The engine used for this research is the 1HC102 single cylinder 4 -stroke, water cooled, spark ignition engine. The engine was chosen for its versatility and robustness of construction which is important because of the intended study of combustion knock. Characteristics of the test bed and engine are shown in Figure 1. A dynamometer applied was a 3x400V, 20 kVA synchronous

generator. Both oxygen concentrations are measured by wide-band (UEGO) electrochemical lambda sensors (Figure 1). In – cylinder pressure measured with Kistler 6055, intake pressure - MPX 4250, fresh charge temperature - DS 18B20, crank angle - encoder with resolution 1024 pulses/rev, respectively. Both air and gaseous fuel consumption by the engine were measured by rotor flow meters. Oxygen content in the exhaust and further lambda ratio was measured with the wide-band oxygen sensor NGK/NTK with the controller UEGO TC 6300A.

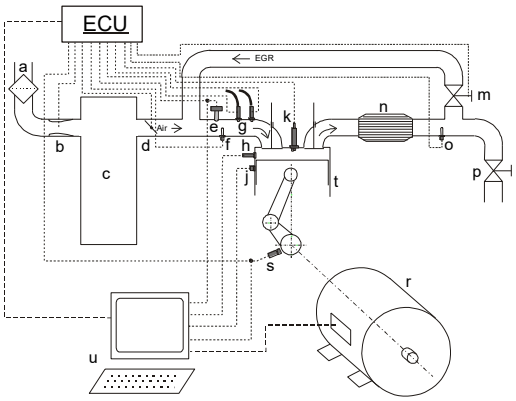


Fig. 1: Diagram of the CFR engine test bed, a – dust filter, b – MAF, c – surge tank, d – throttle, e – MAP, f, o – UEGO sensors, g – gasoline and hydrogen injectors, h – pressure transducer, j – accelerometer, k – ignition system, m – EGR valve, n – catalytic converter, p – gate valve, r – dynamometer, s – crank angle encoder, u – workstation, ECU – electronic control unit

Engine specifications are as follows: bore = 102 mm, stroke = 120 mm, swept volume = 980 cm3.

Sensors monitored required for further analysis the following: flowrates, pressure and temperatures. Sensors included MAF, manifold pressure (MAP), UEGO, and crank position sensor. Electronic actuators included a digital ignition coil, throttle, EGR valve, and port fuel injectors for gaseous fuels.

Data from the in-cylinder pressure and engine mounted piezoelectric accelerometer along with an engine position sensor were acquired with the analog to digital converter. All voltage signals from sensors were collected on a PC computer with aid of the LabVIEW software and the data acquisition system NI USB 6251. Data for 300 engine cycles at 100 kSamples/second-channel was acquired.

Investigation was focused on finding impact of dilution effect caused by either EGR or leaning on knock intensity in the hydrogen rich gas fuelled engine.

The tests were realized at the following parameters:

- Fuel: coke gas (65% hydrogen, 35% methane) and hydrogen with purity of 99.99%,
- EGR varied from 0 to 30%,
- Lambda - relative equivalence ratio for the in-cylinder mixture varied from 1.0 to 1.5,
- Spark timing fixed at 5 CA deg before top-dead-centre (BTDC),
- Compression ratio (CR) of 9.7:1,
- Engine speed 1500 rpm.

III. Methodology

Combustion knock intensity is expressed by filtered pressure pulsations from the in-cylinder combustion pressure. Pressure pulsations from each combustion event were obtained from high-pass filtering using Butterworth filter of 4 order with cut-off frequency of 3.5 kHz. The knock intensity for the single combustion event is defined as maximal amplitude (PP - Peak Pressure) in the pressure pulsations and denoted as PP_{ind} (Figure 2). Next, knock intensity is calculated for the entire combustion test series consisted of 300 combustion events. The averaged knock intensity is denoted as PP_{av}. This methodology was successively used by Naber etal. (2007).

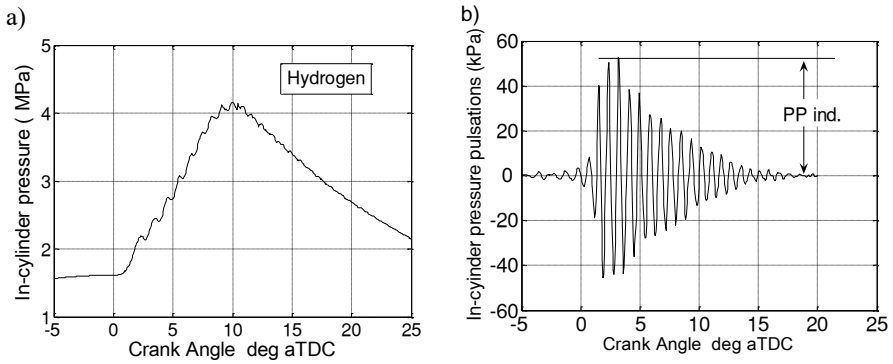


Fig. 2: In-cylinder pressure history from hydrogen fuelled engine (lambda=1, ST=0 deg) (a), pressure pulsations filtered from the in-cylinder pressure (b)

Among others there are works (Nande etal. 2008, Szwaja and Naber, 2008) showing that knock intensity expressed by PP_{av} is in negative correlation with both EGR percentage and relative equivalence ratio – lambda.

As mentioned, the main target of this research was to answer which measure (EGR or lean mixture) for air-fuel mixture dilution with respect to reducing combustion knock is more effective. To solve this problem, the dilution ratio χ was introduced follow the equation (1). This dilution ratio makes it possible to compare knock reduction by EGR with knock reduction by lean mixture.

$$\chi = \frac{n_{st}}{n_{st} + n_{dil}} \cdot 100\% \quad (1)$$

Where, n_{st} – number of moles (including fuel and oxidizer) of the stoichiometric air-gas mixture; n_{dil} – number of moles of additional gas working as a diluent; χ - dilution ratio in percentage.

This dilution ratio χ equals 100% for stoichiometric mixture, in which there is no dilution agents (n_{dil}=0). In case the diluent is air, then dilution ratio defined with the equation 1 depends on relative air-fuel equivalence ratio - lambda. Hence, following the equation (1) a lean combustible mixture can be treated as the stoichiometric mixture diluted in extra amounts of air. If EGR is applied for diluting the combustible mixture, then the dilution ratio χ is a function of the EGR ratio.

For example, dilution ratio for the lean air-hydrogen mixture which is treated as stoichiometric mixture diluted in additional air can be expressed with the equation (2). As seen, the dilution ratio is strictly associated with the lambda.

$$\chi_{\lambda} = \frac{6{,}78}{2 + 4{,}78 \cdot \lambda} \cdot 100\% \quad (2)$$

In case of applying the EGR as diluent, then the dilution ratio can be expressed as follows (3):

$$\chi_{EGR} = \frac{n_{st}}{n_{st} + n_{EGR}} \cdot 100\% \quad (3)$$

Where, n_{EGR} – number of moles of exhaust gases recirculating to the engine intake port.

Number of moles n_i of each gas can be easily calculated from the equation (4):

$$n_i = \frac{m_i}{MW_i} \quad (4)$$

Where, m_i – mass of the i agent; MW_i – molar weight of the i agent.

Finally, correlations between knock intensity PP_{av} vs. dilution ratio χ for both EGR and lean mixtures were worked out.

IV. Results and discussions

As shown in Figure 3, knock intensity decreases with decrease in dilution ratio for both the fuels under investigation: hydrogen and coke gas. Worth of noticing is the knock intensity is more sensitive to applying EGR as diluent rather than to making the combustible mixture lean. For example, for hydrogen only fuel knock intensity at the same dilution ratio is approximately twice lower for EGR in comparison to lean mixture at the same dilution. Moreover, as observed,

this correlation between knock intensity and dilution ratio is almost linear.

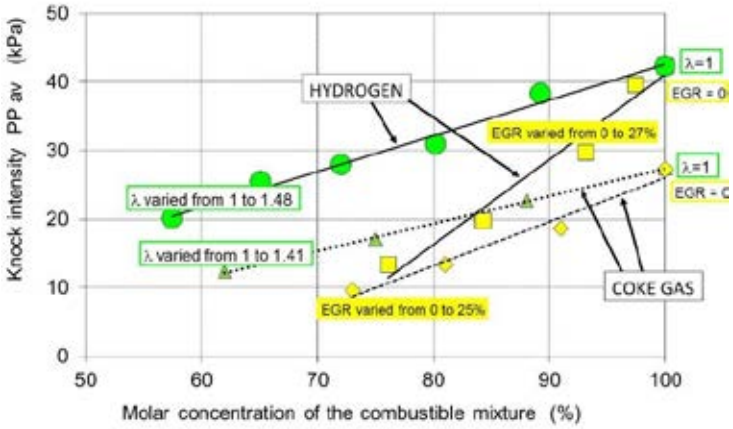


Fig. 3: Knock intensity vs. molar concentration of the combustible mixture

V. Conclusions

The maximal peak in high frequency in-cylinder pressure pulsations were used to evaluate engine knock intensity. As concluded, engine combustion knock can be reduced more effectively by applying EGR rather than applying lean mixture. This EGR impact on knock is approximately twice stronger if compared to lean mixture. The correlation between dilution ratio and knock intensity is almost linear. Hydrogen in comparison to coke gas is more willing to generate knock. It is caused by methane in coke gas, which strongly slows down overall reaction rate for combustion of hydrogen-methane mixture.

Acknowledgements

This project has received funding from the European Union's Horizon 2020 research and innovation programme under grant agreement No 691232 — Knocky — H2020-MSCA-RISE-2015/H2020-MSCA-RISE-2015.

References

d'Adamo, A., Breda S., Fontanesi S., Irimescu A., Merola S.S., Tornatore C., A RANS knock model to predict the statistical occurrence of engine knock, Applied Energy, 191, 251-263 (2017).

Jamrozik A., Tutak W., Modelling of combustion process in the gas test engine, IEEE, Proceedings of VIth International Conference of Perspective Technologies and Methods in MEMS Design (MEMSTECH), 14-17 (2010).

Merola S.S., Vaglieco B.M., Knock investigation by flame and radical species detection in spark ignition engine for different fuels, Energy Conversion and Management, 48(11), 2897-2910 (2007).

Merola S.S., Sementam P., Tornatore C., Vaglieco B.M., Knocking diagnostics in the combustion chamber of boosted port fuel injection spark ignition optical engine, International journal of vehicle design, 49(1-3), 70-90 (2009).

Nande A., Szwaja S., Naber J.D., Impact of EGR on Combustion Processes in a Hydrogen Fuelled SI Engine, SAE Paper No. 2008-01-1039, (2008).

Naber J.D., Blough J.R., Frankowski D., Goble M., Szpytman J.E., Analysis of Combustion Knock Metrics in Spark-Ignition Engines, SAE Transactions Journal of Engines, 115, 223-243 (2007).

Szwaja S., Naber J.D., Dual nature of hydrogen combustion knock, Int J of Hydrogen Energy, 38, 12489-12496 (2013).

Szwaja S., Szwaja M., Conversion of Exhaust Gases from the Internal Combustion Engine to Electrical Power at Small Scale - Waste Heat Recovery Concept, Conference Proceedings by IEEE, International Conference on Green Energy and Applications ICGEA 2017, IEEE Xplore, DOI: 10.1109/ICGEA.2017.7924646, (2017).

Szwaja S., Naber J.D., Impact of leaning hydrogen-air mixtures on engine combustion knock, Journal of Kones - Powertrain and Transport,15, 483-492 (2008).

Influence of hydrogen co-combustion with diesel fuel on performance, smoke and combustion phases in the compression ignition engine

[1]*Romualdas Juknelevičius, [2]Stanislaw Szwaja, [2]Michal Pyrc, [2]Michal Gruca
[1] Vilnius Gediminas Technical University, Faculty of Transport Engineering, J. Basanaviciaus 28, LT-03224 Vilnius, Lithuania
[2] Czestochowa University of Technology, Czestochowa, Faculty of Mechanical Engineering and Computer Science, ul. Dabrowskiego 69, 42-201 Czestochowa, Poland

*E-mail: romualdas.juknelevicius@vgtu.lt

Abstract
Paper presents results from analysis of combustion progress in the internal combustion engine fueled with diesel fuel and hydrogen. Hydrogen was used in amounts up 40% by energy share. The main objective of this study was to examine impact of hydrogen on combustion phases and ignition delay in the diesel engine as well as smoke in the exhaust gases. Literature review shows in general hydrogen in those cases is used in small amounts below lower flammability limits. In this study, the test bench consisted of a single cylinder diesel fueled engine with common rail injection system. Hydrogen was injected into the intake manifold, where it created homogeneous mixture with air. Tests were performed at both fixed and optimal injection timings at full engine load. Results from experiments show that increasing amounts of hydrogen into the engine contribute to shorten ignition delay time that also affect main combustion phase. Complete analysis for heat release rate was presented in the paper. Moreover, decrease in smoke (mainly soot) in the exhaust gases was observed with increase of hydrogen amounts to the engine.

Keywords: Hydrogen, diesel fuel, IC engine, combustion, emission

I. Introduction

The road transport of the World contributes $5.4 \cdot 10^9$ t of CO_2 to the greenhouse effect, due to consumption of fossils fuel containing carbon. EU introduced CO_2 emission regulation of 95 g/km for cars and 820 g/kWh for trucks. Decrease of CO_2 emission could be achieved by use other fuels characterizing with higher H/C ratio (Grab-Rogalinski, 2017). The biodiesel can be considered as substitute of fossil fuels as recommended by Grab-Rogalinski et al. (2016). In combination with hydrogen, it has potential to positively contribute well-to-wheel and reduce the greenhouse effect. One of the possible measures is to use hydrogen as secondary fuel injected to the intake port in the diesel fueled compression ignition (CI) engine. Hydrogen addition below 5% shortens the ignition lag as described by Szwaja and Grab-Rogalinski (2009). They also found that hydrogen energy share (HES) of 5 – 15% does not change combustion duration, but with HES of 15% p_{max} increased. At HES higher than 17%, the mixture got stoichiometric leading to faster combustion and generating combustion knock. Research on the CI engine operated with 20% HES (Gomes Antunes et al. 2009) showed decrease in NO_x emissions by 20% at low loads, however, NO_x increased with increase of engine load. Investigation conducted by Rocha (2017) on biodiesel showed that increase of HES decreases brake specific fuel consumption (BSFC), CO_2, CO and HC, but the NO_X increases. The study by Barrios et al. (2017) on biodiesel with hydrogen addition to 25% in the CI engine with EGR revealed that PM (particle matter) decreased below 63% at engine specific working conditions. As reviewed, there are some gaps in knowledge dealing with hydrogen assisted combustion of various fuels in the CI engine. Results of studies presented in this paper present impact of hydrogen co-combusted with commercial diesel and pure RME (Rapeseed Methyl Ester) on both performance, combustion phases and toxic exhaust emissions from the CI engine. It was observed, that emissions and engine performance are dependent on the following: HES, injection parameters as timing and duration and equivalence ratio.

II. Experimental Set-up and Procedure

Tests were performed on a single cylinder, research CI engine S320, modified to work with dual fuel mode: liquid and gaseous fuels. It was equipped with a high pressure Bosch common rail fuel pump, driven by an electric motor (Fig. 1). Displacement of the engine – 1810 cm^3, compression ratio – 17. The engine was set to operate at the constant speed.

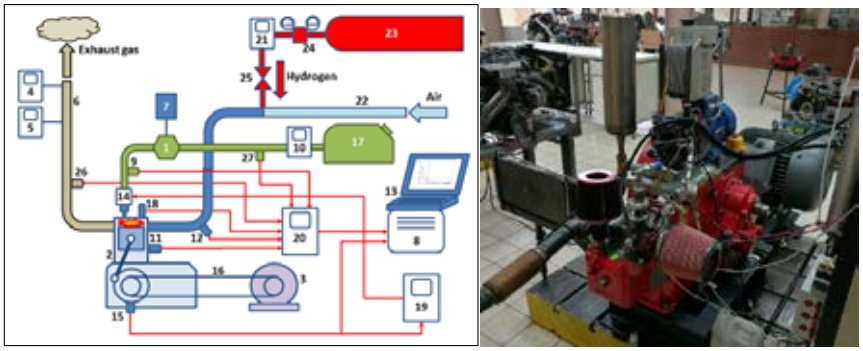


Fig. 1: Test bed. 1 – Diesel Fuel (DF) pump, 2 – CI engine, 3 – Generator, 4 – Smoke analyzer, 5 – Exhaust gas emission analyzer, 6 – Exhaust pipe, 7 – electric motor, 8 – Data acquisition system, 9 – DF pressure sensor, 10 – DF flow meter, 11 – Engine temp. sensor, 12 – Inlet air temp. sensor, 13 – PC with SAWIR software, 14 – DF common rail injector, 15 – Crank angle encoder, 16 – Drive belt, 17 – DF tank, 18 – In-cylinder pressure sensor, 19 – DF injection controller, 20 – Amplifiers & A/D converters, 21 – Hydrogen flow meter, 22 – Air intake pipe, 23 – Hydrogen high-pressure tank, 24 – Hydrogen one-stage pressure controller, 25 – Hydrogen firebreak arrestor, 26 – Exhaust gas temperature sensor, 27 - DF temperature sensor.

The tests were conducted as follows: at various loads (expressed by indicated mean effective pressure – IMEP), various HES, various liquid fuel injection timings and durations. Exhaust gases content was analyzed with aid of the Bosch and the Maha (smoke) analyzers. In-cylinder pressure (p) was measured by the piezo sensor Kistler 6061B. The crank angle (CA) was detected by the encoder Kistler type 2612C. The data acquisition system Measurement Computing Corporation PCI-DAS 6036 was used in line with PC software SAWIR (System of the Indicator Chart on Real Time Analysis). The software SAWIR was used to control and calculate IMEP and combustion phases online. Two types of liquid fuels were tested for this experimental study: Euro diesel fuel (DF) and pure Rapeseed Methyl Ester (RME) biodiesel. Lower Heating Value of DF is 42.5 MJ/kg, RME – 37.4, while H_2 – 120, respectively. The test parameters are shown at Tab.1.

Tab. 1. Injection timings and loads at various composition of combustible mixtures.

Test No.	Composition of combustible mixture	Injection timing φ, deg before the top dead center (BTDC)	Loads
1.	DF + H_2 0%	18°	Low Load
2.	DF + H_2 (16 – 43%)	16°	
3.	DF + H_2 0%	24°	Medium Load
4.	DF + H_2 (15 – 41%)	20°	
5.	DF + H_2 0%	30°	Nominal Load
6.	DF + H_2 (14 – 33%)	26°	
7.	RME + H_2 0%	16°	Low Load
8.	RME + H_2 (19 – 44%)	14°	
9.	RME + H_2 0%	22°	Medium Load
10.	RME + H_2 (16 – 42%)	20°	
11.	RME + H_2 0%	28°	Nominal Load
12.	RME + H_2 (16 – 36%)	26°	

III. Analysis and discussions

The main objective of the presented research, was to examine impact of HES on combustion properties and combustion duration in the CI engine working at the constant speed of 965 rpm and under fixed injection timing with IMEP of low (260 – 298 kPa), medium (380 – 508 kPa) and nominal (520 – 661 kPa) loads. As presence of hydrogen affects the combustion duration, start of diesel injection timing φ, during tests of hydrogen – diesel mixture was set at fixed position, enabling to compare and analyze several MFB profiles at various HES. Experiments revealed that the hydrogen – diesel mixture operation achieve the higher in-cylinder pressure than a conventional DF operation, with HES higher than 20%. BSFC decreases with increase of HES. RME at medium and nominal loads has the highest decrease of BSFC by 23.3% in compare to 19.8% of DF (Fig. 2b). Hydrogen due to high flame speed and short quenching distance extends the flammability range of RME – hydrogen mixture, ensure RME combusted completely under especially higher load conditions which provides reduced BSFC (Baltacioglu 2016). The engine limited performance was achieved as the abnormal combustion (knocking) appeared at the nominal loads and HES more than 35%, as the injection timing was fixed. The hydrogen induction up to 15% decreased the NO levels, however increased the NO levels, with HES of more than 15% (Fig. 3b). NO_x reduction at the low HES of 5% was observed by Senthil Kumar 2003 and Bika et al. 2008. This NO reduction is due to the slower combustion caused by a shorter ignition lag that contributes to advanced ignition, which decreases the combustion rate just after start

of combustion (Szwaja 2009). At higher hydrogen rates of the test, NO pollutants increased. The highest increase rate of NO was at the nominal load at the top HES of experiment. However, the increase of HES, led to a reduction of smokiness (Fig. 3a).

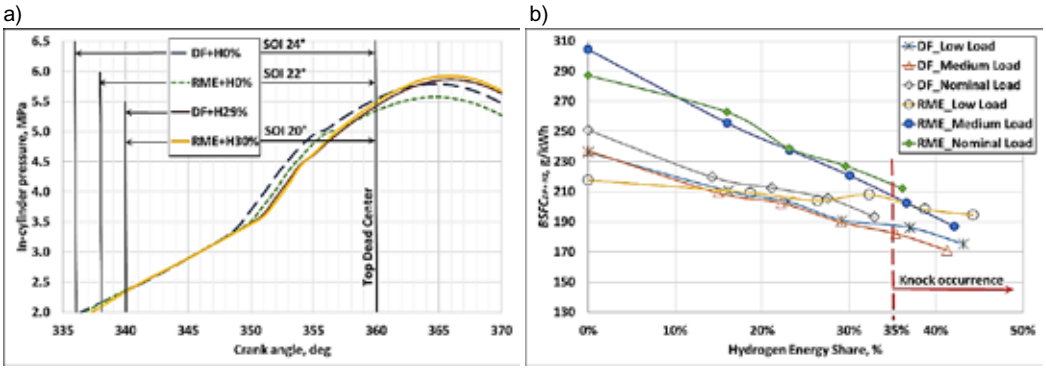


Fig. 2: In-cylinder pressure at Medium Load (a). *BSFC* at Low, Medium and Nominal Loads and HES (b)

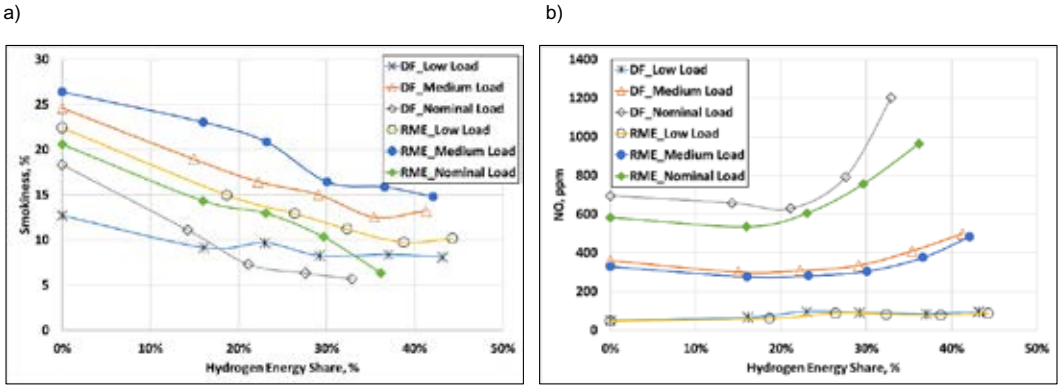


Fig. 3: The dependence of smokiness (a) and NO (b) on fuel used, IMEP and HES.

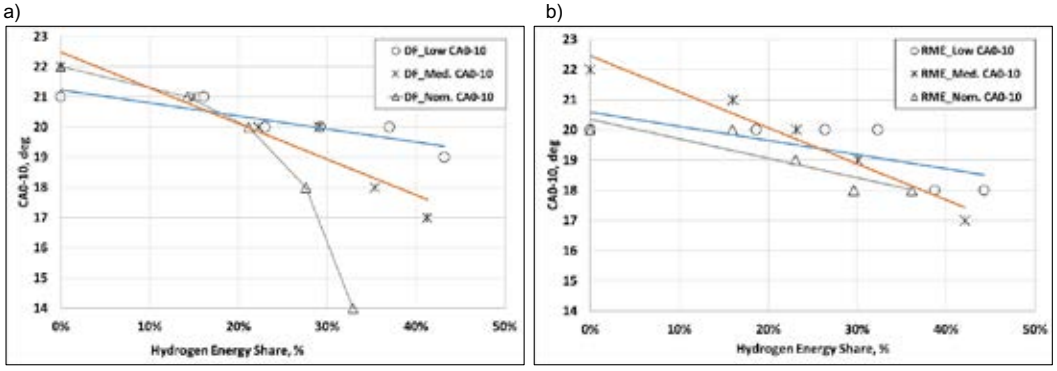


Fig. 4: The combustion delay 0 – 10% MFB at tested HES of DF (a) and RME (b).

The increase of HES shortens the ignition delay (lag) expressed by the initial combustion duration of CA0–10 (Fig. 4 and 5) due to the high premixed combustion rate and impact of higher laminar speed of hydrogen flame. Increase of hydrogen fraction also reduces the main combustion duration CA10–90 which was accelerated by the first combustion phase CA0–10.

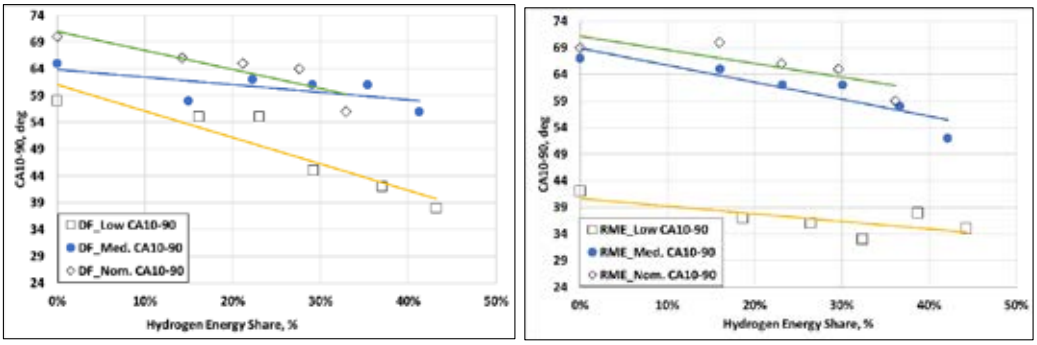


Fig. 5: The main combustion duration 10 – 90% MFB at tested HES of DF (a) and RME (b).

IV. Conclusions

The combustion duration CA0–10 (considered as ignition lag) and CA10–90 (main combustion phase) shorten with increase of HES. Presence of hydrogen also contributes to decrease in BSFC what causes increase in brake thermal engine efficiency. HES of less than 15% decreases the NO emissions, but higher hydrogen fraction increases it significantly at nominal load. The trend of smokiness decreased steadily with increase of HES. Amounts of hydrogen addition by energy share were limited with combustion knock occurring at HES over 35% at nominal load.

Acknowledgements

This project has received funding from the European Union's Horizon 2020 research and innovation programme under grant agreement No 691232 — Knocky — H2020-MSCA-RISE-2015/H2020-MSCA-RISE-2015.

References

Baltacioglu M.K., Arat H.T., Ozcanli M., Aydin K., Experimental comparison of pure hydrogen and HHO (hydroxy) enriched biodiesel (B10) fuel in a commercial diesel engine, Int. Journal of Hydrogen Energy, 41, 8347-8353 (2016).

Barrios C.C., Domínguez-Sáez A., Hormigo D., Influence of hydrogen addition on combustion characteristics and particle number and size distribution emissions of a TDI diesel engine, Fuel, 199, 162-168 (2017).

Gomes Antunes J. M., Mikalsen R., Roskilly A. P., An experimental study of a direct injection compression ignition hydrogen engine, International Journal of Hydrogen Energy, 34, 6516-6522 (2009).

Grab-Rogalinski K., Szwaja S., The combustion properties analysis of various liquid fuels based on crude oil and renewables, IOP Conference Series: Materials Science and Engineering, 148 (1), 012066, DOI:10.1088/1757-899X/148/1/012066, (2016).

Grab-Rogalinski K., Szwaja S., Combustion Of The Biomethane In An IC Over-Expanded Engine, Conference Proceedings by IEEE, International Conference on Green Energy and Applications ICGEA 2017, IEEE Xplore, DOI: 10.1109/ICGEA.2017.7925473, (2017).

Rocha H.M.Z., Pereira R.S., Nogueira M.F.N., Belchior C.R.P., Tostes M.E.L., Experimental investigation of hydrogen addition in the intake air of compressed ignition engines running on biodiesel blend, Int. Journal of Hydrogen Energy, Vol. 42, Issue 7, Pages 4530-4539 (2017).

Senthil Kumar M., Use of hydrogen to enhance the performance of a vegetable oil fuelled compression ignition engine, Int. Journal of Hydrogen Energy, 28(10):11, 43 – 54 (2003).

Singh Bika A., Franklin L.M., Kittelson D.B., Emissions effects of hydrogen as a supplemental fuel with diesel and biodiesel, SAE Pap 2008-01-0648 (2008).

Szwaja S., Grab-Rogalinski K., Hydrogen combustion in a compression ignition diesel engine, International Journal of Hydrogen Energy, 34, 4413–4421 (2009).

Energy and Exergy Analysis of 1 kW Self-humidified PEM Fuel Cell

***Tayfun Özgür*[1], Ali Cem Yakaryılmaz[1], Erdi Tosun[2], Mustafa Atakan Akar[1], Mustafa Özcanlı[1]**

1Department of Automotive Engineering, Çukurova University, Adana, Turkey
2Department of Mechanical Engineering, Çukurova University, Adana, Turkey

Fuel cells are new power generation systems that convert chemical energy into electrical energy. A proton exchange membrane (PEM) fuel cell promises clean energy conversion with nearly zero emission. Since PEM fuel cells have high efficiency and zero emissions levels, many researchers make a lot of investigations on them. PEM fuel cell uses hydrogen as a fuel and oxygen that is generally taken from air. Then, converts these reactants to water and electricity. In this study thermodynamic analysis of a 1 kW self-humidified PEM fuel cell which was produced by Horizon Fuel Cell Technologies was experimentally investigated. The aim of this study is to obtain better performance and better efficiency from the PEM Fuel Cell. A testing apparatus was established to analyze the system efficiencies based on first and second laws of thermodynamics. In this system, pure hydrogen was directly used as a fuel from compressed gas storage tank. Purity of hydrogen was 99.99% and operating pressure was set to 0.5 bar. The effects of different dead state temperature values on system performance were observed at constant operating pressure.

Keywords: PEM fuel cell, dead state, efficiency, energy, exergy.

A Comparative Thermodynamic Analysis of Alternatively Proposed Different Fuel System Models

[1*]Muhammet Yilanli, [2]Önder Altuntaş, [3]Emin Açıkalp
[1 and 2] Faculty of Aeronautics and Astronautics, Anadolu University, Eskisehir TR-26470, Turkey
[3] Mechanical and Manufacturing Engineering Department, Bilecik S.E. University, Bilecik TR-11210, Turkey

*E-mail: muhammetyilanli@anadolu.edu.tr

Abstract
As a baseline model an aircraft fuel system and alternatively proposed different type of aircraft fuel system models analysed in order to assess energy and exergy interactions between fuel system components using Jet A fuel as a working fluid. The aim of this study is to examine and compare energy and exergy changes of four different fuel systems and its components, which are considered to be related to the departure, acceleration, horizontal cruising and landing phases of the aircraft under the different day conditions.

Keywords: Aircarft fuel system, energy, exergy, diffirent type of aircraft fuel systems

I. Introduction

Aircraft technology needs demand that hydrocarbon fuels play dual roles of fuel and coolant over wide ranges between fuel feed system and combustion chamber conditions considering temperature and pressure. Improvements in the performance of advanced gas turbine engines and pulse-detonation engines require a high-heat-sink, thermally stable fuel that can be used to cool hot engine components. So it is necessary to stabilize engine heat load input to fuel through fuel system components (Bruening and Chang, 1999). The use aviation fuel as coolant to remove waste heat loads produced by the turbine engines, is a technological goal of great interest for the aircraft industry. However, kerosene-type aviation fuels, have the tendency to degrade at high temperatures and form solid deposits. Such phenomena are generally referred to as thermal stability of the fuel and is one of the specification required for commercial aviation fuel and one of the most critical fuel properties (Hazlett, 1991).

Because of the importance of fuel temperature limits in the fuel tanks, many researchers studied about fuel temperature prediction and its limits during flight. To determine whether a proposed vehicle design will likely be restricted in operational performance by tank temperature limits, a model (German, 2012) that integrates heat transfer during mission segments to determine the thermal endurance of an aircraft in terms of fuel tank temperature rise developments in cases with and without tank-wall heat transfer presented. Numerical prediction of fuel temperature in the fuel tanks of unmanned air vehicles for both ground static, non-operating and in flight transient conditions (Baek, 2011) calculated by using a modified Dufort-Frankel scheme.

The use of exergy analysis might provide new information in which a comparative study could rely on, since trade-off studies are faulty in evaluating new systems, as they present lack of information (Bejan, 2001; Tona et al., 2008). At this point, thermal engineering, commonly referred to energy engineering, plays a vital role. Exergy in particular, is a prominent tool in this field of engineering, providing benefits, such as the evaluation and optimization of energy systems. Exergy analysis comprises the first and second laws of thermodynamics. Exergy analysis, which benefits from both the first and second laws of thermodynamics, pays attention to the quality of energy consumption and conversion within a system in addition to the quantity. Therefore, it leads us to understand the irreversibility and loss within the examined System (Dinçer and Çengel, 2001; Rocco et al., 2014; Pavelka et al., 2015)

II. Experimental Set-up and Procedure

The main functions of engine fuel system on the aircraft are to safely supply, pressure and heat the fuel to the combustion chamber. Baseline engine fuel system is shown schematically in the Figure 1a. Gear pumps receives fuel from the aircraft fuel tank and delivers fuel to the HX. The fuel then passes through Main Engine Control unit (MEC) to Fuel HX and then it is sent to the fuel injectors in the engine combustors. (Versaw, 1983; Rolls Royce, 1996). The alternatively supposed fuel systems are shown in Figure 1. MEC controls amount of fuel transferred to the combustion chamber by recirculation or by-pass of fuel.

To direct the study following assumptions were made

- All processes are assumed steady-state and steady-flow.
- Potential and kinetic effects are negligible.
- The variation of specific heats with temperature is to be considered.
- By-pass flow of fuel between system components are ignored.
- Fuel filter in the system doesn't taken into consideration.
- Energy losses due to mechanical friction and pressure losses in the components are negligible.

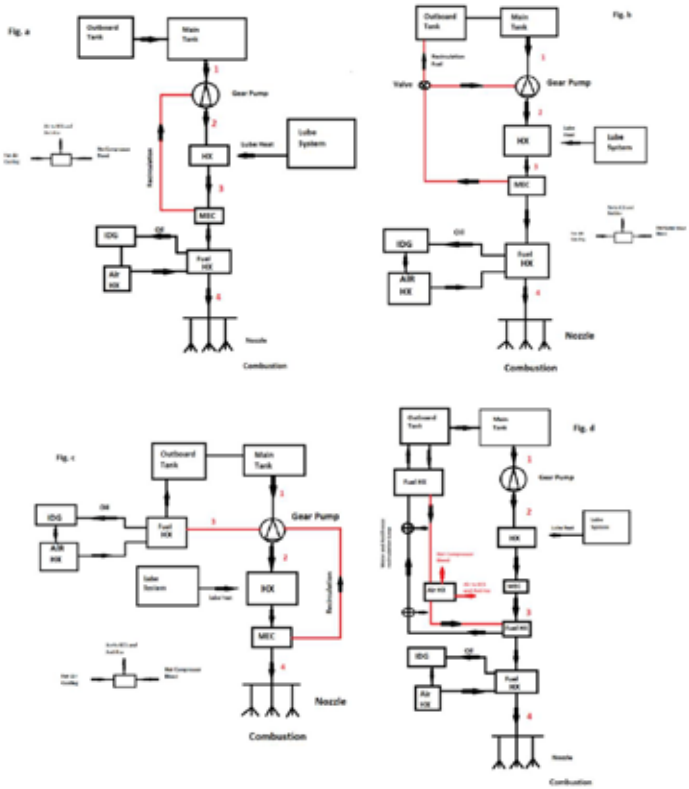


Fig. 1: (a) DC-10-30 baseline fuel system and alternative fuel systems, (b) system a, (c) system b, (d) system c

Reference Aircraft DC-10-30 commercial transport aircraft was selected to serve as the baseline vehicle for evaluating energy and exergy analyses of the fuel system. In the hot day mission, less than one hour, a flight profile containing only one cruise segment is used. However, in the cold day mission, more than 9 hours and two cruise segment is used. The aircraft climbs to the cruise altitude, cruises, and descends to the destination for both flight profile Table 1. For the purpose of exergy analyses the reference temperature (T_0) selected as the ambient temperature profile.

Tab. 1: Cold day 8000 km and hot day 450 km flight mission's flight profile parameters of fuel system models

8000 km flight mission					Main Fuel Pump in Temperature (K)				Heat Exchanger in Temperature (K)				Fuel Heat Excahnger in Temperature (K)				Nozzle in Temperature (K)			
Flight Phase	Cold Flight (min)	Altitude (km)	Main Fuel Flow Rate (kg/min)	System	Baseline	A	B	C	Baseline	A	B	C	Baseline	A	B	C	Baseline	A	B	C
Idle	5.0	0.0	15.0		265.2	255.2	252.2	255.2	341.2	263.2	341.2	323.2	345.2	272.2	343.2	326.2	349.2	299.2	348.2	338.2
Climb	25.0	0-11000	88.0		255.2	254.7	251.2	256.2	325.2	270.2	314.2	306.2	323.8	291.2	322.2	318.2	341.2	291.2	321.2	321.2
Cruise	450.0	11000.0	38.0		237.2	245.2	239.2	234.2	311.2	269.2	316.2	302.7	320.7	277.2	317.2	313.2	331.2	276.2	325.2	317.2
Climb	5.0	11000-12000	60.0		233.2	249.2	235.2	231.7	312.2	264.2	315.2	303.2	321.2	283.2	321.2	315.2	332.2	278.2	319.2	319.2
Cruise	75.0	12000.0	50.0		232.2	253.2	235.2	231.7	316.2	266.2	312.2	312.2	303.2	286.2	322.7	322.7	334.2	291.2	317.2	358.4
Descent	25.0	12000-0	20.0		243.2	259.2	247.2	244.2	345.2	270.2	336.2	321.2	342.2	275.2	339.2	331.2	353.2	294.2	344.2	329.2

450 km flight mission					Main Fuel Temperature Pump in (K)				Main Filter in				Lube				Nozzle in			
Flight Phase	Hot Flight (min)	Altitude (km)	Main Fuel Flow Rate (kg/min)	System	Baseline	A	B	C	Baseline	A	B	C	Baseline	A	B	C	Baseline	A	B	C
Idle	15.0	0.0	10.0		315.2	310.2	313.2	311.2	385.2	321.2	383.2	365.2	297.2	293.2	293.2	286.7	391.2	341.2	384.2	381.2
Climb	5.0	0-6200	95.0		310.2	308.2	311.2	309.2	351.2	327.2	352.2	343.2	291.2	314.2	321.2	304.2	355.2	335.2	352.7	385.2
Cruise	18.0	6200.0	42.0		309.2	305.2	309.2	306.2	367.2	320.2	357.2	347.2	282.9	292.2	283.2	291.2	379.2	337.7	357.4	375.2
Descent	14.0	6200-0	15.0		311.2	306.2	307.7	308.2	376.2	312.2	376.2	363.2	287.2	297.2	298.9	291.7	389.2	338.2	377.2	388.2

III. Analysis

An evaluation of any thermal system or process in the framework of the first law provides insight into how energy is consumed or morphed into another form (Bejan et al. (1985); Çengel et al., 2002). In this framework, fundamental equations should be written to perform exergy analysis of any system. Therefore, for any steady state system, mass and energy conservation equations are written respectively as follows:

$$\dot{Q} - \dot{W} + \sum \dot{m}_{in}\left[h_{in} + \left(V_{in}^2/2\right) + gz_{in}\right] - \sum \dot{m}_{out}\left[h_{out} + \left(V_{out}^2/2\right) + gz_{out}\right] = 0 \quad (1)$$

The work required by the pumps, specific flow exergy of the fuel and Second Law efficiency of fuel pump is evaluated in sequence:

$$\dot{W}_{Fuel\ pump} = \dot{m}_{fuel}(h_{out} - h_{in}) \quad (2)$$

$$\dot{W}_{rev.\ fuel\ pump} = \dot{m}_{fuel}[(h_{out} - h_{in}) - T_0(s_{out} - s_{in})] \quad (3)$$

$$\eta_{II,pump} = \frac{\dot{W}_{rev}}{\dot{W}} \quad (4)$$

Heat absorption rate equation of fuel at heat exchangers, entropy generation rate during heat transferred from heat exchanger to fuel and the rate of exergy destruction during heat transfer to fuel through heat exchanger respectively as follows:

$$\dot{Q}_{fuel} - \dot{m}_{fuel}h_{out} - \dot{m}_{fuel}h_{in} \quad (5)$$

$$s_2 - s_1 = \int_1^2 c(T)\frac{dT}{T} \equiv c_{p.avg}\ln\frac{T_{out}}{T_{in}} \qquad \dot{S}_{gen} = \dot{m}_{fuel}c_{p.avg}\ln\frac{T_{out}}{T_{in}} \quad (6)$$

$$\dot{S}_{gen_{FCOC}} = \dot{m}_{fuel}c_{p.avg}\ln\frac{T_{out}}{T_{in}} \quad (7)$$

To calculate enthalpy of Jet-A fuel at any temperature, the chemical formula $C_{12}H_{23}$ and universal gas constant R_u = 8.31447 kJ/kmolK with a molecular weight of 167.3, thermodynamic functions of specific heat Cpo, enthalpy HT^o and entropy ST^o, need to be expressed as functions of temperature in the form of a fourth order polynomial function (Gracia-Salcedo et al., 1970).

IV. Results and discussions

The 2nd Law efficiency of the fuel pump, HX and Fuel HX, for cold and hot day flight mission, are shown in Figures 2. The 2nd Law efficiency of fuel system's pump component, at the cold day fligt mission, from idle flight stage to the end of first stage of cruise gradually decrease, by climbing phase increase a significient magnitude except baseline model, with the cruise stage tend to decrease and with the landing stage indicate an augment similar to the climbing stage. As for The 2nd Law efficiency of heat exchanger, for the cold day fligt mission, both of them (HX and Fuel HX) have similarity in position of corresponding parts through flight; furthermore, efficiency of 2nd Law going to downwards consequently baseline, system b, system c and system a models.

The flight under hot weather condition flight, the 2nd Law efficiency of fuel pumps which is gradually decreasing in the fuel system tend to increase counting from the end of the cruise phase. The increase in 2nd Law efficiency is sharp for the system a fuel pump component. The 2nd Law efficiency of fuel pumps under cold day condition flight indicate a parallel change in value through the flight stages. At the idle stages 2nd Law efficiency of the fuel pumps indicate remarkable difference in value.

In the case of heat exchangers, the 2nd law is decreasing towards the descent flight after increasing the efficiency on cruise stage. At the both flights and for all the system models, the system a shows the lowest 2nd Law efficiency value, on the other hand the system c nearly indicates the highest 2nd Law efficiency value at all stages.

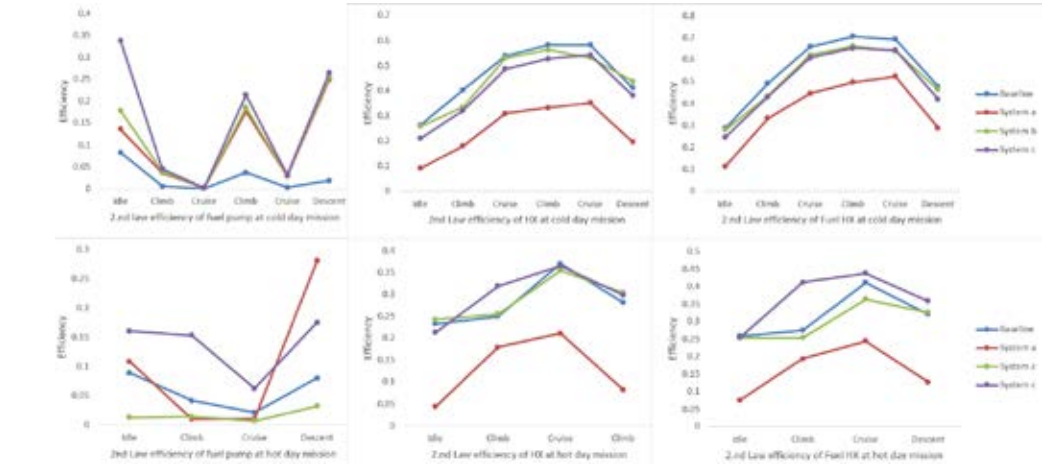


Fig. 2: Second Law Efficiency of fuel system components for both cold and hot day flight mission

V. Conclusions

In this study, aircraft fuel systems have been investigated with energy and exergy analysis. The main conclusions drawn from the results of the present study can be listed as follows:

- For the heat exchangers, the best exergy efficiency was found at the cruise phase for all components. Some improvements could be made at other phases. In addition, fuel pump section, because of the higher exergy destructions and work loads, should be developed with additional equipment.
- The maximum exergy destruction rate was calculated at idle stage for both flight mission. Along with the increase in altitude, according to the reduction of work and heat loads, the destruction of the exergy can be reduced.
- The highest and lowest the exergy destruction rate during the flight has occurred at idle and cruise stage, consequently.
- Exergy destruction rate in the system and system components decreases along with the increase of altitude.
- Most effective system among fuel system models, in term of fuel pump work load, is system c in the hot day flight mission. Furthermore, at the cold day flight mission too, for the fuel pump efficiency, most effective fuel system model is system c.
- In terms of heating fuel, the most effective work condition of heat exchangers occurred with the baseline model at cold day flight mission and with the system c model at the hot day flight mission.

References

Baek, N.G., ve Lim, J.S. (2011). 'Numerical Prediction of Aviation Fuel Temperatures in Unmanned Air Vehicles', International Journal of Aeronautical & Space Sciences, 12(4), 379–384.

Bejan A, Tsatsaronis G, Moran M. (1995) *Thermal design and optimization*. John Wiley & Sons Inc. P.O.Box 17, 3300 AA Dordect, Netherland

Bruening G.B., Chang W.S., (1999) 'Cooled Cooling Air Systems for Turbine Thermal Management' ASME 1999 International Gas Turbine and Aeroengine Congress and ExhibitionVolume 3: Heat Transfer; Electric Power; Industrial and Cogeneration Indianapolis, Indiana, USA

Cengel, Y.A., Wood, B., and Dincer, I., (2002) 'Is bigger thermodynamically better?', Exergy Int. J. 2 62–68.

Dincer I, Cengel YA. (2001). 'Energy, entropy and exergy concepts and their roles in thermal engineering'. Entropy; 3:116-49.

German B.J. (2012). 'A tank heating model for aircraft fuel thermal systems with recirculation', Journal of Propulsion and Power, Vol. 28, No. 1, 204-210.

Gracia-Salcedo, C.M., McBride, B. J., Brabbs, T. A. (1970) Experimental Verification of the Thermodynamic Proporties of a Jet-A Fuel, NASA Lewis Research Center, Cleveland, Thermodynamic data library of the 875-882

Hazlett, R.N. Thermal oxidation stability of aviation turbine Fuels; ASTM: Philadelphia, 1991

Pavelka M, Klika V, Vagner P, Marsík F. (2015) 'Generalization of exergy analysis', Applied Energy;137:158-72

Rocco MV, Colombo E, Sciubba E. (2014) 'Advances in exergy analysis: a novel assessment of the extended exergy accounting method', Applied Energy;113:1405-20.

The Effect of Support Material on the Hydrogen Adsorption-Desorption Characteristics of Ru/SiO2 and Ru/Vulcan Catalysts

***Mustafa Yasin Aslan*, Deniz Üner**

Department of Chemical Engineering, Middle East Technical University, Ankara, Turkey

The role of support material on the adsorption-desorption characteristics of hydrogen over Ru/SiO_2 and Ru/Vulcan catalysts were investigated. 1 wt% Ru loaded Ru/SiO_2 and Ru/Vulcan catalysts were prepared using incipient wetness impregnation method. The metal dispersions of the catalysts were determined via volumetric H_2-chemisorption technique. In order to analyze the adsorption-desorption characteristics of the catalysts, temperature programmed analysis techniques (H_2-TPR, Cooling in H_2, He-TPD) were applied. The fresh catalysts were reduced in the flow of H_2 in Ar up to 650 °C with a temperature ramp of 5 °C/min. After reduction, the catalysts were cooled down to room temperature in the flow of H_2 in Ar and then immediately He-TPD analysis up to 650 °C with a temperature ramp of 5 °C was performed. According to the results of "Cooling in H_2" analysis of 1 wt% Ru/SiO_2 and 1 wt% Ru/Vulcan catalysts, H/Ru ratios were calculated as 11.35 and 22.97, respectively. When He-TPD profile of the catalysts were examined, while 1 wt% Ru/SiO_2 had two desorption peaks at 185 °C and 685 °C, 1 wt% Ru/Vulcan had three desorption peaks at 100 °C, 395 °C, 660 °C. In addition to this, H/Ru ratio of 1 wt% Ru/SiO_2 and 1 wt% Ru/Vulcan were determined as 0.59 and 1.96, respectively. The experimental results showed that the hydrogen uptake amount of 1 wt% Ru/Vulcan is higher than 1 wt% Ru/SiO_2 in both Cooling in H_2 and He-TPD. The effect of surface and structural characteristics of support materials on the hydrogen adsorption-desorption behavior over Ru/SiO_2 and Ru/Vulcan catalysts will be discussed in the framework of relationship between Ru nanoparticles and support materials.

Keywords: Ruthenium, Hydrogen Adsorption-Desorption, Spillover

SnS Photo-electrodes Produced by Sulfurization of Electrodeposited Sn Films for Photo-electrochemical Water Splitting

Sercan Soyöz[1], Bulut Şahin[2], Selim Demirci[2], Cevat Sarıoğlu[1]

[1]Marmara University, Department of Metallurgical and Materials Engineering, Kadiköy, 34722, Istanbul, Turkey
[2]Marmara University, Department of Pure and Applied Science, Kadiköy, 34722, istanbul, Turkey

Recently SnS has become attractive for photovoltaic absorber as well as photo electrodes for solar water splitting because of their promising high electron (2.37x104cm2V-1s-1) and holes (7.35x104cm2V-1s-1) mobility and suitable band gap (Eg: 1.2-1.7 eV). In this work,SnS photo-electrodes were investigated for photo-electrochemical splitting of water. They were prepared on indium-doped tin oxide (ITO) coated glass by sulfurization of electrodeposited Sn films at different temperature (300-500oC) in the sulfur vapor atmosphere The effect of electrodeposition parameter (thickness of the film) and sulfurization temperature on photo-electrochemical (PEC) water splitting were investigated. The crystal structure, surface morphology and optical properties of the SnS photo-electrodes were characterized using an X-ray diffractometer (XRD), scanning electron microscopy (SEM) and UV–VIS spectrophotometer, respectively. PEC performances of the SnS photo-electrodes were determined in the 0.1 M NaOH electrolyte solution. The results showed that electrodeposition parameter (thickness of the Sn films) and sulfurization temperature influenced the PEC performance of SnS photo-electrodes. The photo current and efficiency increased as the SnS became the major phase with decreasing temperature and the thickness of the SnS layer decreased.

Keywords: “SnS, Photo-electrode, Electrodeposition, Sulfurization, Hydrogen generation, Water splitting”

Zirconium Metal-Organic Framework Platform as a Heterogeneous Catalysts for Electrochemical Hydrogen Evolution

Emine Ülker*, Selçuk Demir
Department of Chemistry, Faculty of Arts and Sciences, Recep Tayyip Erdogan University, 53100, Rize, Turkey

E-mails: emine.kapancik@erdogan.edu.tr; selcuk.demir@erdogan.edu.tr

Abstract
Large-scale hydrogen production requires development of alternative low-cost electrocatalysts to be used instead of platinum for hydrogen evolution reaction (HER). Metal-organic frameworks (MOFs) have been attracting great attention because of their porosity, high surface area and modular structural properties. Herein, we prepared a zirconium MOF (MOF-653) which has high chemical and thermal stability that allows post metalation with cobalt acetate to obtain MOF-653@Co via solvothermal deposition method. MOF-653@Co thin film has been used as a scaffold for the deposition of sulphur. HER activity of the prepared MOF-653@Co_S hybrid material was investigated on GC working electrodes in acidic solution. To improve the catalytic activity of GCE_ MOF-653@Co_S electrode, cathodic treatment was performed for two hours. Consequently, two hours cathodic treatment significantly increased the catalytic activity of GCE_Zr-TBA@Co_S hybrid materials according to the as-prepared electrode with an onset potential of 171 mV (vs RHE) and 347 mV for current density of 10 mA cm^{-2}.

Keywords: Hydrogen evolution reaction, Metal-organic frameworks, Heterogeneous electrocatalysis

I. Introduction

The rapid growth of global energy consumption and the associated environmental issues such as greenhouse effect, air pollution and water pollution increased the demand of clean and sustainable alternative energy sources (Wang, 2017; Wu, 2015). Hydrogen is a clean and flexible energy carrier since it does not constitute harmful chemical products. Thus, electrochemical reactions, such as the hydrogen evolution reaction (HER) and oxygen evolution reaction (OER) are the most effective ways to produce hydrogen and oxygen by electrocatalytic water splitting.

However, development of catalysts for hydrogen evolution from water, which is one of the most challenging steps, are needed. Platinum (Pt) and Pt-based materials are the most effective electrocatalysts for hydrogen evolution reaction (HER). However, because it is the most precious and rarest metal on the earth, large scale applications of Pt are unfeasible. Thus, to find a non-noble hybrid material with high activity and low cost as efficient hydrogen evolution catalyst is very challenging.

One of the recent alternatives of hybrid materials as electrocatalysts is metal-organic frameworks (MOFs). MOFs have been attracting great attention because of their superior porosity, high surface areas and tunable properties. Among other applications such as hydrogen storage, separation, solar cell, and biomedical, MOFs are alternative materials for clean energy applications as hydrogen evolution (Furukawa 2017; Nevruzoglu 2016; Tokalioglu 2017; Demir 2017).

II. Experimental Section

Electrochemical experiments, including linear sweep voltammetry (LSV) and cyclic voltammetry (CV) were performed at room temperature using Gamry Instruments Interface 1000 Potentiostat / Galvanostat. A conventional three-electrode electrochemical cell was used with Ag/AgCl electrode (sat. KCl) as the reference electrode, Pt plate as a counter electrode, and catalyst coated glassy carbon electrode (GCE, 3 mm in diameter) as a working electrode. All potentials were measured versus Ag/AgCl reference electrode and were reported versus the reversible hydrogen electrode (RHE) by adding a value of (0.197 + 0.059 pH) V. Electrochemical experiments were performed in 0.1 M HCl (pH 1). All experiments were carried out under a nitrogen atmosphere.

Preparation of MOF-653@Co and MOF-653@Co_S coated GCE

The GCE were polished prior to catalyst deposition by 1 µm, 0.3 µm and 0.04 µm alumina powder and rinsed by sonication in deionized water and ethanol, respectively. The working electrode was prepared as follows: 2 mg of catalyst and 500 µL ethanol were sonicated for 60 min to make a stable suspension. Then, 7.5 µL of the sonicated suspension of the catalyst was dropped onto a clean GCE and electrode was dried in room-temperature, followed by dropping 2 µL of 5 wt % Nafion solution as a binder. CoS was prepared from electrochemically sulfurization of cobalt in structure of MOF-653@Co by CV in 0.5 M of thiourea solution from -1.2 V to 0.2 V versus Ag/AgCl at a scan rate of 5 mV s^{-1} for 5 cycles (Sun, 2013).

III. Results and descussions

Electrocatalytic activity of GCE_MOF-653@Co and GCE_MOF-653@Co_S for H_2 evolution were investigated with a typical three-electrode setup in acidic media (0.1 M HCl). Fig. 1a shows the polarization curve of GCE_MOF-653@Co and GCE_MOF-653@Co_S as compared with blank GCE at a scan rate of 5 mV s^{-1}. As expected, blank GCE is inactive toward hydrogen evolution, also, GCE_MOF-653@Co electrode shows similar

catalytic activity with GCE. Furthermore, GCE_MOF-653@Co_S is able to electrocatalytically generate hydrogen, with an onset overpotential (about 271 mV) and a low cathodic current density. These electrodes were electrochemically treated by cathodic polarization for two hours to improve the catalytic activity (Dekanski, 2001). Electrode found that the catalyst was not good for HER at the beginning, however, the activity significant increased a lot during cathodic polarization, as observed by the onset overpotential shift from 271 mV to 171 mV for a current density of 55 μA cm^{-2} and 505 mV to 347 mV for current density of 10 mA cm^{-2} for GCE_MOF-653@Co_S.

Fig. 1b shows Tafel slope of the preparedelectrodes obtained from LSV at a scan rate of 5 mV s^{-1}. Tafel slopes are 176 and 84 mV dec^{-1} for GCE_MOF-653@Co and GCE_MOF-653@Co_S, respectively before the cathodic polarization. However, Tafel slope decreased for both electrodes after the cathodic polarization as 103 and 67 mV dec^{-1} for GCE_MOF-653@Co and GCE_MOF-653@Co_S, respectively. A smaller Tafel slope shows the faster HER rate with increasing overpotential, which is provided by the electrode surface changes after the electrochemical treatment. Tafel slope of 67 mV dec^{-1} for GCE_MOF-653@Co_S is smaller than the reported value of $CoSe_2$ nanoparticles embedded in defective carbon nanotubes ($CoSe_2$@DC) from selenization of pre-oxidized MOF-Co (82 mV dec-1) at pH 0 (Zhou, 2016), Cobalt-Boride (Co-B) catalyst (102 mV dec^{-1}) at pH 1 (Gupta, 2015). This slope (67 mV dec^{-1}) shows Volmer–Heyrovsky mechanism for HER and electrochemical desorption process as rate-limiting step.

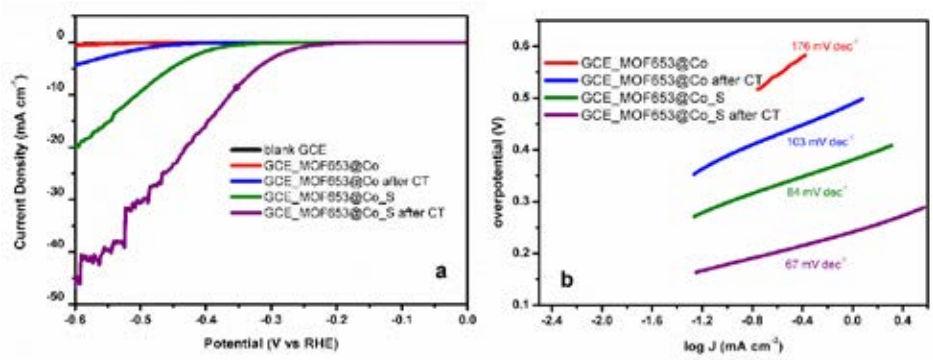


Fig. 1. a) LSV b) Tafel slope of blank GCE (black), GCE_MOF-653@Co before (red) and after cathodic treatment (blue), GCE_MOF-653@Co_S before (green) and after cathodic treatment (purple) in 0.1 M HCl.

IV.Conclusions

In summary, heterogeneous electrocatalyst including of electrodeposited sulphur on a zirconium MOF metalated with cobalt was developed. Also, to improve the catalytic activity of GCE_MOF-653@Co_S towards HER, cathodic treatment was performed for two hours. The prepared GCE_MOF-653@Co_S catalyst after the cathodic treatment shows catalytic activity for HER with an onset potential of 171 mV (vs RHE) in acidic media, which is 100 mV lower than as-prepared GCE_MOF-653@Co_S. In aqueous HCl at pH 1, the catalyst can deliver a catalytic current of 10 $mAcm^{-2}$ at 347mV. Tafel slope of 67 mV dec^{-1} for GCE_MOF-653@Co_S shows that Volmer–Heyrovsky mechanism works for HER. This study indicates that MOF can be used as a suitable support material for further investigations of non-noble-metal sulfide films in the field of HER application.

References

Dekanski, A., Stevanovic, J., Stevanovic, R., Nikolic, B. Z., Jovanovic, V. M., Glassy carbon electrodes I. Characterization and electrochemical activation, Carbon, 39, 1195–1205 (2001).

Demir, S., Usta, S., Tamar, H., Ulusoy, M. Solvent free utilization and selective coupling of epichlorohydrin with carbon dioxide over zirconium metal-organic frameworks, Microporous Mesoporous Mater., 244, 251–257, (2017).

Furukawa, H., Cordova, K. E., O'Keeffe M., Yaghi, O. M., The Chemistry and Applications of Metal-Organic Frameworks, Science, 341 (6149), 1230444 (2013).

Gupta, S., Patel, N., Miotello, A., Kothari, D. C. Cobalt-Boride: An efficient and robust electrocatalyst for Hydrogen Evolution Reaction, Journal of Power Sources, 279, 620-625 (2015).

Li, H., Ke, F., Zhu, J., MOF-Derived Ultrathin Cobalt Phosphide Nanosheets as Efficient Bifunctional Hydrogen Evolution Reaction and Oxygen Evolution Reaction Electrocatalysts. Nanomaterials, 8, 89 (2018).

Nevruzoglu, V., Demir, S., Karaca, G., Tomakin, M., Bilgin, N., Yilmaz, F., Improving the stability of solar cells using metal-organic frameworks, J. Mater. Chem. A., 4, 7930-7935 (2016).

Sun, Y., Liu, C., Grauer, D. C., Yano, J., Long, J. R., Yang, P., Chang, C.J., Electrodeposited Cobalt-Sulfide Catalyst for Electrochemical and Photoelectrochemical Hydrogen Generation from Water, Journal of the American Chemical Society, 135, 17699−17702 (2013).

Tokalioglu, S., Yavuz, E., Demir, S., Patat, S., Zirconium-based highly porous metal-organic framework (MOF-545) as an efficient adsorbent for vortex assisted-solid phase extraction of lead from cereal, beverage and water samples, Food Chemistry, 237, 707-715, (2017).

Wang, W., Xu, X., Zhou, W., Shao, Z. Recent Progress in Metal-Organic Frameworks for Applications in Electrocatalytic and Photocatalytic Water Splitting, Adv. Sci. 4, 1600371 (2017).

Wu, H. B., Xia, B. Y., Yu, L., Yu, X. Y., Lou, X. W., Porous molybdenum carbide nano-octahedrons synthesized via confined carburization in metal-organic frameworks for efficient hydrogen production, Nature Communications, 6, 6512 (2015).

Zhou, W., Lu, J., Zhou, K., Yang, L., Ke, Y., Tang, Z., Chen, S., CoSe2 nanoparticles embedded defective carbon nanotubes derived from MOFs as efficient electrocatalyst for hydrogen evolution reaction, Nano Energy, 28, 143–150 (2016).

Metal-Organic Frameworks as Hydrogen Evolution Catalysts

Selçuk Demir, Emine Ülker*,
Department of Chemistry, Faculty of Arts and Sciences, Recep Tayyip Erdogan University, 53100, Rize, Turkey

E-mails: emine.kapancik@erdogan.edu.tr; selcuk.demir@erdogan.edu.tr

Abstract
Platinum (Pt) and Pt-based materials are the most effective electrocatalysts for hydrogen evolution reaction (HER). However, because it is the most precious and rarest metal on the earth, large scale applications of Pt are unfeasible. Thus, to find a non-noble hybrid material with high activity and low cost as efficient hydrogen evolution catalyst is very challenging. One of the recent alternatives of hybrid materials as electrocatalysts is metal-organic frameworks (MOFs). MOFs have been attracting great attention because of their superior porosity, high surface areas and tunable properties. Among other applications such as hydrogen storage, separation, solar cell, and biomedical, MOFs are alternative materials for clean energy applications as hydrogen evolution. Herein, we summarized recent developments on HER using MOFs as heterogeneous catalyst.

Keywords: Hydrogen evolution reaction, Metal-organic frameworks, Heterogeneous electrocatalysis

I. Introduction

Metal-organic frameworks (MOFs), the new family of porous materials, have been attracting considerable attention because of their high surface area, chemical and thermal stabilities and structural properties which enable us to tune their structures for desired applications. MOFs are hybrid porous materials and consist of organic and inorganic building units. Thus their properties such as surface area, pore apertures, active sites, can be tuned while keeping their structures same. This tailorability allows us to conduct targeted applications such as gas storage, selective separation, solar cells, and catalytic applications (Suh, 2011; Furukawa, 2013; Nevruzoğlu, 2016). Also, it is a great challenge to increase the stability of MOFs in order to increase their application areas (Demir, 2017; Morris, 2012). Since global warming is one of major issues of modern age, hydrogen production as an energy carrier is a promising way to overcome environmental problems. As a raw material water is common and cheaper alternative to produce hydrogen via electrocatalytic process.

Electrocatalytic hydrogen evolution reaction (HER) takes place via electrochemical reduction of protons in acid solutions : $2H^+ + 2e^- \rightarrow H_2$. Catalysts are needed for this reaction to occur at suitably high current densities (Hod, 2015). Platinum with its high price is a good candidate for HER. However, realization of large-scale hydrogen production requires the development of alternative low-cost electrocatalysts with earth abundant elements.

Efficient heterogeneous catalytic materials derived from MOF precursor as sacrificial templates have been used as electrocatalysts for HER (Zhao, 2017), but employing MOF as support materials for HER reaction is in its early stage (Figure 1) (Nohra, 2011; Qin, 2015; Dai, 2016). Nohra *et al*. directly used polyoxometalate-based MOFs (POMOFs) as electrocatalysts briefly for the HER in 2011 (Nohra, 2011) and a detailed investigation of POMOFs reported by Qin *et al*. on 2015 (Qin, 2015). The overpotential of the most active POMOF is 237 mV at a benchmark current density of 10 $mA \cdot cm^{-2}$ with a Tafel slope of 96 $mV \cdot dec^{-1}$ in acidic media. This highest HER activity is attributed to the both presence of POM units and porosity of the MOF (Qin, 2015). Because metal sulfides and selenides containing Co, Fe, molybdenum polysulfide (MoS_x) (Dai, 2016) and Ni display promising catalytic behaviour for the HER, MoS_x appended on a Zr-MOF, (UiO-66-NH_2) by Dai et al. very recently. Prepared composite which is durable in acid medium, showed remarkable electrochemical HER activity with a Tafel slope of 59 $mV \cdot dec^{-1}$, and a cathode current of 10 $mA \cdot cm^{-2}$ at an overpotential of 200 mV (Dai, 2016). Additionally, Hupp *et al.* showed that NU-1000 which used as support materials for the deposition of a Ni-S electrocatalyst, exhibits significantly enhanced performance for HER at pH 1, with an overpotential of 238 mV at 10 $mAcm^2$ and a Tafel slope of 120 $mV \cdot dec^{-1}$ (Hod, 2015).

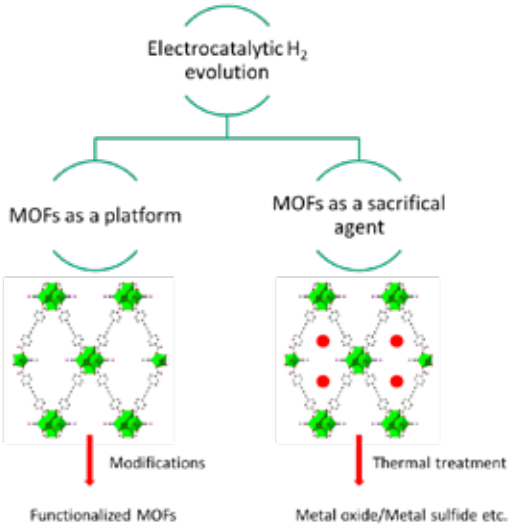


Fig. 1: Utilization of MOFs for hydrogen evolution reactions.

II. Conclusions

Because MOFs are rarely used for hydrogen evolution reaction from water which is a crucial research domain of hydrogen economy, preparation of water stable MOF to be employed as a HER catalyst are highly demanded. The pores of MOFs facilitate the diffusion of the reactants and improve the interaction and efficiency of the catalyst. Additionally robust structure of MOFs prevents the changes on the active sites. Consequently recent literature survey represents that MOFs are very promising materials with their designable structures and properties.

References

Dai, X., Liu, M., Li, Z., Jin, A., Ma, Y., Huang, X., Sun, H., Wang H., Zhang, X., Molybdenum Polysulfide Anchored on Porous Zr-Metal Organic Framework To Enhance the Performance of Hydrogen Evolution Reaction. J. Phys. Chem. C, 120, 12539–12548 (2016).

Demir, S., Usta, S., Tamar H., Ulusoy, M. Solvent free utilization and selective coupling of epichlorohydrin with carbon dioxide over zirconium metal-organic frameworks Microporous Mesoporous Mater., 244, 251–257 (2017).

Furukawa, H., Cordova, K. E., O'Keeffe M., Yaghi, O. M. The Chemistry and Applications of Metal-Organic Frameworks, Science, 341, 1230444 (2013)

Hod, I., Deria, P., Bury, W., Mondloch, J. E., Kung, C.-W., So, M., Sampson, M. D., Peters, A. W., Kubiak, C. P., Farha O. K., Hupp, J. T., A porous proton-relaying metal-organic framework material that accelerates electrochemical hydrogen evolution. Nat Commun., 6, 8304 (2015).

Morris, W., Volosskiy, B., Demir, S., Gándara, F., Mcgrier, P. L., Furukawa, H., Cascio, D., Stoddart, J. F., Yaghi, O. M., Ga F., Mcgrier, P. L., Synthesis, Structure, and Metalation of Two New Highly Porous Zirconium Metal–Organic Frameworks. Inorg. Chem., 51, 6443–6445 (2012).

Nevruzoğlu, V., Demir, S., Karaca, G., Tomakin, M., Bilgin, N., Yilmaz, F. Improving the stability of solar cells using metal–organic frameworks, J. Mater. Chem. A., 4, 7930-7935 (2016).

Nohra, B., El Moll, H., Albelo, L. M. R., Mialane, P., Mellot-draznieks, C., Kee, M. O., Biboum, R. N., Keita, B., Nadjo L., Dolbecq, A., Polyoxometalate-Based Metal Organic Frameworks (POMOFs): Structural Trends, Energetics, and High Electrocatalytic Efficiency for Hydrogen Evolution Reaction. J. Am. Chem. Soc., 133, 13363–13374 (2011).

Qin, J., Du, D., Guan, W., Bo, X., Li, Y., Guo, L., Su, Z., Wang, Y., Lan Y., Zhou, H., Ultrastable Polymolybdate-Based Metal–Organic Frameworks as Highly Active Electrocatalysts for Hydrogen Generation from Water. J. Am. Chem. Soc., 137, 7169−7177 (2015).

Suh, M. P., Park, H. J., Prasad, T. K., Lim, D.-W. Hydrogen Storage in Metal–Organic Frameworks, *Chem. Rev.*, **112**, 782–835 (2011)

Zhao, S.-N., Song, X.-Z., Song S.-Y., Zhang, H., Highly efficient heterogeneous catalytic materials derived from metal-organic framework supports/precursors. Coord. Chem. Rev., 337, 80–96 (2017).

Enhancement of Hydrogen Charging in Metal Hydride-Based Storage Systems By Using Heat Pipe

Fawzi ELHAMSHRI[1], Muhammet Kayfeci[2*]
[1,2]Department of Energy Systems Engineering, Karabuk University, Karabuk, Turkey

E-mail:mkayfeci@karabuk.edu.tr

Abstract
Heat transfer in metal hydride bed is an important factor affecting the performance of metal hydride reactors (MHRs for short). In this study, the hydrogen storage in MHRs is investigated experimentally under various hydrogen supply pressures, e.g. (2 -10 bars) in order to explain the influence of heat pipe and fins in the hydriding process. Three different reactor configurations, consisted of a tubular cylinder with same base dimensions. Reactor 1 is a closed cylinder that exchanges heat through its lateral and base surfaces by cool with natural convection. Heat pipe is made of copper–ethanol combination and situated along the axis of reactor 2. Reactor 3 is a similar to reactor 2 with additional aluminum circulated fins are manufactured around the heat pipe in order to enhance heat transfer with the environmental field. The temperature evolution data for the cylindrical $LaNi_5$ reactors at several locations are recorded under all the certain values of hydrogen charging pressure. The experimental results showed that the use of heat pipe could be a good choice to improve hydrogen storing performance. The finned heat pipe configuration confirms the less temperature increased in the fastest charging time. The charging time was reduced approximately 75% with 10 bar hydrogen supply pressure.

Keywords: Hydrogen storage, Heat transfer, charging pressure, Heat pipe, finned heat pipe.

I. Introduction

Hydrogen as an energy has come to the forefront within the scope of new energy technologies as being a storable and transportable energy with high calorific value and environmental friendliness. Hydrogen is a new clean energy and the best alternative to fossil fuels (Askri et al., 2009; Kaplan, 2009; Kayfeci et al., 2014; Boo et al., 2009; Chung et al., 2013). Several challenges remain to store and to use hydrogen efficiently. However, the problem of storage for hydrogen reduces its use and marketing. A metal hydride is a useful method in the hydrogen storage, because it has features such; generating a large amount of heat with hydrogen absorbing and storing compactly. The MHRs which can store large amounts of hydrogen in small volumes have attracted attention. However, heat management in MHRs is the main concern as a result of kinetic, heat and mass reactions, which are the key factors in the charging/discharging process.

There are many experiments and theoretical studies on several aspects of MHRs to optimize the best reactor performance. Heat exchangers are used in hydrogen storage to accelerate the heat transfer rate in the metal hydride (Askri et al., 2009; Kaplan, 2009; Kayfeci et al., 2014). Askri et al., (2009) indicated that approximately 80% improvement of hydrogen charging time with a concentric heat exchanger tube reactor equipped with fins. Kaplan et al., (2009) confirmed that, the hydrogen storage in MHRs is principally heated transfer dependent, and the tank configuration which has a better cooling system exhibits the fastest charging characteristics. Kayfeci, (2014) investigated the heat transfer mechanism on MHRs under different hydrogen supply pressure. The results showed that, the using of MHRs with fins confirms the less charging time. A heat pipe is a device with high thermal conductance. Recently, Boo and Chung (Boo et al., 2009; Chung et al., 2013) employed the heat pipe in MHRs design. Boo et al., (2009) showed by simulation that, the use of heat pipes in MHRs provided a good enhancement of heat transfer with comparison to heat exchangers. Chung et al., (2013) experimentally showed a good improvement in hydrogen storage capacity by use of a heat pipe. More than half time reduced for absorption process. However, the heat pipe applications in MHRs remain limited. This study presents a pilot design of MHRs equipped with a heat pipe and fins. In experimental studies, 2-10 bars of hydrogen supply pressures are adjusted, and temperature distributions are measured at several points in MHRs. In additional, the stored hydrogen mass is determined.

II. Experimental Set-up and Procedure

Three configurations of MHRs are designed and constructed as shown in (Fig. 1). They are made of St52 steel, and have the same inner and outer diameters of 26 mm and 35 mm, respectively, and the same inner height of 60 mm. A heat pipe made of copper–ethanol combination is situated along the axis of reactor 2. The heat pipe outer diameter and thickness are 6 mm and 1 mm, respectively, with 250 mm length. Aluminum sleeve is made with inner diameter and thickness of 6 mm and 1 mm, respectively, and attached with 30 aluminum fins. The sleeve is situated along the axis of reactor 3 to insert the heat pipe inside the reactor. The fins have a diameter and thickness of 20

mm and 1 mm, respectively, and the spacing between adjacent fins was 3 mm. The temperatures in the hydride beds are monitored by 4 thermocouple probes (P_1, P_2, P_3, and P_4) in each reactor with additional 2 thermocouple probes (P_5 and P_6) attached to the heat pipe section outside the reactor as shown in (Fig. 1). A 0.5 µm grade tubular filter is fixed on the inlet/outlet tubing to prevent metal powders from being drawn out during the discharging process. Each reactor contains 120 g of $LaNi_5$ metal powder.

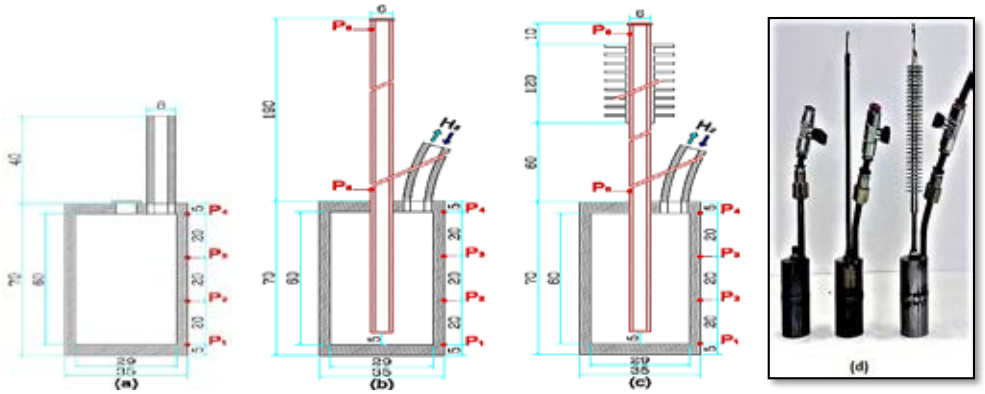


Fig. 1: MHRs a) w/o heat pipe b) with heat pipe c) with finned heat pipe d) photograph of the MHRs

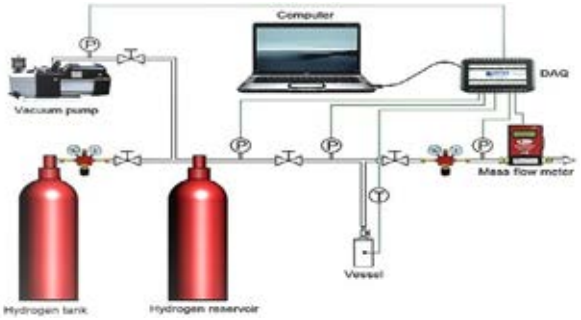


Fig. 2: Schematic of the experimental set-up

Fig. 2 shows the schematic of the experimental setup. In the assembly; a design reactor, a vacuum pump to removing the moisture and the air inside the reactor, temperature thermocouples to measure the temperature during the hydriding process, a regulator for adjusting the hydrogen pressure, data collecting system, a computer laptop, Hydrogen cylinder with 99.999 % of purity.

$LaNi_5$ material is grinded for 2 hours with 600 rpm speed of mechanical grinder machine associated with steel ball at the rate of 1/10 to produce a powder size in between 10 and 50 µm. 120 grams of $LaNi_5$ powders are filled in each reactor at the rate of 60% as a reaction volume. 35% free volume and 5% the volume occupied by internal heat pipe section. The reactor is settled in ceramic resistance by being assembled to the vacuum pump at a low pressure (≈0.01 bar), and assembled to the hydrogen tank with 10 bar pressure to start the activation process. The tank heated to approximately 350-450 °C and vacuumed for 15 minutes under low pressure. Activation consists in executing repeated charging/discharging process more than (20 cycles) until the maximum hydrogen storage reached (~1.3 wt%). When the activation process is completed, the reactor cooled to room temperature and the experimental operations take place by charge the hydrogen for 5000 s duration.

III. Results and Discussion

The experiments in this study were carried out to evaluate the hydrogen reactor by adding a heat pipe and fins. The analysis results are given below for all reactor configurations. The maximum temperature values inside the reactor, the time duration values at which the amount of hydrogen mass is achieved, as well as the absorbed amount of hydrogen mass are all analyzed and discussed.

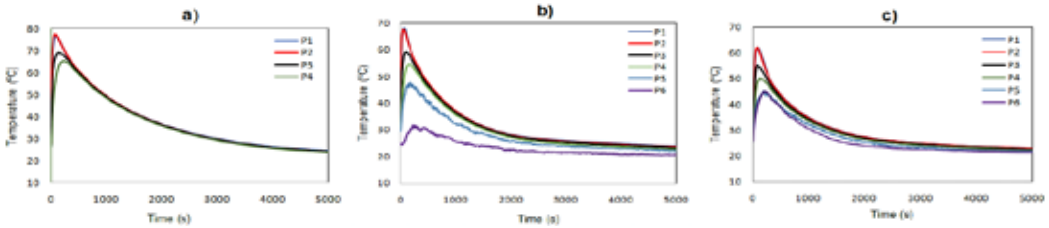


Fig. 3. Temperature profiles of metal hydride bed during the hydriding process for the MHRs under 4 bar pressure a) w/o heat pipe b) with heat pipe c) with finned heat pipe

Fig. 3 shows the temperature variation of metal hydride bed under 4 bar supply pressure during the hydriding process for all MHRs. It is clearly seen a higher temperature was recorded in P_2 position at (z= 20 mm) for all configurations. The P_1 and P_2 presented close temperature because they are located in a reaction volume for metal hydride bed. P_1 is relatively measuring a smaller than the P_2 because the P_1 position is located near the tank bottom through which cooling from bottom side is controlled by convection. Based on the same reason, the P_3 and P_4 presented a smaller temperature than the P_2. They are located out of the reaction volume in the free space (expansion volume), where the heat transfer by convection is playing a role. Accordingly, It is seen the region close to the reactor inlet towards the pores media of the metal hydride powder has the highest temperature in all configurations. These temperature differences involve the absorption process would occur first close to the reactor inlet in the metal regions near the tank wall and then regularly moved toward the central region of the storage tank. Also, ,the heat released during charging process has been removed quickly in case of the reactor with finned heat pipe 62 ºC, and heat pipe reactor 67 ºC, with a comparison to the reactor without heat pipe 77 ºC.

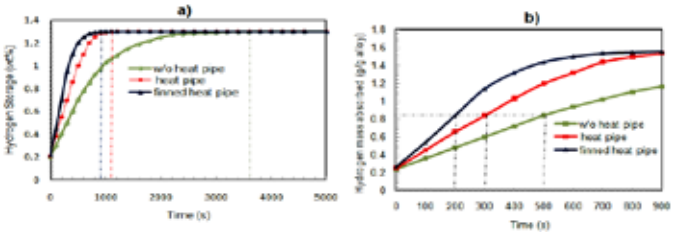


Fig. 4: Time history of the hydrogen stored in the metal hydride bed under 10 bar pressure supply. a) wt%, b) g/g alloy .

The hydryding process was tested at10 bar supply pressure for a duration of 5000 s. The hydrogen storage rates showed in (Fig. 4). The capacity of hydrogen absorbed was approximately 1.3 wt% in all configurations as shown in Fig, 4a. Fig. 4b shows the amount of hydrogen stored by g/g alloy within first 900 s for all MHRs for comparison. For reactor without heat pipe, at 100 s, 200 s, 300 s, 400s, 500 s, 600 s, 700 s, 800 s, and 900s, the storage capacity was: 0.36 g, 0.48 g, 0.60 g, 0.72 g, 0.84 g, 0.94 g, 1.02 g, 1.11 g, and 1.16 g respectively. For heat reactor, at 100 s, 200 s, 300 s, 400 s, 500 s, 600s, 700s, 800s, and 900s, the storage capacity was: 0.46 g, 0.66 g, 0.84 g, 1.03 g, 1.20g, 1.32 g, 1.44 g, 1.5 g, and 1.54 g respectively. And for the finned heat pipe reactor, at 100 s, 200 s, 300 s, 400 s, 500 s, 600 s, 700 s, 800 s, and 900 s, the storage capacity was: 0.54 g, 0.84 g, 1.14 g, 1.32 g, 1.44 g, 1.50 g, 1.54 g, 1.55 g, 1.56 g respectively. It is observed that, the significant improvement of storage performance of the finned heat pipe reactor. For example, the storage duration of 0.84g is required 200s for finned heat pipe reactor, whereas it needs 300 s in the case of the heat pipe reactor, and 500s in the reactor without heat pipe. Furthermore, the time required for the reactor without heat pipe to reach 1.3 wt% was 3600s, whereas in the reactor with heat pipe was 1100 s, and for that one equipped with a finned heat pipe was 900s as shown in Fig. 4a. Thus, the charging time was reduced approximately 75% by using finned heat pipe and 70% by using a heat pipe, this reduction in time shows a development in hydrogen charge by using the heat pipe and fins.

The temperature distribution in the MHRs provides information explaining the improvement in hydiyding process. The hydrogen supply pressure is responsible for enhancing the mass transfer reaction. Therefore, the increased initial hydrogen pressure, simultaneously, raising the absorption reaction speed and charge rates in $LaNi_5$. The temperature profiles on the MHRs at various hydrogen supply pressures, e.g. (2 -10 bars) are shown in (Fig. 5). It is seen that, the reactor temperature increases as the hydrogen inlet pressure increases due to the enhancement of kinetic reaction by development the exothermic absorption reaction between the hydrogen and metal hydride. Accordingly, the maximum temperature was recorded at 10 bar for all MHRs, e.g. 101 ºC (reactor without heat pipe), 93 ºC (reactor with heat pipe), and 83 ºC (finned heat pipe reactor). Comparisons of the

temperature profiles for MHRs during the hydriding process under different pressure are shown in (Fig. 6). It is seen that the device temperature increases as the pressure increases, and the amount of hydrogen stored also increased. The configuration with finned heat pipe shows the most fast charging time and less temperature confirming better heat removal at any pressure value. However, this can be attributed to enhanced heat transfer by utilized a heat pipe and fins in hydriding process. Accordingly, the hydrogen absorption kinetic is improved by helping of the heat pipe and fins.

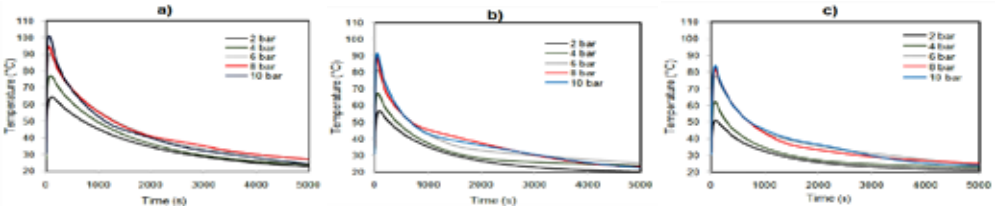


Fig. 5: Effect of the initial hydrogen supply pressure on the average bed temperature at the P_2 position (Z= 20 mm), a) w/o heat pipe, b) with heat pipe, c) with finned heat pipe

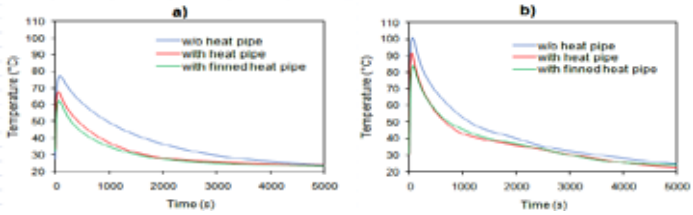


Fig. 6: Comparison of the temperature profiles of the metal hydride bed during the hydriding process for the MHRs w/o heat pipe, with heat pipe and with finned heat pipe a) 4 bar b) 10 bar

IV. Conclusion

This study showed the pilot design of MHRs using $LaNi_5$ material as the storage media to explain the influence of the heat pipe and fins in the hydriding process. Different experiments were done on three reactor configurations, which are manufactured in a laboratory as; a) reactor without heat pipe, b) reactor with a heat pipe, and c) reactor with a finned heat pipe. The study also presents comparisons of the results obtained concerning the hydrogen mass stored and the hydride bed temperature between the reactor configurations. In addition, the effect of the applied hydrogen pressure on the storage time of the proposed configurations was experimentally investigated. The results showed that, the charging of hydride reactors is mainly heat transfer management and the better performance of reactor can be achieved by the configuration which provides successful heat removal. Thus, a significant improvement of storage performance was established by use the finned heat pipe reactor. Consequently, the use of heat pipe could be a good choice to increase hydrogen storage reactor performance. The finned heat pipe configuration confirms the less temperature increased and the fastest charging time. The charging time was reduced approximately 75% with 10 bar hydrogen supply pressure.

Acknowledgements

We would like to thank the Department of Energy Systems Engineering, Karabuk University, Turkey, for authorized us to use their laboratory and providing the experimental equipments.

References

F. Askri, M. B. Salah, A. Jemni, and S. B. Nasrallah, "Optimization of hydrogen storage in metal-hydride tanks," *International journal of hydrogen Energy,* vol. 34, pp. 897-905, 2009.

Y. Kaplan, "Effect of design parameters on enhancement of hydrogen charging in metal hydride reactors," *International Journal of Hydrogen Energy,* vol. 34, pp. 2288-2294, 2009.

M. Kayfeci, F. Bedir, and H. KURT, "Experimental investigation of the effects of vessel design and hydrogen charge pressure on metal hydride based hydrogen storage parameters," *Journal of Thermal Science and Technology,* vol. 34, pp. 83-90, 2014.

Boo, J.H., et al. *Numerical analysis of a metal hydride reactor with embedded heat pipes to enhance heat transfer characteristics*. in *ASME 2009 Heat Transfer Summer Conference collocated with the InterPACK09 and 3rd Energy Sustainability Conferences*. 2009. American Society of Mechanical Engineers.

C. Chung, S.-W. Yang, C.-Y. Yang, C.-W. Hsu, and P.-Y. Chiu, "Experimental study on the hydrogen charge and discharge rates of metal hydride tanks using heat pipes to enhance heat transfer," *Applied energy,* vol. 103, pp. 581-587, 2013.

The Relationship Between Flow Channel Geometry and Pressure Drop in a Direct Methanol Fuel Cell with Parallel Channels

Anil Can Turkmen[1], Didem Demirtas[2], Hatice Esen[2], Cenk Celik[1]

[1]Department of Mechanical Engineering, Kocaeli University, Kocaeli, Turkey
[2]Department of Industrial Engineering, Kocaeli University, Kocaeli, Turkey

In this study, the relationship between the pressure drop on the channels due to the methanol flow and the geometry of the flow channels on the anode side of a direct methanol fuel cell has been investigated. Parallel type channels are used as flow channels. The active area of the fuel cell is 5x5 cm². The system consists of channels that are optimally placed in the active area, with channel widths and distance of the channels kept constant. Combinations of 1, 1.5, 2, 2.5, 3 mm measurements were used for flow channel width and distance between channels. The ratio of the area created by the prepared geometries to the active area (percentage of contact area) is defined as a new parameter. There was a statistically significant difference between the flow channel widths and the distance between the channels and the pressure.

Keywords: methanol fuel cell, flow channel geometry, pressure drop

Hydrogen permeation characteristics through palladium membrane with/without vacuume

[1]Shang-Wei, Lin, [2,*]Wei-Hsin, Chen
[1] National Cheng Kung University, senior undergraduate student, International Degree Program on Energy Engineering, Tainan 70101, Taiwan
[2] National Cheng Kung University, Distinguished Professor, Department of Aeronautics and Astronautics, Tainan 70101, Taiwan

E-mail: weihsinchen@gmail.com; chenwh@mail.ncku.edu.tw

Abstract
A vacuum pump is being applied on the outlet sector of a typical membrane system. Same pressure differences is being controlled with/without vacuum. The permeances and the flow rate of two palladium (Pd) membranes under same pressure difference in pure H_2, binary gas mixtures are investigated experimentally. With binary gas condition of 10% impurities (N_2, CO_2, or CO) in H_2, the result shows that under same pressure difference, the one with vacuum on the outlet sector performs better regardless of gas types. The flow rate for pure H_2 increased by 5% to 17% with vacuum and increased by 15% to 136% for binary gas. The profiles shows that the reduction by the gas impurities is ranked as $CO>CO_2>N_2$ and the effect of vacuum indicates that the worse permeance for the impurities it is, the more it can be improved by vacuum, the improvement is also ranked as. $CO>CO_2>N_2$.

Keywords: Pd-memebrane, vacuum, binary gas, same pressure difference.

Exergetic Comparison of Various Flow Patterns in PEMFCs

*Suha Orçun MERT, M. Mücahid TOPRAK
Yuzuncu Yıl University, Department of Chemical Engineering 65080, Campus, Van

*E-mail: orcunmert@gmail.com

Abstract
Energy need of the civilized world is ever increasing, and as such, the subject of energy production from renewable energy sources is gaining popularity in scientific studies. Amongst these studies are the researches on fuel cell systems. In this study, the flow channels of the "proton exchange membrane" (PEM) type fuel cell were designed, modelled, and studies were conducted on three-dimensional channels of various designs via Comsol Multiphysics simulation software, with hopes to contribute to the renewable energy solutions. Proposed fuel cell designs and geometries of flow channels were compared to existing fuel cells' with exergetically efficient designs, in terms of total exergy efficiency. Exergy efficiency analysis was conducted on the membrane surfaces of the proposed flow channels. Anode and cathode side exergy analyses, polarization curve of the system, voltage, current and produced power parameter results were also inspected.

Key Words: Fuel Cell, PEM, Comsol Multiphysics, Modeling and Simulation, Flow Plates, Exergy

I. Introduction

Fuel cells, having both portable and embedded applications, are becoming increasingly significant alternative energy production systems. In parallel with the developments in nano-technology, PEM fuel cells have drawn the attention of researchers throughout the world with a growing momentum, mostly due to their ability to use various components like hydrogen, methanol and formic acid as fuel. As evidenced by scientific and industrial efforts focused on them, number of fuel cells and related applications are increasing, perhaps affected by advances in nano-technology.

Inspection of literature reveals a substantial amount of research on fuel cell systems. These studies mostly focus on catalyst and membrane improvements, performance analyses for various cell systems, exergy-energy analyses and storage of hydrogen fuel.

One study has used COMSOL software to observe potential improvements in a mobile PEM fuel cell by altering cathode channel geometry (Henriques, César, and Branco 2010). Another study inspected and compared thee different geometric collector designs in a Proton Exchange Membrane fuel cell (PEMFC), while keeping fluid dynamics in mind. The geometries inspected were serpentine, parallel and square layouts (Zahi, Rossi, and Faucheux 2011). One study had designed flow channels for a fuel cell in a planar space by transforming 3D mathematical space into a 2D model, running simulations in this environment (Hamilton and Pollet 2010). In another study a derived mathematical model was used to gather detailed results for for a mechanical fuel cell's parallel flow channels (Ly, Birgersson, and Vynnycky 2012). In one study, two versions of a flow channel plate for PEM fuel cell was inspected under high voltage and current in terms of reactants' spread over catalyst surface (Mehta and Cooper 2003; Springer, Zawodzinski, and Gottesfeld 1991). Another study has inspected three variations of a flow plate (straight, serpentine and mixed) and simulated spread properties, discussing the results (Jithesh et al. 2012; Karthikeyan et al. 2013).

This study however, inspects six types of flow channel designs through COMSOL Multiphysics software modeling and simulation, compares them in terms of exergy and performance analyses, and discusses the reasons behind the most efficient design.

I.1. Fuel Cell

A fuel cell is a system that generates electrical energy as a result of an electrochemical reaction between an oxidant and a suitable fuel. After the fuel cell reaction -which can be described as the reverse of electrolysis reaction- electricity is produced, in the form of direct current (DC). Fuel cells are akin to batteries in terms of their working principles. Traditional batteries also convert energy which has been stored in them into electrical energy through an electrochemical reaction. The energy supplied by batteries and accumulators, however, is limited by their internal energy (EG&G Technical Services, Inc. and EG&G Technical Services 2004; Gregor Hoogers and Hoogers 2003). Fuel cells, on the other hand, produce energy continuously and endlessly, as long as fuel and air are supplied into them.

Basically, a fuel cell is composed of the electrolyte, and electrodes which are in contact with a surface of the electrolyte each; the anode on one side and the cathode on the other.

I.2. PEM (Proton Exchange Membrane) Fuel Cell

The cost of energy keeps increasing, perhaps tied to the ever increasing energy demand. The standards set by civil demands in developed countries also affect trend on developing countries, which lead the world towards new, innovative and green energy sources. One of the few technologies that can answer such demands is the fuel cell systems. In terms of thermal cycles, fuel cell systems are capable of producing electrical energy from the chemical energy stored within the fuel with efficiencies of up to 80%, and without energy transformation. Due to the

nature of PEM fuel cells, the only waste produced are usable water and heat, which makes PEM's quite compatible with nature.

Proton Exchange Membrane fuel cells have a relatively simple design and operation process. PEMs also have a higher power density, and lower volume and weight compared to other fuel cells. All fuel cells contain a thin, polymer membrane. Sized in micron levels, this membrane is proton permeable in PEM type cells, which gives them their name. PEMs work under 100°C, usually at the levels of 60-80°C.

As long as hydrogen fuel is fed towards the anode side, it gets decomposed into its ions here. Meanwhile, protons reach cathode through the proton-permeable membrane, and electrons arrive to the cathode through another circuit. As the oxygen dissipates into its protons and reacts with the H_2 ions over the electrodes, the reaction is completed. This reaction produces water and heat. Since the solid membrane's ion permeability -which is directly affected by the moisture of membrane- is a major factor in these events, humidity of the membrane is a major performance factor. This requires management of moisture levels of the membrane, which usually is handled by an additional water management unit in the cell, tasked with keeping the humidity steadily at optimum levels (Broka and Ekdunge 1997; Karthikeyan et al. 2013).

I.3. Fuel Cell Performance.

Fuel cell performance is generally seen as the sum of performances of its components. These performances are tightly coupled to the reaction's occurrence on the catalyst, generation of current by collection of electrons, transfer of hydrogen ions through membrane, water production as a result of the combustion reaction, and finally, electrical resistances of intracellular components. This is a complex process composed of many chemical thermodynamic processes. As is the case in many thermal systems, operating conditions have strong influences on these processes. The main operating conditions which affect fuel cell performance are temperature, pressure, membrane thickness, humidity and current density. A uniform reaction with constant speed along the catalyst surface depends on optimal distribution of temperature, humidity and concentration. Such a distribution can only be achieved by an optimum distribution of content over the flow plates. In this study, simulation and modeling of alternative flow plate geometries were inspected with an exergetic aspect in search for the most effective distribution pattern as being a frontier study in this respect. As a result, a homogeneous distribution of the performance-affecting criteria of the fuel cell -like the temperature, concentration, and humidity- has been achieved over the cell surface and the results were examined and interpreted.

II. Material and Methods

II.1. Simulation with COMSOL Multiphysics

As the first stage of the study, the proposed fuel cells and their flow channels were designed using Comsol Multiphysics program. This software has an integrated multi-physics infrastructure for various engineering endeavors. It includes various equipment in the simulation environment already modeled (Dickinson, Ekström, and Fontes 2014). The software also gives quick results as the physical interfaces of many theoretical processes are pre-modelled within it. It has a wide coverage of applications from to the fluid flow problems to transport of heat, and from structural mechanics to electromagnetic analyses (Karthikeyan et al. 2013) (Comsol 2010) (COMSOL Inc. 2013).

Figure 1 displays the required parameters to model a fuel cell in a visual overlay. All the proposed designs in this study were based on this model. The anode and cathode flow channels, gas diffusion layers (GDL), the membrane and the porous electrodes are the primary constituents of a fuel cell model.

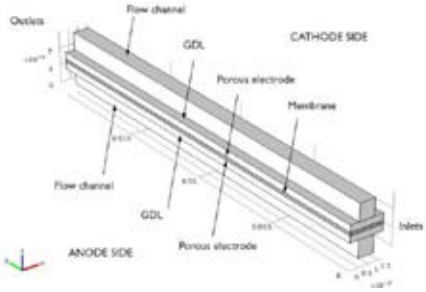


Fig. 1: COMSOL Multiphysics Model View (Water and This 2010)

A total of 6 alternate fuel cell designs were analyzed exergetically in these simulations, and the results were discussed and interpreted afterwards. The modeling of the fuel cell includes modeling of electrochemical currents, mass transfer and momentum transfer.

The electrochemical current modeling is done by using Reacting flow in porous media and current distribution interfaces in Comsol. The models based on Ohms law and solving for these considering the cell GDLs, and in the porous electrodes, and in the electrolyte membrane. These are dependent to the concentration of the species and ionic and electronic potentials.

The current density of the anode of the fuel cell is calculated depending on the following formula locally that is basically based on Butler-Volmer expression

$$H_2 \rightarrow 2H^+ + 2e^- \quad (1)$$

$$i_a = i_{0,a}\left(\frac{c_{H_2}}{c_{H_{2,ref}}}\right)^{0.5}\left(\frac{\alpha_{a,a}+\alpha_{c,a}}{RT}\right)F\eta_a \quad (2)$$

where c_{H2} is the local hydrogen concentration and $c_{H2,ref}$ a hydrogen reference concentration

Cathode reaction is as follows in a PEM fuel cell

$$O_2 + 4H^+ + 4e^- \rightarrow 2H_2O \quad (3)$$

for the oxygen reduction reaction the following current density equation is used that is a version of Tafel-equation which is derived to implement the effect of concentration.

$$i_c = -i_{0,a}\left(\frac{c_{O_2}}{c_{O_{2,ref}}}\right)\exp\left(-\frac{\alpha_{c,c}}{RT}\right)F\eta_c \quad (4)$$

The mass transfer phenomena in the fuel cell is solved using Transport of Concentrated Species interfaces of the Comsol. This interface depends on the Maxwell-Stefan equations and these are used for both flow channels, GDL and electrodes. The mass fractions of the species are set at the inlets and the remaining concentrations are calculated dynamically.

The momentum transfer based on the Navier-Stokes equations in flow channels and Brinkman equations for the porous gas diffusion layers (GDLs) and electrodes.

There are some general assumptions are made regarding the cell geometry. That are

- Boundaries at the anode side are assumed as to have zero electronic potential,
- The boundaries at the cathode side are assumed to be at the cell potential.
- Remaining boundaries are assumed as electrically isolated, and has zero flux for mass transfer

II.2. Proposed flow channel geometries for PEM

Figure 2 displays geometrical views of six proposed fuel cell designs in 3D. The geometries are developed regarding the currently used geometries and the geometries that are thought to be good candidates of having a high and homogen distributed fuel cell exergetic efficiency

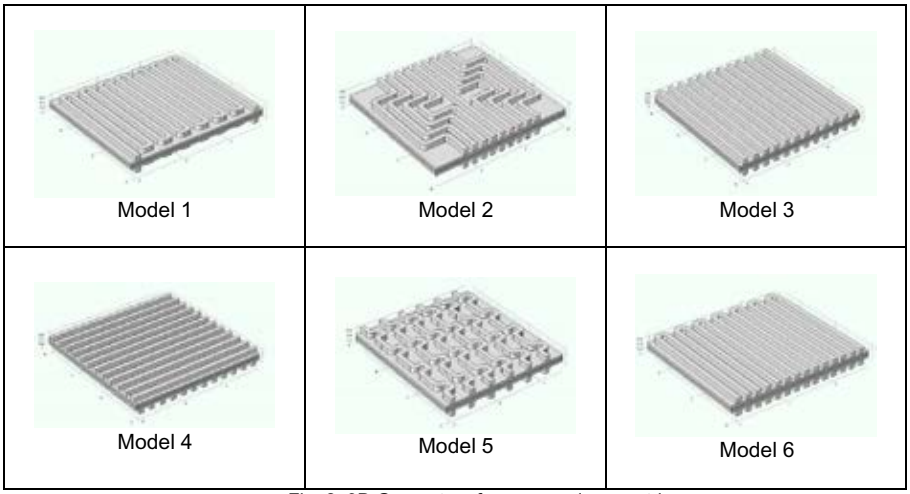


Fig. 2: 3D Geometry of a proposed geometries

The 3D Mesh (Meshwork) for the geometries are developed using physics oriented mesh algorithm of the Comsol with fine meshes in order to have a better results structure. Figure 3 display meshwork for the Model 6 geometric design. The solution based on this meshwork took approximately 8 to 12 hours for each model with the RenderBox Pro workstation (Dual Intel Xeon Processor E5-2620, 32 GB DDR4-1333MHz).

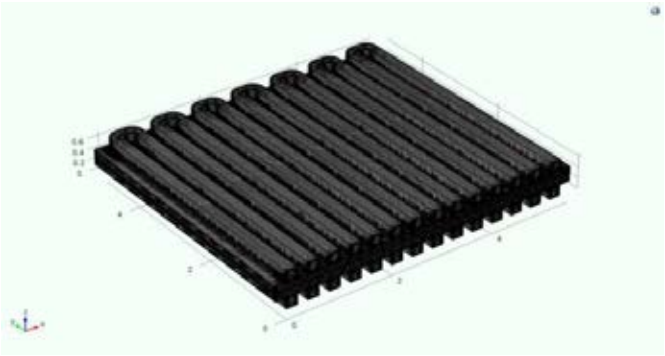


Fig. 3: 3D Mesh view of the 7 Inlet-Outlet Fuel Cell Design

III. Exergy Analysis

Compared to thermodynamics' first law which focuses on the quantity of the energy in a system, exergy analyses utilizes the second law to also inspect the energy's quality (Dincer 2002; Tsatsaronis 2007) . This makes it a very good tool to compare energy systems with similar sizes in terms of work they can produce.

Since the quality of the energy is also evaluated along with quantity, exergy analysis is useful in figuring out the real work-related value of a given system, which in turn helps locating the sources of inefficiencies, energy losses, and thermo-dynamic inadequacies within it.

Considering all these, exergy analysis becomes an unavoidable method if accurate and consistent evaluations and calculations are strived for in determining a system's true potential (Dincer and Cengel 2001; M. Rosen and Dincer 1997).

There are various components of the total of exergy in a system and since other forms except physical and chemical exergies are in extremely small amounts in PEM fuel cells, they are ignored during this study. This means the total exergy in the system can be defined as (Mert, Dincer, and Ozcelik 2012):

$$E = E_{Chem} + E_{Phy} \quad (5)$$

Physical exergy is the definition of work performed by the energy that forms as a result of thermal processes between the initial thermal state of the system and the final, dead state (in which the system is in complete thermal balance with its environment), and is calculated with the below formulae (Mert et al. 2007; Mert, Dincer, and Ozcelik 2012):

$$E_{Phy} = (E - U_0) + P_0(V - V_0) - T_0(S - S_0) \quad (6)$$

$$E_{Phy} = (H - H_0) + T_0(S - S_0) \quad (7)$$

where 0 (reference) indicates the dead state.

The amount of work performed by the energy produced in system until it reaches chemical balance with the environment is called chemical exergy. For pure substances, the work produced until they reach the reference condition concentrations is calculated with the below formula (Mert et al., 2007, 2012).

$$E_{Chem} = RT_0 \ln\left(\frac{P}{P_0}\right) \quad (8)$$

This means substances in the system that contain materials other than reference materials must first be reduced to their components defined in the reference conditions and stabilized. Formula 5 given below is used for this purpose.

$$E_{Chem} = \Delta G - \sum_j \vartheta_j E_{0,che,j} \quad (9)$$

ΔG indicates free Gibbs energy, v indicates stoichiometric coefficient, while $E_{0,che,j}$denotes standard chemical exergy value. After all of these, chemical exergy of the system can be calculated using standard chemical exergy table and equation 6 below (M. A. Rosen and Dincer 2003).

$$E_{Chem} = E_{0,Chem,j} + \sum(x\ln(x)) \quad (10)$$

where x denotes the molar fraction.

Fuel cell voltage and power, and the current feed will also be added to the aforementioned equations in order to analyze the exergy within the system of the fuel cell, with the formula given below.

$$I_{FC} = \sum \dot{E}_{mass,i} - \dot{E}_{mass,o} - \dot{E}_{heat} - \dot{E}_{work} \quad (11)$$

System efficiency is calculated based on the energy and exergy analyzes and is achieved with the below equations:

$$\eta_{sys,en} = \frac{\dot{W}_{net}}{HHV_{H_2} \cdot F_{H_2,in}} \quad (12)$$

$$\eta_{sys,ex} = \frac{\dot{W}_{net}}{\dot{E}_{in}} \quad (13)$$

The derived exergy equations are implemented to the Comsol and the 3d flow of the exergy in the fuel cell is simulated.

III.1. Exergy Analysis Results on Proposed Fuel Cell Designs and Discussion

The results of the analyses on the 6 proposed flow plate designs in this study will be given below. Hydrogen and Oxygen exergies will be indicated on x-y axis, while exergy efficiency, polarization curve, power and current values based on current density will be indicated with graphs. Active membrane surface area was kept the same between all the proposed designs, and channels were designed with the same total area and dispersed on the plate surface as homogenously as possible. Voltages were also kept fixed (0.5V – 0.7V)In order to have consistently accurate comparisons between alternative geometries, channel width and height was fixed, causing the same amount of pressure loss per unit distance travelled in all models.

III.1.1. Exergy Analysis Results for Design 1

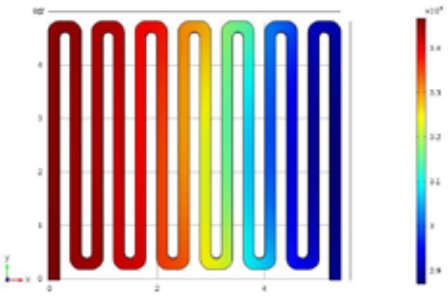


Fig.4: Hydrogen exergy x-y axis for Design 1

x-y axis for the hydrogen within the fuel cell anode side is given in Figure 4. It is evident that towards the +x direction, hydrogen exergy dissipates rather steadily, due to consistent reduction of hydrogen over the channel as it travels on the anode side.

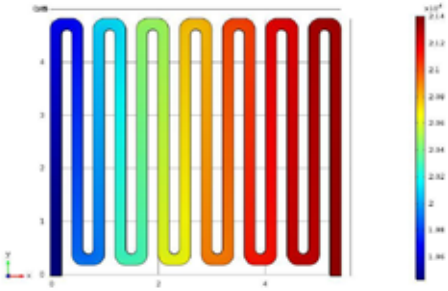


Fig.5: Oxygen exergy x-y axis for Design 1

As can be seen in Figure 5, oxygen exergy in the cathode side drops steadily as it moves in the channel, similar to the hydrogen in the anode side given in Figure 4. As the amount of water produced in the cathode side, the effect of oxygen increases.

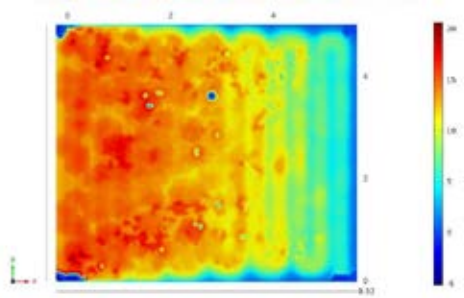


Fig.6: Exergy efficiency for Design 1

Figure 6 displays the exergy efficiency of the system. As evident in the figure, the efficiency is high in the entrance area of the plate where reaction speed and current density is high, while efficiency is comparatively low in the other areas. This is caused by the build-up in the entrance area, which also causes more strain on the membrane.

III.1.2. Exergy Analysis Results for Design 2



Fig.7: Hydrogen exergy x-y axis for Design2

x-y axis for the hydrogen within the proposed fuel cell's anode side is given in Figure 7. Considering the sudden drop of hydrogen amount towards the middle in +y direction, hydrogen exergy could evaluated to be low.

Oxygen exergy for this design can be seen in Figure 8 x-y axis. Oxygen exergy is relatively lower to hydrogen exergy given in Figure 7 due to the water production.

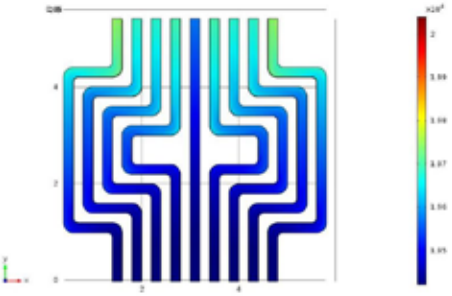


Fig.8: Oxygen exergy x-y axis for Design 2

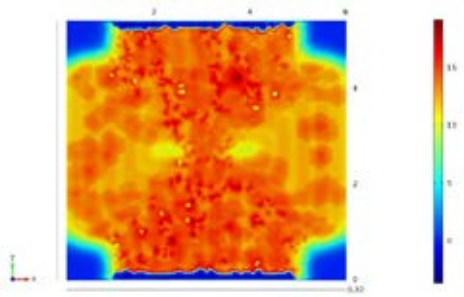


Fig.9: Exergy efficiency for Design 2

Figure 9 displays the total exergy derived from Hydrogen and Oxygen exergies, indicating the exergy efficiency of the system. As evident in the figure, there is a significant build-up towards the middle. Membrane activity is rather high up to this point, but drops suddenly henceforth, plummeting the efficiency. Furthermore, the unused space in the corners of the design effects overall efficiency adversely. All these considered, it is safe to say Design 2 has lower exergy efficiency compared to Design 1.

III.1.3. Exergy Analysis Results for Design 3

Hydrogen exergy x-y values for Design 3 are displayed in Figure 10, while oxygen exergy x-y values are given in Figure 11. As can be seen in these figures, gasses fed to the system have a homogenous distribution on the surface. This is a good indication in terms of operation costs.

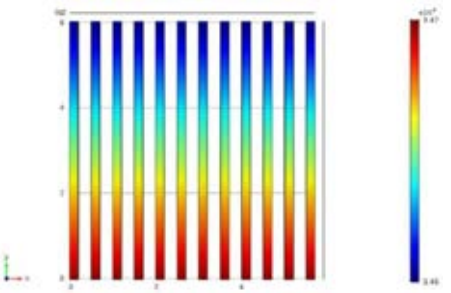


Fig.10: Hydrogen exergy x-y axis for Design 3

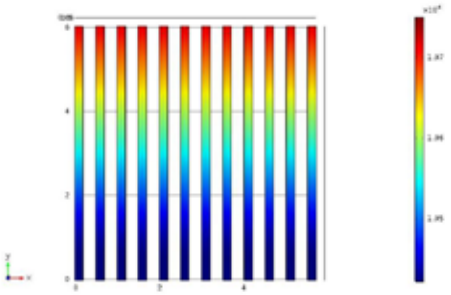


Fig.11: Oxygen exergy x-y axis for Design 3

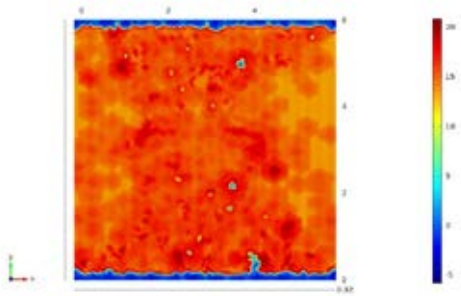


Fig.12: Exergy efficiency for Design 3

Total exergy efficiency for Design 3 can is displayed in Figure 12. The fuel and the oxygen clearly disperses homogenously on the plate, creating a positive impact on the longevity and thus running costs for the system. Moreover, the achievement of a current of 0.4A/cm^2 on the polarization curve further contributes to the cost efficiency.

III.1.4. Exergy Analysis Results for Design 4

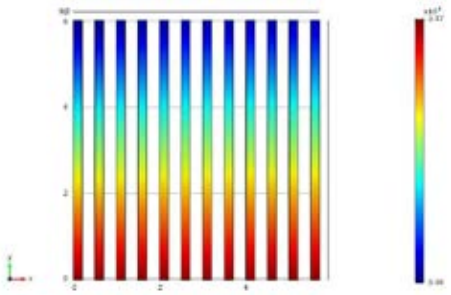


Fig.13: Hydrogen exergy x-y axis for Design 4

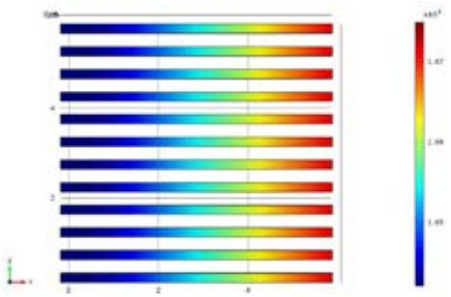


Fig.14: Oxygen exergy x-y axis for Design 4

Hydrogen exergy x-y values for Design 4 are displayed in Figure 13, while oxygen exergy x-y values are given in Figure 14. As can be seen in these figures, the performances are quite similar to that of Design 3.

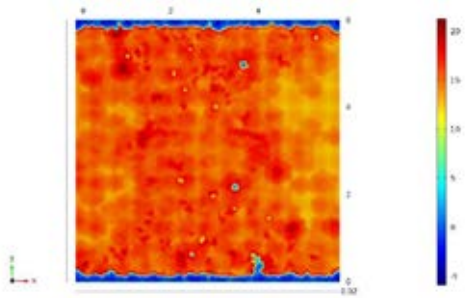


Fig.15: Exergy efficiency for Design 4

Total exergy efficiency for Design 4 fuel cell is given in Figure 15. When exergy values over the active surface are evaluated, the homogenous distribution is clearly evident again, like in the Design 3, which indicates the change in geometry direction of the hydrogen flow of the design did not have much of an effect of efficiency.

III.1.5. Exergy Analysis Results for Design 5

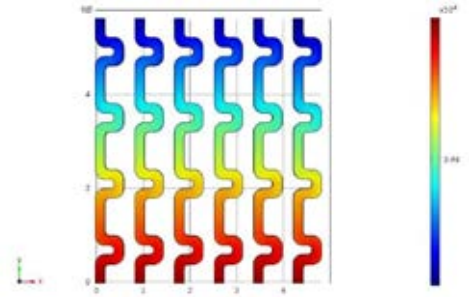


Fig.16: Hydrogen exergy x-y axis for Design 5



Fig.17: Hydrogen exergy x-y axis for Design 5

Hydrogen exergy x-y values for Design 5 are displayed in Figure 16, while oxygen exergy x-y values are given in Figure 17. As evident in these figures, there is a fall in concentration for both the hydrogen on cathode side and oxygen on anode side in +y direction, towards the middle regions. This situation effects exergy efficiency of the design adversely.

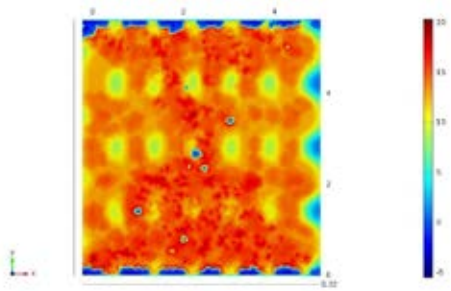


Fig.18: Exergy efficiency for Design 5

Total exergy efficiency for this design is displayed in Figure 18. Due to having more unused space compared to other flow plate designs, Design 5 suffers a lowered exergy efficiency. This situation arises due to the wavy geometrical design of the plate. It causes a lower flow density, which, combined with the unused spaces, ruin the homogeneity of the distribution.

III.1.6. Exergy Analysis Results for Design 6

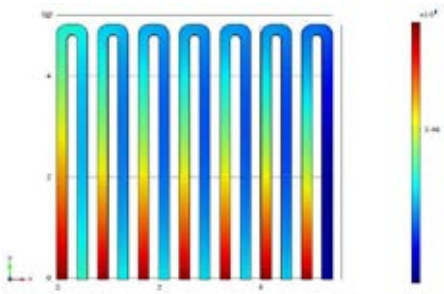


Fig.19: Hydrogen exergy x-y axis for Design 6

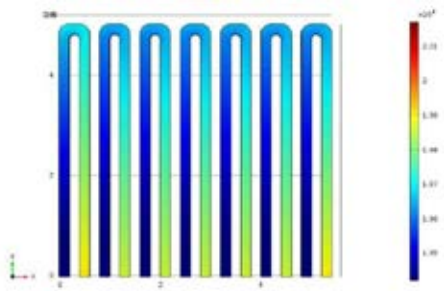


Fig.20: Oxygen exergy x-y axis for Design 6

Hydrogen exergy x-y values for Design 6 are displayed in Figure 19, while oxygen exergy x-y values are given in Figure 20. Both figures indicate their respective gasses are dispersed along the whole channel quite smoothly.

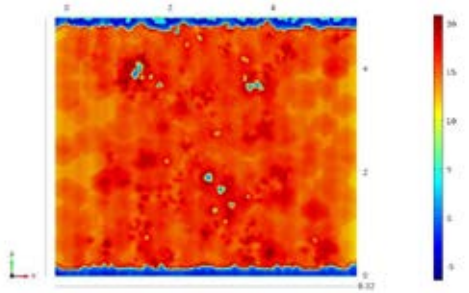


Fig.21: Exergy efficiency for Design 6

Total exergy efficiency for the system proposed in Design 6 is displayed in Figure 21. The high efficiency is clearly visible, and it's due to the uniform distribution of both the air and the fuel over the membrane. Even though there seem to be some spots where the efficiency seems to have gone down a little bit, overall efficiency is still higher than all the other designs'.

IV. Conclusions

In this study, 6 alternative versions of flow channel plate designs were proposed, all of which were modeled in COMSOL Multiphysics software and analyzed under simulation. Exergy changes on the hydrogen and the oxygen, total exergy efficiency, along with polarization curve voltage, power and current values were evaluated. In the end, multiple inlet designs were found have some of an advantage in distributing the fuel over the plate uniformly, enabling them to reach higher efficiency levels. Cross-channel designs were found to have positive effect in case of short channeled designs, while they were found to have negative effects in case of long channel designs. When the fuel cell surface area is utilized homogenously, hydrogen and air reaction inside the system takes place in higher speeds, and the strain of the reaction is distributed evenly along the plate, preventing any over-worn spots that could cause physical damage to the plate. Modeling and simulating various flow plate designs reduce the otherwise expensive actual tests and reduce the time needed to get results, they are henceforth valuable tools for researchers working of fuel cell design.

Acknowledgement

The authors gratefully acknowledge the financial support provided by the Scientific and Technological Research Council of Turkey (TÜBİTAK-MAG-115M741).

References

Broka, K, and P Ekdunge. 1997. "Modelling the PEM Fuel Cell Cathode." *Journal of Applied Electrochemistry* 27: 281–89. doi:10.1023/A:1018476612810.

Comsol. 2010. *Comsol Multiphysics User's Guide*. *Building*. doi:10.1007/s10237-010-0257-z.

COMSOL Inc. 2013. "COMSOL Multiphysics." *Interfaces*.

Dickinson, Edmund J.F., Henrik Ekström, and Ed Fontes. 2014. "COMSOL Multiphysics®: Finite Element Software for Electrochemical Analysis. A Mini-Review." *Electrochemistry Communications* 40 (March): 71–74. doi:10.1016/j.elecom.2013.12.020.

Dincer, Ibrahim. 2002. "The Role of Exergy in Energy Policy Making." *Energy Policy* 30: 137–49. doi:10.1016/S0301-4215(01)00079-9.

Dincer, Ibrahim, and Yunus A. Cengel. 2001. "Energy, Entropy and Exergy Concepts and Their Roles in Thermal Engineering." *Entropy*. doi:10.3390/e3030116.

EG&G Technical Services, Inc., and Inc. EG&G Technical Services. 2004. *Fuel Cell Technology-Handbook, 7th Edition*. U.S. Department of Energy.

Gregor Hoogers, and Gregor Hoogers. 2003. *Fuel Cell Technology – Handbook*. CRC Press.

Hamilton, P. J., and B. G. Pollet. 2010. "Polymer Electrolyte Membrane Fuel Cell (PEMFC) Flow Field Plate: Design, Materials and Characterisation." *Fuel Cells*. doi:10.1002/fuce.201000033.

Henriques, T., B. César, and P. J Costa Branco. 2010. "Increasing the Efficiency of a Portable PEM Fuel Cell by Altering the Cathode Channel Geometry: A Numerical and Experimental Study." *Applied Energy* 87: 1400–1409. doi:10.1016/j.apenergy.2009.09.001.

Jithesh, P.K., A.S. Bansode, T. Sundararajan, and Sarit K. Das. 2012. “The Effect of Flow Distributors on the Liquid Water Distribution and Performance of a PEM Fuel Cell.” *International Journal of Hydrogen Energy*. doi:10.1016/j.ijhydene.2012.08.058.

Karthikeyan, P., M. Muthukumar, S. Vignesh Shanmugam, P. Pravin Kumar, Suryanarayanan Murali, and A.P. Senthil Kumar. 2013. “Optimization of Operating and Design Parameters on Proton Exchange Membrane Fuel Cell by Using Taguchi Method.” *Procedia Engineering* 64: 409–18. doi:10.1016/j.proeng.2013.09.114.

Ly, H., E. Birgersson, and M. Vynnycky. 2012. “Fuel Cell Model Reduction through the Spatial Smoothing of Flow Channels.” *International Journal of Hydrogen Energy* 37: 7779–95. doi:10.1016/j.ijhydene.2012.01.129.

Mehta, Viral, and Joyce Smith Cooper. 2003. “Review and Analysis of PEM Fuel Cell Design and Manufacturing.” *Journal of Power Sources*. doi:10.1016/S0378-7753(02)00542-6.

Mert, S. O., I. Dincer, and Z. Ozcelik. 2012. “Performance Investigation of a Transportation PEM Fuel Cell System.” *International Journal of Hydrogen Energy* 37 (1): 623–33.

Mert, S O, Z Özçelik, Y Özçelik, and I Dinçer. 2007. “Multi-Objective Optimization of A Fuel Cell System for Transportation Application” 3 (1): 2007.

Rosen, M. A., and I. Dincer. 2003. “Exergy-Cost-Energy-Mass Analysis of Thermal Systems and Processes.” *Energy Conversion and Management* 44: 1633–51. doi:10.1016/S0196-8904(02)00179-6.

Rosen, MA, and Ibrahim Dincer. 1997. “On Exergy and Environmental Impact.” *International Journal of Energy Research* 21: 643–54. doi:10.1002/(sici)1099-114x(19970610)21:7<643::aid-er284>3.0.co;2-i.

Springer, T. E., T. A. Zawodzinski, and S. Gottesfeld. 1991. “Polymer Electrolyte Fuel Cell Model.” *Journal of the Electrochemical Society* 138: 2334–42. doi:10.1149/1.2085971.

Tsatsaronis, George. 2007. “Definitions and Nomenclature in Exergy Analysis and Exergoeconomics.” *Energy* 32 (4): 249–53. doi:10.1016/j.energy.2006.07.002.

Water, C, and C This. 2010. “Mass Transport Analysis of a High Temperature PEM Fuel Cell.” *Comsol*. Comsol.

Zahi, I., C. Rossi, and V. Faucheux. 2011. “Micro PEM Fuel Cell Current Collector Design and Optimization with CFD 3D Modeling.” *International Journal of Hydrogen Energy* 36: 14562–72. doi:10.1016/j.ijhydene.2011.08.020.

Quasistatic Model Based Analysis of Direct Methanol Fuel Cell System for Hybrid Vehicular Applications

[1,2*]Mustafa Umut Karaoğlan, [2]Alper Can İnce, [1]Can Özgür Çolpan, [1]Nusret Sefa Kuralay

[1] Dokuz Eylul University, Faculty of Engineering, Mechanical Engineering Department, Tinaztepe, Buca, Izmir, 35397, Turkey
[2] Dokuz Eylul University, The Graduate School of Natural and Applied Sciences, Mechanical Engineering Department, Tinaztepe, Buca, Izmir, 35397, Turkey

*E-mail: mustafa.karaoglan@deu.edu.tr

Abstract
Different operating scenarios can be used in a hybrid system based on a direct methanol fuel cell (DMFC) and a battery. In this paper, a DMFC system model is integrated into a model formed for a hybrid vehicular system which consists of a battery, a DMFC stack and its auxiliary equipments, and the model is simulated in Matlab/Simulink environment using quasistatic approach. An algorithm for the energy management of the system is also developed considering the state of charge (SOC) of the battery. In the DMFC system model, DMFC current and empirical data for the polarization curves, and methanol crossover and water crossover rates are taken as the input parameter; whereas the stack voltage, the remaining methanol in the fuel tank and the power demand of auxiliary equipments are taken as the output parameters. In this model, the methanol consumption, and the water and CO_2 production are found applying mass balances for each component of the system. The results of the simulations helped to give more insights in the operation of both DMFC system and hybrid system.

Keywords: DMFC, fuel cell system, quasistatic model, vehicular application

I. Introduction

Direct methanol fuel cells can be considered to be a source of power and energy conversion device for vehicular system. Pure methanol (CH_3OH) and recycling water (generated at the cathode compartment) are used as fuel in DMFC systems while carbon dioxide (CO_2) occurs as product. Therefore, the balance of fuel concentration and amount of products play a significant role in a DMFC system.

Several studies on DMFC are carried out in the literature at cell and stack level. However, studies that focused on the integration of DMFC model into any system model, are not sufficient. One of the earliest steady-state studies on simulation of the DMFC systems was published by Von Andrian and Meusinger (2000), who examined the effects of operating conditions such as temperature, pressure, air to fuel ratio and methanol permeation on the fuel cell system performance. They calculated the electrical system efficiency and heat balance with varying the selected parameters. They found that reducing the air to fuel ratio leads to a higher system efficiency. In addition, the amount of permeating mathanol was found to reduce the system efficiency dramatically. Heat and power management of a DMFC system was described by Dohle et al. (2002) through modelling and experimental investigation of this system. They presented the modeling equations including mass, energy and heat balances. According to the results of their study, the system pressure and the air flow rate have an important impact on both the system power and efficiency. An alternative approach for modeling a DMFC system was developed by Zeneith et al. (2017). They focused on reducing the high methanol loss by evaporation in the separator and mixer. Therefore, they modified their previous system which they called mingled outlet system to the so-called highly integrated system and both were compared. In addition, they found the amount of methanol crossover and evaporation using simulations.

In this study, the amount of the methanol consumption, water production and consumption, CO_2 production and required air are found for each component of fuel cell by simulation of DMFC in Matlab/Simulink with using experimentally obtained water crossover rate, methanol permeation rate and current density data for various methanol concentrations.

II. System Modeling

A fuel cell hybrid vehicle system contains electric motor, battery, and fuel cell for the power arragenments and DC/DC converters for the voltage arragenments. Apart from those main powertrain elements, power requirement on the electric motor of a vehicular system can be calculated by speed profile of the vehicle, which depends on the selected driving cycle. Power requirement in the electric motor is determined by using longitudinal motion equations with small sized vehicle parameters and a proper drive cycle. In this study, drive cycle profile consists of three acceleration and two deceleration sections in a cycle which consists of 70 seconds and the vehicle (approximately 120 kg with the driver) reaches 12 km/h top speed. Hybrid powertrain model is designed in Simulink environment according to the power requirement on the tire-road surface.

The quasistatic method is similar to the method applied by Guzzella et al. (2005) in which the power outputs and performances of each complex powertrain structures were investigated. This approach offers design flexibly control of each subsystem to optimize the power flows in the powertrain system. Each powertrain element illustrated with its input and output parameters as the basic blocks is shown in Fig. 1. Electric motor block (EM) calculates the current requirement (I_{EM}) of the electric motor by using the operating voltage (U_{EM}) and power (P_{EM}). If the SOC of battery is higher than 85%, operation algorithm block (OA) does not allow fuel cell (FC) operation and power input

to auxiliary units, and current (I_{FC}) and voltage (U_{FC}) of FC have zero values. Battery is the only current source to response the demand of EM when FC is in the off mode. When the SOC is under the 85% level, FC operates from 0.05 A/cm^2 to 0.4 A/cm^2 current density which changes linearly, between 85% and 0% SOC. State of charge control block (SC), which is integrated into battery block (BT), uses energy consumption (E_B) as input and calculates remaining battery capacity (Q_B) to determine SOC and voltage drops (U_D) as output parameters. Methanol fuel control (MC) works inside FC block to calculate the state of fullness of methanol in storage tank (SOF_{MeOH}) as output parameter depending on the methanol consumption rate ($\dot{m}$); and the information about methanol state in the tank is transmitted to the OA block to control FC operation.

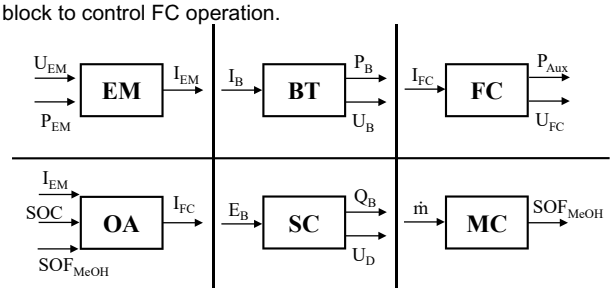


Fig. 1: Parameters of main blocks by quasistatic approach of the system simulation. EM=Electric Motor, BT=Battery, FC=Fuel Cell, OS=Operation Strategy, SC=State of Charge Control, MC=Methanol Fuel Control

The DMFC system consists of a DMFC stack, a condenser, an anode mixing vessel, a circulating pump, a condensate pump, a methanol pump, an air blower, and a methanol tank as shown in Fig. 2. In this system, moist air reaches to the cathode side after passing through an air blower and an air filter, respectively. At the cathode side, water is generated by the oxygen reduction reaction and the reaction of crossed-over methanol with oxygen. Some amount of water also exists at the cathode side because of the water crossover from the anode to the cathode. In addition, CO_2 is produced a result of methanol reaction with oxygen. The fluid mixture consisting of H_2O, CO_2, N_2, and O_2 leaving the stack is cooled down and water is separated to liquid and gas phases after passing through a condenser. Then, liquid water is recycled to the anode mixing vessel and methanol reaches to anode mixing vessel from the methanol tank. These diluted methanol solution is sent to the anode side. Unreacted methanol, CO_2 and water formed in the stack return to the anode mixing vessel and CO_2 is released to the atmosphere from the top of the vessel.

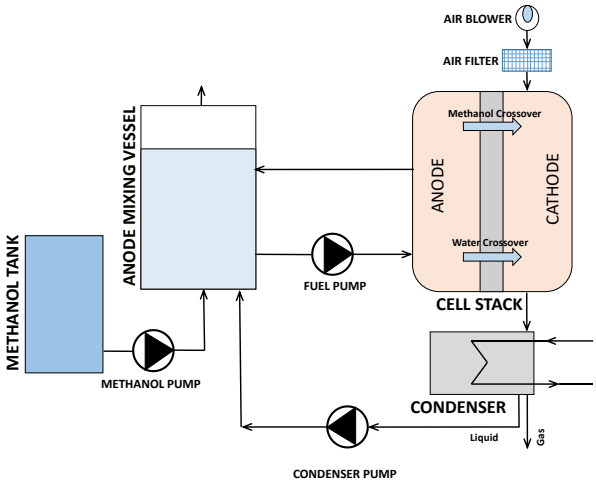


Fig. 2: Layout of DMFC system

In the DMFC sytem, five different fluids exists: methanol, water, oxygen, carbon dioxide, and nitrogen. Calculating the mass flow rate of these fluids at each point of the system is required in the system analysis. According to the Faraday's law, the overall methanol consumption rate [kg/h] in the stack can be expressed as:

$$\dot{m}_{CH_3OH,s} = \frac{(i_{el}+i_{perm})\times A_{cell}}{6\times F} \times n \times \lambda_a \times MW_{CH_3OH} \times 3.6 \quad (1)$$

Where i_{el} and i_{perm} are the current density of the cell and the corresponding crossover current density, respectively. In this study, the value of i_{perm} was taken from experimental data. A_{cell} is the superficial electrode area

of the cell, *n* is the number of cell, *MW* represents the moleculer weight of the species and Faraday's constant *F* represents the charge per mole of equivalent electrons. The Faradic efficiency is a measure of the percent utilization of reactant in a galvanic process. The term stoichiometry (λ) is defined as the inverse of the Faradic efficiency. Its value is taken as constant for both anode and cathode in this study.

The net water production in the cathode is made up of four different sources: i) electrochemical reactions that produce two molecules of water per molecule of methanol, ii) methanol crossoverreaction at the cathode to produce two molecules of water per molecule of methanol, iii) the water crossed over from the anode, and iv) water vapor in the air inlet. Total water generation rate at the cathode [kg/h] by electrochemical reaction is:

$$\dot{m}_{w,el} = \frac{i_{el} \times A_{cell}}{2 \times F} \times n \times MW_{H_2O} \times 3.6 \quad (2)$$

Methanol permeation which is defined as the transport of methanol from anode to cathode is a major problem as it decreases the cell voltage. When methanol reaches the cathode, the methanol is oxidized and water is generated ($\dot{m}_{w,mc}$) [kg/h] as expressed in Eq. (3)

$$\dot{m}_{w,mc} = \frac{i_{perm} \times A_{cell}}{3 \times F} \times n \times MW_{H_2O} \times 3.6 \quad (3)$$

As mentioned before, the moist air enters the cathode. The flow rate of water found in the moist air [kg/h] can be found by Eq. (4). In this equation, y_i is the mole fraction of gas in air, P_{sat} which is a function of temperature, is the saturation pressure of water at a given temperature. Relative humidity ratio (φ) is defined as the ratio of partial pressure of water vapor to the saturation pressure.

$$\dot{m}_{w,a} = \frac{(i_{el} + i_{perm}) \times A_{cell}}{4 \times F} \times n \times \frac{\lambda c}{y_{O_2}} \times (\sum y_i \times MW) \times 3.6 \times 0.622 \times \frac{P_{sat} \cdot \varphi_{in}}{P - P_{sat} \cdot \varphi_{in}} \quad (4)$$

The cathodic CO_2 production rate [kg/h] is:

$$\dot{m}_{CO_2} = \frac{i_{perm} x A_{cell}}{6 \times F} \; x \; n \; x \; MW_{CO_2} x \; 3.6 \quad (5)$$

III. Analysis of DMFC Hybrid System

System structure for the simulation of DMFC hybrid vehicular applications is shown in Fig. 3. Main system components and connections among them are represented by voltage (U), current (I) power (P), SOC and state of fullness (SOF) of methanol with the subscript i (in), a (out), B (battery) and FC (fuel cell) as input and output parameters.

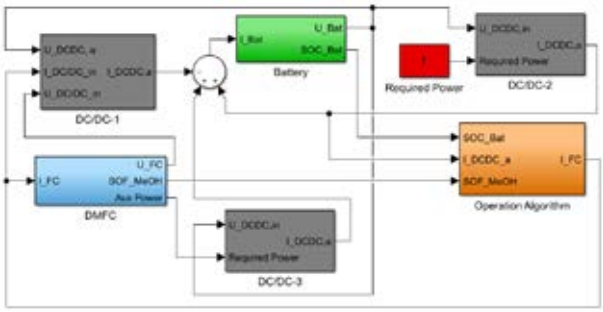


Fig. 3: Simulation structure of the fuel cell hybrid vehicle system

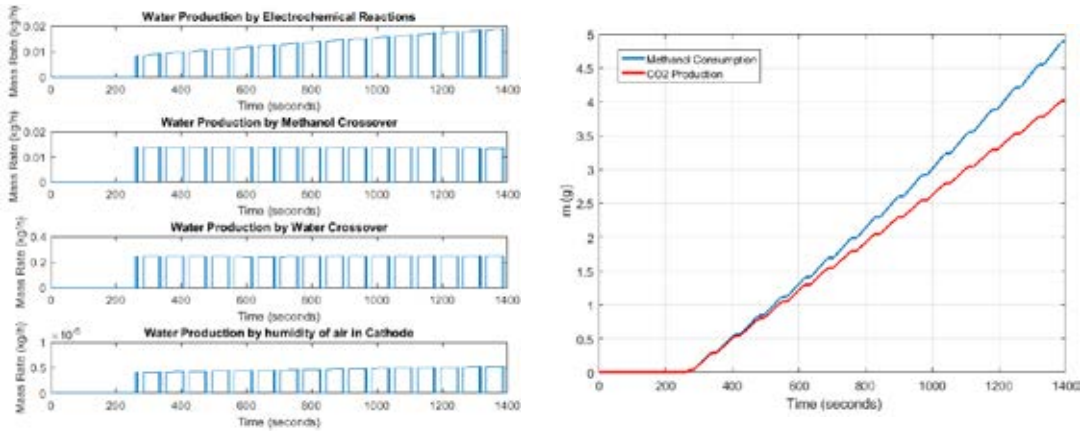
DMFC system model calculates the methanol consumption rate, and water and CO_2 production rates solving mass balance equations for the components of the system. Methanol crossover rate, water crossover rate and cell voltage of the single cell, which are measured experimentally for different methanol concentrations and various current densities, are integrated into Simulink model by surface block that creates a polynomial surface from the data. Power management of the DMFC system is determined by operation algorithms which is discussed in the previous section.

IV. Results and discussion

Required power on electric motor is produced along 70 seconds in the drive cycle time. DMFC hybrid system simulation is performed in Simulink environment for 20 drive cycle time and $3x10^{-4}$ maximum step size, $3x10^{-4}$ relative tolerance and Ordinary Differential Equation (ODE 45) solver type was used as the simulation configuration parameters. SOC of the battery reached 85% level and FC started to operate 12 W power output just before the 300th second of the simulation time. Additionally, SOC level dropped to 70% and power output of FC is about 25 W

at the end of the time.

Fig. 4 presents water production rate in DMFC because of electrochemical reactions, methanol crossover, water crossover and humidity of cathode air during the simulation time. After the FC started the operation, water production rate by electrochemical reactions which is shown in the Fig. 4(a), is increasing due to the current demand of FC. However, changes on water production rate by methanol crossover, water crossover and air humidity are negligible as shown in Fig. 4(a). Methanol consumption and CO_2 production rates of DMFC are calculated using Eqs. 1 and 5, respectively. Fig. 4(b) shows the summation of methanol consumption and CO_2 production rates for the simulation time. Methanol is consumed about 5 g and CO_2 is produced about 4 g at the end of the simulation.



a) b)

Fig. 4: Water production of DMFC stack during simulation time (a) and methanol consumption and CO_2 production of DMFC stack during simulation time (b)

V. Conclusions

System simulation for DMFC hybrid vehicular applications was performed by quasistatic approach in Simulink environment based on mass balance of FC system and the equations discussed in Section 2. Starting time and current demand of DMFC are determined by the operation algorithm for the hybrid system. The simulations give the methanol consumption, water production and CO_2 emission amounts during the simulation time. Additionally, power demand of auxiliary units of FC system are calculated in the DMFC block. In a future study, the effect of the operation of DMFC in the hybrid powertrain will be shown in battery SOC history and power demand. The contribution of DMFC system for vehicle range will be expressed and the results will be compared with pure electric drive system.

References

Colpan C. O., Cruickshank C. A., Matida E., Hamdullahpur F., 1D modeling of a flowing electrolyte-direct methanol fuel cell, Journal of Power Sources, 196, 3572-3582, (2011).

Larminie J., Dicks A., Fuel Cell Systems Explained Second Edition, ISBN 0-470-84857-X, Wiley Press, (2003)

Mench M. M., Fuel Cell Engines, ISBN 978-0-471-68958-4, Wiley Press, (2008).

Dohle H., Mergel J., Stolten D., Heat and power management of a direct-methanol-fuel-cell (DMFC) system, Journal of Power Sources, 111(2), 268-282, (2002).

Zenith F., Krewer U., Modelling, dynamics and control of a portable DMFC system. Journal of Process Control, 20(5), 630-642, (2010).

Colpan C. O., Quellette D., Glüsen A., Müller M., Stolen D., Reduction of methanol crossover in flowing electrolyte-direct methanol fuel cell, International Journal of Hydrogen Energy, 42, 21530-21545, (2017)

Zenith F., Na, Y., Krewer U., Effects of process integration in an active direct methanol fuel-cell system, Chemical Engineering and Processing: Process Intensification, 59, 43-51, (2012).

Jiang R., Chu D., Water crossover: a challenge to DMFC system II. Simulation of water recycling in a 20 W DMFC system, Journal of the Electrochemical Society, 155(8), B804-B810, (2008).

Spiegel C., Designing and Building Fuel Cells, New York: The McGraw-Hill Companies, (2007).

Guzzella L., Sciarretta A., Vehicle Propulsion Systems Introduction to Modeling and Optimization, Springer, (2005)

Investigation of Hydrogen Fuel Usage Affects On Exergetic and Exergeeconomic Performances of a Turbojet Engine

***Ozgur Balli*[1], Yasin Şöhret[2], T. Hikmet Karakoc[3]**

[1]*Turkish Air Forces (TurAF), First Air Supply and Maintenance Center*
[2]*Süleyman Demirel University, School of Civil Aviation, Department of Airframe and Powerplant Maintenance*
[3]*Anadolu University, Faculty of Aeronautics and Astronautics, Department of Airframe and Powerplant Maintenance*

In the present paper a comprehensive exergetic and exergoeconomic analyses of a turbojet engine is performed to determine how the hydrogen fuel usage affects the exergetic and exergoeconomic performances of the engine. According to this study, by hydrogen fuel burnt in the turbojet engine, the product exergy rate decreases from 4.06 GJ/h to 4.02 GJ/h because the exhaust gases mass flow rate decreses from 9.21 kg/s to 9.108 kg/s. The exergy efficiency of the engine deduces from 15.40% to 14.33% while the waste exergy rate increases from 22.31GJ/h to 24.01 GJ/h. Hovewer, the fuel cost rate increases from 264.38 US$/h to 1143.72 US$/h while the specific fuel exergy cost rises dramatically from 10.03 US$/GJ to 40.81 US$/GJ. The high increase in the fuel cost rate and specific fuel exergy cost with the hydrogen fuel causes that the specific product exergy cost rises up from 134.69 US$/GJ to 355.11 US$/GJ.

Keywords: turbojet engine, exergetic analysis, exergoeconomic analysis, hydrogen fuel, aircraft

Catalytic and Non-Catalytic Hydrogen Generation from Chemical Hydrides

Nazrin Abdullayeva and *Mehmet Sankir
Department of Materials Science and Engineering
TOBB University of Economics and Technology, Ankara, 06560, Turkey

*E-mail: msankir@etu.edu.tr

Abstract
Catalytic and non-catalytic methods of hydrogen generation from chemical hydrides have been studied due to their promising performances. For catalytic method, alloys containing precious and nonprecious metals have been simultaneously cosputterred forming catalysts in film and particle forms, which are further dealloyed. At the dealloying step, the nonprecious metal is etched from the surface leaving behind the precious metal as nanoporous catalyst with larger surface area and higher potential for hydrogen generation. Different combinations of Ru-Al, Pt-Al, Ru-Cu were tested at various process conditions. The highest amount of hydrogen generated by particulate catalysts of Ru-Al alloys was found as 110 L $min^{-1}g_{catalyst}^{-1}$. Catalyst free systems, in comparison, consist of directly disulfonated copolymers at various degrees of disulfonation. The highest hydrogen generation rate observed with the catalyst free system was 235 mL min^{-1} for BPSH 45 evaluated in a two-compartment reactor containing acid and $NaBH_4$ solutions separated via proton exchange membranes.

Keywords: Hydrogen generation, catalysts, catalyst morphologies, catalyst free hydrogen generation

I. Introduction

Hydrogen generation is one of the most extensively studied topics in renewable energy field due to its being a clean energy carrier and providing zero-emission energy Sankir (2015). Several limitations related to its on-board storage and generation in high volumetric capacities creates challenges in hydrogen utilization Sankir (2015). In this regard, chemical hydrides such as $NaBH_4$, NH_3BH_3, LiH, $NaAlH_4$, are highly promising due to their energy densities and high volumetric hydrogen capacities as solids Diwan (2009). So far, two major hydrogen generation methods using chemical hydrides have been developed which are, thermolysis and hydrolysis Oh and Kwon (2013). Hydrolysis itself has a very slow kinetics which is why catalytic hydrolysis processes that can be used for higher hydrogen production rates were developed Sankir (2015). However, previously reported systems are highly small and generate a limited amount of hydrogen Sankir (2015). In order to achieve an effective hydrolysis reaction, chemical hydrides should get in contact with a certain catalyst. Ruthenium (Ru), platinum (Pt), nickel (Ni), palladium (Pd), cobalt (Co), Ni-B, Co-B, Co-P, Ni-Co-B can be given as examples to these catalysts Sankir (2015). Utilizing precious metals as catalysts is highly expensive. Metal and alloy catalysts from nickel, iron and cobalt, in comparison to precious metal catalysts, are more inexpensive, yet they are usually not stable in long-term operations Dai and Wang (2013). This means that the catalytic activities of catalysts decay over time Dai and Wang (2013). On the other hand, catalyst free methods for hydrogen generation from chemical hydrides have also been developed, recently Sankir (2015). For instance, hydrogen generation is achieved via liquid acids reacting with chemical hydrides. However, these systems are not so effective due to the continuous fluctuations in hydrogen generation rates Sankir (2015). Alongside liquid acids, the utilization of solid acid membranes containing $–SO_3H$ groups has also been reported Sankir (2015). Yet, these systems have suffered from the poor hydrogen generation since the reaction only occured on the membrane surface Sankir (2015). In this study, three different methods of hydrogen generation are discussed of which two contain particle and film forms of catalysts as well as a catalyst free method.

II. Experimental Set-Up and Procedure

Platinum (Pt) and Ruthenium (Ru) nanoporous catalysts have been used as catalysts in particle forms to investigate their effect on hydrogen generation rates. The experiments were performed by cosputtering precious metal target (Pt or Ru) with Al target used as nonprecious metal. The sputtering power of precious metal has been kept constant at 50W, while it has been varied from 200 to 400W for Al. Chemical etching has been applied in order to remove Al from the alloy for 24 hours by using HCl acid. The remaining Pt (or Ru) nanoparticles have been filtered and washed with deionized water in order to discard acid residues. Catalysts in film forms have been prepared by coating Ruthenium (Ru) and Copper (Cu) simultaneously with sputtering power of Ru at 50W and varying Cu power values (30, 50, 100, 200 and 300W). Deposited Cu-Ru alloys have been dealloyed by using sulfuric acid as etching agent. Similar catalyst of Pt-Al in film forms have also been sputtered in similar conditions with Teflon™ or asymmetric membranes being used as backing layers. Catalyst free hydrogen generation has been achieved via directly disulfonated poly(arylene ether sulfone) (BPSH) copolymers with 25, 35 and 45 molar percent of disulfonation. The prepared membrane solutions described in our previous studies have been dried on flat ordinary glass and allowed to dry under IR lamp at approximately 60 ^{0}C for 12 hours McGrath (2007). After this casting step, membranes have been boiled in 0.5 M sulfuric acid and reboiled again in deionized water McGrath (2005). Hydrogen generation measurements for catalyst

containing systems have been performed in a three-necked, round bottom flask placed in a water bath and equipped with mass flow meter, silica dryer and thermocouple. The flask is connected to drained water containing cylindrical tube, thus, produced hydrogen volume is detected via measuring the change of water level in the gas burette. For catalyst free system two-compartment reactors, with acid and $NaBH_4$ solutions being separated via proton exchange membranes, are used. Protons from acid travel through the $NaBH_4$ half-cell via proton exchange membrane and reacts with $NaBH_4$ to generate hydrogen.

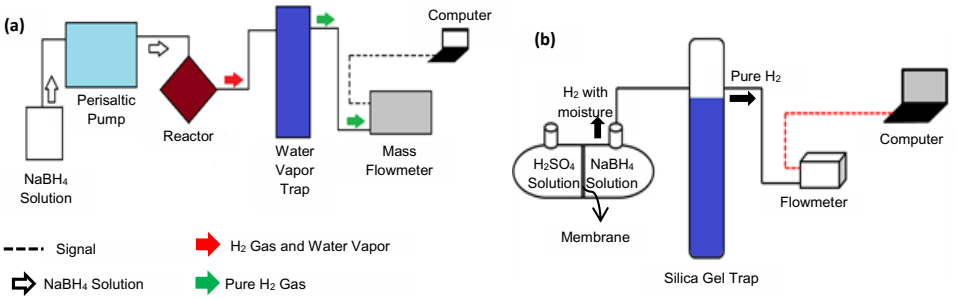


Fig. 1: Experimental set-up for **(a)** catalytic and **(b)** catalyst free hydrogen generation

III. Results and discussions

Sputtering power plays a crucial role in determination of the amount of generated hydrogen for particulate and film catalysts. The main purpose is to minimize the amount of precious metal by decreasing the sputtering power of it in order to make the systems cost-effective Sankir (2018). Therefore, sputtering power of precious metals was kept constant while the overall composition has been varied by changing the sputtering power of nonprecious metals. For particulate catalysts, Pt metal has been sputtered at 50W, while sputtering power for Al varied from 200 to 400W Semiz (2016). At 200W the alloy composition before dealloying consisted of 74 and 26 percent of Pt and Al, respectively Semiz (2016). The weight ratio of Pt to Al has changed to unity when sputtering power of Al has increased to 400W causing a noticeable change in particle sizes which is reduced from 900 to 90nm Sankir (2018). Similarly, this was true for the catalysts in the film form. In this case, along with sputtering power, sputtering and dealloying periods can also be considered as two parameters having an effect on overall hydrogen generation Sankir (2017). By keeping the sputtering power constant at 50W for precious metals, the power for non-precious Cu has been altered from 30 to 300W Sankir (2017) and Serin (2014). The highest hydrogen generation has been achieved at sputtering power of 200W Sankir (2017) and Serin (2014). By taking these power values as reference, the cosputtering time has been altered from 15 to 60 minutes Sankir (2017) and Serin (2014). It can be easily concluded that the film thickness is directly proportional with sputtering time. The optimum thickness of 1.5 μm preventing surface delamination is achieved after 60 minutes of cosputtering. Dealloying time being another variable affecting the hydrogen generation performance has been varied from 15 to 120 minutes Sankir (2017). Here the key parameter influencing the rate of hydrogen generation is the ratio of precious to nonprecious metal. At this point, the highest hydrogen generation rate has been observed with 90 minute dealloying period. The further dealloying causes delamination of film from surface and results in lower performances Sankir (2017). On the other hand, catalyst free hydrogen generation via copolymer membranes have been performed in two compartment reactors in which one of the compartments contained acid and the other contained sodium borohydride solutions Sankir (2015). Rate of hydrogen generation was controlled by tailoring the proton conductivities of membranes by changing their degrees of disulfonation (25, 35 and 45 molar percent). The results obtained from BPSH membranes have been compared with the ones obtained from Nafion™ Sankir (2015). Another variable affecting hydrogen generation rate in these experiments was temperature. This experiment has shown that at temperatures higher than 80^0C Nafion212 membranes deteriorate losing their proton conductivity Sankir (2015). Below given table summarizes all the hydrogen generation values obtained from three different methods described above.

Table 1: Summary of hydrogen generation performances obtained from catalytic and non-catalytic methods

Type of Catalyst		Experimental Parameters	H_2 Generation Rate	Reference
Particulate Form	Pt - Al	○ 50 W Pt – 400 W Al ○ Cosputtering time – 5 min. ○ Etchant HCl; Etching time – 24 hours	At T = 20 ^{0}C 90 L min^{-1} $g_{catalyst}^{-1}$ At T = 70 ^{0}C 460 L min^{-1} $g_{catalyst}^{-1}$	Sankir (2018)
	Ru - Al	○ 50 W Ru – 400 W Al ○ Cosputtering time – 5 min. ○ Etchant HCl; Etching time – 24 hours	At T = 20 ^{0}C 110 L min^{-1} $g_{catalyst}^{-1}$ At T = 70 ^{0}C 590 L min^{-1} $g_{catalyst}^{-1}$	Sankir (2018)
Film Form	Ru - Cu	○ 50 W Ru – 200 W Cu ○ Cosputtering time – 60 min. ○ Etchant H_2SO_4; Etching time – 90 min.	35 mL min^{-1}	Sankir (2017)
No Catalyst	-	○ BPSH Copolymer membranes at 25, 35, and 45 molar percent disulfonation and Nafion 212 ○ H_2SO_4 concentration 18 M ○ Temperature ranging from 15 to 80 ^{0}C	The Highest H_2 generation rate: BPSH 45 At T = 90 ^{0}C 900 mL min^{-1} Nafion 212 At the same conditions: 780 mL min^{-1}	Sankir (2015)

IV Conclusions

In summary, we report three different ways of hydrogen generation by using particle form, film form catalysts and catalyst free systems. For catalyst containing systems, optimum preparation methods resulting in the highest possible hydrogen generation rates have been stated. The effects of sputtering power and time, dealloying time, reaction temperature have been investigated in order to bring out the most beneficial outcome. For catalyst free systems, parameters such as degree of sulfonation of membranes and reaction temperature have been varied. The obtained results were compared with the ones achieved by using commercial Nafion 212 membrane.

Acknowledgements

Authors would like to express their appreciation to “The Scientific and Technological Research Council of Turkey” (TUBITAK) for their support of this research under the contract number 112M474.

References

Dai H.B., Wang P., Zhuang D.W., Kang Q., Muir S.S., Yao X., Ma G.L., Evaluation of a cobalt-molybdenum-boron catalyst for hydrogen generation of alkaline sodium borohydride solution-aluminum powder system, Journal of Power Sources, 224, 304-311, (2013)

Diwan M., Hydrogen Generation for Fuel Cell Applications, PhD Thesis, Purdue University, Indiana, (2009)

McGrath J.E., Sankir M., Bhanu V.A., Harrison L., Ghassemi H., Wiles K.B., Glass T.E., Brink A.E., Brink M.H., Synthesis and Characterization of 3,3’-Disulfonated-4,4’-dichlorodiphenyl Sulfone (SDCDPS) Monomer for Proton Exchange Membranes (PEM) in Fuel Cell Applications, Journal of Applied Polymer Science, 100, 4595-4602, (2006)

McGrath J.E., Sankir M., Kim Y.S., Pivovar B.S., Proton exchange membrane for DMFC and H2/air fuel cells: Synthesis and characterization of partially fluorinated disulfonated poly(arylene ether benzonitrile) copolymers, Journal of Membrane Science, 299, 8-18, (2007)

Oh T.H., Kwon S., Performance evaluation of hydrogen generation system with electroless-deposited Co–P/Ni foam catalyst for NaBH4 hydrolysis, International Journal of Hydrogen Energy, 38, 6425-6435, (2013)
Sankir M., Semiz L., Serin R.B., Sankir N.D., Hydrogen generation from nanoflower platinum films, International Journal of Hydrogen Energy, 40, 8522-8529, (2015)

Sankir M., Semiz L., Sankir N.D., Catalyst free hydrogen generation from directly disulfonated poly (arylene ether sulfone) copolymer membranes, Journal of Membrane Science, 496, 318-324, (2015)

Sankir M., Serin R.B., Abdullayeva N., Dealloyed Ruthenium Film Catalysts for Hydrogen Generation from Chemical Hydrides, MDPI Materials, 10, 1-10, (2017)

Sankir M., Semiz L., Abdullayeva N., Nanoporous Pt and Ru Catalysts by Chemical Dealloying of Pt-Al and Ru-Al Alloys for Ultrafast Hydrogen Generation, Journal of Alloys and Compounds (submitted)

Semiz L., Advanced Energy Materials for Fuel Cell Systems and Flow Batteries, PhD. Thesis, TOBB University of Economics and Technology, Turkey (2016)

Serin R.B., Hydrogen generation from chemical hydrides with high kinetics, MSc. Thesis, TOBB University of Economics and Technology, Turkey (2014)

Artificial Neural Network Modelling of Hydrogen Storage Properties of $LaNi_{4.75}Al_{0.25}$ alloys based metal hydride vessels

Muhammet Kayfeci[1], Fevzi Bedir[2], Ümran Elmas[3]
[1]Department of Energy Systems Engineering, Karabuk University, Karabuk, Turkey
[2]Department of Mechanical Engineering, Gebze Technical University, Kocaeli, Turkey
[3]The scientific and technological research council of Turkey, Ankara, Turkey

*Email: mkayfeci@karabuk.edu.tr (e-mail)

Abstract- Heat transfer is an important factor affecting the performance of metal hydride based hydrogen storage vessels. In the present work an artificial neural network (ANN) model has been created for prediction of the hydrogen storage capacity in finned and non-finned vessels. The ANN was trained and tested by using MATLAB toolbox on a personal computer. As ANN input parameters, time, temperature and hydrogen charge pressure were used, while absorbed hydrogen mass was the output parameter. The model was used to study their influence on the performance of the reactor geometry and hydrogen charging parameters in hydride vessels using $LaNi_{4.75}Al_{0.25}$ as the storage media and comparing vessels with and without fins as named Vessel 1 and Vessel 2. It was found that the maximum mean absolute percentage error (MRE, %) is less than 7.658%. R^2 (%) values for testing were found 99.90 and 99.99 in Vessel 1 and Vessel 2 respectively. The predicted results agreed well with experimental values, verified the applicability of the network model in the estimation of hydrogen storage capacity of non-finned and finned vessels. And also results show that this ANNA models more useful for Vessel 2.

Keywords: Hydrogen storage, metal hydride, ANN, vessel design.

1. Introduction

Modern industrialized societies which their economic growth have been based on the utilization of energy locked in fossil fuels no more pretending not to see effects of the fossil fuels such as global warming, climate changes, natural disasters. It is known that reserves of fossil fuels will be exhausted in a few decades, particularly those of oil and natural gas. On the other hand, the demand for energy continues to rapidly rise because on the continuing increase in world population and because of the growing demand by the developing countries in order to improve their living standards. The solution of this global energy problem must be found with clean energy technologies (Nalbant, 2008). Hydrogen is the ideal candidate to replace fossil fuels in the near future. Considering its massive usage, some technical problems appear in relation to its physical properties. To store it as a gas, high pressures must be achieved due to its low density (0.086 kgm^{-3} at normal conditions), and as a liquid, it requires the use of cryogenic technologies due to its low boiling point (20.4 K). These problems might be addressed by the use of metal hydrides since they offer high hydrogen storage capacity, cycling stability and safety. However, the usage of hydrides as hydrogen storage media has been precluded by the complexity of the heat and mass transfer phenomena, fluid flow and chemical reaction involved during the charge–discharge of hydrogen (Melnichuk et al., 2009).

Jemni et al., (1999) conducted an experimental and numerical study in order to determine the effective thermal conductivity, the equilibrium pressure, and the reaction kinetics of a metal-hydrogen reactor. An analytic expression of the equilibrium pressure and the reaction kinetics have been obtained and presented in good agreement with experimental data under different conditions. Mat et al., (2001) and Aldaş et al., (2002) studied numerically three-dimensional heat and mass transfer in a metal hydride bed during absorption. Spiral type heat exchanger for an MHT is developed. The experimental results showed that when a heat exchanger is used, the charge/discharge times of the tank are considerably reduced. Moreover, the effects of different parameters such as cooling fluid temperature and mass flow, tank volume and operation pressure were investigated and it was concluded that a good choice of these parameters is necessary (Mellouli et al., 2007). The optimization of hydrogen storage in metal hydride beds was investigated (Eustathios et al., 2006). Two novel cooling design options are investigated by introducing additional heat exchangers at a concentric inner tube and an annular ring inside the tank. Effects of heat transfer mechanisms on the charging process in metal hydride reactors under various charging pressures were studied. Three different cylindrical reactors with the same base dimensions are designed and manufactured. The experimental results showed that the charging of MHTs is mainly heat transfer-dependent and the reactor with better cooling exhibits the fastest charging characteristics (Kaplan, 2009). Mellouli et al., (2007) predicted two-dimensional mathematical model to evaluate transient heat and mass transfer in a metal hydride tank with metal foam heat exchanger. The model is validated by comparison with experimental data. A good agreement is obtained. The effect of metal foam exchangers on the charging process is evaluated. The impacts of the foam properties on heat transfer rate and hydrogen storage time are studied. Furthermore, novel cooling design options are investigated by introducing a concentric heat exchanger tube equipped with aluminum foam and filled with flowing cooling fluid. Dhaou et al., (2010) studied an experimental of the geometric and the operating parameter of a finned spiral heat exchanger has been carried out to identify their influence on the performance of the charging process of the MHV. The experimental results show that the charge time of the reactor is considerably reduced, when finned spiral heat exchanger is used. Askri et al., (2009) studied a two-dimensional mathematical model is developed and validated against experimental results. This model is used, first, to evaluate the impact of the tank wall thermal mass

on the hydriding process. Walls in steel and in brass are tested and the obtained results show that there is no significant effect on hydrogen storage time.

In this work presents a study on the effect of hydrogen absorption cycling on hydrogen storage properties, such as storage capacity, charging pressures, metal hydride reactor geometry and particle size distribution, of an annealed $LaNi_{4.25}Al_{0.75}$ alloy. In addition an ANN model has been developed describe hydrogen storage in metal hydride reactors and compared with experimental results.

II. Experimental

Two different reactors designed and manufactured for this study without and with finned vessels, denoted Vessel 1 and Vessel 2, were as shown in Fig.1 to determine the effect of heat transfer between hydride vessel and environment, which is one of the process parameters that affect hydrogen charge/discharge procedures on hydrogen storage (hydrogen pressure and metal hydride reactor geometry). Both of the vessels were made of St 42 steel. Vessel 1 is the base case having 20 mm inner diameter, 125 mm outer length and 2 mm thickness. Vessel 2 has the same dimensions as Vessel 1 but have 23 circular fins spaced by 4 mm with 40 mm outer diameter and 1 mm thickness to obtain a better heat removal from the vessel.

Experimental setup for hydrogen absorption is schematically shown in Fig. 2. Setup mainly consists of a metal hydride vessels, a vacuum pump to evacuate the vessels before, absorption experiments, manometers, thermocouples, a data acquisition system, a tank of containing 99.999% pure hydrogen gas. The vessel contained 135 g of $LaNi_{4.75}Al_{0.25}$. Before the hydriding test $LaNi_{4.75}Al_{0.25}$ powder is grounded for 4 hours. Grinding procedure is conducted by a ball mill which is located in a glow box of 60 mm diameter and 80 mm height. Nitrogen gas is used during the process to prevent possible oxidation. Grinding speed is set at 515 rpm. $LaNi_{4.75}Al_{0.25}$ material is used in the vessels. After milling, the powders were put in to the storage vessel. The packing fraction was approximately 75% of the internal volume. Activation a very important problem for practical applications of metal hydrides is the fact that the surfaces of metals are usually covered with oxide of various thicknesses, depending on the formation process of each process of each particular metal. After grounding, the first hydrogenation is preformed at 220 °C in furnace for 2 h under low pressure. The metal powders were activated by repeatedly evacuating and filling the storage tank with high pressure hydrogen (10 bars) for 2 h at room temperature. After the activation, the hydrogen storage capacity reached a saturated value of approximately 1.12 wt%. The experimental part of the study started after the activation process is fully completed. Vessels are then charged with hydrogen at the range of 2–10 bar pressure, where the pressure is continuously maintained. The hydriding process is monitored by temperature measurements obtained at four locations r=0 and z=5–60 mm from the bottom of the vessels for the first 4000 s of the absorption period. The temperature and storage hydrogen mass variation are recorded on a computer for further processes and for determine of storage rate and the interpretation of hydriding behavior.

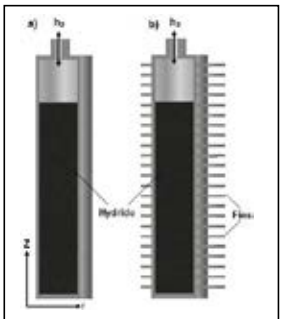


Fig. 1 - Metal hydride vessels cross section, a) Vessel 1 and b) Vessel 2

Some of procedure is followed during the experimental study as; $LaNi_{4.75}Al_{0.25}$ material is grounded for 4 hours. Grinding procedure is conducted by a ball mill which is located in a glow box of 60 mm diameter and 80 mm height. Nitrogen gas is used during the process to prevent possible oxidation. Grinding speed is set 515 rpm. $LaNi_{4.75}Al_{0.25}$ material is used in the reactors. Grounded material is transferred into the reactor in a glove box. The density of the powder is 75% volume of the reactor and is kept constant in all experiments. This process was carried out in a nitrogen atmosphere unless otherwise noted. The reactor is heated to almost 220 °C in furnace for 2 h under low pressure. After the heating process the reactor is cooled down to near room temperature and then hydrogen is charged to the reactor under 10 bar pressure. This heating and cooling process is repeated ten times for complete activation of $LaNi_{4.75}Al_{0.25}$ alloys. The experimental part started after the activation process is completed. Vessels are then charged with hydrogen at a range of pressure 2–8 bar and the pressure is continuously maintained. The hydriding process is monitored with temperature measurements obtained at four locations r=0 and z=5–60 mm from the bottom of the reactors for the first 4000 s of the absorption period. The temperature and mass variation readings are recorded on a computer for further processing, storage rate and interpretation of hydriding behavior. The hydriding and dehydriding processes are monitored with temperature and pressure measurement via three thermocouples positioned at three locations within the hydride bed and with a pressure sensor installed between the reference cylinders and the hydride reactor. The temperature and the pressure readings are recorded on a computer for further processing and interpretation. An ANN with back-propagation algorithm learns by changing the weights, these changes are stored as knowledge. Here ANNs are used for modeling the stored hydrogen mass in metal hydride reactors. Inputs for the network are hydrogen charging pressure, temperature and time: the output is the stored hydrogen mass. Here 98 data points are generated by the simulation of industrial hydrogen plant. Data set was divided in the training, validation, and test subsets in the proportion of 60%, 20% and 20%, respectively.

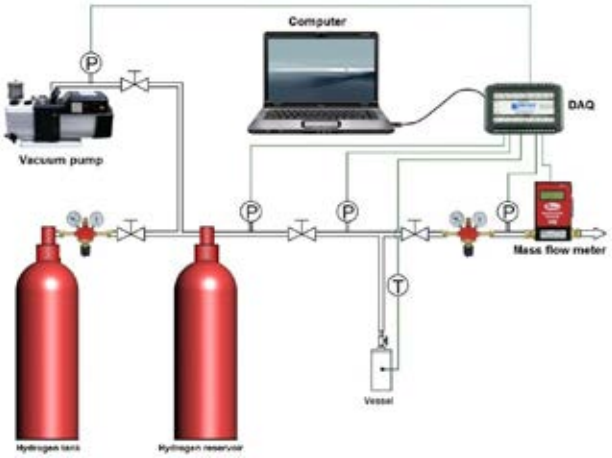


Fig. 2 - Schematic of the experimental set-up

The mean value based on the performance criterion was then considered as the predicting ability of the corresponding model. In each system training network was trained for 1000 epochs as the stopping parameter. For the normalization step, the following function was applied.

$$X_n = \frac{X_r - X_{r,min}}{X_{r,max} - X_{r,min}} \times (X_h - X_l) + X_l$$

where Xn denotes normalized input variable, Xr is raw input variable, and Xr,min and Xr,max denote minimum and maximum of input variable. Moreover, Xh and Xl are set to be 0 and 1. An error during the learning is the root-mean-squared (RMSE) one and defined as follows:

$$RMSE = \left[\frac{1}{n}\sum_{i=1}^{n}(t_i - o_i)^2\right]^{1/2} \quad (1)$$

In addition, the absolute fraction of variance (R^2) and the mean absolute percentage error (MAPE) are defined as follows respectively:

$$R^2 = 1 - \sum_i (t_i - o_i)^2 / \sum_i (o_i)^2 \quad (2)$$

$$RMSE = \left[\frac{1}{n}\sum_{i=1}^{n}(t_i - o_i)^2\right]^{1/2} \quad (3)$$

The FERMI transfer function has been used.

$$F_z = \frac{1}{1 + e^{-4(z-0.5)}} \quad (4)$$

where z is the weighted sum of the input.
Input and output layers are normalized in the (-1, 1) or (0, 1) range.

III. Results and discussions

In this study, two different geometries hydrogen storage vessel are design and manufactured, defined as Vessel 1 and Vessel 2. Input parameters t= 0 to 2400 s; T=36 to 128 and P=4 to 8 bars in Vessel 1, t=0 to 2400; T=37 to 120 and P=4 to 8 bar in Vessel 2. The output parameter is determined via LM algorithm. The experimentally obtained absorbed hydrogen mass results have been compared with ANN predicted absorbed hydrogen mass results. As shown in Fig.3 a and b, increasing of the hydrogen charging pressure was increased absorbed hydrogen mass for both vessels. The performance of the neural network model for prediction of absorbed hydrogen mass in Vessel 1 and Vessel 2 are shown respectively Fig.4 a and b. As can be seen from the figures, the prediction data has a good compatibility with the corresponding experimental data. Therefore, the model can be used to predict the stored hydrogen mass for both hydride reactors. The statistical values such as RMS, R^2 and MRE are also given in Tab. 1 for training and test. The values in the table are for LM and for the hidden layer with 4 to 16 neurons. The values of RMS are $4.2x10^{-6}$-1.5 $x10^{-3}$% for training and 7.5 $x10^{-5}$-$1.2x10^{-3}$% for test in Vessel 1, and $5.8x10^{-4}$-$7.4x10^{-6}$% for training and $1.8x10^{-3}$-$3.4x10^{-5}$% for test in Vessel 2. The maximum and minimum MRE are 0.801% and 0.014% for training and the maximum and minimum MRE are 7.658% and 0.957% for test. On the other hand values of R^2 are 99.68 to 99.98% for training and 97.55 to 99.96% for tests. From a comparison of the actual results with the results of the ANN study, one can see that the results are quite compatible. There is no significant difference between experimental and ANN results. Matching experimental values and predicted values by ANN for testing sets of the absorbed hydrogen for the finned and non-finned reactors are shown in Figs. 4 and 5 respectively; the predictive ability of the network for hydrogen storage capacity of MHVs was very satisfactory.

Tab. 1: The statistical values for absorbed hydrogen mass

		Vessel 1			Vessel 2		
Neuron		R^2	RMS	MRE	R^2	RMS	MRE
8	Training	99.96	5.7×10^{-5}		99.95	8.4×10^{-5}	
8	Test	99.96	4.2×10^{-5}	0.0110	99.95	1.0×10^{-4}	0.0108
10	Training	99.14	1.5×10^{-3}		99.86	2.3×10^{-4}	
10	Test	99.72	3.8×10^{-4}	0.0061	99.85	3.6×10^{-4}	0.0112
12	Training	99.99	4.2×10^{-6}		99.99	1.5×10^{-5}	
12	Test	99.90	3.3×10^{-4}	0.0130	99.98	2.9×10^{-5}	0.0119
14	Training	99.99	1.3×10^{-5}		99.85	5.8×10^{-4}	
14	Test	99.72	6.1×10^{-4}	0.0112	99.88	2.8×10^{-4}	0.0055
16	Training	99.98	2.3×10^{-5}		99.99	7.4×10^{-6}	
16	Test	99.97	5.8×10^{-5}	0.0132	99.17	1.8×10^{-3}	0.0139

The performance of the trained neural network was tested by comparing the predicted normalized storage capacities (for each inlet charging pressures and vessel type) of $LaNi_{4.75}Al_{0.25}$ metal hydride alloys with the experimental data. As noticed above, the number of neurons in the output layer were adjusted accordingly because the different inlet pressure of the hydrogen were improved greatly compared with those in the training sets. Among these pressures and stored hydrogen capacity, were adjusted best result adjusted with 12 neurons for neural network. Which is rather longer than that of the training data sets. Fig.6 and Fig.7 gives the comparison of the prediction results and the experimental data for the normalized storage capacities of each vessels. It can be seen from figure that there is good agreement between the results of the predicted and experimental data in the test data sets.

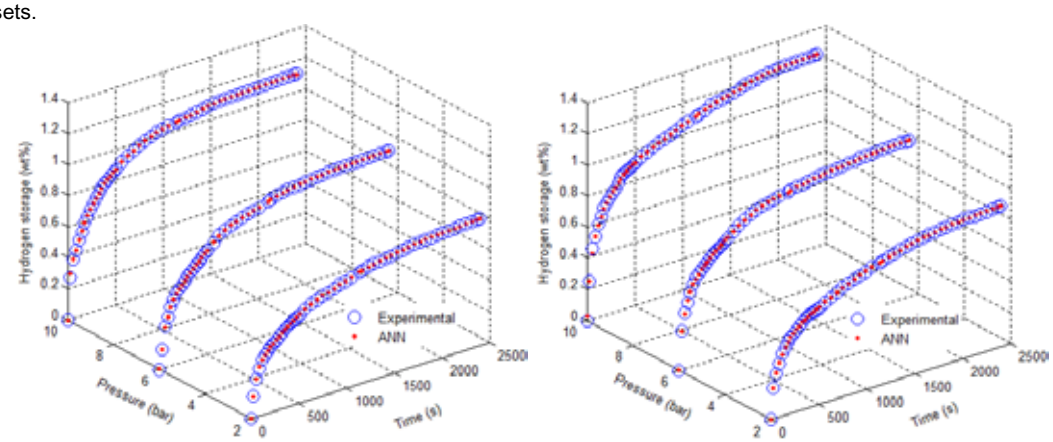


Fig. 3: Absorbed hydrogen mass versus time and hydrogen supply pressure for a) Vessel 1 b) Vessel 2

IV.Conclusions

In this study an ANN has been developed describe hydrogen storage in $LaNi_{4.75}Al_{0.25}$ metal hydride with finned and non-finned reactors. Results for the hydrogen charging process have been obtained and compared to experimental data; the good accord between ANN and experimental values shows that the proposed model is able to predict correctly storage systems. The developed ANN model with an accuracy of about 99%. In ANN model R^2, RMSE and MAPE values for Vessel 1 were found as 0.999, 0.00006 and 0.0214 respectively while for the Vessel 2 these values were found as 0.998, 0.01258 and 0.0042 respectively. Beside this absorption times of the metal hydride reactors are considerably reduced use to the finned reactor. Valuable developments were also observed at reaction kinetics and thermodynamic characteristics by grinding alloys in grinder and activation process. While the hydrogen is charged, an exothermic reaction occurs. For different pressure values, 2, 6 and 10 bar, the temperature increased rapidly during the first 400 s at the vessels. Maximum temperature values for both vessels were reached vary points, depending on the hydrogen charge pressure and depend on the vessel. However, it is possible to say that as pressure increases maximum temperature values increase, too. In addition, depending on the heat transfer, temperature values for the finned vessel were lower than for the un-finned vessel. As the hydrogen charge pressure increases, exothermic reaction also increases and therefore the mass of stored hydrogen rises. Mass of stored hydrogen essentially depends on the cooling of the vessel. Finned vessel stored more hydrogen compared to un-finned vessel, because of the faster heat transfer rate.

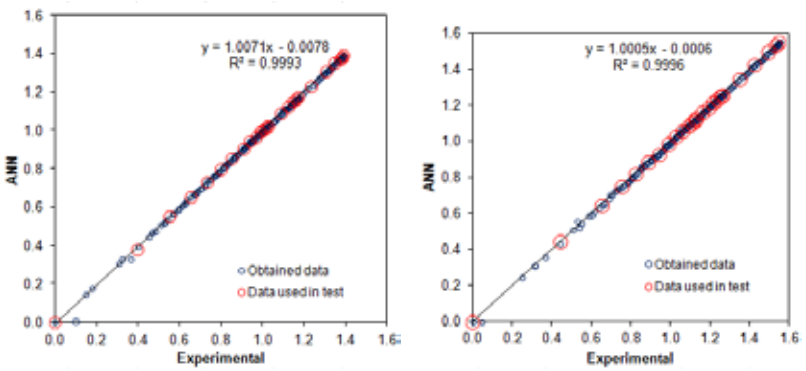


Fig. 4: Comparison of the experimental data and the results obtained from developed ANN model for a)Vessel 1 b) Vessel 2

References

Nalbant M.A., Toz metalurjisi ile üretilen magnezyum-alüminyum alaşımlarının hidrojen depolama kapasitelerinin ölçülmesi, Atatürk Üniversitesi, Fen Bilimleri Enstitüsü, Yüksek Lisans Tezi, 2008; 112s., In Turkish.

Melnichuk M., Silin N., Peretti H.A., Optimized heat transfer fin design for a metal-hydride hydrogen storage container, Int J Hydrogen Energy 2009;34:3417–24.

Jemni A, Ben Nasrallah S, Lamloumi J. Experimental and theoretical study of metal hydrogen reactor. International Journal of Hydrogen Energy 1999;24:631–44.

Mat D, Kaplan Y. Numerical study of hydrogen absorption in an Lm-Ni_5 hydride reactor. Int J Hydrogen Energy 2001;26:957–63.

Aldas K, Mahmutt D, Kaplan Y. A three-dimensional mathematical model for absorption a metal hydride bed. Int J Hydrogen Energy 2002;27:1049–56.

Mellouli S, Askri F, Dhaou H, Jemni A, Ben Nasrallah S. A novel design of a heat exchanger for a metal-hydrogen reactor. Int J Hydrogen Energy 2007;32:3501–7.

Eustathios S, Kikkinides, Georgiadis Michael C, Stubos Athanassios K. On the optimization of hydrogen storage in metal hydride beds. Int J Hydrogen Energy 2006;31:737–51.

Kaplan Y. Effect of design parameters on enhancement of hydrogen charging in metal hydride reactors. Int J Hydrogen Energy 2009;34:2288–94.

Mellouli S, Askri F, Dhaou H, Jemni A, Ben Nasrallah S. Numerical study of heat exchanger effects on charge/discharge times of metal-hydrogen storage vessel. Int J Hydrogen Energy 2009;34:3005–17.

Dhaou H, Souahlia A, Mellouli S, Askri F, Jemni A, Ben Nasrallah S. Experimental study of a metal hydride vessel based on a finned spiral heat exchanger, Int J Hydrogen Energy 2010;35:1674–80.

Askri F, Ben Salah M, Jemni A, Ben Nasrallah S. Optimization of hydrogen storage in metal-hydride tanks. International Journal of Hydrogen Energy 2009;34:897–905.

Kayfeci M. Experimental study for effect of design parameters of metal hydride reactor on hydrogen storage properties. Ph.D. Thesis, S.Demirel University Graduate School of Natural and Applied Sciences; 2011.

Ceylan İ., Kaya M., Gürel A.E. and Ergun A., Energy Analysis of a New Design of a Photovoltaic Cell-Assisted Solar Dryer, Drying Technology: An International Journal, 31:9, 1077-1082, 2013.

Taghavifar H., Mardani A., Mohebbi A. and Taghavifar H., Investigating the effect of combustion properties on the accumulated heat release of DI engines at rated EGR levels using the ANN approach, Fuel 2014;137:1–10.

Synthesis and Characterization of Electrocatalyst with Graphene and Multi-Walled Carbon Nanotube Support Material

[1*]Guvenc Umur ALPAYDIN, [2]Elif Damla ARICA, [2]Yilser DEVRIM, [1]Can Ozgur COLPAN
[1] Dokuz Eylul University, Engineering Faculty, Department of Mechanical Engineering, Izmir, Turkey
[2] Atilim University, Engineering Faculty, Department of Energy Systems Engineering, Izmir, Turkey

*E-mail: guvenc.alpaydin@ogr.deu.edu.tr

Abstract
The aim of this study is to investigate the effect of graphene nano pellets (GNP) and multi-walled carbon nanotubes (MWCNT) based carbon supports on PBI based HT-PEMFC under simulated reformate gases. Pt-Ru/GNP-MWCNT (50:50 wt/wt) was synthesized by microwave (MW) irradiation method. Thermogravimetric analysis (TGA), X-ray diffraction (XRD) and were used to investigate the microstructure and morphology of the as-prepared catalysts. Electrochemical characterization of the catalysts were carried out by cyclic voltammetry (CV) analysis using a conventional three electrode electrochemical cell connected to a potentiostat. The corresponding electrochemical surface area (ECSA) of the catalyst layers are 55 m^2/g and 47.7 m^2/g for Pt-Ru/GNP-MWCNT and commercial Pt-Ru/CB catalysts, respectively. Pt-Ru/GNP-MWCNT has a larger ECSA which was directly related to the number of available catalytic sites. A comparison of the standard, commercial Pt-Ru/CB and Pt-Ru/GNP-MWCNT catalyst is also presented.

Keywords: fuel cell, cyclic voltammetry studies, carbon nanotubes, graphene

I. Introduction

The use of support materials in catalysts is quite common because it is known that supported metal catalysts have improved stability and higher activity compared to unsupported bulk metal catalysts. In addition, each support material has different effects on the reaction occurring on a catalyst. A good support material should provide good electrical conductivity, good catalyst-support interaction, large surface area, easy handling of catalyst nanoparticles of ionomer and polymer electrolyte, and good corrosion resistance. The choice of support material is vital and extremely effective in determining the behaviour, performance, longevity and cost-effectiveness of the catalyst and the fuel cell because a good interaction between catalyst and support not only improves catalyst efficiency but also reduces catalyst losses and improves catalyst performance and durability (Sharma and Pollet, 2012).

Among the fuel cell electrocatalysts, the most common commercial support material is carbon black (CB). CB has some advantages such as large surface area and high electrical conductivity. However, using CB increases the rate of corrosion in the fuel cell environment (Olivera et al., 2013). This will cause the fuel cell to fail to operate stably. Therefore, new support materials have been investigated to increase the durability and performance of the catalysts. In general, the support materials can be carbon based (e.g. activated carbon, graphene nano pellets (GNP), and multi-walled carbon nanotubes (MWCNT)) or non-carbon based (conductive polymers, titanium, indium oxide, alumina, silicon tungsten oxide nanostructures) (Daş et al., 2016). Because of the high thermal and electrical conductivity, chemical stability, surface area, and mechanical durability of MWCNT and, GNP, which are carbon-based support materials, their usage is widespread.

In recent years, CNTs, which can fill and absorb particulate matter due to its pipe-like structure, have attracted great attention as a new support material. Furthermore, CNTs have high electrical conductivity, large surface area, and good thermal and chemical stability. CNTs are more stable in many cases than CBs (Yu et al., 2017). Rahsepar et al. (2013) applied a microwave assisted impregnation method to prepare a Pt/MWCNT as a catalyst. This catalyst exhibited high electrochemical activity in the electrochemical semi-cell characterization. The effects of diameter and length of MWNCTs on the electrocatalytic performance of Pt-Ru/MWCNT catalysts for methanol oxidation were investigated by Li et al. (2007). It has been shown that PtRu nanoparticles supported on MWCNT with large tube diameter exhibit a higher specific activity in the methanol oxidation reaction, while the length of MWCNTs has little effect on the specific activity of the Pt-Ru/MWCNT catalyst. This demonstrated that MWCNTs with larger tube diameters provide higher electrical conductivity.

Graphene, a two-dimensional monolayer of carbon atoms, has excellent electrical conductivity, high specific surface area, high stability, and a large surface to volume ratio. These features have led researchers to believe that graphene may be suitable catalyst support (Daş et al., 2016). Huang et al. (2012) observed that the graphene structure in the Pt/G hybrid is hardly degraded, which significantly increases the electrocatalytic activity of Pt nanoparticles and reduces catalyst poisoning. Lee et al. (2011) synthesized Pt-Ru/G and Pt-Ru/MWCNTs catalysts using the hydrothermal synthesis method. The characterization results showed that the PtRu nanoparticles are better distributed in the Pt-Ru/G catalyst. As a result, Pt-Ru/G catalyst showed a higher mass activity and better long-term performance for the methanol electrooxidation reaction.

In this study, GNP and MWCNT supported Pt-Ru catalysts were synthesized by microwave irradiation method. The microstructure and morphology of the samples were characterized by Thermogravimetric analysis (TGA) and X-ray diffraction (XRD). Electrochemical properties of the catalysts were investigated by cyclic voltammetry (CV) method using a three-electrode electrochemical cell. The synthesized Pt-Ru/GNP-MWCNT (50:50 wt.%) catalyst was compared with commercial (Pt-Ru/CB) catalyst in terms of electrochemical surface area (ECSA). In addition, the potential use of Pt-Ru/GNP-MWCNT based catalyst was demonstrated.

II. Experimental

Synthesis of Pt-Ru/GNP-MWCNT catalyst

The Pt-Ru/GNP-MWCNT catalyst was prepared by the microwave irradiation method. Dihydrogen hexachloroplatinate (IV) hexahydrate (Alfa Aesar) and ruthenium (III) chloride hydrate (Aldrich) were used as metal precursors. MWCNT and GNP were first dispersed to ethylene glycol (EG) and isopropyl alcohol (IPA) mixture (volume ratio of 4:1) under ultrasonic mixing for 1 hour. Then, Pt and Ru metal precursors were added to this mixture and it was again ultrasonically mixed for 10 minutes. After mixing, the pH of the mixture was adjusted to 12 and the ultrasonic mixing continued for another 30 minutes under N_2 gas environment. Then, the mixture was placed in a microwave oven and the catalyst was heated for 40 seconds taking the microwave power as 800 W. After the heating process finished, the mixture was kept in room temperature its temperature reaches to the room temperature. Then, the pH of the mixture was reduced to 2. Finally, the catalyst was stirred for 12 hours and the catalyst solution was put in an oven at 80°C for 1 day.

Characterization of Pt-Ru/GNP-MWCNT nanoparticles

The X-ray diffraction (XRD) was used for identification of the crystal structure of the Pt-Ru/MWCNT nanoparticles. XRD patterns were recorded on Ultima IV X-ray diffractometer using Cu at 40 kV and 30 mA. Electrochemical properties of the catalysts were investigated by cyclic voltammetry (CV) method using three-electrode electrochemical cell, which are the reference electrode (RE), the counter electrode (CE) and the working electrode (WE). TGA was performed on a Perkin Elmer Pyris 1 /TGA instrument. The samples were heated from 25 to 950 °C with a heating rate of 10°C/min.

III. Results and discussions

Characterization of Pt-Ru/GNP-MWCNT nanoparticles

The XRD analysis was performed to identify the crystal structure of the Pt-Ru/GNP-MWCNT electrocatalyst. The XRD patterns of the Pt-Ru/GNP-MWCNT and commercial Pt-Ru/CB are shown in Fig. 1.

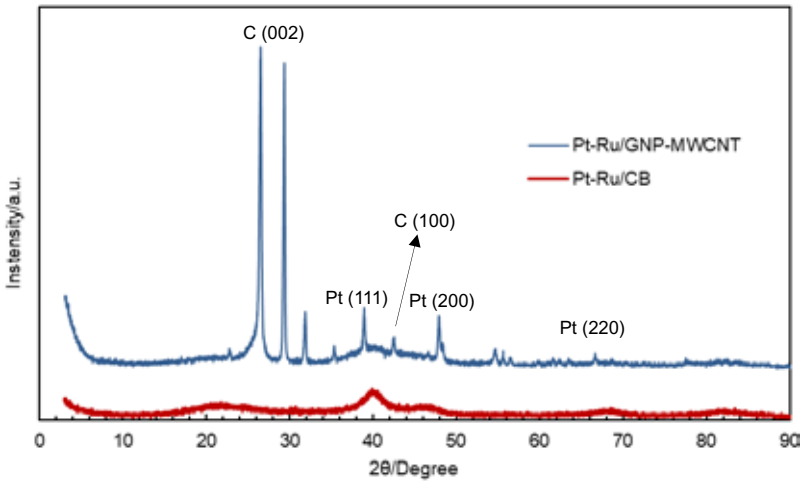


Fig. 1: X-ray diffraction patterns of (a) prepared Pt-Ru/GNP-MWCNT and (b) commercial Pt-Ru/CB samples

As shown in Fig. 1, the diffraction peaks were observed at 26.5° and 42.4°, which corresponds to the (0 0 2) and (1 0 0) crystal planes of graphitic carbon, respectively. These results are consistent with Gopiraman et al. (2014) The XRD results demonstrated that the basic structure of graphitic carbon was maintained during the procedure. In addition, it shows the (1 1 1), (2 0 0), and (2 2 0) reflections of the Pt-patterned face-centred cubic (fcc) crystal structure. On the XRD graph, the peaks for ruthenium do not bounce since in alloys containing about 50% Ru, the reflection causes a slight shift in the peak points. The peak points indicate the characteristic reflections of Pt (Chu and Gilman, 1996). As a result, it can be concluded that the microwave method is suitable for Pt-Ru/GNP-MWCNT catalyst preparation and catalyst has a high alloy phase formation between Pt and Ru.

TGA curves of Pt-Ru/GNP-MWCNT and Pt-Ru/CB are shown in Fig. 2. Weight loss of Pt-Ru/GNP-MWCNT and Pt-Ru/CB catalysts were observed as 75 wt.% and 39 wt.% at 900 °C, respectively. The TGA results showed that the Pt loading over for Pt-Ru/GNP-MWCNT was 25%

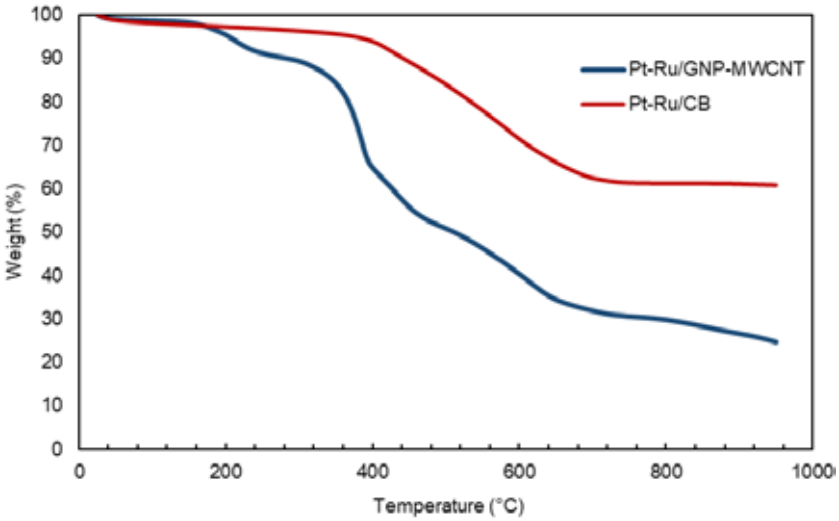


Fig. 2: TGA curves of (a) prepared Pt-Ru/GNP-MWCNT and (b) commercial Pt-Ru/CB (heating rate of 10°C min^{-1})

Electrochemical properties of Pt-Ru/GNP-MWCNT nanoparticles

Figure 3 shows the results of the cyclic voltammetry analysis of the Pt-Ru/GNP-MWCNT and Pt-Ru/CB catalysts over the -0.25-1.2 V potential range.

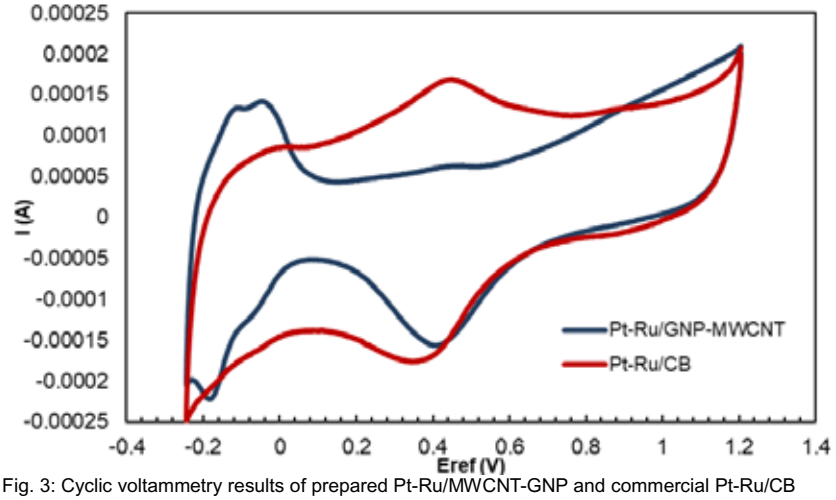


Fig. 3: Cyclic voltammetry results of prepared Pt-Ru/MWCNT-GNP and commercial Pt-Ru/CB

The electrochemical surface area (ECSA) values calculated as shown in Eq. (1) are calculated for every hundred cycles,

$$ECSA\ [cm^2/g] = \frac{Q_{H,}\ [\mu C/cm^2]}{\Gamma\ [\mu C/cm^2] \cdot L\ [g/cm^2]} \quad (1)$$

where ECSA is the electrochemical surface area of the catalyst, Q_H (μC/cm^2) is charge density, L is the metallic content in the electrode (g/cm^2), Γ (μC/cm^2) is the charge required to reduce a monolayer of protons on metallic content of catalyst.

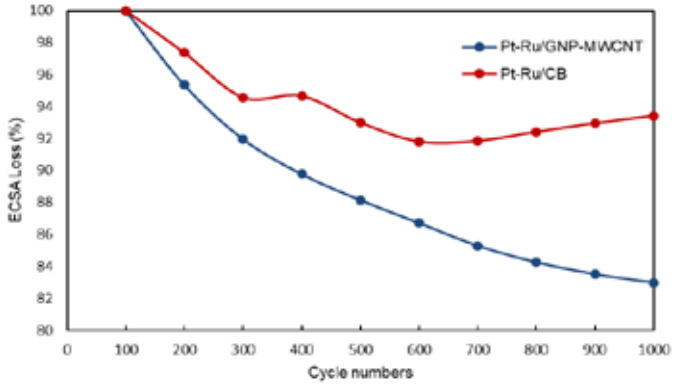


Fig. 4: ECSA loss for (a) prepared Pt-Ru/GNP-MWCNT and (b) commercial Pt-Ru/CB

As shown in Figure 4, both catalysts showed a decrease in ECSA with an increasing number of cycles. For both catalysts, there was about 10% loss of ECSA in the first 500 cycles. After 500 cycles, there was no significant loss of ESCA in the Pt-Ru/GNP catalyst. The Pt-Ru/GNP-MWCNT catalyst continued to decline. At 1000 cycles, the reduction in Pt-Ru/CB catalyst was about 10 percent while the Pt-Ru/GNP-MWCNT catalyst was 20 percent. However, the Pt-Ru/MWCNT-GNP catalyst always has higher ECSA value than Pt-Ru/CB.

IV. Conclusions

Pt-Ru nanoparticles have been successfully attached on MWCNT and GNP supports by using microwave irradiation method. While TGA and XRD analyses demonstrated that the microwave irradiation method is an efficient method for Pt-Ru/GNP-MWCNT catalyst synthesis, the CV results demonstrated that the MWCNT and GNP-supported Pt-Ru catalyst exhibited a larger electrochemical surface area than the CB-supported Pt-Ru. The ECSA values of the Pt-Ru/GNP-MWCNT catalyst ranged from 54 to 45, while for Pt-Ru/CB this change was between 47 and 44. These results are caused by high carbon corrosion in the CB. This situation led to the reduction of the active surface area due to the Pt agglomeration, the collapse of the carbon support, the loss of porous pores, and the clogging of the mass transfer path. Therefore, GNP-MWCNT support material is more suitable than CB. Consequently, the results showed that the GNP-MWCNT is a better support material than CB. These results have encouraged PEMFC performance testing for a future study.

References

Chu D. and Gilman S. Methanol Electro-oxidation on Unsupported Pt-Ru Alloys at Different Temperatures, Journal of the Electrochemical Society, 143(5), 1685-1690, (1996).

Daş E., Gürsel, S. A., Şanli L. I., and Yurtcan A. B., Comparison of two different catalyst preparation methods for graphene nanoplatelets supported platinum catalysts, International Journal of Hydrogen Energy, *41*(23), 9755-9761, (2016).

de Olivera M. C. L., Gerhard E., and Renato A. A., Corrosion and thermal stability of multi-walled carbon nanotube–graphite–acrylonitrile–butadiene–styrene composite bipolar plates for polymer electrolyte membrane fuel cells, Journal of Power Sources, 221, 345-355, (2013).

Gopiraman M., Babu S. G., Karvembu R., and Kim I. S, Nanostructured RuO2 on MWCNTs: Efficient catalyst for transfer hydrogenation of carbonyl compounds and aerial oxidation of alcohols, Applied Catalysis A: General, 484, 84-96, (2014).

Huang H., Chen H., Sun D. and Wang X., Graphene nanoplate-Pt composite as a high performance electrocatalyst for direct methanol fuel cells. Journal of Power Sources, *204*, 46-52, (2012).

Lee S. H., Kakati N., Jee S. H., Maiti J., and Yoon Y. S., Hydrothermal synthesis of PtRu nanoparticles supported on graphene sheets for methanol oxidation in direct methanol fuel cell, Materials Letters, 65(21-22), 3281-3284, (2011).

Li J., Liang Y., Liao Q., Zhu X. and Tian X., Comparison of the electrocatalytic performance of PtRu nanoparticles supported on multi-walled carbon nanotubes with different lengths and diameters, Electrochimica Acta, *54*(4), 1277-1285, (2009).

Rahsepar M., Pakshir M. and Kim, H., Synthesis of multiwall carbon nanotubes with a high loading of Pt by a microwave-assisted impregnation method for use in the oxygen reduction reaction, Electrochimica Acta, 108, 769-775, (2013).

Sharma S., Pollet B. G., Support materials for PEMFC and DMFC electrocatalysts—a review, Journal of Power Sources, 208, 96-119, (2012).

Yu, J. H., Li, W. W. and Zhu, H., Effect of the Diameter of Carbon Nanotubes Supporting Platinum Nanoparticles on the Electrocatalytic Oxygen Reduction. Acta Physico-Chimica Sinica, 33(9), 1838-1845, (2017).

Axane Commitment for a Sustainable, Reliable, and Field Proven Power Source Though Partnership with Laboratories and Design Efforts

***Johan Andre*[1], Marian Chatenet[2], Frédéric Maillard[2], Laetitia Dubau[2], Lionel Flandin[3], Corine Bas[3], Gilles De Moor[3], Olivier Lottin[4], Eric Claude[1], Elisabeth Rossinot[1], Nicolas Caqué[1]**

[1]Axane 2, Rue de Clémencière BP-15 38360 Sassenage, France
[2]LEPMI UMR 5279 CNRS / Grenoble – INP / U. de Savoie / U. Joseph Fourier, France
[3]LEPMI, UMR CNRS 5279 LMOPS, Université de Savoie, Bât. IUT, Campus de Savoie Technolac, France
[4]LEMTA - LEMTA - UMR 7563 CNRS – Université de Lorraine, 2 avenue de la forêt de Haye, France

Axane is a fuel cell system supplier of the Air Liquide group, located in Sassenage. Through the development of systems dedicated to niche markerts and powering of telecom antennas on remote sites, Axane had to cope with technical hurdles to reach ambitious targets in terms of performance, lifetime, availability and system cost. Thanks to a 3-year project dedicated to a better understanding of MEA degradation mechanisms and a 7-year project promoting new technologies for stationary applications and forklift markets, Axane has developed close relations with expertise laboratories to address lifetime and performance issues.

A better understanding of MEA degradation appeared as a priority for the PEMFC industry in order to develop more resistant materials and efficient mitigation strategies. Furthermore, degradations mechanisms are closely linked to operating conditions and as a consequence some damages are specific to the systems in which the MEAs are used.

In this work, detailed post-mortem analyses of different commercial MEAs aged in test benches as well as commercial systems have been carried out. Most of the ageing has been realised in Axane's commercial hardware in order to observe the corresponding specific degradation mechanisms. Multi-scale techniques were involved, giving complementary RESULTS: leak detection with infra-red camera, physic-chemical characterisation of catalyst layers, local performance measurement. This showed that degradations were heterogeneous on the active area: membranes appeared more damaged near the air channels outlet while the cathodic active layers underwent faster degradation in the outlet region of the H2 channels.

The results of this work have been helpful to select MEAs, adapt operating parameters, then optimise hardware geometry (flow-field). Following presentation will detail the key features and benefits of this special partnership, from experience feedback from the field to local analyses and new cell design.

Keywords: fuel cell, lifetime, MEA, degradation, ageing

A Density Functional Theory Study of Molecular Hydrogen Adsorption on Mg site in OFF Type Zeolite Cluster

[1*]Mehmet Ferdi Fellah, [1]Mehmet Çopur, [1]Osman Nuri Şara
[1] Department of Chemical Engineering, Bursa Technical University, Bursa, 16310, Turkey

* E-mail: mferdi.fellah@btu.edu.tr

Abstract
Hydrogen molecule adsorption was investigated on additional framework of Mg atom in OFF type zeolite by way of Density Functional Theory. The electronegativity, HOMO and LUMO energy, chemical hardness, chemical potential, adsorption enthalpy and adsorption energy values have been calculated on a 8T zeolite cluster model and compared with those of Mg exchanged ERI, LTL and DFT zeolite structures. Hydrogen adsorption enthalpy value was computed as -17 kJ/mol. This value is meaningfully larger than the hydrogen molecule's liquefaction enthalpy value. This accordingly specifies that Mg-OFF zeolite structure appears to be an encouraging candidate cryoadsorbent for hydrogen storage.

Keywords: Hydrogen adsorption, DFT, Mg atom, OFF zeolite, Offretite

I. Introduction

The idea of consuming hydrogen as an energy carrier of the future was important over the past three decades due to limited hydrocarbon resources. Large-scale storage of hydrogen safely should be developed in order to make it economically probable. Cryogenically cooled, pressure and containers covering an appropriate adsorbent material are methods known as hydrogen storage. Among the adsorbents for the hydrogen adsorption; zeolites, activated carbon and metal alloys are the most important candidates. Several research groups studied the hydrogen adsorption on exchanged Mg atom site in zeolites such as zeolite X (Song, 2007), zeolite Y and FAU (Otero Areán etal, 2007), zeolites ERI, LTL and DFT (Fellah, 2017a, b and c). There is no study concerning adsorption of hydrogen on Mg metal atom exchanged OFF type zeolite in either theoretical or experimental open literature. The aim of this study is to examine the activity of Mg^{2+} site in OFF (Offretite) type zeolite for the hydrogen molecule adsorption.

II. Model and Method

The theoretical calculations employed were based on Density Functional Theory (DFT) (Kohn, 1965) used in Gaussian 09 software (Frisch etal, 2009) with the B3LYP-Hybrid formalism method in present work. It has been known that one of the DFT methods for high-quality procedure of theoretical calculations for organic chemistry is the B3LYP method. For all atoms 6-31G(d,p) basis set was utilized in calculations.

The lattice constants values of the OFF type zeolite are a = 13.0630 Å, b = 13.0630 Å and c = 7.5650 Å and angles of $\alpha = \beta = 90^o$ and $\gamma = 120^o$ with P6/m2 space group. In current study the cluster utilized for theoretical calculations has been cut from the channel of OFF type zeolite (See Figure 1). The model of 8T OFF zeolite cluster (where T is called as SiO_4 tetrahedral structure) has 24 O and 8 Si atoms. Two Si atoms were replaced by two Al atoms in the ring of 8T cluster model ($[Si_6Al_2O_{24}H_{16}]^{2-}$). The part b of Figure 1 shows the final cluster model. The cluster's negative charge (2-) was saturated by the additional framework of $[Mg]^{2+}$. Free bonds of the Si and Al atoms have been terminated by hydrogen (H) atoms in order to neutralize the charge of the cluster. In this work terminating hydrogen atoms are kept fixed and all other atoms were relaxed during all theoretical calculations. Moreover, additional hydrogen atoms were kept to be fixed in order to direct the next Si site in the tetrahedral direction in OFF type zeolite structure.

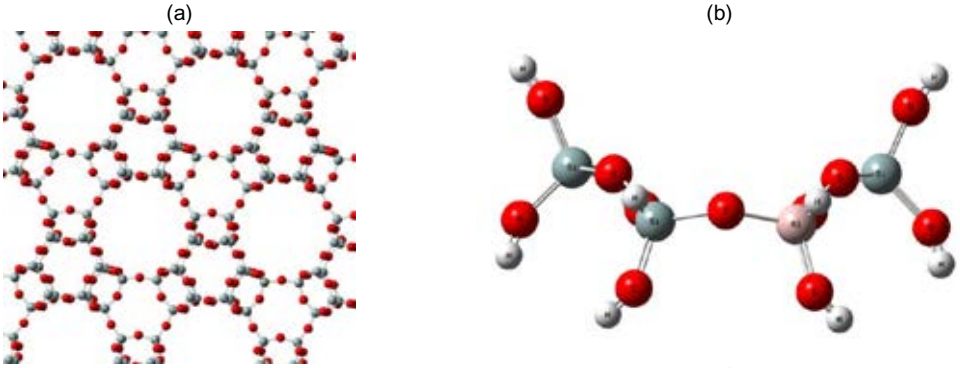


Fig. 1: a) OFF type zeolite structure with crystallographic position of the cluster, b) 8T OFF cluster

Geometries have been optimized by Equilibrium Geometry (EG) calculations. In this study, values of energy difference consist of the zero-point energy (ZPE) corrections which have been calculated by using vibrational frequency calculations through Single Point Energy (SPE) calculations. Additionally, the thermal energy and thermal enthalpy were computed by frequency calculations at 298 K because either theoretical or experimental literature has no thermochemistry data for hydrogen adsorption on Mg-OFF zeolite. These energy values have been computed as follows in Gaussuan.

$$E = E_{electronic} + ZPE + E_{vibrational} + E_{rotational} + E_{translational} \quad (1)$$

$$H = E + RT \quad (2)$$

The chemical potential, electronegativity and chemical hardness values were computed by using below equations. Energy of the highest occupied molecular orbital (ϵ_{HOMO}) and energy of the lowest unoccupied molecular orbital (ϵ_{LUMO}) have been utilized in order to these equations based on the approximation of Koopmans (Parr and Yang, 1989).

$$\text{Chemical Hardness } (\eta) \cong \frac{I-A}{2} \quad (3)$$

$$\text{Chemical Potential } (\mu) \cong -\frac{I+A}{2} \quad (4)$$

$$\text{Electronegativity } (\chi) \cong -\text{ Chemical Potential } (\mu) \quad (5)$$

where $I \cong -\epsilon_{HOMO}$ and $A \cong -\epsilon_{LUMO}$

The theoretical method in this study is the same with the method of our previous studies. In this study the relative energy values for theoretical calculations have been obtained by following equation.

$$\Delta(E/H) = (E/H)_{System} - (E/H)_{Adsortive} - (E/H)_{Cluster} \quad (6)$$

Here, $(E/H)_{System}$ is the energy/enthalpy for the optimized adsorbing molecule-cluster system, $(E/H)_{Adsorbtive}$ is the energy/enthalpy for the adsorbing molecule, and $(E/H)_{Cluster}$ is the energy/enthalpy for the cluster.

III. Results and discussions

Firstly Mg-OFF cluster was optimized by EG calculation with neutral charge and the singlet Spin Multiplicty (SM). Moreover singlet SM was established for the cluster-hydrogen molecule system. EG of 8T Mg-OFF cluster is shown in Figure 2a. Charge and SM determined for the calculation of obtaining EG of adsorbing molecule as hydrogen molecule was neutral charge and singlet state. After the optimization of adsorbing molecule (H_2) and cluster, hydrogen molecule adsorption was examined on Mg-OFF cluster by EG calculation. Optimized geometry of the hydrogen adsorbed 8T Mg-OFF cluster structure is represented in Figure 2b.

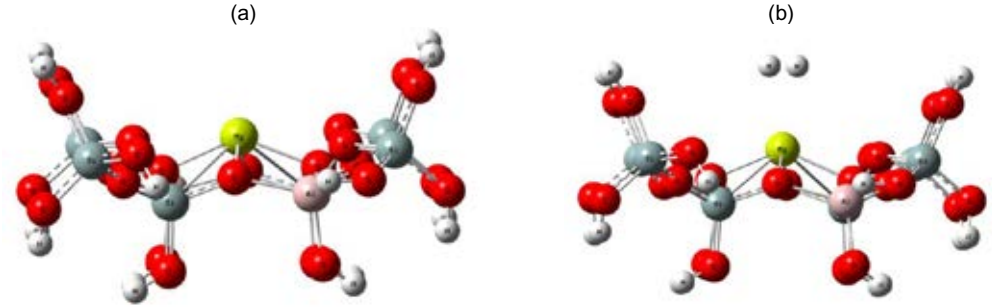


Fig. 2: a) a) Optimized 8T Mg-OFF zeolite cluster, b) Optimized hydrogen adsorbed 8T Mg-OFF cluster

The HOMO and LUMO energy values, chemical potential (μ), chemical hardness (η) and electronegativity (χ) values and the energy change values (ΔE and ΔH) for hydrogen adsorption on M-OFF, Mg-DFT, Mg-ERI and Mg-LTL clusters have been presented in Table 1. Based on the LUMO energies, the LUMO energy changes to more negative values when Lewis acidity increases for Mg-DFT zeolite, Mg-OFF zeolite, Mg-LTL zeolite and Mg-ERI zeolite respectively, that correspondingly parallels for decreasing of adsorption strength (Fellah, 2017a,b,c).

Chemical potential (μ), chemical hardness (η) and electronegativity (χ) values were calculated by using both the HOMO/LUMO values based on the values of free H_2 molecule and model cluster and the HOMO/LUMO values based on the values of cluster with the optimized adsorbed H_2 molecule (Parr and Yang, 1989).The chemical hardness values decreases in the order of Mg-ERI > Mg-LTL > Mg-OFF > Mg-DFT. It should be noted that the

chemical potential values are strongly related with the energy issue of adsorption during a reaction. The lower chemical potential values indicate that during the hydrogen adsorption on cluster the adsorption energies on these clusters should be much lower with respect to the other Mg exchanged zeolite clusters (Parr and Yang, 1989).According to Table 1, chemical potential values, electronegativity values and adsorption energy values are in the order of Mg-DFT > Mg-OFF > Mg-LTL > Mg-ERI. Besides, lower chemical hardness value of Mg–OFF cluster designates that this cluster is softer than other clusters for hydrogen adsorption.

Tab. 1: Comparison of energy values for hydrogen adsorption (Values are in units of kJ/mol).

	Zeolite ERI[a]		Zeolite LTL[b]		Zeolite OFF[c]		Zeolite DFT[d]	
	Cluster	Cluster with adsorbed H_2	Cluster	Cluster with adsorbed H_2	Cluster	Cluster with adsorbed H_2	Cluster	Cluster with adsorbed H_2
HOMO Energy	-733.0	-731.4	-715.1	-716.8	-731.8	-728.1	-737.9	-727.9
LUMO Energy	-103.6	-71.6	-131.4	-70.1	-223.9	-96.0	-266.6	-195.2
Chemical Hardness	314.7	329.9	291.8	323.4	253.9	316.1	235.6	266.3
Chemical Potential	-418.3	-401.5	-423.3	-393.5	-477.8	-412.0	-502.3	-461.5
Electronegativity	418.3	401.5	423.3	393.5	477.8	412.0	502.3	461.5
Adsorption Energy (ΔE)		-1.2		-13.0		-14.6		-23.8
Adsorption Entalphy (ΔH)		-3.6		-14.7		-17.0		-26.2

[a] Fellah, 2017a; [b] Fellah, 2017b; [c] This study; [d] Fellah, 2017c

Adsorption enthalpy values on Mg exchange zeolites were described in the range of -13 to -18 kJ/mol experimentally (zeolite X and zeolite Y) and in the range of -3.6-(-26.2) kJ/mol theoretically (zeolite X, zeolite CHA, zeolite ERI, zeolite LTL and zeolite DFT) in literature. Adsorption enthalpy of hydrogen has been computed as -17 kJ/mol Mg-OFF zeolite cluster model in this study. In order to be able to remark that a material can be a possible applicant cryoadsorbent material for storage of hydrogen the enthalpy value for hydrogen adsorption on that material should be larger than the liquefaction enthalpy of hydrogen molecule. In view of that, if adsorption enthalpy value for hydrogen on Mg–OFF cluster is compared to the hydrogen molecule's liquefaction enthalpy (0.9 kJ/mol, Perry and Green, 1997) and the available literature data, it can be seen that the enthalpy values of hydrogen adsorption involved for Mg–OFF structure is substantially larger than the liquefaction enthalpy of hydrogen and the literature values. Consequently, based on these data, Mg-OFF zeolite structure seems to be talented candidate cryoadsorbent material for hydrogen storage.

IV. Conclusions

For the adsorption of hydrogen molecule DFT calculations with B3LYP method have been utilized on Mg-OFF type zeolite cluster. Adsorption enthalpy value for hydrogen adosorption was computed as -17 kJ/mol, which is principally greater than the hydrogen molecule's liquefaction enthalpy value. This indicates that Mg-OFF zeolite structure looks to be a talented candidate cryoadsorbent for storage of hydrogen molecule.

References

Fellah M.F., A DFT Study of Hydrogen Adsorption on Be, Mg and Ca Frameworks in Erionite Zeolite, Appl. Surf. Sci., 394, 9-15, (2017a).

Fellah M.F., Hydrogen Adsorption: A DFT Study on Be, Mg and Ca Frameworks in LTL Zeolite Cluster, J Mol. Model., 23, 184-202, (2017b).

Fellah M.F., Hydrogen Adsorption on Mg-DFT Zeolite Cluster: A Density Functional Theory Study, J Inno. Sci. Eng., 1, 1-5, (2017c).

Frisch M.F., et al., Gaussian 09. Gaussian Inc.: Wallingford, CT, (2009).

Kohn W., Sham, L.J., Self-consistent equations including exchange and correlation effects, Phys. Rev., 140, A1133-A1138, (1965).

Otero Areán C., Turnes Palomino, G., Llop Carayol, M.R, Variable temperature FT-IR studies on hydrogen adsorption on the zeolite (Mg,Na)-Y, Appl. Surf. Sci., 253, 5701-5704, (2007).

Parr R.G., Yang, W., Density Functional Theory of Atoms and Molecules. New York, Oxford University Press, (1989).

Perry R.H., Green, D.W., Perry's Chemical Engineers Handbook, Seventh Edition (McGraw-Hill International Editors, Sydney, Section 2, (1997).

Song M.K., No KT, Molecular simulation of hydrogen adsorption in organic zeolite, Catal. Today, 120, 374-382, (2007)

Simulation of a novel Alternative Fuelled Hybrid Electric Vehicle (AF-HEV) with Hydrogen Enriched Internal Combustion Engine

[1*]Hüseyin Turan ARAT
[1] İskenderun Technical University, Faculty of Engineering and Natural Sciences, Department of Mechatronics Engineering, İskenderun Campus, Hatay, 31200, TURKEY

* E-mail:hturan.arat@iste.edu.tr

Abstract
There are new issues with very little research on the usage of alternative fuels on internal combustion engines (ICE) used in hybrid electric vehicles (HEV). The use of hydrogen, which has perfect combustion and engineering properties gas fuel, as an additional/enriched fuel on an ICE that used for HEV will be investigated in this simulation study for the first time. In this work, the performance and emission values of the internal combustion engine of a hybrid electric vehicle resulting from hydrogen enrichment are simulated. In the simulation, the energy, performance and emission values are given comparatively in comparison with a driving cycle of model vehicle realized with AVL Cruise and AVL Boost programs. The ICE's experimental results used in this study were compiled from authors' other publications for validating the modelled ICE which was computed with AVL Boost. Then it is placed as ICE of HEV in AVL Cruise. The electric machine, battery and transmission of parallel configuration HEV modelled, determined and compared with the basic model. Increasing performance gained with hydrogen enrichment, beside ICE has become more environmentally friendly with hybrid mode. The Model HEV has delivered promising results both as performance and emission values. Addition of hydrogen showed 3,56 % improvement in ICE torque and 2,37% ICE power. Sum of the total fuel consumption and emission pollutions decreased by 12,6% and 27% respectively with hybrid mode.

Keywords: Alternative fuelled Hybrid Electric Vehicles, Hydrogen Enrichment, Emissions, AVL Cruise & Boost.

I. Introduction

Emission pollution is increasingly threatening the environmental balance of our earth every day. The surplus of vehicles produced against decreasing petroleum reserves and other exhaust emission pollutant applications have created a driving force for researchers to work intensively on alternative fuels and alternative energy sources. In terms of production diversity, availability on the earth and physicochemical properties, hydrogen is the first element that comes to mind when it comes to alternative energy and fuel. It can be reached on the basis of known technical characteristics of hydrogen, production steps, advantages and disadvantages, use as fuel, applications, chemical phases, thermodynamic and energetic properties, cost analysis, etc. can be reachable on Dinçer (2007)'s studies. In the use of hydrogen as a fuel in ICE, the common opinion of many researchers in the literature is that this fuel, which has the highest heating values and very good flammability limit; has side effects such as explosion and knocking. In addition, although improves the energy performance of the engine in the end result of good combustion, it is prevalent in some studies it increases NO_x. In addition to storing the liquid and gas phase in cryogenic tanks, hydrogen is the most important fuel source for fuel cells. Because of its electrochemical structure, it can be obtained by electrolysis of water as it is in fuel cells. With all these advantages, hydrogen, so to say the number one of fuel world has become impossible to escape from the markings of automotive manufacturers.

Nowadays, hydrogen can be applied for transport as a main fuel (or supplement fuel) for ICEs and for fuel cell; and most of the hydrogen stations on over the world are attending to fuel cell vehicles. Hydrogen internal combustion engines have the potential for high power because of more energy per unit mass and high flame speed, high efficiency because of high flame speed that causes high rate of pressure rise in the cylinder and hence near constant-volume combustion and they also have near-zero emissions, except NOx at higher loads, because of the absence of carbon in the fuel molecular structure. Whit this situations, hydrogen can be used as an additional fuel for clean combustion and less pollution for ICEs. This can be performed by three ways for entrance the engine. First one is intake manifold entrance; that can be useful for both SI (spark ignition) and CI (compression ignition) engines. Hydrogen mixed with air before the cylinders which provide the lean burning situation that it minimized the emissions and fuel consumption. Second one is port injected hydrogen situation, which can be preferable for SI engines that needs an additional injector for mixing the fuel and air components with hydrogen in cylinders. Third one is using directly hydrogen ICE. Although H_2 has clean and superior combustion characteristics, it's the most important handicaps; storage, infrastructural difficulties and security are not solved even with today's technology.

Automotive practitioners used in addition to alternative fuels, they have also been used in alternative propulsion systems for the last 30 years. Basically if a vehicle chooses two or more traction devices for energy source to drive, this vehicle called *hybrid vehicle*. If the secondary energy source used as electric and aimed to good driving dynamics and comfort while reducing fuel consumption and emissions, these vehicles are called hybrid electric vehicles (HEV). Last three decades, HEVs are playing a critical position for integration the last technologies uses and placed an important bridge role between the ICEs and fully electrical vehicles (EV). Especially dividing the energy requirement of full vehicle, ICE and electrical assisted (simply consists of electric motor, battery, generators, energy management systems, inverters and converters, power electronics, etc. (Hameş et al (2017, 2018)) HEV is giving an energy efficient and cleaner strategy when compared conventional ICEs.

Classifications, topology architectures and hybridization ratios of HEVs are the first crucial subjects on manufacturing. Generally, HEV topology divided into 3 groups as serial, parallel and combined power split (serial-parallel). In terms of hybridization characteristics, micro HEV (used EM >5 kW), mild HEV (used EM >5-20 kW) and full HEV or plug-in HEV (used EM>40 kW) can be classified. The degree of hybridizations and more important information on HEV system modelling and control is complied by Liu (2017). All the researches related to HEVs focused on the electrification components of the vehicle. System identification, modelling, control strategies, management systems (both battery and thermal), power transmission organs, etc. By the way the ICE is selected according to the hybridization rate. In HEVs the purpose of electrical apparatus usage, while minimized working of ICE under certain conditions, aiming for fuel economy, greener emissions and energy efficiency. With this perspective only two mentioned study welcomed us. He (2006) studied the development and validation of a HEV with hydrogen internal combustion engine. And by Grabowski (2006) patented Hydrogen fuelled hybrid powertrain and vehicle, that returned by a concept car for Ford company with the named H_2RV. Differed from this study, both of them used directly hydrogen ICE. The use of alternative fuel in the ICE of HEVs is more attractively usage has become one of the possible ideas to be considered in the future for the support of the main goal of the electrical part. In this simulation study, an ICE is enriched with hydrogen for coupled on HEVs. AVL Boost and AVL Cruise tools simulated the model engine and model HEV, respectively. In terms of being a guide for this study, author's previous studies Arat et al (2016, 2016) and Kenanoğlu et al (2016) study are used for the modelling the similarly ICE in AVL boost in light of with their experimental results. Then modelled ICE is imported the AVL Cruise for modelling the HEV with appropriate electrical devices. In this manner, hydrogen enriched ICE is used on HEV application for the first time.

II. Simulation Procedure and Numerical Approach

Simulation studies are important steps that researchers can take to optimize their consumption of time and costs prior to prototype production. In this simulation study, AVL simulation tools (Boost and Cruise) are used for validating and modelling an HEV which include hydrogen enriched ICE. Figure 1 illustrated the schematics of study's simulation procedure steps. Modelled HEV specifications are shown in Table 1.

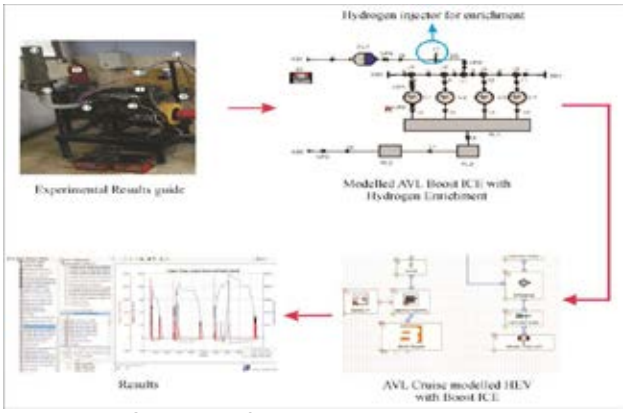


Fig. 1: Schematics of study's simulation procedure steps

Tab. 1: Model Vehicle Specifications

Vehicle	Parallel configuration HEV, Mass: 1310/1620 kg, Frontal area: 2,15 m^2 ,Wheel base: 2690 mm
Engine	Boost modelled H_2 enrichment 4-cylinders gasoline engine, Displacement: 1490 cm^3 , Maximum Power: 88 kW, Peek torque: 134 Nm @ 3550 rpm, Aerodynamic drag coefficient.: 0.3, Vehicle frontal area (m^2): 2.15, Rolling friction coefficient: 0.015, Wheel radius (m): 0.289
Battery	Maximum charge: 6.8 Ah, Nominal voltage: 160 V, SOC=70-90
Electric Machine	Type: ASM, Power Capacity: 10 kW, Maximum Power Torque: 65 Nm, Maximum Speed: 8000 rpm.
CVT	Min/Max Ratio: 0,5 / 2,8726

Understanding the basic principles of HEV is depended on auxiliary numerical analyses. Especially preparing a simulation model, the components formulations and identifications are very important variables. When modelling and control designed of HEV, basic formulations of traction, vehicle torque, total vehicle mass, break mean effective pressure on ICE, fuel consumption, energy losses, engine drag torque, electric motor power, battery model and formulas with SOC are reachable from Liu (2017). [*Related formulas are not written due to the limited number of pages, but they cited with reference*]. Control strategies need to be developed to ensure that all these complex and instantaneous variables work together in highly efficient manner with an optimal situation. The simulation model used in this study is a dynamic, modular, forward-type simulation. That is the model consists of a

driver sub-model trying to follow a predetermined velocity profile, a dynamic vehicle model, and a parallel hybrid vehicle control module that essentially acts as the interface between the driver and vehicle models with the base structures of AVL Cruise and its MATLAB-Simulink interface indices.

III. Results and discussions

The main purpose of this study is to simulate the effects of fumigation/enrichment for ICE with alternative fuel (hydrogen), which is used in modelled HEV. As an another goal for this study, in addition to achieving the lower fuel consumption and emission minimization with electrical apparatuses, it was desired to achieve better performance and lower emission values in the ICE with the use of hydrogen that at the top of alternative fuels. General literature showed that, hydrogen enrichment give promising results on thermal efficiency and reduction of emissions. Notwithstanding it is an important demerit alerted with the importance of knock (especially SI engines) and volumetric ratios of mixtures with air when used in intake manifold fumigation. For this reasons, in this study, SI ICE is operated under lean burning conditions and with the helped of literature in intake manifold, hydrogen enrichment into air is stated with the 8% volumetric mixture ratio. After ICE was decided and modelled, HEV model was created with AVL Cruise. Thank for the connections between each other's of AVL tools, the ICE modelled on Boost is simulated with Cruise for use in HEVs. Results are given into two parts which is suitable for easy understanding. Driving circles are used for the integrity of the experimental parameters of the HEVs. In this study, 780 sec UDC test cycle was used.

Figure 2 illustrated the ICE effects part of HEV. As seen from fig. 2, the stock SI ICE and hydrogen enrichment ICE is compared each other with the graphs of Brake power and torque, fuel consumption, HC, CO_2 and NO_x emissions. In figure 2, H_2 enrichment is playing important improvements on brake torque and brake power. The main reason of this phenomenon is thermal behaviour and fast flammability aspects of hydrogen. Break Specific Fuel Consumption given a cumulative and calculated version. In simulation tool, system programming for analyzed under selected driving cycles. Such ICE engine stock state and hydrogen enriched ICE is simulated with Boost and HEV with H_2 enriched ICE is analyzed with the calculation of Cruise data. For assumed lean burning conditions and partially lower volumetric ratio of hydrogen addition; the H_2 enriched ICE is improved the fuel economy with 5.5%. But when compared between HEV with H_2 enriched ICE to stock ICE, the fuel economy is effected a level that can be counted as much better, achieved the purpose with 12.6%. When it comes to emission perspective; totally HEV with H_2 enriched ICE reached an exceptional goal with the interspaced of approximately 12-28%. Figure 3 showed the electric devices of HEV analyses. Electric machines efficiency maps, transmission's desired ratios and battery parameters are given in related fig.

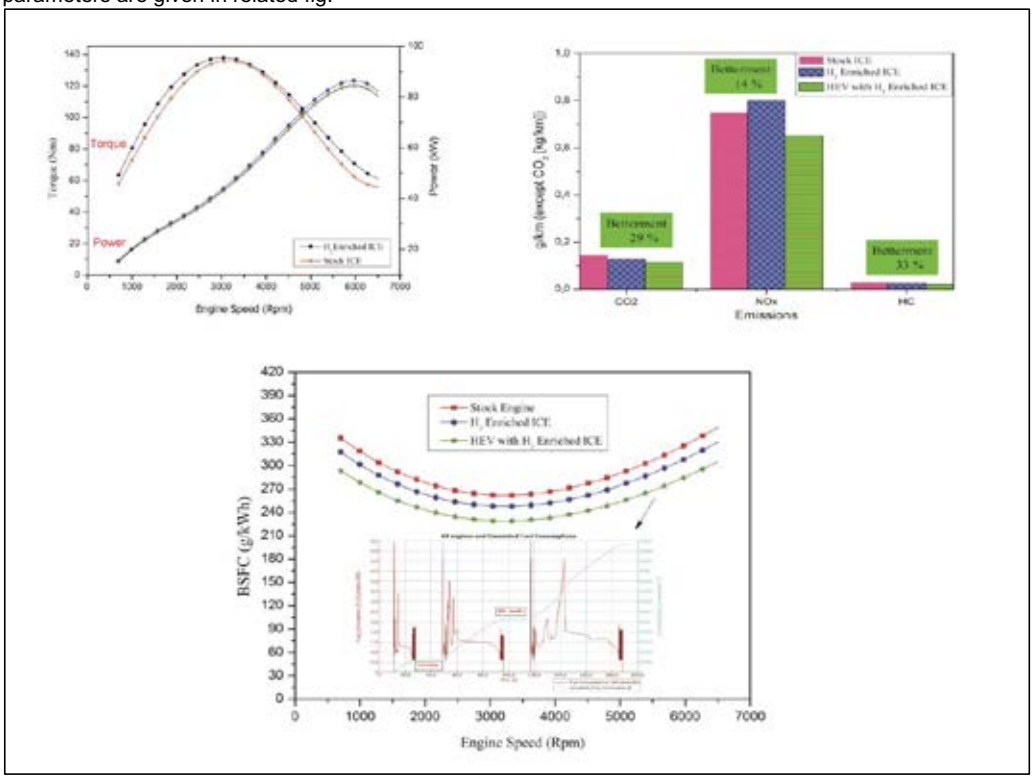


Fig. 2: Stock ICE and H_2 enriched ICE effects of HEV in terms of fuel consumption and emissions

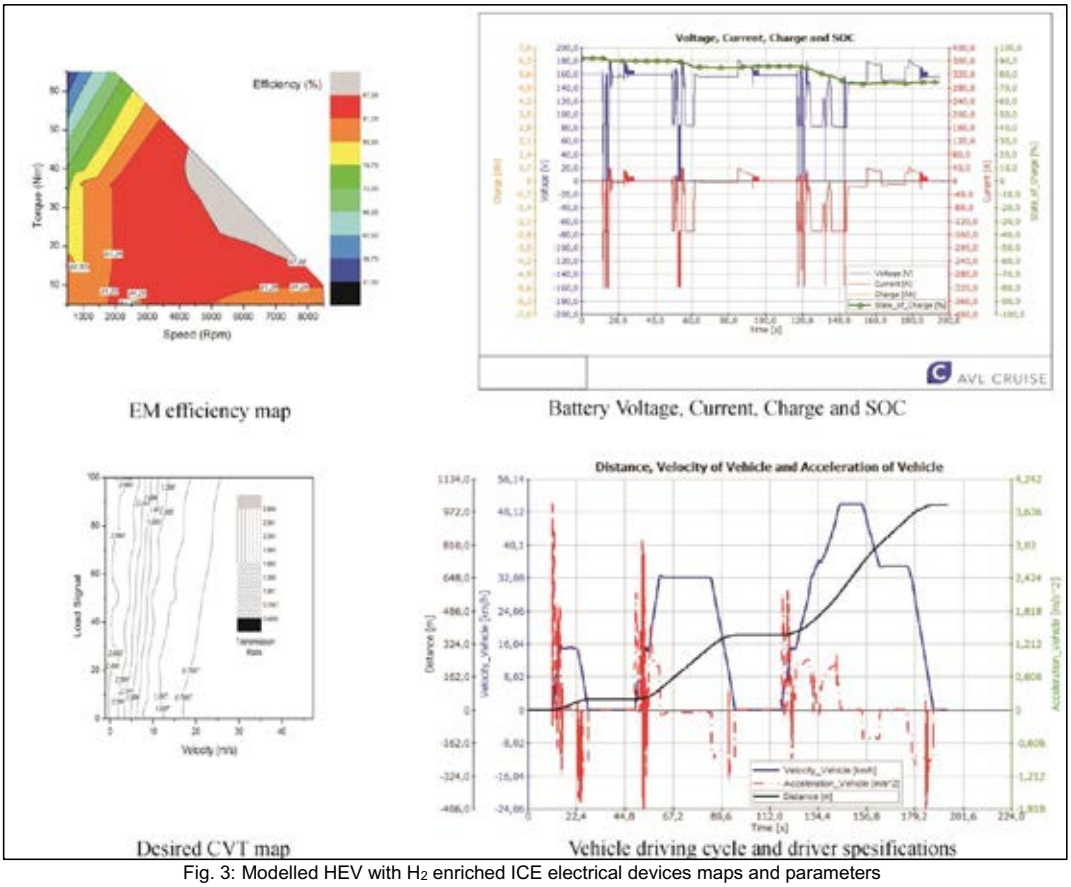


Fig. 3: Modelled HEV with H_2 enriched ICE electrical devices maps and parameters

IV. Conclusions

In this simulation study, a SI ICE is enriched with hydrogen via intake manifold (8% vol.) for master driver on parallel architecture HEV. AVL Boost and Cruise tools were used for simulation. Hydrogen enriched ICE is used on HEV application simulated for the first time with this study. Simulation steps, selected driving cycle (UDC) and vehicles specifications were given detailed with tables and figures. Simulation results showed very promising outputs in the terms of reduction of fuel consumption and emissions while improvement of performance.

Acknowledgements

This study was conducted with AVL CRUISE and AVL Boost. Author acknowledges to AVL-AST, Graz, Austria to provide these programs.

References

Arat H. T., et al., Optimizing the quantity of diesel fuel injection by using 25hhocng gas fuel mixture, Advanced Engineering Forum, Vol. 14, 36-45, (2016).

Arat H. T., et al., Effect of using Hydroxy–CNG fuel mixtures in a non-modified diesel engine by substitution of diesel fuel, International Journal of Hydrogen Energy, 41/19, 8354-8363, (2016).

AVL, 2015, Users Guide Book. AVL CRUISE- AVL Boost Version 2015.

Dinçer İ, Zamfirescu C., Sustainable Hydrogen Production, Elsevier, ISBN: 9780128015636, (2016).

Grabowski T., et al,(Ford Company), Hydrogen fuelled hybrid power-train and vehicle, US patent, US20060174624 A1, (2006).

Gürz M., Baltacıoğlu E., Hameş Y., Kaya K., The meeting of hydrogen and automotive: A review, International Journal of Hydrogen Energy, 42/36, 23334-23346 (2017).

Hameş Y., Kaya K., Baltacıoğlu E., Türksoy A., Analysis of the control strategies for fuel saving in the hydrogen fuel cell vehicles, International Journal of Hydrogen Energy, https://doi.org/10.1016/j.ijhydene.2017.12.150, In press, (2018).

He X., Development and validation of a hybrid electric vehicle with hydrogen internal combustion engine, Ph.D. Thesis, Texas Tech University (2006).

Lui W., Hybrid electric vehicle system modelling and control, John Wiley and Sons Co. Press, ISBN 9781119279327, (2017).

Kenanoğlu R., et al., Numerical comparison of HHO and HHOCNG fuel performance analysis with pilot diesel injection, Advanced Engineering Forum, 18, 58-65, (2016).

Preparation And Characterization Of Polyvinyl Alcohol/Chitosan Blended Anion Exchange Membrane For Direct Borohydride Fuel Cells

Ramiz Gültekin Akay[1], Tuncay Kadıoğlu[1], Cenk Çelik[2]
[1]Department of Chemical Engineering, Kocaeli University, Kocaeli, Turkey
[2]Department of Mechanical Engineering, Kocaeli University, Kocaeli, Turkey

Development of liquid based fuel cells for particularly portable applications which are the clean and efficient substitutes for the batteries such as li-ion became more important in the recent years. Direct borohydride fuel cells (DBFC) is a promising sub-class of fuel cells because an alkaline solution of sodium borohydride (NaBH4) as fuel offers the ease of storage and transportation and oxygen, air or hydrogen peroxide as oxidant could be used. DBFCs have the advantages of having a higher theoretical open circuit voltage (OCV), higher energy density (theoretical energy density for a DBFC using oxygen is 9.3 kW h kg-1) and safety compared to proton exhange membrane fuel cells (PEMFC) and direct methanol fuel cells (DMFC). Since sodium borohydride doesn't have any carbon in it CO can not be formed in the cell preventing CO poisioning occuring in cell's anode. Anode, cathode and overall reactions and the potentials (in strongly alkaline media) are as follows:

Anode (Oxidation): $BH4^- + 8OH^- \rightarrow BO2^- + 6H2O + 8e^-$ E0=1.24 V (1)
Cathode (Reduction): $O2 + 2H2O + 4e^- \rightarrow 4OH^-$ E0=0.40 V (2)
Overall Cell Rxn: $NaBH4 + 2O2 \rightarrow NaBO2 + 2H2O$ E0CELL=1.64V (3)

As in other types of fuel cells, electrolyte membrane is one of the most important component for the commercialization of DBFCs. Both anion-exchange membranes (AEMs) and cation-exchange membranes (CEMs) can be used for DBFCs. AEMs can transport OH- from cathode to anode side with efficient way and naturally suitable for an alkaline FC but BH4- crossover is higher than that of CEM. Alkaline stability of AEMs is limiting their use for long-term operation in DBFCs. The fuel-cell operation conditions, temperature, basicity of environment directly effect stability. Another factor is the ion exchange capacity (IEC) which depends on the degree of swelling ratio and water uptake, or number of the cationic sites of the membrane.

In this study, PVA/CS AEMs were prepared by a modified solution casting method and glutaraldehyde is used as a cross-linking agent. The amount of glutaraldehyde was inestigated on the membrane performances. Another investigated parameter is the preparation METHOD: AEMs were prepared by direct and indirect chemical cross-linking. The membranes were studies in their OH- forms and characterized for their ion conductivity with electrochemical impedance spectroscopy (EIS), ion exchange capacity (IEC) with titration, mechanical stability by tensile tests, chemical stability with fenton's tests, water uptake, chemical characterization by FTIR. The permeability tests were also performed in a lab made permeability cell with a potentiometric electrochemical method. Results showed that these membranes have a potential if the balance between the crosslinking and the other needed properties could be balanced. Further single fuel cell tests will be performed in the near future.

Keywords: direct borohydride fuel cell, anion exchange membrane, polyvinyl alcohol, chitosan

Colloidal Synthesis and Characterization of $CuInS_2$ Nanoparticle for Solar Hydrogen Production

[1]Çiğdem Tuc Altaf, [1,2,*]Nurdan Demirci Sankir
[1] TOBB University of Economics and Technology, Micro and Nanotechnology Graduate Program, Sogutozu Cad. No:43, Ankara,06560, Turkey
[2] TOBB University of Economics and Technology, Materials Science and Nanotechnology Engineering, Sogutozu Cad. No:43, Ankara,06560, Turkey

* E-mail:nsankir@etu.edu.tr

Abstract
The renewable energy sources, including solar cells have been growing interest since they are perfect alternatives for fossil fuels which cause serious enviromental problems. The major problems of solar energy are the low efficiency and high cost. Thin film $CuInS_2$ solar cells are being under investigation as their primary advantage is low cost. The aim of this research is to develop low cost $CuInS_2$ thin films for solar cells by practical solution based techniques on FTO coated glass substrate. For this purpose, chalcopyrite, zincblende and wurtzite crystal types of nanoparticles were prepared via facile hot-injection process and they have been characterized by XRD, EDS and TEM. The as-synthesized nanoparticles were redispersed in *N,N*-dimethylformamide which would faciliate the practical application of these nanoinks. The photoelectrochemical performance (PEC) study has been performed under the condition of 1-sun illumination. 6.72% and 0.91% of the illumination and photo-conversion efficiencies have been evaluated, respectively.

Keywords: Copper indium sulfide; nanoink; hydrogen; thin film solar cells

I. Introduction

Photoelectrochemical solar cells (PEC-cells) are known for their ability to split water into hydrogen and oxygen gases by utilizing solar energy. Thus, hydrogen generation by PEC-cells draws great attention for being one of the most attractive chemical methods for renewable energy conversion. Along with increasing demand in finding low cost routes for the production of photoelectrodes for PEC-cells, I-III-VI ternary nanocrystals have been suggested as promising materials for solar hydrogen production. Among these materials, $CuInS_2$ nanocrystals have gained a great influence in this field due to its large absorption coefficient ($\alpha = 5\times10^5\,cm^{-1}$) in the visible spectral range, which makes it an attractive material for the applications in solar energy conversion, photodetectors, light-emitting devices, photocatalysis, and biolabelling as previously reported by Kolny-Olesiak (2013). In addition, $CuInS_2$ exhibit a suitable direct band gap of ~1.5 eV. Solvent based synthetic routes leading to stable $CuInS_2$ nanoparticles are additionally attractive since they avoid high cost and energy intensive vacuum techniques for the production of active materials. $CuInS_2$ nanoparticles have been prepared by various solution based routes by Rosenthal (2012). $CuInS_2$ exists in three polymorphs: a stable phase with a tetragonal chalcopyrite structure, metastable phases with a cubic zinc-blende and a hexagonal wurtzite structures depending on temperatures. The metastable phase exhibits more flexibility of stoichiometry as compared to chalcopyrite structure. Consequently, the disordered structure and the potential application in solar cells have been investigated in the controlable synthesis of metastable $CuInS_2$ by Cui (2009). More recently, the formation of two crystal phases in single nanocrystals with various shapes has gained interest due to their ability of providing new possibilities to enhance the optoelectronic properties Liu (2013). The heterocrystalline polytypic $CuInS_2$ with zinc-blende or chalcopyrite structure growing on wurtzite structure have been reported by Yu (2016). $CuInS_2$ are dispersed in various solvents to form ‘‘nanoinks’’ which was applied on glass substrates by Chen (2015). In this manuscript, we present the detailed process for the synthesis of $CuInS_2$ by hot injection method. The as-prepared nanoparticles are re-dispersed in N,N-dimethyl formamide to form stable nanoink paste which can easily be applied on glass to fabricate PEC-cells for solar hydrogen generation.

II. Experimental Set-up and Procedure

Synthesis of $CuInS_2$ Nanoparticles. All the synthesis procedure has been carried out through sthandard Schlenk system under N_2 gas atmosphere. A 15 ml oleylamine (OLA) solution of 1.5 mmol $CuCl_2$, 1.5 mmol $InCl_3$ was heated to 130 °C in a three-neck flask to dissolve completely. Then, the temperature has been raised to 225°C. 20 ml of freshly prepared OLA solution of thiourea (3.0 mmol) was rapidly added to previous solution at this temperature and the reaction was refluxed for additional 1 h under N_2 gas circulation and then cooled down to room temperature (RT). The obtained $CuInS_2$ nanoparticles were precipitated by addition of 5.0 ml of toluene and 10.0 ml of ethanol and centrifuged. Decantate was discarted and the black powder was washed with ethanol for three times. Same procedure was applied for other $CuInS_2$ nanoparticles by changing precursors, solvent and temperature (Table 1).

PEC-Cell Fabrication. Prior to use, FTO coated glass substrates were cleaned by ultrasonic bath in acetone for 10 min, in Alconox® for 10 min, washed with distilled water and dried. $CuInS_2$ nanoink were applied a by doctor blade technique. Typically, a concentrated N,N dimethyl formamide (NMF) solution of nanoink (30.0 mg/ml) was dropped at one edge of glass substrate and heated at 300 °C for 3 min to remove organics.



Fig. 1: Experimental set-up

III. Analysis

The crystal structure of the films was confirmed by using Panalytical X'pert Pro MPD X-Ray diffractometer (CuKα, λ=1.5405 A). $CuInS_2$ nanoparticles were dispersed in ethanol and dropped on Mo grid for HRTEM anaylsis which were performed by Jeol 2100F 200kV RTEM instrument. Energy dispersive spectrometry (EDS) was carried on FEI, Quanta 200 FEG. The photoelectrochemical (PEC) performance of the samples (area=1cm^2) was examined by using the conventional three-electrode cell with an aqueous 0.05 M Na_2S and 0.95 M Na_2SO_3 electrolyte solution (pH 12.5). For electrode connections copper wires have been attached on glass contacts by silver paste. Silver contact and back contact of the photoanodes was isolated by epoxy resin. Current density of the photoanodes as a function of applied potential versus the Ag/AgCl reference electrode was analyzed using Gamry 750 Potentiostat/Galvanostat/ZRA system in the range of -1 to 0 V. Platinum sheet was used as a counter electrode. All measurements were carried out at room temperature. Illuminated measurements were performed with back light illumination of photoanodes using Lot Oriel low cost solar simulator with 150 W Xenon Lamp.

IV. Results and discussions

The $CuInS_2$ nanoparticles synthesized by hot-injection process have been characterized by XRD spectroscopy to determine crystal structures. The corresponding XRD patterns of the $CuInS_2$ synthesized from either oleylamine (OLA) or diethylene glycol (DEG) solution of Cu/In/S precursors in 1:1:2 ratio at 225 °C are displayed in Figure 2. The XRD pattern belonging on sample (1) (Fig. 1a) exhibited a small peak indexed as (200) at 33° as a good match with previously reported zincblende crystal structure [JCPDS No. 75-0106]. The pattern exhibits well indexed diffraction peaks (110) and (102) of the standard wurtzite structure (Fig. 2b) maching well with the bulk wurtzite $CuInS_2$ peaks. In addition, the peak position and relative peak intensities identical with the powder diffraction data reported for wurtzite $CuInS_2$ by Wang (2014). Although the difference in XRD patterns between chalcopyrite and zincblende is very small, the low intensity characteristic peak of chalcopyrite structure (101) appears at 15.4°, and zincblende characteristic peak (200) disappears at 32.6° indicating that the sample (3) possesses a chalcopyrite structure (Fig. 2c) (JCPDS card file no. 85-1575). The diffraction peaks of the product are sharp and intense indicating that the as-synthesized $CuInS_2$ nanoparticles have an excellent crystallinity or large crystal size. The absence of diffraction peaks from other species, indicating that as-prepared sample is pure $CuInS_2$ crystals without any binary sulfides of Cu_2S, CuS, or In_2S_3.

Tab. 1: List of the prepared CIS *NCs*.

Sample	Cu	In	S	Solvent	Crystal Form	Cu/In/S ratio by EDS
(1)	CuCl	$InCl_3$	Elemental Sulfur	OLA	Zb	1.00/1.00/1.86
(2)	$CuCl_2$	$InCl_3$	Thiourea	OLA	Wz	1.03/1.00/1.99
(3)	CuCl	$InCl_3$	Thiourea	DEG	Ch	1.00/1.13/1.80
(4)	$Cu(acac)_2$	$In(acac)_3$	Thiourea	OLA	Poyltypic	1.00/1.13/1.90

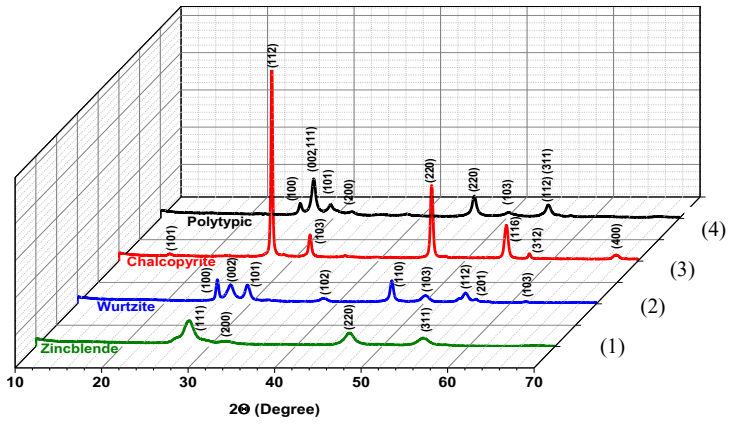


Figure 2. XRD pattern of the syhthesized $CuInS_2$ nanoparticles in (a) zincblende (b) wurtzite (c) chalcopyrite (d) polytypic structures

The stoichiometric compositions of $CuInS_2$ could be analyzed by using energy dispersive spectrometric (EDS) data. Based on these data, the Cu/In/S atomic ratio is found very close to the theoretical stoichiometric composition for each sample indicating the high purity and good crystallinity corroborating the XRD results. The absence of oxygen peaks in the given spectra also approves the formation of $CuInS_2$ free of undesired metal oxides. HRTEM images of Ch-$CuInS_2$ exhibited large crystal size (~120 nm) formation but highly aggregated.

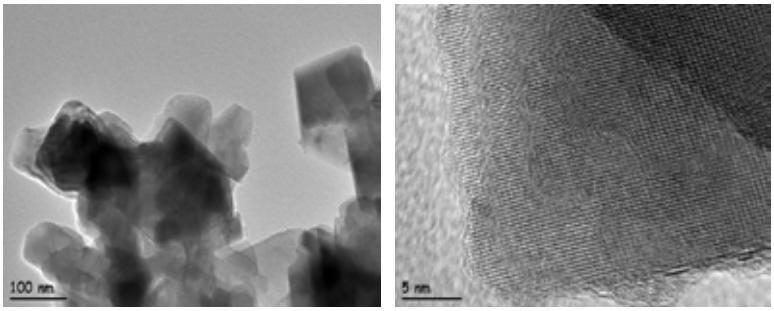


Figure 3. TEM and HRTEM images of Chalcopyrite CIS NCs

Photoelectrochemical Measurement of prepared thin films. In order to demonstrate the potential applications of chalcopyrite $CuInS_2$ nanoink in solar harvesting, a device structure of FTO coated glass/ $CuInS_2$ has been prepared and the photocurrent density–voltage (J – V) characteristics of thin film was invested in a PEC cell containing 0.95M Na_2SO_3-0.05M Na_2S electrolyte solution (Fig 4). The applied bias photon-to-current efficiency, which is also called ABPE, of the photoelectrodes has been calculated by using the following equation:

$$\eta_{photo}(\%) = \frac{J_{photo}(1.23 - V_{bias})}{P_{light}} x100 \qquad (1)$$

where the J_{photo} is the difference between the illuminated and dark current densities, 1.23 is the redox potential for water, and P_{light} is the illumination power density, which equals to the 100 mW/cm^2 for the 1 sun condition on the surface of the earth. For the three-electrode configuration, V_{bias} should be converted into the potential vs. RHE according to:

$$V_{bias} = V_{Ag/AgCl} + 0.059\,pH + E^0_{Ag/AgCl} \left(E^0_{Ag/AgCl} = +0.199V\right) \qquad (2)$$

when Ag/AgCl acts as a reference electrode and Pt as cathode electrode.

The photocurrent value at 0V vs RHE was observed as 14.8 mA cm^{-2} for prepared thin film. In order to estimate solar-to-hydrogen conversion efficiency (STH) we calculated η_{photo} as 0.91% (equation 1). We found a comparable result to that reported by Gunawan (2017). The PEC efficiency for the fabricated thin film is aimed to be improved by the insertion of In_2S or CdS layers into the system in further study.

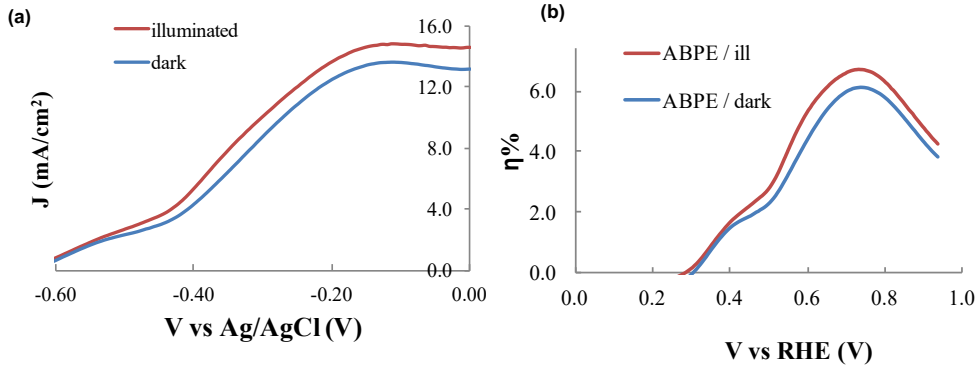


Figure 4 (a) *J-V* characteristics of the resulting thin film solar cells; (b) PEC efficiency vs VrHE graph under both illumination and in the dark

V. Conclusions

We have demonstrated a facile colloidal synthesis for the selective $CuInS_2$ nanoparticles growth as well as polytypic crystal formation. Later on, a practical thin film fabrication was performed to investigate the photoelectrochemical performance for hydrogen generation. The major problem on non-vacuum techniques is the adhesion of nanoink to the substrate during the fabrication process. It is observed that the use of *N,N*-DMF solvent improved the adhesion of the ink to glass substrate resulting in a crack free and uniform thin film formation. As prepared thin films were applied in water reduction to generate hydrogen gas and thus, 0.91% photo-conversion efficiency was observed during PEC study.

Acknowledgements

Autors would like to appreciate "The Scientific and Technological Research Council of Turkey" (TUBİTAK) for their support of this research under the contract number 114F360.

References

Chen, B., Chang, S., Li, D., Chen, L., Wang, Y., Chen, T. ,Template synthesis of $CuInS_2$ nanocrystals from In_2S_3 nanoplates and their application as counter electrodes in dye-sensitized solar cells, Chem Mater., 27, 5949-5956, (2015).

Conner, S.T., Hsu, C.M.; Weil, B.D., Aloni, S., Cui, Y., Phase Transformation of Biphasic Cu_2S−$CuInS_2$ to Monophasic $CuInS_2$Nanorods, J.Am.Chem.Soc, 131, 4962-4966, (2009).

Gunawan, Haris A., Widiyandari, H., Septina, W., Ikeda, S., Surface modifications of chalcopyrite CuInS2 thin films for photocathodes in photoelectrochemical water splitting under sunlight irradiation, Material Science and Engineering, 172, 012021(2017)

Kolny-Olesiak, J., Weller, H. Synthesis and Application of Colloidal $CuInS_2$ Semiconductor Nanocrystals. ACS Appl. Mater. Interfaces, 5,12221 – 12237, (2013).

Liu, M., Jing, D., Zhou, Z., Twin-induced one-dimensional homojunctions yield high quantum efficiency for solar hydrogen generation., L. Nat. Commun., 4, 2278, (2013).

Niezgoda, J. S., Harrison, M. A., McBride, J. R., Rosenthal, S. J., Novel Synthesis of Chalcopyrite $Cu_x In_y S_2$ Quantum Dots with Tunable Localized Surface Plasmon Resonances. Chem. Mater., 24, 3294, (2012).

Wang Y, Zhao XD, Liu FY, Zhang XH, Chen HW, Bao FX, et al. Selective synthesis of cubic and hexagonal phase of $CuInS_2$nanocrystals by microwave irradiation. RSC Advance.,4:16022–6, (2014).

Wu, L., Chen, S-Y., Fan, F.J., Zhuang, T.T., Dai, C.M., Yu, S.H., Polytaypic nanocrystals of Cu-based ternary chalcogenides: colloidal synthesis and photochemical properties, J.Am. Chem. Soc., 138, 5576-5586, (2016).

Novel Pd-Co/C Bimetallic Alloy Electrocatalyst for Direct Borohydride Fuel Cell

[1*]Cem Gözlü, [2]Cenk Çelik, [1]Ayşe Nilgün Akın, [1]Ramiz Gültekin Akay
[1] Kocaeli University Chemical Engineering Department, Umutttepe Campus, İzmit, 41380, Turkey
[2] Kocaeli University Mechanical Engineering Department, Umutttepe Campus, İzmit, 41380, Turkey

* E-mail: cemgozlu@gmail.com

Abstract
A novel Pd-Co/C electrocatalyst was prepared via modified polyol method to be used in direct borohydride fuel cell anode. The structural characterization was done by XRD, ICP-OES, TEM, EDX and XPS analysis. XRD results showed no oxidation peaks for Co and Pd oxides. The calculated particle size was 3,0 nm. ICP-OES results showed the metal loading of the catalyst was %12 by weight and the ratio of Pd:Co by weight is 1:1. CV results showed a good selectivity towards BOR and ECSA value calculated was 71,0 cm²/mg. According to chronoamperomety study, compared to Pd/C prepared via the same method under same conditions Pd-Co/C catalyst showed more current density and stability.

Keywords: Direct Borohydride Fuel Cells, Pd-Co Nanoparticles, Anode Catalyst

I. Introduction

In the recent decades, with the increase in the number and variety of portable electronic devices demand in power for these has also increased. Fuel cells and particularly liquid fuel based ones are becoming alternatives of conventional batteries with being clean, their high efficiency and energy/power density promises. H_2-O_2 polymer electrolyte membrane fuel cells (PEMFC) and direct methanol fuel cells (DMFC) are vastly studied. But, fuel cells such as direct borohydride fuel cells (DBFC) are also very good candidates and needs more improvements. Also, they have some advantages over PEMFC and DMFC. Since sodium borohydride doesn't have any carbon in it CO can not be formed in the cell preventing CO poisioning occuring in cell's anode. Also, DBFC uses borohydride ion directly as fuel, meaning no H_2 is formed, removing the need of a reformer and the problem of H_2 storage. Since there is no H_2 production in DBFC the efficiency of the fuel cell is lower than Indirect borohydride fuel cell so DBFC can be used in military devices with low power need.

The anode and cathode reactions and overall reaction is shown in Eq 1 to Eq 3. Anode reaction is called borohydride oxidation reaction (BOR) and cathode reaction is called oxygen reduction reaction (ORR). In theory 8 electrons can be produced by BOR in alkaline media but because of the hydrolysis of borohydride this amount of electron production can not be achieved.

$$\text{Anode: } NaBH_4 + 8OH^- \longrightarrow NaBO_2 + 6H_2O + 8e^- \ (E^0 = -1{,}24V) \quad (1)$$
$$\text{Cathode: } 2O_2 + 4H_2O \longrightarrow 8OH^- \ (E^0 = +0{,}4V) \quad (2)$$
$$\text{Overall: } NaBH_4 + 2O_2 \longrightarrow NaBO_2 + 2H_2O + 8e^- \ (E^0 = 1{,}64V) \quad (3)$$

Behmenyar (2015) and Merino - Jiménez etal (2012) reported that commonly studied catalysts for BOR is noble metals such as Pt, Pd, Au; transion metals such as Ni and Cu and the alloys of these metals. Hydrogen storage alloys were also studied for DBFC anodes. Lam (2012) reported that gold is the most studied metal as BOR because it is not active towards borohydride hydrolysis so 8 electrons can be produced as the result of BOR. Chatenet etal (2006) studied the activity of carbon supported pt towards BOR and reported that 4 electrons can be produced because of borohydride hydrolysis. Pt alloys such as Pt-Cu, Pt-Zn, Pt-Au and Pt-Ni can produce higher electrons as the result of BOR. Ag is another metal studied for BOR. Molina Concha and Chatenet (2009) reported that Ag alloy of Pt shows higher activity than Pt or Ag. Atwan etal (2007) prepared different Ag alloys and reported Ag-Ir and Ag-Pt shows highest activities. Liu etal (2004) and Dong etal (2005) reported that Ni produces 4 electron rather than theoretic 8 electrons. The reason is basically the formation of Ni oxides in the alklyne medium. Even though Co is highly active towards borohydride hydrolysis its alloys were studied for BOR. Li etal (2013) used Co-W-B as anode and the single cell tests reveals higher power densities than Au/C and Pt/C. Pd is another metal studied for DBFC anode. Çelikkan etal (2006) reported that Pd, like Pt, shows activity towards borohydride hydrolysis and produces less electrons than 8. Behmenyar and Akın (2014) studied Pd-Cu/C for DBFC anode and reported that Pd-Cu produces more power density than Pd/C which was prepared by the same method.

I. Experimental Set-up and Procedure

Pd-Co/C bimetallic alloy electrocatalyst was prepared by a modified polyol method. Calculated amounts of palladium acetate and cobalt acetate which were used as precursor salts were dissolved in 1,4 Dioxane and ethylene glycol respectively. Vulcan XC-72 which was used as carbon catalyst support was mixed with ethylene glycol. Precursor solutions were kept in the ultrasonic bath for 15 minutes and then mixed with carbon and ethylene glycol. The mixture was set to pH value of 10 using 1M NaOH solution. A PARR pressured reactor, shown in Fig. 1, was used to prepare the electrocatalyst. Nitrogen gas was used to create oxygen-free media and pressuring agent. The pressure of the reactor was 20 bars. The catalyst preparation reaction lasts 2 hours. After the reaction the catalyst

was kept in ice bath overnight. Then, the solvent was filtered using 50 μm filter and the cake was washed with distilled water and acetone for one time. Then the catalyst was filtered again and dried at 105 °C at 24 hours in a Nüve EV018 vacuum oven.



Fig. 1: Experimental installation: PARR/USA 4525 pressured reactor system

III. Analysis

XRD, ICP-OES, TEM, EDX and XPS analyses were used to determine the structural characterization of Pd-Co/C. XRD analysis was performed using Rigaku Miniflex II X-ray diffractometer, between 2θ values of 10° and 80° with the rate of 1°/minute and 0,02° step length. ICP-OES analysis was performed using Perkin Elmer Optime 4300 DV. The solvent used to dissolve the catalyst contains 3:1 by volume of HNO_3:HCl.

CV and chronoamperometry analyses were used for electrocharacterization of Pd-Co/C and LSV was used to determine the number of electrons produced as the result of BOR. CV was used to determine the selectivity of the catalyst towards BOR and the ECSA of Pd-Co/C. Chronoamperometry was used to determine the stability of the catalyst. CV and LSV analysis were carried out between -1V vs Ag/AgCl and 0,5V vs Ag/AgCl with 20 mV/s scanning speed and 1mV step length. Chronoamperometry analysis was performed for 60 seconds. The step change was from -0,2V vs Ag/AgCl to -1,2V vs Ag/AgCl. These analyses were performed using Gamry Reference 3000 Potensiostat, RDE360 rotating disk electrode system and Dr. Bob's Cell. Glassy carbon RDE (R = 5mm) was used as working electrode, a graphite rod was used as counter electrode and Ag/AgCl electrode containing 3M KCl solution was used as reference electrode.

The ink preparation and catalyst coating on RDE method fallows as: 10 mg catalyst and 1 mL ethanol was mixed in ultrasonic bath for 30 minutes. 5 µL Nafion solution (%15 Nafion w/w) was dripped on RDE then 10 µL catalyst ink was dripped and dried at 80 °C for 30 minutes.

IV. Results and discussions

XRD patterns of Pd-Co/C and commercial Pd/C was shown in Fig. 2. The shifts to the right at Pd peaks suggests the formation of Pd-Co alloys and 2θ values of the peaks were consisted with studies made by Liu etal. (2014) on Pd-Co/C. The particle size calculated from Debye – Scherrer Equation was found 3,0 nm.

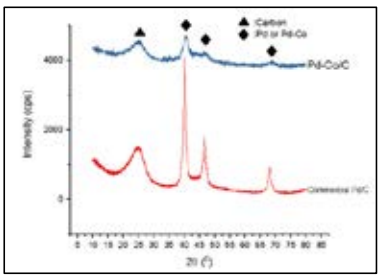


Fig. 2: XRD patterns of commercial Pd/C and Pd-Co/C

Table 1 shows the ICP-OES results of Pd-Co/C. The desired amounts of Pd and Co can not be achieved. It is thought that the reaction of Pd and Co reduction in ethylene glycol is not efficient enough to get desired results.

Tab. 1: ICP-OES results of Pd-Co/C

	%Pd	%Co
Pd-Co/C	*6,2*	*6,0*

Fig. 3 shows CV voltammograms of Pd-Co/C in different electrolytes. First voltammogram which was obtained in %20 NaOH by weight and 1M $NaBH_4$ could not be analysed because the $NaBH_4$ concentration was too high to get a clear voltammogram. The more $NaBH_4$ concentration reduces the more voltammogram became clear. In 3M NaOH and 0,05M $NaBH_4$ medium the voltammogram was clear enough to analyse so this electrolyte concentration was used in other analyses.

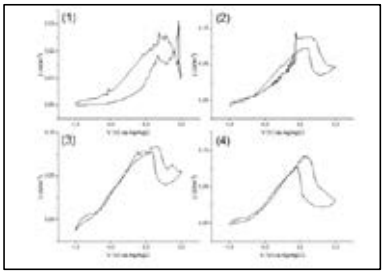


Fig. 3: CV voltammograms of Pd-Co/C using different electrolytes. (1) %20 NaOH by weight + 1M $NaBH_4$ (2) 3M NaOH + 0,2M $NaBH_4$ (3) 3M NaOH + 0,1M $NaBH_4$ (4) 3M NaOH + 0,05M $NaBH_4$

Fig 4 shows the CV voltammogram of Pd-Co/C which was used to analyse the selectivity of the catalyst towards BOR. Behmenyar and Akın (2014) and Liu etal (2015) performed the same analysis with Pd-Cu/C and Pd-Zn/Nanoporous Carbon and obtained the same peaks. According to their studies peak a1 which was obtained between -0,8V vs Ag/AgCl and -0,7V vs Ag/AgCl represents H_2 electrooxidation which is the product of borohydride hydrolysis. a2 peak which was obtained nearly at 0V vs Ag/AgCl represents direch BH_4^- electrooxidation. c1 peak obtained at approximately -0,1V vs Ag/AgCl represents BH_3OH^- electrooxidation which was adsorbed on catalyst. Since the c1 peak is too big the catalyst shows high activity towards BH_3OH^- adsorbtion.

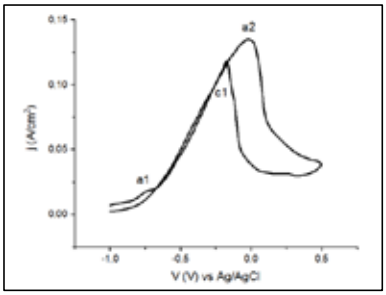


Fig. 4: CV voltammogram of Pd-Co/C (Electrolyte: 3M NaOH + 0,05M $NaBH_4$)

Fig. 5 shows the CV voltammogram used to determine the ECSA value of Pd-Co/C catalyst. ECSA was calculated from the area of single-layer Pd oxidation peak which is obtained at approximately -0,3V vs Ag/AgCl at backward sweep. The calculated ECSA value is 71.0 cm^2/mg which is lower than Pd-Cu/C and Pd-Zn/Nanoporous Carbon calculated by Bahmenyar and Akın (2014) and Liu etal (2015) respectively.

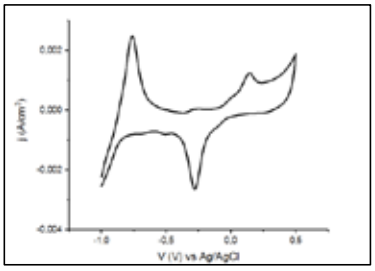


Fig 5: CV voltammogram of Pd-Co/C (Electrolyte: 3M NaOH)

Fig. 6 shows the chronoamperometry result for Pd-Co/C. After 60 seconds of the voltage drop from -0,2V vs Ag/AgCl to -1,2V vs Ag/AgCl Pd-Co/C catalyst remained stable. The current density value showed no change which

indicates the raction rates of the reactions occurring at the anode was stabled. This can be explained by the stability of the Pd-Co/C.

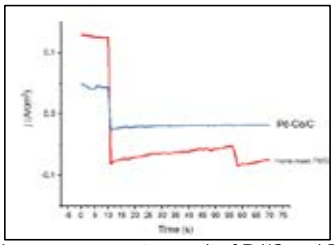


Fig 6: Chronoamperometry result of Pd/C and Pd-Co/C

V. Conclusions

Carbon supported Pd-Co nanoalloy catalyst was prepared via a modified polyol method. XRD pattern of the catalyst revealed Pd-Co structure formation and particle size of the alloy was calculated to be 3,0 nm which showed polyol method is an efficient method to prepare nano-sized alloy particles. CV analyses showed high selectivity towards BOR. Chronoamperometric study revealed Pd-Co/C is a stable catalyst.

Acknowledgements

This research was supported by the Scientific and Technological Research Council of Turkey (TÜBİTAK) (Project code: 215M255). This support is gratefully acknowledged by the authors.

References

Behmenyar G., Düşük Sıcaklık Yakıt Pilleri İçin Pd-Cu/C Katalizörünün Geliştirilmesi, Ph.D. Thesis, Kocaeli Üniversitesi (2015).

Behmenyar G., Akın A. N., Investigation of crbon supported Pd-Cu nanoparticles as anode catalysts for direct borohydride fuel cells, Journal of Power Sources, 249, 239-246 (2014).

Chatenet M., Micoud F., Roche I., Chainet E., Kinetics of sodium borohydride direct oxidation and oxygen reduction in sodium hydroxide electrolyte Part I. BH4- electro-oxidation on Au and Ag catalysts, Electrochemica Acta, 51, 5459-5467 (2006).

Dong H., Feng R., Ai X., Cao Y., Yang H., Cha C., Electrooxidation Mechanisms and Discharge Characteristics of Borohydride on Different Catalytic Metal Surfaces, The Journal of Physical Chemistry, 109, 10896-10901 (2005).

Li S., Yang X., Zhu H., Wei X., Liu Y., Ultrafine amorphous Co-W-B alloy as the anode catalyst for a direct borohydride fuel cell, International Journal of Hydrogen Energy, 38, 2884-2888 (2013).

Liu B. H., Li Z. P., Suda S., Electrocatalysts for anodic oxidation of borohydrides, Electrochemica Acta., 49, 3097-3105 (2004).

Liu J., Yi L., Wang X., Zhao Q., Zhang Y., Gao J., Wei W., Investigation of nanoporous carbon supported palladium-zinc nanocomposites as anode catalysts for direct borohydride-hydrogen peroxide fuel cell, International journal of Hydrogen Energy, 40, 7301-7307 (2015).

Merino-Jimenez I., Ponce de Leon C., Shah A. A., Walsh F. C., Developments in direct borohydride fuel cells and remaining challenges, Journal of Power Sources, 219, 339-357 (2012).

Molina Concha B., Chatenet M., Direct oxidation of sodium borohydride on Pt, Ag and alloyed Pt-Ag electrodes in basic media Part II. Carbon-supported nanoparticles, Electrochemica Acta, 54, 6130-6139 (2009).

A Comparative Study on the Determination of Borohydride Permeability of Cation Exchange Membranes for DBFC

***Kürşat Can Ata*[1], *Tuncay Kadıoğlu*[1], *Ramiz Gültekin Akay*[1], *Cenk Çelik*[2]**

[1]*Kocaeli University, Department of Chemical Engineering, Kocaeli, Turkey*
[2]*Kocaeli University, Department of Mechanical Engineering, Kocaeli, Turkey*

Direct borohydride fuel cell technology is a promising technology for especially protable applications because of the high theoretical energy density and for the advantageous liquid fuel. For Turkey in particular, technologies utilizing boron containing compounds are important since a vast share of world boron sources are located in the country. However, there are a number of technical obstacles to be solved. One of them is the borohydride crossover to the cathode which will cause a mixed potential as a result of the oxidation at the cathode part.

Similar to the other classes of fuel cells, membrane is one of the key components to the commercialization of DBFCs. A good polymer electrolyte membrane must have the impermeability for the reactant and oxidant used (problem in particular for liquid reactant systems). Membrane properties affects all the system performance and electro-catalyst choice and preparation method at first. Nafion® still seems to be the membrane used mostly for DBFCs also because of its teflon like fluorinated backbone and related high chemical-mechanical- thermal stabilities for both PEMFCs and DMFCs. But Nafion® has also well-known drawbacks such as being very expensive (an important barrier for commercializaton), being dependent on full hydration (sharp decrease at temperatures over 80 °C) and high permeability to reactants especially methanol because of its well separated channels and the dependence of water. One of the difficulties in the research on borohydride-based systems is related to the determination of the borohydride concentration particularly for permeability determination.

For this purpose, there are a number of methods are avaliable but it must be fast, non-destructive and should not change the concentration. Therefore, a potentiometric electrochemical method seems to be a good choice. When immersed in sodium borohydride alkaline solutions, different electrode materials give very different responses to the borohydride presence. So the choice and comparison of the electrode materials are very important.

Another technique that we choose includes the combined usage of the acid-base and iodometric titration methods. The acid-base titration method, which simultaneously uses the technique of differentiation and computer simulation of titration curves, allows one to determine the contents of hydroxide and total “borate +borohydride” content. The iodometric titration method allows one to selectively determine borohydride. The average determination error depends on the number and ratio of compounds in a mixture. In this study both the gold and platinum electrode responses for portentometric measurements were investigated and the results are compared with combined acid-base and iodometric method. The two membranes fort he comparison of permeability results are CEM membranes which are commercial Nafion 117 and sulfonated polyether ether ketone (SPEEK) produced in laboratory. Specific details of the both analysis’ of two different techniques will be discussed.

Keywords: dbfc, crossover, permeability, borohydride, ocp, titration

A Labview-FPGA Based Process Control and Power Conditioning Prototype Application of a Fuel Cell Powered Range Extender for Unmanned Aerial Vehicles

[1*]Betül Erdör Türk, [2]Mustafa Hadi Sarul
[1] TUBITAK Marmara Research Center, Energy Institute, Gebze, Kocaeli, 41470, Turkey
[2] Yildiz Technical University, Faculty of Electrical&Electronics, Department of Electrical Engineering, Esenler, Istanbul, 34220, Turkey

* E-mail:betul.turk@tubitak.gov.tr

Abstract
This paper will focus on an embedded Labview-FPGA based data acquisition and control system, which was designed to provide a self-regulated process of the hydrogen generation and power conditioning systems of a fuel cell powered small unmanned aerial vehicle. The hydrogen generation system utilizing sodium borohydride solution is able to produce 4 L/min of hydrogen with the aim of extending the range of the UAV. The critical parameters for on-site hydrogen production like temperature, pressure, mass flow, chemical sensor's output signals and voltage were monitored in real time via the NI sbRIO-9626 control card and Labview FPGA toolkit software. On the power conditioning side, according to the real time output values of the sensors; the required analog and digital signals were evaluated to actuate valves and drive the brushless DC motor and the MOSFETs to manage the power properly. In this study, the combined hardware-software implementation of the experimental and prototype control set-ups will be introduced and performance test results will be given as well.

Keywords: Fuel cell, embedded process control, power conditioning, range extender, UAV, sodium borohydride

I. Introduction

Unmanned air vehicles (UAVs) have many fields of use such as discoveries, observations, target detection/follow-up, determining damage in battlefields, electronic war, physical attack and damage, detecting and eliminating mines, detecting and follow-up of fires, atmospheric observations, search&rescue operations, civil security, using agricultural pesticides, and scientific research.

The most important development in UAVs is the range extension; in other words, the extension of the flight distance or flight time. Many UAVs use batteries because other power supplies have lower efficiencies. However, battery ensures that unmanned air vehicles stay in air for 60-90 minutes, which is a relatively short duration. When the fact that lithium-based batteries have 200 Wh/kg energy density is considered, it is clear that other energy systems with more energy densities are needed. There are several publications reporting application of fuel cells to power UAVs (Bradley, 2009 and Okumus, 2016).

Right at this point, fuel cells are among the important alternative technologies for batteries with their high energy density (pressurized gas hydrogen:1000 Wh/kg, liquid hydrogen:10.000 Wh/kg). The most important problem in fuel cells is the storage and distribution of the hydrogen. Hydrogen may be stored as gas or liquid in pure form. It may also be stored physically in nano-tubes and chemically in the form of hydride. Sodium Borohydride ($NaBH_4$) may be used directly in Fuel Cells; or may be used in Polymer Electrolyte Membrane Fuel Cells (PEMFC) with catalysts after hydrogen is produced by using sodium borohydride as the source of hydrogen (Kim 2011). This process eliminates all the risks and difficulties of storing hydrogen. As a result of the hydrolysis of $NaBH_4$ solution, which is not flammable or explosive and which does not have the risk of exploding even in accumulation in the reactor, with a proper catalyst, H_2 gas is obtained. By feeding this hydrogen to the fuel cell stack, the fuel cell system (FCS) is obtained.

In such a system, accurate reading and processing of the process data and management of the input-output signals that are needed by the power conditioning system are of great importance. A real-time data acquisition and control system must be created for these purposes. In this study, the combined hardware and software implementation of the experimental and prototype control set-ups will be introduced and performance test results will be given as well.

II. Experimental Control Set-up

Experimental studies conducted so far show that it is possible to examine the system under two main headings, which are; the process control of the hydrogen generation system (HGS) and power conditioning unit of the FCS. In the context of the present study, the primary target is to establish a process system that produces min. 4 liters of hydrogen per minute to feed the 200 W fuel cell stack that will be used as the main power unit of the mini type UAV that has a wing opening of 2.5 m. The basic process variables in the system have been defined as temperature (below and upper part of the reactor), flow (the mass flow of the hydrogen), pressure (the pressure in the tank where the hydrogen is stored) and the control system has been designed in terms of its hardware requirements (Erdör Türk, 2014). In addition, an engine controlled drainage system was developed to eliminate the chemicals that are produced as a result of the reaction and that have to be removed from the system via the control equipment.

In terms of the control and data acquisition studies, the c-dAQ 9178 control chassis, NI 9211 differential thermocouple input module, NI 9474 24 V digital output module, NI 9207 voltage/current combined analog input

module, which are the products of National Instruments (NI) were used as the hardware in the experimental design (Fig.1a). The Labview 2015 version and the Real Time Software Module were used as software. It is desired that the system control has a user friendly interface as much as possible especially in the experimental stage, because the variables in the process must be monitored as real time and necessary changes must be made in the interface without interfering to the background of the software (Fig.1b, 1c).

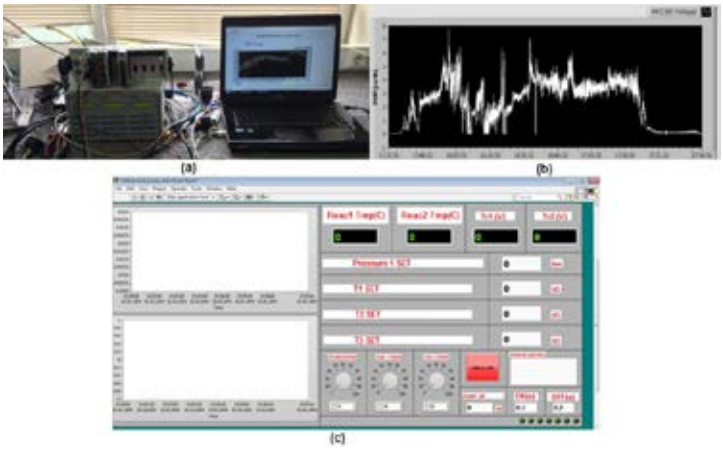


Fig. 1: (a) Experimental set-up of HGS (b)Flow rate chart (c)Labview user interface of the HGS process

As it was foreseen that the UAV would stay in air for approximately 2 hours with the support of the fuel cell, the HGS was run for 2 hours. The hydrogen production graphic of the experiment is given in Figure 1b.

After the design experiments of HGS were completed successfully, the next stage was the transfer of the process control software codes into the Field Programmable Gate Array (FPGA) processor in an embedded form. The FPGA means programmable gate index that is programmable in the field and consists of programmable logic blocks and the inter-connections among these blocks. It is a digital integrated circuit and has a wide application area. Such integrated circuits are produced to perform the logical functions needed by the designer and the function of each logic gate may be designed by the user. In order to create the FPGA design, either the Very High-Speed Hardware Description Language (VHDL) or the schematic design must be created by the user.

In the context of the study, the Labview Program, which is a graphic programming language for software and the FPGA card was programmed by using the VHDL Compiler feature of the program. Since the same programming language was used in the experimental design, it became easy in terms of adaptation to embedded software. In terms of the working principle of the Labview based FPGA software, the task of the FPGA module in the software is to compile the VI file created in the Labview for the FPGA hardware. In the background, the graphic code written is converted into text-based VHDL code. Then, the Xilinx ISE compiler synthesizes how the hardware is synthesized and performed the compilation work to the VHDL code. This process also applies time limitations to the design and makes the design become suitable for low-level hardware sources of the FPGA. The sb-RIO 9626 control card of NI was used in the study as the FPGA Card by considering the hardware requirements of the system. This card has Xilinx-Spartan-6 LX45 FPGA processor, 16-channel Analog 16-bit input, 4-channel Analog 16-bit Output, and 4-channel Digital Input/Output.

III. Control System Procedure

The basic working principle of the control system is as follows; the process data in the fuel cell stack and the HGS are collected via the real time operated system. Main process variables are; temperature, voltage, current, level of the chemicals, pump speed, fan speed, mass flow and pressure. Depending on the structures of the sensors and the levels of the signals, the relevant data may be read by the FPGA card directly or may be sent to the FPGA card by processing or amplifying via the analog card. According to the real time output values of the sensors, the required analog and digital signals were evaluated to actuate valves and drive the brushless DC motor and the MOSFETs to manage the power properly.

The complete system diagram which includes the fuel cell stack, HGS and the power conditioning unit is shown in Fig. 2. As seen in this figure, while fuel is fed to the HGS and hydrogen is generated, a solid chemical is also produced as waste.

Fuel cell stack generates DC power with hydrogen produced by the HGS and with air through the fans on the air breathing fuel cell stack. The FPGA based control card NI-sbRIO 9626, controls the HGS, fuel cell and an analog card in the system. A DC/DC converter on the analogue card provides the internal power requirement of the peripheral circuits and the FPGA platform.

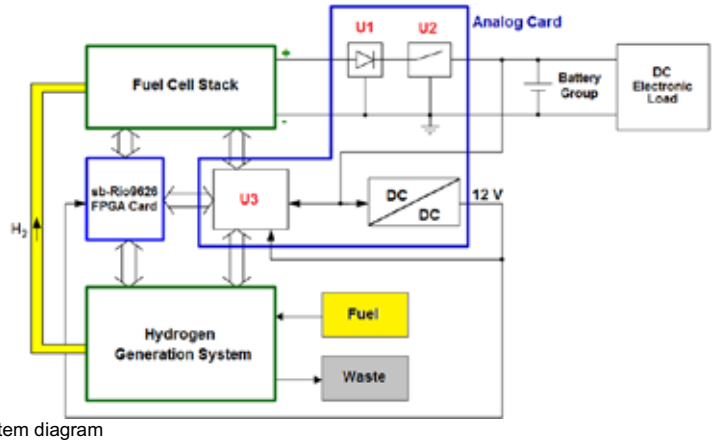


Fig. 2: Complete system diagram

Output terminals of the stack are connected to the Li-ion battery group (22.2 V, 5Ah) over the U1 and U3 circuits on the analog card. The aim of the U1circuit is protecting the fuel cell stack from the reverse current flow. This function could be performed by using a power diode; however, in order to reduce the power losses that would occur in the diode, a power MOSFET was used. The power MOSFET is controlled with an integrated “diode-OR” control circuit and it allows only for a unidirectional power flow as power diodes. As seen in the same figure, if the load requires more power input than that produced by the fuel cell, the fuel cell stack charges the battery. U2 circuit is an excessive charge protection circuit that avoids that the battery is charged over 25 VDC.

NI sb-Rio 9626 card manages online data acquisition and signal generation processes that are needed for the control of the FCS and HGS. Although the U3 circuit block on the analog card produces the signals that sense the chemical waste and water levels of the reactor and collector tanks on the HGS. U3 also consists of temperature and pressure sensing circuits on the required points and MOSFET drivers.

The control algorithms of the whole system were compiled with Labview-FPGA tool and an embedded system control structure was performed. In this way, a self-regulated control system was created that was enabled to run on its own without the support of a PC when it was energized. The system software algorithm consists of 27 cyclical blocks nested within each other.

IV. Flight scenario test and results

All the systems produced in the context and the Amrel 1.5K-120-300 DC electronic load were integrated in the inner design of the UAV and the flight test was performed in laboratory conditions (Fig. 3)

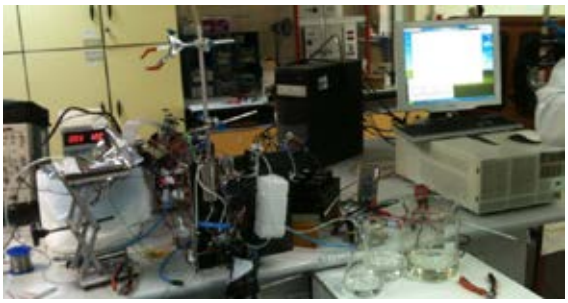


Fig. 3: Flight scenario test of the integrated UAV system

When this test was performed, according to the data received from the UAV producer company, the flight scenario was accepted as follows:

1- Along the first 15 seconds, the system will be loaded with 50 A and the UAV will accelerate and take off
2- Along 3 minutes, the system will be loaded with 25 A and the UAV will climb
3- The system will be loaded with 5-8 A during the stall condition and the range extension period will be measured

Performance tests with/ without fuel cell system are made according to the loading conditions and results are given in Table 1.

Tab. 1: Performance test results

Load	50 A (take off)	25 A (climb)	5A (stall)
Flight period without FCS	*15 sec.*	*3 min.*	*21.75 min.*
Flight period with FCS	*15 sec.*	*3 min.*	*46.75 min.*

As it may be observed in the relevant performance results, the system was targeted to extend the distance with a fuel cell and the system reached a flight duration that was doubled under the existing test conditions.

V. Conclusions

The combined hardware-software implementation of the experimental and prototype control set-ups are introduced and performance test results are given in this study. The transition from the experimental data monitoring chassis to the embedded system was performed succesfully in terms of both software and hardware. This yields a significant advantage of time consumption in design projects that usually require intense experimental works.

The performance results also approve that fuel cell based hybrid power conditioning systems are capable of powering UAVs during diffent phases of flight with longer duration.

Acknowledgements

This study is funded by Yildiz Technical University (YTU) with Project No: 2016-04-02-DOP02 and National Boron Research Institute (BOREN) with Project No: 2013-Y0418.

References

Bradley TH., Parekh DE., Comparison of design methods for fuel cell powered unmanned aerial vehicles, Journal of Aircraft, 46(6),1945-1956, (2009)

Erdör Türk B., Okur O., Karadağ Ç., Boyacı San F.G., Kılıç M., Yazıcı M.S., Okumuş E., Investigation of control parameters for sodium borohydride based hydrogen generation system, HİTEK Congress 2014, İstanbul , (2014)

Kim K., Kim T., Lee K., Kwon S., Fuel cell system with sodium borohydride as hydrogen source for unmanned aerial vehicles, Journal of Power Sources, 196, 9069-9075, (2011)

Okumus E., Boyaci San FG., Okur O., Erdör Türk B., Çengelci E., Kılıç M., Karadağ Ç., Development of boron-based hydrogen and fuel cell system for small unmanned aerial vehicle, International Journal of Hydrogen Energy, 42, 2691-2697, (2017)

www.ni.com/white-paper/6983/en/

www.xilinx.com/training/fpga/fpga-field-programmable-gate-array.htm

Electrochemical Characterization of Carbon-Supported Bimetalic PdZn Nanoparticles as Anode Catalyst for Direct Borohydride Fuel Cells

Merve Doğan Özcan[1], Cenk Çelik[2], Ayşe Nilgün Akın[1], Ramiz Gültekin AKAY[1]*
[1]Kocaeli University, Department of Chemical Engineering, 41380, Kocaeli, Turkey
[2]Kocaeli University, Department of Mechanical Engineering, 41380, Kocaeli, Turkey

* E-mail: gultekin.akay@gmail.com

Abstract
In this work, Pd and PdZn supported on Vulcan XC-72 carbon catalysts have been prepared by $NaBH_4$ impregnation-reduction technique with ultrasound irradiation method. The physical properties of the electrocatalysts are identified by X-ray diffraction (XRD). Successful PdZn alloy formation was observed in the XRD patterns. The electrochemical properties of catalysts were detected by cyclic voltammetry (CV) and chronoamperometry (CA) techniques. The electrochemical surface areas (ECSA) were determined from the areas of the peaks in voltammograms obtained by cyclic voltammetry. The first set of results show that the Pd_2Zn/C catalyst can be a promising catalyst for the direct borohydride fuel cells (DBFC) according to electrochemical characterization results and low-cost.

Keywords: Anode electrocatalyst, Direct borohydride fuel cell, PdZn nanoparticles

I. Introduction

The demand for new and clean energy production sources is increasing due to the increasing environmental concern of emissions derived from the use of fossil fuels. Hydrogen based fuel cells are one of the alternative technologies providing highly efficient energy conversion systems, in which electrical energy is produced directly from the chemical energy of hydrogen. However, hydrogen storage and handling problems must be resolved for successful commercialization of fuel cells (Liu et al. 2015). Direct borohydride fuel cells differ from conventional fuel cells as aqueous solution of sodium borohydride is fed to DBFC. Moreover, DBFC has many advantages such as high energy density (9300 Wh kg^{-1}), high theoretical open cell voltage (1.64 V), easy start-up and low toxicity. Therefore, one approach for solving the problem of hydrogen production and storage by using high-pressure cylinders is the use of DBFC for portable applications (Li et al. 2013).
The following reactions are involved in the DBFC (Behmenyar et al. 2014);

$$\text{Anode: } BH_4^- + 8OH^- \longrightarrow BO_2^- + 6H_2O + 8e^- \qquad E^0 = -1.24V \qquad (1)$$

$$\text{Cathode: } 2O_2 + 4H_2O + 8e^- \longrightarrow BO_2^- + 6H_2O + 8e^- \qquad E^0 = -0.4V \qquad (2)$$

$$\text{Overall: } BH_4^- + 2H_2O \longrightarrow BO_2^- + 2H_2O + 8e^- \qquad E^0 = -1.64V \qquad (3)$$

The DBFC applications are believed to be more favorable then other fuel cells. However, because of the limitations like high cost of electrocatalyst and expensive fuel the commercialisation of DBFC technologies are not in the desired level. Therefore, careful selection of the anode catalyst is very important to decrease the electrocatalyst cost and increase the fuel utilization in DBFC. In the past decades, many researches have been studied on transition metals (Zn, Co, Ni) and precious metals (Ag, Pt, Pd, Au) as anode catalysts. Although they have high cost and limited storage, Pd and Pt are the most favored precious metals due to fast electrode kinetics. Nowadays, Pd-based bimetallic alloy catalysts have been mostly investigated due to reduce the use of the precious metals (Fathirat et al. 2016).

In this study, Pd/C and bimetallic PdZn/C nanoparticles catalysts with a fixed molar ratio of Pd:Zn (2:1) were prepared by $NaBH_4$ impregnation-reduction technique with ultrasound irradiation. Physical properties of the catalysts were described by using X-ray diffraction technology. The electrochemical properties and performance of electrocatalysts were evaluated by cyclic voltammetry and chronoamperometry techniques. The results show that the Pd_2Zn/C bimetallic catalyst could be utilized for the DBFC application.

II. Experimental Set-up and Procedure

Pd/C and Pd_2Zn/C electrocatalysts with fixed Pd/Zn (2:1) molar ratio were prepared by $NaBH_4$ impregnation-reduction technique with ultrasound irradiation. $PdCl_2$ (Merck) and $ZnCl_2$ (Merck) metal salts were used as received for Pd and Zn sources respectively. Prior to experiments, successfully preparation of H_2PdCl_4 solution was achieved at 60 °C for 1h. Catalysts were prepared with 20 wt% metal loading on Vulcan XC-72 carbon support. The Pd_2Zn/C electrocatalyst with a Pd/Zn molar ratios of 2:1 was prepared as follows: 8.98 mL of H_2PdCl_4 solution, 2.24 mL of 0.2 M $ZnCl_2$ and 0.5 g of Vulcan XC were added into 100 mL deionized water and mixtured with magnetic stirring for 30 min. The Ph value of the solution was slowly adjusted to 12.70 prior to $NaBH_4$ addition. The solution was irradiated with ultrasonic wave (200 W, 45% amplitude) for 30 min at room temperature while 5 ml of $NaBH_4$ solution was dropped continuously to solution.The precipitate was filtered, washed with deionized water, and dried at 80 °C under vacuum overnight.

III. Analysis

The X-ray Diffraction (XRD) analysis of the prepared catalysts was conducted to examine the crystallinity by using a Rigaku Miniflexs II diffractometer equipped with a CuK_α (λ = 0.154 nm) radiation source. The diffractograms were recorded between 2θ = 10-80° scanning angles with a scanning speed of 2°/sec. Electrochemical tests of catalysts were performed on a GAMRY Reference 3000 Potentiostat/Galvanostat by using rotating disc electrode (RDE710) system. The rotating disc glassy carbon (GC, 5 mm in diameter) electrode coated with electrocatalyst ink was used as working electrode, Ag/AgCl (saturated KCl) electrode was used as reference electrode and a graphite road was used as a counter electrode. The electrolyte was 0.05 M $NaBH_4$ + 3.0 M NaOH. The CV curves of the catalysts recorded from -0.1 V to 0.5 V with a scan rate of 20 mV/s. The working electrode was prepared as follows: the catalyst (10 mg) is added to Nafion-water solutions. The catalyst ink was mixed for 2 h to obtain homogeneity. Then 10 µl of the ink was dropped onto the glasy carbon electrode. The electrode was dried at 40° for 30 min. After drying, applied 5µl Nafion solution (wt%5) onto the electrode and dried again for 30 min at 40°C.

IV. Results and discussions

The crystalline structure of catalyst determined by XRD analysis, and the results are shown in Fig. 1. In the XRD pattern, the first broad diffraction peak at 2θ=24° is related with the carbon (002) crystal face. For Pd/C catalyst 2θ=40°, 47° and 68° that are assigned to the (111), (200) and (220) planes of face-centered cubic Pd (Liu et al. 2016). The location of (111) peak of PdZn/C are softly moved to higher values of 2θ with the addition of Zn, which demonstrates the formation of alloy. The peak of metallic Zn or ZnO wasn't detected in the XRD pattern. The average particle size for the catalyst is calculated by Scherrer equation (Eg. 4) (Behmenyar et al. 2014).

$$D = 0.9\lambda/B\cos\theta \quad (4)$$

Where D is the average particle size (nm), λ is the X-ray wavelength (1.54056 Å), B is the full width at half maximum in radians (FWHM) and θ is the angle of (111) peak. The average particle size of PdZn nanoparticle is around 3.4 nm.

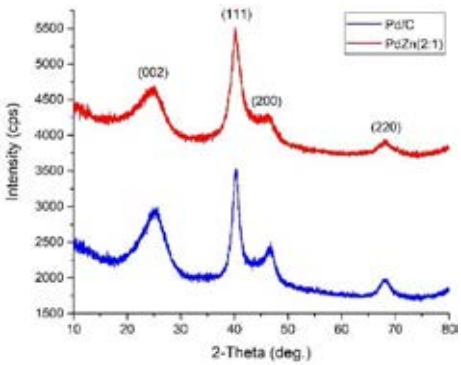


Fig.1: XRD patterns of catalysts

Electrochemical characterization of PdZn nanoparticle catalyst was performed by cyclic voltammetry (CV), chronoamperometry (CA). The catalytic activity of the Pd_2Zn/C catalyst for borohydride electrooxidation was investigated by CV and the results are shown in Fig. 2. As shown in Fig.2, Hydrogen oxidation (Eqs. 5 and 6) peak a1 and direct oxidation of borohydride peak a2 (Eq. 7) are observed in the positive-going sweep In the reverse potential sweep, the oxidation peak c1 is attributed to the electrooxidation of absorbed BH_3OH^- formed as a byproduct in the process of the BH_4^- electrooxidation (Eq. 8) In Fig.2.a, The peak current density of direct oxidation of borohydride is 21.5 mA/cm^2. Hydrogen oxidation peak (a1) is obtained 8 mA/cm^2 from the cyclic voltammogram. For Pd/C catalyst, direct oxidation of borohydride (a2) and Hydrogen oxidation peak (a1) current density was obtained 20 mA/cm^2 and 20 mA/cm^2 respectively. Evidently, the catalytic activity of Pd_2Zn/C electrocatalyst is enhanced for borohydride electrooxidation while hydrogen oxidation reaction is eliminated by the addition of Zn to Pd/C catalyst.

$$BH_4^- + H_2O \longrightarrow BH_3(OH)^- + H_2 \quad (5)$$

$$H_2 + 2OH^- \longrightarrow 2H_2O + 2e^- \quad (6)$$

$$BH_4^- + 8OH^- \longrightarrow BO_2^- + 6H_2O + 8e^- \quad (7)$$

$$BH_3OH^- + 3OH^- \longrightarrow BO_2^- + 3/2\ H_2 + 2H_2O + 3e^- \quad (8)$$

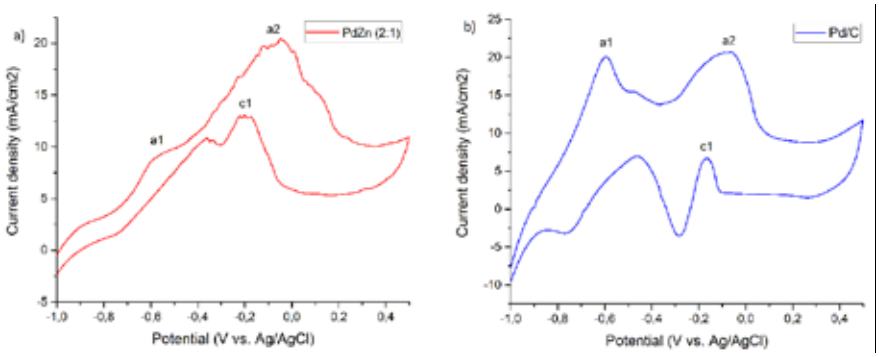


Fig.2:Cyclic voltammograms of Pd_2Zn/C and Pd/C electrodes in 3 M NaOH+0.05 M $NaBH_4$ solution at a scan rate of 20 mV s^{-1}

The electrochemical surface areas (ECSA) of the catalysts were determined from cyclic voltammograms obtained by CV. The results are shown in Fig. 3. The ECSA of the catalysts are calculated by using Eq. 9.

$$ECSA = \frac{Q}{0.424 \times mcat} \quad (9)$$

Where Q is the coulombic charge (mC) found by integrating peak area of the reduction of PdO (peak a), m_{cat} is the catalyst loading amount on the electrode (mg), 0.424 represents the charge required for the reduction of PdO monolayer (mC/cm^2) (Duan et al. 2015). The calculated ECSA of Pd_2Zn/C and Pd/C catalysts are 658 cm^2/mg and 617 cm^2/mg respectively.

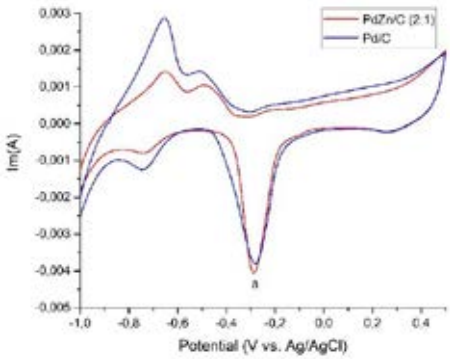


Fig.3: Cyclic voltammograms of Pd_2Zn/C and Pd/C electrodes in 3 M NaOH solution at a scan rate of 20 mV s^{-1}

Chronoamperometry is an important method to determine the electrochemical activity and stability in fuel cells. Chronoamperometric measurement is performed in 3 M NaOH + 0.05 M $NaBH_4$ solution for 1000 s with a potential step from -1.2 to - 0.2 V. As shown in Fig. 4, the current density of catalyst dropped fastly at the initial stage and the pseudo-steady state condition was attained. This result indicate that the Pd_2Zn/C catalyst has stability for the BH_4 electrooxidation.

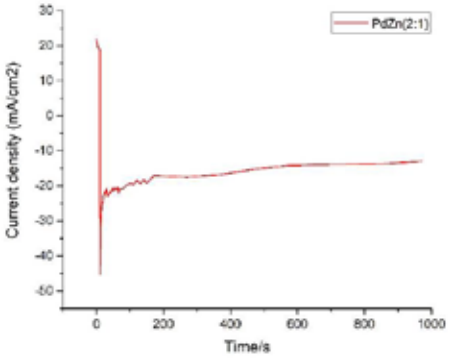


Fig.4: Chronoamperometric curve of Pd_2Zn/C in 3 M NaOH + 0.05 M NaOH solution at a scan rate of 20 mV s^{-1}

V. Conclusions

In this study, Vulcan XC-72 carbon-supported Pd and Pd_2Zn bimetallic nanoparticles were prepared by a $NaBH_4$ impregnation reduction method with ultrasound irradiation method. The average size of Pd_2Zn/C nanoparticles was about 3.4 nm. It was shown that the Pd_2Zn/C bimetallic nanoparticles shows the same catalytic behavior like Pd/C. Solely, the Pd_2Zn/C catalyst becames not only a economical but also presents higher electrochemical catalytic activity for the electrooxidation of BH_4^- when compared to Pd/C. The addition of Zn to Pd/C catalyst was indicated to improve the catalytic activity toward BH_4^- electrooxidation and decrease the hydrogen oxidation reaction owing to the synergistic effect between Pd and Zn. Therefore, the results show that the Pd_2Zn/C catalyst could be a good alternative for low cost catalyst choice for DBFC applications. Further research especially on single cell performance tests should be planned and conducted.

Acknowledgements

This work was funded by TUBITAK (1003) with project number 215M255.

References

Behmenyar G., Akın A. N., Investigation of carbon supported Pd-Cu nanoparticles as anode catalysts for direct borohydride fuel cell, Journal of Power Sources, 249, 239–246, (2014).

Duan D., You X., Liang J., Liu S., Wang Y., Carbon supported Cu-Pd nanoparticles as anode catalyst for direct borohydride-hydrogen peroxide fuel cells, Electrochimica Acta, 176, 1126–1135, (2015).

Fathirad F., Afzali D., Mostafavi A., Bimetallic Pd-Zn nanoalloys supported on Vulcan XC-72R carbon as anode catalysts for oxidation process in formic acid fuel cell International Journal of Hydrogen Energy, 41,13220–13226, (2016).

Li S., Yang X., Zhu H., Wei X., Liu Y., Ultrafine amorphous Co-W-B alloy as the anode catalyst for a direct borohydride fuel cell, International Journal of Hydrogen Energy, 38, 2884-2888, (2013).

Liu J., Yi L., Wang X., Zhao Q., Zhang Y., Gao J., Wei W., Investigation of nanoporous carbon supported palladium-zinc nanocomposites as anode catalysts for direct borohydride-hydrogen peroxide fuel cell, International Journal of Hydrogen Energy, 40, 7301-7307, (2015).

HHO Enrichment of Bio-Diesohol Fuel Blends in a Single Cylinder Diesel Engine

[1]Mustafa Kaan Baltacioglu, [2*]Raif Kenanoglu, [3]Kadir Aydın
[1] Department of Mechatronics Engineering, İskenderun Technical University, Hatay, 31200, Turkey
[2] Department of Mechanical Engineering, İskenderun Technical University, Hatay, 31200, Turkey
[3] Department of Mechanical Engineering, Çukurova University, Adana, 01330, Turkey

* E-mail:raif.kenanoglu@iste.edu.tr

Abstract
One of the primary aims of this experimental investigation is to examine hydroxy-gas enrichment effects on environmentally friendly but performance-reducing alternative fuels such as ethanol and biodiesel. Entire HHO system has integrated into engine test rig for this purpose. Two different fuel mixtures were prepared and named by their volumetric compositions which are Biodiesohol (10/5/85) and Biodiesohol (15/5/80). Biodiesohol was used to describe biodiesel, ethanol and standard diesel blends. Specific fuel properties are measured and ensured to be in EN590 and EN 14214 standards. Experiments were conducted on a single cylinder diesel engine which was fuelled with diesel-biodiesel-ethanol fuel blends those enriched by 1 liter per minute HHO gas fuel during the entire tests. All the experiments were performed under full load condition within the range of 1200 to 3200 rpm and graphical points were selected at intervals of 100 rpm. From the view of performance; brake power, brake specific fuel consumption and thermal efficiency results were discussed; additionally carbon monoxide and nitrogen oxides as exhaust emission results were also measured and presented. Standard diesel fuel outputs were determined as the reference line to compare experimental results. A number of studies have been conducted with fuels used in this experimental study and their mixture in different ratios as well, but an examination of the HHO addition to biodisohol is performed for the first time in this research area of the literature.

Keywords: Hydroxy gas enrichment, single cylinder diesel engine, ethanol, biodiesel, performance, emission

I. Introduction

The number of internal combustion engine vehicles will decrease in the next decades and will be out of use in the mid-term, but research and developments will continue in the meantime to make those vehicles more economical and environmentally friendly. Harmful environmental impact of greenhouse gas emissions and dependency on fossil fuels has been expecting to be reduced from existing and close future vehicles. Nowadays, scientists who investigate the use of alternative fuels in internal combustion engines have used the hydrogen as supplementary fuel and referred as secondary fuel. Most common way to bring together hydrogen and ICEs is electrolysis of water by an HHO system. Some of the main reasons for using HHO system in ICEs have been summarized by Suleman, F et al (2015) and Baltacioglu, M. K et al (2016) as below:

- Easy installation and no need expensive maintenance,
- Hydrogen is a high quality energy carrier,
- 33% oxygen presence that provides enhanced combustion,
- Technically proven that hydrogen can be used for transportation,
- Hydrogen offers the highest heating value per mass among all chemical fuels.
- Additionally, it is regenerative and environmentally friendly
- Reduces exhaust emissions and improves performance rates by increasing efficiency of the fuel combustion.

On the other hand sole usage of hydrogen in ICEs is not suitable without any modification. To be more independent of fossil fuel, also some alternative and renewable fuels are blending into the standard diesel fuel is necessary. These criteria have been supported by government obligatory and laws. Fuel suppliers are obliged to achieve a certain biofuel share. In 2016, the blending of bioethanol and biodiesel in transport fuels was reported at European Union Biofuel Annual (2017) respectively 3.3% and 5.8% (energy basis), and thus well below the 10 percent target for 2020. Renewable Energy Directive (RED) which announced by European Commission (EC) deals with biofuels in several ways, of which the most important was the mandatory target which states that 10 % of final energy consumption in transport should be met by renewable energy by 2020 (Shahir, S. A. et al.,2014, Amezaga, J. M. et al, 2010). As a result of these, biodiesel and ethanol consumptions are increasing annually to achieve greenhouse gas targets according to the declaration of energy associations and commissions. The continuing examinations and the already reported results about the volumetric replacement of standard diesel fuel with the combination of biodiesel and ethanol in compression ignition engines found to be relevant. Because these blends have the similar fuel properties as the commercial diesel fuel even at high biofuel content (Shahir, S. A. et al., 2014, Barabás, I., & Todoruț, I. A, 2011, Zoeldy, M, 2011). Some of the fuel specifications are important to prescience the combustion, such as density, viscosity, cetane number and calorific value to which are represented and explained with details in materials and method section. Among them, the calorific value is that most affect the combustion result. The calorific value of the aforementioned ternary blend fuel is much lower than the fossil diesel. Biodiesel and ethanol can cause the engine performance to decline while improving the exhaust emission. HHO enrichment can be the key solution to prevent performance losses while keeping emissions improvements. The hydrogen used in this study constitutes 66% of the HHO gas obtained by electrolysis and also has the highest heating value per

mass among all chemical fuels (Suleman, F et al, 2015).

Thus, the aim of this experimental study is to investigate the effects of HHO gas usage on performance and emissions with two different ternary biodiesehol fuel blends. Diesel fuel results will be the reference point to compare and interpret combustion results. Citrus sinensis oil was preferred as biodiesel raw metarial. Citrus sinensis oil can be produced from the waste and rotten peel of the orange fruit which has no market value. Since peel of the orange is non-edible except used as animal feedstuffs in our country. With these common issues, Tüccar, G. et al (2014) mentioned that conversion of citrus sinensis oil into biodiesel will be reasonable.

II. Experimental Set-up and Analysis

Ternary liquid fuel blends which contain the various combinations of biodiesel, anhydrous ethanol and diesel were enriched by hydroxy gas (HHO) to compare with the diesel fuel base condition. Two different abbreviations were used during the test fuels definitions to avoid ambiguity which is BED (10/5/85) + HHO (1L/min) and BED (5/15/80) + HHO (1L/min). Fuel blends named by their volumetric composition of the new fuel contents; As an example, the mixture BED (10/5/85) + HHO (1L/min) describes the proportions in the fuel mixture: 10 % biodiesel + 5 % ethanol + 85 % diesel fuel blend with hydrogenated gas enrichment with 1 liter per minute volumetric flow rate. HHO gas was inducted into the combustion chamber via intake manifold of the test engine and kept constant during the entire tests with a needle vane and Allicat flow meter. The single cylinder test engine was coupled to hydrolic dynamometer in order to load the engine. Shematic view of the test rig is presented in figure 1. Engine specifications are shown in table 1.

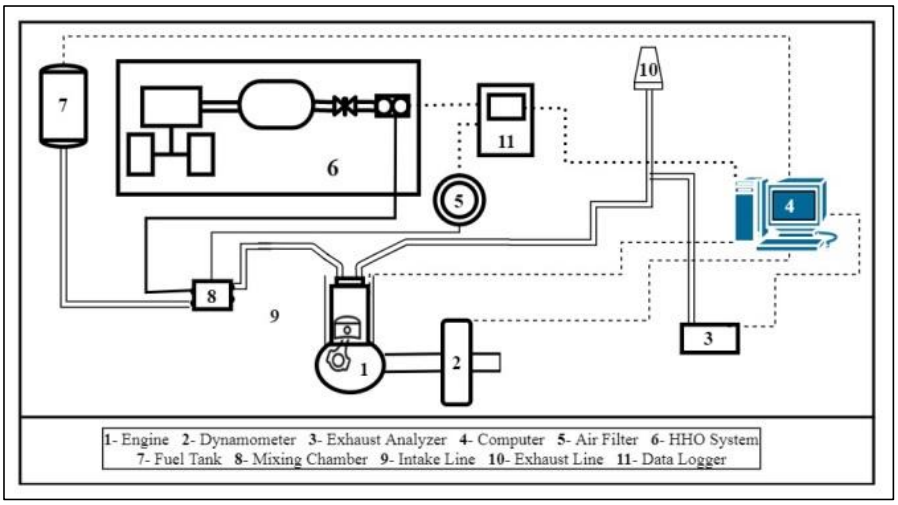


Fig. 1: Experimental Set-up

The oil required for the citrus biodiesel used in this study was first extracted from the shell of citrus fruits supplied from the regional producer. The orange fruit (citrus sinensis) is crushed and distillation method is applied to recover the oils through evaporation. However, since the efficiency of the method was very low (0,003 ml/kg) with the existing equipment, it was necessary to produce bio-oil in some accomplished laboratories. Therefore, commercial orange fruit oil was purchased and citrus sinensis biodiesel (CSB) is produced by transesterification method. Volumetric proportions of CSB in test fuel blends were 10% and 15%, respectively. Fuel analyzes were carried out and the specific fuel properties of diesel, 100% CSB, ethanol, and experimental fuel mixtures are presented in Table 2 and compared. The ethanol mixture ratio was set at 5% for both fuel blends in this study because the ethanol is not completely miscible in diesel fuel and concluded by Pidol, L. et al (2012) that anhydrous ethanol shows complete miscibility up to 5% by volume.

Tab. 1:Test engine specifications

Type	4 stroke, single cylinder, diesel engine
Swept volume (cc)	219 cc
Bore/stroke (mm)	70mm /57mm
Compression Ratio	17:1
Rated power	2.5 kW @ 3600 rpm

Tab. 2. Specific fuel properties and European fuel standards

	Measurement Device	Diesel	EN590 Standard	CSB100	EN 14214 Standard	Anhydrous ethanol	BED (10/5/85)	BED (15/5/80)
Viscosity (cSt)	Tanaka AKV-202	3.10	2-4.5	3.223	3.5 - 5.0	1.074	3.011	3.017
Density (g/cm³)	Kyoto Electronics DA-130	0.841	0.820-0.845	0.868	0.86-0.90	0.789	0.8411	0.842
Cetan Number	Zeltex ZX440	55.2	Min. 51	45.2	Min. 51	10,1	51,945	51,445
LHV (kJ/kg)	IKA Werke C2000	43200	-	38257	-	27000	41896	41649
Flash Point (°C)	Tanaka Automated Pensky-Martens	76	Min. 55	79.1	Min. 101	12.23	73.12	73.28
Pour Point (°C)	Tanaka MPC-102	-16	-	-11	Sum< 4.0 Win<-1.0	-	-26.9	-25,8

Carbon monoxide and nitrogen oxide as exhaust emission results were obtained by MRU Delta 1600 V gas analyzer during the experiments and data were transferred to host computer which has measuring ranges for CO and NOx emissions 0-10% and 0-4000 ppm, respectively.

IV. Results and discussions

The brake power – engine speed graph is given in figure 2.a. The overall results showed that BED (10/5/85) + HHO fuel blend had the best improvement with 11.33 % while BED (15/5/80) + HHO blend had 8.65 % with respect to neat diesel operation. These improvements can be explained with positive effects of HHO enrichments on heating values and also combustion characteristics. The hydrogen usage affects volumetric efficiency adversely at lower engine speed (<1800 rpm) and it causes to obtain more improvement at middle and higher engine speed in internal combustion engines as seen from the figure 2.

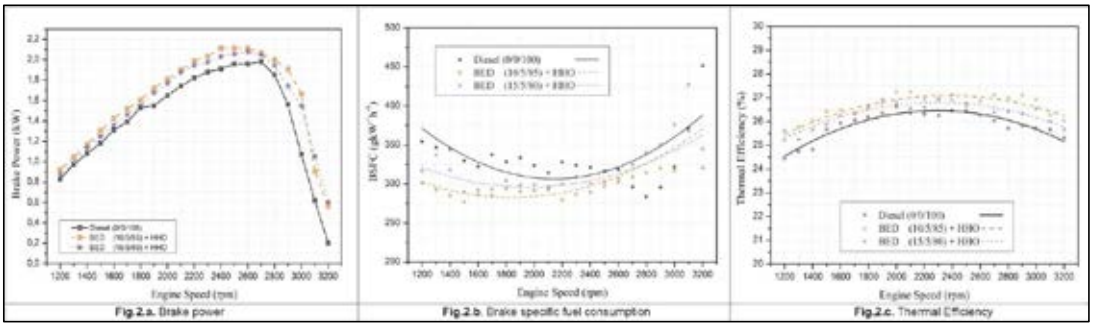


Fig.2. Engine performance results versus engine speed

Figure 2.b. represents Brake specific fuel consumption-engine speed graph. When overall fuel consumption regarded (include hydrogen as calculated equivalent to liquid diesel) the BED (10/5/85) + HHO fuel blend achieved minimum fuel consumption when compared to BED (15/5/80) + HHO blend and neat diesel operations. The improvements ratios of fuel blends, BED (10/5/85) + HHO and BED (15/5/80) + HHO, were 8.3% and 5.5%, respectively. Figure 2.c. represents the thermal efficiency versus engine speed graph. The thermal efficiency is measured by the ratio of the heating value of the overall fuel sent to the cylinder to the work output obtained from this fuel. Hydrogen enrichment caused increasing heating value of the fuel blends. Therefore, as it is seen from figure, BED (10/5/85) + HHO and BED (15/5/80) + HHO improved thermal efficiency thanks to their extra hydrogen contents when compared to the standard diesel operations. The overall improvements were obtained 2.82% and 1.76% by using BED (10/5/85) + HHO and BED (15/5/80) + HHO blends, respectively.

The CO emission versus engine speed graph is given in figure 3.a. It is obviously seen that the fuel mixtures usage caused the CO values to decrease. Due to improvement of the combustion at mid and high engine speed and lower carbon content of fuel mixtures, the amounts of CO values were further reduced. BED (10/5/85) + HHO and BED (15/5/80) + HHO were reduced 8.39% and 12.20 % in average, respectively.

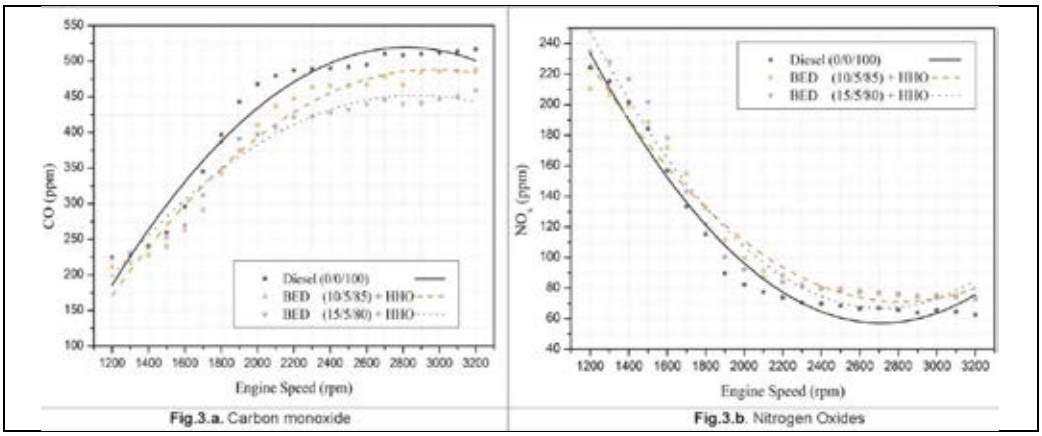


Fig.3.a. Carbon monoxide **Fig.3.b.** Nitrogen Oxides

Fig.3. Engine emission results versus engine speed

The NO_x – engine speed graph is shown in figure 3.b. When the overall results were investigated, NO_x values were increased, due to the formation of NO_x depends on combustion temperature. Both the HHO enrichment of the fuel blends and extra oxygen content of biodiesel were increased combustion temperature in cylinder. Because of the higher combustion temperature, BED (10/5/85) + HHO and BED (15/5/80) + HHO increased NO_x formation with 8.57% and 9.47% in average, respectively.

V. Conclusions

Performance and emission changes of HHO (1 L/min) enrichment to citrus sinensis biodiesel (10% - 15%), anhydrous ethanol (5%) and standard diesel (80% - 85%) ternary blends performed for the first time successfully. Results showed that hydrogenated oxygen addition prevents the power reductions resulting from the use of biofuels, additionally, 11.33% maximum overall improvement is obtained by BED (10/5/85) + HHO fuel blend with respect to base diesel fuel brake power results. From the view of exhaust emission; carbon monoxide formation was reduced around 8 to 10 % significantly while NOx formation was increased at similar percentages as carbon monoxide.

References

Amezaga, J. M., Boyes, S. L., & Harrison, J. A. Biofuels policy in the European Union. In *7th international biofuels conference, New Delhi* (pp. 1-12) (2010).

Baltacioglu, M. K., Arat, H. T., Özcanli, M. & Aydin, K. Experimental comparison of pure hydrogen and HHO (hydroxy) enriched biodiesel (B10) fuel in a commercial diesel engine. Int. J. Hydrogen Energy 41, 8347–8353 (2016).

Barabás, I., & Todoruț, I. A. Utilization of biodiesel-diesel-ethanol blends in CI engine. In *Biodiesel-Quality, Emissions and By-Products*. InTech. (2011).

Flach, B., Lieberz, S.,Rosetti, A. EU-28 Biofuels Annual 2017. in *Global Agricultural Information Network* 42 doi: NL7015 (2017).

Pidol, L., Lecointe, B., Starck, L. & Jeuland, N. Ethanol-biodiesel-Diesel fuel blends: Performances and emissions in conventional Diesel and advanced Low Temperature Combustions. Fuel 93, 329–338 (2012).

Shahir, S. A. et al. Feasibility of diesel-biodiesel-ethanol/bioethanol blend as existing CI engine fuel: An assessment of properties, material compatibility, safety and combustion. Renewable and Sustainable Energy Reviews 32, 379–395 (2014).

Shikida, P. F. A. et al. A comparison between ethanol and biodiesel production: The Brazilian and European experiences. Lect. Notes Energy 27, 25–53 (2014).

Suleman, F., Dincer, I. & Agelin-Chaab, M. Environmental impact assessment and comparison of some hydrogen production options. Int. J. Hydrogen Energy 40, 6976–6987 (2015).

Tüccar, G., Tosun, E., Özgür, T. & Aydın, K. Diesel engine emissions and performance from blends of citrus sinensis biodiesel and diesel fuel. Fuel 132, 7–11 (2014).

Zoeldy, M. Ethanol-biodiesel-diesel blends as a diesel extender option on compression ignition engines. Transport 26, 303–309 (2011).

Bio-ethanol Reforming for Hydrogen and Methane Production

[1*]Yuji Ando
[1] Research Institute of Energy Frontier, National Institute of Advanced Industrial Science and Technology, 16-1, Onogawa, Tsukuba, Ibaraki prefecture 305-8569, Japan

* E-mail:ando-yuji@aist.go.jp

Abstract
Ethanol steam reforming over various catalysts was studied to clarify the best conditions for selective methane production from ethanol. In the sequence of catalyzed reactions, H_2 production was followed by reduction of CO and CO_2 to CH_4. The compositions of the product gases obtained over Ru/CeO_2 and Ru/SiO_2 were close to the chemical equilibrium composition at 673 K. However, the product gas compositions obtained over Ru catalysts and Ru-based alloy catalysts were far from the chemical equilibrium composition at 623 K. Ethanol steam reforming was then conducted with a two-stage catalyst system that involved ethanol C–C bond cleavage in the first stage and reduction of CO and CO_2 to CH_4 in the second stage. The product gas compositions obtained over $Ru\text{-}Pt/SiO_2+Ru/Al_2O_3$ and $Pd/Al_2O_3+Ru/Al_2O_3$ were close to the chemical equilibrium composition at 623 K.

Keywords: Ethanol, hydrogen, methane

I. Introduction

There have been many efforts to commercialize solid oxide fuel cells (SOFCs). One problem is that a simple electrochemical oxidation of hydrogen in a fuel cell can lead to the formation of local hot spots (Eq. 1).

$$H_2 + 1/2O_2 \rightarrow H_2O \quad (1)$$

The thermal stresses in the cell generated by the hot spots may cause crack initiation and consequent damage to the fuel cell. One of the ideas to mitigate the formation of hot spots in SOFCs is co-feeding of methane and steam together with hydrogen to promote the endothermic steam reforming of methane (Eq. 2) in the fuel cell and to use the hydrogen produced by the steam reforming of methane as a fuel for the SOFC.

$$CH_4 + 2H_2O \rightarrow CO_2 + 4H_2 \quad (2)$$

Bioethanol has several advantages among renewable energy sources. It has low toxicity, it has a high energy density per unit volume because it is a liquid at room temperature, and hydrogen can be produced by steam reforming of ethanol (Eq. 3).

$$CH_3CH_2OH + 3H_2O \rightarrow 2CO_2 + 6H_2 \quad (3)$$

Methane as well as hydrogen can be produced by reforming of ethanol (Eq. 4).

$$2CH_3CH_2OH \rightarrow 3CH_4 + CO_2 \quad (4)$$

Development of efficient ways to produce methane and hydrogen from ethanol and use of the methane and hydrogen as a fuel for SOFCs will be important to realize efficient use of biomass resources and reliable operation of the SOFCs. Although many researchers have used ethanol steam reforming to produce hydrogen (Haryanto et al., 2005), few studies have been undertaken to produce methane from ethanol. In this study, ethanol steam reforming over various catalysts was investigated to clarify the best conditions for selective methane production from ethanol.

II. Calculation of Chemical Equilibrium

Chemical equilibrium in ethanol+water reaction system

Chemical equilibrium calculations in an ethanol+water reaction system were performed with the National Aeronautics and Space Administration Chemical Equilibrium with Applications program (McBride and Gordon, 1996). Figures 1–5 show the product yields from 100 mol of ethanol under various reaction conditions. The results of the calculations indicated that hydrogen production via ethanol steam reforming (Eq. 3) becomes predominant at temperatures greater than 723 K (Fig. 1); however, methane production (Eq. 4) becomes predominant at lower temperatures. Ethanol steam reforming was therefore conducted in the temperature range 623–673 K.

III. Experimental Set-up and Procedure

III-I. Catalyst preparation

Various supported noble metal catalysts and Ru-based alloy catalysts were prepared by an impregnation method (Table 1). The support material was SiO_2, Al_2O_3, TiO_2, CeO_2, or MgO. The catalyst precursors included $RuCl_3 \cdot 3H_2O$, K_2PtCl_4, $PdCl_2$, and $NiCl_2 \cdot 6H_2O$. A pre-determined amount of support material was impregnated at room

temperature with an aqueous solution (20 mL) containing a catalyst precursor and then dried at 313 K for 12 h in air. The impregnated, dried sample was reduced with an aqueous solution of $NaBH_4$ at room temperature. After filtration and washing with a large amount of water (500 mL), the obtained solid was dried at 313 K for 12 h. A commercial 0.5 wt%-Ru/Al_2O_3 pellet (N.E. Chemcat, Japan) was also used for comparison. The total amount of metal in each catalyst was 3.0 mmol, except for catalysts 1, 11, and 13 (Table 1).

III-II. Ethanol steam reforming

Ethanol steam reforming was conducted at atmospheric pressure in a quartz reactor (i.d., 20 mm; height, 300 mm) at 623–673 K. The reactor temperature was controlled via a heater with a thermocouple in the catalyst bed. The reactant feed consisted of a gaseous mixture of ethanol, water, and N_2. The mixture was generated as follows. A mixture of ethanol and water was injected with a syringe pump into a vaporizer at 573 K. Before entering the reactor, the vapor was mixed with a stream of N_2 supplied by a mass flow controller. The ethanol/water/N_2 molar ratio was 1:5:0.9 or 1:3:0.9. The outlet products were analyzed on-line by gas chromatography (GL Sciences Inc., Micro GC CP4900). They were separated on a packed column (molecular sieves 5A or Porapak Q) and detected with a thermal conductivity detector.

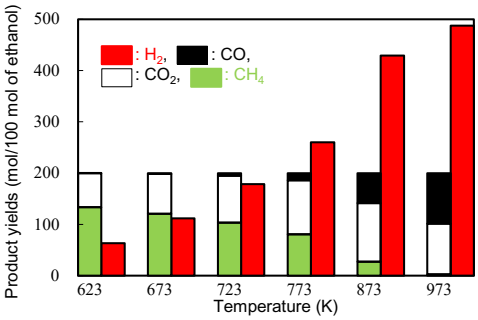


Fig. 1: Chemical equilibrium in ethanol+water reaction system

Tab. 1: Prepared Catalysts

Catalyst number	Catalyst	Amount of metal (mmol)	Support material (g)	Notes
1	Ru/Al_2O_3	Ru (2.5)	Al_2O_3 (50)	0.5wt%-Ru/ Al_2O_3 (N.E.Chemcat)
2	Ru/MgO	Ru (3.0)	MgO (30)	
3	Ru/CeO_2	Ru (3.0)	CeO_2 (20)	
4	Ru/Al_2O_3	Ru (3.0)	Al_2O_3 (20)	
5	Ru/TiO_2	Ru (3.0)	TiO_2 (20)	
6	Ru/SiO_2	Ru (3.0)	SiO_2 (20)	
7	$Ru-Pt/SiO_2$	Ru (1.5), Pt (1.5)	SiO_2 (20)	
8	$Ru-Pd/SiO_2$	Ru (1.5), Pd (1.5)	SiO_2 (20)	
9	$Ru-Ni/SiO_2$	Ru (1.5), Ni (1.5)	SiO_2 (20)	
10	$Ru-Pt/SiO_2$	Ru (1.0), Pt (1.0)	SiO_2 (15)	Two-stage catalyst system
	$+Ru/Al_2O_3$	Ru (1.0)	Al_2O_3 (20)	
11	$Ru-Pt/SiO_2$	Ru (1.0), Pt (1.0)	SiO_2 (15)	First stage of catalyst 10
12	Pd/Al_2O_3	Pd (2.0)	Al_2O_3 (20)	Two-stage catalyst system
	$+Ru/Al_2O_3$	Ru (1.0)	Al_2O_3 (20)	
13	Pd/Al_2O_3	Pd (2.0)	Al_2O_3 (20)	First stage of catalyst 12

IV. Results and Discussion

IV-I. Ethanol steam reforming over supported Ru catalysts

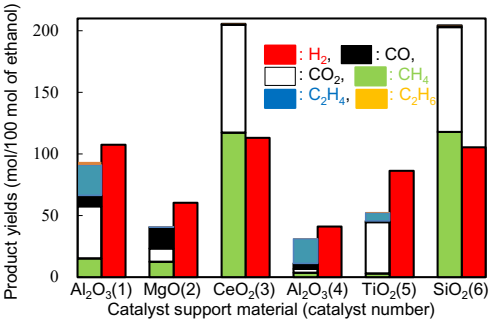
The yields of the products of ethanol steam reforming over supported Ru catalysts at 673 K were strongly influenced by the support material (Fig. 2). The product gas compositions obtained over the Ru/CeO_2 and Ru/SiO_2 catalysts, which showed the highest activities, were close to the chemical equilibrium composition at 673 K.

IV-II. Mechanism of methane production during ethanol steam reforming

Ando et al. (2012) reported that H_2 and CO_2 production decreases and CH_4 production increases over SiO_2-supported noble metal catalysts as the ethanol partial pressure increases. They explained this behavior based on rapid reduction of CO_2 to CH_4. To verify the hypothesis of methane production during ethanol steam reforming, the effect of the amount of Ru/SiO_2 on product yield was examined. Hydrogen was the principal product if only 5 g of catalyst was used (Fig. 3); H_2 yields declined and CO and CO_2 reduction to CH_4 increased with increasing catalyst amount. This result supports the hypothesis of Ando et al. (2012).

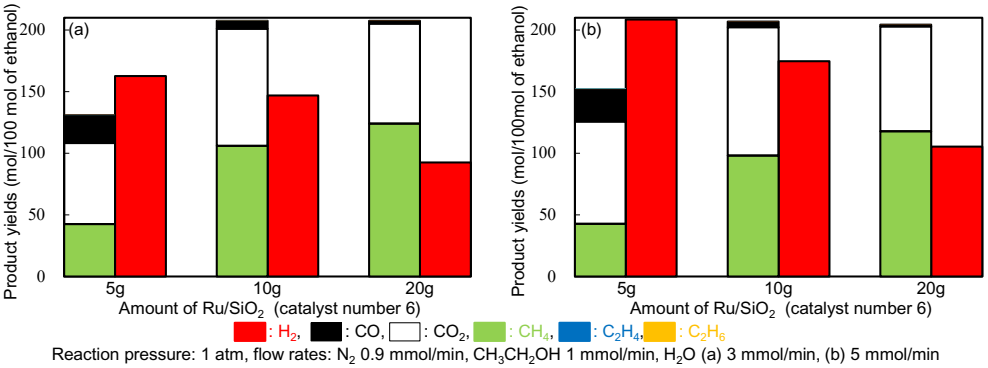
IV-III. Ethanol steam reforming at 623 K

Ethanol steam reforming over supported Ru catalysts was conducted at 623 K to increase the CH_4 yield. The Ru/CeO_2 and Ru/SiO_2 catalysts again showed the highest activities (Fig. 4a). The carbon conversion and CH_4 yields were higher over Ru-alloy/SiO_2 than over Ru/SiO_2 (Fig. 4b). However, the product gas compositions obtained over all catalysts were far from the chemical equilibrium composition at 623 K. This result was probably due to the slow reaction rate at this temperature.



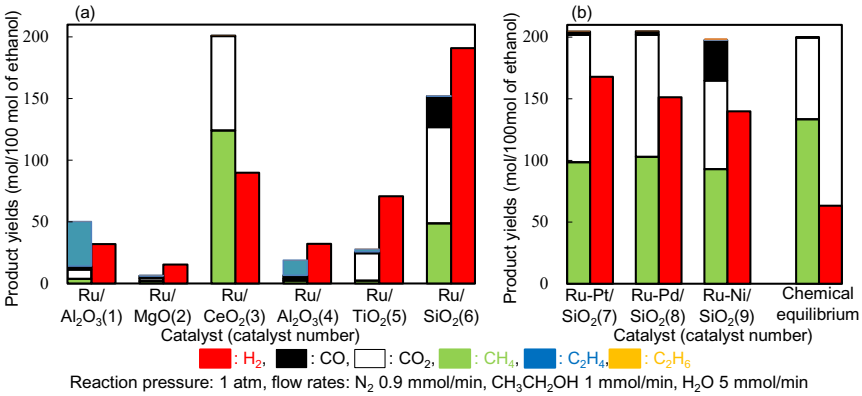
Reaction pressure: 1 atm, flow rates: N_2 0.9 mmol/min, CH_3CH_2OH 1 mmol/min, H_2O 5 mmol/min

Fig. 2: Effect of catalyst support material on product yields during ethanol steam reforming at 673 K over supported Ru catalysts.



Reaction pressure: 1 atm, flow rates: N_2 0.9 mmol/min, CH_3CH_2OH 1 mmol/min, H_2O (a) 3 mmol/min, (b) 5 mmol/min

Fig. 3: Effect of amount of Ru/SiO_2 on product yields during ethanol steam reforming at 673 K.



Reaction pressure: 1 atm, flow rates: N_2 0.9 mmol/min, CH_3CH_2OH 1 mmol/min, H_2O 5 mmol/min

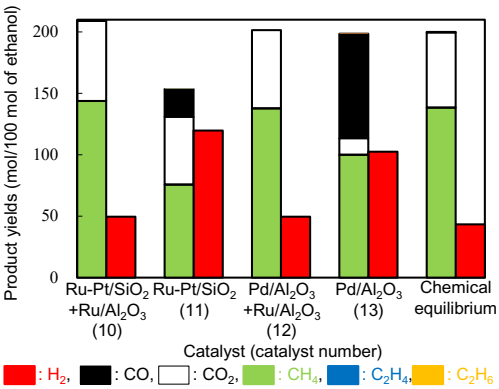
Fig. 4: Ethanol steam reforming over supported Ru catalysts and Ru-based alloy catalysts at 623 K.

IV-IV. Ethanol steam reforming with two-stage catalyst system

To speed up the reaction at 623 K, ethanol steam reforming was conducted via a two-stage process involving ethanol C–C bond cleavage followed by CO and CO_2 reduction to CH_4. Pd and Ru-Pt are candidates for promoting C–C bond cleavage. Davis et al. (1987) reported that Pd catalyzes thermal decomposition of ethanol to CH_4, CO, and H_2. Facile C–C bond cleavage of ethanol occurs over $Ru\text{-}Pt/SiO_2$ at 623 K was already shown in this manuscript (Fig. 4b).

Ru is a promising material for facile reduction of CO and CO_2 to CH_4. Hydrogenation of CO_2 on Ru/Al_2O_3 occurs at a measurable rate above 443 K and yields CH_4 almost exclusively (Solymosi et al., 1981). Rehmat et al. (1970) studied the selective methanation of CO in a gas mixture containing H_2, CO_2, and CO and concluded that Ru was the most effective CO methanation catalyst.

Figure 5 compares the results of ethanol steam reforming with the two-stage catalyst system at 623 K to the results of the first catalyst of the two-stage system ($Ru-Pt/SiO_2$ and Pd/Al_2O_3). The product gas compositions obtained over $Ru-Pt/SiO_2+Ru/Al_2O_3$ and $Pd/Al_2O_3+Ru/Al_2O_3$ were close to the chemical equilibrium composition at 623 K. As expected, ethanol C–C bond cleavage in the first stage was apparently followed by CO and CO_2 reduction to CH_4 in the second stage.



Reaction pressure: 1 atm, flow rates: N_2 0.9 mmol/min, CH_3CH_2OH 1 mmol/min, H_2O 3 mmol/min

Fig. 5: Ethanol steam reforming with two-stage catalyst system at 623 K.

V. Conclusions

Ethanol steam reforming was investigated over various catalysts to clarify the best conditions for selective methane production from ethanol. Product gas compositions obtained over Ru/CeO_2 and Ru/SiO_2 were close to the chemical equilibrium composition at 673 K. However, product gas compositions obtained over Ru catalysts and Ru-based alloy catalysts were far from the chemical equilibrium composition at 623 K. Product gas compositions obtained over two-stage catalyst systems were close to the chemical equilibrium composition at 623 K. The author concludes that ethanol C–C bond cleavage in the first stage was followed by reduction of CO and CO_2 to CH_4 in the second stage.

References

Ando Y., Matsuoka K., Takagi H., and Kuramoto K., Hydrogen Production from Ethanol Steam Reforming over Noble Metal Catalysts Supported on SiO_2: Mechanism of Methane Production and Reaction Conditions for Suppression of Methane Production, Bull. Chem. Soc. Jpn. Vol. 85, No. 4, 517 (2012).

Davis J. L., Barteau M. A., Decarbonylation and decomposition pathways of alcohol's on Pd(111), Surface Sci., Vol. 187, No. 2–3, 387 (1987).

Haryanto A., Fernando S., Murali N., and Adhikari S., Current Status of Hydrogen Production Techniques by Steam Reforming of Ethanol: A Review, Energy & Fuels, 19, 2098 (2005).

McBride B. J. and Gordon S., Computer Program for Calculation of Complex Chemical Equilibrium Compositions and Applications, NASA Reference Publication, 1311 (1996).

Rehmat A., Randhava S. S., Selective Methanation of Carbon Monoxide, Ind. Eng. Chem. Prod. Res. Dev., 9 (4), 512 (1970).

Solymosi F., Erdöhelyi A. and Kocsis M., Methanation of CO_2 on supported Ru catalysts, J. Chem. Soc., Faraday Trans. 1, Vol. 77, 1003 (1981).

A Design of Automated HHO System for Optimum Volumetric Efficiency

[1*]Mustafa Kaan Baltacıoğlu, [2]Raif Kenanoğlu, [3]Kemal Kaya, [3]Yakup Hameş, [2]Ertuğrul Baltacıoğlu
[1] Department of Mechatronics Engineering, İskenderun Technical University, Hatay, 31200, Turkey
[2] Department of Mechanical Engineering, İskenderun Technical University, Hatay, 31200, Turkey
[3] Department of Electrical and Electronics Engineering, İskenderun Technical University, Hatay, 31200, Turkey

* E-mail:mkaan.baltacioglu@iste.edu.tr

Abstract
As demonstrated in scientific studies; hydrogen which is produced by electrolysis method can be a supplementary fuel for diesel engines. On the other hand, it has been determined that the adaptation of the HHO system to the operating principles of internal combustion engines is highly necessary in terms of total energy efficiency and it is aimed to be solved by this study. For this purpose, a control unit was designed to control the amount of HHO production automatically by adjusting the current drawn from the engine's battery so that the stable volumetric efficiency could be sustained at any determined engine speed ranges.The continuous constant volumetric flow rate of produced hydrogen as HHO and variable mass airflow rate related to engine speed has provided without degrading the volumetric efficiency, thus can lead better combustion. Amount of necessary HHO can be produced interdependent to the low, medium and high engine speeds by the aid of designed HHO control system which is designed to control with the current automatically. HHO control system is designed in MATLAB/ Simulink. The flow chart and the structure of the generated electronic control mechanism are presented with figures.

Keywords: HHO Control System, volumetric efficiency, hydrogen, engine speed

I. Introduction

Many years, to bring down the negative effects of fossil fuels on the environment and along with fossil fuel dependency to the lowest levels, researchers focused on alternative energy, and they agreed the idea that hydrogen will play a crucial role in this issue in the near future (Veziroglu, T.N., 1997, Midilli, A., 2005, Dincer, I., 2000). The using of hydrogen as a fuel in internal combustion engines have studied by many researchers. These studies have revealed the many advantages of hydrogen, whereas, relatively fewer disadvantages were expressed by researchers.

Hydrogen has many significant fuel properties. One of the most significant properties of hydrogen is lower heating value, approximately three times higher than conventional liquid fuels. Also high flammability limit, auto ignition temperature, minimum ignition energy, quenching distance and heat of combustion are some advantages of hydrogen usage as a fuel solely or fuel enrichment. These advantages improve performance and emission characteristics of diesel and spark ignition engine, except one parameter. Hydrogen usage adversely affects engine volumetric efficiency, due to its too low density. Wang, J. et al., 2007, mentioned that the negative point of the using hydrogen on the port-injected CI engine is the reduction of volumetric efficiency because the gas fuel will substitute a certain portion of the intake air in terms of volume, which will cause a reduction in the power output.

In another study, Ganesh, R.H., 2008, expressed that in the case of lower loads, there is no decrease in volumetric efficiency was observed when the throttle was wide open condition. However, in the case of high loading, the volumetric efficiency is considerably reduced because hydrogen occupies more space in the cylinder. Due to decreasing of volumetric efficiency, the cylinder cannot take enough air for combustion when hydrogen using as a fuel enrichment in C.I. engine. Kumar, M. S. et al., 2003, reported that in dual fuel operations with hydrogen, it was observed that volumetric efficiency was decreased for all power outputs. The reason for the reduction was that occupying the volume of some of the cylinder by hydrogen which has a lighter density than air.

Although hydrogen is considered a high potential fuel for alternative fuel applications, there is still a need to develop some risks in storage, safety, and use. Therefore, the usage of HHO obtained by electrolysis is more promising for on-road systems. The using of HHO as fuel enrichment improves performance data, contributing to improved combustion, albeit to a lesser extent, thanks to the extra oxygen in the contents. Yilmaz, A. C. et al., 2010, performed their study with a manual circuit is designed to reduce the amount of HHO sent to the cylinders at low revs to prevent reduction of volumetric efficiency with the use of HHO.

The literature researchers show that the usage of hydrogen in internal combustion engines negatively affects volumetric efficiency and thus performance output, especially at low engine revolutions. The aim of the study is to produce HHO that will keep the performance and volumetric efficiency values at an optimum level with an electronic circuit.

II. Methodology and Control Strategy

In this study, a new control card was designed and an algorithm was constructed to optimize volumetric efficiency under full load conditions. The control logic and the circuit elements used in the design are given by figure 1 and figure 2, in this section.

The volumetric efficiency (ηv) of an engine is defined as the ratio of the actual air mass flow rate ($\dot{m}_a$) taken to the cylinders divided by the maximum air mass flow rate that could be entered into the cylinder with respect to the engine geometry. It can be written as;

$$\eta v = \frac{\dot{m}_a}{\dot{m}_{th}} \quad (1)$$

Where;

$\dot{m}_a$: Actual mass flow rate of air through the engine

$\dot{m}_{th}$: Maximum possible mass flow rate of air according to engine geometry

Heywood, J. B., 1988, has presented a formula (2) for calculating the maximum air mass flow rate that could be taken into a cylinder.

$$\dot{m}_{th} = \frac{\rho_a * V_d * N}{2*60} \quad (kg/s) \quad (2)$$

Where;

ρ_a: Density of air

V_d: Displacement volume of the Cylinder

N : Engine Speed

when the equations (1) and (2) are combined, the volumetric efficiency could be written as;

$$\eta v = \frac{2*60*\dot{m}_a}{\rho_a * V_d * N} \quad (3)$$

The general scheme of the control unit was designed as shown in Fig.1. First of all, the information of the total engine volume (V_d) should be entered by users. After defining the volume information, the appropriate control strategy is determined according to the engine speed range. According to this control strategy; the number of revolutions taken from the sensor is saved and the control level which are the low speed, the middle speed, and the high speed, is adjusted.

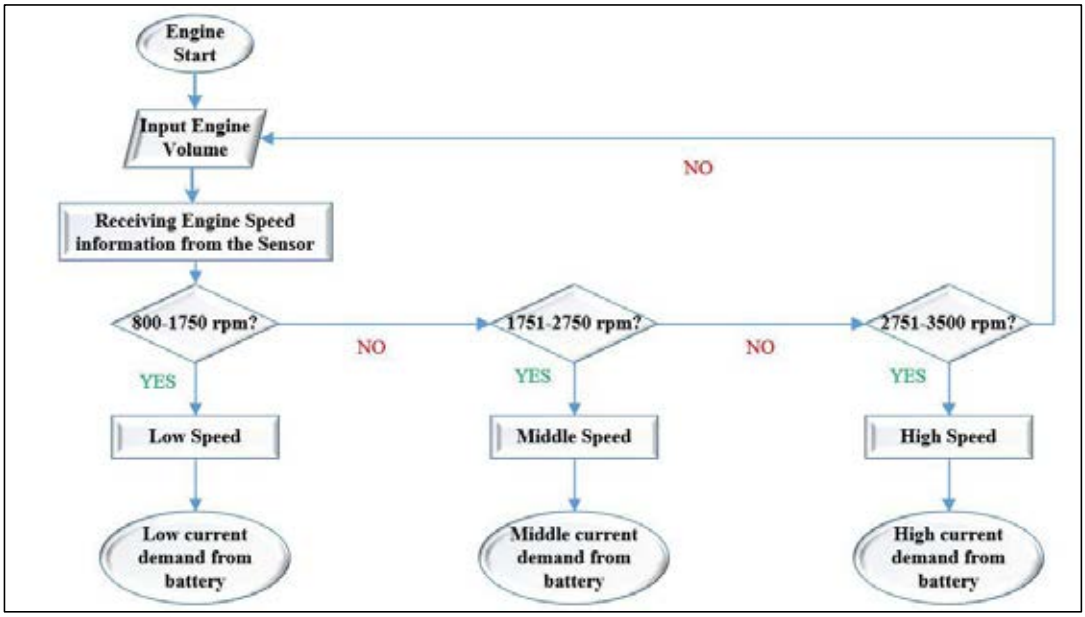


Fig. 1: Flow chart of the designed electronic control unit

The schematic of the electronic control unit design in MATLAB / Simulink is given in Fig. 2. The volumetric efficiency (η_v) calculations were made according to the volume and divided in three sub level with respect to the number of revolutions of the engine which are read by the sensor of the control board. For the volumetric efficiency, three different intervals are determined as 800-1750 rpm, 1751-2750 rpm, and 2751-3500 rpm. Also, considering these stages, the minimum volumetric efficiency value for each stage is defined as 70% for the first stage, 80% for the second stage and 90% for the third stage. This designed control unit automatically controls the amount of HHO production by adjusting the current drawn from the battery so that the volumetric efficiency is not reduced at any rpm intervals.

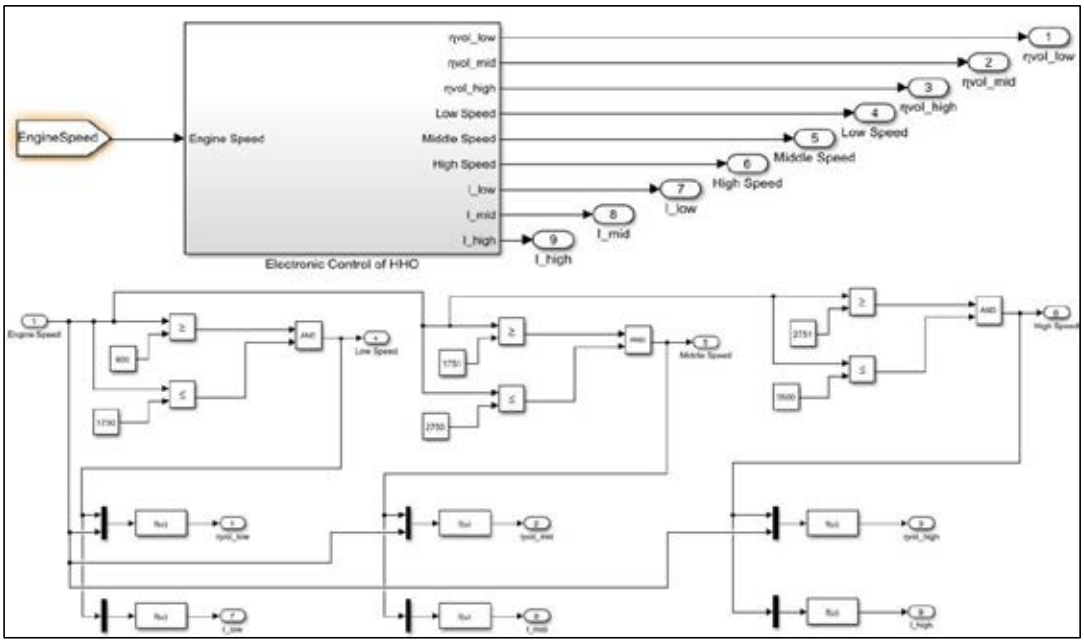


Fig. 2: The structure of the generated electronic control mechanism

III. Results and Discussion

It is known that the amount of air taken into the cylinders during HHO enrichment is reduced and the oxygen required for complete combustion could not be taken in the cylinders. Especially at low engine speeds, when HHO enrichment is kept in constant flow rate, the amount of oxygen decreases in the cylinders due to the light density of the hydrogen. Therefore, both performance and emission values are adversely affected. The designed model controls the HHO production by changing the electrolysis current according to the changing engine speeds. Designed to optimize the volumetric efficiency problem, especially at low engine speeds, this card determines the volumetric efficiency ratio by calculating the maximum amount of theoretical air that can be taken into cylinders for each engine speeds. After all received data, it provides sending the variable current to the electrolyzers according to engine speeds intervals to ensure that the HHO production quantity is maintained at the defined level, 70%, 80% and 90%, for the specified engine speed ranges (low, mid, and high speeds) as it is presented by 3-D graph, in figure 3. In this way, it improves engine performance and emissions at optimum levels even at low engine speeds.

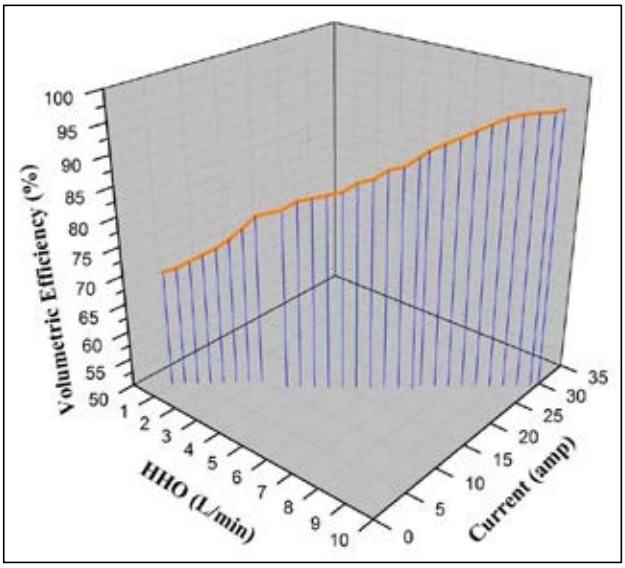


Fig. 3: HHO production rates vs current drawn to optimize volumetric efficiency

The amount of HHO produced by electrolysis is limited by the capacity of the reactors. Masjuki, H. H. et al., 2016, were conducted their experiments with HHO gas obtained from electrolysis. As they reported in their study, when electrolyzers reached maximum capacity, the increasing of water electrolysis amount almost stop and after this point overcurrent could not be increased more HHO gas flow. Furthermore, the lifetime of the reactors is extended by arranging optimum current flow drawn by the HHO system. Therefore, the maximum current delivered to the reactors, as shown in Figure 3, is limited to 30 amperes which is produce 10 liter per minute HHO gas.

IV. Conclusions

The main aim of this study was to obtain optimum HHO production by electrolysis for defined diesel engines volume by any user. It is a scientifically proven fact that the use of hydrogen in internal combustion engines is beneficial to performance and emissions until a certain limit. Although, improvements in performance and emissions have been reported by researchers; the designed control system offers an option to approach the highest achievable rate for HHO usage in CI engines. At the same time, the methodology of HHO enrichment to CI engine is taken one step forward by the designed control unit. System efficiency was improved with instantaneous calculations and feedback algorithm on HHO production rate and enrichment amounth. Automated HHO system is designed to work between 0-30 amp ranges and cooler operating temperetures to prolong the service life of engine batteries and HHO reactors.

References

Dincer, I. Renewable energy and sustainable development: a crucial review. Renewable and sustainable energy reviews, 4(2), 157-175. (2000)

Ganesh, R. H., Subramanian, V., Balasubramanian, V., Mallikarjuna, J. M., Ramesh, A., & Sharma, R. P.. Hydrogen fueled spark ignition engine with electronically controlled manifold injection: An experimental study. Renewable energy, 33(6), 1324-1333. (2008)

Heywood, J. B.. Internal combustion engine fundamentals. (1988)

Kumar, M. S., Ramesh, A., & Nagalingam, B. Use of hydrogen to enhance the performance of a vegetable oil fuelled compression ignition engine. International Journal of Hydrogen Energy, 28(10), 1143-1154. (2003)

Masjuki, H. H., Ruhul, A. M., Mustafi, N. N., Kalam, M. A., Arbab, M. I., & Fattah, I. R. Study of production optimization and effect of hydroxyl gas on a CI engine performance and emission fueled with biodiesel blends. International Journal of Hydrogen Energy, 41(33), 14519-14528. (2016)

Midilli, A., Ay, M., Dincer, I., & Rosen, M. A. On hydrogen and hydrogen energy strategies: I: current status and needs. Renewable and sustainable energy reviews, 9(3), 255-271. (2005)

Veziroğlu, T. N. Hydrogen movement and the next action: fossil fuels industry and sustainability economics. International journal of hydrogen energy, 22(6), 551-556. (1997)

Wang, J., Huang, Z., Fang, Y., Liu, B., Zeng, K., Miao, H., & Jiang, D.. Combustion behaviors of a direct-injection engine operating on various fractions of natural gas–hydrogen blends. International Journal of Hydrogen Energy, 32(15), 3555-3564. (2007)

Photocatalytic Hydrogen Production with Metal Oxide Bulk Structures

***Gizem Yanalak*[1], Abdalaziz Aljabour[2], Emre Aslan[1], Faruk Ozel[3], Imren Hatay Patir[4]**

Three types of metal oxide catalysts (NiO, Co3O4, Mn3O4) have been synthesized by solid state method and characterized by using Scanning Electron Microscopy (SEM) and X-ray Powder Diffraction (XRD). These structures have been used as catalysts for the photocatalytic hydrogen evolution from water without using any co-catalyst under the visible light irradiation by using triethanolamine as an electron donor and Eosin-y dye as a photosensitizer. It is found that the photocatalytic hydrogen evolution activities follow the order as: Mn3O4<Co3O4<NiO (135 µmolg-1h-1, 901 µmolg-1h-1, 937 µmolg-1h-1, respectively). These results demonstrated that NiO and Co3O4 catalysts have been showed approximately 7 times higher photocatalytic hydrogen activities than Mn3O4. This is thought to be due to the difference in the electronegativity, charge carrier separation and transport efficiency of metals.

This study has been supported by TUBITAK-1003 project (215M309), UNESCO-Loreal “For Women in Science” program scholarship and Turkish Academy of Sciences GEBIP fellowship.

Keywords: Metal oxide, hydrogen evolution, co-catalyst free

Hydrogen Evolution at the Water/DCE Interface Catalyzed by Cu2WS4

Faruk Ozel[1], Emre Aslan[2], Adem Sarilmaz[1], Imren Hatay Patir[3]

[1]Karamanoglu Mehmetbey University Department of Metallurgical and Materials Engineering, Karaman/Turkey
[2]Selcuk University Department of Chemistry Konya/Turkey
[3]Selcuk University Department of Biotechnology Konya/Turkey

A novel inorganic highly crystalline ternary electrocatalyst for the hydrogen evolution reaction (HER) is reported as cheap and active. Ternary cubic and cubiclike Cu2WS4 have been synthesized by simple and low-cost hot-injection method to minimize the reaction time and required pressure. The synthesized Cu2WS4 have been characterized by XRD, SEM, TEM, Raman spectra methods. The catalytic activity of Cu2WS4 has been investigated at water/DCE interface by two-phase reactions and 4-electrode methods. Kinetic study of HER has been carried out by integrated rate law. The rate of hydrogen evolution reaction in the presence of Cu2WS4 catalyst results in the enhanced catalytic activity by about 1000-fold, when compared to that in the absence of Cu2WS4 catalyst [1].

This study has been supported by TUBITAK-1003 project (215M309), UNESCO-Loreal “For Women in Science” program scholarship and Turkish Academy of Sciences GEBIP fellowship.

Keywords: hydrogen evolution, liquid/liquid interfaces, metal sulfide catalyst

Electricity Generation and Wastewater Treatment with Microbial Fuel Cells Using Homemade Beer Wastewater

***Ömer Faruk Coşkun*, Kürşat Can Ata, Ramiz Gültekin Akay**

Kocaeli University, Department of Chemical Engineering, Kocaeli, Turkey

Fuel cells (FC) are devices that directly convert chemical energy into electrical energy. Microbial fuel cells (MFC) are FC types that use microbial organisms (bacteria, yeast, etc.) on the anode surface as catalyst in fuel cells, so that these bio-electrochemical systems convert chemical energy of the substrates directly into electrical energy by catalytic reaction of bacteria with electrochemical activity. (Moon et al, 2006)

Interest in MFCs began in the 20th century by first measuring the potential difference between chambers of a FC in one section of the metabolic microorganism and the substrate in the other. Obtained potential difference (voltage) was observed to generate electric current when a resistance was applied between the two compartments. (He and Angenent, 2015)

In the preliminary studies, the power obtained was very low because of the problem in the transport of electrons to the electrode surface, to overcome this problem mediators were used to accelerate the electron transfer to the anode surface. Subsequent studies have shown that some bacteria can use their active microbial intermediates as internal mediators, and these systems are called “mediatorless” MFCs. It has been observed that the electrons of bacterial species such as Shewenalla and Geobacter can be directly transferred to the anode electrode. (Allen and Bennetto, 1993)

MFCs may also be utilized to process and treat waste water during electricity generation. This is particularly beneficial for the industries producing wastewaters having microorganisms such as beer factories. MFC’s that will be utilized in industries like this may be used to purify the wastewater without excess electricity consumption and by even producing some amount of electricity by microbes (bacteria) oxidizing organic compounds in the anode chamber. Another advantage is that; compared to activated sludge process and anaerobic digestion, MFC’s can operate at room temperature. (Mengqian et al)

In this study homemade beer wastewater was used as the substrate in the laboratory, the parameters affecting the system outputs related to the electrical potential generation and treatment. A two-chamber plexiglass MFC reactor was designed and constructed, Nafion TM membranes were used as the separator and ion-exhange medium and carbon fiber paper was used as electrode material. The system operated continuously was monitored for 3 days and chemical oxygen demand (COD) decreased over time. The power density obtained and normalized to the anode chamber volume. MFC system constructed is being studied to investigate the effects of different microorganisms, wastewater compositions and substrates on the power and COD removal.

Keywords: electricity, wastewater, mfc, treatment, home-made

The Hydrogen Evolution Reaction Catalyzed by Metal Oxide and Metal Sulfide Catalysts at Soft Interfaces

Emre Aslan[1], Gizem Yanalak[1], Imren Hatay Patir[2]

[1]Selcuk University Department of Chemistry Konya/Turkey
[2]Selcuk University Department of Biotechnology Konya/Turkey

Cheap, active, and consisted of abundant element catalysts are crucial for the development of efficient hydrogen evolution. Electrocatalytic hydrogen evolution reaction has been usually working with modified solid electrodes. Electrochemistry at the interface between two immiscible electrolyte solutions (ITIES) is also known as another approach to study electrocatalytic reactions. Hydrogen evolution reaction (HER) at the liquid/liquid interface by organic electron donor decamethylferrocene (DMFc) is taken place very slow rate [1]. For this reason, some catalysts are needed to increase the reaction rate. In this study, HER at the water/DCE interface have been investigated by metal oxide and metal sulfide catalysts such as NiO, Co3O4, WS2, MoS2 and Cu2WS4 [2-4]. Catalytic activities of these catalysts have been also compared to each other.

This study has been supported by TUBITAK-1003 project (215M309), UNESCO-Loreal “For Women in Science” program scholarship and Turkish Academy of Sciences GEBIP fellowship.

Keywords: hydrogen evolution, liquid/liquid interfaces, metal sulfide catalysts, metal oxide catalysts

Effect of Channel Bend in Serpentine Flow Field Design Pattern for PEMFC

***Mohammad Ziauddin Chowdhury*[1], *Yahya Erkan Akansu*[2], *Omer Genc*[2], *Serkan Toros*[2], *Yusuf Sahin*[2]**

[1]*Mechanical Engineering Department, Istanbul University, Istanbul, Turkey*
[2]*Mechanical Engineering Department, Nigde Omer Halisdemir University, Nigde, Turkey*

Proton exchange membrane (PEM) fuel cell becomes more viable for fulfilling growing demand of alternative energy. For this reason, it is very important to develop an efficient system for PEM fuel cell. Numerical analysis facilitates better technical tools to analyze suitable and optimal design criteria with an understanding into the internal phenomena of PEM fuel cell instead of experimental measurements, which are highly expensive and time consuming. Flow field design is one of the major research parameter of the system since the appropriate flow field design can improve the cell performance significantly. Among the different types of flow field design patterns, serpentine flow field is one of the most suitable design for better PEM fuel cell. However, one of the biggest drawback of serpentine flow field is high channel pressure drop. In this study, a mathematical model including computational fluid dynamics, electrochemistry and species transport is developed. The model is first solved for traditional serpentine design and the mathematical model is validated with experimental results. Channel bend effect on single serpentine channel is numerically analyzed with consideration of channel pressure drop as well as cell performance. The aspect ratio of bipolar plate with different number of channel bend is taken into account for more effective serpentine flow field design.

Keywords: Aspect ratio, Bipolar Plate, Flow field design, Pressure drop, Proton exchange membrane fuel cell.

Numerical investigation of conventional flow field patterns in proton exchange membrane fuel cell

Mohammad Ziauddin Chowdhury
Istanbul University, Faculty of Engineering, Mechanical Engineering Department, Istanbul, Turkey-34310.

Email: zia72822@gmail.com

Abstract
Flow field pattern intricately facilitates reactive species transport along the reactive zone in the proton exchange membrane fuel cell (PEMFC). Every flow field pattern has its own distinctive flow characteristics having pros and cons. Therefore, a suitable flow field pattern can enhance the cell performance significantly. In this study, the most common flow field patterns (parallel, pin, serpentine and interdigitated) are comparatively studied investigating the transport phenomena and cell performance to identify the pros and cons of the conventional flow field patterns. A validated three dimensional numerical model of an active area of 2 cm^2 is considered analyzing the mass transport, pressure drop and water concentration. The predicted results showed that cell performance as well as transport phenomena are highly dependent on the cathode side of the flow field. The model predicted better mass transport and water management especially of the cathode compartment for the interdigitated, serpentine and pin flow fields through a descendant order where severe mal-distribution of mass transport and excessive water accumulation indicated in the parallel flow field. As a whole outcome of the study, interdigitated flow field has the best cell performance, while parallel has the least.

Keywords: parallel serpentine interdigitated pin flow field design, mass transport, water distribution, pressure drop, cell performance.

I. Introduction

Since the last two centuries, fossil fuels have been the most dominating energy resource for the industrialization and modernization. But considering the environment friendliness and sustainability PEM fuel cell can be a replacement of the fossil fuel energy system. So it is an utmost importance to develop better fuel cell technology for the well-being of human society. The PEMFC has flow-fields which is responsible for carrying the reactant gases from the inlet manifold to the catalyst layer and then to the electrode where the reaction actually takes place. Therefore, the flow field is an important structural feature of a PEM fuel cell and there have been abundant research carried and it's ongoing. Different flow field patterns have their unique features and its effect on reactant gas delivery, flow distribution, water removal characteristics as well as associated pressure drop have been studied in detail. Most common flow field patterns found in the literature are serpentine, parallel, interdigitated, pin, spiral, radial and bio-inspired flow field pattern etc. A 3D numerical model was employed by Jang et. al. (2008) for the analyses of parallel, Z-type and serpentine flow fields performance. The simulation results revealed that serpentine is better than Z-type and parallel, and the later one exhibited worst performance. However, serpentine flow field was found to be superior in terms of oxygen mass transport, velocity and water removal characteristics at the expense of high pressure drop. Interdigitated, serpentine, parallel and mesh flow fields were investigated by Hsieh et. al. (2008) for transient local current density distribution and liquid water accumulation for certain time period. It was found more uniform and highest current density existed in interdigitated flow field followed by serpentine, parallel and mesh types. For water accumulation analyses in parallel and interdigitated flow fields were numerically performed by Wang et. al. (2008) with different level of RH% for the anode and cathode. Hsieh et. al. (2009) conducted pressure drop measurements for different flow fields on the cathode side under various mass flow rates and temperatures on the basis of water accumulation. Arbabi et. al. (2012) adapted Navier-Stokes equation into two dimensional numerical model for a comparative analysis between conventional flow field patterns. It was found out that total pressure drop in bio-inspired is the lowest, followed by the parallel, 3-serpentine, 1-serpentine. The same order was also obtained for the case of pressure uniformity in the channels of each flow field patterns.

In this study, conventional flow field design of parallel, pin, serpentine and interdigitated are comparatively studied. A three dimensional isothermal model is considered for the investigation of transport characteristics and cell performance. The numerical results are explained at the 0.4 V operating voltage for 80℃ cell temperature and 100% RH.

II. Numerical Method

The geometry of the conventional flow fields are shown in Figure 1. The active area of the flow fields are considered as 2 cm^2 with the channel depth and width of 1 mm, rib width of 0.5 mm for all the flow field design. The channel geometry of the flow field designs are optimized in the previous ref. study [Chowdhury et. al. 2017, 2018]. For the case of the Pin flow field, the pin diameter is 0.5 mm where pins are designed as a regular arrangement having 1 mm distance between the two centers irrespective of vertical or horizontal arrangement. The mathematical model is validated with the experimental study as well as the mesh independency test procedures in the ref. study [Chowdhury et. al. 2018]. Also, the major parameters of the numerical model are same as the previous study while the flow rate is taken as a mean of stoichiometry of the experimental study considering the relative active area.

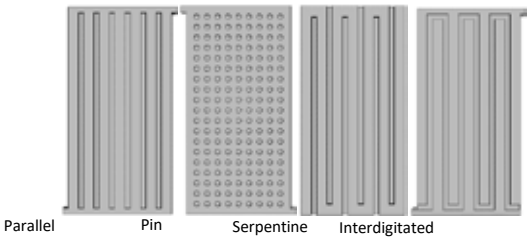


Fig. 1: Geometry of the numerical model of the conventional flow fields

III. Results and Discussion

The hydrogen and oxygen mass transports of the flow fields are shown in the Figure 2 (a) and 2 (b) respectively. It can be seen that, the hydrogen mass transport at the anode for the flow fields is almost same considering consumption and distribution. Meanwhile, oxygen mass transport at the cathode side is not like the anode side where lack of oxygen transport indicated specially for the parallel flow field. The pressure distribution of the anode and cathode flow fields are shown in the Figure 3. From the predicted results, it can be observed that the anode pressure drop is almost negligible compare to that of cathode for all of the cases. The cathode pressure drop is minimum for the pin flow field while maximum for serpentine one following the interdigitated.

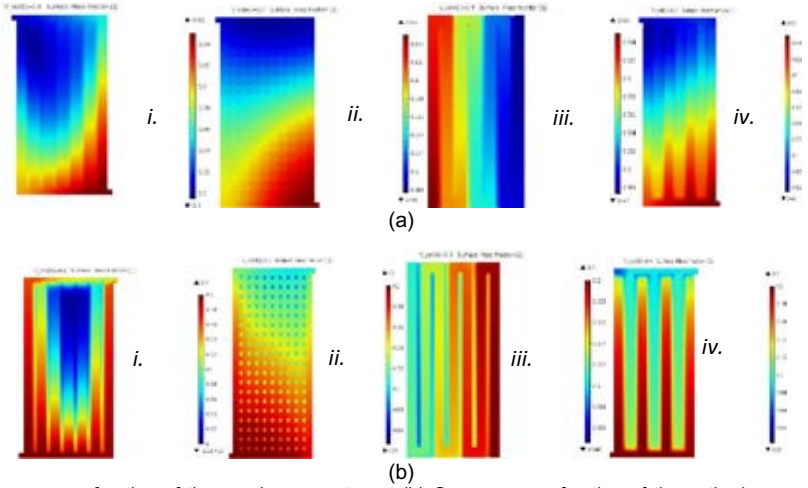


Fig.2: (a) Hydrogen mass fraction of the anode compartment (b) Oxygen mass fraction of the cathode compartment for the conventional flow fields of: i. Parallel, ii. Pin, iii. Serpentine and iv. Interdigitated

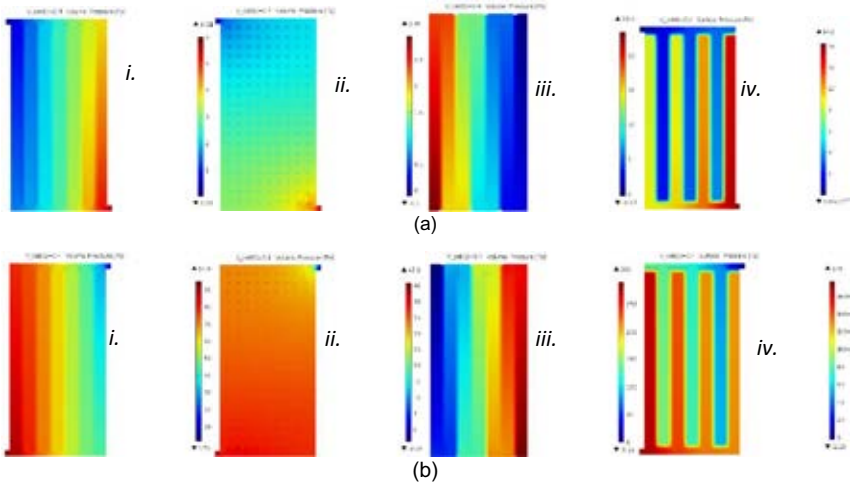


Fig. 3: (a) Pressure distribution of the anode compartment (b) Pressure distribution of the cathode compartment for the conventional flow fields of: i. Parallel, ii. Pin, iii. Serpentine and iv. Interdigitated

The water distribution at the anode and cathode side of the flow fields are shown in the Figure 4. Alike the previous cases, anode side for water distribution is also less significant than the cathode. The water accumulation occurred at the mid-parallel flow field while in the other cases, water removal seems to be effective considering no water accumulation occurred.

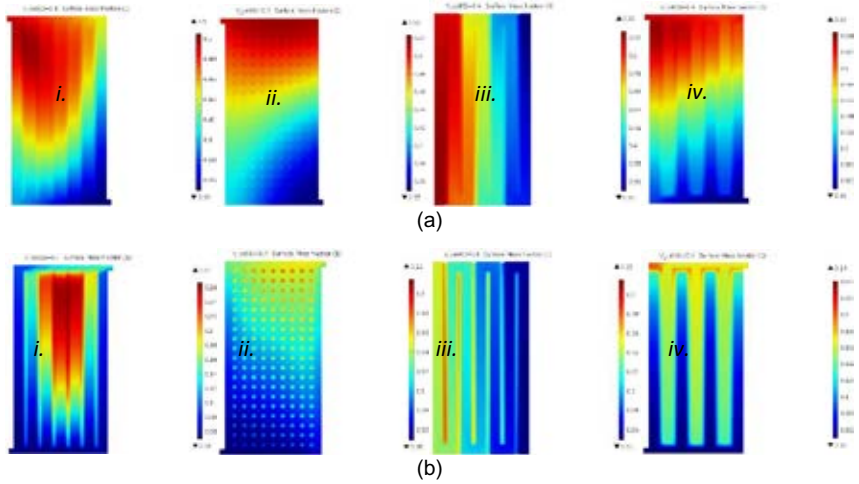


Fig. 4: (a) Water distribution along the anode compartment (b) Water distribution along the cathode compartment for the conventional flow fields of: i. Parallel, ii. Pin, iii. Serpentine and iv. Interdigitated

The cell performance of the flow fields are shown in the Figure 5. From the polarization and power curve, it is found that, there is small difference among the pin, serpentine and interdigitated flow fields of power density. On the other hand, parallel flow field has a noticeable lower performance than the others.

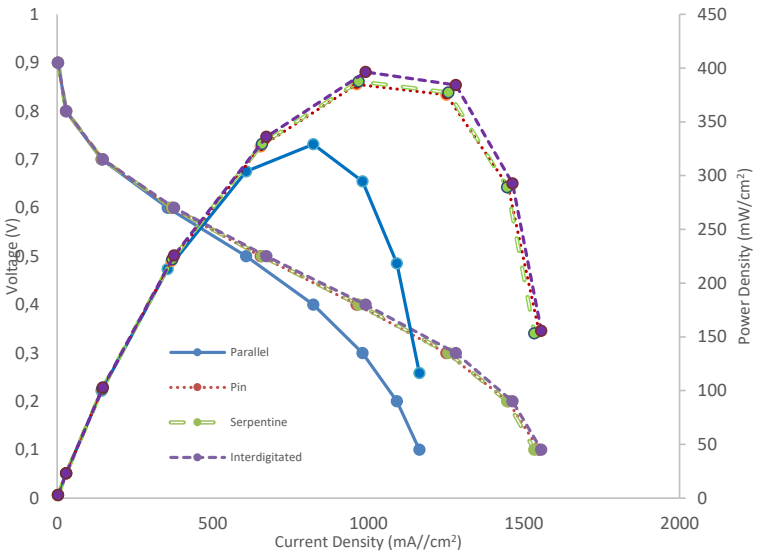


Fig. 5: Cell performance of the conventional flow fields

Conclusion

From this numerical study of the comparative analyses of the conventional flow fields, interdigitated flow field found to be the most suitable although there is little difference with the serpentine one following the Pin type with a small margin. The anode side flow field is found to be less significant on the cell performance compare to the cathode compartment. The pressure drop is maximum for the serpentine whilst minimum for Pin type. The water accumulation along the mid-parallel channels cause lack of reactant transport in the parallel flow field which is the main reason of the cell performance deviation from the other three cases.

References

Arbabi, F., Roshandel, R. and Moghaddam, G.K., "Numerical modeling of an innovative bipolar plate design based on the leaf venation patterns for PEM fuel cells", International Journal of Engineering 25 (3), 177-186, (2012).

Chowdhury MZ, Akansu YE. Novel convergent-divergent serpentine flow fields effect on PEM fuel cell performance. Int J Hydrogen Energ, 42:25686-25694, (2017).

Chowdhury MZ, Genc O, Toros S. Numerical optimization of channel to land width ratio for PEM fuel cell. Int J Hydrogen Energ, (2018). https://doi.org/10.1016/j.ijhydene.2017.12.149

Chowdhury MZ, Akansu YE. Effect of Convergent-Divergent Flow Fields in Single Serpentine Flow Pattern on PEMFCs Performance, 9th International Conference on Sustainable Energy and Environmental Protection (SEEP), Erciyes University, Kayseri, Turkey, 22-25 September, (2016).

Chowdhury MZ, Timurkutluk B, Toros S. Numerical Investigation of the Effect of Channel Depth on PEM Fuel Cell Performance', 2nd International Defense Industry Symposium, Kirikkale University, Ankara, Turkey, (2017).

Chowdhury MZ, Genc O, Toros S. Numerical Investigation of the Effect of Channel Width to Land Ratio on PEM Fuel Cell Performance, 2nd International Hydrogen Technologies Congress, Cukurova University, Adana, Turkey, (2017).

Jang, J.H., Yan, W.M., Li, H.Y. and Tsai, W.C., "Three-dimensional numerical study on cell performance and transport phenomena of PEM fuel cells with conventional flow fields", International Journal of Hydrogen Energy 33, 156–164, (2008).

Hsieh, S.S. and Huang, Y.J., "Measurements of current and water distribution for a micro PEM fuel cell with different flow fields", Journal of Power Sources 183, 193–204, (2008).

Wang, X.D., Duan, Y.Y., Yan, W.M. and Weng, F.B., "Effect of humidity of reactants on the cell performance of PEM fuel cells with parallel and interdigitated flow field designs", Journal of Power Sources 176, 247–258, (2008).

System Design and Optimization of a Hydrogen Fuel Cell Vehicle in the Different Road Models

[1]Yakup Hameş, [1*]Kemal Kaya
[1] Iskenderun Technical University, Faculty of Engineering and Natural Sciences, Electrical and Electronics Engineering Department, ISTE Central Campus, Iskenderun-HATAY, 31200, Turkey

* E-mail:kemal.kaya@iste.edu.tr

Abstract
With the acceleration of the development process of hydrogen fuel cell vehicles, it has become very important to maximize the energy stored in the vehicle and to use the vehicle with high efficiency. The fuel cell, which is located within a hydrogen fuel cell vehicle, is inadequate to require at the first working time and high power demands. For the solution of this, the battery and supercapacitor technologies are used to supply the extra power and energy demands of the fuel cell. These demands vary according to the road conditions of the region. In this study, the system design and optimization of a hydrogen fuel cell vehicle that improves fuel economy and energy efficiency in various road conditions have realized.

Keywords: Fuel cell, battery, supercapacitor, fuel economy, road models.

I. Introduction

One of the most important threats that human beings may face in the future is the increasing need for energy in the world. The reserves of conventional fuels required to meet increased energy demand are limited and exhausted Rodatz etal. (2005). With the use of these fuels, the global warming problem is increasing day by day and the climate conditions are being adversely affected in various regions of the world. For this reason, alternative energy systems are beginning to be used to compensate the high-energy needs of the automotive sector where petrol and its derivatives, which make up a large proportion of the environmental pollution, are used Gao (2005). Particularly hydrogen fuel cells, which have high-energy efficiency and low emission, have started to be used in transportation systems, contributing to the technological developments Marzougui etal. (2017). Besides all of these advantages, hydrogen fuel cells have problems that should be solved, such as low power density and slow power response. In order to overcome these problems, energy storage technologies such as batteries and supercapacitors can be used together with hydrogen fuel cells in vehicles Ahmadi etal. (2018). Of course, the most important goal here is to design this compact structure and save fuel and energy.

Energy sources and storage technologies of hydrogen fuel cell vehicles should work in harmony with each other. For this, system control and energy management are very important Fathabadi (2018). Firstly, it is necessary to determine the system design according to the road conditions of the vehicle. The ability to store and reuse the energy lost by the vehicle is crucial in terms of fuel economy and energy efficiency, especially in road models such as deceleration and downhill. Moreover, supplying the power demands of the vehicle during ramp or sudden acceleration depends on how well the power and energy variables are controlled. This varies depending on the power conversion units in the vehicle, the structure of the traction motor, control strategies and road conditions.

In this paper, system design of a hydrogen fuel cell vehicle has realized by modelling different road conditions. The energy management of the vehicle has been controlled in terms of fuel economy and energy efficiency in various road conditions. Finally, the results of this control mechanism have simulated with the MATLAB / Simulink program.

II. The road models

Automotive manufacturers need to consider road conditions when designing vehicles. Particularly, there is a great effect of the road conditions on the energy consumption and the fuel saving of the energy use in the vehicle. When designing a system for a hydrogen fuel cell vehicle, the road conditions to be encountered should be modelled and the vehicle should be optimized accordingly.

Generally, as a load of the vehicle, reference is made to situations that the vehicle will encounter in various road models. In order to be able to determine the realistic gain rates in the model, it is necessary to model the road conditions that a hydrogen fuel cell vehicle may encounter in the actual driving environment. It has been approved appropriate to examine two different models for this. These are; "stop-go" and "uphill-downhill" road models.

The stop-go road model has created by modelling the road conditions that hydrogen fuel cell vehicles most frequently encounter when they enter urban traffic. In urban transport, vehicles can be exposed to heavy traffic. In addition, they may encounter traffic lights during driving. As the vehicle travels from one traffic light to another, momentum increases with stop, go and acceleration positions. At this time, some of the kinetic energy obtained can be stored in the vehicle not to be wasted by the braking energy when approaching the other traffic light and can be used again in the vehicle starting position. Thus, the fuel consumption is increased.

According to the stop-go road model designed in Fig. 1, the vehicle stop and go 3 times at 100-meter intervals on a flat road of 300-meter in total.

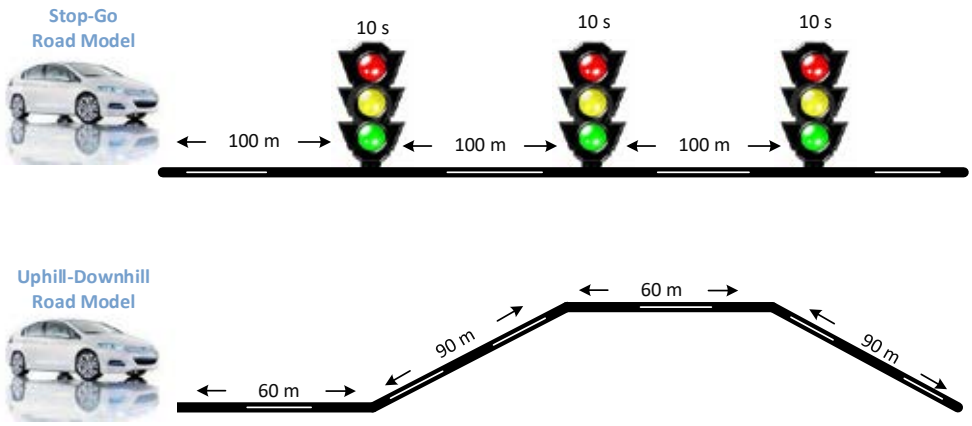


Fig. 1: Stop-go and uphill-downhill road models

One of the most common road models in the real driving environment is also the uphill-downhill road model. A hydrogen fuel cell vehicle demands a lot of power when it goes uphill or at rapid acceleration. To supply this demand, the battery and supercapacitor support the fuel cell. In the meantime, the potential energy of the vehicle increases and more hydrogen is consumed. When the vehicle is going downhill, the potential energy that is earned starts to turn into kinetic energy. Here, just as in the stop-go road model, kinetic energy, which the vehicle will lose during braking, can also be stored in the vehicle by regenerative braking.

In order to reduce the load on the traction motor of the vehicle according to the uphill-downhill road model designed in Fig. 1, the vehicle is accelerated on a straight road of 60 meters after the go. Later, the vehicle is going up a 90-meter ramp. At the end of the ramp, there is a 60-meter straight road to make it easier to observe the vehicle's gains. At the end of this distance, the vehicle has completed the road model by descending from the 90-meter ramp.

III. System design and optimization

Energy saving in the models applied in different road conditions is achieved by storing the kinetic energy gained in the system battery and supercapacitor during regenerative braking for the stop-go road model and during downhill for the uphill-downhill road model. The mathematical model equations for the regenerative braking charge of the battery used in the system are as follows:

$$f(i_t, i^*, \mathrm{i}) = E_0 - K * \frac{Q}{i_t + 0.1 * Q} * i^* - K * \frac{Q}{Q - i_t} * i_t + Ae^{(-B * i_t)} \quad (1)$$

and filtered current is:

$$i^* = \frac{E_{batt} - U}{r_{in} + r_k} \quad (2)$$

Where A is the voltage at the start, E_0 is the voltage at the start of the battery, K is the polarization constant, Q is the maximum battery capacity, B is the variable capacity, r_{in} is the internal resistance of the battery, E_{batt} is the rated voltage of the battery with internal resistance, U is the rated voltage at the external ends of the battery, i is the battery current, i_t is the separated capacity and r_k is the variable capacity of the battery.

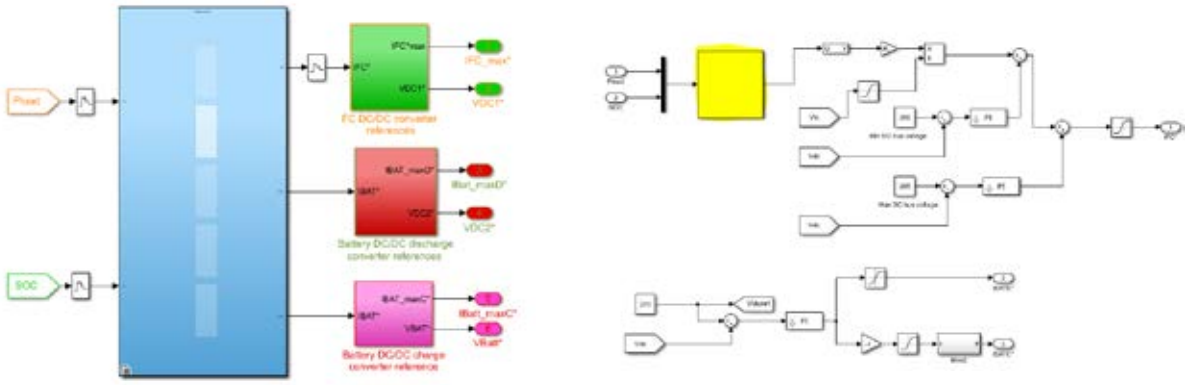
The mathematical model equations for the regenerative braking charging of the supercapacitor used in the system are as follows:

$$E = \frac{1}{2} C (V_r^2 - V_{cf}^2) \quad (3)$$

and

$$SOC = \frac{\frac{1}{2} C V_{Cap}^2}{\frac{1}{2} C V_r^2} = \left(\frac{v_{cap}}{v_r}\right)^2 \quad (4)$$

Where E is the regenerative braking energy, C is the capacitance of the capacitor, V_r^2 is the rated voltage of the supercapacitor, V_{cf} is the cut-off voltage, V_{sc} is the terminal voltage at any point in the supercapacitor, V_r is the terminal voltage at which the supercapacitor is fully charged and SOC is equal to the square of the ratio of these two terminal voltages.



(a) System Control Design (b) Optimization Model

Fig. 2: Hydrogen fuel cell vehicle system control design and optimization model

All of these optimization values have been added to the MATLAB/Simulink model while the system is being designed. Fig. 2 shows the system designed according to the optimization values.

IV. Results and discussions

In this study for a hydrogen fuel cell vehicle, the simulation results are examined according to different road models. The stop-go and uphill-downhill road models as road models are considered as the load of the vehicle's traction motor. First, the system optimization for the stop-go road model has done. In mathematical modelling, the energy gained by regenerative braking has taken into consideration in order to determine the hydrogen consumption in response to the demand. The power demanded by the vehicle for the stop-go road model, the power changes in the fuel cell, battery and supercapacitor, the change in the percentage of SOC of the battery and the fuel consumption of hydrogen connected to them are shown in Fig. 3.

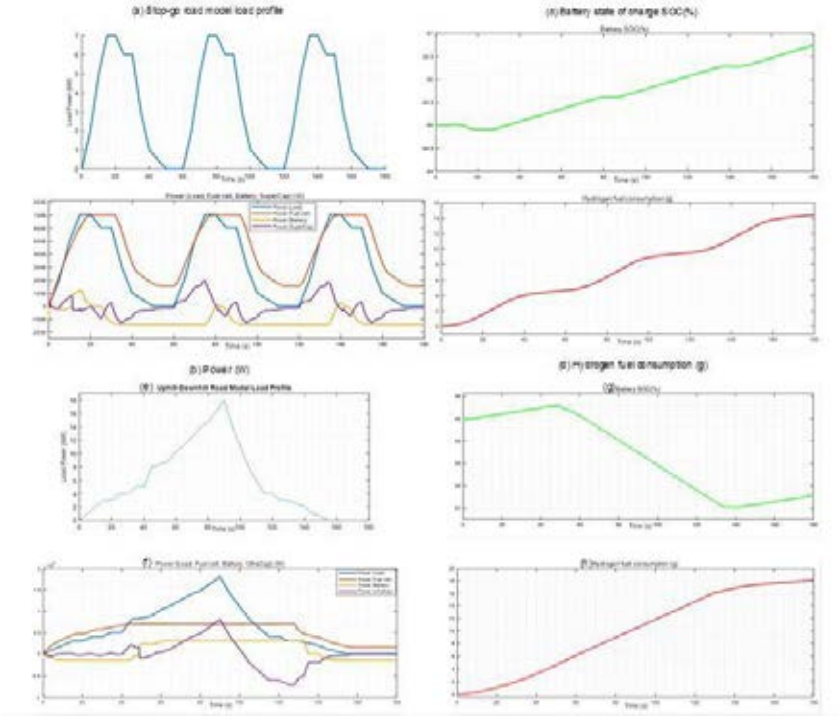


Fig. 3: Simulation results of a hydrogen fuel cell vehicle on stop-go and uphill-downhill road models

Firstly, according to the stop-go road model, the car started to move from the stationary position. As the vehicle has travelled on a 100-meter straight road, it has encountered traffic light and stopped by slowing its speed. After waiting for 10 seconds of light, it has gone back to action and it has repeated this three times in total and travelled 300 meters in 180 seconds. The vehicle used the fuel cell as the primary energy source in this model. In addition, the battery and supercapacitor have stored some of the kinetic energy lost by the regenerative braking and stopping of the vehicle. Here, the battery state of charge (SOC) is 65% at initially, while it is 66.7% at the final position. This means that the energy stored in the battery of the vehicle will be available for re-start. Also in the stop-go road model, the vehicle's hydrogen fuel consumption has been 14.5 g total along the way.

Secondly, the simulation results for the uphill-downhill road model are shown in Fig. 3. In this model, the vehicle is accelerated on a straight road of 60 meters first to reduce the load on the traction motor when the vehicle moves uphill from the stand position. At the end of 60 meters, there has been a demand for heavy power in a 90-meter ramp. Because of the fact that this power-demand will not be supplied by fuel cell alone, the extra power to the vehicle has been provided by the battery and supercapacitor technologies. Additionally, during this excessive power demand of the vehicle, the hydrogen fuel consumption has also increased. After completing the ramp, the vehicle has continued to move on a straight 60-meter road and the 90-meter ramp has descended to complete its movement. The potential energy that the vehicle gains when it comes down downhill has begun to turn into kinetic energy. The vehicle stores some of this kinetic energy in the battery and supercapacitor for reuse with regenerative braking. Moreover, the supercapacitor ensures power in a sudden and high power demands.

In this 300-meter road model, which the vehicle has taken in 180 seconds, the battery's initial SOC dropped from 65% to about 61%, and it has reached to about 62% on the downhill. Furthermore, the vehicle has consumed 18 g of hydrogen fuel in total.

V. Conclusions

Hydrogen fuel cell vehicles are intended to provide the extra power and energy demands of the vehicle with the use of batteries and supercapacitors. The power demanded by the vehicles vary according to different road conditions. In this study, the system design and optimization of a hydrogen fuel cell vehicle has been realized in stop-go and uphill-downhill road models. In addition, fuel efficiency and energy efficiency in different road models have shown with simulation results. Consequently, as the power demanded by the vehicle increases, the hydrogen fuel consumption increases, but the battery and supercapacitor suppress this increase substantially by providing extra power to the fuel cell.

References

Ahmadi S., Bathaee S.M.T., Hosseinpour A.H., Improving fuel economy and performance of a fuel-cell hybrid electric vehicle (fuel-cell, battery, and ultra-capacitor) using optimized energy management strategy, Energy Conversion and Management, 160, 74-84, (2018).

Fathabadi H., Novel fuel cell/battery/supercapacitor hybrid power source for fuel cell hybrid electric vehicles, Energy, 143, 467-477, (2018).

Gao W., Performance comparison of a fuel cell-battery hybrid powertrain and a fuel cell-ultracapacitor hybrid powertrain, IEEE Transactions on Vehicular Technology, 54, 846-855, (2005).

Marzougui H., Amari M., Kadri A., Bacha F., Ghouili J., Energy management of fuel cell/battery/ultracapacitor in electrical hybrid vehicle, International Journal of Hydrogen Energy, 42, 8857-8864, (2017).

Rodatz P., Paganelli G., Sciarretta A., Guzzella L., Optimal power management of an experimental fuel cell/supercapacitor-powered hybrid vehicle, Control Engineering Practice, 13, 41-53, (2005).

Integration of Renewable Energy Systems with Hydrogen Technologies

***Alper Saydam*, Tanay Sıdkı Uyar**

Department of Engineering, Marmara University, İstanbul, Turkey

Renewable energy systems becomes more important as conventional energy generation methods gets more expensive and less reliable. This will lead a transition to 100% renewable energy systems from the current situation which will require smart grid technologies. The excess energy generated from renewable energy sources needs to be stored in a convenient way in order to use when one or some of the renewable energy source is not available. Fuel cells and hydrogen can play a big role in the smart grid area.

There is already applications of co-production of hydrogen and electricity such as DFC-H2 plants in California. This technology can be used with all renewable energy sources and Turkey has a huge potential for producing hydrogen and electricity from wind energy. There are many possibilities for a wind – hydrogen smart grid as Turkey is only beginning the transition to renewable energy systems.

Keywords: Smart grid, hydrogen cell, wind energy

Effective TiO_2 Supported Cu-Complex Catalyst in $NaBH_4$ Hydrolysis Reaction to Hydrogen Generation

[1*]Dilek Kılınç,[2] Ömer Sahin
[a] Faculty of Science and Letters, Department of Chemistry, Siirt University, 56100 Siirt
[b]Faculty of Engineering and Architecture, Department of Chemical Engineering, Siirt University, 56100 Siirt

* E-mail: dkilinc@siirt.edu.tr

Abstract

Hydrogen and fuel cell technology are currently in an intense development phase and many improvements have been accomplished, however the set-up of appropriate hydrogen storage technologies still represents a challenge (Bennici, 2011)

Between the most suitable and safe technologies for H_2 storages metal borohydrides have a potential for portable and portable and stationary applications due to their high energy density storage at room temperature and atmospheric pressure (Demirci, 2009).

$NaBH_4$ can be utilized as sources of a high purity hydrogen generatedby the hydrolysis reaction which is easily controlled by catalyst.

$$NaBH_4 + 2\ H_2O \xrightarrow{\text{cat.}} 4H2 + NaBO_2 + Q\ (217\ kJ\ )$$

In this study, Cu-Schiff Base complex which we synthesized before (Kilinc.2012) was used to support TiO_2 for getting TiO_2 supported-Cu-Schiff Base complex. And this complex was used as a catalyst for hydrolysis of $NaBH_4$ to H_2 generation. TiO_2 supported-Cu(II) complex catalyzed $NaBH_4$ hydrolysis reaction was researched based on several parameters. Also the catalyst were caracterized with some analysis techniques like XRD, FT-IR, BET, SEM. As a result it seen that TiO_2 supported-Cu(II)-Schiff Base complex was highly efficent catalyst in $NaBH_4$ hydrolysis to H_2 generation.

Keywords: $NaBH_4$, Hydrolysis, Schiff Base Complex, H_2 Generation.

References

Bennici S., Yu H., Obeid E., Auroux A., International Journal of Hydrogen Energy 36 (2011) 7431-7442

Demirci U.B., Akdim O., Miele P., International Journal of Hydrogen Energy 34 (2009) 2638-2645

Kilinc D., Saka C., Sahin O., Journal of Power Sources 217 (2012) 256-261.

Thermodynamic Analysis of a New Solar Power Tower Based Integrated System for Hydrogen Production and Liquefaction

[1]Yunus Emre Yüksel, [2*]Murat Öztürk, [3]İbrahim Dinçer,
[1] Afyon Kocatepe University, Education Faculty, Math and Science Education, ANS Campus, Afyonkarahisar, 03200, Turkey
[2] Suleyman Demirel University, Faculty of Technology, Department of Mechatronics Engineering, Cunur West Campus, Isparta, 32200, Turkey
[3] University of Ontario Institute of Technology, Faculty of Engineering and Applied Science, 2000 Simcoe Street North, Oshawa, Ontario L1H 7K4, Canada

* E-mail: muratozturk@sdu.edu.tr

Abstract
In this paper, thermodynamic analysis of a solar power tower based integrated system with hydrogen production and liquefaction is investigated for better environmentally-benign operation. The proposed integrated system is consisted of mainly eight sub-systems; a solar power tower, a high temperature steam electrolysis, a steam Rankine cycle with two turbines, a hydrogen liquefaction process, a quadruple effect absorption cooling system, a drying process, a membrane distillation unit and a domestic hot water tank to supply hydrogen, electrical power, heating, cooling, dry products, fresh water and hot water production for a community. The energy and exergy efficiencies of the integrated system are found as 65.17% and 62.35%, respectively. The parametric studies are carried out to investigate the impact of various system design parameters on the sub-systems exergy destruction rates and exergy efficiencies. In addition, the effect of ambient temperature on exergy destruction rate and exergy efficiency for the integrated system components and whole system.

Keywords: Solar energy, hydrogen, energy, exergy, multigeneration

I. Introduction
Energy has always been recognized as one of the most critical issues of modern life. Fluctuating oil prices and depletion of fossil sources with growing environmental concerns cause to open new gates for meeting of energy needs. One of the solutions for these problems is to use renewable energy sources instead of fossil fuel sources. If current energy technologies remain stable and there is not be a transition to a renewable energy sources, it will not be sustained for next generations. Among renewable energy sources, solar energy is one of the cleanest ways to generate necessary energy, if sufficient radiation is available. Generation of energy in clean, economic and continuous way is challenging because of disadvantages of current energy infrastructure. Single generation energy systems are simple and easy to install however their efficiencies are low. Therefore, popularities of cogeneration, trigeneration and even multigeneration energy systems increase. Relatedly, multigeneration energy systems offer some advantages such as high performance, less thermal losses and wastes, less operation cost, less emission, better usage of sources, fewer distribution units with shorter transmission lines, increased reliability and energy safe (Dincer and Zamfirescu, 2012). Multigeneration energy systems can either use fossil fuels or renewables as source of the system. Therefore, in order to sustain a clean and economic energy options multigeneration energy systems should use renewables as a source. These sources can be selected according to the geographic position, solar radiation, wind potential and/or geothermal availability. In this study, solar tower is selected as primary energy source because of its high efficiency when it is connected to a high temperature storage tank. Also, solar towers can reach higher temperatures than parabolic trough collectors when heat losses are minimized (Atif and Al-Sulaiman, 2017). The main purpose of this paper is to investigate the thermodynamic analysis of solar energy based integrated system, consisting of the solar power tower, the high temperature steam electrolysis, the steam Rankine cycle with two turbines, the hydrogen liquefaction process, the QEAC system, the drying process, the membrane distillation unit and the domestic hot water tank, for multigeneration application, through both energy and exergy analyses. In addition, the specific objectives of this paper are listed as follows:

- A novel integrated, solar power tower based system for multi-generation aims is proposed and thermodynamically investigated in detail through energy and exergy assessment approaches.
- The performance of all subcomponents, mainly eight sub-systems and whole system are calculated and comparatively determined.
- The exergy destruction rates for the system components are determined and analyzed to examine the possibility of improving the investigated integrated system.
- The parametric studies are undertaken to analyze the impacts of changing design parameters and reference temperature on the system exergy destruction rate and exergy efficiency of the investigated integrated system.

II. System Description
A schematic overview of the integrated system is illustrated in detail in Fig. 1. The detailed definition of the multi-generation sub-systems and operating conditions are investigated to analyze for thermodynamic analysis of solar power tower based integrated system for electricity, hydrogen, heating, cooling, dry product, fresh water and hot water production. In this paper, solar thermal energy is selected as the prime-mover of proposed integrated system, and is concentrated in the solar power tower sub-system. The hot thermal energy storage (TES) is integrated with

the solar power tower to product the working fluid temperature, which else should be intermittent. The hot TES component is connected to make use of thermal energy, when the solar radiation coming on heliostats is not strong enough for the desired temperature at the output flow of solar tower sub-system at point 1. Also, it is assumed that, 75,000 heliostats with 2.5 m^2 surface area each are used to reflect solar energy onto the solar power tower receiver with 10% efficiency. The hot working fluid is pumped from the hot TES to the HEX-II and HEX-III for supplying heat to the solid oxide steam electrolyzer (SOSE) for hydrogen production and to drive a steam Rankine cycle with two turbines, respectively.

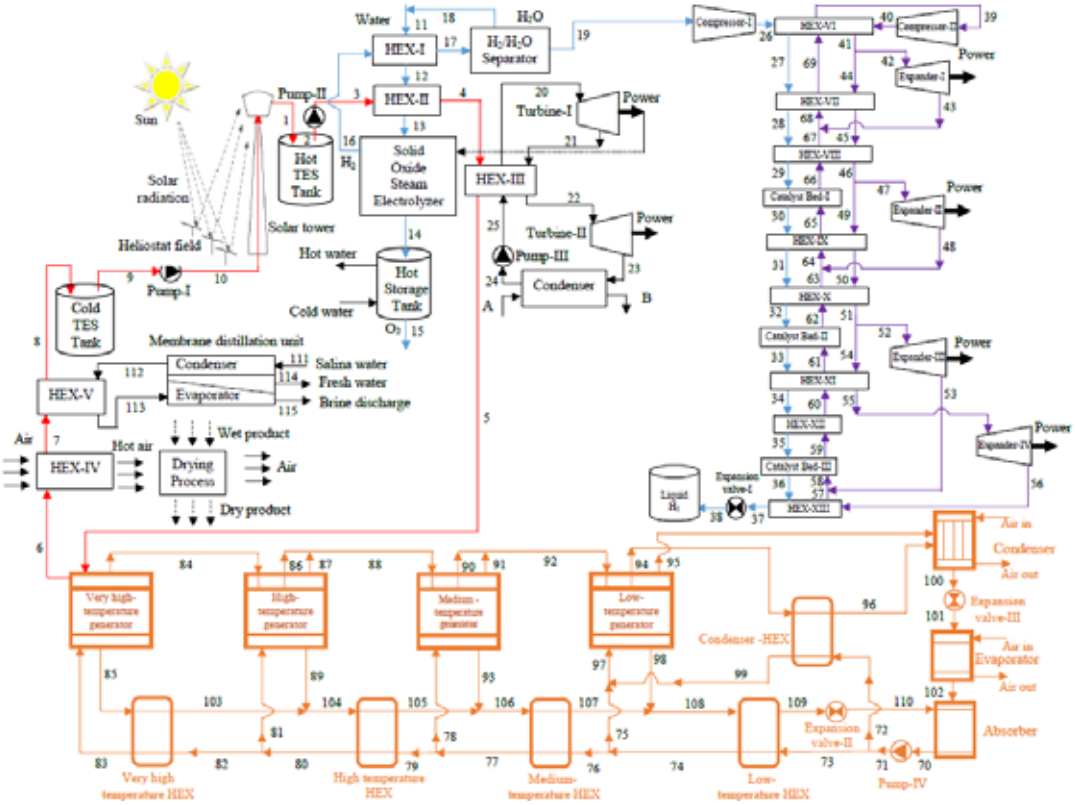


Fig. 1: Schematic diagram of solar based hydrogen production and storage system

III. Thermodynamic Analysis

The thermodynamic analysis of mass, energy and exergy analyses in the integrated system is crucial for describing the indicators affecting the system performance. Exergy analysis is a useful tool understanding the trends of the exergy destruction rates that determine the efficiency of the integrated system. For a real process, the exergy input to the system boundary always more than the exergy output from the system boundary. This difference is called as irreversibility or exergy destruction rate. For each part in the integrated system for multigeneration, the three balance equations are given to investigate the work output, heat input, exergy destruction rate, energy and exergy efficiencies. The general balance equations can be given as (Ahmadi et. al, 2012; Al-Sulaiman et. al, 2011);

- The mass balance equation can be written as follows:

$$\sum \dot{m}_{in} = \sum \dot{m}_{out} \quad (1)$$

- The energy balance equation can be given as follows:

$$\dot{Q} + \sum \dot{m}_{in} h_{in} = \dot{W}_{net} + \sum \dot{m}_{out} h_{out} \quad (2)$$

- The exergy balance equation can be written as follows:

$$\sum_i \dot{m}_{in} ex_{in} + \dot{E}x_Q = \sum_e \dot{m}_{out} ex_{out} + \dot{E}x_W + \dot{E}x_D \quad (3)$$

where $\dot{m}$ is the mass flow rate, subscript *in* is the inlet of matter, subscript *out* is the outlet of the matter, $\dot{Q}$ is the heat transfer rate, $\dot{W}$ is the work transfer rate, h is the specific enthalpy, $\dot{E}x_D$ is the exergy destruction rate, ex is the specific exergy of the process, $\dot{E}x_Q$ is the heat exergy flow rate, $\dot{E}x_W$ is the work exergy flow rate.

$$\dot{E}x_Q = \left(1 - \frac{T_o}{T}\right)\dot{Q} \quad (4)$$

$$\dot{E}x_W = \dot{W} \quad (5)$$

$$ex = ex_{ke} + ex_{pe} + ex_{ph} + ex_{ch} \quad (6)$$

where ex_{ke}, ex_{pe}, ex_{ph} and ex_{ch} are the kinetic, potential, physical and chemical exergies, respectively. In this paper, kinetic and potential exergy changes are negligible.

$$ex_{ph} = (h - h_o) - T_o(s - s_o) \quad (7)$$

where s is the specific entropy. The chemical exergy of gaseous is given as

$$ex_{ch} = \sum x_i ex_{ch}^o + RT_o \sum x_i ln\,(x_i) \quad (8)$$

The net solar energy falling on the heliostat field is calculated according to the literature (Ratlamwala et. al, 2012; Xu et. al, 2011).

IV. Results and discussion

In this study, thermodynamic analyses of solar tower based integrated system are conducted for the evaluation of the system efficiency. As seen from Table 1, the lowest exergy efficiency occurs in QEACS and the probable improvements should be focused on this part. Total energy and exergy efficiency of the integrated system are 65.17% and 62.35, respectively.

Tab. 1: Thermodynamic assessment data for integrated system and its sub-systems

Sub-systems/whole system	Energy efficiency (%)	Exergy efficiency (%)	Exergy destruction rate (kW)	Exergy destruction ratio (%)
Concentrating solar collector	54.15	48.41	8,557	37.89
Rankine cycle	42.18	46.93	3,219	14.25
H_2 production and liquefaction	58.86	56.24	4,302	19.05
QEACS	27.16	18.58	3,763	16.66
Drying process	64.74	61.49	618	2.74
Fresh water production	78.27	75.62	495	2.19
Whole system	65.17	62.35	22,585	100

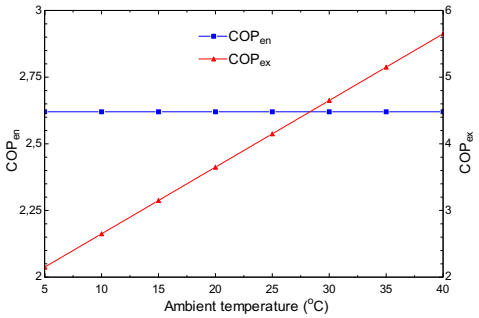


Fig. 2: The impacts of ambient temperature on COP_{en} and COP_{ex} of QEACS

Figure 2 shows that the effects of varying ambient temperature on coefficient of performance of quadruple effect absorption cooling system. As seen from figure, changing ambient temperature does not have any effect on COP_{en}, however COP_{ex} increases with increasing ambient temperature.

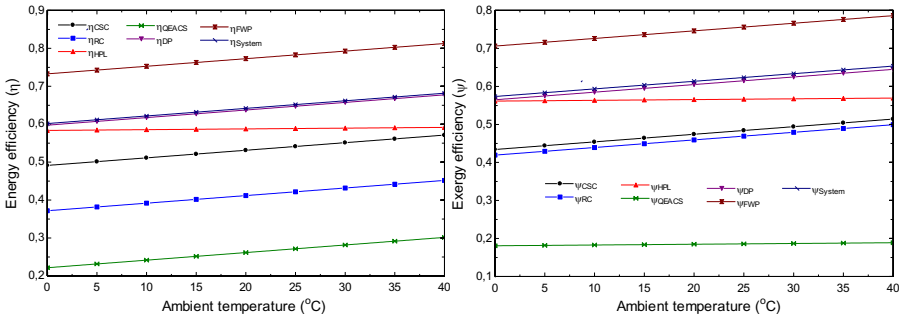


Fig. 3. The impacts of ambient temperature on energy and exergy efficiency of sub-systems and whole system

The effect of ambient temperature on energy efficiencies of subsystems and whole system can be seen at the left side of Fig. 3. This result reveals that increasing ambient temperature has positive effect on energy efficiencies of all subsystems and whole system. Similarly, exergy efficiencies of all systems except for QEACS increase with

increasing ambient temperature as seen from the right side of Fig. 3.

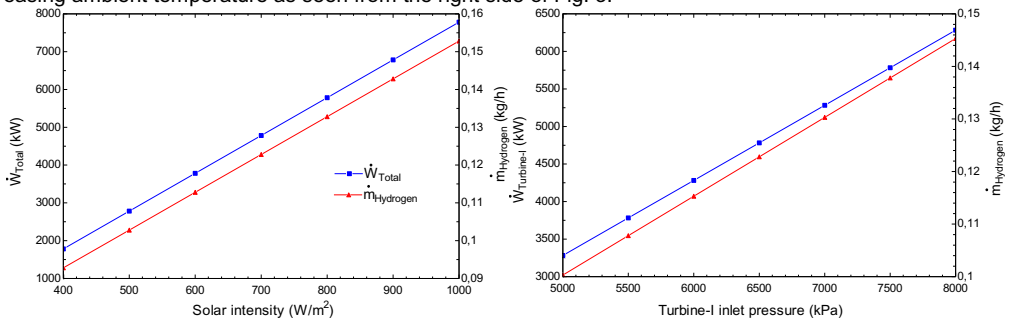


Fig. 4. a) The impacts of solar intensity on total work and hydrogen production rate b) The impacts of turbine-I inlet pressure on work production rate from turbine-I and hydrogen production rate

Fig. 4a demonstrates how solar intensity affects the total work and hydrogen production rate. As solar intensity increases from 400 W/m^2 to 1000 W/m^2, both total work and hydrogen production increases linearly. Fig. 4b shows the effect of turbine-I inlet pressure on total work and hydrogen production. As seen from that figure, as turbine-I inlet pressure rises from 5 MPa to 8 MPa, total work done nearly doubles and hydrogen production rate increases from 0.1 kg/h to 0.145 kg/h.

V. Conclusions

In this paper a novel integrated solar power tower based for multigeneration is developed. The comprehensive thermodynamic assessment analysis is performed on the integrated system components and whole system. The parametric studies are very essential for improving the performance of integrated system and sustainable operations of energy production. As seen from the findings, the most important parameter affecting the system efficiency and hydrogen production rate is solar intensity. So, before installing of such systems solar intensity as primary source should be calculated carefully. Here are some esults:

- The overall energy efficiency of Rankine cycle with two turbine is 42.18% while exergy efficiency is 46.93%.
- The COP_{en} of the QEAC system is 2.62 whereas the COP_{ex} is 2.15.
- The overall energy efficiency of the integrated system is calculated as 65.17% while exergy efficiency is calculated as 62.35%.

Nomenclature

E	Energy [kJ]
$\dot{E}$	Energy rate [kW]
ex	Specific exergy [kJ/kg]
$\dot{E}x$	Exergy rate [kW]
$\dot{E}x_D$	Exergy destruction rate [kW]
h	Specific enthalpy [kJ/kg]
$\dot{m}$	Mass flow rate [kg/s]
$\dot{Q}$	Heat rate [kW]
R	Universal gas constant [kJ/mol-K]
s	Specific entropy [kJ/kgK]
T	Temperature [K]
$\dot{W}$	Work Rate [kW]
x	Molar concentration
η	Energy efficiency
ψ	Exergy efficiency

References

Ahmadi P., Dincer I., Rosen M., Energy and exergy analyses of hydrogen production via solar-boosted ocean thermal energy conversion and PEM electrolysis, International Journal of Hydrogen Energy, 38(4), 1795-1805 (2012).

Al-Sulaiman F.A., Dincer I., Hamdullahpur F., Exergy modeling of a new solar driven trigeneration system, Solar Energy, 85(9), 2228-2243 (2011).

Atif M., Al-Sulaiman F.A., Energy and exergy analyses of solar tower power plant driven supercritical carbon dioxide recompression cycles for six different locations, Renewable and Sustainable Energy Reviews, 68, 153–167 (2017).

Dincer I., Zamfirescu C., Renewable-energy-based multigeneration systems, International Journal of Energy Research, 36(15), 1403-1415 (2012).

Ratlamwala T.A.H., Dincer I., Aydin M., Energy and exergy analyses and optimization study of an integrated solar heliostat field system for hydrogen production, International Journal of Hydrogen Energy, 37, 18704-1812 (2012).

Xu C., Wang Z., Li X., Sun F., Energy and exergy analysis of solar power tower plants, Applied Thermal Engineering, 31, 3904-3913 (2011).

Energy and exergy analyses of an integrated hydrogen production and liquefaction system with waste material gasification

[1]Yunus Emre Yüksel, [2*]Murat Öztürk, [3]İbrahim Dinçer,
[1] Afyon Kocatepe University, Education Faculty, Math and Science Education, ANS Campus, Afyonkarahisar, 03200, Turkey
[2] Suleyman Demirel University, Faculty of Technology, Department of Mechatronics Engineering, Cunur West Campus, Isparta, 32200, Turkey
[3] University of Ontario Instıtute of Technology, Faculty of Engineering and Applied Science, 2000 Simcoe Street North, Oshawa, Ontario L1H 7K4, Canada

* E-mail: muratozturk@sdu.edu.tr

Abstract
In this paper, the comparative energetic and exergetic analyses of a waste material gasification based integrated system is conducted to achieve hydrogen production and liquefaction. The waste materials gasifier component is utilized in integration with a Brayton cycle, a Stirling engine cycle, a single effect absorption cooling system, and a PEM electrolyzer for the purpose of multigeneration. The present integrated system generates power, heating, cooling and domestic hot water along with liquid hydrogen production. The design indicators of integrated system and the influences of operating conditions on the energetic and exergetic efficiency of multigeneration system and also other sub-systems are investigated. The energetic and exergetic efficiency of waste materials gasification based integrated system are calculated as 61.57% and 58.15%, respectively. Furthermore, a parametric study is carried out to investigate the effects of different system design indicators on the integrated system exergy destruction rates and exergy efficiencies.

Keywords: Exergy, waste material gasification, Brayton cycle, Stirling engine, hydrogen, liquefaction.

I. Introduction

One of the most important sign of development for countries is energy. Also, energy is necessary for humanbeing to live in every aspect. Therefore, current energy sources are being given out unless major precautions are applied. One of these precautions is to use energy sources efficiently (Yuksel and Ozturk, 2016). This paper tries to use waste materials as energy source for power, cooling and hydrogen production. According to Arena (2012), gasification of waste materials is a good option to get benefit from waste materials and reduce the emissions.

Recently, single generation energy systems are losing their popularity due to their low efficiencies and high amount of waste heat. So, cogeneration, trigeneration and multigeneration energy systems are substituting for single generation energy systems. Multigeneration systems use an energy source for production of more than three products. Integrated multigeneration systems offer higher advantages than the other options because they also offer continuous energy production with by-products. There are many examples in literature showing higher efficiency and feasibility when another source is integrated the system (Lund and Münster, 2006; Pelet et. al, 2005; Mancarella, 2014).

In this paper, waste material gasification process is integrated with Brayton cycle and Stirling engine to produce power. Produced power can be either used directly or used for hydrogen production. In order to utilize waste heat from these cycles a single effect absorption cooling system is integrated to the system. Lastly for hydrogen production and storage, PEM electrolyzer and hydrogen liquefaction system is integrated. In analysis part, thermodynamic analysis consisting of energy and exergy analyses and parametric studies are applied. Because energy analysis is not enough to show where losses occur, exergy analysis is necessary (Ahmadi et. al, 2013).

The main objective of this paper is to perform thermodynamic analyses, through energy and exergy approaches, and parametric analyses to the waste material gasification based integrated system. Parametric analyses target to find the effects of reference temperature, gasifier temperature and exhaust gas temperature on system energy and exergy efficiency as well as power and hydrogen production rates.

II. System Definition

Figure 1 exhibits the schematic diagram of the waste material gasification based integrated system. This integrated system consists of gasifier, Brayton cycle, Stirling engine, single effect absorption cooling system, PEM electrolyzer and a hydrogen liquefaction unit. As seen from figure 1, syngas produced from waste materials is combusted in combustion chamber and the stream 13 drives the gas turbine to produce power. The remaining heat energy is used in Stirling engine again for power production. Waste heat of Stirling engine with number 15 enters the absorption cooling system to supply cooling. The power produced from Stirling engine drives the PEM electrolyzer to produce hydrogen and oxygen from water. The produced hydrogen is then sent to the mixer and compressor and therefore liquid hydrogen is lastly stored in liquid hydrogen tank.

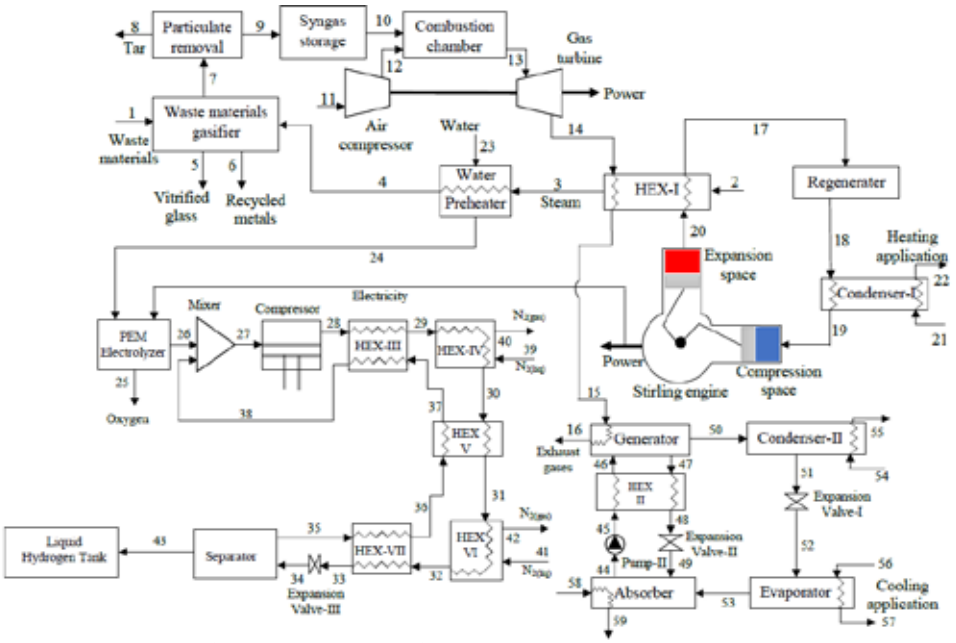


Fig. 1: The schematic diagram of the waste material gasification based integrated system

III. Thermodynamic Analysis

The thermodynamic assessment of waste material gasification based integrated system is investigated by conducting quantitative energy and exergy analyses. The assumptions, basic concepts, procedure, and equations utilized to investigate integrated system performance are defined and expressed. The following assumptions are made for the thermodynamic analysis of integrated gasification combined cycles.

- The ambient temperature (T_o) and ambient pressure (P_o) are taken as 25 °C and 1 atm, respectively.
- All processes take place in steady-state and steady-flow conditions.
- The pressure drops and heat losses in piping are negligible,
- The system parts are well insulated and therefore are taken as adiabatic,
- The kinetic and potential energy and exergy changes in all processes are negligible.

In this sub-section, the overall mass, energy, entropy and exergy balance equations are defined based on the assumptions and operating conditions of waste materials gasification based integrated system for multi-generation.

The heat and work input/output rates, entropy generation rates, and exergy destruction rates, and energy and exergy efficiencies can be calculated by using these balance equations.

In the steady-state and steady-flow condition, the mass balance equation can be given as

$$\sum \dot{m}_i = \sum \dot{m}_e \quad (1)$$

where m and $\dot{m}$ are the mass and mass flow rate, respectively.

In the steady-state and steady flow condition, the energy balance can be written as

$$\sum \dot{m}_i h_i + \sum \dot{Q}_i + \sum \dot{W}_i = \sum \dot{m}_e h_e + \sum \dot{Q}_e + \sum \dot{W}_e \quad (2)$$

where $\dot{Q}$ and $\dot{W}$ are the transfer rates of heat and power, and also h is the specific enthalpy. Based on the steady-state and steady-flow condition, entropy balance equation can be defined as

$$\sum \dot{m}_i s_i + \sum \frac{\dot{Q}_{cv}}{T_o} + \dot{S}_{gen} = \sum \dot{m}_e s_e \quad (3)$$

where s is the specific entropy, and $\dot{S}_{gen}$ is the entropy generation rate. In the steady state and steady flow condition, the exergy balance equation can be given as follows;

$$\sum \dot{m}_i ex_i + \sum \dot{E}x_i^Q + \sum \dot{E}x_i^W = \sum \dot{m}_e ex_e + \sum \dot{E}x_e^Q + \sum \dot{E}x_e^W + \dot{E}x_D \quad (4)$$

where $\dot{E}x_Q$ and $\dot{E}x_W$ indicate the exergy transfer rates associated with heat and shaft work, respectively.

$$\dot{E}x_Q = \left(1 - \frac{T_o}{T}\right)\dot{Q} \quad (5)$$

where $(1 - T_o/T)$ is the dimensionless exergetic temperature, usually defined as Carnot efficiency working between the ambient temperature at T_o and the process temperature at T.

$$\dot{E}x_W = \dot{W} \quad (6)$$

The exergy related to a stream flow is consisted of four major elements: physical exergy (ex_{ph}), chemical exergy (ex_{ch}), potential exergy (ex_{pt}) and kinetic exergy (ex_{kn}). Thus, the specific flow exergy can be defined as follows:

$$ex = ex_{ph} + ex_{ch} + ex_{pt} + ex_{kn} \quad (7)$$

The ex_{pt} and ex_{kn} are assumed to be negligible. The specific physical exergy can be written as

$$ex_{ph} = h - h_o - T_o(s - s_o) \quad (8)$$

where h_o and s_o are the enthalpy and entropy at the reference environment states, respectively. The chemical exergy is the part of the flow exergy that is created by process involving heat transfer rate and exchange of materials with the surroundings to bring the material to the dead state. The chemical exergy of an ideal gas mixture can be defined as follows;

$$ex_{mix}^{ch} = \sum y_i ex_i^{ch} + RT_o \sum y_i \, lny_i \quad (9)$$

where y_i is the mole fraction of the part i in the gas mixture. The exergy destruction rate defines the process irreversibility and it is illustrated in the equation as $\dot{E}x_D$. Also, it can be defined as follows;

$$\dot{E}x_D = T_0 \dot{S}_{gen} \quad (10)$$

IV. Results and discussion

In this study, thermodynamic analysis and parametric analyses of the waste material gasification based integrated system are performed and their results are presented. Engineering Equation Solver (EES) is used for thermodynamic analysis of this integrated system. Energy and exergy efficiencies with exergy destruction rates of whole system and sub-systems are given in Table 1. According to the results, energy and exergy efficiencies of whole system are 61.57% and 58.15%, respectively. The largest exergy destruction ratios occur in waste material gasification and Brayton cycle with 36.68% and 32.38%, respectively.

Table 1. Thermodynamic assessment data for sub-systems of waste materials gasification based integrated system and whole system

Sub-systems/whole system	Energy efficiency (%)	Exergy efficiency (%)	Exergy destruction rate (kW)	Exergy destruction ratio (%)
Waste materials gasification	53.28	49.95	32,486	36.68
Brayton cycle	48.97	45.86	28,680	32.38
Stirling engine	31.23	46.37	12,312	13.9
Single effect absorption cooling	15.48	13.94	4,847	5.472
Hydrogen production and liquefaction	59.36	57.15	10,251	11.57
Whole system	61.57	58.15	88,576	100

Coefficient of performance (COP) is a useful tool for comparing absorption cooling systems which can be analysed either energetically or exergetically. The effect of reference temperature on coefficient of performance of absorption cooling system is seen in Fig. 2. According to the Fig. 2, energetic coefficienct of performance (COP_{en}) does not change with changing reference temperature, however exergetic coefficient of performance increases from nearly 0.32 to about 0.39. The reason for this situation lies on the definition of exergy (Dincer and Rosen, 2012).

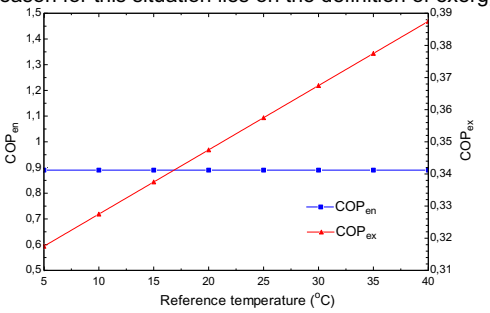


Fig. 2: COP_{en} and COP_{ex} of the single effect absorption cooling system with respect to the reference ambient temperature

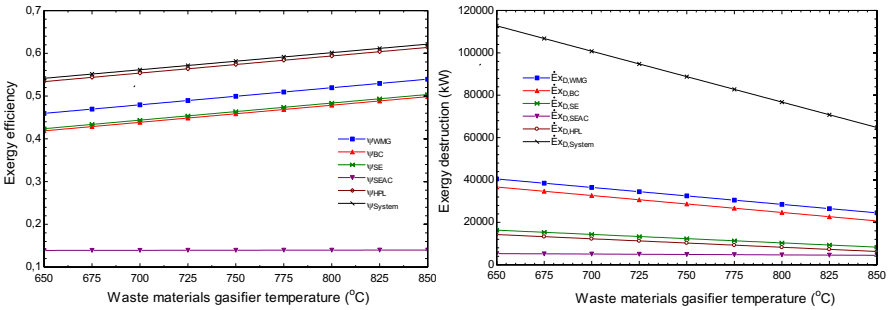


Fig.3: The effect of waste materials gasifier temperature on a) exergy efficiency and b) exergy destruction rate

Fig. 3 demonstrates the effect of waste materials gasifier temperature on exergy efficiency at the left and destruction rate at the right side. As seen from that figure, while waste materials gasifier temperature increases from 650°C to 850°C, exergy efficiencies of all subsystems increase, too. In that change of temperature, exergy efficiency of whole system increases from about 54% to approximately 60%.

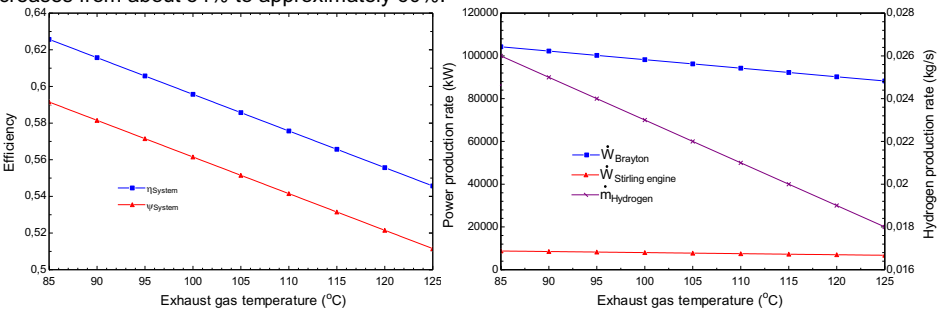


Fig.4: The effect of exhaust gas temperature on a) energy and exergy efficiency and b) power and hydrogen production rate

Another important parameter affecting system performance and power and hydrogen production rates is exhaust gas temperature. As exhaust gas temperature increases from 85°C to 125°C both energy and exergy efficiencies decrease. This happens because as exhaust gas temperature increases the difference between inlet temperature and outlet temperature decreases, so this makes system works less. In this change of temperature energy efficiency of whole system decreases from 62% to 55% and exergy efficiency decreases about 7%. At the right side of Fig. 4, power production rates of Brayton cycle and Stirling engine can be seen. Also, it shows how hydrogen production rate changes with changing exhaust gas temperature. Similar to the efficiencies, the increase of exhaust gas temperature has negative effect on power and hydrogen production rates.

V. Conclusions

A comprehensive thermodynamic analysis of integrated system proposed in this study is performed. The integrated multigeneration energy systems offer higher advantages than conventional power conversion systems. According to the results of the study, waste materials gasification and Brayton cycle have higher exergy destruction rates than the other subsystems. In order to improve the system performance, these subsystems should be focused on. The other concluding remarks are as follows:

- An increase in reference temperature has positive effect on COP_{ex} of absorption system.
- An increase in waste material gasifier temperature has negative effect on exergy efficiencies of all subsystems and whole system.
- Increasing exhaust gas temperature decreases both energy and exergy efficiencies of the integrated system.

Nomenclature

E	Energy [kJ]
$\dot{E}$	Energy rate [kW]
ex	Specific exergy [kJ/kg]
$\dot{E}x$	Exergy rate [kW]
$\dot{E}x_D$	Exergy destruction rate [kW]
h	Specific enthalpy [kJ/kg]
$\dot{m}$	Mass flow rate [kg/s]
$\dot{Q}$	Heat rate [kW]
R	Universal gas constant [kJ/mol-K]
s	Specific entropy [kJ/kgK]
T	Temperature [K]
$\dot{W}$	Work Rate [kW]
η	Energy efficiency
ψ	Exergy efficiency

References

Ahmadi P., Dincer I., Rosen M.A., Thermodynamic modeling and multi-objective evolutionary-based optimization of a new multigeneration energy system, Energy Conversion and Management, 282-300 (2013).

Arena U., Process and technological aspects of municipal solid waste gasification. A review, Waste Management, 625-639 (2012).

Dincer I., Rosen M.A., Exergy : Energy, Environment and Sustainable Development, Elsevier Science, 2nd Ed, (2012).

Lund H., Münster E., Integrated energy systems and local energy markets, Energy Policy, 1152-1160 (2006).

Mancarella P., MES (multi-energy systems): An overview of concepts and evaluation models, Energy, 1-17 (2014).

Pelet X., Favrat D., Leyland G., Multiobjective optimisation of integrated energy systems for remote communities considering economics and CO_2 emissions, International Journal of Thermal Sciences, 1180-1189 (2005).

Yuksel, Y.E., Ozturk, M., Energy and exergy analyses of an integrated solar and biomass assisted multi-generation system with hydrogen production, International Journal of Exergy, 203-235 (2016).

Thrust Modelling for a Solid Oxide Fuel Cell and Gas Turbine (SOFC/GT) Hybrid Propulsion System

[1*]Yasin Şöhret, [2]Arif Hepbasli, [3]T. Hikmet Karakoc
[1] Süleyman Demirel University, School of Civil Aviation, Department of Airframe and Powerplant Maintenance, Isparta, TR-32700, Turkey
[2] Department of Energy Systems Engineering, Faculty of Engineering, Yaşar University, TR-35100, Bornova, Izmir, Turkey
[3] Anadolu University, Faculty of Aeronautics and Astronautics, Department of Airframe and Powerplant Maintenance, TR-26470, Eskisehir, Turkey

* E-mail:ysohret@gmail.com

Abstract
The economical crisis and depletion of conventional fuel resources are major concerns of the 21st century. Facing these challenges are the main drivers of the researches and studies in the field of energy associated with science and engineering. In aerospace science, one of the prominent energy consuming fields, it is required to achieve either more efficient or alternative energy conversion systems. However, efficiency improvement in conventional propulsion systems is considered to be reached limits as more as possible depending on materials science limitations. That implication leads to development of novel and alternative propulsion systems. The mostly preferred system is electric motor driven propulsion system. Additionaly, the main goal of all these researches is to realize all electric arcraft concept. In the light of these considerations, all energy demand of an aircraft, including thrust, should be supplied by an electric power generator. Thermal batteries were used at first to partially supply energy to the aircraft systems. But over the last decade, numerous new generation propulsion systems have been studied. The main objective of this study is to provide a basis for future researches on Solid Oxide Fuel Cell and Gas Turbine (SOFC/GT) hybrid propulsion systems. In this regard, a SOFC/GT hybrid system is studied and thrust generated by a SOFC/GT is parametrically modelled.

Keywords: Aircraft, hybrid propulsion, more electric aircraft, propulsion, SOFC/GT, thrust.

The Role of Temperature on Aluminium Oxide Embedded MWCNTs for Hydrogen Adsorption

***Songül Kaskun*[1], *Muhammet Kayfeci*[2]**

[1]*Department of Environmental Engineering, Engineering Faculty, Karabük University*
[2]*Department of Energy Systems Engineering, Technology Faculty, Karabük University*

Multi walled carbon nanotubes (MWCNTs) are widely used in Hydrogen adsorption studies because of their unique confirmation, porous structure and high aspect ratio. As hydrogen storage medium, generally MWCNTs have been supplemented with alkali metals or compounds to enhance the storage capacity. In this work, hydrogen adsorption of aluminium oxide (Al2O3) nanopowder decorated MWCNTs (Al2O3-MWCNTs) was examined under -273˚C, 0 ˚C and 25 ˚C temperatures at ambient pressure. The structure confirmation of the synthesized Al2O3-MWCNTs was characterized by X-ray diffraction (XRD) analysis, Energy Dispersive X-ray (EDX) and Scanning Electron Microscopy (SEM) observations. A sieverts-like apparatus was used for hydrogenation of Al2O3-MWCNTs under -273˚C, 0 ˚C and 25 ˚C temperatures. The results present that, the highest hydrogen storage capacity of Al2O3-MWCNTs was observed at the cryogenic temperature.

Keywords: Hydrogen adsorption, aluminum oxide, MWCNTs

A Comparative Study of Control Strategies for Vehicles with Hydrogen Fuel Cell/Battery/Supercapacitor in the Electrical Grid-Independent Applications

[1]Yakup Hameş, [1*]Kemal Kaya
[1] Iskenderun Technical University, Faculty of Engineering and Natural Sciences, Electrical and Electronics Engineering Department, ISTE Central Campus, Iskenderun-HATAY, 31200, Turkey

* E-mail:kemal.kaya@iste.edu.tr

Abstract
This paper depicts a means of using a Proton Exchange Membrane (PEM) Fuel Cell (FC) as the primary energy source and a Li-ion battery (BAT) and a supercapacitor (SC) as energy storage technology. These in-vehicle technologies are connected to the DC-bus with DC-DC power converters for suitably supply the power demanded by the traction motor. Thus, the system performance of the vehicle is examined independently of the electrical grid. Here, an appropriate energy management system and a well-designed control strategy both increase productivity and vehicle dynamics. At the same time, different control strategies have been compared that are designed according to the same power demands of the vehicle. The results have been analyzed in terms of hydrogen fuel consumption, energy efficiency and sustainability of control systems.

Keywords: PEM fuel cell, Li-ion battery, hydrogen fuel cell vehicles, supercapacitor, control strategy, hydrogen consumption.

I. Introduction

Today, when the world energy demand is increasing rapidly, energy sources cannot provide this demand Dutta (2014). In this context, the tendency towards renewable energy sources has started to increase. In particular, automobile manufacturers are setting up a competitive environment to drive vehicles with fuel hydrogen to the market Bauman and Kazerani (2008). In terms of energy resources, the trend towards this field is increasing day by day. This, in turn, demonstrates that energy can be used more efficiently with various strategies.

The primary energy source for hydrogen fuel cell vehicles (HFCEV) is the fuel cell (FC) Zhang etal. (2017). The result of the fuel cell alone managing the energy in the vehicle is the fuel consumption and the costs that are very high Zheng etal. (2012). The use of energy storage systems such as batteries (BAT) and supercapacitors (SC) in combination with FC in the vehicle can prevent this Fathabadi (2018). This solution will increase energy efficiency, reduce fuel consumption, extend FC lifetime and reduce costs. Compared with all of these, control strategies are needed to ensure that vehicles equipped with power supply, conversion and drivetrain such as a PEM fuel cell, Li-ion battery, supercapacitor, DC-DC converter, DC-AC inverter and traction motor can manage these systems in a harmonious manner García etal. (2013).

Due to the lower power density and slower power response of a PEM fuel cell, working with a high energy density battery and supercapacitor technology with high power density will significantly increase system efficiency Gao (2005). What it needs to do here is to manage in a correct way the control of the energy and power distribution. The aim of the study is to study system efficiency, fuel consumption, vehicle technology lifespan and vehicle performance by working with different control mechanisms of an electrical grid independent hydrogen fuel cell vehicle.

II. System Modelling and Design

A system model has been developed for HFCEV with a PEM fuel cell and a Li-ion battery and supercapacitor that powers the traction motor with power conversion units. An improved and designed hydrogen fuel cell vehicle configuration is shown in Fig. 1. BAT and SC in the vehicle are connected to the DC-bus via a DC-DC converter. Thus, the output of FC converter can be controlled and control strategies can be determined according to vehicle power demand Hames etal. (2018).

The PEM FC model is formed as a result of the modelling with mathematical expressions of the change in FC potential due to parameters such as temperature, current and pressure. FC electrical equivalent circuit diagram is shown in Fig. 2(a). Accordingly, the mathematical equations of the fuel cell are as follows Graber etal. (2017):

$$V_0 = n * V_{fc} \quad (1)$$

and

$$m_{H2} = \frac{I_{fc} * n}{2F} * 10^{-3} \quad (2)$$

Here, V_0 is the output voltage of n series connected fuel cells, V_{fc} is the voltage of FC, m_{H2} is the FC hydrogen fuel consumption, I_{fc} is the FC current, and F is the faraday constant. System modelling of the PEM FC is created by substituting equations.

A mathematical model of the Li-ion battery used in the system has made. The electrical equivalent circuit of the BAT is modelled as shown in Fig. 2(b). The output voltage of BAT (V_{batt}) in the discharge state is as follows:

$$V_{batt} = E_i - I_{batt} * R_{dch} \ [1 - e^{\left(-\frac{t}{R_{dch} * c_{ov}}\right)}] \quad (3)$$

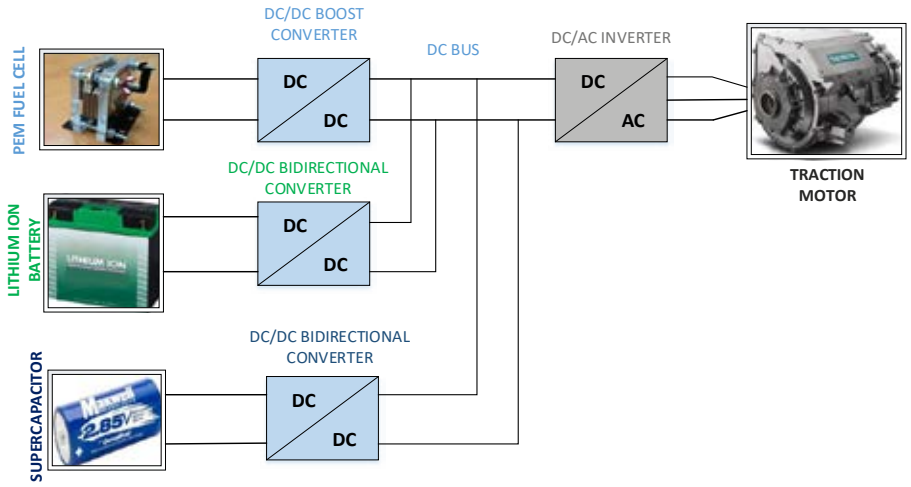


Fig. 1: Drive-train configuration design of hydrogen fuel cell vehicle

In the equation (3), E_i is the idle operating voltage, I_{batt} is the BAT current, R_{dch} is the discharge resistance, c_{ov} is the polarization capacity, and t is the sampling time of BAT output voltage. The output voltage of BAT in the state of charge (SOC) is calculated as follows:

$$V_{batt} = E_i + I_{batt} * R_{ch} \ [1 - e^{\left(-\frac{t}{R_{ch} * c_{ov}}\right)}] \quad (4)$$

Here, R_{ch} is the charging resistor. BAT state of the charge (SOC) is as follows:

$$\%SOC = \%SOC_0 - \left(\frac{1}{C_b} \int I_{batt} * dt\right) * 100 \quad (5)$$

Here, C_b is the BAT capacity. When the equations are written in the system, a Li-ion battery model is created.

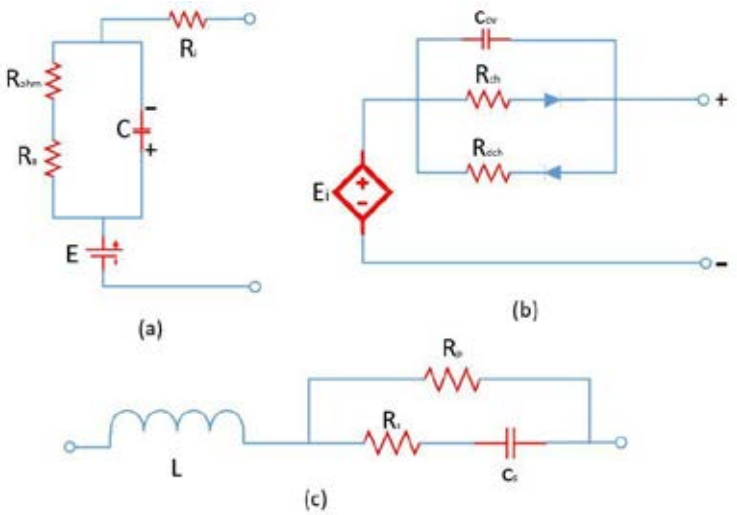


Fig. 2: (a) FC equivalent circuit, (b) BAT equivalent circuit, (c) SC equivalent circuit

Mathematical modeling of the supercapacitor used in the system together with the fuel cell and the battery has been established. The electrical equivalent circuit of SC in the system model is shown in Fig. 2(c). The equations for SC model are:

$$V_{SC} = V_{c_s} - V_{R_s} - V_L \quad (6)$$

$$\%SOC = \frac{V_{SC}}{V_{max}} * 100 \quad (7)$$

$$E = \frac{1}{2} C_s (V_f^2 - V_{cf}^2) \quad (8)$$

In Equation (6), SC output voltage is V_{SC}, when the Kirchoff voltage law is applied according to the equivalent circuit. At the same time, V_{c_s} is the terminal voltage of SC main capacity, V_{R_s} is the series resistor, and V_L is the terminal voltage of inductor. In addition, SOC is one of the most important factors affecting supercapacitor performance. Equation (8) is the energy equation provided by SC. Where V_f is the rated voltage at discharge of SC, and V_{cf} is the cut-off voltage. All of these equations were written in MATLAB/Simulink environment for system modelling and a hydrogen fuel cell vehicle design was realized.

III. Results and discussions

Control strategies of a hydrogen fuel cell vehicle for electrical grid-independent applications have been created as a result of the modelling of the equations obtained. Accordingly, the primary source of energy for the vehicle is the fuel cell. Two different control strategy scenarios have been created in the study. For these scenarios, the changes according to the power demand of vehicle are shown in Fig. 3.

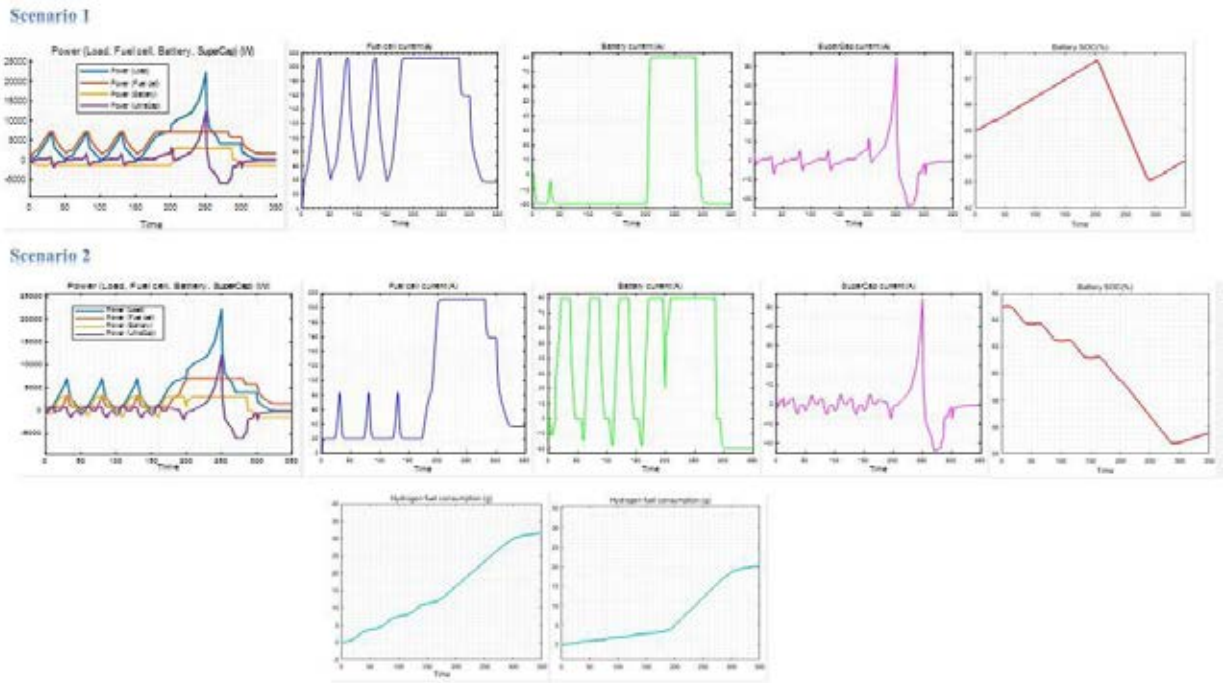


Fig. 3: Simulation results of a hydrogen fuel cell vehicle

In the first scenario, supercapacitors have provided with support to the fuel cell to meet the power demanded by the vehicle at rapid accelerations. The battery has been included in the system only in the high power density demands that the fuel cell/supercapacitor system's total power is not enough. In other cases, the battery stores only the regenerative braking energy. Thus, the battery, which is ready to enter the system in the overload demands of the vehicle, has also increased its charge status.

The total movement duration of the vehicle is 350 seconds. The power demand of the vehicle from 0-150 seconds has beed provided by the only fuel cell. The supercapacitor has provided power to the system at sudden

accelerations. Meanwhile, the initial SOC of the battery has increased from 65% to 67.8%. The vehicle has provided the increased power demand of the system from the fuel cell/supercapacitor between 150-250 seconds, but when the power demand has exceeded the total power of these two systems, the battery has been included in the system. Meanwhile, the battery SOC has decreased to 63%. Braking, decelerating and stopping commands have performed between 250 and 350 seconds on the vehicle. Meantime, while the supercapacitor has discharged rapidly and power has supplied to the system for a certain period from the fuel cell and the battery. Then the vehicle has did not demand power, and during this time the battery has recharged the regenerative braking energy, increasing the charge to 64%.

In the control strategy created for the second scenario, the battery and supercapacitor have provided extra power to the fuel cell at any time. The current has been drawn from the battery to 80 Amps between 0 and 150 seconds. In the developed control strategy, the current drawn from the battery has been limited by controlling the battery converter. Battery SOC has decreased from 65% to 61%. In this scenario, when compared to the first scenario, the current drawn from the fuel cell has reduced and the battery/supercapacitor currents have increased. While the power demand of vehicle has raised between 150 to 250 seconds, the fuel cell/battery/supercapacitor system have worked together to supply the vehicle's power demand. During this time, the battery SOC has decreased to 54.5%. Between 250-350 seconds, a similar situation emerged with the first scenario. However, with regenerative braking, the battery was able to increase the SOC up to 55.5%.

According to the simulation results, in the first scenario, the hydrogen fuel consumption is about 31 grams along the total road, while this value is 20 grams in the second scenario. The reason is to reduce the hydrogen consumption of the fuel cell by more incorporating the battery and supercapacitor into the system. Although the second case provides fuel savings, however, significant losses can occur as a result of the battery operating at high currents. Consequently, the battery life reduces and the system cost increases.

IV. Conclusions

To reduce the disadvantages of the lower power density and slower power response characteristics of the hydrogen fuel cell used in vehicles, it is crucial for energy efficiency and fuel economy to work with appropriate control strategies in combination with a battery with high energy density and a supercapacitor with high power density. In this study, two different control scenarios that created for the same power demands have been examined. The results have revealed the importance of designing the right control system in terms of hydrogen fuel economy, energy efficiency and cost.

References

Bauman J., Kazerani M., A Comparative Study of Fuel-Cell–Battery, Fuel-Cell–Ultracapacitor, and Fuel-Cell–Battery–Ultracapacitor Vehicles, IEEE Transactions on Vehicular Technology, 57, 760-769, (2008).

Dutta S., A review on production, storage of hydrogen and its utilization as an energy resource, Journal of Industrial and Engineering Chemistry, 20, 1148-1156, (2014).

Fathabadi H., Novel fuel cell/battery/supercapacitor hybrid power source for fuel cell hybrid electric vehicles, Energy, 143, 467-477, (2018).

Gao W., Performance comparison of a fuel cell-battery hybrid powertrain and a fuel cell-ultracapacitor hybrid powertrain, IEEE Transactions on Vehicular Technology, 54, 846-855, (2005).

García P., Torreglosa J.P., Fernández L.M., Jurado F., Control strategies for high-power electric vehicles powered by hydrogen fuel cell, battery and supercapacitor, Expert Systems with Applications, 40, 4791-4804, (2013).

Graber G., Galdi V., Calderaro V., Piccolo A., A power split control algorithm for fuel cell electric vehicles using batteries or supercapacitors as auxiliary storage system, 6th International Conference on Clean Electrical Power (ICCEP), ISSN: 2474-9664, pp. 625-630, (2017).

Hames Y., Kaya K., Baltacioglu E., Turksoy A., Analysis of the control strategies for fuel saving in the hydrogen fuel cell vehicles, International journal of hydrogen energy, https://doi.org/10.1016/j.ijhydene.2017.12.150, (2018).

Zhang W., Li J., Xu L., Ouyang M., Optimization for a fuel cell/battery/capacity tram with equivalent consumption minimization strategy, Energy Conversion and Management, 134, 59-69, (2017).

Zheng C.H., Oh C.E., Park Y.I., Cha S.W., Fuel economy evaluation of fuel cell hybrid vehicles based on equivalent fuel consumption, International Journal of Hydrogen Energy, 37, 1790-1796, (2012).

Integrating of PEM electrolyzer for hydrogen production in a Kalina cycle driven by low-grade geothermal energy

*Hadi Ganjehsarabi
[1] Erzincan University, Faculty of Engineering, Department of Mechanical Engineering, Yalnızbağ Campus, Erzincan, 24100, Turkey

* E-mail:Ganjehsarabi@erzincan.edu.tr

Abstract
The possibility of utilizing low temperature heat source systems for producing electricity has been significant due to increasing energy demand. The Kalina cycle is a power generation cycle which uses ammonia-water mixture as working fluid. In this study, Kalina cycle integrated with proton exchange membrane (PEM) electrolyzer is analyzed thermodynamically through exergy method. The exergy efficiency of proposed system is computed to be 66.42 %. In addition, the effect of key parameters such as concentration at the turbine inlet and turbine inlet temperature is discussed. An analysis based on the first and second laws of thermodynamics and basic heat transfer relations is used to illustrate the operational limits and performance characteristics of these power plants.

Keywords: PEM electrolyzer, Kalina cycle, Geothermal energy

I. Introduction

The fossil fuel resources have become limited and their combustion pollutants have adverse effects on the environment. Based on this fact, most countries around the world are now investigating to reduce their dependence on fossil fuels for our energy needs and seeking new and alternative energy resources. The world's energy production from renewable energy resources is expected to triple from 2010 to 2035 reaching 31% of total production IEA (2012). In the meantime, geothermal energy is considered as one of the types of renewable energies that can replace fossil fuels. Due to a lot of low temperature geothermal resources in the world, it is estimated that in the future low temperature geothermal energy will be used more often, which the kalian cycle is the best cycle for utilizing geothermal energy Michaelides (2016).

Hydrogen has been known as a clean energy and it is an efficient fuel for reducing environmental pollution. In addition, it can be produced by using alternative energy resources such as wind, solar and geothermal energy Dincer (2002). Recently, for production of hydrogen, the proton exchange membrane (PEM) electrolyzer is used due to production of pure hydrogen and the ability to operate with a variety of renewable energies. In recent years, considerable research has been done on the development of hydrogen production methods Holladay etal. (2009). Yilmaz etal. (2015) examined various integrated systems for hydrogen generation and liquefaction by using geothermal energy. They concluded the higher geothermal fluid temperature results in the lower cost of hydrogen generation and liquefaction. Balta etal. (2010) thermodynamically simulated the geothermal based hydrogen production via four-step copper –chlorine cycle. The energy and exergy efficiencies of the system are found as 21.67 % and 19.35 %, respectively.

In this research study, in order to achieve higher hydrogen production rate, the Kalina cycle is integrated to PEM electrolyzer. The basic objectives of this present work are given as follows:

- To utilize low- grade geothermal energy as a heat source for power generation and hydrogen production.
- To use Kalina cycle for hydrogen production via PEM electrolyzer.
- To thermodynamically model the entire system.
- To undertake a parametric study to examine the influence of various design parameters on the performance of the entire system.

II. System Description

In this study, Kaline cycle is integrated to PEM electrolyzer for power and hydrogen production. The heat source for Kalina cycle is geothermal energy. The working fluid at the condenser outlet is an ammonia-water mixture at saturated liquid conditions. The pump raises working fluid pressure and fees it to the preheater where it is heated by using geothermal energy. In the evaporator, the working fluid evaporates with an effective heat transfer from the geothermal fluid. The working fluid leaves the evaporator and enters the phase separator. As a result of the separation process, the solution rich in ammonia supplied to the turbine and the solution weak in ammonia. The solution rich in ammonia expanded and leaves the turbine at a low temperature and pressure. The solution weak in ammonia is sent to mixer via expansion valve where it is mixed with the solution leaving the turbine. Therefore, the initial ammonia-water solution is recovered. The mixture is condensed in the air-cooled condenser. Accordingly, the ammonia-water mixture in an adequate liquid condition is recovered and the kalina cycle is completed.

Then the power generated in a kalian cycle in an electric generator is converted into electricity and 200 kilowatts can be consumed directly, and the rest is transferred to the electrolyzer for hydrogen production. In the electrolyzer system, as shown in the figure, the inlet water is introduced into the heat exchanger at ambient temperature and pressure and heated to the electrolysis temperature and enters the electrolyzer. Process 10 shows the production of hydrogen, in which hydrogen drains from its cathode at the environment and stored in a storage tank, as well as the oxygen produced in anode side is separated by a separator of the mixture of water and oxygen. In order to produce hydrogen again, the remaining water from separator is returned to the electrolyzer.

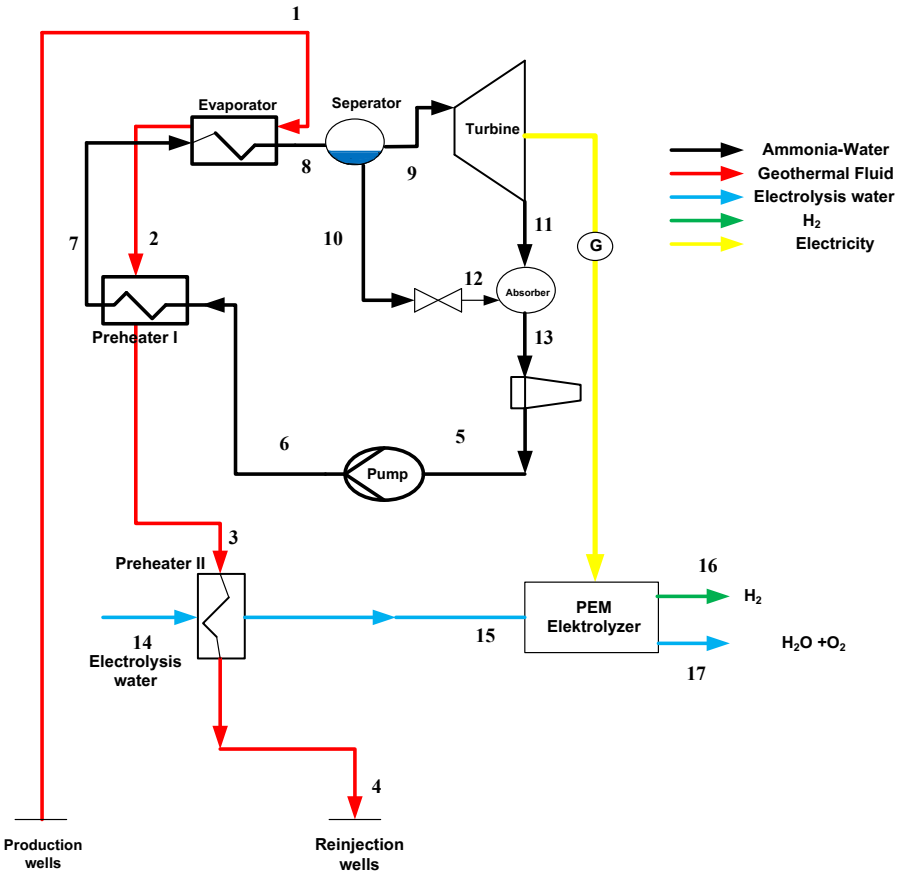


Fig. 1: Schematic of the Kalina cycle integrated with PEM electrolyzer.

III. Analysis

Several simplifying assumptions are made in the following analysis such as that the operation of the kalian cycle is considered in steady-state state, the geothermal fluid is treated as water, and air is taken as ideal gas. Based on these assumptions, the general mass, energy and exergy balance equations are given as follows:

$$\sum \dot{m}_i = \sum \dot{m}_e \tag{1}$$

$$\sum \dot{m}_i h_i + \sum \dot{Q}_i + \sum \dot{W}_i = \sum \dot{m}_e h_e + \sum \dot{Q}_e + \sum \dot{W}_e \tag{2}$$

$$\sum \dot{m}_i \, ex_i + \sum \dot{E}x_i^Q + \sum \dot{E}x_i^W = \sum \dot{m}_e ex_e + \sum \dot{E}x_e^Q + \sum \dot{E}x_e^W + \dot{E}x_D \tag{3}$$

here $\dot{m}$ donates the mass flow rate, $\dot{Q}$ is the heat transfer rate, $\dot{W}$ is the power, and h is the specific enthalpy. Subscripts i and e represent the inlet and outlet conditions, respectively.

The exergy efficiency of the proposed integrated system can be computed as follows:

$$\eta_{ex} = \frac{\dot{W}_{net} + \dot{m}_{H_2} \dot{E}x_{H_2}}{\dot{E}x_{in}} \tag{4}$$

here $\dot{E}x_{in}$ is the exergy of geothermal fluid as the exergy input to the system.

The energy balance quations for the components of the proposed system are givenin Table1.

Tab. 1: Energy balance equations for the components of the investigated system.

Component	Energy balance equations
Evaporator	$\dot{Q}_{evap} = \dot{m}_1(h_1 - h_2) = \dot{m}_7(h_8 - h_7)$
Pump	$\dot{W}_P = \dot{m}_5(h_6 - h_5) = \frac{\dot{m}_5(h_{6s} - h_5)}{\eta_P}$
Preheater I	$\dot{Q}_{Pre-I} = \dot{m}_2(h_2 - h_3) = \dot{m}_6(h_7 - h_6)$
Seperator	$\dot{m}_8 h_8 = \dot{m}_9 h_9 + \dot{m}_{10} h_{10}$
Turbine I	$\dot{W}_T = \dot{m}_9(h_9 - h_{11}) = \dot{m}_9(h_9 - h_{11s})\eta_T$
Absorber	$\dot{m}_{13} h_{13} = \dot{m}_{11} h_{11} + \dot{m}_{12} h_{12}$
Preheater II	$\dot{Q}_{Pre-II} = \dot{m}_3(h_3 - h_4) = \dot{m}_{14}(h_{15} - h_{14})$
Throttling valve	$h_{10} = h_{12}$

IV. Results and discussions

Ammonia mass fraction and turbine inlet pressure are the basic parameters that affect the performance of the proposed system. Fig. 2 shows the influence of turbine inlet pressure on exergy efficiency and net power output. As can be seen from this figure, as turbine inlet pressure increases from 5 bar to 25 bar, both exergy efficiency and net power output increases as a result of increase in the turbine work.

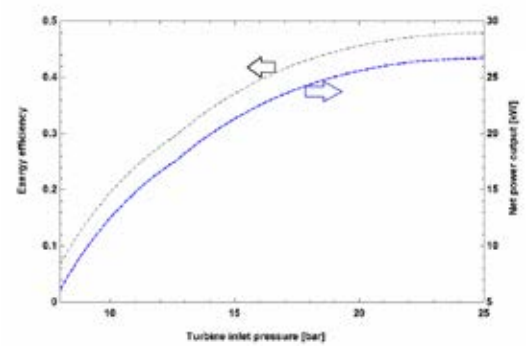


Fig. 2: Exergy efficiency and net power output variation with respect to the turbine inlet pressure.

Fig. 3 illustarate the effect of ammonia mass fraction on exergy efficiency of the system. As can be seen from this figure, as ammonia mass fraction increases from 0.6 to 0.95, exergy efficiency increases as a result of increase in the turbine work. In addition, the results indicate that an increase in the turbine inlet pressure with higher ammonia mass fraction leads to an increase in the exergy efficiency.

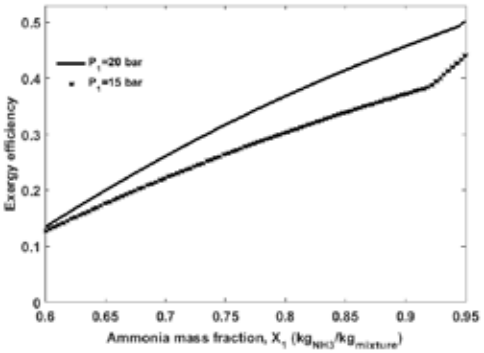


Fig. 3: The variation of exergy efficiency with respect to the ammonia mass fraction at various turbine inlet pressure.

V. Conclusions

In this study, in order to produce power and hydrogen, geothermal based integrated system is examined. The thermodynamic evalustion is performed. The several concluding outputs can be given as follows; Thermodynamic analysis results show that the exergetic analysis represents a better sensitivity analysis of the system performance than energy.

- The integrated kalina cycle with PEM elecktrolyzer has the highest exergy efficiey.
- An increase in the turbine inlet pressure leads to an increase in power output, exergy efficiency and hydrogen production rate.
- A higher ammonia mass fraction at the inlet of the turbine results in a higher turbine work and, as a result, more steam generation in the HRSG.

References

IEA., World energy outlook 2012. Paris (2012).

Michaelides E., Future directions and cycles for electricity production from geothermal resources, Energy Conversion and Management, 107, 3-9, (2016).

Dincer I., Technical, environmental and exergetic aspects of hydrogen energy systems, International Journal of Hydrogen Energy, 27, 265-285, (2002).

Holladay J.D., Hu J., King D.L., Wang Y., An overview of hydrogen production technologies, Catalysis Today 139, 244-260 (2009).

Yilmaz C., Kanoglu M., Bolatturk A., Gadalla M., Economics of hydrogen production and liquefaction by geothermal energy, International Journal of Hydrogen Energy 37, 2058-2069 (2012).

Balta M .T., Dincer I., Hepbasli A., Energy and exergy analyses of a new four-step copper–chlorine cycle for geothermal-based hydrogen production, Energy 35, 3263-3272 (2010).

Investigation of Hydrogen Generation from Sodium Borohydride Hydrolysis Reaction with Different Catalyst

Arife Sağlam, Elif Damla Arıca, *Yılser Devrim
[1] Atılım University, Faculty of Engineering, Energy Systems Engineering Department, Kızılcaşar Mah., Gölbaşı, Ankara, 06830, Turkey

*E-mail:yilser.devrim@atilim.edu.tr

Abstract
In this study, hydrogen gas (H_2) was generated from sodium borohydride ($NaBH_4$), a chemical compound that stores significant amount of H_2 and plays a role in H_2 generation, at the moment of need for portable fuel cells, thereby eliminating all the risks and difficulties of H_2 storage to obtain high efficiency of generation H_2. Based on Proton Exchange Membrane Fuel Cell (PEMFC) which is the most suitable for portable fuel cell applications, $NaBH_4$ weight (2.582 %, 3.823 % and 5.033 %), the effects of different temperatures (27°C, 47°C and 67°C) and the different types of catalysts (platinum/carbon (Pt/C), platinum/grafen (Pt/G) and platinum/multiwall carbon nanotube (Pt/MWCNT)) experiments was carried out by keeping the Pt mass constant were studied experimentally and kinetic study was made. An on-demand H_2 generation system for portable PEMFC has more than 90% conversion rate was developed.

Keywords: Hydrogen generation, hydrolysis, catalyst, sodium borohydride

I. Introduction

Fuel cell is an electrochemical device that directly converts the chemical energy of reactant gases into electrical energy and heat. Fuel cell technologies have many advantages such as low or zero emissions, high efficiency, no noise, having no moving parts and simplicity when compared with the other conventional energy conversion technologies. Among various kinds of fuel cells, polymer electrolyte fuel cell (PEMFC) is the most popular type because of its fast start-up, low operation temperature and high efficiency (Ous and Arcoumanis, 2013). PEMFC systems are useful and preferable for those who need portable, distributed, and mobile electrical power generation due to their high volumetric and specific energy densities, high conversion efficiencies and low associated pollutant emissions (Tuber etal., 2003).

Chemical hydrides such as CaH_2, LiH, $LiAlH_4$, and $NaBH_4$ are used for H_2 generation due to their safety and high storage efficiency. Among these, $NaBH_4$ is a popular H_2 storage material (Kong etal, 1999) considered as H_2 storage material .Also, it has received the most extensive attention owing to its combined advantages such as, the high H_2 storage capacity (10.8 wt. %), the high stability and no flammability of its alkaline solutions. Moreover, the optimal control on H_2 generation rate by supported catalysts, the convenient H_2 generation rate and having environmental friendly product sodium metaborate ($NaBO_2$) (Kojima and Haga, 2007) which is shown in the Eq. (1)

$$NaBH_4 + 2H_2O \xrightarrow{catalyst} NaBO_2 + 4H_2 + heat \quad (1)$$

Various transition metal catalysts including platinum have been extensively studied for H_2 generation. Among them, Pt/C, which has been widely used in PEMFC, seems attractive with NaOH to control H_2 generation. Also, CNT is studied widely for H_2 generation (Pena-Alonso etal, 2007). The aim of this study is to develop the catalyst for an on-demand H_2 generation system to use in PEMFC technologies. Moreover, the influences of the generation amount and reaction rate of H_2 parameters were discussed and kinetic study was made. Finally, catalyst supports were also investigated to use on demand H_2 generator PEMFC applications.

II. Experimental Set-up and Procedure

The proposed H_2 generation experimental set up includes only glass and Teflon pipe which is used in order to connect parts between reactor and moisture trapper and measurement equipment. The batch reaction occurs in the glass reactor fed with $NaBH_4$, distilled water and catalyst. Pt/C (commercial), Pt/G (Devrim and Albostan, 2016) and Pt/MWCNT (Arıca and Devrim, 2017) catalysts were used in this study.

In the first experimental set up, in order to to analyze the H_2 generation rate and amount change with respect to $NaBH_4$ concentration change, was prepared 3 mL distilled water with different $NaBH_4$ wt. percentage 2.582 %, 3.823 % and 5.033 %, repectively. Other parameters such as the amount (0.02 g) and type of catalyst (20 % Pt/C), pressure (approximately 1 atm) and temperature (27°C) were kept constant. In the second experimental set up, to analyze the H_2 generation rate change with respect to temperature change, prepared 3 mL distilled water with different temperatures 27°C, 47°C and 67°C repectively. Other parameters such as the amount and type of catalyst (0.02 g, 20 % Pt/C), the $NaBH_4$ wt. percentage (3.823 wt. %), pressure (approximately 1 atm) and temperature (27°C). After the analysis of $NaBH_4$ wt. percentage and temperature, the other two types of catalyst which are Pt/G (45.13 % Pt) and MWCNT (40.6 % Pt) were used at constant $NaBH_4$ wt. percentage (3.823 wt. %), pressure (approximately 1 atm) and temperature (27°C) to show the H_2 generation rate change and compared with Pt/C by keeping Pt mass 0.004 g.

III. Analysis

Before making analysis, some assumptions and considerations, evaporation from the water tank, solubility of H_2 in the water and effect of the solubility of $NaBO_2$ was neglected. During the hydrolysis reaction the tube reactor was well mixed and temperature of the system was kept constant. Also, experimets were made in the same place and in the same month in order to neglect the little pressure changes.

$$\frac{d(N_{H_2})}{d(t)} = r_{H_2} \tag{2}$$

Where r is the reaction rate and when stoichiometric ratio is taken into account, Eq. (2) becomes;

$$-r_{NaBH_4} = r_{NaBO_2} = -\frac{H_2O}{2} = \frac{r_{H_2}}{4} \tag{3}$$

In the first experimental set up, it was observed thet the amount of the generation H_2 and slope of the best fitting line slope of the generation of H_2 graph increased with the increasing $NaBH_4$ concentration as shown in the Fig.1. a. The slope directly influenced on reaction rate of H_2.

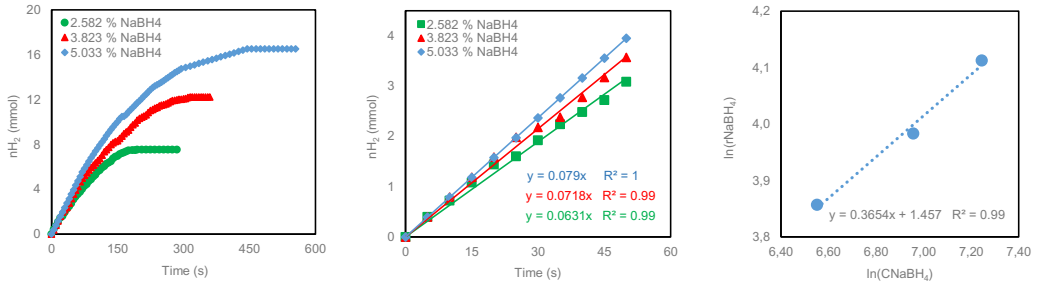


Fig. 1: a) Effects of $NABH_4$ dosage on H_2 generation b) Best fitting line to the H_2 generated versus time data c) ln($rNABH_4$) versus ln (C_{NaBH_4}) graph

The H_2 generation rate was calculated from the slope of the line which was best fitted to the cumulative H_2 generated (mmol) versus Time (second). Fig. 1. (a) shows this linear fit of the curves.

$$r'_{H_2} = \frac{slope(\frac{mmol}{min})}{m_{cat}(g_{cat})} \tag{4}$$

In the second experimental set up, the effect of the increasing temperature of the bach reactor was investigated. The reaction rate of the H_2 increases whereas the maximum amount of the generated H_2 does not change. The temperature of the reactor was successfully kept constant at the desired temperature. However, deviations are acceptable since the reaction was highly exothermic and 0.5-1°C temperature change was assumed that had no effect on the reaction rate. The results of the experiments can be seen in Fig.2.

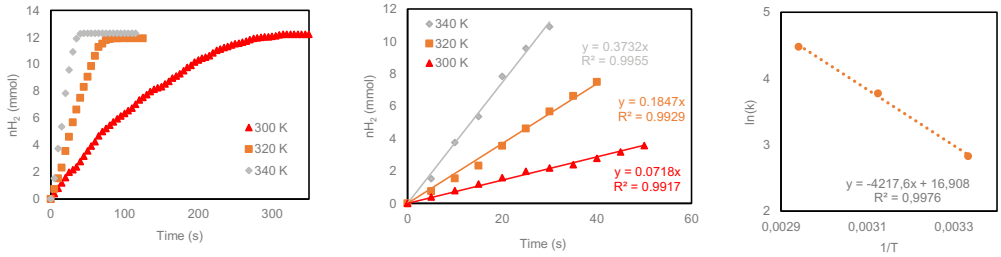


Fig. 2: a) Effect of temperature change on H_2 generation b) Best fitting line to the H_2 generation versus time data c) ln(k) versus 1/T

Reaction rate of the H_2 is a function which depends on the Temperature (T) of the bach reaction and

Concentration of $NaBH_4$ (C_{NaBH_4}) can be formulated as Eq. (5).

$$r'_{H_2} = f(T, C_{NaBH_4}) \quad (5)$$

$$r'_{H_2} = kC^{\alpha}_{NaBH_4} \quad (6)$$

k and α was calculated 17.172 and 0.3654, respectively in Fig.1.c

Where k is,

$$k = Ae^{-Ea/RT} \quad (7)$$

Where Ea is the activation energy; A is Arhenius constant; R is ideal gas constant.
With the linearization of the Eq. (6) becomes;

$$ln\, r'_{H_2} = \alpha ln C_{NaBH_4} + lnk \quad (8)$$

$$lnk = lnA - \frac{Ea}{R}\frac{1}{T} \quad (9)$$

k values for 47°C and 67°C were calculated as 43.616 and 88.129, respectively. When R is considered as 8.314 $J.K^{-1}.mol^{-1}$, Ea was calculated as 33702.92 J/mol and A value was found as 30401424.

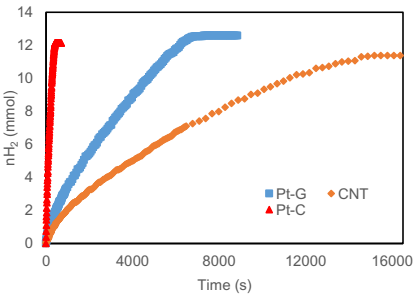


Fig. 3: Effect of catalyst type on H_2 generation

In the last experimental set up, effects of other two types of catalyst supports were investigated on the reaction rate of H_2. It was observed that the reaction rate of H_2 generation was changed with the changing catalyst supports as shown in Fig. 3.
Efficiencies was also calculated for each of the experiments by using Eq. (10) and all of the experiments efficiency is more than 90 %. Therefore, they can be comparable with each other.

$$\eta_{eff} = \frac{actual\ moles\ of\ H_2\ generated}{theoretical\ moles\ of\ H_2\ generated} = \frac{n_{H_{2,actual}}}{n_{H_{2,theoretical}}} \quad (10)$$

IV. Results and Discussions

Four main parameters; $NaBH_4$ wt. percentage, catalyst amount, catalyst support and temperature which affect the H_2 generation rate were investigated. When wt. percentage of $NaBH_4$ was increasing, generated H_2 amount and reaction rate of the H_2 was also increased. To analyse the H_2 generation rate and amount change with recpect to $NaBH_4$ concentration change, $NaBH_4$ amount was changed and others are kept constant. 3 mL solution was prepared with 2.58, 3.82 and 5.033 wt. % $NaBH_4$ and the reaction rates were calculated as 189.3, 214.8 and 244.5 $mmol.min^{-1}.g_{cat}^{-1}$ respectively.

Initially, all reactions occured approximately linear but then they were decreasing with the decreasing concentration of $NaBH_4$ in contact with the catalyst. After a while, the reactions progressed more slowly. Solutions must be prepared at high $NaBH_4$ concentrations up to 26 wt. % because it is limit to increase $NaBH_4$ wt. % because of the decrease of the solubility of $NaBO_2$ (Kojima et al., 2004). Therefore, H_2 generator should be designed by considering the solubility limit of $NaBH_4$ and $NaBO_2$ to avoid suspending solid particules in the solution. The second experimental set up, with increasing temperature 27, 47 and 67°C, the reaction rates of the H_2 generation increased which were calculated 214.8, 554.1 and 1119.6 $mmol.min^{-1}.g_{cat}^{-1}$, respectively. To analyse the effects of the types of catalyst support with keeping constant Pt mass Pt/C, Pt/G and Pt/MWCNT were used and the reaction rates of the experiments were calculated 214.8, 46.9 and 20.1 $mmol.min^{-1}.g_{cat}^{-1}$, respectively.

V. Conclusions

The H_2 generated from the hydrolysis reaction can be used for PEMFC applications and based on this work an on demand H_2 generator can be designed for portable applications. Three main parameters, wt. percentage of $NaBH_4$, temperature of the batch reactor and catalyst supports of Pt, affect the H_2 generation rate were investigated. The reaction rates and efficiencies of H_2 generation is given in Tab. 1. Also, an experiment without catalyst was made in order to see the catalyst effects on H_2 generation amount obviously.

Tab. 1: Reaction rate and efficiency according to different parameter

Experiment No	Wt. % $NaBH_4$	Catalyst Type	T (°C)	Reaction Rate ($mmol.min^{-1}.g_{cat}^{-1}$)	Efficiency %
I	2.582	Pt/C	27	189.3	90
II	3.823	Pt/C	27	214.8	97
III	5.033	Pt/C	27	244.5	98
IV	3.823	Pt/C	47	554.1	94
V	3.823	Pt/C	67	1119.6	97
VI	3.823	Pt/G	27	46.9	99
VII	3.823	Pt/MWCNT	27	20.1	90
VIII	3.823	-	27	-	47

Moreover, H_2 generation rates were calculated and kinetic reaction study was made. Experiment no VI is the most efficient experiment while experiment no VII is the steadiest with keeping Pt mass constant (0.004 g). Therefore, Pt/MWCNT could be used as a convenient catalyst for an on demand portable PEMFC applications due to the low reaction rate.

References

Arıca E.D., Devrim Y., Proton Değişim Yakıt Hücreleri için Platin Karbon Nanotüp Kompozit Elektro Katalizörlerin Hazırlanması, 29. Ulusal Kimya Kongresi, 81 (2017).

Devrim Y., Albostan A., Graphene-Supported Platinum Catalyst-Based Membrane Electrode Assembly for PEM Fuel Cell, Journal of Electronic Materials , 45, 8, 3900–3907 (2016).

Kong V.C.Y., Foulkes F.R., Kirk D.W., Hinatsu J.T., Development of hydrogen storage for fuel cell generators. I: Hydrogen generation using hydrolysis hydrides Int. J. Hydrogen Energ, 24, 665 (1999).

Kojima Y., Haga T., Hydrogen generation from hydrolysis of alkaline sodium borohydride solution using Pt/C catalyst, Int. J. Hydrogen Energy, 28, 989 (2003).

Kojima Y, Suzuki KI, Fukumoto K, Kawai Y, Kimbara M, Nakanishi H, Matsumoto S. Development of 10kW-scale hydrogen generator using chemical hydride. Journal of Power Sources; 125:22–26. 20 (2004).

Ous T., Arcoumanis C., Degradation aspects of water formation and transport in proton exchange membrane fuel cell J Power Sources, 240, 558-582 (2013).

Pena-Alonso R., Sicurelli A., Callone E., Carturan G., Raj R., A picoscale catalyst for hydrogen generation from NaBH4 for fuel cells, J Power Sources, 165, 1, 315-323, (2007).

Tuber K., Zobel M., Schmidt H., Hebling C.A., Polymer electrolyte membrane fuel cell system for powering portable computers, J Power Sources, 15, 1-8(2003).

Mathematical Modeling of a Flowing Electrolyte-Direct Methanol Fuel Cell Using Comsol Multiphysics

[1]O. Faruk Atacan, [2]David Ouellette, [3]Deniz Yilmaz, [4]Pasa Yaman, [5*]C. Ozgur Colpan

[1,3,4,5] Dokuz Eylul University, The Graduate School of Natural and Applied Sciences, Mechanical Engineering Department, Tinaztepe, Buca, Izmir, 35397, Turkey
[2]University of Toronto Institute for Sustainable Energy, Faculty of Applied Science and Engineering, Department of Mechanical and Industrial Engineering, University of Toronto, 5 King's College Road, Toronto, ON M5S 3G8, Canada
[5]Dokuz Eylül University, Faculty of Engineering, Mechanical Engineering Department, İzmir, 35397, Turkey

* E-mail: ozgur.colpan@deu.edu.tr

Abstract

Direct methanol fuel cell is a promising candidate for portable applications because fuel is liquid at low temperatures, easily stored and cheap. However, the problem of methanol crossover from anode to cathode is the main problem for the commercialization of this fuel cell due to performance degradation. In order to prevent methanol crosover, the flowing electrolyte-direct methanol fuel cell (FE-DMFC) is considered as a potential solution. In this type of fuel cell, the anode and the cathode are separated by the porous flowing electrolyte channel, where a liquid electrolyte (for example, sulfuric acid) flows. Membranes are placed on both sides of this porous channel and the methanol crossover is mostly prevented by the flowing electrolyte. Many researchers have modeled this fuel cell, however the majority of these studies are single phase and developed using 1D or 2D techniques. In this study, a three dimensional and two phase FE-DMFC model has been modelled to examine the baseline condition of this fuel cell to obtain more realistic modeling predictions. Main equations such as continuity, momentum, charge, and transport of methanol, water and oxygen species are combined with basic mixture equations and auxiliary equations using the commercial software Comsol Multiphysics.

Keywords: DMFC, Comsol Multiphysics, FE-DMFC, simulation, two phase

I. Introduction

Direct methanol fuel cell (DMFC) is one of the low temperature fuel cell types that can be used in some specific portable and vehicular applications. Using liquid diluted methanol solution provides several advantages as it is easy to store and access methanol. However, unwanted methanol crossover from anode to cathode and poor electrochemical kinetics of the electrochemical reactions at both anode and cathode cause low performance. To eliminate this crossover and enhance the performance, flowing electrolyte-direct methanol fuel cell (FE-DMFC) can be used. In this fuel cell type, methanol is carried away from the cell by means of the flow of sulfuric acid through the flowing electrolyte channel. This FE-DMFC design was initially proposed by Kordesch et al. (2001) and then developed by numerous numerical and experimental methods. For example, in single cell-level, Colpan et al. (2011) and Ouellette et al. (2015) developed 1D models of the FE-DMFC in different levels of details. Colpan et al. (2011) developed a 2D model of FE-DMFC to estimate the performance of this fuel cell for different values of inlet velocities of fluids entering through the channels. In stack-level, recently, Colpan and Ouellette (2018) developed a FE-DMFC stack model including the details of the flow pattern in 3D environment using Comsol Multiphysics environment. In addition to these single-phase models, there are some multiphase FE-DMFC models in the literature. For example, in the studies by Ouellette et al. (2015a, 2015b) and Atacan et al. (2017), an advanced modeling technique including the effects of multi-phase has been used to have a better understanding of the transport phenomena inside the fuel cell. In terms of experimental works on FE-DMFC, the most significant studies were carried out by Sabet-Shargi et al. (2013) and Colpan et al. (2017). In these studies, the superiority of FE-DMFC over DMFC was shown.

Although there are several models in the literature, a detailed 3D multiphase model of FE-DMFC has not been developed. In this study, a three dimensional and two-phase FE-DMFC model has been developed to find the distributions of chemical species (saturation and methanol) within 3D geometry of the cell for the baseline conditions.

II. Modeling

In this study, in order to solve the governing equations (mass, momentum, chemical species and charge) and other auxiliary equations (e.g. Butler-Volmer equation) COMSOL Multiphysics has been used by coupling equations together.

$$\nabla \cdot (\rho \mathbf{u}) = S_{gen} + S_{trans} \quad (1)$$

$$\frac{\rho}{\varepsilon_p}\left[(\nabla\cdot\mathbf{u})\frac{\mathbf{u}}{\varepsilon_p}\right]=\nabla\cdot\left[-P\mathbf{I}+\frac{\mu}{\varepsilon_p}\left\langle(\nabla\mathbf{u})+(\nabla\mathbf{u})^T\right\rangle-\frac{2\mu}{3\varepsilon_p}(\nabla\cdot\mathbf{u})\mathbf{I}\right]-\left(\frac{\mu}{K}+\beta|\mathbf{u}|+\frac{S_{gen}}{\varepsilon_p^2}\right)\mathbf{u}+\mathbf{f} \quad (2)$$

$$\nabla\cdot\left[-D_{\mathrm{lg}}^k\left(\nabla C_i^k\right)+\mathbf{u}_{\mathbf{lg}}^{\mathbf{k}}C_i^k\right]=S_{gen}^k+S_{trans}^k \quad (3)$$

$$\nabla\cdot\left[-\sigma_l(\nabla\phi_l)\right]=S_{c,l} \quad (4)$$

$$\nabla\cdot\left[-\sigma_s(\nabla\phi_s)\right]=S_{c,s} \quad (5)$$

Mixture velocity (**u**) and pressure (P) distributions are found by using Eqs. (1) and (2). By using this velocity, the convective mode of transport within Eq. (3) is accounted for. The concentration profile of each species (methanol, water, oxygen) is taken from Eq. (3) and the current distributions for electrolyte and solid phase are obtained from Eqs. (4) and (5). The main parameters of the fuel cell geometry is given in Tab.1; and other relevant parameters are taken from Atacan et al. (2017).

Tab.1 Main parameters of fuel cell geometry

Parameter	Value	Units
Cell Length	42×10^{-3}	m
Active Area	1.764×10^{-3}	m^2
Thickness		
ABL and CBL	0.175×10^{-3}	m
AFC and CAC	1×10^{-3}	m
AM and CM	0.127×10^{-3}	m
FEC	0.175×10^{-3}	m
ACL and CCL	38×10^{-6}	m
Channel Dimensions		
Width	1.5×10^{-3}	m
Depth	1×10^{-3}	m

In order to get mesh independent model, current density change is taken in consideration. Number of mesh is increased until the error margin is less than 0.1% between two consecutive values. This process is done for each layer and mesh size is determined accordingly. As a result of this process, total number of mesh is found as 1.2 million. To gain time in calculations symmetry property is given at the center of the fuel cell as shown in Fig.1.

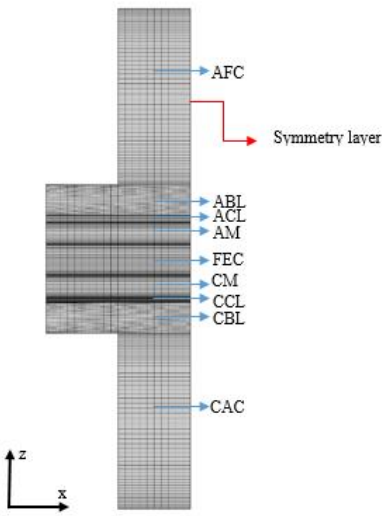


Fig. 1 – Meshing of the geometry in Comsol Multiphysics

III. Results and discussions

Methanol concentration and saturation distributions have been examined with the developed two-phase and three dimensional FE-DMFC model. Fuel cell operates at 80°C with 1 M methanol solution at the anode inlet and 101325 Pa air at the cathode inlet at baseline condition. In addition, the stoichiometric flow ratios at the anode and cathode flow channels are set to 2 and 3, respectively.

III.1. Methanol Concentration

Fig. 2 illustrates the methanol concentration distribution for a cell voltage of 0.2 V (i =1926.4 $A \cdot m^{-2}$). Methanol concentration decreases along the length-wise (y-direction) and thickness-wise (z-direction) directions because of increasing consumption of methanol within ACL. Methanol passes through membrane due to the electro-osmotic drag. This electro-osmotic drag occurs due to production of protons in the ACL. As seen in the FEC, the methanol concentration mostly decreases due to the convective crossflow. This causes reducing the crossover current density, with a maximum of ~30 $A \cdot m^{-2}$ at 0.5 V.

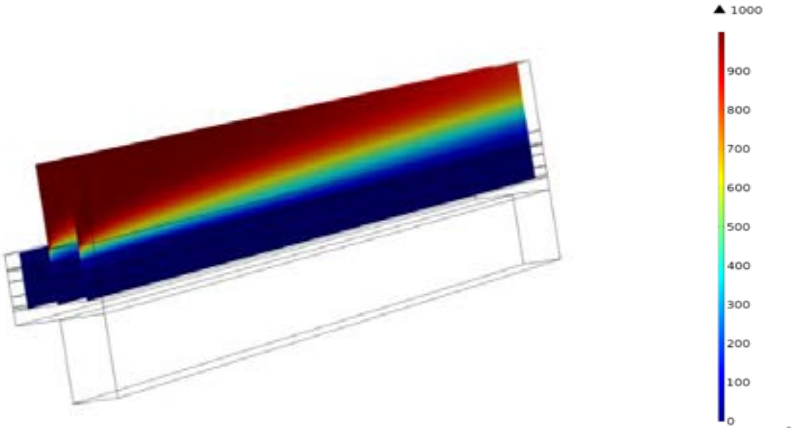


Fig. 2 Distribution of methanol concentration

III.2. Saturation Concentration

The saturation distribution at a cell voltage of 0.2 V is shown in Fig. 3. As shown in this figure, the liquid saturation within the anode and FEC is very high, ~0.9, and constant for both cell voltages. Because of the consumption of methanol and water solution, and the production of carbon dioxide, the cell voltage and the liquid saturation within the ACL decrease. The liquid saturation decreases to a value of 0.894 at the lower cell voltage (0.2 V). However, in this situation, at a cell voltage of 0.2 V, the liquid saturation increases from a value of 0.11 to 0.127. This increase in liquid saturation is owing to the combination of water crossover from the FEC to the cathode and due to the generation of water from the ORR and MOR from any crossed over methanol. Because of the lack of chemical reactions, saturation negligibly changes in the FEC.

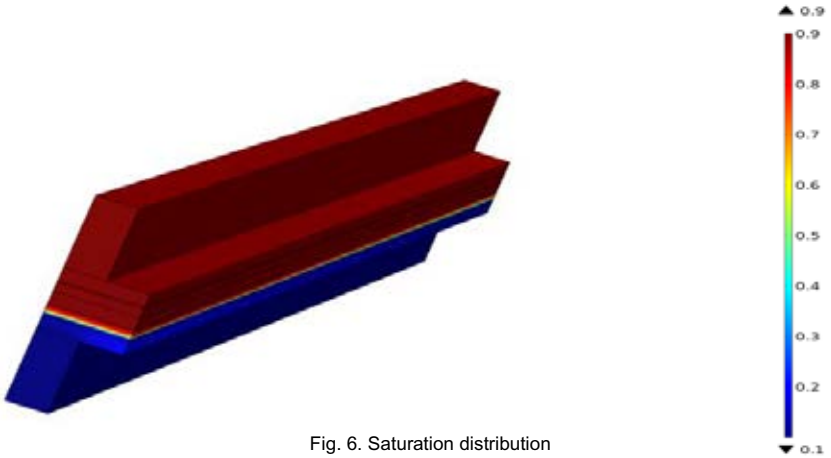


Fig. 6. Saturation distribution

V. Conclusions

Comsol Multiphysics (a commercially available software) is used to find methanol, saturation and oxygen concentration distrubituions. In order to develop a three dimensional and two phase model, the governing conservation equations of momentum, mass, species and charge are solved by using built-in modules in this software. However, mixture equations used in model has been entered manually. The following conclusions have been made in this study:

- The effect of convective crossflow in the FEC decreases crossover density with a maximum of ~30 $A \cdot m^{-2}$ at 0.5 V.
- The increase in liquid saturation is found ~15.5% due to the combination of water crossover from the FEC to the cathode and due to the generation of water from the ORR and MOR from any crossed over methanol.

Acknowledgements

The authors thank TUBITAK (The Scientific and Technological Research Council of Turkey) for their financial support in this work under contract number: 213M257.

Abbreviations

ABL	Anode backing layer
ACL	Anode catalyst layer
AFC	Anode fuel channel
AM	Anode membrane
CAC	Cathode air channel
CBL	Cathode backing layer
CCL	Cathode catalyst layer
CM	Cathode membrane
DMFC	Direct methanol fuel cell
FEC	Flowing electrolyte channel
FE-DMFC	Flowing electrolyte-direct methanol fuel cell

References

Atacan, O. F., Ouellette, D., & Colpan, C. O. Two dimensional multiphase non-isothermal modeling of a flowing electrolyte–direct methanol fuel cell. *International Journal of Hydrogen Energy*, *42*(4), 2669-2679, (2017).

Colpan, C. O., Cruickshank, C. A., Matida, E., & Hamdullahpur, F. 1D modeling of a flowing electrolyte-direct methanol fuel cell. *Journal of Power Sources*, *196*(7), 3572-3582, (2011).

Colpan, C. O., Ouellette, D., Glüsen, A., Müller, M., & Stolten, D. Reduction of methanol crossover in a flowing electrolyte-direct methanol fuel cell. *International Journal of Hydrogen Energy*, (2017).

Colpan, C.O., Ouellette, D. 2018. Three dimensional modeling of a FE-DMFC short-stack. International Journal of Hydrogen Energy. (In Press)

Kordesch, K., Hacker, V., & Bachhiesl, U. Direct methanol–air fuel cells with membranes plus circulating electrolyte. *Journal of Power Sources*, *96*(1), 200–203, (2001).

Ouellette, D., Colpan, C. O., Cruickshank, C. A., & Matida, E. Parametric studies on the membrane arrangement and porous properties of the flowing electrolyte channel in a flowing electrolyte–direct methanol fuel cell. *International Journal of Hydrogen Energy*, *40*(24), 7732-7742, (2015).

Ouellette, D., Colpan, C. O., Matida, E., & Cruickshank, C. A. A single domain approach to modeling the multiphase flow within a flowing electrolyte–direct methanol fuel cell. *International Journal of Hydrogen Energy*, *40*(24), 7817-7828, (2015).

Ouellette, D., Colpan, C. O., Matida, E., Cruickshank, C. A., & Hamdullahpur, F. A comprehensive 1D model of a flowing electrolyte - direct methanol fuel cell with experimental validation. *International Journal of Energy Research*, *39*(1), 33-45, (2015).

Sabet-Sharghi, N., Cruickshank, C. A., Matida, E., & Hamdullahpur, F. Performance measurements of a single cell flowing electrolyte-direct methanol fuel cell (FE-DMFC). *Journal of Power Sources*, *230*, 194-200, (2013).

Wood char - Active carbon production for H_2 adsorption and storage

[1*]Yıldırım İsmail Tosun
[1] Şırnak University, Engineering Faculty, Mining Engineering Department, Şırnak, 73000, Turkey

* E-mail: yildirimismailtosun@gmail.com

Abstract
Şırnak nut shell char, waste wood and lignite were pyrolized and carbonized as powder in industrial furnaces and carbonized by microwave furnace. Turkish lignite fine and coal fine have great economic and ecological benefits in burning after being washed and cleaned. The distribution and quality of Şırnak biochar reserves makes it possible to consume in the water treatment as high reactivity by porosity of 42,7 %, high micro mesoporous and nanoporous content with 7,8% and at high adsorption value of 126mg/kg will be considered. The modified pyrolyzing method was using agglomerated pyrolyzing and microwave carbonization as active carbon and char in the form of micron sized. The parameters of this pyrolyzing method produced there active char by this method and test results of adsorption with active carbon was not effective as biochar. The size of the large agglomerate managed high flow adsorption. It is an effective method especially in high metal load and backwash. It has been determined to be successful in high density and low porous active carbon and less carbonized lignite.

Keywords: microwave, modified carbonized, agglomerated char, biochar, metal adsorption, water treatment

I. Introduction

Biochar is produced by heating biomass in the total or partial absence of oxygen. Pyrolysis is the most common technology employed to produce biochar, and also occurs in the early stages of the combustion and gasification processes. Besides biochar, bio-oil and gas can be collected from modern pyrolysers. These could be refined to a range of chemicals and/or used as sources of renewable energy if derived from sustainably produced biomass. Carbonization the most common technology employed to produce biochar, and also occurs in the early stages of the combustion and gasification processes.



Fig. 1: Low temperature Slow Pyrolyser

The pyrolysis gas is mainly a mixture of carbon monoxide (CO) and hydrogen (H_2) with lower quantities of CO_2, CH_4, H_2O, and a range of volatile compounds. Pyrolysis gas is costly to store and transport and therefore, it is usually combusted on-site to meet the heat requirements of the pyrolyser. However, if the heat energy released during combustion of the pyrolysis gas exceeds the demand of a biochar system and opportunities exist nearby the plant, then the pyrolysis gas could be used to provide heat for external processes. If the energy provided by the pyrolysis gas is converted into electricity, then this can be fed into the grid.

Bio-oil consists of a complex mixture of oxygenated hydrocarbons with a considerable fraction of water. Bio-oil is attractive for the energy industry due to the fact that it is transportable, storable, and a potential replacement of fuel oil or diesel in stationary applications including boilers, furnaces, engines, and turbines for electricity generation. However, it cannot be used directly as a transport fuel unless it is upgraded, which is technically feasible but expensive. In addition, bio-oil can be a source of a number of valuable chemical products such as acetic acid, resins, sugars, food flavourings, slow release fertilisers, adhesives and preservatives.



Fig. 2: Wood Pyrolyser

Charcoal has been produced from woody biomass for thousands of years. In developing countries, traditional earth-mound, brick, and metal kilns are inefficient in producing charcoal and usually do not include burning of the exhaust gases. Therefore, they are regarded as an important source of deforestation and greenhouse gas emissions. Moreover, small-scale pyrolysis stoves are promoted to decrease fuel consumption and deforestation in developing countries, improve respiratory health, and increase soil fertility by incorporating the biochar into soils.

Two toxic compounds, polyaromatic hydrocarbons (PAHs) and dioxins can be also present in chars and bio-oils produced during pyrolysis. Large quantities of PAHs are formed in chemical reactions at temperatures over 700°C and evidence suggests that small amounts of PAHs can also be formed in pyrolysis reactors operating between 350 and 600°C. Dioxins predominantly form at temperatures above 1,000°C and are significantly reduced when chlorine and metals are not present. It is important to note that in any modern biochar manufacturing process these toxins must be avoided.

To ensure that biochar production does not contribute to air pollution and GHG emissions, biochar must be produced in a facility that captures and combusts the gases released when biomass is heated. The heat produced through combustion of these gases can be used as a form of renewable energy. Biochar production can occur at scales ranging from a cook stove to large engineered industrial-scale plants. Slow pyrolysis could be used in intensive animal production or landfill systems as a waste management solution, delivering renewable energy and converting end-of-life biomass to valuable stable carbon-based soil amendments that facilitate nutrient recycling.

II. Adsorption Characterisation of biochar-active carbons

Several physical properties have been identified to measure the quality of biochar: pH, volatile compound content, water holding capacity, ash content, bulk density, pore volume, and specific surface area. The IBI (2015) has formalised these and other properties into a proposed reporting standard.

The characteristics of feedstock and production parameters determine the physico-chemical properties and nutrient content of biochar. Based on surface area, pH, and cation exchange capacity (CEC), Lehmann (2007) proposed a temperature between 450-550°C to optimise the characteristics of biochar for use as char adsorbant (Figure 3).

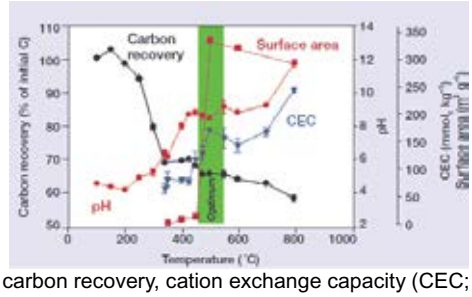


Figure 3. Temperature effects on carbon recovery, cation exchange capacity (CEC; measured at pH 7), pH, and surface area for dried wood from Robinia pseudacacia L. (Lehmann, 2007).

Balancing parameters depend on what is desired. For example, the higher the process temperature the less biochar produced (less soil amendment and less C sequestered) but the higher its carbon stability (longer C sequestration) and co-products yield (more energy). It is important to note that the structure of biochar offers pore networks for gas retention and adsorption. Further characterisation of biochar-liquid and gas dynamics is required and need analysis of the many factors:

- test conditions, duration, and adsorption and desorption study (eg. soil remediation, crop production, carbon sequestration);
- temperature
- type of char
- type of ingredients, reactivities
- feedstock for producing biochar (e.g. rice husk, corn stover, etc)
- type of carbonization technology and respective parameters (e.g. temperature, heating rate, residence time);
- post- treatment (e.g. acidic activation or cleaning);
- effects of soot, steam unveil capacity, pH, leaching, toxins mobilisation).

II.1.The heterogeneous chemical nature of biochar.

Charred biomass consists not only of recalcitrant aromatic ring structures, but also of more easily degradable aliphaticand oxidized carbon structures (Schmidt and Noack 2000). The range of carbon forms within a biochar particle may depend on the carbon properties of the plant cell structure, on the charring conditions, and on the formation process (by either condensation of volatiles or by direct charring of plant cells). The consequence of this heterogeneity is that some portions of biochar may indeed be mineralized very rapidly, as are aliphatic carbon forms (Cheng *et al*. 2006). An extrapolation from relatively easily mineralizable carbon forms to the entire biochar may therefore lead to erroneous projections.

II.2. The particulate form of biochar.

Because biochar exists as particulates, biotic or abiotic decay must be initiated on its surface. (Figure 3) Such surface oxidation may be initiated quite rapidly (ie within a few months; Cheng *et al*. 2006), but is restricted to the outer areas of a particle, even after several hundred years in soils (Lehmann *et al*. 2005b). Quantification of the decomposition of fresh biochar by short-term experiments may therefore lead to an overestimation of long-term decay.

References

Bridgwater A.V., Renewable fuels and chemicals by thermal processing of biomass, Chemical Engin J: 87–102.(2003).

Brodowski S., John B., Flessa H., Amelung W., Aggregate-occluded black carbon in soil, Europ J Soil Sci, 539–46, (2006).

Czernik S. and Bridgwater A.V., Overview of applications of biomass fast pyrolysis oil, Energy Fuels: 590–98 (2004).

Day D., Evans R.J., Lee J.W., Reicosky D., Economical CO2,SOx, and NOx capture from fossil-fuel utilization with combined renewable hydrogen production and large-scale carbon sequestration, Energy: 2558–79, (2005).

J Lehmann Biochar bio-energy, DeLuca T.H., MacKenzie M.D., Gundale M.J., Holben W.E., Wildfire-produced charcoal directly influences nitrogen cycling in ponderosa pine forests, Soil Sci Soc Am J: 448–53, (2006).

Glaser B., Balashov E., Haumaier L., Guggenberger G., and Zech W., Black carbon in density fractions of anthropogenic soils of the Brazilian Amazon region, Org Geochem: 669–78, (2000).

Goldberg E.D., Black carbon in the environment. New York, NY: John Wiley and Sons, (1985).

He B.J., Zhang Y., Funk T.L., Riskowski G.L., Yin Y., Ther-mochemical conversion of swine manure: an alternative process for waste treatment and renewable energy production, Trans ASAE: 1827–34, (2000).

Lee J.W. and Li R,. Integration of coal-fired energy systems with CO2 sequestration through NH4HCO3 production, Energy Convers Manage: 1535–46, (2003).

Lehmann J., da Silva Jr J.P., Steiner C., Nutrient availability and leaching in an archaeological anthrosol and a ferralsol of the Central Amazon basin: fertilizer, manure and charcoal amendments, Plant Soil: 343–57, (2003).

Lehmann J., Lan Z., Hyland C., Long-term dynamics of phosphorus forms and retention in manure-amended soils, Environ Sci Technol: 6672–80, (2005).

Lehmann J., Gaunt J., and Rondon M., Biochar sequestration in terrestrial ecosystems: a review, Mitig Adapt Strategy Global Change : 403–27, (2006).

Liang B., Lehmann J., Solomon D., Black carbon increases cation exchange capacity in soils, Soil Sci Soc Am J: 1719–30, (2006).

Patzek T.W. and Pimentel D., Thermodynamics of energy production from biomass, Crit Rev Plant Sci: 327–64, (2005).

Rumpel C., Alexis M., Chabbi A., Black carbon contribution to soil organic matter decomposition in tropical sloping and under slash-and-burn agriculture. Geoderma: 35–46. (2005).

Dark Earths as carbon stores and sinks. In: Lehmann J., Kern D.C., Glaser B., Woods W.I. (Eds). Amazonian Dark Earths: origin, properties, management. Dordrecht, Netherlands: Kluwer Academic Publishers.

A Parametric Study on Exergetic Performance of Hydropower Integrated Hydrogen Production: A Case Study for East Black-Sea Region of Turkey

Adnan Midilli and *Mert Ozsaban
[1]Mechanical Engineering Department, Faculty of Engineering, Recep Tayyip Erdoğan University, Zihni Derin Campus, Fener, 53100, Rize, Turkey

*E-mail: mert.ozsaban@erdogan.edu.tr

Abstract
The main objective of this study is to perform a parametric study on exergetic performance of the run-of-the-river hydropower integrated hydrogen production via high-pressure-PEM electrolyser in terms of the second law of thermodynamics. For this purpose, the following parameters are taken into consideration: i) Gross head (=50-300m), ii) Discharge (=0.2-0.4 m^3/s), iii) Pure water flow. In this regard, in order to determine the exergetic performance of the run-of-the-river hydropower integrated high-pressure-PEM electrolyser, the hydrogen production rates have been calculated based on the power generated from this hydropower plant. It is determined that run-of-the river mini hydropower plant generates power between 75.5 kW and 905 kW based on the gross head, ranging from 50 m to 300 m, and the discharge, ranging from 0.2 m^3/s to 0.4 m^3/s. Depending on these values, it is estimated that the PEM electrolyser produces hydrogen gas ranging from 1.325 kg/h (=14.928 Nm^3/h) to 15.966 kg/h (=180 Nm^3/h) at 30 bar and 70 °C. Moreover, exergy efficiency is found to be 0.543 at 0.4 m^3/s for 50 m and 0.545 at the discharge of 0.2m^3/s for 300 m of gross head. Accordingly, it can be said that exergetic efficiency of the process decreases with the rise of the discharge at a constant gross head while the hydrogen production rate increases with the rise of electricity generation.

Keywords: Exergy efficiency, Hydrogen, PEM electrolyzer, run-of-river mini hydropower, discharge, gross head.

I. Introduction
Hydropower, more environmental benign and cheapest renewable energy (Dursun, 2011), is an essential tool as a renewable energy source that can be converted into electricity by means of the run-of-the river hydropower plant, as well. The run-of-the river hydropower plant is inviting a global attention because it is clean, cost effective and it has not environmental impact (Manders, 2016). These types of many power plants are particularly appropriate for east Black-sea region of Turkey. East Black Sea Region has a significant role in terms of hydropower energy potential in Turkey. This region has 48478 GWh/year potential energy and it has 24239 GWh/year technical potential energy (Koç, 2014). The present hydropower plants in this region produce almost 3420.9 GWh in a year. However, the installing capacity of those under construction is estimated to be nearly 9553 GWh/year. It means that east black sea region has high quantity of hydropower for different applications such as renewable hydrogen production that has minimum impacts on the environment and society (Cilogluları, 2016). In order to produce renewable hydrogen by using electricity from run-of-the-river hydropower plant PEM electrolysers may be used (Nieminen, 2010; Ahmadi, 2013). This system (the run-of-the-river hydropower integrated hydrogen production via high-pressure-PEM electrolyser system) should be exergetically evaluated in terms of the Second Law of Thermodynamics. Under these considerations

II. Main Consideration
a) System Description
Assumptions:
1. Slope angle of the penstock has been accepted to be 60 degree in accordance with the land structure of East Black Sea Region.
2. Penstock diameter has been accepted to be 1 m.
3. Turbine, generator and transformer, PEM electrolyser, pumps efficiencies have been accepted to be 0.90, 0.95, 0.90, 0.60 and 0.80, respectively.
4. The pressure and heat losses through the system have been neglected.
5. Operating pressure and temperature of PEM electrolyser have been accepted to be 30 bar and 70°C, respectively.

Tab. 1: Operating Parameters of run-of-the-river Hydropower Plant

Parameter	Symbol	Unit	Values	Comment
Local friction factor in valve	k_v	-	0.5	(Featherstone, 1995)
Local friction factor outlet of forebay	k_h		0.5	(Featherstone, 1995)
Reference environment pressure	P_∞	bar	1	Assumed
Reference environment temperature	T_∞	K	298.15	Assumed
Gravity	g	(m/s^2)	9.81	(Featherstone, 1995)
Efficiency of turbine	η_t	%	90	Assumed
Efficiency of generator	η_g	%	95	Assumed
Efficiency of transformator	η_{trs}	%	90	Assumed

In terms of mini hydroelectric power generation it has five main components. These are forebay, penstock and power house. Power house includes turbine, electricity generator and transformer.

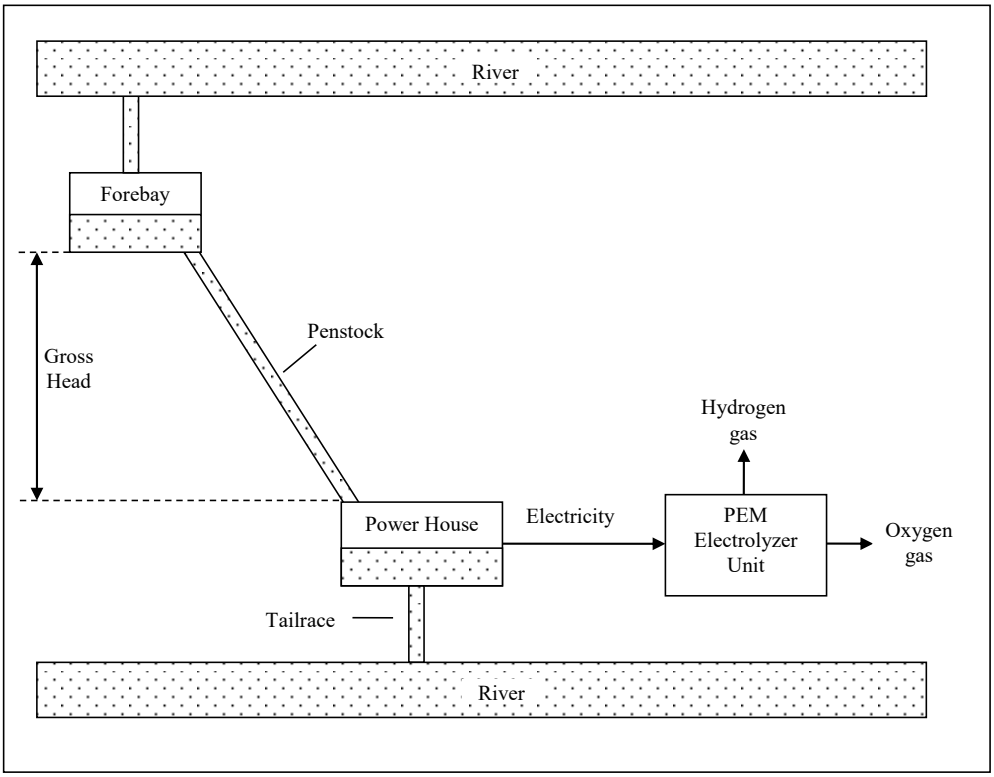


Fig. 1: Schematic illustration of the run-of-the-river hydropower integrated hydrogen production system for East Black Sea Region.

b) Exergy Analysis

Calculations of some constructive parameters for the system,

a) Local losses through the penstock is calculated as below,

$$\xi_l = \frac{k\, v^2}{2\, g} \tag{1}$$

b) Darcy-Weisbach friction factor (Barr equation) can be written as below (Featherstone, 1995),

$$\frac{1}{\sqrt{\lambda}} = -2log\left[\frac{k_s}{3.7D} + \frac{5.1286}{Re^{0.89}}\right] \tag{2}$$

c) Friction Loss in Penstock is calculated as below (Ozgur, 1957),

$$\xi_s = \frac{\lambda\, L\, v^2}{2\, g\, D} \tag{3}$$

d) Total losses in the system is shown as below,

$$\Sigma\xi = \Sigma\xi_l + \Sigma\xi_s \tag{4}$$

e) Calculation of Net Head can be written as below,

$$H_o = H_{gr} - \Sigma\xi \tag{5}$$

f) Calculation of exergy output of the hydropower plant (Kacar, 2009):

$$\dot{E}x_w = 9.81\, \dot{Q}\, H_0\, \eta_t\, \eta_j\, \eta_{trs} \tag{6}$$

g) PEM Electrolyzer electricity demand is shown as below (Inac, 2009):

$$\begin{aligned}\dot{W}_{PEM} &= \dot{m}_{H_2}\left[T_{H_2}\left(s^o_{H_2} + c_{H_2}\ln\left(\frac{T_{H_2}}{298}\right) - Z_{H_2}R\ln\left(\frac{P_{H_2}}{1bar}\right)\right) - c_{H_2}\left(T_{H_2} - 298\right)\right]\\ &+\dot{m}_{O_2}\left[T_{O_2}\left(s^o_{O_2} + c_{O_2}\ln\left(\frac{T_{O_2}}{298}\right) - Z_{O_2}R\ln\left(\frac{P_{O_2}}{1bar}\right)\right) - c_{O_2}\left(T_{O_2} - 298\right)\right]\\ &-\dot{m}_{H_2O}\left[T_{H_2O}\left(s^o_{H_2O} + c_{H_2O}\ln\left(\frac{T_{H_2O}}{298}\right)\right) - \left(h^o_{H_2O} + c_{H_2O}\left(T_{H_2O} - 298\right)\right)\right]\\ &+\dot{m}_{H_2O}\left(-h^o_{H_2O} - c_{H_2O}\left(T_{H_2O} - 298\right)\right) + \dot{m}_{H_2}\left(c_{H_2}\left(T_{H_2} - 298\right)\right) + \dot{m}_{O_2}\left(0.5c_{O_2}\left(T_{O_2} - 298\right)\right)\end{aligned} \tag{7}$$

h) High-pressure water pump electricity demand is calculated as below;

$$\dot{W}_{hpp} = \frac{\dot{m}_{pw} \times v_{pw}\left(P^{hpp}_{out} - P^{hpp}_{in}\right)}{\eta_{hpp}} \tag{8}$$

i) Required electricity for hydrogen production can be written as below;

$$\dot{W}_{H_2} = \dot{W}_{PEM} + \dot{W}_{hpp} \tag{9}$$

j) Exergy expression can be written by depending on the physical and chemical exergies of the hydrogen;

$$\dot{E}x_{H_2} = \dot{E}x^{ch}_{H_2} + \dot{m}_{H_2}((h - h_o) - T_0(s - s_o) \tag{10}$$

k) Exergy of water (potential energy) in the reservoir;

$$\dot{E}x_{pot} = \dot{E}x_{rw_i} = 9.81\, \dot{Q}\, H_{gr} \tag{11}$$

l) Exergy efficiency of the system can be written as below;

$$\eta_{ex} = \frac{\dot{E}x_{H_2}}{\dot{E}x_{pot}} \tag{12}$$

III. Results and Discussions

Variation of exergy efficiency of the system as a function of discharge are presented in Fig. 2. According to Fig. 2, it is determined that minimum exergy efficiency of the system is 0.543 at 50 m of gross head and 0.4 m^3/s of discharge and at the same point, exergy of hydrogen produced is obtained to be 106.707 kW. However, maximum exergy efficiency is estimated to be 0.544 at 300 m of gross head and 0.2 m^3/s of discharge, and at the same

point exergy of hydrogen produced is found to be 320.465 kW. Accordingly, it is found out that exergy of hydrogen produced increases with the rise of discharge while exergy efficiency of the system decreases.

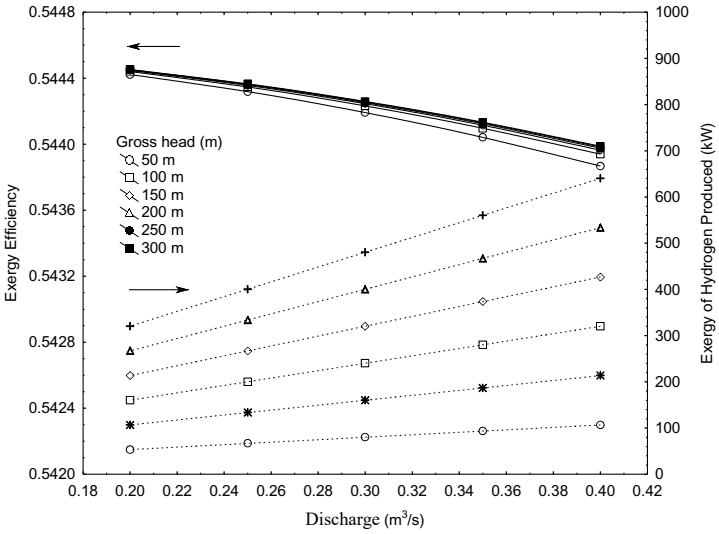


Fig. 2: Variation of exergy efficiency of the system as a function of discharge

IV. Conclusion

The results are obtained from a parametric study on exergetic performance of the run-of-the-river hydropower integrated hydrogen production system. In this regard, depending on the operating values of the system, the following concluding remarks may be briefly drawn under given operating conditions:

- Minimum value of exergy efficiency is calculated to be 0.543 at 0.4 m^3/s for 50 m.
- Maximum value of exergy efficiency is estimated to be 0.545 at 0.2m^3/s for 300 m.
- Minimum exergy by hydrogen is 53.408 kW at 50 m gross head and 0.2 m^3/s of discharge.
- Maximum exergy by hydrogen is 640.383 kW at 300 m gross head and 0.4 m^3/s of discharge.

Consequently, it is recommended that, based on the gross head and discharge values for East Black Sea Region of Turkey, a small hydrogen production station including the run-of-the-river hydropower integrated hydrogen production via high-pressure-PEM electrolyser system in this region be developed for hydrogen production.

V. Acknowledgement

We would like to thank Recep Tayyip Erdoğan University in Turkey for academic and technical support.

Nomenclature

k_v	Local friction factor in valve
k_h	Local friction factor outlet of forebay
P_∞	Reference environment pressure (bar)
T_∞	Reference environment temperature (Kelvin)
H_g	Gross head (m)
H_o	Net head (m)
$\dot{Q}$	Discharge (m^3/s)
v	Velocity (m/s)
L	Length (m)
D	Diameter (m)
g	Gravity (m/s^2)
s	Entropy (J/gK)
h	enthalpy (J/g)
c	Specific heat capacity (J/gK)
Z	Compressibility factor
R	Universal gas constant (J/kg K)
$\dot{m}$	Mass flow rate (kg/s)

$\dot{E}x$ Exergy (kW)

Greek Letters

η Efficiency
ξ Losses
λ friction factor

Acronyms

PEM Proton exchange membrane
Re Reynolds number
gr gross head
pot potential
rw river water

References

Ahmadi P., Dincer I., Rosen M.A., Energy and exergy analyses of hydrogen production via solar-boosted ocean thermal energy conversion and PEM electrolysis, International Journal of Hydrogen Energy, 38(4), 1795-1805, (2013).

Cilogulları M., Erden M., Karakilcik M., Dincer I., Investigation of hydrogen production performance of a Photovoltaic and Thermal System. International Journal of Hydrogen Energy, 42(4), 2547-2552, (2017).

Dursun B., Gokcol C., The role of hydroelectric power and contribution of small hydropower plants for sustainable development in Turkey, Renewable Energy, 36(4), 1227-1235, (2011).

Featherstone R.E., and Nalluri C., Civil Engineering Hydraulics, 3rd Edition, Blackwell Science Ltd., Oxford, 399, (1995).

Inac S., Thermodynamic modeling and energy sustainability analysis of high pressure hydrogen Production System (in Turkish), Graduate School of Natural and Applied Science, MSc Thesis, Nigde University, Turkey, (2009).

Kacar O., Thermodynamic Modeling of Power Generation via A Run-Of-River-Type-Hydropower Plant (in Turkish), Master thesis, Niğde University, Graduate Scholl of Natural and Applied Sciences, (2009).

Koç C., A study on the development of hydropower potential in Turkey, Renewable and Sustainable Energy Reviews, 39, 498-508, (2014).

Manders T.N., Höffken J.I., Vleuten E.B.A., Small-scale hydropower in the Netherlands: Problems and strategies of system builders, Renewable and Sustainable Energy Reviews, 59, 1493-1503, (2016).

Nieminen J., Dincer I., Naterer G., Comparative performance analysis of PEM and solid oxide steam electrolysers, International Journal of Hydrogen Energy, 35(20),10842-10850, (2010).

Ozgur C., Pratik Hidrolik Problemleri, Teknik Kitaplar Yayınevi, 6th Edition, İstanbul, (1957).

Metal-Schiff Base Complex Catalyst in KBH_4 Hydrolysis Reaction for Hydrogen Generation

[1*]Dilek Kılınç , [2]Ömer Şahin

[1] Faculty of Science and Letters, Department of Chemistry, Siirt University, 56100 Siirt
[2]Faculty of Engineering and Architecture, Department of Chemical Engineering, Siirt University, 56100 Siirt

* E-mail: dkilinc@siirt.edu.tr

Abstract
Hydrogen is often presented as one of the potential, sustainable alternatives to fossil fuels as it has the highest energy per mass. Hydrogen storage is a major obstacle in the way of the development of a near-future hydrogen economy. A number of potential solutions have been investigated so far (Demirci, 2017).

Among others, potassium borohydride (KBH_4) appears to be a promising candidate because of its hydrogen storage capacity exceeds 7.4 wt. % H_2 and similar to that of NaBH4 (hygroscopicity, self-hydrolysis, exothermic hydrolysis with -220 kJ/mol, better stability in basic medium, accelerated kinetics in the presences of Co catalysts (Zhu, 2008)

In this research, the new Co-Schiff Base complex that prepared 5-Amino-2,4-dichlorophenol-3,5-ditertbutylsalisylaldimine ligand (Kilinc, 2017) was synthesed. This complex was used as a catalyst to hydrolysis of KBH_4 for H_2 production. KBH_4 hydrolysis reaction which catalyzed with Co-Schiff Base complex was investigated depend on concentration of KBH_4, concentration of NaOH, temperature, percentage of Co complex and amount of catalyst. In addition the catalyst and products were caracterized with some analysis technique like XRD, FT-IR, BET, SEM. As a result it seen that Co-Schiff Base complex was effective catalyst in KBH_4 hydrolysis for H_2 production.

Keywords: KBH_4, Co-Complex, H_2 Production

References
Demirci U., Int. Journal of Hydrogen Energy 42, 21048-21062, (2017).

Zhu L., Kim D., Kim H., Masel R. I., Shannon M. A., J. Power Sources 185, 1334-1339, (2008)

Kilinc D., Sahin O., Saka C., Int. Journal of Hydrogen Energy, 42, 20625-20637, (2017).

Biohydrogen Upgrading Towards a Cleaner Energy Production

*Emre Oguz KOROGLU, Bestami OZKAYA, Ahmet DEMIR
Yildiz Technical University, Civil Engineering Faculty, Department of Environmental Engineering, 34220, Istanbul, Turkey

* E-mail:emreoguzkoroglu@gmail.com

Abstract
From a variety of biological wastes, biohydrogen production through anaerobic fermentation process is growing worldwide. It is considered as a cleaner solution in current energy scenario and this technology is environment friendly, economical, and known as the most efficient - as compared to all other technologies of energy production - through biological energy conversion processes.

In this technology, there is an increasing demand for upgraded biohydrogen, to be used as vehicle fuel or in proton exchange membrane (PEM) fuel cell. Because biogas derivered from anaerobic fermentation is mainly composed of hydrogen (H_2) and carbon dioxide (CO_2) and trace amounts of other impurities such as carbon monoxide and sulphur compounds. However, the presence of CO_2 in H_2 in a fuel cell would reduce the fuel cell performance and could degrade the catalyst activity. The high percentage of CO_2 (up to 25%) and some other impurities, poison especially platinum based catalysts, and limit economic feasibility. Also CO_2 is found to form a cloud and block H_2 from reaching the platinum sites. Because of this unavailability of hydrogen a performance loss exists in fuel cells. Therefore upgrading biogas by removing CO_2 could make hydrogen to become acceptable for more advanced utilisation. Depending on the end use, biogas upgrading is necessary and it is important to optimize upgrading process in respect to low energy consumption, high efficiency and giving high hydrogen content in the upgraded biogas.

For this purpose several biogas upgrading processes including pressure or temperature swing adsorption, pressurized water scrubbing, amine swing absorption, cryogenic separation and membrane technologies have been developed for CO_2 removal. Therefore this study aims to thoroughly evaluate and describe the biogas upgrading technologies that are commercially available and in operation today. The technologies are described in detail by presenting the theory behind the separation mechanism, the upgrading process as a complete system and operational issues.

Keywords: Biohydrogen, biogas upgrading, carbon dioxide, membrane gas permeation

Hydrogen Gas Formation from Wastewater by Electro-hydrolysis

[1*]Serkan EKER, [2]Fikret KARGI
[1,2] Dokuz Eylul University, Department of Environmental Engineering, İzmir, Turkey

* E-mail: serkan.eker@deu.edu.tr

Abstract
Hydrogen gas production was obtained from organics present in wastewater by electro-hydrolysis. Electrical current generated by a using photovoltaic cells and was applied to wastewater using electrodes. Hydrogen gas production from electrolysis of pure water was less than 15% of that obtained from wastewater. Hydrogen gas yields up to 7.14 L H_2/g TOC were obtained. Hydrogen gas fraction in the gas phase varied between 75 and 99%. The results indicated that the major fraction of hydrogen gas was generated by electro-hydrolysis of organic compounds. Hydrogen gas production from electro-hydrolysis of wastewater using electrical power from photovoltaic cells was proven to be an inexpensive, fast and energy efficient method with TOC removal.

Keywords: Hydrogen gas, wastewater, electro-hydrolysis, photovoltaic cells

I. Introduction

Fossil fuels cause serious air pollution problems by formation of undesirable gases (SOx, NOx, COx) in the atmosphere despite being used as a major energy source for many years. Today, hydrogen gas is considered the main energy source of the future. Hydrogen gas is a clean, high-energy fuel (122 kJ/g) compared to fossil fuel. Currently, many technologies can be used for hydrogen production. However, many challenges are known to shift from fossil fuels to H_2 energy. Hydrogen gas, which is not readily available naturally, is produced by expensive processes such as natural gas reforming, electrolysis of water. These methods require high energy input.
Hydrogen gas production is achieved by providing fermentation of raw materials with high carbohydrate content. Dark and photo fermentation or sequential fermentations were used for bio-hydrogen gas production. Although these methods are carried out under proper operating conditions, low hydrogen gas formation rates are the drawbacks of these methods by Kapdan (2006). Electrolysis of water for hydrogen gas production has been studied extensively by Stojic (2003); Nagai (2003); Varkaraki (2003). Energy requirement for electrolysis of water is 4 kW h/m^3 H_2 while the energy content of hydrogen gas is 3.55 kW h/m^3 H_2. Water electrolysis using PEM containing cells requires net energy input for hydrogen gas production by Grigoriev (2006). Electro-hydrolysis of organic compounds present in waste materials is developed as a new approach for hydrogen gas production. Hydrogen gas production by DC current application to organic wastes and fermentation effluents have been reported in a few patents by Day (1980); Roychowdhury (2000); Paterek (2005). Photovoltaic cells have been applied to generate electrical power required for electrolysis of water by Khaselev (2001). Hydrogen gas production from industrial wastewater using electrical power generated by photovoltaic cell (PVC) was investigated in this study. A well-sealed and mechanically mixed reactor with stainless-steel electrodes was used. A voltage regulator and a battery were used to adjust the applied DC voltage and to store the electrical energy for use at the nighttime.

II. Experimental Set-up and Procedure

The experimental system consisted of a PVC panel with 80*120 cm dimensions, a voltage regulator, a battery and a stainless-steel sealed reactor with dimensions of 21 cm, heiht of 48 cm and volume of 16.8 L (Fig.1). Wastewater volume in the reactor was 13.2 L with a head space of 3.6 L. The PVC panel contained 32 cells providing 115 W, 18 V voltage with 6 A current. A voltage regulator was used to adjust voltage to the desired level of 13.5 V. A battery was used to store electrical energy generated by the PVC panel and to provide constant current to the reactor when the sunlight was not available. Mechanically mixed and sealed stainless-steel reactor contained aqueous organic waste, electrodes and a pressure gauge. Electrodes were used to transmit the electrical current (electrons) generated by the PVC to the aqueous medium in the reactor. Dimensions of the electrodes were L= 49.5 cm and D_o= 0.9 cm which were mounted on the head plate of the reactor and immersed in wastewater inside the reactor.

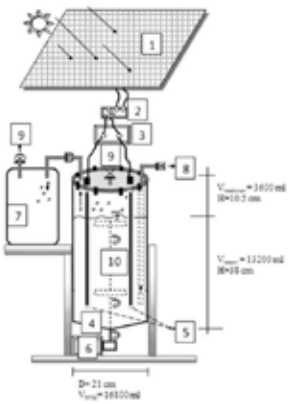


Fig. 1: A schematic diagram of the experimental set up used for hydrogen gas production from wastewater using photovoltaic cells. (1) Photovoltaic cell (PVC) or solar panel, (2) voltage regulator, (3) battery, (4) stainless-steel reactor containing aqueous organic waste, (5) electrodes, (6) mixing motor and blades, (7) hydrogen storage tank, (8) liquid feed/effluent port, (9) gas release port, (10) aqueous organic waste.

III. Analysis

Hydrogen gas was sampled from the headspace of the reactor by using gas-tight glass syringes and hydrogen concentration was determined by using a gas chromatograph (Agilent 6890). Nitrogen gas was used as carrier with a flow rate of 30 ml/min and the head pressure was 22 psi. The amount of total gas produced was determined by water displacement method everyday using sulfuric acid (2%) and NaCl (10%) containing solution. The cumulative hydrogen gas production was determined by Argun (2008). pH and ORP of the fermentation medium were monitored by using pH and ORP meters with relevant probes (WTW Scientific, Germany). Samples removed from fermentation media everyday were centrifuged at 7000 g to remove solids. Total organic carbon (TOC) content of wastewater was determined using clear supernatants after centrifugation of samples. TOC measurements were done using a TOC analyzer (Teledyne Tekmar Apollo 9000 Combustion TOC Analyzer, USA). Fe(II) ions released to the medium were measured by using an ICP analyzer (Optical Emission Spectrometer Optima 2100 OV ICP Analyzer, Perkin Elmer, USA).

IV. Results and discussions

The experiments were carried out using diluted wastewater and tap water to determine the extent of hydrogen gas evolution from water as compared to the wastewater. Fig. 2 depicts cumulative hydrogen production from water and wastewater with application of electrical power. Nearly 9.4 L hydrogen gas was produced within 432 h (18 days) from water electrolysis with 700 ml water loss from the reactor yielding hydrogen formation rate of 0.522 L/d. pH of water increased from 7.7 to 8.3 due to removal of hydrogen ions from water to form hydrogen gas. When the same DC power was applied to wastewater with an initial TOC of 4500 mg/L and nearly 95 L hydrogen gas was released within 22 days yielding hydrogen production rate of 4.32 L/d. Hydrogen gas production rate from wastewater was nearly 8 times grater than that obtained from water. Hydrogen gas was mainly produced by electrohydrolysis of organic compounds releasing protons to the medium. Stainless-steel electrode (anode) was ionized and anode released Fe(II) ions and electrons into the solution with the application of electric power. The released electrons reacted with the protons released from the decomposition and dissociation of organic compounds present in wastewater according to the following reaction.

$$\text{Organic compounds} \rightarrow 2H^+ + \text{decomposed organics}^- \quad (1)$$

$$2H^+ + 2e^- \rightarrow H_2(g) \quad (2)$$

Total organic carbon (TOC) analyses were carried out during the course of experiments, in order to determine TOC removal along with hydrogen gas evolution, Fig. 3 depicts variation of TOC content of wastewater with time. TOC decreased from nearly 4500 mg/L to 4200 mg/L. Total wastewater volume decreased from 13.2 L to 11.88 L with a 1.32 L water loss within 22 days. Hydrogen gas yield was nearly 10 L H_2/g TOC. pH of wastewater decreased slightly from 6.8 to 6.7. Hydrogen ion release from electrohydrolysis of organic compounds present in wastewater. Hydrogen ions reacted with electrons released from the stainless-steel anode to form hydrogen gas. Approximately, 2.03 mg/L Fe(II) was detected in the medium at the end of operation yielding a total of 27 mg Fe(II) release to the medium.

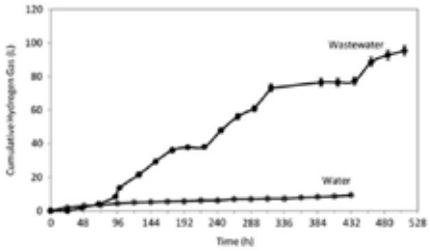


Fig. 2: Comparison of hydrogen production from water and wastewater using photovoltaic cell.

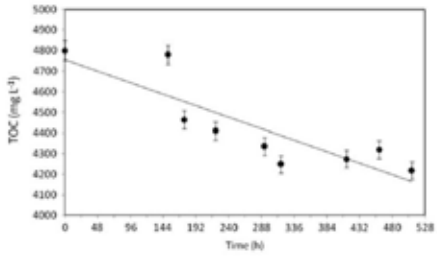


Fig. 3: Variation of TOC content of wastewater

V. Conclusions

Hydrogen gas production from electrolysis of pure water was lower than 15% of that obtained from wastewater. The results showed that the major fraction of hydrogen gas was produced by electrohydrolysis of organic compounds. Hydrogen gas yields up to 7.14 L H_2/g TOC were obtained. Hydrogen gas fraction in the gas phase varied between 75 and 99%. Hydrogen gas production from electrohydrolysis of wastewater using electrical power from a PVC panel was demonstrated to be an inexpensive, fast and energy efficient method as compared to electrolysis of water.

References

Argun H., Kargi F., Kapdan I.K., Oztekin R., Biohydrogen production by dark fermentation of wheat powder solution: effects of C/N and C/P ratio on hydrogen yield and formation rate, Int J Hydrogen Energy, 33:1813-9, (2008).

Day D.L., Steinberg M.P., Electrochemical conversion of organic material, US Patent no 4200505, April, (1980).

Grigoriev S.A., Porembsky V.I., Fateev V.N., Pure hydrogen production by PEM electrolysis for hydrogen energy, 31:171-175, (2006).

Kapdan I.K., Kargi F., Biohydrogen production from waste materials, Enzym Microb Technol, 38:569-82, (2006).

Khaselev O., Bansal A., Turner J.A., High-efficiency integrated multijunction photovoltaic/electrolysis systems for hydrogen production, Int J Hydrogen Energy, 26:127-32, (2001).

Nagai N., Takeuchi M., Kimura T., Oka T., Existence of optimum space between electrodes on hydrogen production by water electrolysis, Int J Hydrogen Energy, 28:35-41, (2003).

Paterek J.R., Method and apparatus for hydrogen production from organic wastes and manure, US Patent no: 6887692, May (2005).

Roychowdhury S., Process for production of hydrogen from anaerobically decomposed organic materials, US Patent no 6090266, July (2000).

Stojic D., Marcta M., Sovilj S., Miljanic S., Hydrogen generation from water electrolysis-possibilities of energy saving, J Power Sources, 118:315-9, (2003).

Varkaraki E., Lymberopoulos N., Zoulias E., Guichardot D., Poli G., Hydrogen based uninterruptible power supply. Int J Hydrogen Energy, 32:1589-96, (2007).

Electrohydrolysis application on metal plating wastewater to produce hydrogen gas

*Ebru Çokay, Yasin Gürler
Department of Environmental Engineering, Dokuz Eylül University, Turkey

*E-mail: ebru.cokay@deu.edu.tr

Abstract
Hydrogen gas production was investigated by electrohydrolysis method using metal plating washing wastewater. Different voltages generated by DC power supply were applied to metal plating wastewater in order to produce hydrogen gas. Effects of the voltage, reaction time and kind of metal on percent hydrogen gas production were investigated. Cumulative hydrogen gas volume increased up to 4V and then decreased with increasing voltages above 4V. Percent hydrogen gas in the gas phase also varied during the course of experiments and reached to nearly pure H_2 gas (95-99% H_2) at 4 V. The optimum DC voltage maximizing cumulative hydrogen gas volume (4000 mL), H_2 production rate (985 mL H_2 d^{-1}) and hydrogen percentage (99%) in the gas phase was obtained with wastewater which contains chrome at 4V. Nearly pure hydrogen gas formation in the gas phase is a significant development since the produced hydrogen gas can directly be used in fuel cells.

Keywords: Electrohydrolysis, Metal plating wastewater, Hydrogen gas production, TOC removal

I. Introduction

Search for clean and high energy fuels has gained significant attention over the last fifty years due to recent energy shortages and air pollution caused by the utilization of fossil fuels (Winter, 2005). Hydrogen gas is identified as one of the major clean energy sources of the future due to its high energy content (122 kJ g^{-1}) and reduced green house gas emissions as compared to fossil fuels. Hydrogen gas is not readily available in nature and is produced by costly processes such as steam reforming of natural gas or electrolysis of water requiring high energy inputs (Das, 2001). Hydrogen gas production by fermentation of carbohydrate rich renewable raw materials such as biomass has been considered as a viable approach due to operation under mild conditions. Major obstacles in bio-hydrogen production by fermentation are low hydrogen yields and formation rates due to slow bacterial metabolisms (Kapdan, 2006). For that reason, hydrogen gas production by electrohydrolysis of organic compounds and metals present in waste materials is a rather new approach. A few recent patents on hydrogen gas production by DC current application to wastes and fermentation effluents have been reported (Kargı, 2011). The major objective of this study is to investigate the effects of the applied DC voltage and kind of metals in wastewater on percent hydrogen gas production and cumulative hydrogen production.

II. Experimental procedure

The experimental set-up consisted of a DC power supplier, two aluminum electrodes and 1 L serum bottles. Wastewaters were obtained from metal plating industry. Wastewater contains chrome, copper and nickel metals. The metallic wastewater (300 mL) was placed inside serum bottles. Aluminum electrodes were immersed inside the bottles containing wastes and connected to the DC power supply by wires. The applied DC voltages (V) and the amperes (A) were monitored during the course of experiments. Produced hydrogen gas was collected in the head space of the serum bottles. Hydrogen gas was sampled from the head space of the bottles by using gas-tight glass syringes and hydrogen concentration was determined by using a gas chromatograph.

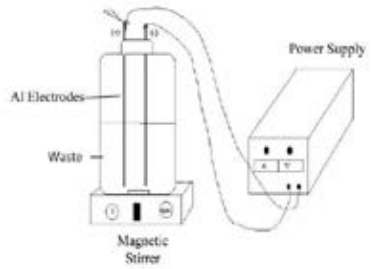


Fig. 1. A schematic diagram of the experimental set-up.

III. Results and discussion

Three set of experiments were performed to determine the effects of applied DC voltage on the rate and extent of hydrogen gas production from each metallic wastewater. Variation of cumulative hydrogen formation with time for different applied DC voltages between 1 V and 5 V were investigated. Two control bottles containing metallic wastewater with no voltage application (control-I) and water with DC voltage application (control-II) were added to each set. The first control bottle was used to evaluate effects of natural anaerobic decomposition of washing wastewater on hydrogen gas production. The second control bottle was used to determine H_2 production by electrolysis of water. According to results of control experiments, cumulative hydrogen gas evolution from electrolysis of water and natural decomposition of metallic wastewater are negligible. Hydrogen gas evolution (approximately 10 mL) was observed in the experimental bottle when no voltage was applied to the metallic wastewater for a period of 97.5 hours.

Cumulative hydrogen gas volume and hydrogen gas percentage were evaluated by different voltages. For all kind of wastewater, cumulative hydrogen volume generally increased up to 4V and then decreased or no significantly raised with increasing voltages above 4V. Percent hydrogen gas in the gas phase also varied during the course of experiments and reached to pure H2 gas (95-99% H_2) at 4 V.

Variation of cumulative hydrogen gas volume for chromic wastewater at different DC voltages by electrohydrolysis is shown in Figure 2. The optimum hydrogen gas production varies depending on the initial DC voltage. It also depends on reaction time. At high reaction times and high DC voltages, cumulative hydrogen gas volume was increased.

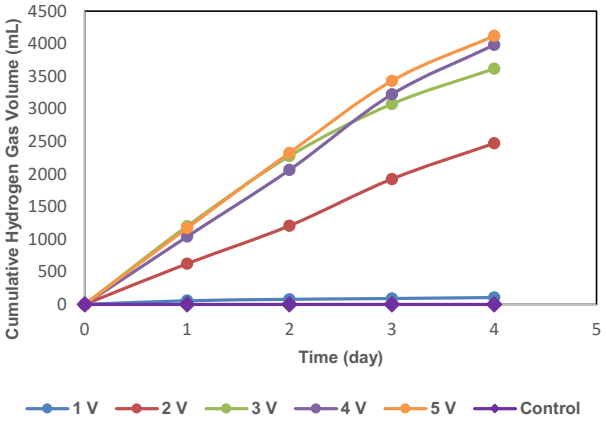


Fig. 2: Variation of cumulative hydrogen gas volume at different DC Voltages by electrohydrolysis using chrome washing wastewater

Therefore, the optimum DC voltage maximizing cumulative hydrogen gas volume (4000 mL), H_2 production rate (985 mL H_2 d^{-1}) and hydrogen percentage (100%) in the gas phase was 4V. In addition to this, the highest TOC removal (43%) was also obtained with 4 V DC voltage.

Variation of cumulative hydrogen gas volume for all wastewater with different reaction times at different metallic wastewaters by electrohydrolysis is shown in Figure 3. The optimum hydrogen gas production varies depending on the kind of metalic wastewater. It also depends on reaction time. After application of different DC voltages on metalic wastewater, cumulative hydrogen gas production and percentage of hydrogen gas were evaluated. Maximum cumulative hydrogen gas production was observed with chromic wastewater at 4 V. Cumulative hydrogen volume increased up to 4V and then decreased with increasing voltages above 4V. Percent hydrogen gas in the gas phase also varied during the course of experiments and reached to pure H_2 gas (95-99 % H_2) at 4 V.

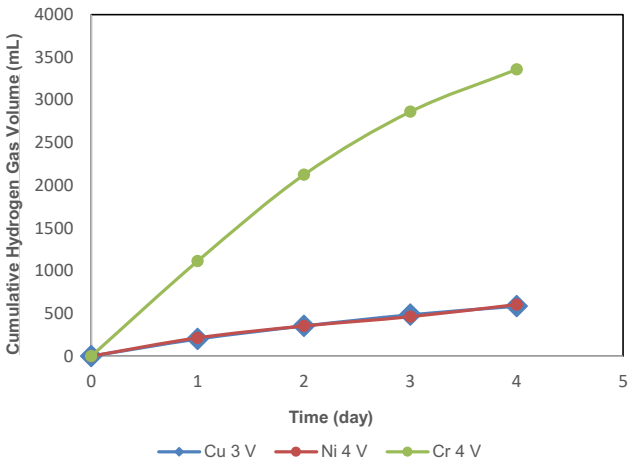


Fig. 3: Variation of cumulative hydrogen gas volume with different reaction times at different metallic wastewater by electrohydrolysis

IV. Conclusion

Hydrogen gas production by electrohydrolysis of metalic wastewater was realized by applying DC voltages between 1 and 5V through aluminum electrodes. The applied voltage affected the rate and extent of H_2 gas formation. According to results, the highest cumulative hydrogen gas evolution (4000 mL) and hydrogen formation rate (985 mL H_2 d^{-1}) were obtained with chromic wastewater at 4V DC voltage. Electrohydrolysis of metalic wastewater was proven to be an effective method for hydrogen gas production. The highest TOC removal (43%) was also obtained with 4 V DC voltage. Pure hydrogen gas formation in the gas phase is a significant development since the produced hydrogen gas can directly be used in fuel cells.

References

Das D, et. al, Int J Hydrogen Energy 26 (2001)

Kapdan IK. et. al, Enzyme Microb Technol.38, 569-82, (2006).

Kargi F. et. al, Int J Hydrogen Energy 36,3457-64, (2011)

Winter, CJ. Int J Hydrogen Energy 30, 681-5 (2005)

Langmuir–Hinshelwood kinetic model to capture the manganese(0) nanoparticles supported on ceria-catalyzed hydrolysis of sodium borohydride

[1*]Sibel Duman, [2]Saim Özkar
[1]Department of Chemistry, Bingol University, 12000 Bingol, Turkey
[2]Department of Chemistry, Middle East Technical University, 06800 Ankara, Turkey

* E-mail:sduman@bingol.edu.tr

Abstract
Because of depletion of fossil fuel resources, environmental pollution and global warming caused by a steep increase in carbon dioxide and other greenhouse gases in the atmosphere, there has been an increasing demand for the renewable energy sources, on the way towards a sustainable energy future. Hydrogen has been considered as a clean and environmentally benign new energy carrier for heating, transportation, mechanical power and electricity generation. Long term exploration has shown that the most effective and safest way of storing hydrogen is to use solid media such as sorbent materials or hydrides. Among the chemical hydrides considered as hydrogen storage material, sodium borohydride ($NaBH_4$) has received the most extensive attention owing to its combined advantages of: (i) the high hydrogen storage capacity (10.8wt%); (ii) the high stability and no flammability of its alkaline solutions; (iii) the optimal control on hydrogen generation rate by supported catalysts; (iv) the acceptable hydrogen generation rate even at low temperature; (v) the availability and easy handling ; (vi) an efficient hydrogen source which releases hydrogen gas in the amount double of its hydrogen content upon hydrolysis in water.

The present study focused on kinetics of hydrogen release through hydrolysis of sodium borohydride $NaBH_4$ in the presence of manganese(0) nanoparticles supported on ceria. From the hydrogen evolution curves, the reaction constant versus the $NaBH_4$ concentration, apparent activation energy, rate constant were determined. It was noticed that the hydrolysis kinetics depends on temperature of reaction (i.e. 20–40°C) and $NaBH_4$ concentration (1.0-5.0 mmol). Hence, the kinetic constants were analyzed using existing kinetic models. The bimolecular Langmuir–Hinshelwood model satisfactorily captured the behavior of our catalyst consisting of manganese(0) nanoparticles supported on ceria. Herein, the kinetic data, the kinetic model, the hydrolysis mechanism and the issues still to be addressed are reported and discussed.

Keywords: Ceria, hydrolysis mechanism, manganese, sodium borohydride,

Acknowledgements
Partial support by the Turkish Academy of Sciences is acknowledged. SD is thankful to the Scientific and Technological Research Council of Turkey (TUBITAK) for the fellowship (National Postdoctoral Research Scholarship Program 2218).

References
Andrieux J., Umit B.D., Mielea P., Langmuir–Hinshelwood kinetic model to capture the cobalt nanoparticles-catalyzed hydrolysis of sodium borohydride over a wide temperature range. Catalysis Today. 170, 13– 19 (2011).

Asli B., Serdar E., Saim O. Inci E., Kinetics of hydrogen generation from hydrolysis of sodium borohydride on Pt/C catalyst in a flow reactor, Int. J. Energy Res., 37, 443–448 (2013)

Germain J., Freechet M.J., Svec F., Nanoporous Polymers for Hydrogen Storage. Small, 10, 1098–1111 (2009).

IAC Report. Lighting the way towards a sustainable energy futures. Interacademy Council: Amsterdam (2007).

Lee J., Kong K.Y., Jung C.R., Cho E., Yoon S.P., Han J., Lee T.G., Nam S.W., A structured Co–B catalyst for hydrogen extraction from NaBH4 solution. Catalysis Today, 120, 305–310 (2007).

Rand D.A.J., Dell R.M., Hydrogen Energy Challenges and Prospects 1st ed. RSC Publishing: Cambridge (2008).

Sandrock G., A panoramic overview of hydrogen storage alloys from a gas reaction point of view. Journal of Alloys and Compounds, 293, 877–888 (1999).

Turner J., Sverdrup G., Mann K., Maness P.G., Kroposki B., Ghirardi M., Evans R.J., Blake D., Renewable hydrogen production. International Journal of Energy Research, 32, 379–407 (2008).

Xu D., Zhang H., Ye W., Hydrogen generation from hydrolysis of alkaline sodium borohydride solution using Pt/C catalyst. Catalysis Communications, 8, 1767–1771 (2007).

Zhang J., Fisher T.S., Gore J.P., Hazra D., Ramachandran P.V., Heat of reaction measurements of sodium borohydride alcoholysis and hydrolysis. International Journal of Hydrogen Energy, 31, 2292–2298 (2006).

Green dehydrogenation of dimethylamine borane catalyzed by Nickel(0) and Copper (0) nanoparticles

Hakan DEMİR, Ali ÖZDEMİR and *Sibel DUMAN
Department of Chemistry, Bingol University, 12000 Bingol, Turkey

* E-mail:sduman@bingol.edu.tr

Abstract
The synthesis of metal nanoparticles (NPs) by a sustainable technology is very important to solve many challenges in modern materials science. “Top-down” approach which utilizes physical methods and the “bottom-up” approach which employs solution-phase colloidal chemistry are traditional methods of synthesis of metal NPs. Size distributions of NPs obtained by top-down methods are very broad and typically large (>10 nm) and are giving irreproducible catalytic activities. In contrast, bottom-up method is the most widely used approach and provides more convenient ways to control the size of the NPs than top down methods. However, preparation of monodisperse NPs on large scales, which can be used in practical applications, is very difficult to obtain via both of these methods. Therefore, in recent years, atom-economy and solvent-free approaches have attracted the attention for a permanent solution to this problem. Moreover, solvent-free approaches have drawn considerable attention and popularity, both from an environmental point of view and for synthetic advantages in terms of yield, selectivity, and simplicity of the reaction procedure.

Herein, DMAB that has low melting point (~35°C) was used as both reducing and stabilizing agent for synthesis of Ni(0) and Cu(0) NPs. We report that Ni(0) and Co(0) NPs are normally obtained by decomposition of $NiCl_2$ and $Cu(acac)_2$, respectively, during the solvent-free dehydrogenation of DMAB under inert gas atmosphere at room temperature. The solvent-free dehydrogenation of DMAB in the presence Ni(0) and Cu(0) NPs corresponding to an initial turnover frequency of 21 and 19 h^{-1}, respectively. The Ni(0) and Cu(0) NPs were characterized by TEM, HRTEM, TEM-EDX, UV-Vis. and XRD techniques. The heterogeneity of the in situ generated Ni(0) and Cu(0) NPs in the solvent-free dehydrogenation of DMAB were identified by carbon disulfide poisoning experiments. Also, the detailed kinetics in the solvent-free dehydrogenation of DMAB was studied by varying catalyst and substrate loadings and temperature.

Keywords: Copper, dimethylamine-borane, green dehydrogenation, hydrogen storage, nickel.

Acknowledgements
We are grateful to the Bingol University Scientific Research Projects (BUBAP, Grant Number: BAP-130-96/97-2011) for financial support.

References

Bonnemann H., Richards R.M., Nanoscopic metal particles-synthetic methods and potential applications. Eur. J. Inorg. Chem., 10, 2455-2480 (2001).

Crooks R.M., Zhao M.Q., Sun L., Chechik V., Yeung L.K., Dendrimer-encapsulated metal nanoparticles: Synthesis, characterization, and applications to catalysis. Acc. Chem. Res., 34, 181-190 (2001).

Dahl J.A., Maddux B.L.S., Hutchison J.E., Toward greener nanosynthesis. Chem. Rev., 107, 2228-2269 (2007).

Fu X.Y., Wang Y.A., Wu N.Z., Gui L.L., Tang Y.Q., Shape-selective preparation and properties of oxalate-stabilized Pt colloid. Langmuir, 18, 4619-4624 (2002).

Hakan D., Sibel D., Monodisperse nickel nanoparticles in the solvent-free dehydrogenation of dimethylamine borane. Int. Hydrogen Energy, 40, 10063-10071 (2015).

Kalidindi S.B., Sanyal U., Jagirdar B.R. Metal nanoparticles via the atom-economy green approach. Inorg. Chem., 49, 3965-3967 (2010).

Sheldon R.A., Green solvents for sustainable organic synthesis: state of the art. Green Chem., 7, 267-278 (2005).

Quinones L., Grazul J., Martinez-Inesta M.M., Synthesis of platinum nanostructures in zeolite mordenite using a solid state reduction method. Mater. Lett., 63, 2684-2686 (2009).

Rogach A.L., Talapin D.V., Shevchenko E.V., Kornowski A., Haase M., Weller H., Organization of matter on different size scales: Monodisperse nanocrystals and their superstructures. Adv. Funct. Mater.,12, 653-664 (2002).

Willner I., Mandler D.. Characterization of Pd-betacyclodextrin colloids as catalysts in the photosensitized reduction of bicarbonate to formate. J. Am. Chem. Soc., 111, 1330-1336 (1989).

Hydrogen Generation From the Hydrolysis of Dimethylamine- Borane at Room Conditions by Using Polyvidone Protected Ruthenium Nanocatalyst

***Mehmet Gülcan*, Yaşar Karataş**

Van Yüzüncü Yıl Üniversitesi, Fen Fakültesi, Kimya Bölümü, Tuşba-Van

Boron based chemical hydrides (LiBH4, NaBH4, Ca(BH4)2, Mg(BH4)2) and boron-nitrogen (B–N) compounds (NH-3BH3, NR3BH3 (R = H or alkyl), (CH3)2NHBH3, NH3B3H7, NH4B3H8, N2H4BH3) have been considered as solid hydrogen storage materials. Among these materials, B–N compounds are much better suited for this purpose due to their high gravimetric hydrogen storage capacity. Dimethylamine-borane ((CH3)2-NHBH3, DMAB) is appropriate material due to its high efficiency of H2 production, high stability, and nontoxicity (Caliskan et al. 2012; Wechsler et al. 2008; Zahmakiran and Özkar 2009). Hydrolysis of DMAB produces 3 mol of H2 per mole by using 2 mol of water (1):

Herein we report highly active nanocatalyst for the room temperature dehydrogenation of dimethylamine-borane in water. Polyvidone protected Ru nanocatalyst was synthesized via a classical alcohol reduction technique and were characterized by carrying out TEM, HR-TEM, TEM/EDX, P-XRD analysis, UV/Vis and XPS spectroscopy. Moreover, detailed kinetic studies on the catalytic hydrolysis reaction were applied to assess the activation parameters.

Keywords: Nanocatayst, dimethylamine-borane, polyvidone, hydrolysis, ruthenium

Highly Effective PVP-stabilized Rh-Ru Bimetallic Nanoparticles for the Dehydrogenation of Methylamine-borane in Water

***Mehmet Gülcan*, Yaşar Karataş**

Van Yüzüncü Yıl University, Faculty of Science, Department of Chemistry, Tuşba-Van Turkey

Methylamine-borane (CH3NH2-BH3, MeAB) is an ammonia-borane derivative and it has been studied in hydrolysis reaction over the past years due to its very high hydrogen density of 11.1%. According to the eqn (1), 3 moles of hydrogen can be obtained from the dehydrogenation of MeAB in water per mole MeAB in the presence of a suitable catalyst, which is considered to be a more advantageous method when compared to other systems that produce hydrogen using MeAB such as thermolysis and non-aqueous catalytic dehydrogenation (Gülcan and Karataş, 2017; Staubitz et al. 2010; Yang et al. 2012).

In the current work, we aimed to prepare and characterize PVP-stabilized Rh-Ru bimetallic nanoparticles and to use them as an highly effective catalyst for dehydrogenation of MeAB in water at room temperature. The PVP-stabilized Rh-Ru bimetallic nanoparticles were synthesized using a classical alcohol reduction method (Gülcan and Karataş, 2017) and characterized by using TEM, HR-TEM, TEM/EDX, P-XRD, UV/Vis and XPS techniques.

Keywords: Nanoparticles, methylamine-borane, PVP, dehydrogenation, rhodium, ruthenium

Thermodynamic Analysis of a Unique Integrated Photoelectrochemical System for Multigeneration Purposes

Canan Acar[1], Ibrahim Dincer[2]
[1] Faculty of Engineering and Natural Sciences, Bahcesehir University
Çırağan Caddesi No: 4 – 6 34353 Beşiktaş, Istanbul, Turkey
[2] Faculty of Engineering and Applied Science, University of Ontario Institute of Technology
2000 Simcoe Street North, Oshawa, Ontario, L1H 7K4, Canada, and Faculty of Mechanical Engineering, Yildiz Technical University, Besiktas, Istanbul, Turkey

Email: Canan.Acar@eng.bau.edu.tr

Abstract
Hydrogen is a highly versatile energy carrier that may become one of the key pillars to support the future CO_2-free energy infrastructure. When used in fuel cells, H_2 is converted to water and it gives little or zero exhaust of greenhouse gases. For H_2 economy to succeed, it needs to be produced in a clean, sustainable, reliable, and feasible way. The main objective of this study is to develop and investigate a continuous type hybrid photoelectrochemical-chloralkali H_2 production reactor that converts the by–products into useful industrial commodities (i.e., Cl_2 and NaOH). This system maximizes solar spectrum use by taking advantage of photocatalysis and PV/T. Furthermore, by using electrodes as electron donors to drive the photochemical reaction, the potential of pollutant emissions is minimized. The final products of this novel integrated system can be listed as H_2, Cl_2, NaOH, heat, and electricity. In this study, the effects of operating temperature on H_2, Cl_2, heat, and electricity production, energy and exergy efficiencies, and exergy destruction rates are presented.

Keywords: Energy, exergy, efficiency, hydrogen production, multigeneration, sustainability, solar energy

I. Introduction

One of the most important challenges of the twenty–first century is keeping up with the growing worldwide energy needs due to increasing population and rising standards of living. In 2013, 9,301 Mtoe energy was consumed by approximately seven billion people worldwide. By 2050, these numbers are expected to go up to 20,000 Mtoe and nine billion, respectively (IEA, 2015; Friedlingstein et al., 2014). Meeting the significantly escalating global energy requirements with no or minimal environmental damage and fossil fuel dependence can only be accomplished by employing clean energy systems. These systems can present substantial environmental, energetic, financial, and societal advantages. To be considered sustainable, an energy system ought to meet these conditions: (i) insignificant or zero undesirable environmental or societal influence; (ii) negligible or no natural source exhaustion; (iii) capable of meeting the present and forthcoming population's energy requirements; (iv) reliable, affordable, and effective fashion; (v) air, land, and water safety; (vi) minor or zero net GHG emissions; and (vii) well-being at present with no burden to prospect generations (Dincer and Acar, 2015).

By taking sustainability as the primary motivating factor, this study aims to develop and thoroughly investigate an integrated photoelectrochemical cell for H_2, Cl_2, NaOH, heat, and electricity generation. The integrated system consists of (i) solar splitter which sends the low energy content of solar spectrum to the PV/T subsystem, (ii) PV/T for cogeneration of heat and electricity; and (iii) a hybrid photoelectrochemical cell which can produce H_2, Cl_2, and NaOH. In this study, comprehensive thermodynamic analysis is conducted to calculate the H_2, Cl_2, heat and electricity generation, energy and exergy efficiencies, and exergy destruction rates. The effects of operating temperature on H_2, Cl_2, heat and electricity generation, energy and exergy efficiencies, and exergy destruction rates are also investigated.

II. System Deescription and Analysis

A block illustration of the integrated system is shown in Fig. 1 which describes the large scale conceptual system. The solar irradiation (Stream 1) is sent to the solar spectral splitter (Unit I). Here, photons with wavelengths up to 400 nm is sent directly to the hybrid reactor (Unit III). Rest of the spectrum (Stream 2) is sent to the PV/T (Unit II) where the produced electricity (Stream 4) is sent to support Unit III. Excess electricity (Stream 5) is served as a product of the integrated multi-generation system. In order to minimize any efficiency losses, PV/T is cooled down and the recovered heat is used to heat up Unit III (Stream 6) when operating at temperatures higher than the environmental temperature. Stream 7 is the heat product, which is recovered from the PV/T and not used by Unit III.

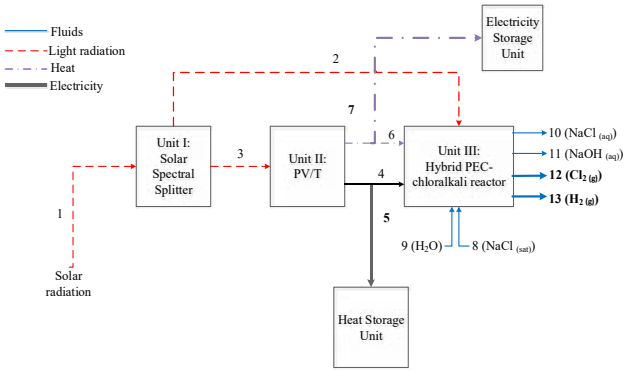


Fig. 1: Conceptual block diagram of integrated system for solar H_2, Cl_2, electricity, and heat production.

Thermodynamic performance of the system is examined by conducting quantitative energy and exergy analyses. Throughout this study, the following assumptions are utilized:

- Environmental temperature (T_0) and pressure (P_0) are 20°C and 1 atm, respectively.
- All streams and components are at operating temperature and pressure at all times.
- All processes take place in steady-state and steady-flow.
- All processes proceed to completion.
- Changes in potential and kinetic energies are negligible.
- Change in the control volumes (reactor and integrated system units) is disregarded.
- H_2, O_2, and Cl_2 gases are presumed to be ideal.
- The heat losses to environment are neglected.
- The auxiliary components are assumed to be well insulated and conduct electricity with no loss.
- The spectral splitting system is evaluated as reported by Zamfirescu and Dincer (2014).

For the integrated multi-generation system, a hypothetical location is chosen where sufficient solar irradiation exists, which is presumed to be 1 kW/m^2 with AM1.5G solar spectrum. Number of annual operational sunlight hours is taken as 2000 h (Zamfirescu and Dincer (2014). The integrated systems' energetic and exergetic performance can be evaluated based on the number of valuable products definition (Tab. 1).

Tab. 1: Summary of energy and exergy efficiencies of integrated system.

	Valuable products	Energy efficiency	Exergy efficiency
1	H_2	$\eta_1 = \frac{\dot{E}_{13}}{\dot{E}_1}$	$\psi_1 = \frac{\dot{E}x_{13}}{\dot{E}x_1}$
2	H_2, Cl_2	$\eta_2 = \frac{\dot{E}_{12}+\dot{E}_{13}}{\dot{E}_1}$	$\psi_2 = \frac{\dot{E}x_{12}+\dot{E}x_{13}}{\dot{E}x_1}$
3	H_2, Cl_2, Electricity	$\eta_3 = \frac{\dot{E}_5+\dot{E}_{12}+\dot{E}_{13}}{\dot{E}_1}$	$\psi_3 = \frac{\dot{E}x_5+\dot{E}x_{12}+\dot{E}x_{13}}{\dot{E}x_1}$
4	H_2, Cl_2, Electricity, Heat	$\eta_4 = \frac{\dot{E}_5+\dot{E}_7+\dot{E}_{12}+\dot{E}_{13}}{\dot{E}_1}$	$\psi_4 = \frac{\dot{E}x_5+\dot{E}x_7+\dot{E}x_{12}+\dot{E}x_{13}}{\dot{E}x_1}$

III. Results and Discussion

The integrated system performance is investigated based on varying the operating temperature: between 20°C and 80°C. The effect of the operating temperature on the integrated system's H_2 and Cl_2 production is presented in Fig. 2. Fig. 2 shows that both H_2 and Cl_2 production rates increase with increasing operating temperatures. At 20°C, the H_2 production rate is about 4.1 g/h (~ 48 L/h) and the Cl_2 production rate is around 124 g/h (~ 42 L/h). These amounts increase up to 4.9 g/h (70 L/h) for H_2 and 148 g/h (60 L/h) for Cl_2 at 80°C. The reason of these increases is the enhanced conductivity of the system components and the membrane with increasing operating temperatures. With enhanced conductivities, potential losses are reduced, resulting an increased production from the same amount of input energy.

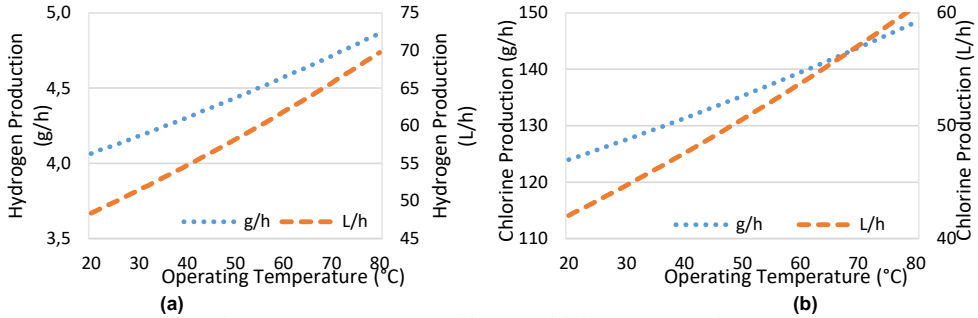


Fig. 2: Effect of operating temperature on (a) H_2 and (b) Cl_2 production of integrated system.

Fig. 3 shows the effect of the operating temperature on the electricity and heat production in the integrated system. Fig. 3 shows that with increasing operating temperatures, both electricity and heat production rate decreases. At 20°C, the electricity production is about 158 W and the heat production is around 792 W. These amounts decrease to 104 W for electricity and 296 W for heat at 80°C. The reason of these decreases is the increased electricity and heat consumption of the reactor with increasing operating temperatures. The solar irradiation is considered the only input to the integrated system which is assumed to be set to 1000 W/m^2 and only excess electricity and heat are the products of the integrated system. Therefore, when the reactor electricity and heat demand increases, the electricity and heat productions decrease.

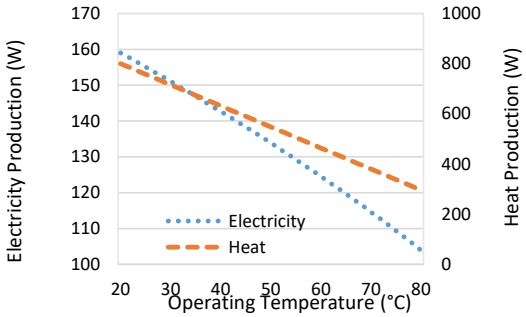


Fig. 3: Effect of operating temperature on electricity and heat production of integrated system.

When investigating the effect of the operating temperature on the exergy destruction rate, inlet flow rate is 1g/s NaCl and 1 g/s H_2O, environmental temperature is 20°C, and irradiation level is 1000 W/m^2. The total photoactive area is 4 m^2. The effect of the operating temperature on the exergy destruction rate is presented in Fig. 4. The exergy destruction rate increases with increasing operating temperatures. At 20°C, the exergy destruction rate is about 23 W. This amount increases to 348 W at 80°C. The primary reason of this trend is the increased heat consumption of the reactor.

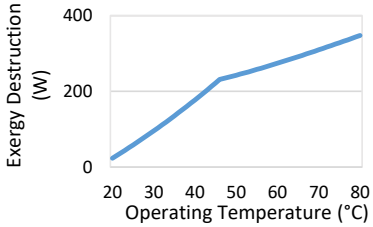


Fig. 4: Effect of operating temperature on exergy destruction of integrated system.

When investigating the effect of the operating temperature on the energy and exergy efficiencies, the inlet flow rate is 1g/s NaCl and 1 g/s H_2O, environmental temperature is 20°C, and the irradiation level is 1000 W/m^2. The total photoactive area is 4 m^2. The results are presented in Fig. 5. There are four different efficiency descriptions, each one is based on the number of useful products, which are explained in Tab. 1. In all cases, the input energy is constant since the irradiation level is fixed to 1000 W/m^2 and the photoactive area does not change.

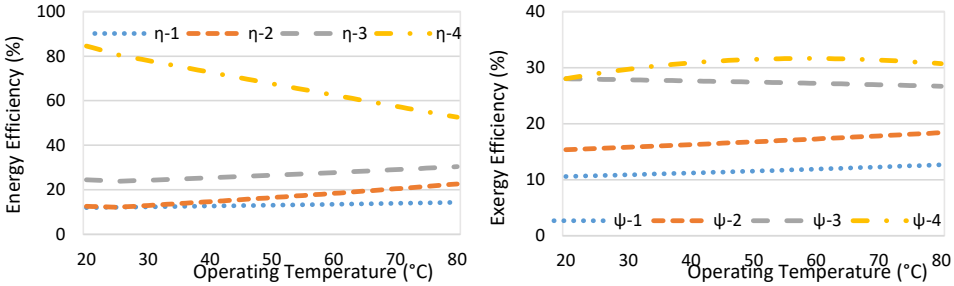


Fig. 5: Effect of operating temperature on (a) energy and (b) exergy efficiencies of integrated system.

Fig. 5 shows that the energy and exergy efficiencies of the H_2 (η-1 and ψ-1) and H_2-Cl_2 (η-2 and ψ-2) increase with increasing operating temperature since higher H_2 and Cl_2 production rates are observed at higher operating temperatures. At 20°C, η-1 and ψ-1 are 12% and 11%, respectively; and they increase to 14% and 13% at 80°C. Similarly, η-2 and ψ-2 are 13% and 15% at 20°C and they are 23% and 18% at 80°C. When the electricity is considered as a useful amount as well, η-3 rises from 25% to 28% and ψ-3 decreases from 30% to 27% between 20°C and 80°C. When H_2, Cl_2, electricity, and heat are considered all as useful outputs, the overall energy efficiency (η-4) decreases from 85% to 53% when operating temperature is increased from 20°C to 80°C. However, within the same operating temperature interval, the overall exergy efficiency (ψ-4) increases from 28% to 31%. This is due to the increasing exergetic content of the heat with increasing operating temperatures as environmental temperature is fixed to 20°C.

V. Conclusions

The present integrated system is thermodynamically investigated under various operating temperatures. Under the operating temperature increases from 20 to 80°C, the following are achieved:

- The hydrogen production rate increases from 4.1 g/h (~ 48 L/h) to 4.9 g/h (70 L/h)
- The chlorine production rate increases from 124 g/h (~ 42 L/h) to 148 g/h (60 L/h)
- The electricity production rate decreases from 158 W to 104 W
- The heat production rate decreases from 792 W to 296 W
- The exergy destruction rate increases from 23 W to 348 W
- The overall energy efficiency decreases from 85% to 53%
- The overall exergy efficiency increases from 28% to 31%

References

Dincer, I., Acar, C. (2015). A review on clean energy solutions for better sustainability. *International Journal of Energy Research*, 39(5), 585–606.

Friedlingstein, P., Andrew, R. M., Rogelj, J., Peters, G. P., Canadell, J. G., Knutti, R., Luderer, G., Raupach, M. R., Schaeffer, M., Van Vuuren, D. P., Le Quéré, C. (2014). Persistent growth of CO_2 emissions and implications for reaching climate targets. *Nature Geoscience*, 7(10), 709–715.

International Energy Agency (IEA) Technical Report. 2015 Key World Energy Statistics. (2015). *Website*, [accessed on 06.02.2018] https://www.iea.org/publications/freepublications/publication/KeyWorld_Statistics_2015.pdf.

Zamfirescu, C., Dincer, I. (2014). Assessment of a new integrated solar energy system for hydrogen production. *Solar Energy*, 107, 700–713.

Biohydrogen Production From Fruit And Vegetable Wastes Through Dark Dry Anaerobic Fermentation Under Thermophilic Condition

[1,2]Haris Nalakath Abubackar, [1]Okyanus Yazgın, [1]Bensu Günay, [3]Kubra Arslan, [1]Tuğba Keskin Gündoğdu, [1,3,*]Nuri Azbar
[1] Ege University, Engineering Faculty, Bioengineering Department, Izmir, 35100, Turkey
[2] University of La Coruña, Faculty of Sciences and Center for Advanced Scientific Research (CICA), La Coruña, E15008, Spain
[3] Ege University, Center for Environmental Studies, Izmir, 35100, Turkey

* E-mail:nuri.azbar@ege.edu.tr

Abstract
Dark fermentative hydrogen production from organic waste is an attractive technique that simultaneously treats waste along with generation of renewable fuel (Keskin et al., 2018). In this study, a relative new technology named dark dry fermentation was tested in a 55-L reactor to treat fruit and vegetable waste (FVW) along with simultaneous generation of biohydrogen. To understand the effect of autoclaving as a pretreatment method on FVW for subsequent biohydrogen production, two independent experiments were performed; one with autoclaved waste (EXP1) and another by using non autoclaved waste (EXP2). From the analyses, it was found that maximum hydrogen % obtained for EXP1 was 41% whereas, for EXP2 was 21%. In terms of total hydrogen produced, around 30% higher production was observed with EXP1 compared to EXP2. The hydrogen yields for EXP1 and EXP2 were respectively, 27.19 and 20.81 $mLH_2.gVS^{-1}$, and the metabolites (VFAs) preferentially produced were acetic acid and butyric acid.

Keywords: Biohydrogen, dry fermentation, fruit and vegetable waste (FVW), bioenergy

I. Introduction

The worldwide generation of organic fraction of municipal solid waste (OFMSW) is estimated to be around 1012 million by 2025. These biodegradable wastes are generally disposed by landfilling or by open dumping. One way to treat them properly together with generation of energy is by applying anaerobic digestion (Pavi et al. 2017). This not only mitigates the climate change caused from the greenhouse gas emissions but also helps to achieve sustainability in terms of energy. Several countries set targets to reduce the emission of environmentally harmful gases. In this respect, European Environment Agency target in the transport sector is to achieve a reduction of 80–95 % greenhouse gas emissions by 2050. According to the revised European Directive 2009/28/EC, by 2030 27% renewable energy consumption should be achieved. Overall, to meet these requirements, a huge leap in research has been noticed for the past decade to find an alternative renewable energy source (Yun et al. 2017).

Hydrogen is considered as a promising energy source in terms of its high energy content (143 MJ/Kg) compared to any existing fuel, and its combustion generates water as the only by-product. To date, hydrogen was produced mainly from fossil fuels with 48% from natural gas, 30% from heavy oils and naphtha, and 18% from coal (Nikolaidis and Poullikkas 2017). An alternative method of producing hydrogen is through a technology named anaerobic digestion (AD) by using strict or facultative anaerobes. These anaerobes have the ability to degrade and convert the complex polysaccharides present in the biomass to valuable products such as hydrogen, acetic acid, butyric acid and various other higher fatty acids (Ghimire et al., 2015).

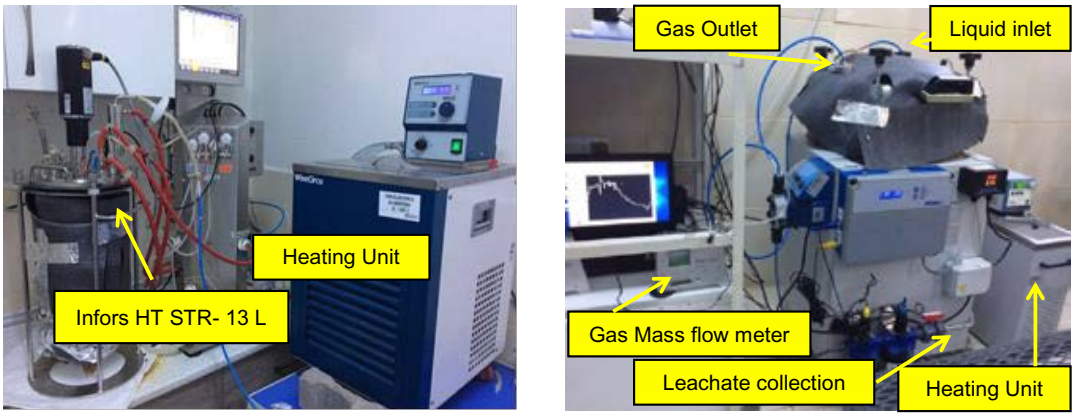
AD can be classified into: wet fermentation where the total solid content is less than 10% and dry fermentation with total solid content greater than 10%. Dry fermentation is a promising technology due to its several advantages like requirement of smaller reactor volume, easiness in handling digestate and lesser water wastage (Karthikeyan and Visvanathan, 2013). Although many studies have performed for the biogas production through dry fermentation still not much studies on biohydrogen production using this process. In this study, dry fermentation were performed under thermophilic condition to understand the effect of pretreatment (autoclaving) of FVW on biohydrogen production under thermophilic condition.

II. Experimental Set-up and Procedure

The experiments were performed in a fully automated stirred tank (ST) single walled reactor of a total volume of 13-L (INFORS HT Labfors 5 reactor, Switzerland) which was inoculated with hydrogen producing microbes and a 55-L custom made reactor (DF) where the wastes and hydrogen producers were mixed and filled for treatment (Fig.1). Temperature of the ST reactor was controlled via an inbuilt temperature sensor (pt100) that was inserted in a blink pocket of the reactor and by using cold finger to circulate the cooling water. Dry fermentor was fabricated from an autoclave unit and an aluminum basket with holes around the sides and bottoms were placed inside the unit for introducing the FVWs and holding it, allowing the leachate to flow freely to the bottom of the DF unit to the leachate collection tube. Inside temperature of the DF unit was controlled by circulating controlled temperature water through the stainless steel coil which is placed inside the DF unit. A sprayer was fixed under the cap of the DF to spray the ST liquid through the FVWs for continuous addition of microbes and also to washout the metabolites adhere on the FVWs.

A volumetric gas flow meter (μFlow, Bioprocess Control AB, Sweden) having detection range from 20 to 4000 ml/h was connected each to the gas outlet of the ST and the DF to monitor the total gas produced. The gas flow

rate and total gas volume were normalized by the gas flow meter with real-time pressure and temperature and were accurately measured and read. Gas sampling ports were also connected to the gas outlets to collect the gas samples for characterizing using gas chromatography.



(A) (B)

Fig. 1: Experimental installation: (A) stirred tank reactor and (B) dry fermentor.

Two independent dry fermentation experiments were performed: one with autoclaved FVWs (pretreated, EXP1) and second one with raw FVWs (unpretreated, EXP2). For both experiments, the ST reactor was filled with pretreated 4.3 L sludge from the biogas plant along with 200 ml of 40 (X) times concentrated basal medium. The composition of basal medium ((X) per liter of distilled water) used were 1.25 g/l $NaHCO_3$; 0.5 g/l NH_4Cl; 0.25 g/l KH_2PO_4; 0.25 g/l $CaCl_2$, 0.032 g/l $NiSO_4$; 0.32 g/l $MgSO_4 \cdot 7H_2O$; 0.02 g/l $FeCl_2$; 0.0144 g/l $Na_2MoO_4 \cdot 2H_2O$; 0.023 g/l $ZnCl_2$; 0.021 g/l $CoCl_2 \cdot 6H_2O$; 0.01 g/l $CuCl_2 \cdot 6H_2O$ and 0.03 g/l $MnCl_2 \cdot 4H_2O$. The working volume of 8 L was then made up with FVWs liquid (the liquid collected after grinding the FVW) and remaining amount with distilled water. The ST was then undergo heat pretreated at 105^0C for 10 min using an autoclave and later flushed for few minutes with argon before starting the experiment to ensure anaerobic conditions. It was maintained at constant temperature of 55± 1^0C with a constant agitation of 250 rpm throughout the experiment. The pH was maintained uncontrolled throughout the experiment.

Dry fermentor (DF) basket was filled by mixing 4.83 kg FVWs (< 5 cm) with 0.7 L of preheated inoculum and 17.5 ml of 40(X) basal medium. During the feeding days, the leachate (L) from the DF was drained from the leachate collection tube and the respective volume of liquid from the ST was removed and introduced to DF. Leachate (L) was then introduced into the ST. Argon was flushed through the DF once each day to remove the head space CO_2.

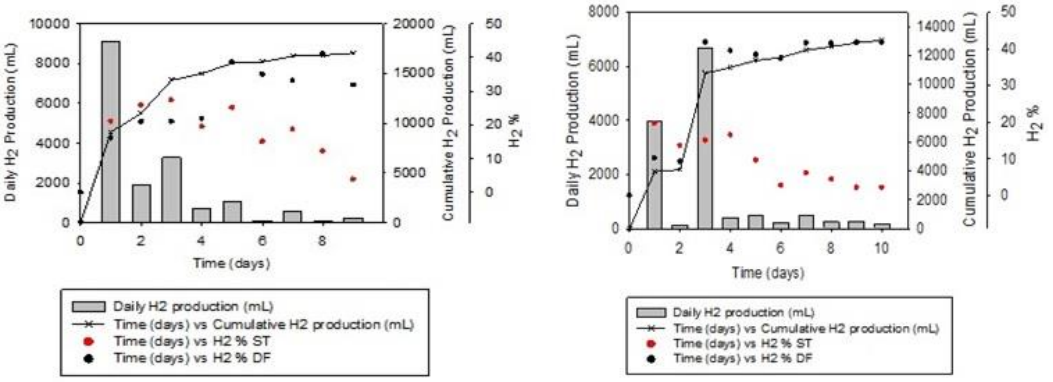
III. Analysis

Gas sample of 2 ml was taken from the outlet sampling port of the ST and DF to monitor the concentrations of various gas components (H_2, CO_2 and CH_4). Similarly 10 ml of liquid samples were withdrawn in order to measure the metabolites concentrations, NH_4^+, soluble COD and soluble sugar concentrations

Gas-phase H_2 concentrations were measured by 6890N (Agilent technologies) gas chromatograph (GC) equipped with a thermal conductivity detector (TCD) by injecting 3-5 ml of headspace sample collected using a gas tight syringe (Agilent). The GC was fitted with HayesepD 80/100 packed column. The injector, oven and detector temperatures maintained at 150, 35 and 150^0C, respectively. Argon was used as the carrier gas at a flow rate of 20 ml/min. The soluble metabolites were analysed by GC (6890N Agilent) equipped with a flame ionization detector (FID) and TR-FFAP 30 m × 0.25 mm ID × 0.25 µm (Thermo Scientific). The initial temperature of the column was 40^0C for 3 min followed with a ramp of 20^0C/min to 60^0C for 3 min and then increased at 30^0C/min to 120^0C for 4 min and reach a final temperature with ramp of 30^0C/min to 240^0C for 6 min. The temperatures of the injector and detector were both 240^0C. Helium was used as the carrier gas at constant pressure of 103 kPa. The liquid sample is centrifuged and filtered using 0.2 µm nylon syringe filter and was acidified using ortho-phosphoric acid before analysing via GC. The soluble chemical oxygen demand (SCOD) was determined by using Hach LCK 114 COD kit and concentration was read directly using the Hach Pocket Colorimeter II. NH_4+ concentration determination was performed using Spectroquant Ammonium Test kit.The soluble carbohydrate concentrations were measured using phenol sulphuric acid method by Masuko et al. (2005). Total solids (TS) and volatile solids (VS) were also determined using standard methods (APHA-AWWA-WPCF, 1998).

IV. Results and discussions

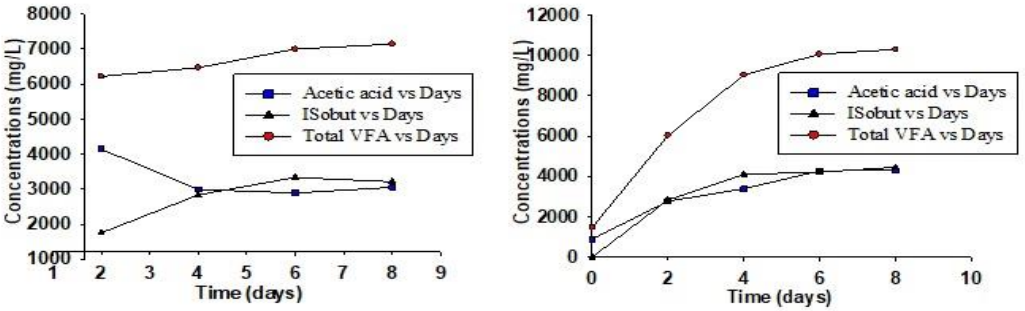
Two independent experiments were performed to understand the extent of influence of autoclaving the waste as a pretreatment method for subsequent biohydrogen production under thermophilic condition. Identical FVW were used for these experiments with EXP1 used autoclaved and EXP2 used non-autoclaved waste. The results of total hydrogen produced (ml) and percentage of H_2 (%) at the headspace of both ST and DF were measured is shown in Fig: 2. As expected experiments using autoclaved waste produced more hydrogen than without autoclaving as it favours solubilisation of complex waste biomass. However, an enhancement in overall hydrogen production was observed in any thermophilic (autoclaved or non-autoclaved) conditions tested than in mesophilic (data not shown) conditions. However, a 30% increase in hydrogen production was obtained in EXP1 compared to EXP2.



(a) (b)

Fig. 2: Hydrogen percentage and hydrogen production in Exp1 (a) and Exp2 (b).

Dark fermentative biohydrogen production is associated with volatile fatty acid production. The maximum concentrations of the VFAs obtained from the studies were 7366.2 mg/L acetic acid and 7662 mg/L isobutyric acid in EXP1, and 10535 mg/L acetic acid and 10847.9 mg/L isobutyric acid in EXP2 (Fig. 4 and Fig. 5). High concentrations of VFAs accumulation was occurred due to high organic loading rate in DF. This might be one of the possible reasons for the relatively low amount of hydrogen production obtained from these studies as high concentration of VFAs is detrimental for microbes (Ren et al. 2018). In addition, ethanol and propionic acid presence were also noticed in the DF and ST which might be another reason as metabolic pathway of former does not leads to hydrogen production, whereas, the latter is a hydrogen consuming pathway (Ghimire et al. 2015).



(a) (b)

Fig. 3: VFA production profile of Exp1: (a) DF and (b) ST

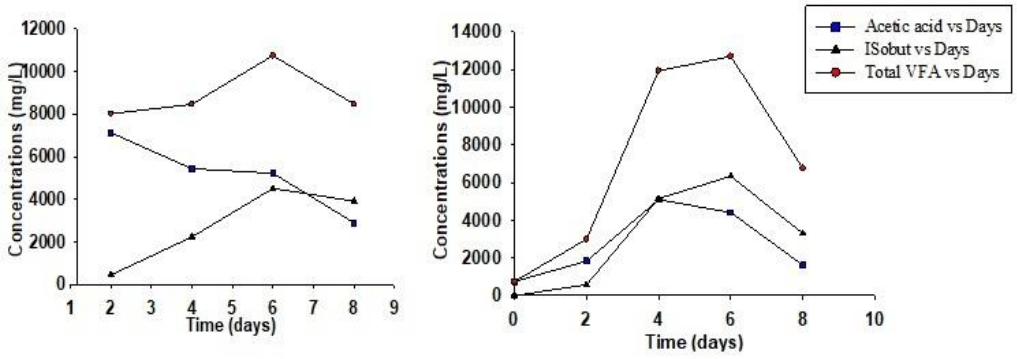


Fig. 4: VFA production profile of Exp2: (a) DF and (b) ST

pH of the ST was monitored regularly and was maintained between 5.5 to 6.75. This is to ensure optimal growth condition for the hydrogen producers and to inhibit methanogens. However, pH of DF was in the range of 4 to 5.5 due to acidification effect of VFA. In order to avoid the consumption of hydrogen by homoacetogens, CO_2 was also removed intermittently from the head space of the DF.

V. Conclusions

Dry anaerobic fermentation of FVWs for biohydrogen generation was successfully performed in a 55-L reactor. From the studies, EXP1 using autoclaved waste was found to generate a cumulative total of 17033.89 mL H_2 (27.19 mLH_2 gVS^{-1}) and 13041.39 mL H_2 (20.81 mLH_2 gVS^{-1}) in EXP2. VFAs are profoundly produced in both experiments (EXP1, maximum total VFAs = 17432.6 mg/L and EXP2, maximum total VFAs = 23447.5 mg/L) which could influence the overall performance of the process. It can be concluded that although thermophilic autoclaved improved the overall hydrogen productivity, further optimization studies are warranted for commercialization of this process.

Acknowledgements

The authors wish to thank TUBITAK-MAG-215 M 314 for financial support of this study. HNA thanks the Xunta de Galicia (Spain) for his postdoctoral fellowship (ED 481B-2016/195-0). The authors Bensu Günay and Okyanus Yazgın would also like to thank the Tubitak 2209-A University Student Research Projects Support Program for this research.

References

Ghimire, A., Frunzoc, L., Pirozzi, F., et. al., A review on dark fermentative biohydrogen production from organic biomass: Process parameters and use of by-products, Applied Energy, 144, 73–95 (2015).

Karthikeyan, Obuli P., Visvanathan, C., Bio-Energy recovery from high-solid organic substrates by dry anaerobic bio-conversion processes: A review, Reviews in Environmental Science and Biotechnology, 12, 257–284 (2013).

Keskin,T., Arslan,K., Abubackar, H.N., et.al., Determining the effect of trace elements on biohydrogen production from fruit and vegetable Wastes, International Journal of Hydrogen Energy, doi: 10.1016/j.ijhydene.2018.01.028 (2018).

Masuko, T., Minami, A., Iwasaki, N., et. al., Carbohydrate analysis by a phenol-sulfuric acid method in microplate format, Analytical Biochemistry 339, 69–72 (2005).

Nikolaidis, P., Poullikkas, A., A comparative overview of hydrogen production processes, Renewable and Sustainable Energy Reviews 67, 597–611 (2017).

Pavi, S., Kramer, L.E., Gomes, L.P., Miranda, L.A.S., Biogas production from co-digestion of organic fraction of municipal solid waste and fruit and vegetable waste, Bioresource Technology 228, 362–67 (2017).

Ren, Y., Yu, M., Wu, C., A comprehensive review on food waste anaerobic digestion: research updates and tendencies, Bioresource Technology, 247, 1069-1076 (2018).

Yun, Y-M., Lee M.K., Im, S.W., Biohydrogen production from food waste: current status, limitations, and future perspectives, Bioresource Technology, 248, 79–87 (2017).

Optimization of Thermal Pre-treatment Conditions By Box-Wilson Method For Dark Fermentative Biohydrogen Production From Fruit and Vegetable Wastes

***Bensu Günay*[1], Okyanus Yazgın[1], Kubra Arslan[3], Haris Nalakath[2], Tugba Keskin[1], Nuri Azbar[1]**

[1]*Engineering Faculty, Bioengineering Department, Ege University, Izmir, Turkey*
[2]*Faculty of Sciences and Center for Advanced Scientific Research (CICA), University of La Coruña, La Coruña, Spain*
[3]*Graduate School of Natural and Applied Science, Biotechnology Department, Ege University, Izmir, Turkey*

One of the biggest challenges of the next decade is to identify alternative renewable energy sources that are environmentally friendly; as fossil fuels are non-renewable, polluting and harmful to nature. Nevertheless, fossil fuels are highly used amongst other energy sources. On the other hand, as an alternative way, hydrogen is a clean and high energy (122 kj/g) resource. Dark anaerobic fermentation is considered as one of the most promising hydrogen production methods due to its low energy demand and production process using renewable sources. The rate limiting step of dark fermentation is the hydrolysis stage of complex substrate. For easily accessible to microbial attack, several pre-treatment methods can be implemented.

Thermal pre-treatment is known as one of the best methods for enhancing hydrogen production yields. In this study, eight different thermal pretreatment conditions, which are determined by Box-Wilson statistical approach (100°C-10 min, 105°C-1.5 min, 105°C-8.5 min, 110°C-5 min, 110°C-10 min, 117°C-1.5 min, 117°C-8.5 min and 120°C-10 min) have been used for biohydrogen production from fruit and vegetable wastes. Totally, 9 samples (including one control) in triplicates were prepared, using 60 mL as working volume. The maximum hydrogen production of 61 mL H2/g VS was observed with 1.5 min treatment at 117°C. The Box-Wilson statistical model was significant (R2=0.91). The results showed that the optimum temperature conditions were 98-102°C for long treatment time (8-11mins) and 118-122°C for short treatment time (1-4mins). The kinetic results were performed by Gompertz equation and the hydrogen production rates changed between 1.24-2.91 mL H2/min. A maximum volatile fatty acids concentration of 23 g/L was observed with 110°C-10 min treatment. The dominant volatile fatty acids were acetic acid and butyric acid; however, the ethanol production was observed in low H2 producing reactors. Hence, this study showed an alternative approach to conventional heat treatment operations (80°C-1 h) with short treatment time.

Acknowledgment: The authors wish to thank the Tubitak 2209-A University Student Research Projects Support Program for financial support of this study. Also, thank TUBITAK-MAG-215 M 314 project. HNA thanks the Xunta de Galicia (Spain) for his postdoctoral fellowship (ED 481B-2016/195-0).

Keywords: Biohydrogen, Thermal Pretreatment, Fruit and Vegetable Wastes, Box-Wilson Method, Dark Fermentation

Analysis of Biohydrogen Production via Dry Anaerobic Digestion of Fruit And Vegetable Waste

***Okyanus Yazgın*[1], Bensu Günay[1], Haris Nalakath Abubackar[2], Tuğba Keskin Gündoğdu[1], Nuri Azbar[1]**

[1]Ege University, Engineering Faculty, Bioengineering Department, 35100, Izmir, Turkey
[2]University of La Coruña, Faculty of Sciences and Center for Advanced Scientific Research (CICA), La Coruña, Spain

The dry anaerobic digestion for biohydrogen production is relatively novel technology that requires less water and smaller reactor volume. In addition, the digestate obtained from the process can be easily handled and can be used as soil amendment. In this study, fruit and vegetable waste (FVW) (6.4 kg, wet weight) collected from the local municipality (Izmir, Turkey) was treated in a 55 L custom made dry fermenter (DF). The inoculum used was collected from a local biogas plant that uses dairy product as feed (Izmir, Turkey) and was undergone pre-treatment at 105°C for 10 min in order to gather hydrogen producers. A 13 L fully automated reactor (ST) (INFORS HT Labfors 5 reactor, Switzerland) was placed adjacent to the DF for the purpose of treating the daily collected leachate. Throughout the experiment, the leachate was collected from the DF twice a day and was introduced into the ST. Respective amounts of liquid from the ST were taken out and sprayed over the DF. The experiment was performed under mesophilic condition without any pH control. The amount of gas produced were continuously monitored using gas flow meters (µFlow, Sweden) attached to the outlet of each reactor. The percentage of hydrogen present in the produced gas was measured using a gas chromatography (Agilent, 6890N). Periodically the liquid samples were also collected to monitor the VFAs using GC. Other parameters analyzed were total sugar, soluble COD, ammonia concentrations, total solids (TS) and volatile solids (VS). The maximum percentage of hydrogen measured at the head space of the reactor was 30 % and the cumulative hydrogen production was 5700 mL. The major VFAs produced were isobutyrate (maximum: 5048 mg/L) and acetic acid (maximum: 3563 mg/L). Compared to the previous studies (data not shown) with less frequent feeding, this study with twice daily feeding couldn't improve the overall hydrogen production. As thus, it can be concluded that feeding frequency does not significantly enhances the hydrogen production through dry fermentation and this is important as it plays a major role in the economy of the process.

Keywords: Biohydrogen, renewable energy, dry fermentation, anaerobic digestion

Copper(II)Phthalocyanine/Metal Organic Frameworks (Cupc/MOF) Composite with Improved Electrocatalytic Efficiency for Hydrogen Production

[1]Gobeng Release Monama, [1*]Kwena Desmond Modibane, [1]Kabelo Edmond Ramohlola, [2]Kerileng Mildred Molapo, [1]Mpitloane Joseph Hato, [1]Mogwasha Daphney Makhafola, [1]Gloria Mashao, [2]Siyabonga Beizel Mdluli, [2]Emmanuel I. Iwuoha
[1]University of Limpopo, Private Bag X1106, Sovenga, 0727, South Africa,
[2]University of the Western Cape, Private Bag X17, Bellville, 7535, South Africa

* E-mail: kwena.modibane@ul.ac.za

Abstract
The hydrogen evolution reaction (HER) of CuPc/MOF composite was investigated for hydrogen production. The SEM and EDS analyses showed that CuPc was incorporated into MOF through impregnation method. The electrochemical measurements were studied using cyclic voltammetry (CV) and it was found that CuPc/MOF composite exhibited favourable catalytic activity for HER. The Tafel slope value of the CuPc/MOF composite was found to be 185.3 mV.dec^{-1} and noticeably lower than that of the bare MOF (236.7 mV.dec^{-1}) at 0.30 M of the acid, and the charge transfer coefficients are all close to 0.5, suggesting the Volmer reaction coupled with either Heyrovsky or Tafel reaction for hydrogen production. The exchange current density, (i_0) of all the samples increased with increasing the concentration of the hydrogen source. Nonetheless, the CuPc/MOF composite showed a higher i_0 as compared to bare MOF. These observations provide a platform to synthesize promising low-cost CuPc/MOF electrocatalyst with high efficiency and excellent electrocatalytic performance for HER.

Keywords: Metal organic frameworks**;** Phthalocyanine**;** Hydrogen evolution reaction

I. Introduction

In recent years, fossil fuels are considered as the main energy resources. Nonetheless, they possess some disadvantages such as limited resources, global warming and environmental pollution. One solution to the problem is the use of alternative energy sources instead of fossil fuels. In this context, hydrogen fuel cell technology is one of the promising technology for sustainable energy applications owing to its various advantages such as recyclability, pollution-free and fuel efficiency (Ren et al., 2013). In addition, H_2 gas yields more energy, which is about 2.75 times greater as compared to traditional gasoline-based energy resources. However, the problem for practical usage of H_2 gas as an energy carrier lies in the production and storage technology (Ehan and Wahid, 2016). Up to this stage, electrochemical reduction of water is preferred as an effective and alternative route to produce hydrogen with high purity and in large quantity because of its simplicity and cost effectivenss (Ren et al., 2013). Ren et al. (2013) and Benck (2014) proposed a number of porous materials, such as carbon nanotubes, metal organic frameworks (MOFs), graphite nanofibers, zeolites and activated carbon as candidates for HER. Among these materials, MOFs hold greater promise as potential candidates in the design of advanced multifunctional materials due to their unique structures (Zheng and Jiao, 2017). MOFs are inorganic-organic hybrid compounds built from metal ions or clusters and organic ligands by coordination bonds, providing highly crystalline porous structures with large surface area, high pore volume as well as uniform nanoscale cavities (Ramohlola et al., 2017). Thus, MOFs have been used in various applications such as energy storage, CO_2 adsorption, hydrocarbon adsorption/separation, catalysis, advanced sorbents for solids extraction and sensors. However, MOFs possess some drawbacks as HER material because of H_2 embrittlement, moisture instability and poor H_2 adsorption and desorption at ambient conditions (Ramohlola et al., 2017). To the best of our knowledge, there are no studies reported on the formation and observation of HER using copper phthalocyanine (CuPc) incorporated on the MOF surface to prepare an effective electrocatalyst. Therefore, this study reports on the synthesis, characterization and application of the hybrid-hybrid CuPc/MOF composite as a suitable electrocatalyst for HER.

II. Experimental Set-up and Procedure

MOF was synthesized following the methodology of Ramohlola et al. (2017). In brief, 4.5 mmol of $Cu(NO_3)_2.3H_2O$ was dissolved in 10 mL of distilled water and then mixed with 0.525 g (2.5 mmol) of H_3BTC dissolved in 10 mL of ethanol. The mixture was stirred for 30 min and then transferred into a 23 mL teflon stainless-steel autoclave, sealed and the mixture reacted for 36 h at 120 °C in thermostatic drying oven. CuPc was synthesised from phthalimide according to previous method reported elsewhere by Chiang et al. (2012). Typically, a mixture of phthalimide (3.00 g, 0.0200 mol) in the presence of excess urea (3.00 g, 0.0500 mol), ammonium heptamolybdate (0.0800g, 0.0600 mmol) and copper nitrate (1.40 g, 0.0058 mol) in nitrobenzene (15.00 mL) was refluxed for 5 h at 180 ^oC to give a target compound. CuPc/MOF composite (Scheme 1) was prepared by reacting the synthesized CuPc with MOF. Briefly, 0.1 g of the as-synthesized MOF sample was dehydrated at 150 ^oC for 1 h and then suspended in 10 mL DMF. An appropriate amount of 1.4 mL DMF in CuPc (0.12 mol.L^{-1}) was added to the suspension of MOF solution and the mixture was stirred for 24 h at room temperature.



Scheme 1. Synthesis of CuPc/MOF composite through impregnation in DMF.

Morphological characterizations were performed using field-emission scanning electron microscope (FE-SEM, Auriga® Carl Zeiss) operated at a voltage of 30 kV coupled with EDS for elemental analysis. Electrochemical measurements were carried out using EPSILON electrochemical workstation. The data was collected using a conventional three-electrode set-up with gold electrode (3 mm diameter, 0.071 cm^2 area) as a working electrode, Pt wire as a counter electrode and Ag/AgCl wire as a reference electrode. Repetitive scanning of the solutions of CuPc, MOF and CuPc/MOF composite (~2.0 x 10^{-3} $mol.L^{-1}$) was measured from -2.0 to 1.25 V at the scan rate of 0.02 - 0.10 $V.s^{-1}$. Electrochemical experiments were performed in 10 mL of 0.1 M TBAP/DMSO electrolytic system. HER studies were done using different concentrations of 0.03 - 0.45 M H_2SO_4 as H_2 source in 0.1 M TBAP/DMSO system and ~2.0 x 10^{-4} $mol.L^{-1}$ of CuPc, MOF and CuPc/MOF composite as electrocatalysts.

III. Analysis

The Tafel plot was constructed from current density-potential data at various concentrations ranging from 0.033 to 0.45 M H_2SO_4. From this analysis, two important parameters such as Tafel slope (b) and exchange current density (i_o) can be deduced and they are essential for monitoring the kinetics and performance of HER electrocatalyst (Ramohlola et al., 2017). In our recent work, Monama et al. (2018), we reported that the b could also serve as an indicator of either Volmer, the Heyrovsky and the Tafel in a multi-step proton transfer process and i_o the measure of performance of an electrocatalyst. In this study, the values of b and i_o were estimated by linear polarization curves and the results are presented in Table 1. In addition, another important parameter that can give insight of reaction mechanism is the cathodic transfer coefficient (1-α) which was calculated using high overpotential region, where Butler-Volmer equation simplifies to the Tafel equation, from the Tafel slope b given by the relationship:

$$b = \frac{-2.303\ RT}{(1-\alpha)F} \quad (1)$$

IV. Results and discussions

The SEM microphotograph were used to provide further insight into the morphology and microstructure of CuPc, MOF and CuPc/MOF composite (Fig. 2). As shown in Fig. 2(a), MOF demonstrates typical irregular crystals with octahedral/pyramidal shapes confirming a low control on the crystal growth parameters and its corresponding EDS (Fig. 2(b)) reveals the presence of C-, O- and Cu- atoms in the MOF structure (Ramohlola et al., 2017). The inset image of Fig. 2(a) shows that MOF crystals have smooth surfaces. This observation confirmed that hydrothermal synthesis gives pure, highly crystalline MOF materials. The SEM images of CuPc crystals and CuPc/MOF in parts c and e of Figu. 2 show similar needle/rod-like structures. This observation is in good agreement with the work reported by Ge et al. (2016). It is also noticeable that the rod-like structures change the surface of MOF when the composite is formed. This observation can be attributed to the morphology of CuPc on the MOF structure. Magnification of the octahedral MOF crystals (inset images in Fig. 2 (c) and (e)) of CuPc/MOF composite showed that an introduction of CuPc crystals in the composite developed a rough-surfaced morphology, which may suggest a strong interaction between MOF and CuPc crystals.

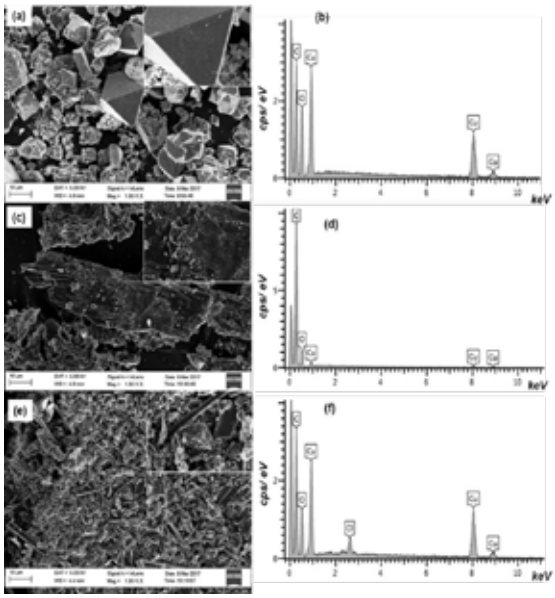


Fig. 2: SEM images of (a) parent MOF, (c) CuPc, (e) CuPc/MOF composite and EDS spectra of (b) MOF, (d) CuPc, (f) CuPc/MOF composite (inset: magnification on the crystal structure to view the surface of the crystal).

Fig. 3 shows Tafel plots (V versus log i_o plots) for blank electrode, CuPc, MOF and CuPc/MOF composite. The present study exhibits that the MOF electrode gives Tafel slope of 320.8 mV.dec^{-1} at 0.033 M H_2SO_4 as compared to 184.4 mV.dec^{-1} of the composite at the same condition. At the same acid conditions, CuPc, MOF and the composite showed lower Tafel slope values as compared to the bare electrode. High values of the Tafel slopes were observed in the case of MOF and CuPc electrocatalysts though the values are lower than the bare electrode at low concentrations. It was reported that Tafel slopes in the ranges of 105-150 mV.dec^{-1} may be explained on the basis of a Volmer rate determining step for HER (Ramohlola et al., 2017). Nonetheless, the presence of the CuPc on the surface of MOF results in an increase in the Tafel slope value. These results are in good agreement with the work reported by Kubisztal et al. (2007) when studying the HER behaviour of nickel-based composite coatings containing molybdenum powder. Furthermore, the charge-transfer coefficient (α = 0.5**)**, describes a mechanism where the rate determining step is the Volmer reaction or the Volmer reaction coupled with one of the other two reactions. As given in Table 1, the charge transfer coefficients for MOF and CuPc/MOF composite are close to 0.5. Thus, the rate determining step of HER for the MOF and the composite maybe the Volmer reaction or the Volmer reaction coupled with one of the other two reactions (Ramohlola et al., 2017).

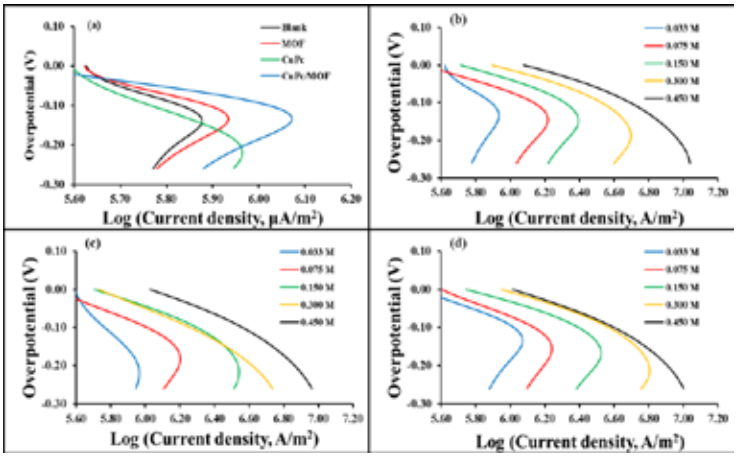


Fig. 3. (a) Tafel plots of blank, MOF, CuPc and CuPc/MOF composite in the presence of 0.033 M H_2SO_4; and Tafel plots of (b) MOF, (c) CuPc and (d) CuPc/MOF composite in the presence of 0.033 – 0.450 M H_2SO_4 at 0.10 Vs^{-1} on Au electrode in 0.1 M TBAP/DMSO electrolyte.

Tab. 1: Experimental values of Tafel slope (b), charge transfer coefficient (1–α) and exchange current density (i_0) of blank, MOF, CuPc and CuPc/MOF composite.

Material	H_2SO_4 ($mol.L^{-1}$)	Slope (b) ($V.dec^{-1}$)	-b ($mV.dec^{-1}$)	1-α	$\log i_0$ ($\mu A.m^{-2}$)	i_0 ($A.m^{-2}$)
MOF	0.033	-0.3208	320.8	0.1844	5.93	0.851
	0.300	-0.2367	236.7	0.2499	6.70	5.012
CuPc	0.033	-0.4526	452.6	0.1307	5.95	0.891
	0.300	-0.2063	206.3	0.2867	6.73	5.370
CuPc/MOF	0.033	-0.1844	184.4	0.3207	6.07	1.175
	0.300	-0.1853	185.3	0.3193	6.81	6.457

V. Conclusions

In this work, a highly active CuPc/MOF composite for the HER was prepared through impregnation method of MOF and CuPc. The influences of CuPc on the morphology and crystalline structure of MOF surface, as well as the resulting electro-catalytic activity in hydrogen evolution were systematically investigated. The electrocatalytic activity of the CuPc/MOF composite is higher than that of the neat MOF. Furthermore, the Tafel slope and charge-transfer coefficients showed that the rate determining step of HER on the studied MOF and CuPc/MOF composite maybe the Volmer reaction or the Volmer reaction coupled with one of other two reactions. The results demonstrate that microstructured MOF-based composite may be used as alternative electrocatalyst for hydrogen fuel cell applications.

Acknowledgements

Thanks for the financial supports from the National Research Foundation (NRF) of South Africa under the Unique Grant No. 99278.

References

Kubisztal J., Budniok A., Lasia A., Study of the hydrogen evolution reaction on nickel-based composite coatings containing molybdenum powder, Int. J. Hydrogen Energy, 32, 1211-1218 (2007).

Ge S., Zhang Y., Huang B., Huang S., Tie W., Lei Y., He Q., G. Tu Q, Q. Qin, S. Niu, M. Li, D. Li, Z. Zheng, Synthesis of highly crystalline copper phthalocyanine needles by solvothermal method, Mater. Letters, 163, 61-64 (2016).

Ramohlola K.E, Masikini M, Mdluli S.B, Monama G.R., Hato M.J, Molapo K.M., wuoha E.I., Modibane K.D., Electrocatalytic hydrogen production properties of poly (3-aminobenzoic acid) doped with metal organic frameworks, Int. J. Electrochem. Sci., 246, 1174-1182 (2017).

Chiang C.Y., Aroh K., Ehrman S.H., Copper oxide nanoparticle made by flame spray pyrolysis for photoelectrochemical water splitting–Part I. CuO nanoparticle preparation, Int. J. Hydrogen Energy, 37, 4871-4879 (2012).

Ramohlola K.E, Masikini M., Mdluli S.B, Monama G.R., Hato M.J., Molapo K.M., Iwuoha E.I., Modibane K.D., Electrocatalytic hydrogen evolution reaction of metal organic frameworks decorated with poly (3-aminobenzoic acid), Electrochimica Acta, 246, 1174-1182 (2017).

Zheng J., Jiao Z., Modified Bi_2WO_6 with metal-organic frameworks for enhanced photocatalytic activity under visible light, J. Colloid. Interface. Sci., 488, 234–239 (2017).

Benck J.D., Hellstern T.R., Kibsgaard J., Chakthranont P., Jaramillo T.F., Catalyzing the hydrogen evolution reaction (HER) with molybdenum sulfide nanomaterials, ACS Catal., 4, 3957-3971 (2014).

Ehan S., Wahid M.A., Hydrogen production from renewable and sustainable energy resources: Promising green energy carrier for clean development, Renew. Sustain. Energy Rev., 7, 850–856 (2016).

Ren Y., Chia G.H, Gao Z., Metal-organic frameworks in fuel cell technologies, Nano Today, 8, 577–587 (2013).

Monama G.R., Mdluli S.B., Mashao G., Makhafola M.D., Ramohlola K.E., Molapo K.M., Hato M.J., wuoha E.I, Modibane K.D., Palladium deposition on copper(II) phthalocyanine/metal organic framework composite and electrocatalytic activity of the modified electrode towards the hydrogen evolution reaction, Ren. Energy, 119, 62-72 (2018).

Graphene Oxide/Metal Organic Framework Nanocomposite with Improved Electrocatalytic Activity for Hydrogen Evolution Reaction

[1]Mogwasha Daphney Makhafola, [1]Kabelo Edmond Ramohlola, [1]Thabang Ronny Somo, [1]Gobeng Release Monama, [1]Mpitloane Joseph Hato, [2]Kerileng M. Molapo, [2]Emmanuel I. Iwuoha,[1]Kwena Desmond Modibane*
[1]University of Limpopo, Private Bag X1106, Sovenga, 0727, South Africa,
[2]University of the Western Cape, Private Bag X17, Bellville, 7535, South Africa

*E-mail addresses:kwena.modibane@ul.ac.za

Abstract
In this study, a composite of graphene oxide (GO) and HKUST-1-type metal organic framework (MOF) was synthesized by impregnation method, and its application as electrocatalyst for hydrogen production via hydroge evolution reaction (HER) was studied. X-ray diffraction (XRD), Fourier Transform Infrared spectroscopy (FTIR), Scanning electron microscopy (SEM) and Transmission electron microscopy (TEM) were used to characterize GO, MOF, and GO/MOF catalysts. The XRD and FTIR results of the composite showed the phases and characteristic bands for both parent materials as indicative of the composite. The SEM and TEM images revealed the presence of octahedral structure of MOF in the GO sheet-like structure. The performance of the proposed electrolytic system for electrochemical HER was studied by cyclic voltammetry and Tafel plots. The results showed that the addition of GO/MOF in the electrolytic system reveals better catalytic characteristics such as highest catalytic activity and lowest onset potential.

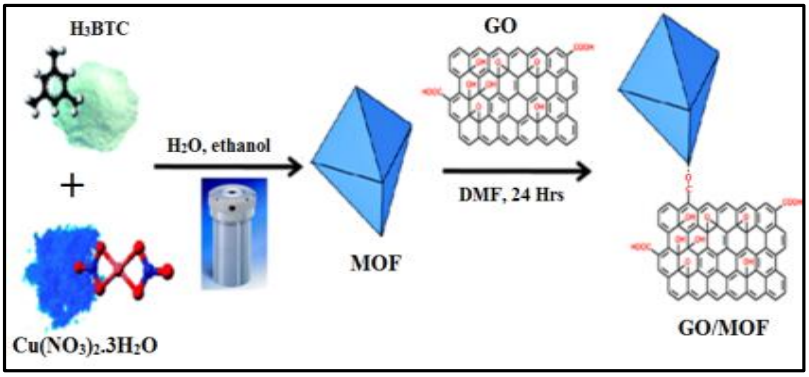
Keywords: Hydrogen evolution reaction, HKUST-1-type Metal organic framework, Graphene oxide

I. Introduction

In developing countries, energy supplies are mainly based on combustion of fossil fuels accompanied by a number of environmental problems such as green house emission. In order to overcome those challenges, renewable energies are needed, since the supply of non-renewable energy sources is finite. Owing to its excellent properties (i.e. light weight and high energy density), hydrogen has been designated as the best energy carrier. However, there are significant challenges hindering the large-scale applications and commercialization of hydrogen fuel especially in mobile transportation. These problems include the lack of safe handling and effective methods for hydrogen production and storage (Salehabadi, Salavati-Niasari and Gholami, 2017). With this being noted, electrochemical reduction of water is considered as one of the promising route for hydrogen production due to its simplicity and economical way to produce hydrogen with large and quantity high purity. Even though in the electrochemical studies platinum (Pt) is known as an excellent electrode for hydrogen generation, it is limited by its high cost and low abundance (Satyapal *et al.*, 2007). MOFs have shown to be very promising HER electrocatalysts mainly due their extremely large surface area, high porosity, adjustable pore sizes as well as defined hydrogen occupation sites (Ramohlola *et al*., 2017). Unfortunately, these MOF materials have been reported to exhibit several weak points such as the relative low stability in solution and conductivity hampering their realistic applications. Combining MOF materials with other substrates has been proposed in order to mitigate the above-mentioned drawbacks (Zhou *et al.*, 2013). Graphene oxide (GO) with rich functional groups is very suitable to construct graphene-based hybrid composites (Zhou *et al.*, 2015). Petit and Bandosz (2015) have reported the formation of GO/MOF composites using hydrothermal method, where the synergetic effect between MOF units and GO layers was responsible for enhanced adsorption amounts compared to the parent material. To the best of our knowledge, there are no studies reported on HER using composite of GO/MOF prepared by impregnation procedure. Hence in this study, a composite of MOF with GO (GO/MOF) was prepared through impregnation method and applied for electrochemical hydrogen generation.

II. Experimental Set-up and Procedure

GO/MOF composite (Scheme 1) was prepared through impregnation method of directly mixing of GO and MOF. Briefly, 0.1 g of as-synthesized MOF sample was dehydrated at 150 ^{o}C for 1 h. It was then suspended in 10 mL DMF. In a separate beaker, 0,1 g of graphene oxide was dispersed in 1,4 mL DMF, and then the two mixtures were mixed together and stirred magnetically for 24 h at 50 ^{o}C. Electrochemical measurements were carried out using EPSILON electrochemical workstation. The data was collected using a conventional three-electrode set-up with gold electrode (3 mm diameter, 0.071 cm^2 area) as a working electrode, Pt wire as a counter electrode and Ag/AgCl wire as a reference electrode. Repetitive scanning of the solutions of MOF, GO and MOF composite (~2.0 x 10^{-3} mol.L^{-1}) was measured from -1.0 to 1 V at the scan rate of 0.02 - 0.10 V.s^{-1}. Electrochemical experiments were performed in 10 ml of 0.1 M TBAP/DMSO electrolytic system. HER studies were done using different concentrations of 0.03 - 0.45 M H_2SO_4 as H_2 source in 0.1 M TBAP/DMSO system and ~2.0 x 10^{-4} mol.L^{-1} of MOF, GO and MOF composite composite as electrocatalysts.



Scheme 1: Synthesis of MOF and GO/MOF composite through hydrothermal and impregnation method respectively.

III. Analysis

The FTIR spectra were acquired on a Cary 600 series FTIR spectrometer (Agilent Technologies). The crystal structure was analyzed by using Phillips PW 1830 model XRD. Morphological characterizations were performed using field emission scanning electron microscopy (FE-SEM, Auriga® Carl Zeiss) operated at a voltage of 30 kV and transmission electron micrographs were collected using an FEI Tecnai G2 20 field-emission gun (FEG) TEM, operated in bright field mode at an accelerating voltage of 200 kV.

The overall electrocatalytic HER can also be explained by means of mechanism. In an acid medium, the HER pathway could proceed via three main steps (Konieczna *et al.*, 2017):

$H+ + e- \rightarrow$ Had Volmer reaction (1)

$H_{ad} + H+ + e- \rightarrow H_2$ Heyrovsky reaction (2)

$H_{ad} + H_{ad} \rightarrow H_2$ Tafel reaction (3)

It has been reported that for the HER on platinum electrode in acidic solutions, the reactions above show the Tafel slope values of 120 mV, 40 mV and 30 mV for the Volmer, the Heyrovsky and the Tafel, respectively (Ramohlala *et al.*, 2017). From these reactions, the HER process can either proceed by combination of Volmer-Heyrovsky or Volmer-Tafel mechanism.

Kinetic analysis and electrocatalytic activity of HER for MOF, GO and GO/MOF composite was performed by Tafel plot analysis. The Tafel plot was constructed from current density-potential data at various concentrations ranging from 0.033 to 0.450 M H_2SO_4. From this analysis, two important parameters such as Tafel slope (b) and exchange current density (io) can be deduced and they are essential to monitor the kinetics and performance of HER electrocatalyst. It was reported that the b could also serve as an indicator of either Volmer, Heyrovsky or Tafel in a multi-step proton transfer process and io the measure of performance of an electrocatalyst (Ramohlala *et al.*, 2017). In this study, the values of b and io were estimated by linear polarization curves and the results are presented in Table 1. In addition, another important parameter that can give insight of reaction mechanism is the cathodic transfer coefficient (1-α) which was calculated using high overpotential region, where Butler-Volmer equation simplifies to the Tafel equation, from the Tafel slope b given by the relationship:

$$b = \frac{-2.303\ RT}{(1-\alpha)F} \quad (4)$$

IV. Results and discussions

Fig. 1(a) shows FTIR spectra of MOF, GO and GO/MOF. The characteristic bands of MOF are well observed on the spectrum. Since MOF consisted of benzene-1,3,5-tricarboxylicacid(H_3BTC), the bands of the spectrum are essentially derived from H_3BTC (Petit, Burress and Bandosz, 2011; Zhou *et al.*, 2015). The bands of both GO and MOF are clearly observed in the IR spectrum of the composite GO/MOF. The diffraction pattern of MOF presented in Fig. 1(b), is in accordance with the one reported in the literature (Topologies, Stock and Biswas, 2012). The SEM image of GO in Fig. 1(c) is seen as dense fakes of graphene sheets stacked together by dispersive forces (Zhou *et al.*, 2015). The formation of the composite is hypothesized to occur via the reaction between the copper sites of HKUST-1 and the oxygen-containing groups on GO, which has been deduced by Bandosz group (Petit and Bandosz, 2015). In Fg. 1(d), the graphene phase seems to be mainly separated from the MOF-origin phase and large aggregates can be easily distinguished. It is known that electron beam illumination can cause the break down of HKUST-1 and can thus prevent any visualization of its lattice structure (Petit, Burress and Bandosz, 2011).

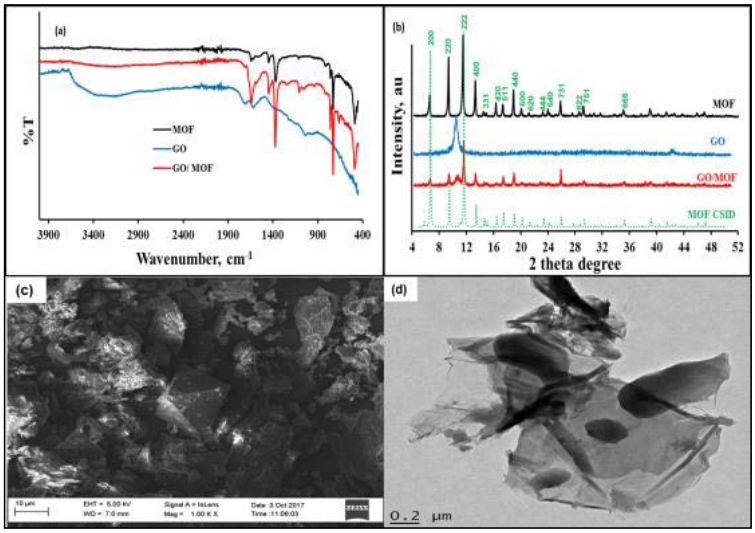


Fig. 1: (a) FTIR spectra, (b) XRD patterns of MOF, GO and MOF/GO composite, (c) SEM and (d) TEM imgaes of MOF/GO composite

Electrochemical behaviour of the composite has been studied by cyclic voltammetry to understand the redox chemistry of the prepared composites. Fig. 2(a) and (b) showed typical current-potential curves of the gold electrode in 0.1 M TBAP/DMSO system of blank, MOF, GO and GO/MOF composite. It was noticeable that the Faradaic contributions (redox process) onto gold electrode was observed at around -0.50 V. This is a typical redox process of bare Au electrode (Ramohlala *et al*., 2017). Nila and Gonzales reported that the electrochemical reduction of Cu^{2+} in solution proceeds in two one electron reversible waves via a Cu+ intermediate, in which the stability of the intermediate was due to the presence of ions in the solution (Nila *et al*., 1996). The increase in the cathodic current in CV of GO/MOF composite encourages strong interaction between MOF and GO.

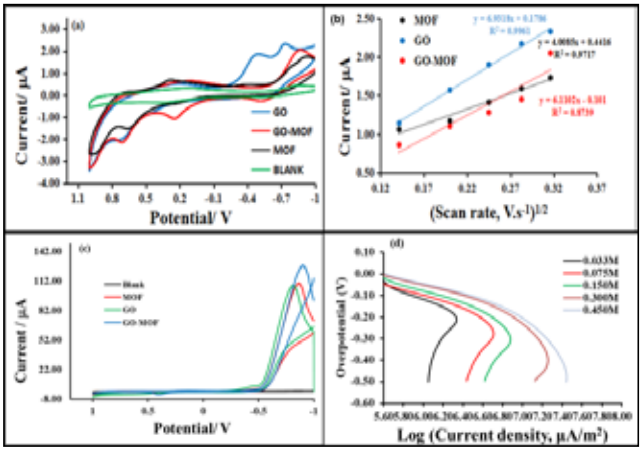


Fig. 2: (a) Cyclic voltagrams of blank, GO, MOF and GO/MOF in 0.1 M TBAP/DMSO electrolyte solution on Au electrode; (b) Peak current as a function of square root of scan rate); (c) CV curves of GO, MOF and GO/MOF composite (~2.0 x 10^{-4} mol.L^{-1}) in the presence 0.300 M H_2SO_4 at 0.10 V.s^{-1}; and (d) Tafel plots of GO/MOF composite in different concentrations of H_2SO_4 on Au in 0.1 M DMSO/TBAP electrode system at various scan rate (0.02 – 0.10 V.s^{-1})

Fig. 2(c) and (d) show Tafel plots (V versus log io plots) for GO, MOF and GO/MOF composite. The present study exhibits that the GO, MOF and GO/MOF composite showed Tafel slope values ranging from 105-211 mV.dec^{-1} at different concentration, and it was reported that Tafel slopes in the ranges of 105-150 mV.dec-1 may be explained on the basis of a Volmer rate determining step for HER (Ramohlala *et al*., 2017). Nonetheless, the

presence of the GO on the surface of MOF results in an increase in the Tafel slope value. Furthermore, the charge-transfer coefficient (α = 0.5), describes a mechanism where the rate determining step is the Volmer reaction or the Volmer reaction coupled with one of the other two reactions (Ramohlala *et al*., 2017). As given in Table 1 below, the charge transfer coefficients for MOF and GO/MOF composite are close to 0.5. Thus, the rate determining step of HER on the studied MOF and the composite maybe the Volmer reaction or the Volmer reaction coupled with one of the other two reactions (Nila *et al*., 1996).

Tab. 1: Experimental values of Tafel slope (b), charge transfer coefficient ($1–\alpha$) and exchange current density (i_0) of MOF, GO and GO/MOF composite.

Material	H_2SO_4 (mol.L^{-1})	Slope (b) (V.dec^{-1})	$-b$ (mV.dec^{-1})	$1-\alpha$	logi_0 (μA.m^{-2})	i_0 (A.m^{-2})
MOF	0.075	-0.2119	211.9	0.279	6.65	4.466
	0.300	-0.1057	105.7	0.559	7.17	14.79
	0.450	-0.1257	125.7	0.470	7.35	22.38
GO	0.075	-0.1759	175.9	0.336	6.73	5.370
	0.300	-0.1437	143.7	0.411	7.15	14.12
	0.450	-0.1887	188.7	0.313	7.36	22.90
GO/MOF	0.075	-0.1529	152.94	0.386	7.36	22.90
	0.300	-0.1251	125.1	0.472	7.24	17.37
	0.450	-0.1162	116.2	0.508	7.4	25.11

V. Conclusions

A highly active GO/MOF composite for the HER was prepared through impregnation method of MOF and GO. The influences of GO on the morphology and crystalline structure of MOF surface, as well as resulting electro-catalytic activity in hydrogen evolution were systematically investigated. The presence of GO on the MOF surface can significantly increase the HER exchange current density, and reduce the electrochemical reaction resistance. The observed promotional roles of incorporated GO is ascribed to possible synergetic effects between GO crystals and the MOF matrix, leading to a facilitation of HER as part of hydrogen production. Furthermore, the Tafel slope and charge-transfer coefficients showed that the rate determining step of HER on the studied MOF and GO/MOF composite maybe the Volmer reaction or the Volmer reaction coupled with one of other two reactions. The results demonstrated that microstructured MOF based composite may be used as alternative electrocatalyst for hydrogen production.

Acknowledgements

This work was supported by the National Research Foundation (NRF) (Unique Grant No. 99278) South Africa for financial support.

References

Konieczna, D.D., Biller, H., Witte, M., Gero, W.G., Neuba, A. and Wihelm, R. 'New pyridinium based ionic dyes for the hydrogen evolution reaction', Tetrahedron, 11-53, (2017).

Nila, C. and González, I., Thermodynamics of Cu-H_2SO_4-Cl−-H_2O and Cu-NH_4Cl-H_2O based on predominance-existence diagrams and Pourbaix-type diagrams, Hydrometallurgy 42, 63-82, (1996).

Petit, C. and Bandosz, T.J., 'Engineering the surface of a new class of adsorbents: metal-organic framework/graphite oxide composites.', Journal of Colloid and Interface science, 447, 139–51, (2015),

Petit, C., Burress, J., Bandosz, T. J., 'The synthesis and characterization of copper-based metal-organic framework/graphite oxide composites', Carbon. 49, 563–572, (2011).

Ramohlola, K.E., Masikini, M., Mdluli, S.B., Monama, G.R., Hato, M.J., Molapo, K.M., Iwuoha, E.I. and Modibane, K.D., 'Electrocatalytic hydrogen evolution reaction of metal organic frameworks decorated with poly(3-aminobenzoic acid)', Electrochim. Acta 246, 1174-1182, (2017).

Salehabadi, A., Salavati-Niasari, M. and Gholami, T., 'Effect of copper phthalocyanine (CuPc) on electrochemical hydrogen storage capacity of $BaAl_2O_4$/$BaCO_3$ nanoparticles', International Journal of Hydrogen Energy, 42, 15308–15318, (2017).

Satyapal, S., Petrovic, J., Read, C.; Thomas, G. and Ordaz, G., 'The U.S. Department of Energy's National Hydrogen Storage Project: Progress towards meeting hydrogen-powered vehicle requirements', Catalysis Today, 120, 246–256, (2007).

Topologies, M. O. F., Stock, N. and Biswas, S., 'Synthesis of Metal-Organic Frameworks (MOFs): Routes to Various', 933–969, (2012).

Zhou, H., Liu, X., Zhang, J., Yan, X., Liu, Y. and Yuan, A., 'Enhanced room-temperature hydrogen storage capacity in Pt-loaded

graphene oxide / HKUST-1 composites', International Journal of Hydrogen Energy, 39, 2160–2167, (2013).

Zhou, H., Zhang, J., Zhang, J., Yan, X-F., Shen, X-P. and Yuan, A-H., 'Spillover enhanced hydrogen storage in Pt-doped MOF / graphene oxide composite produced via an impregnation method', Inorganic Chem. Com., 54, 54–56, (2015).

Phase Transition and Photoelectrochemical Properties of Copper Oxide Photoelectrodes Fabricated by Electrodeposition

Meral Balık, Veysel Bulut, Ibrahim Y. Erdogan*
Bingöl University, Faculty of Health Sciences, 12000, Bingöl, Turkey
* E-mail: ibrahimyerdogan@gmail.com

Abstract
In this study, photoactive materials containing copper oxides have been prepared with high quality and stability in various compositions by electrodeposition method. These materials based on copper oxide have been characterized and compared using XRD, EDX, UV-Vis, FTIR, and electrochemical techniques. Based on the electrochemical production conditions; phase changes of photoactive materials and, at which conditions which phase or phases are present, were evaluated in detail. It was carried out that a full phase change from single-phase Cu_2O to single-phase CuO. Here, copper oxide compounds with different optical properties were prepared without the addition of any element or impurity except from copper and oxygen. The semiconductors have been found to have direct band gap that is more preferred for solar energy applications. Photoelectrochemical (PEC) performances of the copper oxide electrodes containing a different phase structure were determined, and the changes of PEC activities were examined comparatively.

Keywords: Copper oxides, electrodeposition, phase transition, photoelectrocatalytic activity

I. Introduction

Semiconductors based on photoactive materials can transform water into hydrogen. Hydrogen is a promising alternative energy source for a cleaner and greener future (Solmaz et al. 2016). Hydrogen can be produced directly from water using solar energy and semiconductors based on photoactive materials (Li and Wu 2015). Copper oxides are widely used in many fields due to contain earth-abundant elements, low costs, nontoxic, high absorbing properties, excellent photoelectrochemical characteristics, high performance energy conversion and ease production (Erdogan and Gullu 2010). Cu_2O and CuO enabling good solar light harvesting are intrinsic p-type semiconductors (Mizuno et al. 2005). They are promising materials as photocathodes due to their p-type semiconductor properties and suitable band gap that responds to visible light. Copper oxides have valence and conduction band capable of oxidizing and reducing water. Two distinctly different phases, Cu_2O and CuO, of this binary semiconductor can be prepared by the methods, which differ in the oxidation state of copper (Jiang et al. 2002). Among these techniques, electrodeposition method is an alternative to complex and costly vacuum-based methods due to its low cost, simplicity and environmental friendliness (Sasano et al. 2011).

There are few studies regarding the phase structure of copper oxide in the literature; said studies examined the partial phase changes of the copper oxide materials, majority of which had been prepared using non-electrochemical methods, at several different temperatures (Johan et al. 2011). These studies contain no detailed information on how a full phase change from single-phase Cu_2O to single-phase CuO, which were prepared via the electrodeposition based method was completed, and on the step-by-step monitoring of this phase change. The popularity of copper oxides would surely increase in many areas, provided that the band gap energies of copper oxide semiconductors could be changed in a wide spectrum without adding any elements or impurity into their compounds.

In this study, copper oxides have been prepared with high quality in various compositions by an electrodeposition method. The phase changes of photoactive materials and, at which electrochemical conditions which phase or phases are present, were evaluated in detail. PEC performances of the copper oxide coated electrodes containing a different phase were determined.

II. Experimental Set-up and Procedure

All electrochemical experiments were performed in a conventional three electrode glass cell, with a potentiostat/galvanostat system (CHI 660D) at room temperature. The working electrode was an indium tin oxide (ITO) single-side coated conducting glass (Rs<10 Ω/sq). A platinum wire (99.99% pure) was used as a counter electrode. All the potentials were referenced to a saturated calomel electrode (SCE). Cu_2O electrodeposition was carried out from a 0.02 M $CuSO_4.5H_2O$, 0.2 M Na_2SO_4 and 0.3 M lactic acid ($C_3H_6O_3$) solution for 15 minutes. Cyclic voltammetry (CV) and controlled potential electrolysis (CPE) techniques were used to prepare the copper oxide samples. Cu_2O semiconductors prepared by electrodeposition were annealed in air for different temperatures ranging from 50 to 400 °C for 1 h. The thermal treatment was done in a furnace (GSL-1500X) with temperature control. The optical absorbance spectra of electrochemically prepared copper oxide semiconductors were measured by an UV-VIS-NIR spectrophotometer (Shimadzu UV-3600). The X-ray diffraction (XRD) patterns of semiconductors were obtained on an X-ray diffractometer (Rigaku Ultima IV) using monochromatized Cu-Kα radiation (λ=0.15418 nm). The elemental compositions (Cu/O) of the semiconductors were determined by EDX with a JEOL JSM-6510 system. The Fourier transform infrared (FTIR) spectra of copper oxides semiconductors were measured by using a FTIR spectrometer (Perkin Elmer Spectrum 100). The photoelectrochemical measurements were conducted with combined electrochemical workstation (CHI660D) and solar simulator (Class a Solar Light 16S-002) system. The electrodes based on copper oxide were set to face an optical fiber leading from 150W xenon

arc lamp containing an air mass filter (AM1.5). During the PEC measurements, the working electrodes were illuminated with chopped sun light (light/dark cycles of 10 s). 0.1 M Na_2SO_4 solution was used as electrolyte.

III. Results and discussions

The CV technique was used in the first step to prepare copper oxide semiconductors and, the voltammogram was taken in the range from +500 to –500 mV. This technique was utilized for the following purposes; to determine the electrodeposition potential for the preparation of semiconductors, to provide a methodical nucleation. Second step involved the utilization of the CPE technique in the determined potential, electrodeposition was realized throughout 15 minutes. The underpotential deposition region, where surface-limited electrochemical reactions were realized, was preferred as the electrodeposition potential region over the bulk deposition or overpotential deposition region. It was seen here that single-phase Cu_2O can be prepared with high quality in basic medium via the electrodeposition method, that CuO is obtainable when subjecting Cu_2O to heat-treatment. With the company of various characterization techniques, it was seen that the most ideal, optimal Cu_2O can be prepared from basic water solutions whose pH are 9.5. Cu_2O that was prepared with the electrodeposition method for 15 minutes was subjected to various annealing temperatures, and the formed structures and phase change instances were examined. Phase changes were observed to start at 250 °C and continue up to 350 °C. It was determined that CuO began to form at 250 °C, the Cu_2O phase diminished along with the increasing heat, the CuO phase increased, and in the wake of the heat treatment conducted at 350 °C, CuO was the only phase in the structure. This is why the focus was on the 250 °C-350 °C range. Conclusively, by using the electrodeposition based method, single-phase Cu_2O, single-phase CuO and copper oxide phase mixtures were successfully prepared.

The structures and phases, which the copper oxide semiconductors that were prepared with the electrodeposition method contain, were determined with the XRD, and FT-IR methods. Peaks that were obtained from the entire XRD data belong to Cu_2O (cuprite), CuO (tenorite) and ITO (Fig. 1). According to the data, Cu_2O grew dominantly in the (111) plane, which was observed approximately at 36.6 degrees (2θ) with a *d* value of 0.246 nm; and CuO grew dominantly in the (111) plane, which was observed at 38.9 degrees (2θ) with a *d* value of 0.231 nm. This shows that Cu_2O grows dominantly in the (111) plane and CuO decides to follow suit. Only the Cu_2O phase was observed in the structure according to the XRD diffractogram of the material, which was not subjected to any annealing treatment after its preparation using the electrodeposition method. Only the Cu_2O phase was observed in the structure according to the XRD diffractograms of the materials, which were prepared by being subjected to an one-hour long heating treatment that increased in 25 °C intervals from 50 °C to 225 °C annealing temperatures. The Cu_2O and CuO phases were both observed in the XRD data analysis obtained from the annealing treatment conducted at 250 °C. In the diffractograms obtained from the annealing treatments conducted at 275, 300 and 325 °C, it was reported that both Cu_2O and CuO phases were present, however the Cu_2O phase decreased gradually with the increasing annealing temperature, and the CuO phase increased gradually. Only the CuO phase was observed in the structure according to the XRD data of the materials annealed at 350 °C.

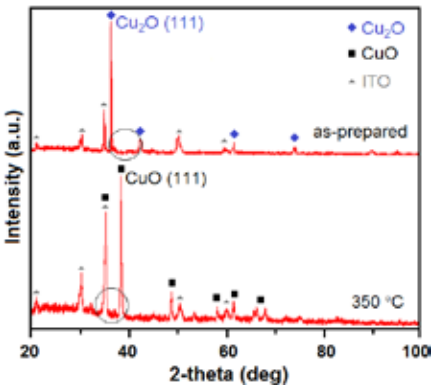


Fig. 1: XRD patterns of the copper oxides before and after heat treatment at different temperatures

Fig. 2 presents the FTIR spectra of the copper oxide semiconductors. All FTIR peaks belong to Cu_2O or CuO phases. Only the Cu_2O phase was observed in the structure according to the FTIR spectrum of the material, which was not subjected to any annealing treatment after its preparation using the electrodeposition method. The FTIR spectrum of non-annealed sample consists of a single peak at 624 cm^{-1} can be assigned to the F_{1u} modes of Cu_2O. This FTIR peak correspond to characteristic stretching vibration of Cu(I)–O bond in the Cu_2O phase. The Cu_2O and CuO phases were both observed in the FTIR spectra obtained from the annealing treatment conducted at 250 °C. In the FTIR spectra obtained from the annealing treatments conducted at 275, 300 and 325 °C, it was reported that both copper oxide phases were present, however the Cu_2O phase decreased gradually with the increasing annealing temperature, and the CuO phase increased gradually. Only the CuO phase was observed in the material

according to the FTIR spectrum of the material annealed at 350 °C. The FTIR spectrum of the sample annealed at 350 °C consists of three peaks at 432, 530 and 606 cm^{-1} can be assigned to the A_u mode, B_u mode, and the other B_u mode of CuO, respectively. These FTIR peaks correspond to characteristic stretching vibrations of Cu(II)–O bond in the CuO phase.

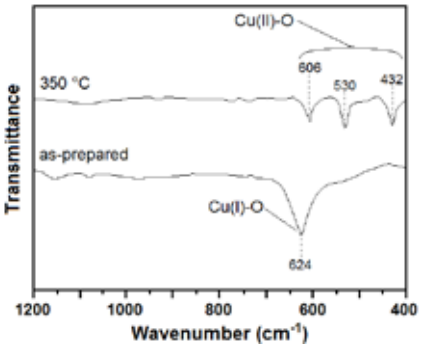


Fig. 2: FT-IR spectra of the copper oxides before and after heat treatment at different temperatures

The stoichiometry (Cu/O) of the samples was determined by EDX method (Tab. 1). The EDX spectra of different regions of the samples gave the same results. The EDX results were confirmed that the Cu_2O diminished along with the increasing temperature, the CuO increased. The quantitative atomic ratios of Cu and O for the samples of non-annealed and annealed at 350 °C are approximately 2:1 (Cu_2O) and 1:1 (CuO) stoichiometry, respectively.

Tab. 1: The EDX results of copper oxide samples.

Sample	Atomic percent		Cu/O
	Cu	O	
Non-annealed	66.44	33.56	1.98 (2:1)
Annealed at 250 °C	64.16	35.84	1.79
Annealed at 275 °C	61.09	38.91	1.57
Annealed at 300 °C	57.63	42.37	1.36
Annealed at 325 °C	53.49	46.51	1.15
Annealed at 350 °C	49.24	50.76	0.97 (1:1)

In the absorption spectrums of the copper oxide semiconductors prepared via the electrodeposition method, a very clear shift from the blue to red was observed due to the increasing annealing temperature (Fig. 3). The absorbance edge value of the sample no annealing treatment was applied upon is approximately 590 nm. This value is rather similar to the values in the literature and is the proof that the prepared material is Cu_2O.

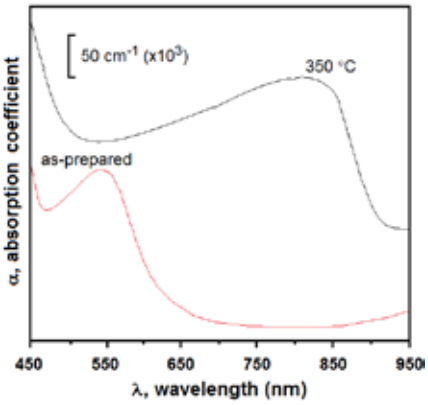


Fig. 3: Absorption spectra of the semiconductors

Absorbance edge values of the samples subjected to heating treatments at 250, 275, 300, 325 and 350 °C are approximately 640, 700, 765, 825 and 880 nm, respectively. 880 nm value had been reached with the 350 °C annealing treatment, this number complies with the literature and shows the prepared phase to be CuO.

The photocurrent–time curves show a cathodic current spike at first occurs before a steep decay to a steady-state photocurrent (Fig. 4). The reasons of sudden decay are attributed to the e^-/h^+ recombination/overproduction, or the presence of pre-adsorbed electrolyte in the semiconductors at momentary time. The photocurrent values are 22, 26, 35, 48, 59 and 72 $\mu A/cm^2$ at zero bias voltage vs Ag/AgCl reference electrode, corresponding to the copper oxides before and after heat treatment at 250, 275, 300, 325, and 350 °C, respectively. As compared with the copper oxides not subjected to any annealing temperatures, the photocurrent shifted to more negative values in the annealed copper oxide semiconductors. Fig. 4 also shows a good stability and reproducibility over 15 cycles of light-on and off states over 300 s. No changes in shape of photocurrent curves occurred during the PEC measurements. PEC studies reveal photocathode characteristic and the p-type nature of copper oxides. The p-type semiconductors act as photocathodes and consequently hydrogen is generated at p-type semiconductor photocathodes ($4H^+ + 4e^- \rightarrow 2H_2$) and oxygen is also generated at the counter electrode ($2H_2O + 4h^+ \rightarrow O_2 + 4H^+$).

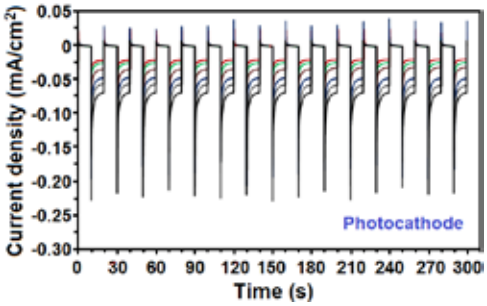


Fig. 4: The photocurrent−time curves of the copper oxides before and after heat treatment at different temperatures

IV. Conclusions

Copper oxides that were prepared with the electrodeposition method was subjected to various annealing temperatures, and the formed structures and phase change instances were examined. Copper oxides with different optical properties were prepared and the wavelength of the materials were altered within a broad scale. PEC performances of the copper oxide electrodes containing a different phase structure were determined, and the changes of PEC activities were examined comparatively. The cathodic photocurrent density increased with increasing annealing temperature.

Acknowledgements

The authors are greatly thankful to Bingöl University Scientific Research Projects Coordination Unit (BÜBAP) for financial supporting and Bingöl University for providing instrument and laboratory facilities.

References

Erdogan I.Y., Gullu O., Optical and structural properties of CuO nanofilm: Its diode application, J. Alloys Compd, 492, 378–383 (2010).

Jiang X.C., Herricks T., Xia Y.N., CuO nanowires can be synthesized by heating copper substrates in air, Nano Lett. 2, 1333-1338 (2002).

Johan M.R., Suan M.S.M., Hawari N.L., Ching H.A., Annealing effects on the properties of copper oxide thin films prepared by chemical deposition, Int. J. Electrochem. Sci. 6, 6094-6104 (2011).

Li J., Wu N., Semiconductor-based photocatalysts and photoelectrochemical cells for solar fuel generation: a review, Catal. Sci. Technol. 5, 1360-1384 (2015).

Mizuno K., Izaki M., Murase K., Shinagawa T., Chigane M., Inaba M., Tasaka A., Awakura Y., Structural and electrical characterizations of electrodeposited p-type semiconductor Cu_2O films, J. Electrochem. Soc. 152, C179-C182 (2005).

Sasano J., Motomura K., Nagai M., Mohamad F.B., Izaki M., Pulse electrodeposition of CuO thin films to improve crystallinity for the enhancement of photoelectrochemical response, Electrochem. 79, 831-837 (2011).

Solmaz R., Doner A., Dogrubas M., Erdogan I.Y., Kardas G., Enhancement of electrochemical activity of Raney-type NiZn coatings by modifying with PtRu binary deposits: application for alkaline water electrolysis, Int. J. Hydrogen Energy 41, 1432-1440 (2016).

Enhanced Photoelectrocatalytic Performance of ZnO/Cu_2O Photoelectrodes

Ako Mahmood Qadir, *Ibrahim Y. Erdogan
Bingöl University, Faculty of Health Sciences, 12000, Bingöl, Turkey

* E-mail: ibrahimyerdogan@gmail.com

Abstract
This work reports on a systematic study of the influence of Cu_2O doping on the structural, optical and photoelectrochemical characteristics of ZnO. ZnO doped with Cu_2O were prepared by a practical electrochemical method. Characterization of the materials was performed by XRD, EDX, UV–Vis spectroscopy and photoelectrochemical (PEC) techniques. The XRD and UV–Vis spectroscopy results showed a single phase of ZnO for the lower Cu_2O deposition time (at time≤3 min), while a secondary phase of Cu_2O evolved for 5 min deposition time. The absorbance spectra, and EDX results confirm the presence of ZnO and Cu_2O. This work showed that ZnO doped with Cu_2O grown for 3 min have the best PEC performance. ZnO/Cu_2O photoelectrodes are suggested as a competitive candidate for advanced PEC detection, may be for the extended field of PEC water splitting.

Keywords: ZnO/Cu_2O photoelectrodes, electrodeposition, photoelectrochemistry

I. Introduction
Sun light-induced photoelectrocatalysis is an effective clean approach for water splitting to generate clean solar fuels (Zou et al. 2001). Oxide-based semiconductors have been utilized as active photocatalysts in photoelectrochemical water splitting to produce hydrogen (Hisatomi et al. 2014). Hydrogen is an important intermediary or secondary form of energy or an energy carrier (Solmaz et al. 2016). The majority of hydrogen is produced from natural gas, oil or coal. This situation cause which on the one hand consumes non-renewable sources, and on the other hand raise serious environmental issues (Grimes at al. 2008). Water splitting is considered the most efficient renewable method of hydrogen production (Montoya et al. 2017). Oxide semiconductor materials are the most important candidate, because of low cost of raw materials and high optical absorption (Erdogan 2010). ZnO is a semiconductor with a direct wide band gap of 3.3 eV and a large exciton binding energy of 60 meV at room temperature (Lakehal et al. 2014). Cu_2O has a direct band gap of 2.1 eV. These band gap values would make them very suitable for PEC applications. In this work, we reported on a systematic study of the influence of Cu_2O doping on the structural, optical and PEC characteristics of ZnO. ZnO/Cu_2O photoelectrodes that have the best PEC performance determined.

II. Experimental Set-up and Procedure
The electrochemical experiments were performed in a three electrode glass cell, with a potentiostat/galvanostat system (CHI 660D). The working electrode was an indium tin oxide (ITO) single-side coated conducting glass. A platinum wire (99.99% pure) was used as a counter electrode. All the potentials were referenced to a saturated calomel electrode (SCE). ZnO electrodeposition was carried out from a 0.02 M $Zn(NO_3)_2.6H_2O$ and 0.2 M KNO_3 solution for 1 hour. Cu_2O electrodeposition on ZnO/ITO substrate was carried out from a 0.02 M $CuSO_4.5H_2O$, 0.2 M Na_2SO_4 and 0.3 M lactic acid ($C_3H_6O_3$) solution for different deposition times (1, 3, 5, 10 and 15 minutes). Cyclic voltammetry (CV) and controlled potential electrolysis (CPE) techniques were used to prepare the ZnO/Cu_2O samples. The absorbance spectra of electrochemically prepared ZnO/Cu_2O were measured by an UV-VIS-NIR spectrophotometer (Shimadzu UV-3600). The X-ray diffraction (XRD) patterns of materials were obtained on an X-ray diffractometer (Rigaku Ultima IV) using monochromatized Cu-Kα radiation. The elemental compositions (Zn/Cu/O) of the materials were determined by EDX with a JEOL JSM-6510 system. The photoelectrochemical measurements were conducted with combined electrochemical workstation (CHI660D) and solar simulator (Class a Solar Light 16S-002) system. The electrodes based on zinc oxide and copper oxide were set to face an optical fiber leading from 150W xenon arc lamp containing an air mass filter (AM1.5). 0.1 M Na_2SO_4 solution was used as electrolyte.

III. Results and discussions
In order to determine a deposition potential of the ZnO from the solution, the cyclic voltammetric measurements of zinc were recorded at the underpotential deposition region in the aqueous medium. The results showed that the bulk zinc deposition does not occur until −700 mV. If the potential of the working electrode is kept constant at a more positive potential than −700 mV, Zn and O are supposed to deposit underpotentially at the electrode surface. These electrodeposited Zn and O react to form the ZnO film on ITO coated glass surface. ZnO film deposited on ITO coated glass surface for 1 h. In order to determine a deposition potential of the Cu_2O from the solution, the cyclic voltammetric measurements of copper were also recorded at the underpotential deposition region. The results showed that the bulk copper deposition does not occur until −200 mV. If the potential of the ZnO coated working electrode is kept constant at a more positive potential than −200 mV, Cu and O are supposed to deposit underpotentially at the electrode surface. The amount of electrodeposited Cu_2O will depend on the deposition time. Thus, electrodeposition of Cu_2O with various amounts on ZnO coated surface could be achieved by this method using different deposition times. Cu_2O electrodoped on ZnO coated surface at different deposition times (1, 3, 5, 10

and 15 minutes).

Fig.1.a shows the XRD patterns of the electrodeposited ZnO films on ITO coated glass. The XRD diffractogram of ZnO electrodeposited for 1 h consists of a strong diffraction peak at 36.5° (2θ scale) arising from (1 0 1) reflections from ZnO. The weaker diffractions at 32.1°, 34.5°, 47.8°, 57.2°, 63.1°, and 68.5° corresponds to (1 0 0), (0 0 2), (1 0 2), (1 1 0), (1 0 3), and (1 1 2) reflections of ZnO. The other peaks belong to ITO coated glass which belongs to working electrode in this study. In XRD diffractograms of ZnO films doped with Cu_2O electrodeposited for 1 and 3 min, all the peaks belong to ZnO and ITO coated glass. No peaks belong to Cu_2O was detected in XRD patterns. The single-phase ZnO was observed for ZnO films doped with Cu_2O electrodeposited for 1 and 3 min. When the deposition time increased to 5 min, the weak peaks appeared at around 36.6°, 42.5°, 61.7° and 73.9°, corresponding to the (1 1 1), (2 0 0), (2 2 0) and (3 1 1) peaks of Cu_2O. It was revealed that a secondary phase of Cu_2O evolved when Cu_2O at more high deposition times than 5 min was doped into ZnO films. As the deposition time increases, the intensity of Cu_2O reflections increases (Fig.1.b).

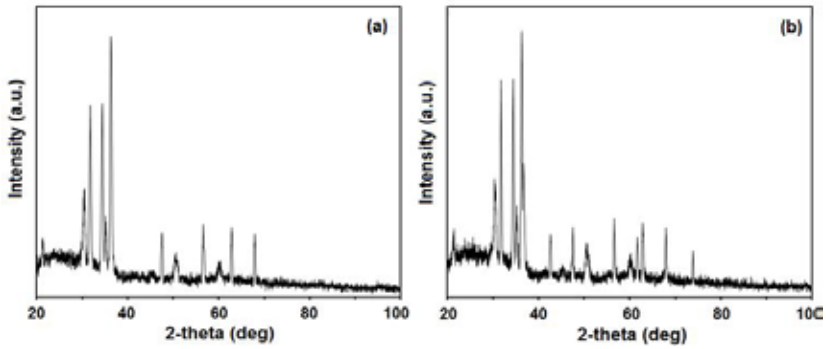


Fig. 1.a: XRD diffractogram of ZnO films electrodeposited onto ITO coated glass surface, b: XRD diffractogram of ZnO films doped with Cu_2O electrodeposited for 15 min

The elemental compositions of the electrodeposited ZnO films and Cu_2O were determined by the EDX. The absence of any other peaks indicates that the ZnO and Cu_2O are homogeneous in composition and formed from Zn-O and Cu-O. EDX analyses of different regions gave the same results. For the ZnO films electrodoped with Cu_2O, the quantitative atomic ratios of Zn/O and Cu/O are close to 1/1 and 1/2 stoichiometry, respectively.

Fig.2.a shows the optical absorption spectra of ZnO films electrodeposited onto ITO coated glass surface in the range of 300–800 nm. Only an absorption in the UV-Vis region can be observed. The absorption edge measured for the films is 365 nm. The fundamental absorption edge at 365 nm corresponds to bulk ZnO.

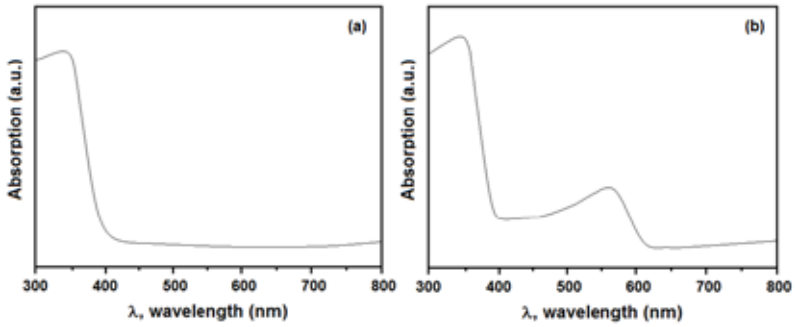


Fig. 2.a: Absorbance spectrum of ZnO films electrodeposited onto ITO coated glass surface, b: Absorbance spectrum of ZnO films doped with Cu_2O electrodeposited for 15 min

In absorbance spectrum of ZnO films doped with Cu_2O electrodeposited for 1, and 3 min, one absorption bands in the UV-Vis region observed. This fundamental absorption edge corresponds to ZnO. In absorbance spectrum of ZnO films doped with Cu_2O electrodeposited for 5 min, two absorption bands in the UV-Vis region observed. The absorption edge measured for the electrodes are 368 and 540 nm. In absorbance spectra of ZnO films doped with Cu_2O electrodeposited for 7, 10, and 12 min, the absorption edges measured for the electrodes are 370/555, 373/570, 375/580 nm respectively. Absorbance spectrum of ZnO films doped with Cu_2O electrodeposited for 15 min is shown in Fig.2.b. In this spectrum, the absorption edge measured for the electrodes are 380 and 590 nm. These fundamental absorption edges correspond to ZnO and Cu_2O.

Fig. 3 shows the effect of Cu_2O growth time on the light and dark currents of semiconductor films. Fig.3.a exhibits linear sweep voltammograms of ZnO films electrodeposited onto ITO coated glass surface in dark and light. This voltammogram show a photoanodic behavior due to the n-type nature of the ZnO semiconductors. Fig.3.b exhibits linear sweep voltammograms of ZnO films doped with Cu_2O for 3 min. The photocurrents increase with longer deposition time. The ZnO films doped with Cu_2O for 3 min exhibit the highest photocurrents between the investigated all semiconductor films. Despite the higher surface area of ZnO films doped with Cu_2O for higher deposition times, they show lower photocurrents than the ZnO films doped with Cu_2O for 3 min. This may be due to the increased bending of ZnO films doped with Cu_2O for higher deposition times, which may reduce the effective area for surface reactions leading to lower photocurrents.

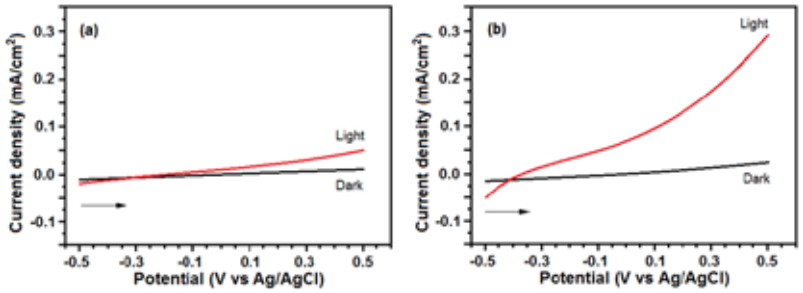


Fig. 3.a: Linear sweep voltammograms of ZnO films electrodeposited onto ITO coated glass surface, b: Linear sweep voltammograms of ZnO films doped with Cu_2O electrodeposited for 3 min in 0.1 M Na_2SO_4

IV. Conclusions

ZnO and ZnO/Cu_2O electrodes were prepared by practical electrochemical method. The influence of Cu_2O on the structural, optical and photoelectrochemical characteristics of ZnO films investigated. Electrodepositions of Cu_2O with various dimensions on ZnO coated surface could be achieved by this method using different deposition times. XRD and UV-Vis spectroscopy results of ZnO films doped with Cu_2O electrodeposited for 1 and 3 min, all the peaks belong to ZnO and ITO coated glass. When the deposition time increased to 5 min, the weak peaks appeared the peaks corresponding to Cu_2O. It was revealed that a secondary phase of Cu_2O evolved when Cu_2O at more high deposition times than 5 min was doped into ZnO films. As the deposition time increases, the intensity of Cu_2O increases. Linear sweep voltammograms show a photoanodic behavior due to the n-type nature of the semiconductors. The ZnO films doped with Cu_2O for 3 min exhibit the highest photocurrents between the investigated all semiconductor films. ZnO films doped with Cu_2O exhibit good switching behavior for different Cu_2O growth times.

Acknowledgements

The authors are greatly thankful to Bingöl University for providing instrument and laboratory facilities.

References

Erdogan İ.Y., The alloying effects on the structural and optical properties of nanocrystalline copper zinc oxide thin films fabricated by spin coating and annealing method, J Alloys Compd 502, 445-450 (2010).

Grimes C.A., Varghese O.K., Ranjan S., Water Light Hydrogen−The Solar Generation of Hydrogen by Water Photoelectrolysis Springer (2008).

Hisatomi T., Kubota J., Domen K., Semiconductor heterojunction photocatalysts: design, construction, and photocatalytic performances, Chem. Soc. Rev., 43, 7520-7535 (2014).

Lakehal S., Achour S., Ferrari C., Buffagni E., Rossi F., Fabbri F., Photoelectrochemical properties of ZnO nanorods decorated with Cu and Cu_2O nanoparticles, Superlattices and Microstructures, 72, 253-261 (2014).

Montoya J.H., Seitz L.C., Chakthranont P., Vojvodic A., Jaramillo T.F., Norskov J.K., Materials for solar fuels and chemicals Nat. Mater., 16, 70-81 (2017).

Solmaz R., Doner A., Dogrubas M., Erdogan I.Y., Kardas G., Enhancement of electrochemical activity of Raney-type NiZn coatings by modifying with PtRu binary deposits: application for alkaline water electrolysis, Int. J. Hydrogen Energy 41, 1432-1440 (2016).

Zou Z.G., Ye J.H., Sayama K., Arakawa H., Direct splitting of water under visible light irradiation with an oxide semiconductor photocatalyst, Nature, 414, 625-627 (2001).

Bio-Hydrogen Production From Waste Rice Husk using Co-Culture

[1]S. Ozmihci, [2]G.G. Taylan
[1,2]Dokuz Eylül University, Environmental Engineering Department

E-mail:serpil.ozmihci@deu.edu.tr, gizem.taylan@ogr.deu.edu.tr

Abstract
Research of clean energy alternatives accelerate after the growing energy demand such as biohydrogen production. Hydrogen gas is a clean fuel and an important energy carrier with a high energy content of 122 kJ g−1. Replacement of fossil fuels with bio-hydrogen gas would overcome air pollution problems and helps to reduce global warming. It's eco-friendly, has high gravimetric energy, waste materials such as rice husk may be used as substrates.

The aim of this study is to investigate the best ratio of co-cultures (Clostridium termitidis, C. intestinale) for batch dark bio-hydrogen fermentation with 5 g/L rice husk. C. termitidis is a celluloytic microorganism that has the ability to hydrolize both cellulose and hemicellulose and C. intestinale was used in the fermentation media to fasten the hydrogen production yield and rate. 6 different co-culture ratios (1:1 ,2:1, 5:1, 10:1, 15:1, 20:1 , C. termitidis :C. intestinale) were tested in submerged dark fermentation at 37°C for 14 days.

The highest CHF (29.15 mL) was detected with a ratio of 5:1 at the end of the fermentation period. The hydrogen production yield and specific hydrogen production rates at the same ratio were 5.83 mL H_2/ gr rice husk and 0.28 mL H_2/ gr biomass.h, respectively.

Keywords: Biohydrogen, submerged fermentation, rice husk.

I. Introduction

Search for clean energy sources to replace fossil fuels has increased over the last fifty years. Hydrogen gas is a clean fuel and an important energy carrier with a high energy content of 122 kJ g^{-1}. Hydrogen can also be used in fuel cells for electricity generation. Costly chemical processes such as steam reforming of natural gas and electrolysis of water are used for hydrogen gas production since it is not readily available in nature. Fermentative hydrogen gas production processes operate under mild conditions and offer considerable advantages over costly chemical processes. The major problems for large scale bio-hydrogen production are low yields and formation rates requiring large fermenter volumes (Kapdan and Kargı, 2006).

Waste biomass, such as agricultural and domestic wastes can be used for bio-hydrogen production as inexpensive and abundant raw materials. Waste grains such as wheat, corn and rice are inexpensive and reliable resources for bio-hydrogen production due to high starch content. Carbohydrate rich renewable resources can be used for bio-hydrogen production by dark and light anaerobic fermentation (Kapdan and Kargı,2006)The first step in bio-hydrogen production is acid or enzymatic hydrolysis of starch/cellulose yielding highly concentrated sugar solution. Anaerobic fermentation of concentrated sugar solution using acetogenic-anaerobic bacteria, such as Clostridia sp., Enterobacter sp. and mixed culture of heat treated anaerobic sludge to volatile fatty acids (VFA), hydrogen and CO_2 isthe nextstep (Manish and Banerjee, 2008) Volatile fatty acids (VFA) produced by dark fermentation can be further fermented by photo-heterotrophic bacteria such as Rhodobacter sp to H_2 and CO_2 by photo-fermentation (Kotay and Das, 2008). Boiled (partially hydrolyzed ground wheat) has been used for bio-hydrogen production by dark and light fermentations (Ozmihci and Kargı, 2010).

Most of the bio-hydrogen production studies by dark fermentation of carbohydrate rich raw materials were realized by batch operation (Yokoi,at al, 1998). Limited number of continuous culture studies was reported for bio-hydrogen production by dark fermentation (Arooj at al, 2008).

II. Experimental Set-up and Procedure

Serum bottles (Isolab-Germany Boro 3.3) with 310 mL total volume were used. Silicone stoppers were used to avoid gas leakage from the bottles. 5 gr of rice husk with different co-culture ratios (1:1 ,2:1, 5:1, 10:1, 15:1, 20:1 , C. termitidis ATCC-21846: C. intestinale ATCC-BAA 1027) were placed in serum bottles. Anaerobic conditions were maintained by passing argon gas from the head space of the bottles for 10 min at the beginning of the experiments. Serum bottles were placed in an incubator at 37˚C.

III. Analysis

Total sugar concentration, mono sugar compositon and total volatile fatty acids analyses were carried out on daily removed samples. The samples were centrifuged at 7500 rpm to remove solids from the liquid media and the analyses were carried out using clear supernatants. Total sugar concentration was determined by using the phenol-acid spectrometric method (Dubois et al, 1956). The mono sugar compositon and total volatile fatty acids analyses were carried out by HPLC (Agilent 1100). Total gas volume was determined by water displacement method using 2% sulfuric acid and 10% NaCl containing solution at room temperature. Hydrogen gas percentage was determined by using a gas chromatograph (Agilent 6890 N-GC). Cumulative hydrogen gas volumes were calculated using the method described in our previous publications (Ozmihci, Kargi, and Cakir, 2011). Medium pH was controlled at 6 by manual addition of 1 M NaOH everyday. Protein concentration was detected by using Modified Lowry protein assay kit (Thermo Scientific).

IV. Results and discussions

In this study effects of microorganism ratio on the rate and yield of bio-hydrogen formation were investigated in submerged fermentation. The highest cumulative hydrogen formation (CHF) was detected as 29.15 mL with the 5:1 ratio of microorganisms (Fig. 1). Additionally the highest yield (5.83 ml H_2 g^{-1} substrate) was obtained at the same production medium. In this medium, initial and final total sugar concentrations were detected as 170 and 147 mg/L, respectively.

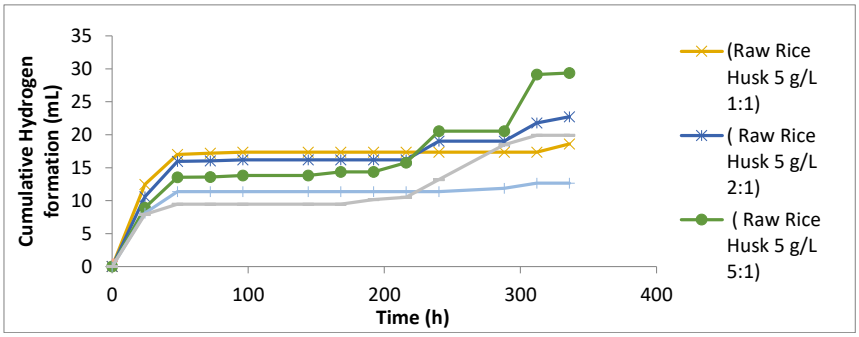


Fig. 1: Cumulative hydrogen formation with different microorganism ratio

The second best production yield (4.54 ml H_2 g^{-1} substrate) was obtained with 1:2 ratio of microorganisms with a CHF of 22.73mL (Fig.1).

Butyric acid was the main volatile fatty acid, glucose and cellobiose were the main sugar components that were produced in the fermentation media.

V. Conclusions

Effects of different organism ratios of C.termitidis and C. intestinale were tested for maximizing hydrogen gas production with waste rice husk. The highest cumulative gas production (29.15 mL) was obtained with C.ter:C.int ratio of 5:1. The highest yield was obtained with the same ratio and was 5.53 mL g^{-1} substrate. A co-culture of C.termitidis and C. intestinale may be a promising process for bio-hydrogen production with lignocellulosic substrates.

Acknowledgements

This research was supported by The Scientific and Technological Research Council of Turkey under grant 115Y301.

References

Arooj M.F., Han S.K., Kim S.H., Kim D.H., Shin S.H., Continuous bio- hydrogen production in a CSTR using starch as a substrate, Int J Hydrogen Energy, 33:3289-94, (2008).

Kapdan I.K., Kargi F., Bio-hydrogen production from waste materials, Enzyme Microb Technol, 38:569-82, (2006).

Kotay S.M., Das D., Biohydrogen as a renewable energy resource - Prospects and potentials, Int J Hydrogen Energy, 33:258-63, (2008).

Manish S., Banerjee R., Comparison of bio-hydrogen production processes, Int J Hydrogen Energy, 33:279-86, (2008).

Ozmihci S., Kargi F., Bio-hydrogen production by photo- fermentation of dark fermentation effluent with intermittent feeding and effluent removal, Int J Hydrogen Energy, 35:667-6680, (2010).

Yokoi H., Tokushige T., Hirose J., Hayashi S., Takasaki Y., H2 production from starch by mixed culture of Clostridium butyricum and Enterobacter aerogenes, Biotechnol Lett, 20: 143-7, (1998).

Effects of Rice Husk Particle Size On Biohydrogen Production under Solid State Fermentation

[1]S. Ozmihci, [2]Z. Velioglu Tosuner

[1] Dokuz Eylül University, Environmental Engineering Department
[2]Dokuz Eylül University, Biotechnology Department

serpil.ozmihci@deu.edu.tr, zulfiyevelioglu@gmail.com

Abstract
The search for eco-friendly, economical, alternative energy sources has begun due to the insufficient fossil fuels to meet the energy demand. As a renewable energy source bio-hydrogen production from lignocellulosic wastes is a novel and promising approach which can produce clean fuel with no CO_2 emissions. Utilization of agro-industrial residues in solid state fermentation (SSF) known as an eco-process with its lower energy requirements, low wastewater production and offering a solution to solid wastes disposal; provides an economical production process of value-added products such as hydrogen. Clostridium sp. (Clostridium termitidis and Clostridium intestinale) which have the ability to produce hydrogen in anaerobic conditions can be subjected to waste lignocellulosic substrates such as rice husk with high carbon content.
In this study three different particle size of rice husk (crude, below 50 mesh, below 200 mesh) was subjected to batch dark fermentation with a *Clostridium termitidis: Clostridium intestinale* ratio of 5:1. *C. termitidis is a cellulolytic microorganism that has the ability to hydrolyze both cellulose and hemicellulose. Therefore, combined fermentation of C. termitidis and C. intestinale is appropriate for the production of hydrogen in fermentation media where various lignocellulosic wastes are used as the substrate.* 5 g rice husk with 75% humidity was used as substrate. The highest CHF (29.26 ml) and the highest yield (5.9 ml H_2 g^{-1} substrate) were obtained with the smallest particle size (below 200 mesh). The second best production yield (3.99 ml H_2 g^{-1} substrate) was obtained with the middle particle size (below 50 mesh) rice husk with a CHF of 19.71 mL.

Keywords: Biohydrogen, solid state fermentation, rice husk.

I. Introduction

The rapid developments in technological and industrial areas in recent years have created a need for more energy and this has accelerated the accumulation of greenhouse gases by causing more fossil fuel consumption. The search for eco-friendly, economical, alternative energy sources has begun due to the insufficient fossil fuels to meet the energy demand (Chandrasekhar, Lee, Lee, 2015). Hydrogen (H_2) gas is one of the most promising, eco-friendly, and renewable energy sources which has a high-energy yield. Additionally, the combustion of H_2 with O_2 produces water as the only by-product (Ghimire et al. 2015).

Among the different methods used for hydrogen production, the production of H_2 from biomass through biological pathways is an emerging technology because it is a sustainable, cost-effective and eco-friendly method (Yasin, Mumtaz, Hassan, 2013). Rice is the second most produced crop in the world wide and rice husk mainly consists of lignin, hemicellulose, and cellulose that make it a suitable lignocellulosic waste substrate for different bioprocesses (Dagnino et al, 2012).

The choice of microorganism strain to be used with lignocellulosic substrate is important. *Clostridium* sp. are obligate anaerobic bacteria including the hydrogen producer strains such as *C.termitidis* and *C.intestinale*. *C. termitidis* is a cellulolytic microorganism that has the ability to hydrolyze both cellulose and hemicellulose (Ramachandran et al, 2008). Therefore, combined fermentation of *C. termitidis* and *C. intestinale* is appropriate for the production of hydrogen in fermentation media where various lignocellulosic wastes are used as the substrate.

Solid state fermentation (SSF) is the fermentation which involves solids in absence or near absence of free water. Substrate must possess enough moisture to support growth and metabolism of microorganism (Pandey, 2003).

SSF is a suitable alternate for productions where agro-industrial wastes are used as substrates (Rahardjo et al, 2006). The desired final product yield and speed in the SSF depends on the organism and substrate used. The main process variables in SSF are water content, culture amount, temperature, pH, particle size and mixing speed(Pandey, 2003).

Particle size is a critical factor in SSF. The density and specific surface area of the substrate are the key parameters. The porosity of the particals has to allow masss transfer. Gas diffusion between particals and homogenizing the fermentation media likewise liquid fermentation may earier the control of processing which is very difficult on SSF (Pandey, 2003).

II. Experimental Set-up and Procedure

Serum bottles (Isolab-Germany Boro 3.3) with 310 mL total volume were used. Silicone stoppers were used to avoid gas leakage from the bottles. 5 gr of rice husk with different particle sizes (crude, below 50 mesh, below 200 mesh) were placed in serum bottles and mineral medium (Medium 1191; pH 7.0) was added as 75% moisture. Anaerobic conditions were maintained by passing argon gas from the head space of the bottles for 10 min at the beginning of the experiments. Serum bottles were placed in an incubator at 37˚C, 30 rpm. *C. termitidis*

ATCC-21846 and *C. intestinale* ATCC-BAA 1027 cultures were inoculated with ratio of 5:1, respectively.

III. Analysis

Total sugar concentration, mono sugar compositon and total volatile fatty acids analyses were carried out on daily removed samples. The samples were centrifuged at 7500 rpm to remove solids from the liquid media and the analyses were carried out using clear supernatants. Total sugar concentration was determined by using the phenol-acid spectrometric method (Dubois et al, 1956). The mono sugar compositon and total volatile fatty acids analyses were carried out by HPLC (Agilent 1100). Total gas volume was determined by water displacement method using 2% sulfuric acid and 10% NaCl containing solution at room temperature. Hydrogen gas percentage was determined by using a gas chromatograph (Agilent 6890 N-GC). Cumulative hydrogen gas volumes were calculated using the method described in our previous publications (Ozmihci, Kargi, and Cakir, 2011). Medium pH was controlled at 6 by manual addition of 1 M NaOH everyday. Protein concentration was detected by using Modified Lowry protein assay kit (Thermo Scientific).

IV. Results and discussions

In this study effects of substrate size on the rate and yield of bio-hydrogen formation were investigated in solid state fermentation. Crude, below 50 mesh, below 200 mesh partical sizes were used. The highest cumulative hydrogen formation (CHF) was detected as 29.26 mL with the smallest particle size (below 200 mesh) (Fig. 1). Additionally the highest yield (5.9 ml H_2 g^{-1} substrate) was obtained at the same production medium. In this medium, initial and final total sugar concentrations were detected as 692 and 1042 mg/L, respectively. This is an indication that the solid substrate in the medium may be degraded by *C. termitidis*.

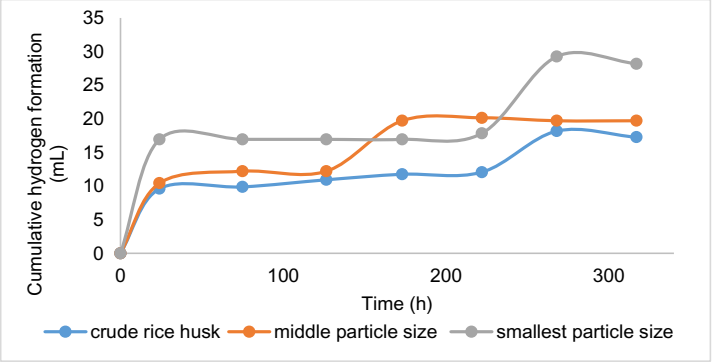


Fig. 1: Cumulative hydrogen formation with different rice husk particle size

The second best production yield (3.99 ml H_2 g^{-1} substrate) was obtained with the middle particle size (below 50 mesh) rice husk with a CHF of 19.71 mL (Fig.1). With crude rice husk 18.17 mL CHF and 3.63 ml H_2 g^{-1} substrate yield was detected. That means the increased surface area of the substrate by reducing the size of the substrate has increased the usability of the microorganism.

Butyric acid was the main volatile fatty acid, glucose and cellobiose were the main sugar components that were produced in the fermentation media.

V. Conclusions

This study is important to investigate the effect of particle size on biohydrogen production using rice husk in solid state fermentation with *C. termitidis* and *C. intestinale*. A co-culture performing with combined fermentation under solid state fermentation showed a promising hydrogen production yield of 5.59 ml g^{-1} substrate. An increase in production yield was detected with decreasing particle size. The highest CHF and yield were obtained with the smallest particle size (below 200 mesh).

Acknowledgements

This research was supported by The Scientific and Technological Research Council of Turkey under grant 115Y301.

References

Chandrasekhar K., Lee K.J., Lee D.W., Biohydrogen production: Strategies to improve process efficiency through microbial routes, International Science of Molecular Science, 16, 8266-8293, (2015).

Dagnino E.P., Chamorro E.R, Romano S.D., Felissia F.E., ve Area M.C., Optimization of the acid pretreatment of rice hulls to obtain fermentable sugars for bioethanol production, Industrial Crops and Products, 363-368. (2012).

Dubois M., Gilles K.A., Hamilton J.K., Rebers P.A., Smith F., Colorimetric method for determination of sugars and related substances, Analitycal Chemistry, 8, 350-66, (1956).

Ghimire A., Frunzo L., Pirozzi F., Trably E., Escudie R., Lens P. N., Esposito G. A review on dark fermentative biohydrogen production from organic biomass: process parameters and use of by-products, Applied Energy, 144, 73-95, (2015).

Ozmihci S., Kargi F., Cakir A, Thermophilic dark fermentation of acid hydrolyzed waste ground wheat for hydrogen gas production. International Journal of Hydrogen Energy, 36, 2111-7, (2011)

Pandey A., Solid-state fermentation. Biochemical Engineering Journal, 13(2-3), 81-84, (2003).

Rahardjo Y.S., Tramper J., Rinzema A., Modeling conversion and transport phenomena in solid-state fermentation: a review and perspectives, Biotechnology Advances, 24(2), 161-179, (2006).

Ramachandran U., Wrana N., Cicek N., Sparling R., Levin D.B., Hydrogen production and end-product synthesis patterns by *Clostridium termitidis* strain CT1112 in batch fermentation cultures with cellobiose or α-cellulose, International Journal of Hydrogen Energy, 33, 7006–7012, (2008).

Yasin N.H.M., Mumtaz T., Hassan M.A., Food waste and food processing waste for biohydrogen production: a review, Journal of Environmental Management, 130, 375-385, (2013).

The Investigation of Three-Dimensional Copper Nanodomes as Anode Materials for Direct Methanol Fuel Cells

Fatih Baştürk[1], Handan Yüksel[1], Ramazan Solmaz[2]

[1]Bingöl University, Faculty of Health Sciences, Occupational Health and Safety Department, 12000, Bingöl, Turkey
[2]Bingöl University, Science and Letters Faculty, Chemistry Department, Bingöl, 12000, Turkey

In this study, three-dimensional (3D) copper nanodomes (CuNDs) were fabricated and characterized as potential anode materials for direct methanol fuel cells. The CuNDs were fabricated by a combined method of soft lithography-nanosphere lithography and physical vapor deposition (PVD) using polydimethylsiloxane (PDMS) as template. The nano structures were characterized using scanning electron microscopy and atomic force microscopy. Their electrochemical activity against methanol electrooxidation was studied in KOH solution with the help of electrochemical measurements. Their electrochatalytic activity was compared to that of bulk and polished Cu. It was found that the well-structured and homogenously distributed CuNDs could be fabricated using these combined methods. The methanol electrooxidation activity of the 3D-NDs in alkaline solution was considerably improved when compared to bulk Cu. The improved activity of the nanostructures was related to good intrinsic activity of Cu for this reaction and their large real surface area.

Acknowledgements: The authors are greatly thankful to Bingöl University Scientific Research Projects Coordination Unit (BÜBAP) (Project Number: BAP-FEF.2016.00.009) for supporting of materials and Bingöl University Central Laboratory for characterization measurements. The authors also would like to thank to Assoc. Prof. Dr. Mehmet Kahraman for his kind helps to prepare PDMS templates.

Keywords: Copper nanodomes, methanol electrooxidation, direct methanol fuel cells

Pt, Pd and Ag Modified NiCuZn Raney Electrodes for Alkaline Water Electrolysis

***Ramazan Solmaz*[1], Ayşe Ongun Yüce[2], Ali Döner[3], Ibrahim Şahin[2], Gülfeza Kardaş[2]**

[1]Bingöl University, Faculty of Health Sciences, Occupational Health and Safety Department, 12000, Bingöl, Turkey
[2]Çukurova University, Science and Letters Faculty, Chemistry Department, 01330 Balcalı, Adana, Turkey
[3]Şırnak University, The Faculty of Engineering, Energy Systems Engineering Department, 73000 Ş ırnak, Turkey

Pt, Pd and Ag modified alkaline leached NiCuZn composite coatings were electrochemically fabricated on a copper electrode. The electrocatalysts were characterized by scanning electron microscopy and energy dispersive X-ray spectroscopy. The hydrogen evolution activity of the modified electrodes was tested in 1 M KOH solution. For this aim, cathodic current-potential curves and electrochemical impedance spectroscopy (EIS) techniques were used. Furthermore, the electrochemical and physical stability of the electrodes as a function of electrolysis time were tested in the same electrolyte using electrochemical and spectroscopic techniques.

The modification of alkaline leached NiCoZn ternary coating by deposition of small amounts of Ag, Pd and Pt can further enhance the hydrogen evolution performance of this Raney-type electrode when compared to NiCoZn individually. It was found that modification of the alkaline leached NiCuZn coatings with the platinum group metals enhances its hydrogen evolution activity greatly. The improved activity was realated to large real surface area, good intrinsic activity of Pt, Pd and Ag as weel as possible synergistic effect between the metal. Their hydrogen evolution activity and stability depend on the type of loaded metal.

Acknowledgements: The authors are greatly thankful to Çukurova University research fund (Project Number: FEF2006D8) and TUBITAK (Project Number: 106T542) for financial support.

Keywords: Pt, Pd, Au- modified NiCuZn electrocatalysts, alkaline water electrolysis, hydrogen energy

Effect of inlet air temperature on exergetic performance of hydrogen production from car tires via plasma gasification

Handan DEMIRCAY[1], Merve MEHAN[1], Muhammed Emin TOPAL[2], Yildiz KALINCI[3], Senol BAYRAKTAR[4], Ugur AKBULUT[4], Haydar KUCUK[4], Hayati OLGUN[5], Adnan MIDILLI[4*], Ibrahim DINCER[6,7]
Project Scholarship[1], Mechanical Engineering Department[1,2,4], Faculty of Engineering, Recep Tayyip Erdogan University, Fener Campus, 53100, Rize, Turkey.
[3]Dokuz Eylul University, Izmir Vocational School, Department of Technical Programs, Education Campus Buca, Izmir, Turkey.
[5]Solar Energy Institute, Ege University, Izmir 35100, Turkey
[6]University of Ontario Institute of Technology, Faculty of Engineering and Applied Science, Mechanical Engineering Department, 2000 Simcoe Street North, Oshawa, Ont., L1H 7K4, Canada
[7]Yildiz Technical University, Faculty of Mechanical Engineering, Besiktas, Istanbul, Turkey

* E-mail: amidilli@gmail.com

Abstract
In this study, exergetic performance of hydrogen production from car tires via air plasma gasification is parametrically investigated. The required data are taken from the literature studies for testing the exergy balance equation developed for the air plasma gasification process. In order to estimate the exergetic efficiency of this process, some important data including the results of ultimate and proximate analyses, air flow rate and specific power input for plasma gasification, yield of steam, etc. are used. In terms of the Second Law of Thermodynamics, the variation of exergetic hydrogen production efficiency as a function of exergetic efficiency is discussed. Furthermore, during the plasma gasification process, the effect of air inlet temperature on hydrogen gas production efficiency is investigated. Consequently, under the selected operating conditions, exergetic hydrogen production efficiency increases linearly with the rise of exergetic efficiency ranging from 0.868 to 0.881 while it increases and decreases parabolically with the rise of the air inlet temperature ranging from 298 K to 1023 K. The minimum and maximum hydrogen production efficiencies are calculated to be 0.199 and 0.202 respectively. It is concluded that, under the selected operating conditions, optimum air inlet temperature for hydrogen production from car tires via plasma gasification is 573 K.

Keywords: Car tires, plasma gasification, hydrogen production, exergetic performance evaluation.

I. Introduction

In the World wide, large number of waste car tyres is produced every year (e.g. about 2.7 billion units of tyres were produced in 2017 and 1 billion units were disposed (Machin et al., 2017). Due to the negative environmental impacts, the waste tryres is no longer permitted to be lanfilled in some countries (US. EPA, 2012; EEA, 2014). Presently, the preferred ways for the disposal of waste tires are basically: the reconstruction of the tyre, recovery of material and recovery of energy (Torretta et al., 2015). The composition (wt%) of the tyre makes up, roughtly from rubber 66.7%; textile cord, 15% and metal cord, 18.3%. Also, its elemental composition consists of C, 60.16%; H, 5.66%; O, 10.74%; N, 0.77%; Fe, 18.3% and others, 4.37% (Lotosh, 2007; Straka et al., 2018). It is similar to the black coal with its the chemical composition and lower heating value (LHV) (approximately 33.9 MJ/kg) (Lerner et al., 2012). The three technologies for waste tyre treatment are preferred in practical applications, which are pyrolysis, combustion and gasification (Kandasamy and Gokalp, 2015). Gasification of tyres is a process in which air, oxygen and/or steam reacts with tyres in an endothermic reaction to produce mainly syngas (CO and H_2) and other by-products are CO_2, light hydrocarbons and char. But the process is a so complex process. As stated by Raman et al. (1981), it includes two key processes which are primary decomposition reactions and secondary recations. The primary reactions include decomposition of tyres into heavy and light hydrocarbons and solid car. The secondary reactions include the craking of the heavy hydrocarbons, the reforming of the light and heavy hydrocarbons and gasification of the solid car material in a conventional gasification system.

Many researchers in the literature focused on the gasification proceses for waste tires. For example, a laboratory scale bubbling fluidized bed gasifier was used to gasify the waste tyre by Karatas et al (2012). The experimetal study examined gasification agents as air and CO_2, air&steam and steam. They reported that the LHV of the product gas was obtained 9.59, 7.34 and 15.21 MJ/Nm^3, respectively. Also, the authors presented effects of some operation paramters on gasification of waste tire using air as gasification agent (Karatas et al., 2013). Portofino et al. (2013) conducted a study of steam gasification of waste tyre in a continuous bench scale reactor. The experimetal study was carried out at 850-1000 °C by keeping the eye on other parameters. They stated that higher temperature results in a higher syngas production (86 wt%).

Recently, plasma gasification has come forward in the waste-to-energy systems due to the fact that the high temperature range of thermal plasma (between 1500 ºC and 5000 ºC) improves LHV of the product gas, also most of the harmful compounds, such as polyaromatic hydrocarbons, volatiles, dioxins and furans are broken into simple molecules, and tar formation are impeded. So, the syngas quality will increase to be used in gas turbines and fuel cells. Despite the advantages, power required for torches is a significant hindrance. Several studies, related to the plasma gasification of tyre have been published in the literature. Indeed, for the plasma gasification of car tire, Rutberg et al. (2012) estimated to be 4.988 MJ/Nm^3 of the LHV of the product gas at 1500 K and 1 atm of operation conditions. Lerner et al. (2012) conducted a study about steam plasma gasification of 1 kg of used car tires. Their

system made up two stages which were plasma gasification and catalytic conversion of the produced gas. They yield 3.0 m^3 (at 298 K) of syngas, consisting of 99.5% of hydrogen + carbon monoxide and having heat energy of 1.1 kW h. At the second stage, the catalytic conversion of the syngas with steam flow rate of 4 mol per mol carbon in the presence of a CaO absorber produced 2.9 m^3 gas containing ~99.5% hydrogen. Another study was presented by Kuznetsov et al. (2012) about equilibrium analysis of hydrogen production using the steam-plasma gasification process of the used car tires. They investigated the syngas compositions according to temperature and plasma flow rate variation. According to their results, it was possible to produce ~4.2 Nm^3 of the syngas consisting of H_2-60.3%, CO-39.0% for 1 kg of the used tires at 1350 K and the steam plasma flow rate of ~1.2 kg/kg of tires. Also, Janajreh et al. (2013) studied a gasification model based on non-stoichiometric chemical equilibrium. The model was used for a broad range of feedstocks. The developed plasma reactor model was based on a non-transferred arc DC plasma torch operating in an insulated reactor chamber and adiabatic environment. The syngas produced from tires consisted of H_2-54.69%, CO-34.42% and others at feedstock flow-1 kg/s; plasma gas flow-0.74 kg/s; steam ratio-1 and torch power-11.71 MW. Also, efficiency of plasma gasification was calculated as 43%.

Although plasma gasification is a promising technology for waste treatment, studies on the plasma gasification of car tires are insufficient. Considering these important expanations, a parametric study on exergetic performance evaluation of hydrogen production from car tires via plasma gasification is undertaken.

II. System Description

For the parametric investigation, the following schematic illustration (Fig. 1) reflecting the developed model indicating the main procedure of hydrogen production from car tires via plasma gasification process. For this purpose, the raw data required is taken from the literature (Rutberg et al., 2012) as listed in Table 1.

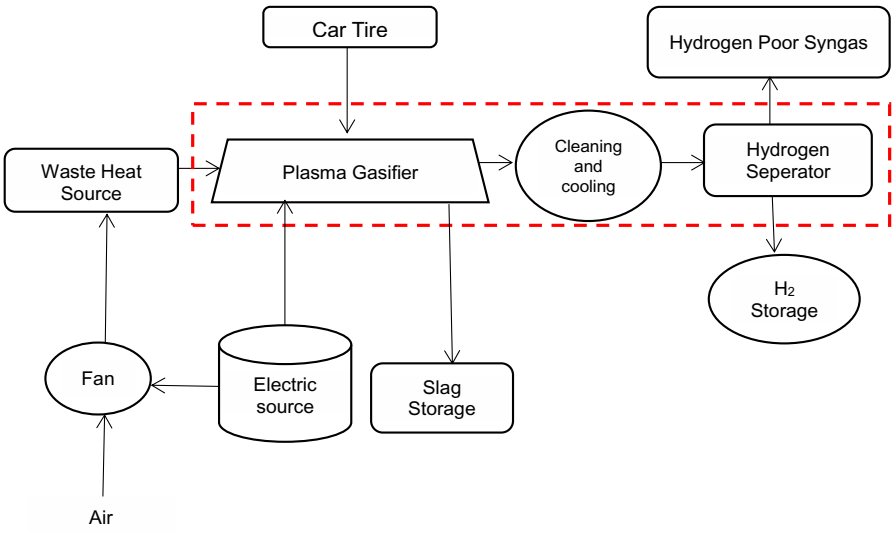


Fig. 1: Schematic illustration of the developed model for hydrogen production from car tyre via air plasma gasification process.

Tab.1: Raw data for plasma gasification of waste tires (Rutberg et al., 2012)

Parameter		Value
Car tire composition (%mass)	C	*86.13*
	H	*6.93*
	N	*0.57*
	S	*1.73*
	O	*3.47*
	Cl	*1.16*
Feedstock moisture		*1.14*
Car tire ash content (%mass)		*13.35*
Car tire LHV (kJ/kg)		*31110*
Air flow rate (kg/kg)		*4.064*
Specific power input (kJ/kg)		*1519*
Specific yield of syngas (Nm^3/kg)		*4.954*
Syngas Composition (% vol.)	*CO*	*30.25*
	H2	*14.54*
	N2	*54.18*
	CO2	*0.01*
Yield of steam (kg/kg)		*0.001*

III. Analysis

The following calculation procedure that is, in terms of the Second Law of Thermodynamics, derived for our project (TUBITAK Code: 117M436) will be tested in this study by using raw data taken from the literature (Rutberg et al., 20012). In the analysis, some common assumptions are made as follows:

- The raw data for the parametric investigation are taken from Rutberg et al. (2012).
- The components and process in system developed for the study are considered to be steady state steady flow.
- The air inlet temperatures ranges from 298 K to 1023 K at 1 atm.
- The operating pressure and temperature are 1 atm and 1500 K.

The exergy balance equation:

$$\sum Ex_{in} = \sum Ex_{out} + \sum Ex_{loss} \quad (1)$$

$$\sum Ex_{in} = Ex_{in}^{ct} + Ex_{in}^{air} + W_{torch} + Ex_{in}^{Q_{wh}} \quad (2)$$

If $\frac{O}{C} \leq 0.667$ then $f_{ct} = 1.0437 + 0.1882\frac{H}{C} + 0.0610\frac{O}{C} + 0.0404\frac{N}{C}$ is used (Kotas, 1995).

In this study, (O/C) is equal to 0.0403.

The exergetic efficiency:

$$\eta_{ex,PG} = \left(1 - \frac{Ex_{loss}}{Ex_{in}}\right) \quad (3)$$

The exergetic hydrogen production efficiency:

$$\eta_{ex,H_2} = \frac{(ex_{H2}^{ph} + ex_{H2}^{ch})}{\sum Ex_{in}} \quad (4)$$

IV. Results and discussions

In this study, exergetic performance of hydrogen production process from car tires via air plasma gasification has been evaluated. Figure 2 evaluates the variation of exergetic hydrogen production efficiency as a function of exergetic efficiency of plasma gasification of car tires. As shown in Fig. 2, exergetic hydrogen production efficiency increases linearly with the rise of exergetic efficiency. The minimum and maximum hydrogen production efficiency is found to be 0.199 and 0.202 at 0.868 and 0.881 respectively.

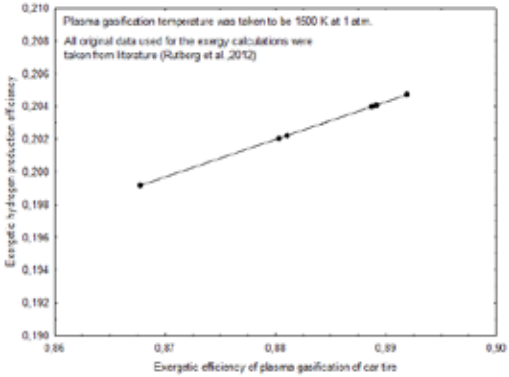


Fig. 2: Variation of exergetic hydrogen production efficiency as a function of exergetic efficiency of gasification of car tires

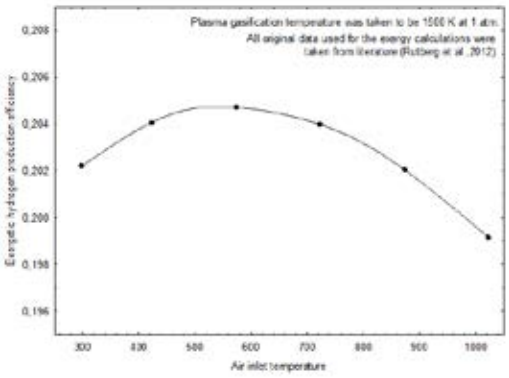


Fig. 3: Variation of exergetic hydrogen production efficiency as a function of air inlet temperature

Figure 3 illustrates the variation of exergetic hydrogen production efficiency as a function of air inlet temperature. In Fig. 3, it is observed that the exergetic hydrogen production efficiency increases and decreases parabolically with the rise of the air inlet temperature. This curve has a maximum at 573K air inlet temperature and the minimum and

maximum exergetic hydrogen production efficiency is calculated to be 0.199 at 1023K and 0.205 at 573 K.

V. Conclusions

In this study, exergetic performance of hydrogen production process from car tires via air plasma gasification has been evaluated. Under the given operating conditions, the following concluding remarks can be drawn:

- The exergetic hydrogen production efficiency increases linearly with the rise of exergetic efficiency. The minimum and maximum hydrogen production efficiency is found to be 0.199 and 0.202 at 0.868 and 0.881 respectively.
- The exergetic hydrogen production efficiency curve has a polynomial character and a maximum at 573K air inlet temperature. The minimum and maximum exergetic hydrogen production efficiency is calculated to be 0.199 at 1023K and 0.205 at 573 K.
- Under the selected operating conditions, optimum air inlet temperature for hydrogen production from car tires via plasma gasification is found to be 573 K.

Acknowledgement

This paper was produced in the scope of the project works. The financial support provided to this project by the Turkish Scientific and Technical Research Council-TUBITAK (Project Code: 117M436) is greatly appreciated.

References

Europeran Commision-Environment. Landfill of Waste, European Commsion; Brussels, Belguim (2014)

Janajreh I., Raza S.S., Valmundsson A.S., Plasma gasification process: modeling, simulation and comparison with conventional air gasification, Energy Conversion and Management 65, 801–809 (2013).

Kandasamy J., Gokalp I., Pryolysis, Combustion and Steam Gasification of various types of crap tires for energy recovery. Energy and Fuels 29, 346-354 (2015).

Karatas H., Olgun H., Akgun F., Experimental results of gasification of waste tire with air&CO_2, air&steam and steam in a bubbling fluidized bed gasifier, Fuel Process Technol 102,166-174 (2012).

Karatas H., Olgun H., Akgun F., Experimental results of gasification of waste tire with air in a bubbling fluidized bed gasifier, Fuel 105, 566–571 (2013).

Kotas, T.J., The Exergy Method of Thermal Plant Analysis. Krieger Publishing Company, Malabar, Florida (1995).

Kuznetsov V.A., Kumkova I.I., Lerner A.S., Popov V.E., Equilibrium analysis of hydrogen production using the steam-plasma gasification process of the used car tires, Journal of Physics: Conference Series. 406, 012023 (2012).

Lerner A.S., Bratsev A.N., Popov V.E., Kuznetsov V.A., Ufimtsev A.A., Shengel' S.V., Subbotin D.I., Production of hydrogen-containing gas using the process of steam-plasma gasification of used tires, Glass Physics and Chemistry 38 (6), 511–516 (2012).

Lotosh V.E., *Pererabotka otkhodov prirodopol'zovaniya* (Processing of Waste of the Nature Management),

Yekaterinburg: Poligrafist, 2007 [in Russian].

Machin E.A, Pedroso D.T, Carvahlo J . Energetic valorization of waste tires, Renewable and Sustainable Energy Reviews 68, 306-315 (2017).

Oboirien B.O., North B.C., A Review of Waste Tyre Gasification, Journal of Environmental Chemical Engineering 5, 5169–5178 (2017).

Portofino S., Donatelli A., Iovane P., Innella C., Civita R., Martino M., Matera D. A., Russo A., Cornacchia G., Galvagno S., Steam gasification of waste tyre: Influence of process temperature on yield and product composition. Waste Management 33, 672–678 (2013).

Raman K.P., Walawender W.P., Fan L.T., Gasification of waste tires in a fluid bed reactor, Conservation&Recycling 4 (2), 79–88 (1981).

Rutberg P.G., Bratsev A.N., Kuznetsov V.A., Kumkova I.I., Popov V.E., Surov A.V., Plasma gasification of organic containing substances as a promising way of development of alternative renewable power engineering, J. Phys. Conf. Ser. 406 (012024), (2012).

Straka P., Kriz V., Bucko Z., Co_Gasification of Rubber with Brown Coal, Acta Geodyn. Geomater, 5 (151, 329-334 2008.

Torretta V., Rada E.C., Ragazzi M., Trulli E., Istrate I.A., Cioca L.I, Treatement and disposal of tyres. Two EU approaches : A review , Waste Management 24, 563-569 (2015).

United States Enviomental Protection Agency (US. EPA). Wastes-Resource- Conservation-Common Waste and Materials-Scrap Tires. US EPA, Washington D.C (2012).

Xiao G., Ni M.J., Chi Y., Cen K.F., Low-temperature gasification of waste tire in a fluidized bed. Energy Convers Manage 49, 2078–2082 (2008).

Design of Thin Film Membranes for Intermediate-Temperature Hydrogen Separation

[1,2*]Fatih Pişkin and [1]Tayfur Öztürk

[1]ENDAM, Center for Energy Materials and Storage Devices, Dept. of Metallurgical and Materials Engineering, Middle East Technical University, Ankara, Turkey
[2]Dept. of Metallurgical and Materials Engineering, Muğla Sıtkı Koçman University, Muğla, Turkey

* E-mail: fatihpiskin@mu.edu.tr

Abstract
Separation membranes allow purification of hydrogen from gas mixtures that could be generated by various production methods such as steam reformation of hydrocarbons, coal gasification or biomass-based fermentation process. Here, each production method sets conditions for separation membranes in terms of operating conditions. Thus, the separation membranes are required to meet different process temperatures varying from ~600 °C to as low temperature as possible. The temperature intervals for hydrogen separation processes might be expressed into three categories such as; low temperature, RT-200 °C, intermediate-temperature, 300-450 °C, and high temperature, ≥450 °C.

The current study concentrates on intermediate-temperature separation membranes, i.e. temperature 300-450 °C which are applicable to steam reformation of natural gas including the water gas shift reaction. Metallic membranes used for this purpose are quite attractive due to their high permeability together with a selectivity that is exceptional among other alternatives. The study adopts a membrane design methodology based on combinatorial material science. This approach makes use of magnetron sputtering whereby a library of thin film membranes are produced in a single experiment each membrane with a different composition. The library is then screened by four-probe resistivity measurements so as to identify compositions that react with hydrogen. A map of reactive index is prepared in the compositional field from which candidates were identified for hydrogen separation. The membranes were then fabricated in the form of foils and tested for hydrogen permeability. Using the above methodology, three ternary alloy system were evaluated, namely Nb-Pd-Ti, Pd-Ag-Ti, and Pd-Ag-Ni.

$Mg_{60}Ni_{40}$ Alloy Synthesis and Investigation of Hydrogen Storage Properties

***Gözde Bayazıt*[1], Sefa Emre Sünbül[1], Sultan Öztürk[2], Kürşat Icin[2], Şadan Özcan[1]**

1Department of Physics Engineering, SNTG Lab., Hacettepe University, Beytepe, Ankara, 06800, Turkey
2Department of Metallurgical and Materials Engineering, Karadeniz Technical University, Trabzon, 61080, Turkey

In this study, rapidly solidified Mg60-Ni40 (wt. %) alloy ribbons were synthesized by melt spinning method. According to this process, inductively melted liquid alloys were ejected on the copper wheel by rotating high speed and gas pressure via a nozzle and was quenched as ribbons. Relatively uniform and continuous ribbons were synthesis nearly 60 µm thickness with this process. The structural and hydrating properties of the ribbons were investigated with scanning electron microscope (SEM), X-ray diffraction (XRD). Its hydrogen storage properties were determined by Sievert type hydrogen storage physical measurement method. XRD patterns of produced and hydrated ribbons were characterized by presence of two different phases of Mg and Mg2Ni and their hydrides. The difference between hydrated and unhydrated ribbons were determined with SEM pictures. When the ribbons were synthesized, they were not active for absorbing the hydrogen. Their activation were done in 350 ^{0}C and 19 bar hydrogen gas atmosphere along 24 hours. Its maximum hydrogen absorption and desorption capacity was found as more than 5 % weight. According to pressure-concentration-temperature (PCT) measurement, two different plateau pressure was found. This results can be attributes to their different phases.

Keywords: Hydrogen storage, melt spinning, rapid solidification, magnesium nickel hydride, Sievert, PCT

International Association for Hydrogen Energy

International Journal of Hydrogen Energy

IHTEC 2018

www.ihtec2018.org

3rd International HYDROGEN TECHNOLOGIES Congress

March 15-18, 2018
Asia Beach Resort Hotel
Alanya, Turkey

ORGANIZATION SECRETARIAT

BROS
Congress, Incentive and Events

Cumhuriyet Mah. Tavukçu Fethi Sok. Köşe Palas Apt. No:28/3
Osmanbey - Şişli - İstanbul / TURKEY
Tel: + 90 212 296 66 70 / **Fax:** + 90 212 296 66 71
alen.demirel@brosgroup.net / www.brosgroup.net

ISBN: 978-605-66381-5-2